

AD-A059 752

STANFORD UNIV CALIF INTEGRATED CIRCUITS LAB  
COMPUTER AIDED ENGINEERING OF SEMICONDUCTOR INTEGRATED CIRCUITS--ETC(U)  
JUL 78 J D MEINDL, K C SARASWAT, R W DUTTON DAAB07-77-C-2684

F/G 9/5

UNCLASSIFIED

DELET-TR-77-2684-2

NL

1 OF 5  
ADA  
059752





LEVEL III

A056914

2

AD A059752

DDC FILE COPY

Research and Development Technical Report

18 DELET/19 TR-77-2684-2

6 COMPUTER AIDED ENGINEERING OF SEMICONDUCTOR INTEGRATED CIRCUITS

16 prepared by

J.D./Meindl,  
K.C./Saraswat,  
R.W./Dutton,  
J.F./Gibbons  
W./Tiller

J.D. Plummer  
B.E. Deal  
T.I. Kamins

INTEGRATED CIRCUITS LABORATORY  
STANFORD UNIVERSITY  
Stanford, CA 94305



12 July 1978

9 Interim Report for Period 1 May 1977 - 31 October 1977

Distribution Statement

Approved for public release;  
distribution unlimited.

Prepared for:

ADVANCED RESEARCH PROJECTS AGENCY  
1400 Wilson Boulevard  
Arlington, VA 22209

15 US Army Electronics Technology & Devices Laboratory

ERADCOM

US ARMY ELECTRONICS RESEARCH AND DEVELOPMENT COMMAND  
FORT MONMOUTH, NEW JERSEY 07703

409 117 78 10 10 094

JLB

The findings in this report are not to be construed as an official Department of the Army position unless so designated by other authorized documents.

Citation of manufacturers' or trade names does not constitute an official endorsement or approval of the use thereof.

Destroy this report when it is no longer needed. Do not return it to the originator.

UNCLASSIFIED

SECURITY CLASSIFICATION OF THIS PAGE (When Data Entered)

REPORT DOCUMENTATION PAGE		READ INSTRUCTIONS BEFORE COMPLETING FORM	
1. REPORT NUMBER <b>DELET-TR-77-2684-2</b>	2. GOVT ACCESSION NO	3. RECIPIENT'S CATALOG NUMBER	
4. TITLE (and Subtitle) Computer-Aided Engineering of Semiconductor Integrated Circuits		5. TYPE OF REPORT & PERIOD COVERED Interim Report for the Period 1 May 1977 - 31 October 1977	
7. AUTHOR(S) J.D. Meindl, K.C. Saraswat, R.W. Dutton, J.F. Gibbons, W. Tiller, J.D. Plummer, B.E. Deal and T.I. Kamins		6. PERFORMING ORG. REPORT NUMBER	
9. PERFORMING ORGANIZATION NAME AND ADDRESS Integrated Circuits Laboratory Stanford University Stanford, California 94305		8. CONTRACT OR GRANT NUMBER(S) DAAB07-77-C-2684	
11. CONTROLLING OFFICE NAME AND ADDRESS Advanced Research Projects Agency (ARPA) 1400 Wilson Blvd. Arlington, Virginia 22209		10. PROGRAM ELEMENT, PROJECT, TASK AREA & WORK UNIT NUMBERS 6.1 1T1 61101 A 00A 00 690000.211.13.27.00	
14. MONITORING AGENCY NAME & ADDRESS (if diff. from Controlling Office) ERADCOM ATTN: DELET-IS Fort Monmouth, NJ 07703		12. REPORT DATE July 1978	13. NO. OF PAGES 436
16. DISTRIBUTION STATEMENT (of this report)  Approved for public release: distribution unlimited.		15. SECURITY CLASS. (of this report)  UNCLASSIFIED	
17. DISTRIBUTION STATEMENT (of the abstract entered in Block 20, if different from report)		15a. DECLASSIFICATION/DOWNGRADING SCHEDULE	
18. SUPPLEMENTARY NOTES This research was sponsored by the Defense Advanced Research Projects Agency (DARPA) pursuant to ARPA Order No. 2985, dated 18 February 1975, Program Code W15P87.			
19. KEY WORDS (Continue on reverse side if necessary and identify by block number) MODELING SEMICONDUCTOR DEVICES SEMICONDUCTOR PROCESSING PROCESS MODELING SEMICONDUCTORS			
20. ABSTRACT (Continue on reverse side if necessary and identify by block number) Economical procurement of small quantities of high performance custom integrated circuits for military systems is severely impeded by inadequate process, device and circuit models that handicap accurate computer-aided design at low cost. The salient objective of this program is to formulate physical models of fabrication processes, devices and circuits to allow total computer-aided design of custom large-scale integrated circuit subsystems to reduce development cycle time and cost. The basic areas under investigation are: (1) ion implantation and diffusion of dopants; (2) thermal oxidation; (3) chemical vapor deposition of silicon epitaxy.			

DD FORM 1 JAN 73 **1473**  
EDITION OF 1 NOV 65 IS OBSOLETE

UNCLASSIFIED  
SECURITY CLASSIFICATION OF THIS PAGE (When Data Entered)

78 10 10 094

UNCLASSIFIED

SECURITY CLASSIFICATION OF THIS PAGE (When Data Entered)

19. KEY WORDS (Continued)

20. ABSTRACT (Continued)

and (4) device simulation and statistical circuit modeling. This report discusses the results of the second year of the program.

DD FORM 1473 (BACK)  
1 JAN 73

EDITION OF 1 NOV 65 IS OBSOLETE

UNCLASSIFIED

SECURITY CLASSIFICATION OF THIS PAGE (When Data Entered)

# CONTENTS

	<u>Page</u>
INTRODUCTION - - - - -	1
1. ION IMPLANTATION - - - - -	5
1.1 A Theoretical Approach to the Calculation of Annealed Impurity Profiles of Ion Implanted Boron into Silicon - -	287
2. THERMAL OXIDATION - - - - -	9
Introduction - - - - -	9
Summary of Principal Accomplishments to Date - - - - -	11
Detailed Discussion of Results - - - - -	15
3. CHEMICAL VAPOR DEPOSITION OF SILICON - - - - -	72
Introduction - - - - -	72
Epitaxy - - - - -	74
Transient and Steady-State Study of the Dopant System - - -	74
Physicochemical Model of the Dopant System - - - - -	81
Low-Pressure Chemical-Vapor-Deposition of Silicon: Structure and Stability - - - - -	105
4. DEVICE SIMULATION AND STATISTICAL CIRCUIT MODELING - - - - -	134
Introduction and Project Goals - - - - -	134
One-Dimensional Semiconductor Device Analysis (SEDAN) - - - -	143
Finite Elements for Semiconductor Device Simulation - - - -	177
Measurement Tools for Extracting Two-Dimensional Profiles - -	198
Latch-Up in CMOS Integrated Circuits - - - - -	218
A Charge-Oriented Model for MOS and Transistor Capacitances -	240
Statistical Circuit Analysis - An Example - - - - -	257
APPENDIX A - Partial List of Distributed Copies of SUPREM - - - -	281
APPENDIX B - Publications Resulting from Work Done - - - - -	283
APPENDIX C - (see 1.1, above) - - - - -	287

ACCESSION for	
NTIS	<input checked="" type="checkbox"/> File Section
DDC	<input type="checkbox"/> Bull. Section
UNANNOUNCED	
JUSTIFICATION	
BY DISTRIBUTION/AVAILABILITY CODES	
Dist.	Special
A	

## COMPUTER-AIDED ENGINEERING OF SEMICONDUCTOR INTEGRATED CIRCUITS

### Introduction

In military, industrial, commercial, and consumer applications, frequently there is a great necessity for "customizing" the design of an integrated circuit to fulfill the critical needs of a specific system or class of systems. A major barrier which prevents the economic production of small quantities of high performance custom integrated circuits is the cost of design. The source of this difficulty lies in empirical, and costly, engineering techniques used currently both in integrated circuit design, and production. Optimal system design requires accurate computer models for silicon fabrication processes, elemental device structures, monolithic circuit configurations and system architectures. Current capability to predict changes in system performance resulting from silicon fabrication process modifications is impeded by deficiencies in process, device, circuit and system models.

The overall objectives of this program are:

- (1) Develop process engineering models which predict key technological design parameters and facilitate process control.
- (2) Develop methods to utilize geometrical process information to specify simple device models for high performance devices including all two-dimensional effects.
- (3) Develop circuit analysis capabilities which reflect statistical model effects including parameter correlation so that correct parameter specifications for optimized yield are possible.
- (4) Disseminate the results to the industry.

This report describes the progress which has been made during the past 12 months of this program.

Apart from photolithography which may be viewed as a fixed process that simply provides flexibility in chip layout, the primary fabrication processes which determine the electrical characteristics of silicon electronics are ion implantation, diffusion, thermal oxidation and chemical vapor deposition of silicon. In Part 1 a multistream diffusion model has been described, which apart from simple thermal diffusion of dopants, can also predict diffusive annealing behavior of ion implanted dopants and proton enhanced diffusion. The case of boron has been investigated by taking into account boron ions, positively charged vacancies and neutral boron vacancy pairs and their generation - recombination kinetics to predict the resulting impurity profile of boron implanted in the dose range of  $10^{16}$  to  $10^{16}$  ions/cm<sup>2</sup> and annealed at temperatures of 800°C, 900°C, and 1000°C. Transmission electron microscopy studies were conducted to relate the diffusion mechanism of boron to the negatively charged vacancies and boron vacancy complexes. Using these studies the phenomenon of precipitation of boron at higher dose implants was investigated. The generalized diffusion model can predict electrically active, inactive and precipitated boron as a function of time and temperature of diffusion.

Part 2 describes the results of the work on thermal oxidation of silicon. In an effort to understand physically the observed O<sub>2</sub>/HCl kinetics, oxidations in O<sub>2</sub>/H<sub>2</sub>O, O<sub>2</sub>/Cl<sub>2</sub> and H<sub>2</sub>O/Cl<sub>2</sub> mixtures have been investigated and a physical model has been developed. The kinetics of H<sub>2</sub>O and H<sub>2</sub>O/HCl mixtures using a pyrogenic system have been studied. Complete experimental characterization of the thermal oxidation of heavily phosphorus doped silicon has been

completed and relationships of the linear and parabolic rate constants have been derived. A physical model based entirely upon the electrical effects has been developed relating higher equilibrium vacancy concentrations at high doping levels to the observed enhanced oxidation rate in heavily phosphorus doped silicon. Initial results of the work on correlating the two principal oxide charges,  $Q_{ss}$  and  $N_{st}$ , with process conditions are also presented.

Part 3 deals with chemical vapor deposition of silicon. Dopant incorporation process in the epitaxial growth of silicon and properties of thin Si films deposited by low-pressure, chemical vapor deposition (LPCVD) have been studied. The transient and steady-state response of the dopant system of a horizontal, atmospheric-pressure, epitaxial reactor have been studied at different growth rates to learn the effect of the growth rate on the parameters entering into the transfer function of the reactor. A physicochemical model for the dopant incorporation into the Si epitaxial films has been developed. In the model developed, the different mechanisms entering into the doping process and their relative importance is analyzed. The results from the transient and steady-state study are used to confirm the model. The structure of Si films obtained by the LPCVD process in the 600°C temperature range and the effect of annealing them in the temperature range of 800°C to 1200°C has been investigated by x-ray diffraction and transmission electron microscopy.

Part 4 discussed the results of device simulation and statistical circuit modeling. The material discussed in this chapter has two key objectives. First, fabrication process information is used directly as input for device simulation so that technology variables are correctly reflected in device characteristics. While the present examples of this process/device

simulation coupling focus primarily on one-dimension, progress on the two-dimensional analysis programs is encouraging. Second, equivalent circuit and statistical analysis capabilities are being developed with emphasis on predicting geometry and process dependent effects. The impact of this work on both reliability and circuit yield will be discussed.

The procurement of small quantities of high performance custom integrated circuits for military systems is presently impeded by inadequate process device and circuit models which would facilitate accurate computer aided design and which would consequently provide rapid availability of LSIC subsystems at reasonable cost. Nevertheless, the demand for LSIC subsystems for military equipment is expected to increase during the nineteen-eighties. This program is relevant to military needs since it will result in computer aided engineering capabilities that will increase design efficiency, facilitate fabrication, and improve the availability of custom LSIC's, thereby leading to reduced DOD electronics procurement costs.

Part 1  
ION IMPLANTATION

J.F. Gibbons, A. Chu, K.C. Saraswat

Research on ion implantation performed during the past year under the ARPA-supported Process Modelling program at Stanford has been directed toward the development of a mathematical model that is capable of predicting the annealing behavior of boron-implanted silicon over a wide range of experimental conditions.

The principal result of the research is a new model which can be used to calculate the complete annealing behavior of boron-implanted silicon for any dose level up to  $10^{16}$  B/cm<sup>2</sup> and any annealing temperature in the range  $800^{\circ}\text{C} \leq T \leq 1000^{\circ}\text{C}$ . A full and careful development of this model and its application to a number of problems of practical interest are the subject of the attached doctoral thesis of A. Chu entitled "A Theoretical Approach to the Calculation of Annealed Impurity Profiles of Ion Implanted Boron Into Silicon".\* This thesis represents what we believe to be the most comprehensive treatment of the problem available at the present time and is currently being incorporated into the SUPREM process modelling program. In what follows we give a brief description of its principal contents.

The general problem to which the work is addressed is as follows. Boron implanted into room temperature silicon under specific conditions of dose and energy will produce a spatial distribution of boron that can be calculated from the theory of Lindhard, Scharff and Schiott [1]; and a spatial distri-

---

\*Appendix C.

bution of damage in the crystal that can be calculated from the theory of Brice [2]. To realize the electrical properties of the implanted dopant, the crystal must be annealed to repair the damage and place the implanted boron atoms on substitutional sites. In general this annealing step requires raising the implanted material to a relatively high temperature (800-1000°C), and the implanted boron will then diffuse into a new distribution. The problem is to calculate, for given implantation and annealing conditions, (a) the time required to completely anneal the implantation damage and (b) the spatial distribution of the substitutional boron at that time. A critical feature of the annealing process is that, until the damage is annealed, the boron will diffuse at extraordinary rates because the defect concentration in the implanted crystal is above its equilibrium value for the given annealing temperature.

A multistream diffusion model has been developed to describe the annealing process, in which the boron is visualized as being in one of several possible atomic sites or complexes within the silicon crystal. In the simplest cases boron exists as either a simple substitutional acceptor or it is complexed with a positively charged vacancy to form a fast-diffusing, electrically-inactive species. For doses  $\Phi \leq 10^{15} \text{ B/cm}^2$  and annealing temperatures in excess of 900°C, the annealing behavior can be well-approximated by a set of three coupled diffusion equations in which interactions between substitutional boron ( $B_s$ ), lattice vacancies ( $V$ ) and boron-vacancy pairs ( $B-V$ ) are modelled in terms of departures of the corresponding concentrations from their thermal equilibrium values. The relevant equations are

$$\text{B-V pair:} \quad \frac{\partial C_{BV}}{\partial \tau} = D_{BV} \frac{\partial^2 C_{BV}}{\partial x^2} - \frac{C_{BV} - k_0 C_B C_V}{\tau_0}$$

$$\text{Lattice Vacancy:} \quad \frac{\partial C_V}{\partial \tau} = D_V \frac{\partial^2 C_V}{\partial x^2} + \frac{C_{BV} - k_0 C_B C_V}{\tau_0} + \frac{C_V - C_{Veq}}{\tau_V}$$

$$\text{Substitutional Boron:} \quad \frac{\partial C_B}{\partial \tau} = D_B \frac{\partial^2 C_B}{\partial x^2} + \frac{C_{BV} - k_0 C_B C_V}{\tau_0}$$

The last term in each equation describes the coupling between species referred to above. The diffusion coefficients  $D_i$  and the relaxation time  $\tau_0$  are found in the literature or obtained from thermodynamics.

The general annealing problem for  $\phi \leq 10^{15}/\text{cm}^2$  and  $T_{\text{anneal}} \geq 900^\circ\text{C}$  is then solved by starting with a set of initial conditions for B, V and (B-V) that are determined by the implantation and then calculating the time-space evolution of each species from the given equations. As a conservative but practical set of initial conditions, it was found that for all cases studied,

- (1) all of the implanted boron can be assumed to be in (B-V) pairs, and
- (2) the vacancy concentration can be assumed to relax quickly to its equilibrium value.

The diffusion and dissociation of (B-V) pairs then provides the mechanism that causes the system to ultimately reach thermal equilibrium. Substrate doping effects are included by using a Fermi level argument to establish the concentration of positively-charged vacancies in terms of the concentration of

of neutral vacancies.

This relatively simple model fails to predict the annealing behavior of boron-implanted silicon when (a) the dose exceeds  $10^{16}/\text{cm}^2$  and/or (b) the annealing temperature is reduced to  $800^\circ\text{C}$ . In the first of these cases, boron precipitates will form during the early phases of the anneal and may subsequently dissolve if the annealing is carried out for a sufficiently long time. These precipitates form whenever the concentration of boron exceeds the solid solubility of boron in silicon at the annealing temperature.

This effect can be included quantitatively by adding terms to each of the equations above that describe the formation and dissolution of the precipitate.

At low annealing temperatures a similar effect occurs in which defect loops and dislocation dipoles are formed during the early stages of the annealing and diffusing boron is subsequently adsorbed on these defect loops. This effect is included in the model in a manner similar to that used for precipitated boron. In both cases the boron will dissolve from the precipitation or adsorption site if the anneal is carried out for a sufficient period of time.

The addition of precipitation and adsorption effects to the basic model lead to a comprehensive annealing model that is capable of predicting the amount and distribution of any form of boron (substitutional, complexed, adsorbed or precipitated) at any time during the annealing sequence. Taken together with the theories that predict the initial range and damage distributions, this comprehensive annealing model provides a complete process model for boron-implanted silicon.

## Part 2

### THERMAL OXIDATION

J.D. Plummer, B.E. Deal, W.A. Tiller,  
C.P. Ho and R.R. Razouk

#### 2.1 INTRODUCTION

Thermally grown silicon dioxide ( $\text{SiO}_2$ ) is one of the key components of modern integrated circuit structures. The oxide acts as a mask against dopant diffusion, passivates the active device regions and junctions, insulates "field" regions and, as the gate dielectric, is an actual component in MOS devices. Thus, the control and predictability of oxide growth and the resulting electrical properties are critical if reproducible device performance is to be achieved.

The overall goals of the thermal oxidation portion of this program may be stated as follows.

1. To achieve accurate analytic prediction of oxide thickness under all process conditions encountered in modern technologies. These include the effects of high substrate doping levels, arbitrary silicon substrate orientation, the presence of a chlorine species during the oxidation, and the use of multiple species (such as  $\text{O}_2/\text{H}_2\text{O}$  mixtures) during oxidation.
2. To achieve accurate analytic prediction of oxide charge densities, also under all process conditions important to modern devices. These conditions include arbitrary silicon substrate orientation, ambient conditions

---

\* This work represents a joint effort by the Stanford University Integrated Circuits Laboratory, Fairchild Camera and Instrument Corporation Research and Development Laboratory and the Stanford University Department of Materials Science.

during oxidation and high and low temperature anneals.

3. To achieve accurate analytic prediction of segregation and redistribution effects at the Si-SiO<sub>2</sub> interface. This includes accurate prediction of dopant profiles in both the SiO<sub>2</sub> and Si.
4. A further important goal is the determination of an atomic level, electrically accurate model of the Si-SiO<sub>2</sub> interface. Such a model is believed to be essential for achieving physical understanding of oxidation kinetics, the origin of oxide charges and segregation and redistribution.

Realization of these goals will allow accurate prediction of oxide and surface properties for an arbitrary device structure. This in turn will minimize costly iterative, empirical techniques in the development and characterization of new and improved technologies.

An illustration of the importance of these goals is shown in Fig. 2-1. The device shown here is an oxide isolated NMOS transistor, similar in configuration to many devices currently in production. The numbers indicated on the figure refer to practical, current problems in oxidation kinetics and SiO<sub>2</sub> charge densities which are addressed by the above goals. Referring to the figure:

- 1,5 : Over the N<sup>+</sup> source and drain diffusions, enhanced oxidation rates due to high dopant concentrations are important as are impurity redistribution and segregation effects.
- 2,3 : In the thin gate oxide, the kinetics of multiple species oxidations (O<sub>2</sub>/H<sub>2</sub>O for example) and the use of a Cl species may be important.

- 4 : The three-dimensional nature of the device is illustrated in the oxide isolation region where the effective surface crystal orientation changes with position and affects the oxidation kinetics and charge densities.
- 5 : Redistribution and segregation are also extremely important under the thick field oxide where a lightly doped P type layer is often ion implanted to prevent surface inversion.
- 6 : Fixed oxide charges ( $Q_{ss}$ ) and interface state charges ( $N_{st}$ ) located near the Si-SiO<sub>2</sub> interface affect device threshold voltage, carrier mobilities, junction leakage currents and breakdown voltage and numerous other important device properties. These cannot at present be predicted analytically.

Similar arguments could be made with respect to other technologies and other devices currently being manufactured. The major point to be made here is that the goals presented above for this program are addressed to important practical problems. Understanding on a more basic physical level of oxidation kinetics, charges and redistribution will permit optimization of present device structures and will minimize the amount of empiricism needed to develop new structures.

## 2.2 SUMMARY OF PRINCIPAL ACCOMPLISHMENTS TO DATE

The thermal oxidation work to be described here is the result of an extensive interdisciplinary effort and is the result of three main groups - the Stanford University Integrated Circuits Laboratory, Fairchild Camera and Instrument's Research and Development Laboratory and the Department of Materials Science at Stanford.

At the beginning of this program, understanding of silicon oxidation kinetics was based largely upon the general oxidation relationship developed in 1965 by Deal and Grove [2.1], and given by

$$\frac{x_o^2}{B} + \frac{x_o}{B/A} = t + \tau \quad (2.1)$$

where  $x_o$  = oxide thickness,  $t$  = oxidation time, and  $A$ ,  $B$  and  $\tau$  are constants which are functions of oxidation conditions. The parabolic rate constant  $B$  dominates the overall reaction at high temperatures and for thick oxides and includes such factors as solubility of the oxidant in the oxide, oxidant diffusion rate in the  $\text{SiO}_2$  and the partial pressure of the oxidant. The linear rate constant  $B/A$  dominates the reaction for low temperatures and short times and includes oxidant solubility, partial pressure and the reaction at the  $\text{Si-SiO}_2$  interface. Such surface variables as silicon orientation and dopant concentration can affect this surface oxidation reaction and hence  $B/A$ .

The use of this first order kinetic relationship allows prediction of oxide thickness given that  $B$  and  $B/A$  may be expressed as functions of orientation, doping level, ambient conditions and temperature. Since  $B$  and  $B/A$  are based on a model in which oxidant diffusion through an existing oxide layer, and  $\text{Si-SiO}_2$  interface reaction kinetics respectively determine the overall oxidation rate, some understanding of the underlying physical mechanisms involved may also be obtained from this model.

An even more basic physical understanding of the mechanisms involved in thermal oxidation will be needed, we feel, to fully understand oxidation kinetics and in particular to analytically predict oxide charge densities.

What is really needed here, and what we are now pursuing is a more microscopic model of the oxidation process.

Many of the important oxidation kinetic processes and most of the charges associated with  $\text{SiO}_2$  are determined by the 5-40 $\text{\AA}$  transition region between Si and  $\text{SiO}_2$ . A clear understanding on an atomic level of this region appears to be necessary for a physical understanding of the kinetic and charge density experimental data obtained here and elsewhere.

Toward these ends, a large portion of the initial effort in this program was aimed at gathering sufficient kinetic data to make modeling of the physical processes involved possible. More recently, with this kinetic data as a basis, considerable effort has been devoted to developing underlying physical models to explain the data. The following list summarizes our efforts in both these areas.

1. Complete characterization of  $\langle 111 \rangle$  and  $\langle 100 \rangle$  orientation kinetics for dry  $\text{O}_2$  and wet  $\text{O}_2$  between 700 and 1200°C has been completed. These results were described in last year's annual report [2.2].
2. Complete experimental characterization of  $\text{O}_2/\text{HCl}$  oxidation kinetics for 0-10% HCl and  $T = 900\text{-}1100^\circ\text{C}$  has been completed. These results were described in last year's annual report [2.2] and are the subject of journal publication [2.3].
3. In an effort to understand physically the observed  $\text{O}_2/\text{HCl}$  kinetics, oxidations in  $\text{O}_2/\text{H}_2\text{O}$ ,  $\text{O}_2/\text{Cl}_2$  and  $\text{H}_2\text{O}/\text{Cl}_2$  mixtures have been investigated. The results will be described in detail later in this report, and are the subject of a forthcoming journal article [2.4].

4. The kinetics of  $H_2O$  and  $H_2O/HCl$  mixtures using a pyrogenic system have been studied and the results are described later in this report.
5. Complete experimental characterization of heavily doped phosphorus substrate oxidation kinetics for  $N_D = 10^{15}$  to solid solubility,  $T = 800-1100^\circ C$  in dry  $O_2$  has been completed. Empirical relationships for both the linear and parabolic rate constants as  $f$  (phosphorus chemical concentration) have been derived. These results are described later in this report and are the subject of a journal article to be published [2.5].
6. A physical model based entirely upon electrical effects (higher equilibrium vacancy concentrations at high doping levels), has been derived to explain the observed enhanced oxidation rate in heavily phosphorus doped substrates. This model explains our experimental data extremely well and allows prediction of oxidation kinetics for B, As, Sb and other impurity doped substrates. It will be described in detail later in this report.
7. Within the last several months, work on correlating the two principal oxide charges,  $Q_{ss}$  and  $N_{st}$ , with process conditions has begun. Initial results will be presented later in this report.
8. Installation and programming of a flexible, computer controlled C-V measurement system for characterization of oxide charge densities has been completed.
9. Implementation of computer prediction of first order oxidation kinetics has been realized.

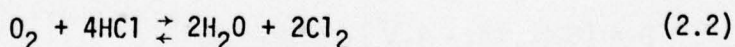
The remainder of this report summarizes the principal results of the past year's effort. The reader is referred to last year's annual report for a discussion of previous results achieved in this program.

## 2.3 DETAILED DISCUSSION OF RESULTS

### A. Chlorine Oxidation Kinetics and Mechanisms

During this past year, experiments were carried out to gain a better insight into the mechanism of the HCl/O<sub>2</sub> oxidation process. It was found in the previous work [2.2] that as the HCl concentration in O<sub>2</sub> increased from 0 to 10 percent for a given temperature or silicon orientation, the oxidation rate increased. This increase was reflected by a continuous increase in the parabolic rate constant B, but the linear rate constant B/A leveled off with increasing HCl after 1-2 percent. The effects on the activation energies were complex and unclear.

An expression involving the gas phase reaction of O<sub>2</sub> with HCl, previously reported [2.6], was used as basis for the current studies:



Therefore, the oxidation of silicon in O<sub>2</sub> with added amounts of H<sub>2</sub>O, Cl<sub>2</sub>, or H<sub>2</sub>O + Cl<sub>2</sub>, equivalent to 0-10% HCl, was investigated. Log-log plots of oxide thickness vs. oxidation time for H<sub>2</sub>O and Cl<sub>2</sub> additions at 1000°C are shown in Figs. 2-2 and 2-3. In Figs. 2-4 and 2-5, plots of parabolic and linear rate constants as a function of H<sub>2</sub>O concentrations are presented. Rate data at other temperatures were also obtained for both HCl and Cl<sub>2</sub>

additions. Overall results for the  $\text{H}_2\text{O}/\text{O}_2$  mixtures were pretty much as expected, although some departures from predicted theory were observed at lower  $\text{H}_2\text{O}$  concentrations. The  $\text{Cl}_2/\text{O}_2$  rate constant data were somewhat erratic; no rate constant data are presented here.

An attempt was made to establish a "combination" general oxidation relationship, that is, one that assumes parallel but independent oxidation by two separate species. These two species might be  $\text{O}_2$ , which is the major component in all the mixtures in question, and either  $\text{H}_2\text{O}$  or  $\text{Cl}_2$  from Eq. 2.2 above, or  $\text{H}_2\text{O}$  or  $\text{Cl}_2$  from the special  $\text{Cl}_2/\text{O}_2$  and  $\text{H}_2\text{O}/\text{O}_2$  mixtures investigated. Such an expression could help to establish the  $\text{HCl}/\text{O}_2$  oxidation mechanism. The relationship developed was similar to that reported earlier [2.7]. It is:

$$t = \frac{1}{E} \left\{ x_0^2 - x_i^2 + C(x_0 - x_i) - D \ln \left[ \frac{2EX_0 + F}{2EX_i + F} \right] \right\} \quad (2.3)$$

where  $C = (A_1B_1 + A_2B_2)/(B_1 + B_2)$ ,

$$D = [B_1B_2 (A_1 - A_2)^2] / [2(B_1 + B_2)^2],$$

$$E = B_1 + B_2,$$

$$F = A_1B_2 + A_2B_1,$$

and  $A_1$  and  $B_1$  are the constants in Eq. 2.1 for one oxidation species and  $A_2$  and  $B_2$  the constants for the second species.  $B_1$  and  $B_2$  are proportional to the partial pressure of components 1 and 2 in the oxidation ambient.

The other terms have the same meaning as in Eq. 2.1.

Log-log plots of oxide thickness vs. oxidation time were prepared for experimental and calculated 5%  $\text{H}_2\text{O}/\text{O}_2$  mixtures and for experimental 10%  $\text{HCl}/\text{O}_2$  mixtures (10%  $\text{HCl}$  should produce 5%  $\text{H}_2\text{O}$  according to Eq. 2.2). These plots plus dry  $\text{O}_2$  data are shown in Fig. 2-6 for 900°C, 1000°C, and 1100°C. It can be noted that the 10%  $\text{HCl}/\text{O}_2$  plot approaches those for 5%  $\text{H}_2\text{O}/\text{O}_2$  (calculated and experimental) at 1100°C.

These and other results led to the following general conclusions.

1. The relationship  $\text{O}_2 + 4\text{HCl} \rightleftharpoons 2\text{H}_2\text{O} + 2\text{Cl}_2$  does appear to be valid for silicon oxidation in  $\text{HCl}/\text{O}_2$  mixtures.
2. The equilibrium of the above relationship is established very rapidly, since identical results were obtained starting with equivalent amounts of either  $\text{HCl} (+\text{O}_2)$  or  $\text{H}_2\text{O} + \text{Cl}_2$ .
3. The reaction of  $\text{O}_2 + \text{HCl}$  goes to completion at 1200°C or above. Gas phase thermodynamics apparently does not predict this, but in the silicon oxidation system the  $\text{SiO}_2$  may provide a catalytic effect which reverses the thermodynamic predictions.
4. At high temperatures (1200°C), the oxidation rate in  $\text{HCl}/\text{O}_2$  mixtures is determined by the oxygen and water concentrations. Therefore the rate increase (compared to  $\text{O}_2$  oxidation above), is maximum in accordance with the combination relationship.
5. At lower temperatures (900°C), the rate increase due to  $\text{HCl}$  additions to  $\text{O}_2$  is less. Apparently  $\text{Cl}_2$  tends to retard the reaction at the  $\text{Si-SiO}_2$  interface and at low temperatures the oxidation is dependent

in large part on this interface reaction.

6. The oxidation is not affected to any extent by HCl itself, only by the reaction products  $H_2O$  and  $Cl_2$ .
7. Chlorine diffuses towards the Si-SiO<sub>2</sub> interface during the oxidation process. While it may be negatively charged during the high temperature oxidation, it exhibits no charge at room temperature.

Details of the above investigation will be reported in a forthcoming publication [2.4].

#### B. H<sub>2</sub>O and HCl/H<sub>2</sub>O Pyrogenic Steam Oxidation Kinetics

The kinetics of steam oxidation of silicon over the temperature range 900° to 1100°C was investigated using a pyrogenic system. This system involves the direct reaction of H<sub>2</sub> and O<sub>2</sub> in the oxidation furnace to form H<sub>2</sub>O. It was found that such a system does not permit 100 percent (760 Torr) water to be produced. Therefore, a ratio of H<sub>2</sub> to O<sub>2</sub> was selected which provides a vapor pressure of water equal to that obtained in a previous investigation where O<sub>2</sub> was bubbled through 95°C H<sub>2</sub>O [2.1]. This H<sub>2</sub>O pressure is 640 Torr.

A log-log plot of oxide thickness versus oxidation time is presented in Fig. 2-7 for <111> and <100> oriented n-type silicon ( $C_B = 10^{15} \text{ cm}^{-3}$ ). Data from [2.1] obtained at 1200°C for wet O<sub>2</sub> are also included in the figure, with little difference between <111> and <100> silicon being observed at this temperature. Data were also obtained in the pyrogenic system at 950° and 1050°C but are not included in Fig. 2-7 because of space limitations.

Rate constants,  $B$  and  $B/A$ , were obtained and are plotted versus  $1/T$  in Figs. 2-8 and 2-9. Activation energies are indicated and agree reasonably well with previous results. In the case of the linear rate constant,  $B/A$ , a constant ratio of 1.68 is obtained between the pre-exponential constants of  $\langle 111 \rangle$  to  $\langle 100 \rangle$  oriented silicon. On the other hand, the  $B/A$  activation energies of the two orientations (2.05 eV) are equal.

Included in Figs. 2-8 and 2-9 are corresponding data for dry  $O_2$  oxidations. The one important observation is that previously the  $\langle 100 \rangle$  Si  $B/A$  activation energy data for dry  $O_2$  did not permit a straight line to be drawn through the scattered points. If the constant  $\langle 111 \rangle / \langle 100 \rangle$  ratio of 1.68 from steam oxidation is assumed, then a plot can be forced through the dry  $O_2$   $\langle 100 \rangle$  data points. This has been done in Fig. 2-9 and a reasonable fit for the data results.

Oxidations in  $H_2O$  with additions of 5 volume percent  $HCl$  were carried out over the temperature range  $900^\circ$  to  $1100^\circ C$ . Not only did the oxidation rate not increase, it actually decreased. This decrease was found to be approximately 5 percent, the same amount as the  $HCl$  added. It was therefore concluded that the addition of  $HCl$  to an  $H_2O$  oxidation ambient only serves to dilute the oxidizing species. On the other hand, the presence of the  $HCl$  provides a cleaning action, and the oxides produced exhibit much less contamination effects.

C. Thermal Oxidation of Heavily Phosphorus Doped Silicon - Experimental Results and Empirical Models

A brief review of general oxidation theory indicates qualitatively what may be expected in the case of heavily doped substrates or diffused regions. The macroscopic model of Deal and Grove [2.1] for silicon oxidation by water or dry oxygen involves the diffusion of the oxidizing species from the ambient through an existing oxide to react with silicon at the Si/SiO<sub>2</sub> interface. Analysis based upon requiring continuity of steady-state flux of the oxidant through the ambient/oxide/interface structure yields the familiar linear-parabolic growth relationship

$$\frac{x_o^2}{B} + \frac{x_o}{B/A} = t + \tau \quad (2.4)$$

where the terms have the same meaning as in Eq. 2.1.

For thick oxides and oxidation times long relative to a characteristic time  $A^2/4B$ , the first term on the left hand side of Eq. 2.4 dominates, resulting in parabolic, diffusion limited growth. Under these conditions, B is the dominant rate constant and is given by

$$B = 2D_{\text{eff}} C^* / N_1 \quad (2.5)$$

where  $D_{\text{eff}}$  = effective diffusion coefficient of the oxidant in the oxide,  $C^*$  = equilibrium concentration of the oxidant in the oxide, and  $N_1$  = number of oxidant molecules incorporated per unit volume of oxide grown. B exhibits an Arrhenius temperature dependence with activation energies of 1.2 eV for dry O<sub>2</sub> and 0.71 eV for H<sub>2</sub>O, apparently reflecting the activation energies for the diffusivity of O<sub>2</sub> and H<sub>2</sub>O, respectively, in SiO<sub>2</sub> [2.1].

For thin oxides and oxidation times short relative to  $A^2/4B$ , the second term on the left hand side of Eq. 2.4 dominates, resulting in linear interface reaction limited growth.  $B/A$  is the governing rate constant under these conditions and is given by

$$\frac{B}{A} = \frac{kh}{k+h} \frac{C^*}{N_1} \approx k \frac{C^*}{N_1} \quad (2.6)$$

where  $h$  = gas phase transport coefficient for the oxidizing species from the ambient to the outer oxide surface and  $k$  = Si/SiO<sub>2</sub> interface reaction rate constant. An activation of energy of 2 eV is observed for  $B/A$  for both dry O<sub>2</sub> and H<sub>2</sub>O ambients, apparently determined by the energy required to break a Si-Si bond [2.1, 2.8].

In an idealized interpretation, then, factors likely to influence the interface reaction rate should alter  $B/A$ , while those affecting oxidant diffusion will change  $B$ . Sufficiently high impurity levels in the substrate should be expected to modify the interface reaction. Similarly, high impurity content in the oxide may affect diffusivity of the oxidizing species. The relative magnitudes of such effects should depend on the particular impurity involved and its behavior during oxidation.

Specifically, phosphorus, as with the other commonly used donor impurities arsenic and antimony, diffuses more slowly in the oxide than in the silicon and tends to segregate at the interface in favor of greater phosphorus levels on the silicon side. As a result, a pile-up of phosphorus at the interface to levels greater than bulk concentrations in the silicon may occur during oxidation, with relatively much lower levels in the oxide. In addition, the pile-up should be more substantial for H<sub>2</sub>O than for dry O<sub>2</sub>

oxidation due to even slower diffusion relative to oxide growth rates [2.9].

Therefore, oxidation regimes dominated by the linear rate constant should exhibit greater dependence on heavy phosphorus doping level than should regimes dominated by the parabolic rate constant. Shorter oxidations which are interface reaction rate limited should show greater variation with heavy phosphorus doping than should longer oxidations which are diffusion limited. The influence of heavy phosphorus doping via large B/A variations should also diminish or saturate with increasing oxidation temperature, since diffusion-limited oxidation dominates at shorter oxidation times with increasing temperature.

Overall, then, this qualitative model indicates that greater influence of heavy doping levels of phosphorus (and also arsenic and antimony) should be seen at shorter oxidation times and lower oxidation temperatures, and that these effects should be greater for  $H_2O$  than for dry oxygen oxidations. The validity of this simple model for the enhanced oxidation rates observed over  $N^+$  regions will now be considered quantitatively.

An extensive series of oxidations were done in a dry  $O_2$  ambient at temperatures of 800, 900, 1000, and 1100°C. The data produced are shown in Figs. 2-10 and 2-11 as oxide thickness vs. oxidation time curves for each of five heavily doped sample types and the lightly doped control. At each temperature, the bottom curve represents the lightly doped control and agrees well with published data for  $\langle 111 \rangle$  substrates, while the additional curves represent the heavily doped samples, in order of increasing substrate doping. Specific doping levels are indicated in Table I. Both SIMS and AES techniques

were used to measure chemical phosphorus concentration  $C_{BC}$ ; spreading resistance and anodic oxidation techniques were used to measure the electrically active concentrations  $C_{BE}$ .

The data in Figs. 2-10 and 2-11 already lends qualitative support to the predictions based on the simple interpretations of doping effects presented earlier. Clearly the greatest relative variations of oxide thickness occur at the shorter times and lower temperatures, the regions in which the interface reaction and hence  $B/A$  are expected to dominate, indicating that the increasing substrate phosphorus level has a very strong effect on the interface reaction. At the longer times and higher temperatures, in the diffusion-limited regime, substantially less variation of thickness with doping is seen, implying that oxidant diffusion and the parabolic rate constant are influenced to a much smaller extent by the increasing substrate phosphorus levels. Indeed, a few selected oxidations at  $1200^{\circ}\text{C}$ , when the characteristic time  $A^2/4B$  for lightly doped substrate oxidations is only about 0.5 minutes and therefore oxidation is effectively entirely  $B$  dominated, produced essentially no variation of oxide thickness with increasing phosphorus doping that could be resolved within the limits of interferometer accuracy.

The variation of the effective  $B/A$  and  $B$  values with increasing initial substrate total chemical phosphorus concentration, representatively illustrated in Fig. 2-12 for  $900^{\circ}\text{C}$  dry  $\text{O}_2$  oxidation, exhibits dramatically the expected behavior.  $B/A$ , reflecting interface reaction-limited oxidation, increases sharply by more than an order of magnitude as the phosphorus level

risers toward solid solubility. On the other hand,  $B$ , which represents the diffusion-limited regime, is affected only slightly by the increasing substrate phosphorus doping. Clearly, the predictions of the simplified interpretations presented have been convincingly confirmed. We now consider the effects on  $B/A$  and  $B$  in detail.

i) Linear Rate Constant

The temperature dependence of  $B/A$  is shown in Fig. 2-13, where  $\log (B/A)$  is plotted against  $1/T$  with substrate doping level as a parameter. The lowest points are the values found for the lightly doped control samples, while the higher points correspond, respectively, to the increasingly heavily phosphorus doped substrate types used. To a reasonable approximation, Arrhenius temperature dependence may be assumed for the effective  $B/A$  values corresponding to each substrate doping level, leading to the least-squares fitted lines and apparent activation energies of the figure.

High impurity levels may produce the large increases of effective  $B/A$  by altering the activation energy and/or the pre-exponential factor. Apparently the basic limiting activation energy of approximately 2 eV associated with the interface reaction is not substantially altered by the high phosphorus levels, while significant dependence on dopant concentration may be found in the pre-exponential factor. A physical explanation for this relatively constant activation energy will be given later in this report.

Some indication of the nature of this dependence may be gained via examination of the variation of  $B/A$  with concentration at a given temperature, as was done in Fig. 2-12 for 900°C. The sharp increase of the linear rate constant suggests an exponential dependence on  $C_{B_0}$ , the initial chemical substrate phosphorus concentration, a possibility that is tested further by

investigating the variation of  $\log (B/A)$  with  $C_{BC}$  in Fig. 2-14. Evidently  $\log (B/A)$  eventually exhibits roughly a linear dependence on  $C_{BC}$ , and hence  $B/A$  an exponential dependence on  $C_{BC}$ , at each given temperature, but only after a stronger initial increase. There may be a slight temperature dependence in the magnitude of this initial increase, but to a large extent the substrate background phosphorus concentration dependence is very similar at all temperatures.

Clearly, many closed-form relationships for this  $C_{BC}$  dependence may be used to approximate this data to varying degrees of complexity, in the absence of an accurate physical model for that dependence. A fairly simple form, producing a reasonable first order approximation, might be

$$\frac{(B/A)}{C_0 e^{-E_1/kT}} \equiv (B/A)' = 1 + k_1 C_{BC}^{n_1} e^{k_2 C_{BC}} \quad (2.7)$$

where  $C_0 e^{-E_1/kT}$  is the published temperature dependence of the linear rate constant for lightly doped substrates with  $E_1 \approx 2$  eV [2.1]. Thus, the exponential eventually dominates, but the power law dependence produces the stronger initial increase. Optimal  $k_1$  and  $k_2$  values may be found by rewriting Eq. 2.7 in the alternative form

$$\log \left[ \frac{(B/A)' - 1}{C_{BC}^{n_1}} \right] = \log k_1 + k_2 C_{BC} \quad (2.8)$$

Plotting  $\log \left[ \frac{(B/A)' - 1}{C_{BC}^{n_1}} \right]$  vs.  $C_{BC}$  should therefore produce a linear dependence with intercept  $\log k_1$  and slope  $k_2$ , for an appropriate value of  $n_1$ . Such analysis indicates that a value of  $n_1 \approx 0.5 - 1.0$  should be used, with  $n_1 \approx 0.5$  giving particularly consistent linear dependences. Thus, the curves plotted together with the experimental B/A values in Fig. 2-14 have been calculated using  $n_1 = 0.5$  and the resulting appropriate  $k_1$  and  $k_2$  values. Agreement appears very reasonable. The fitted  $k_1$  and  $k_2$  values are presented vs.  $1/T$  in Fig. 2-15, confirming that the temperature dependence is relatively slight when compared with the overall dependence of B/A. In fact, appropriate constant values of  $k_1$  and  $k_2$  independent of  $T$  conceivably could be used for all temperatures. While agreement not surprisingly is not as good, using values of  $k_1 = 5.9 \times 10^{-11} \text{ cm}^{3/2}$  and  $k_2 = 3.0 \times 10^{-21} \text{ cm}^3$  gives reasonable agreement with the experimental results over the entire temperature range investigated. Use of eq. 2.7 with these values for  $k_1$ ,  $k_2$  and  $n$ , allows calculation of effective linear rate constants for arbitrary substrate phosphorus doping levels.

## ii) Parabolic Rate Constant

B has been found to be a much weaker function of high phosphorus concentrations. Nevertheless, it does appear to increase somewhat with concentration, as seen in Fig. 2-16, where  $\log B$  is plotted vs.  $1/T$  with substrate doping as a parameter. At each temperature, the lowest point represents the lightly doped control while the higher points correspond to the heavily doped samples. It is apparent that, unlike the case for B/A, the concentration dependence of B varies significantly with temperature. Dopant level has a greater effect at lower temperatures and virtually no effect at

1100°C. Also, for a given doping level, the net temperature dependence is not readily reconcilable with a single activation energy Arrhenius relation, implying changes in activation energy and a temperature-dependent pre-exponential factor, or addition of a new, phosphorus-related term with different activation energy. Fig. 2-17, presenting  $\log B$  vs.  $C_{BC}$  with temperature as parameter, emphasizes this additional temperature dependence. Further, the dopant concentration effects at a given temperature become evident. As substrate doping level increases (and consequently the lower phosphorus level in the oxide also rises),  $B$  first increases rapidly and then begins to "saturate," increasing only very slowly, if at all.

As with  $B/A$ , a convenient closed-form approximation of the  $B$  variations may be made. For convenience, no new explicit  $T$  dependence is included, but the fitted "constants" should then reflect any dependence thus hidden. The initial rapid rise and subsequent sluggishness suggest a possible power law dependence on dopant levels. Initial substrate phosphorus level is used as the variable for this analysis, though actual levels in the oxide should be more directly relevant, as discussed in [2.5].

$$\frac{B}{B_0 e^{-E_2/kT}} \equiv B' = 1 + k_3 C_{BC}^{n_2} \quad (2.9)$$

where  $B_0 e^{-E_2/kT}$  is the published temperature dependence of the parabolic rate constant for lightly doped substrates with  $E_2 \approx 1.2$  eV for dry  $O_2$  [2.1].

Appropriate  $k_3$  and  $n_2$  values may be extracted in a manner analogous to Eq. 2.8. This approach was used with the extracted B values for 800, 900, and 1000°C, with surprisingly good linear relations found. The calculated curves in Fig. 2-17 illustrate the very reasonable fit to the extracted B values produced by the above relation with the  $k_3$  and  $n_2$  values shown vs.  $1/T$  in Fig. 2-18. The expected additional T dependence is clearly evident in  $k_3$  and possibly, to a lesser extent, in  $n_2$ . A new additional activation energy is strongly suggested, and this will be explored. Until a model related to basic physical phenomena is derived to explain these effects on B, eq. 2.9 can be used to calculate effective parabolic rate constants for substrates with arbitrary phosphorus doping levels.

#### D. Physical Modeling of the Thermal Oxidation of Heavily Doped Silicon

A considerable body of kinetic data was presented in the previous section for the thermal oxidation of heavily phosphorus doped, <111> oriented silicon in dry oxygen. The observed enhancement of oxidation rate for the heavily doped substrates, when reduced to the effective rate constants B and B/A of the Deal and Grove macroscopic oxidation model, was shown to be manifested primarily in a substantial increase of the linear rate constant B/A, implying significant change of the Si-SiO<sub>2</sub> interface reaction rate, though apparently with only slight effect on the associated effective activation energy of ~ 2 eV. This section will describe a model based upon fundamental physical parameters which we believe can be used to explain these observations.

Consideration of the possible physical mechanisms by which these increases of B/A may be produced has included qualitatively chemical, electrical, and even mechanical effects of the doping. The relative importance of these postulated effects would be more evident if the precise nature of the interfacial oxidation reaction were known.

In this regard, Dobson [2.10, 2.11] has suggested that, since oxidation occurs by the flow of oxygen through the oxide to the Si-SiO<sub>2</sub> interface, the interface reaction may proceed by an oxygen atom's filling a silicon lattice vacancy at the interface to annihilate a silicon vacancy and/or the oxygen atom's occupying a silicon site to create a silicon interstitial. Thus, an overall flow of material (silicon atoms) away from the interface into the substrate may occur by either a vacancy flux to the interface from the substrate and/or an interstitial flux into the substrate from the interface to incorporate the growing oxide. In fact, consideration of the atomic structure of the Si-SiO<sub>2</sub> interface clearly demonstrates that this effective movement of Si atoms away from the interface must occur to "make room" for the oxygen atoms.

Expansion upon these possibilities leads to the several possible Si vacancy and interstitial mechanisms indicated in Fig. 2-19 that may be involved in the interfacial oxidation reaction. For example, interstitials may be generated in the interface reaction, to flow into the bulk Si, as Dobson speculates; alternatively, some of these interstitials may move outward into the oxide, perhaps to meet and react with the incoming oxygen species. In addition, Si vacancies, whether generated at the interface and/or flowing to the interface from the bulk Si, may provide reaction sites for the oxygen species at the interface.

Should any or all of these Si defect-related possibilities exist, then indeed the statistics of point defects in the crystalline silicon substrate, and their dependence upon such substrate parameters as doping level, become relevant to the oxidation process. The relative contributions and possible dominance of the various defect mechanisms should vary with these substrate parameters.

In this regard, while apparently relatively little quantitative data on interstitials has been gathered, considerable work on vacancy statistics may be found in the literature. For example, vacancies are found to exist in neutral ( $V^X$ ) and charge states ( $V^+$ ,  $V^-$ ,  $V^{=}$ ). In thermal equilibrium, the neutral vacancy concentration  $C_{V^X}$  is a function of temperature only, while the charged vacancy concentrations are dependent on  $C_{V^X}$ , the Fermi level  $E_F$ , the ionized vacancy energy levels ( $E_{V^+}$ ,  $E_{V^-}$ ,  $E_{V^{=}}$ ) in the bandgap, and temperature [2.12]. At sufficiently high doping levels,  $E_F$  will vary from the intrinsic level  $E_i$  even at oxidation temperatures; the charged vacancy concentrations, and therefore the total equilibrium vacancy concentration, will vary from their intrinsic concentrations (i.e., concentrations at lower doping levels for which  $E_F = E_i$ ) [2.13].

If vacancies do contribute to the interface oxidation reaction then, a significant effect of heavy substrate doping level on the interface reaction rate may very well be an electrical one - the shifting of the Fermi level to alter the vacancy concentrations.

A first-order calculation may now be done to test the validity of this interpretation. The interface oxidation reaction rate, as reflected in the linear rate constant  $B/A$ , may be the result of multiple "additive" mechanisms, one of which is postulated to be a vacancy mechanism. Thus,  $B/A = R_1 + R_2$ , where

$R_1$  = all other contributions; e.g., a Si interstitial contribution

$R_2 = KC_{V_T} = \text{Si vacancy contribution}$

and  $C_{V_T}$  is the total vacancy concentration.

(For simplicity, the charge states of the vacancies have been neglected and only  $C_{V_T}$  considered. In fact, the dominant charge state and concentrations will depend on Fermi level position and therefore on the nature of dopant, n- or p-type. This dependence would demand consideration should charge state prove to be a determining factor in the vacancy contribution. Thermal equilibrium is assumed, and the contribution(s) in  $R_1$  are assumed relatively unaffected by heavy doping electrical effects.

For substrates of low doping levels less than the intrinsic carrier concentration  $n_i(T)$ , where  $E_F = E_i$  and  $C_{V_T} = C_{V_T}^i$ ,

$$(B/A)^i = R_1 + KC_{V_T}^i = C_1 e^{-2.0/kT} \quad (2.10)$$

For substrates of heavy doping levels such that  $n \neq n_i(T)$ , where  $E_F \neq E_i$  and  $C_{V_T} \neq C_{V_T}^i$ ,

$$(B/A) = R_1 + KC_{V_T}. \quad (2.11)$$

Rewriting and suitable manipulation produces

$$(B/A) = (B/A)^i \left[ 1 + \left( \frac{K}{C_1} \right) C_{V_T}^i e^{+2.0/kT} \left( \frac{C_{V_T}}{C_{V_T}^i} - 1 \right) \right] \quad (2.12)$$

$$\log \left[ \underbrace{(B/A)/(B/A)^i}_{(B/A)^i} - 1 \right] = \log \left[ \underbrace{\left( \frac{K}{C_1} \right) C_{V_T}^i}_{K'} e^{+2.0/kT} \right] + \log \left[ \underbrace{\frac{C_{V_T}}{C_{V_T}^i}}_{\frac{C_{V_T}}{C_{V_T}^i}} - 1 \right] \quad (2.13)$$

So, if in fact a direct correlation exists between the effective  $(B/A)$  and silicon vacancies, then  $\log [(B/A)' - 1]$  should be linearly related to  $\log [C_{V_T}' - 1]$  with slope = 1, as both vary with electrically active heavy doping levels, with constant (relative to doping) offset  $\log [K' C_{V_T}^i e^{+2.0/kT}]$ .

$(B/A)'$  has been determined experimentally for heavy phosphorus doping and corresponding measured "bulk"  $n > n_i$  values (Fig. 2-13).  $C_{V_T}' (n > n_i)$  may be calculated directly from vacancy statistics, to varying levels of rigor. For a first approximation, mass-action balance is assumed and degeneracy effects neglected, to give

$$\begin{aligned} C_{V_T} &= C_{V^x} + C_{V^+} + C_{V^-} + C_{V^=} \\ &= C_{V^x} + C_{V^+}^i \left( \frac{n_i}{n} \right) + C_{V^-}^i \left( \frac{n}{n_i} \right) + C_{V^=}^i \left( \frac{n}{n_i} \right)^2 \end{aligned} \quad (2.14)$$

from which  $C_{V_T}'$  may be found readily from published values for  $n_i$ ,  $E_i$ ,  $E_{V^+}$ ,  $E_{V^-}$ , and  $E_{V^=}$  at relevant oxidation temperatures (but with no need to assume values for  $C_{V^x}$ , which cancels out of  $C_{V_T}'$ ).

When the experimental  $\log [(B/A)' - 1]$  is compared to the calculated  $\log [C_{V_T}' - 1]$ , for heavy  $n > n_i$ , the relation is found indeed to be linear, with slope  $\sim 1$ , to reasonable approximation at each of the temperatures 800, 900, 1000, and 1100°C for which  $(B/A)'$  values are available, lending credence to the postulated existence of a Si vacancy contribution to the effective linear rate constant.

If, for the moment, the validity of this vacancy contribution-multiple mechanism system is assumed, then the accurate modeling of enhanced B/A values found for the oxidation of heavily phosphorus-doped silicon is straightforward. Fitting lines of slope = 1 to the  $\log[(B/A)' - 1]$  vs.  $\log[C_{V_T}' - 1]$  plots determines the value of the only previously unknown and therefore effectively the single fitted parameter of this vacancy contribution model, the offset  $\log K' C_{V_T}^i e^{2.0/kT}$  in Eq. 2.13. The resulting values, shown in Fig. 2-20, appear very reasonably approximated as an activated process, for which

$$K' C_{V_T}^i \approx 2.62 \times 10^3 e^{-3.10/kT} \quad (2.15)$$

With this one fitted parameter, then, the B/A dependence on heavy phosphorus doping levels through  $n \gtrsim n_i$ , and a temperature T, may be calculated directly from basic physical parameters and their published values. Comparisons of these calculated  $(B/A)'$  curves with experimental  $(B/A)'$  data points as functions of n are presented in Figs. 2-21 to 2-24, for oxidation temperatures of 800-1100°C, respectively. Agreement appears reasonable in all cases. Thus, assumption of a vacancy contribution to the interface reaction (and not considering possible vacancy charge states and degeneracy effects, to this point) yields an adequate quantitative model for the observed (B/A) dependence in heavy substrate phosphorus doping by utilizing a single fitted parameter with published physical parameters.

The proposed vacancy contribution has been found to be

$$K C_{V_T} = K C_{V_T}^i C_{V_T}' = C_1 K' C_{V_T}^i C_{V_T}' \quad (2.16)$$

Since  $C_{V_T}^i$  indicates the dependence on doping level of the total equilibrium vacancy concentration, regardless of ongoing oxidation, it seems reasonable to assume that  $C_1 K' C_{V_T}^i$  must therefore reflect the nature of the vacancy contribution to the interface oxidation reaction, regardless of doping level. Specifically, then, the energetics of the fitted parameter  $K' C_{V_T}^i$  may be revealing.  $C_{V_T}^i$  may be calculated from and follows very closely the Arrhenius temperature dependence of  $C_{V^x}$  (a quantity that has not been needed in the analysis to this point). Physical interpretation of the vacancy contribution will therefore be dependent on the precise determination of the behavior of  $C_{V^x}$  with temperature.

Van Vechten and Thurmond [2.14] conclude from quenching data that  $C_{V^x} \propto e^{-(2.4 \pm 0.2)/kT}$ . The observed behavior of  $K' C_{V_T}^i$  would then necessitate an additional  $K'$  temperature dependence. Since Van Vechten [2.15] also indicates that vacancy migration requires an additional  $(1.2 \pm 0.3)$  eV, regardless of charge state,  $K'$  may possibly be related to vacancy diffusivity. So, the vacancy contribution reflected in  $K' C_{V_T}^i$  may indeed consist of a vacancy flux to the interface, entirely consistent with Dobson's speculation.

On the other hand, Seidel and MacRae [2.16] propose that  $C_{V^x} \propto e^{-3.4/kT}$ . In this event, the vacancy contribution may possibly be linked to vacancy generation at or near the interface, as  $K'$  would then seem temperature insensitive. In either case, the 3.1 eV activation energy in eq. 2.15 and in Fig. 2-20 seems to tie in well with independently measured physical parameters, again lending credence to the overall vacancy model presented here.

Also in either case, a vacancy situated at the interface presumably contributes to the interface reaction by providing a site for an oxygen species to occupy.

Overall, then, should the effects of heavy substrate doping prove to be Si vacancy-linked, as suggested here, it would appear that the interface oxidation reaction, discussed so frequently to date only in terms of the breaking of a Si-Si bond, may actually result from multiple contributors - both a vacancy term and the other contributors that have been grouped together as  $R_1$  in this analysis. Fig. 2-25 compares the total  $(B/A)^i = R_1 + KC_{V_T}^i$  with the vacancy term  $KC_{V_T}$ , for several heavy  $n$  values, alone. It is evident that for lightly doped substrates with  $n = n_i(T)$  the vacancy term makes negligible contribution to the overall  $(B/A)^i$ , and the mechanism(s) in  $R_1$  must dominate to produce the overall apparent  $(B/A)$  activation energy of 2.0 eV. Possibly, as proposed by Dobson, interstitial flow into the substrate may be significant. As further suggested in Fig. 2-19, perhaps some interstitials may move into the oxide. (Such a flow would then very probably be intimately related to the observed oxide charge  $Q_{ss}$  that has been discussed as incompletely oxidized silicon atoms.) Or, perhaps even the breaking of a Si-Si bond may be the limiting step of the interface oxidation reaction under low doping level conditions.

As substrate doping levels increase such that  $n > n_i(T)$ , and if as assumed the  $R_1$  contributors are relatively unaffected by increasing electrical effects of heavy doping, then the vacancy mechanisms suggested in Fig. 2-19 increase in magnitude and become proportionately more significant until they begin to dominate at sufficiently high  $n$  values, as illustrated

rather strikingly in Fig. 2-25. It is the  $R_1$  term that now makes the smaller contribution and ultimately may be neglected. The dominant increased magnitude and apparent reduced activation energy of the vacancy contribution under such conditions, due to shifting of the Fermi level  $E_F$  by the heavy substrate doping even at oxidation temperatures, then produces an apparent increase of the linear rate constant  $(B/A)$  "pre-exponential factor" with little apparent change of the effective activation energy from  $\sim 2$  eV. The similarity of this behavior, remarkable because of the proposed shift from one to another dominant mechanism(s) as substrate doping increases, can be compared with the experimentally determined  $(B/A)$  behavior in Fig. 2-13. The agreement is evident. We are currently actively pursuing verification of this vacancy model. If proven to be correct, it should allow analytic prediction of oxidation kinetics under a wide range of process conditions not well modelled at present.

#### E. Oxide Charge Effects

We are starting the phase of the overall program where an attempt will be made to incorporate oxide charges into the process modeling computer program, possibly even into the oxidation general relationship. The charges most closely associated with the oxidation process are  $Q_{ss}$ , fixed oxide charge, and the structural type of  $N_{st}$ , interface states.\* These along with the other two oxide charge types, are indicated in Fig. 2-26, which shows their location in the oxidized silicon structure.

Quite a little is already known about the relationship of  $Q_{ss}$  to process conditions. This information is included in [2.17]. A short set of experiments was carried out, however, to familiarize current personnel with the sensitivity of  $Q_{ss}$  to high temperature anneal and cooling

---

\*Other types of interface states include metallic impurity induced states, radiation induced states, and those caused by high currents or voltages.

conditions immediately following oxidation. Results are summarized in Table II. A series of oxides was prepared in dry  $O_2$  at  $1200^\circ C$  for 60 minutes, resulting in approximately  $0.20 \mu m$  thick oxides. Subsequent anneal and cooling conditions were varied according to the final column in Table II. As can be noted,  $Q_{ss}/q$  values for  $\langle 111 \rangle$  silicon ranged from  $1.60$  to  $7.90 \times 10^{11} \text{ cm}^{-2}$ , while  $\langle 100 \rangle$  values ranged from  $0.20$  to  $2.65 \times 10^{11} \text{ cm}^{-2}$ . Similar results were obtained for interface state densities ( $N_{st}$ ), which will be in a later report. The main conclusion is that extreme care should be used in controlling process conditions when oxide charges are being studied.

This portion of the program involves determining  $N_{st}$  (structural type) dependence on process conditions and comparing the results with similar  $Q_{ss}$  relationships. Therefore, a quasistatic C-V analysis system has been assembled [2.18]. Figure 2-27 contains a schematic description of the set-up. The analysis program has been optimized and  $N_{st}$  densities across the middle region of the silicon band gap can be determined in the range  $10^{10}$  to  $10^{13}/\text{cm}^2\text{-eV}$ .  $N_{st}$  is now being determined as a function of silicon orientation and type, oxidation temperature, time and ambient, annealing and cooling conditions, and low temperature hydrogen annealing conditions.

Preliminary results are indicated in Figs. 2-28 and 2-29. The dependence of  $N_{st}$  values at midgap on oxidation temperature for  $\langle 111 \rangle$  and  $\langle 100 \rangle$  silicon and three different anneal/cool conditions is shown in Fig. 2-28. In this case, no low temperature  $H_2$  anneal has been employed. The interesting result is that  $N_{st}$  values follow the same trend with oxidation temperature as does  $Q_{ss}$ , i.e. the  $Q_{ss}/O_2$  triangle [2.19]. In Fig. 2-29, midgap

values of  $N_{st}$  for a number of samples are plotted against  $Q_{ss}/q$  for both  $H_2$ -annealed and no low temperature anneal. A definite relationship between  $Q_{ss}$  and  $N_{st}$  is observed for both cases. These results help to demonstrate (a) a common origin for  $Q_{ss}$  and the structural type of  $N_{st}$ , and (b)  $N_{st}$  can be characterized by particular oxidation conditions.

## REFERENCES

- [2.1] B.E. Deal and A.S. Grove, "General Relationship for the Thermal Oxidation of Silicon," J. Appl. Phys., 36, 3770-3778, Dec 1965.
- [2.2] J.D. Meindl et al., "Final Report on Computer-Aided Semiconductor Process Modeling," Stanford Electronics Laboratories, TR-4969-73-F, Oct 1976.
- [2.3] D.W. Hess and B.E. Deal, "Kinetics of the Thermal Oxidation of Silicon in  $O_2/HCl$  Mixtures," J. Electrochem. Soc., 124, 735-739, May 1977.
- [2.4] B.E. Deal, D.W. Hess, J.D. Plummer and C.P. Ho, "Kinetics of the Thermal Oxidation of Silicon in  $O_2/H_2O$  and  $O_2/Cl_2$  Mixtures," to be published Feb 1978 J. Electrochem. Soc.
- [2.5] C.P. Ho, J.D. Plummer, B.E. Deal and J.D. Meindl, "Thermal Oxidation of Heavily Phosphorus Doped Silicon," to be published in J. Electrochem. Soc..
- [2.6] R.J. Kriegler, "The Uses of  $HCl$  and  $Cl_2$  for the Preparation of Electrically Stable  $SiO_2$ ," Semiconductor Silicon 1973 Proceedings, H.R. Huff and R.R. Burgess, Eds., The Electrochemical Society, Princeton, N.J., p. 63.
- [2.7] K. Hirabayashi and J. Iwamura, "Kinetics of Thermal Growth of  $HCl-O_2$  Oxides on Silicon," J. Electrochem. Soc., 120, 1595, 1973.
- [2.8] L. Pauling, The Nature of the Chemical Bond, 3rd ed., p. 85, Cornell University Press, Ithaca, New York, 1960.
- [2.9] A.S. Grove, O. Leistiko, Jr., and C.T. Sah, "Redistribution of Acceptor and Donor Impurities During Thermal Oxidation of Silicon," J. Appl. Phys., 35, 2695, 1964.
- [2.10] P.S. Dobson, "The Effect of Oxidation on Anomalous Diffusion in Silicon," Philosophical Mag., 24, 1971, 567-576.
- [2.11] P.S. Dobson, "The Mechanism of Impurity Diffusion in Silicon," Philosophical Mag., 26, 1301-1306, 1972.
- [2.12] W. Shockley and J.L. Moll, "Solubility of Flaws in Heavily-Doped Semiconductors," Phys. Rev., 119, 1480-1482, Sept 1960.
- [2.13] R.K. Jain and R.J. Van Overstraeten, "Theoretical Calculations of the Fermi Level and of Other Parameters in Phosphorus Doped Silicon at Diffusion Temperatures," IEEE Trans. Electron Devices, ED-21, 155-165, Feb 1974.

- [2.14] J.A. Van Vechten and C.D. Thurmond, "Comparison of Theory with Quenching Experiments for the Entropy and Enthalpy of Vacancy Formation in Si and Ge," Phys. Rev. B, 14, 3551-3557, Oct 1976.
- [2.15] J.A. Van Vechten, "Enthalpy of Vacancy Migration in Si and Ge," Phys. Rev. B, 10, 1482-1506, Aug 1974.
- [2.16] T.E. Seidel and A.U. MacRae, "Some Properties of Ion Implanted Boron in Silicon," Trans. Metall. Soc. AIME, 245, 491-498, March 1969.
- [2.17] B.E. Deal, "The Current Understanding of Charges in the Thermally Oxidized Silicon Structure," J. Electrochem. Soc., 121, 198C, 1974.
- [2.18] M. Kuhn, Solid State Electronics, 13, 873, 1970.
- [2.19] B.E. Deal, M. Sklar, A.S. Grove, and E.H. Snow, J. Electrochem. Soc. 114, 266 (1967).

Table I  
Electrically Active  $C_{BE}$  and Chemical  $C_{BC}$  Dopant  
Concentrations in Heavily Phosphorus Doped Samples

Sample	$C_{BE}$	$C_{BC}$	
		SIMS	AES
A	$(\sim 10^{15})$	_____	_____
B	$5.1 \times 10^{19}$	$5.5 \times 10^{19}$	$5.2 \times 10^{19}$
C	$7.2 \times 10^{19}$	$1.5 \times 10^{20}$	$8.2 \times 10^{19}$
D	$1.8 \times 10^{20}$	$2.4 \times 10^{20}$	$2.8 \times 10^{20}$
E	$2.8 \times 10^{20}$	$4.5 \times 10^{20}$	$5.0 \times 10^{20}$
F	$3.2 \times 10^{20}$	$7.0 \times 10^{20}$	$6.8 \times 10^{20}$

TABLE II  
Q<sub>SS</sub> VARIATIONS DUE TO POST-OXIDATION VARIATIONS

(DRY O<sub>2</sub>, 1200°C, 60min; x<sub>0</sub> = 0.2 μm)

RUN NO.	Q <sub>SS</sub> /q (10 <sup>11</sup> /cm <sup>2</sup> )		ANNEAL/COOL CONDITIONS*	
	(111)Si	(100)Si		
SA-142	1.60	0.40	2O <sub>2</sub> , FP, OPEN,	UR
SA-143	2.50	0.60	" " "	F
SA-144	1.80	0.40	" " CLOSED, UR	UR
SA-145	4.35	0.95	" " "	F
SA-146	6.00	1.25	2O <sub>2</sub> , SP, CLOSED, UR	UR
SA-147	6.40	2.65	" SSP "	"
SA-148	6.15	2.10	" " "	F
SA-149	2.00	0.20	IN <sub>2</sub> , SP, CLOSED, UR	UR
SA-150	2.25	0.30	4N <sub>2</sub> " "	"
SA-153	7.90	2.15	2N <sub>2</sub> " OPEN	"
SA-154	2.25	0.40	4N <sub>2</sub> FP "	"

RANGE 1.60-7.90 0.20-2.65

\* 1, 2, or 4 = gas flow rate (ℓ/min) OPEN OR CLOSED ELEPHANT  
 FP = fast pull (<3 sec) UR = upright boat  
 SP or SSP slow pull (2 or 10 min) F = flat boat  
 N<sub>2</sub> anneal time = 10 min

R71002

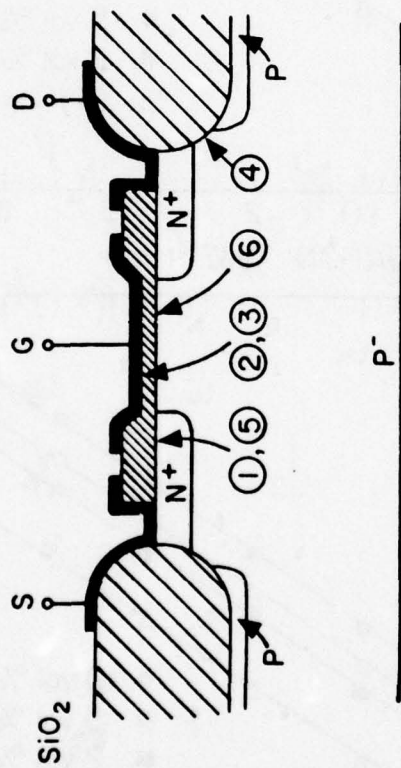


Fig. 2-1. Cross-Section of Oxide Isolated NMOS Transistor.

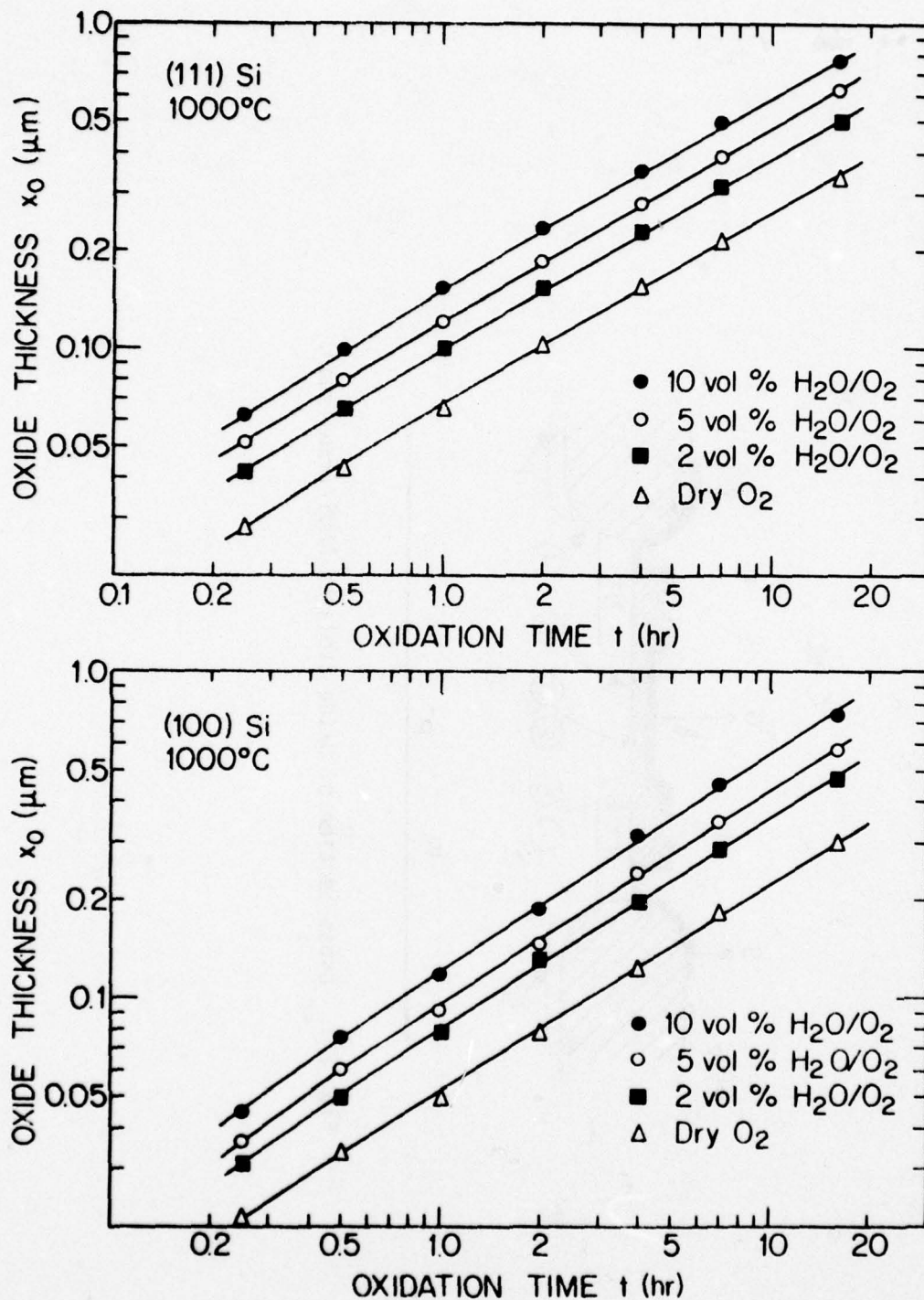


Fig. 2.2. Oxide thickness versus oxidation time for the oxidation of (111) and (100) oriented n-type silicon in various  $O_2/H_2O$  mixtures at 1000°C.

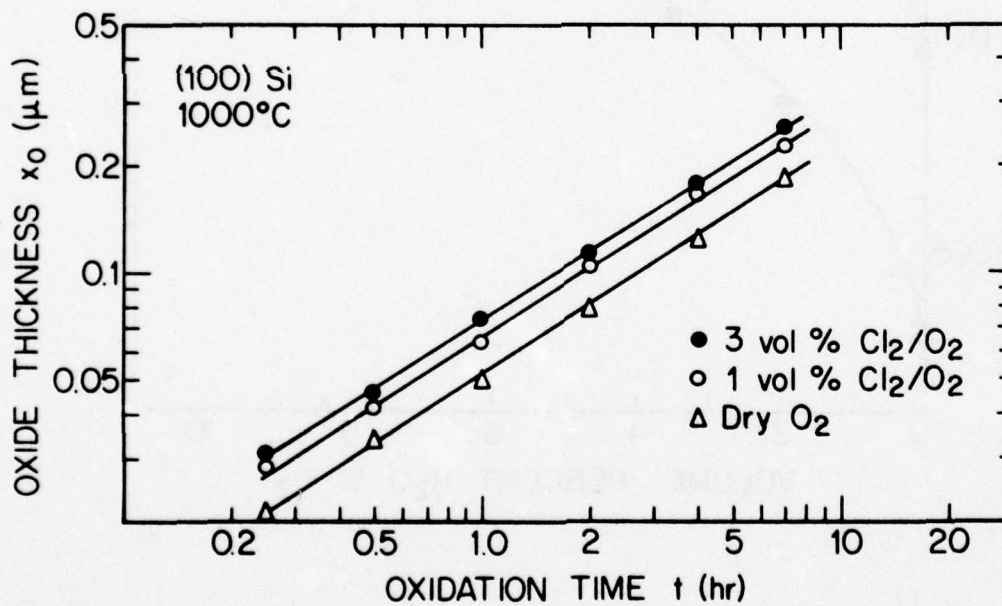
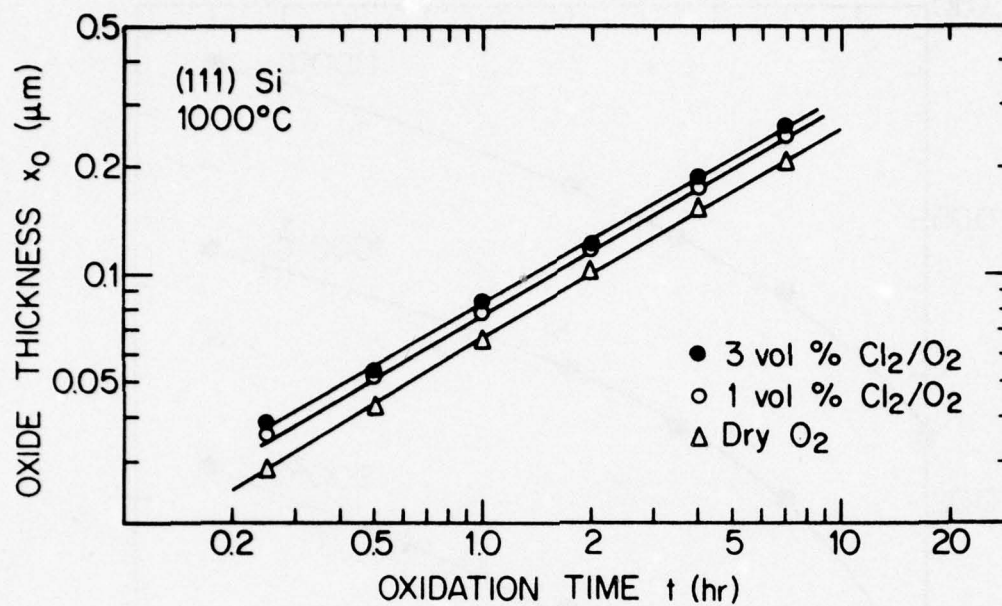


Fig.2-3. Oxide thickness versus oxidation time for the oxidation of (111) and (100) oriented n-type silicon in various  $\text{O}_2/\text{Cl}_2$  mixtures at 1000°C.

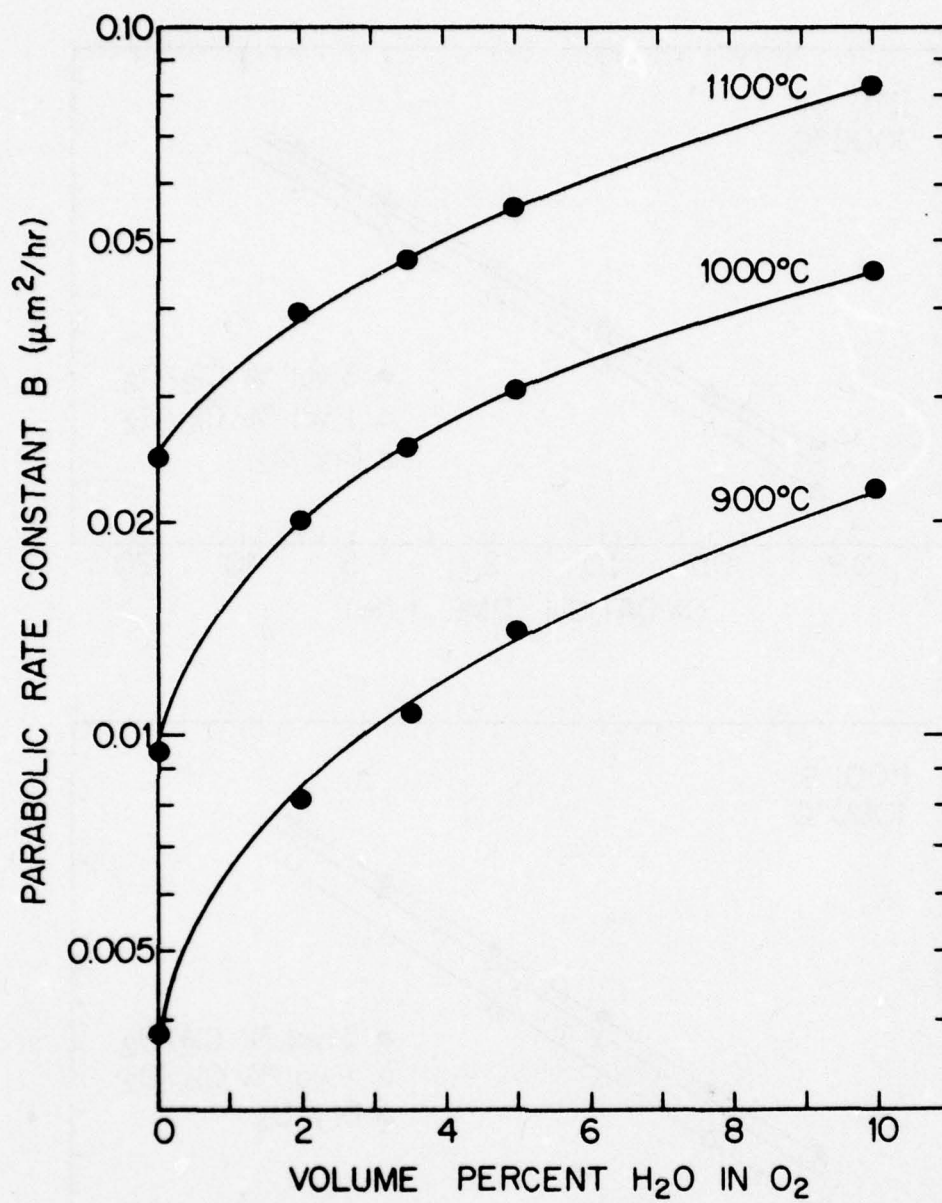


Fig. 2-4. Parabolic rate constant versus volume percent  $\text{H}_2\text{O}$  in  $\text{O}_2$  for oxidation of n-type silicon at 900°, 1000°, and 1100°C. Data are for both (111) and (100) silicon orientations.

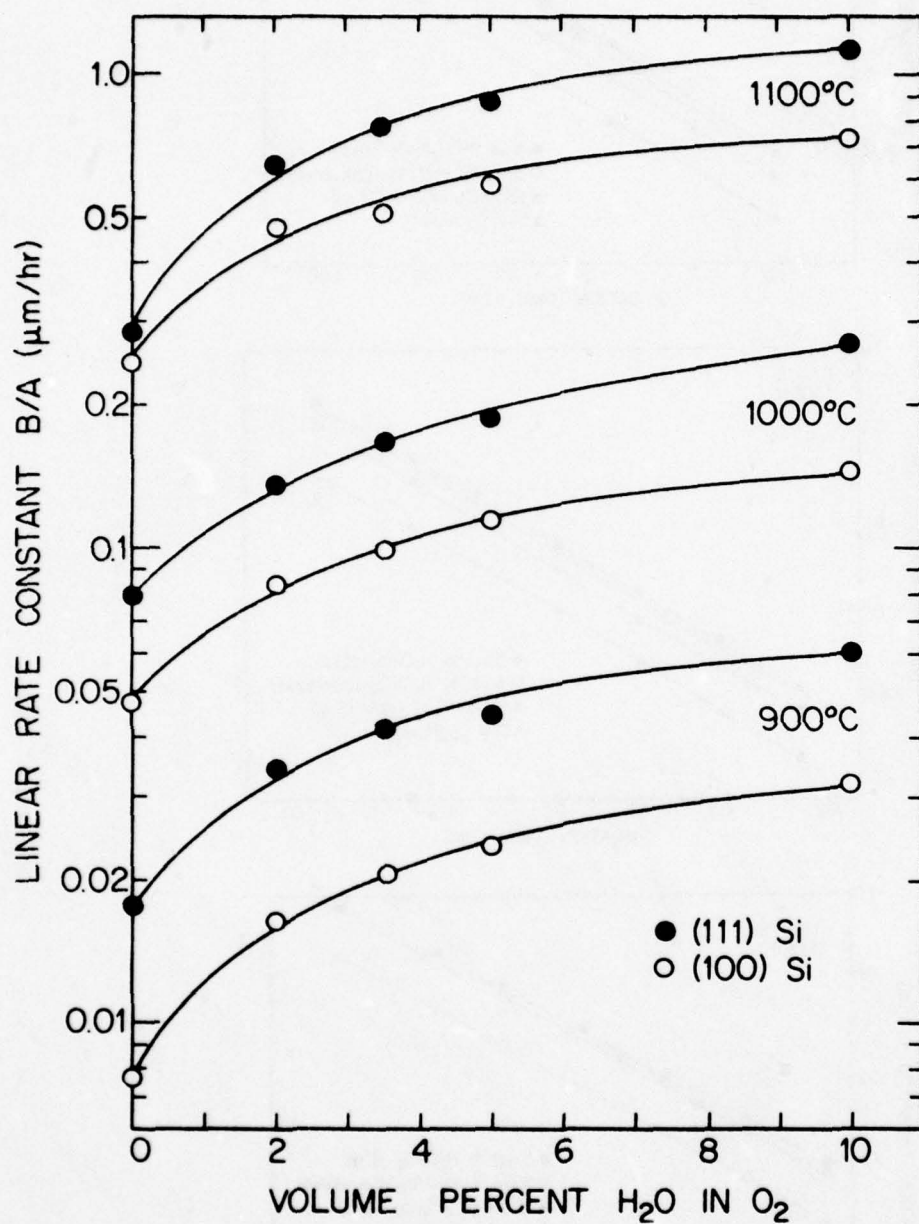


Fig. 2-5. Linear rate constant versus volume percent  $\text{H}_2\text{O}$  in  $\text{O}_2$  for oxidation of (111) and (100) oriented n-type silicon at 900°, 1000°, and 1100°C.

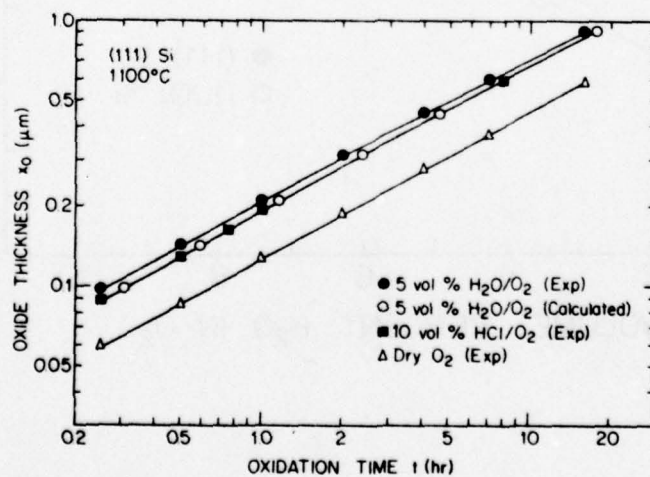
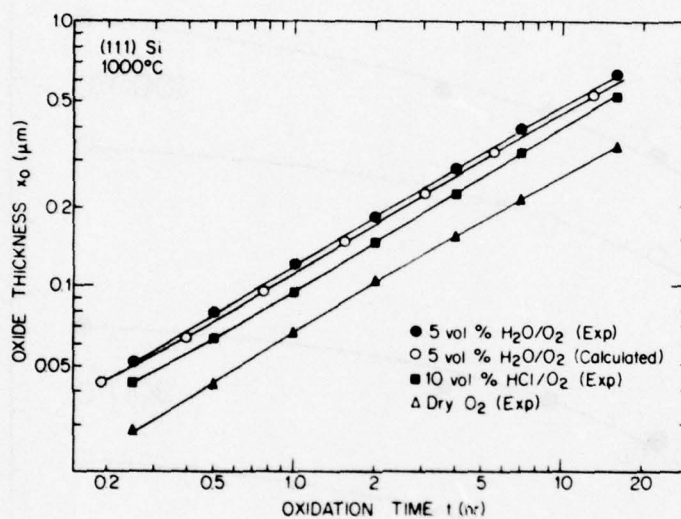
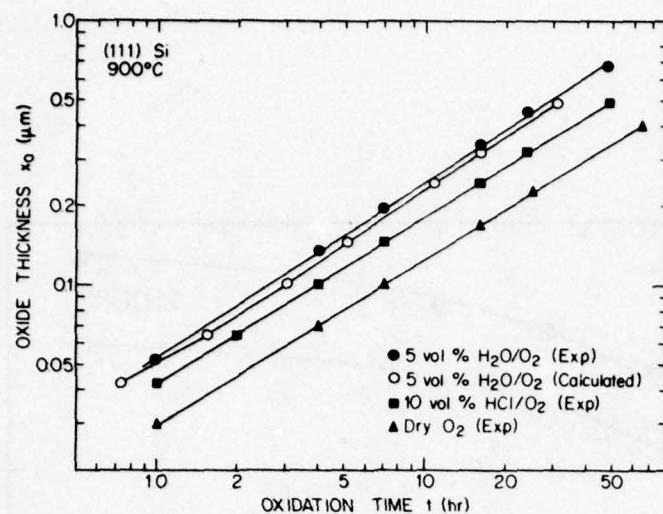


Fig. 2-6. Oxide thickness versus oxidation time for the oxidation of (111) oriented n-type silicon at 900°, 1000°, and 1100°C in 5 volume percent  $\text{H}_2\text{O}/\text{O}_2$ , 10 volume percent  $\text{HCl}/\text{O}_2$ , and dry  $\text{O}_2$  mixtures. Also included are data for 5 volume percent  $\text{H}_2\text{O}/\text{O}_2$  mixture calculated from Eq. [3].

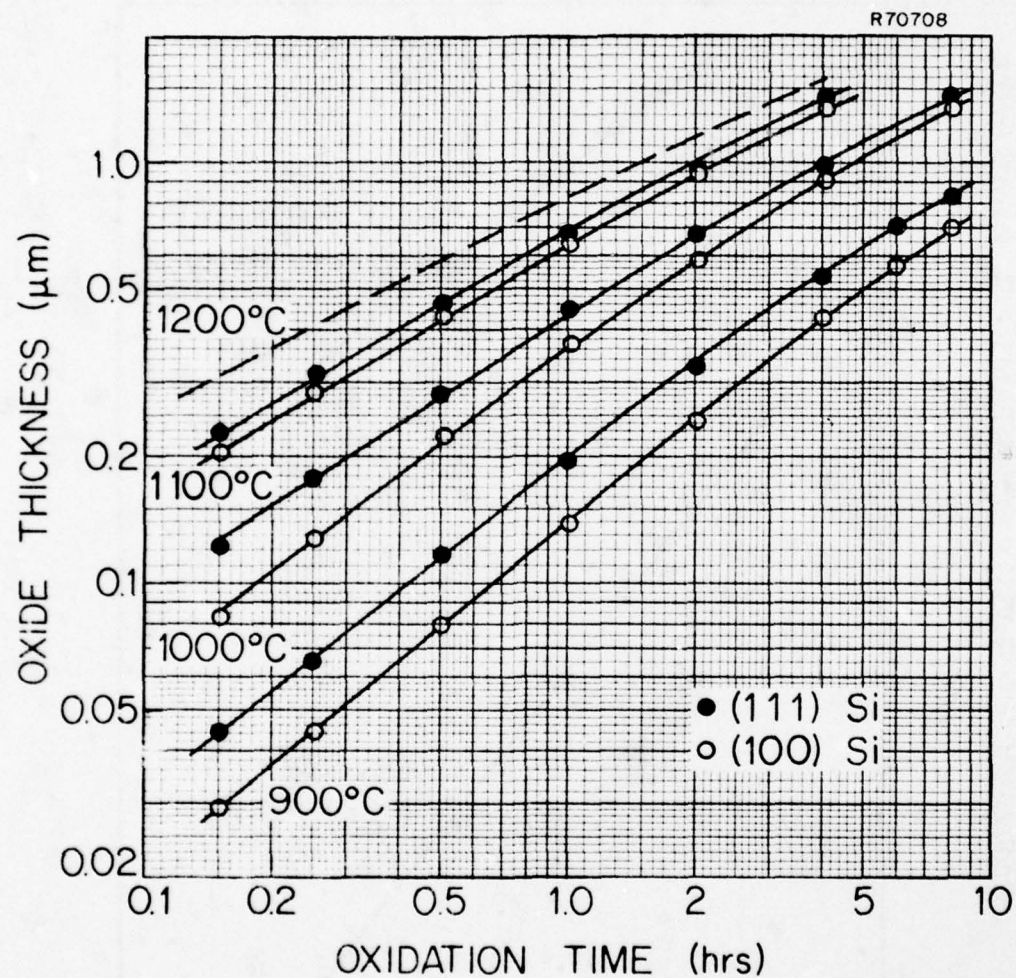


Fig. 2-7. Oxide thickness vs oxidation time for silicon oxidation in  $\text{H}_2\text{O}$  (640 Torr).

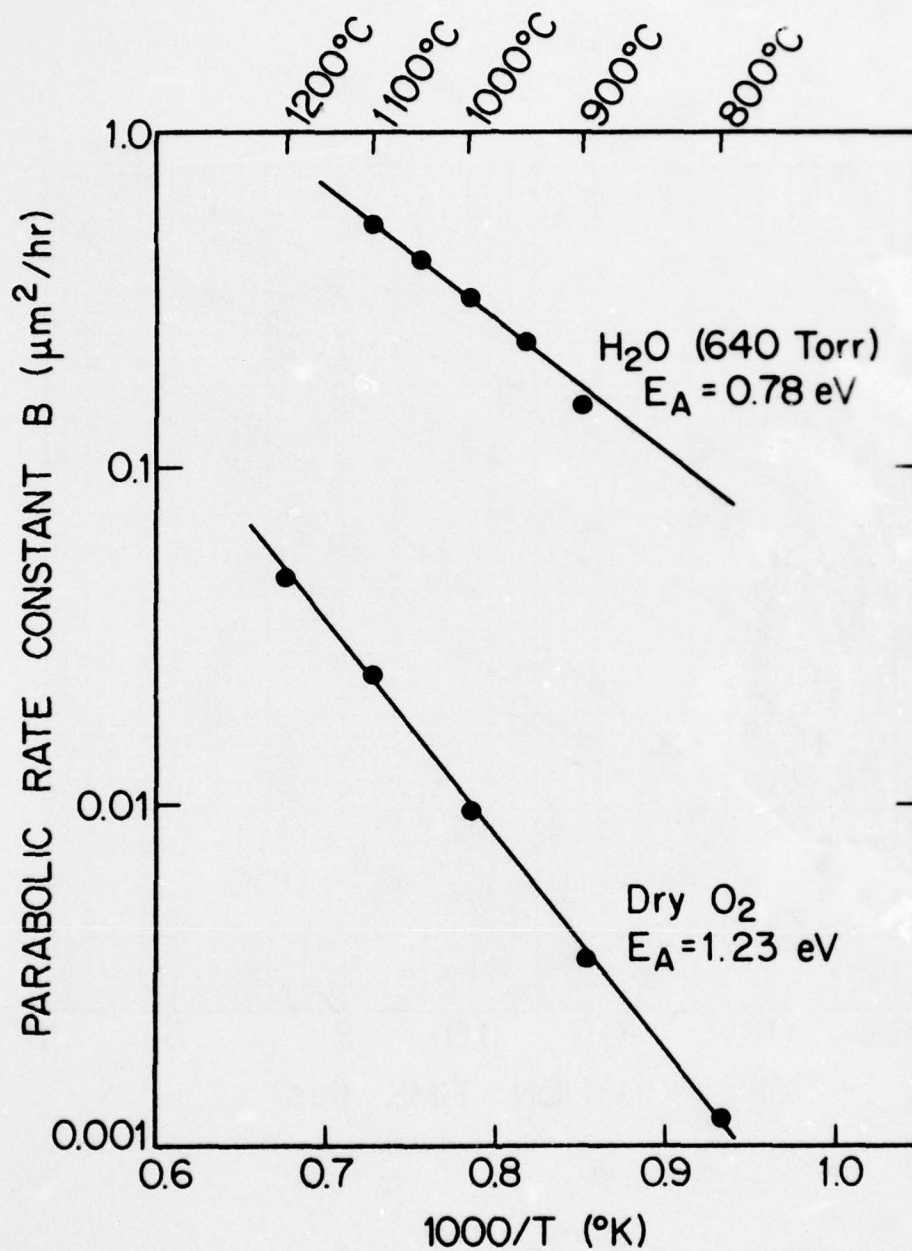


Fig. 2-8. Dependence of parabolic rate constant B on temperature for the thermal oxidation of silicon in pyrogenic H<sub>2</sub>O (640 Torr) or dry O<sub>2</sub>.

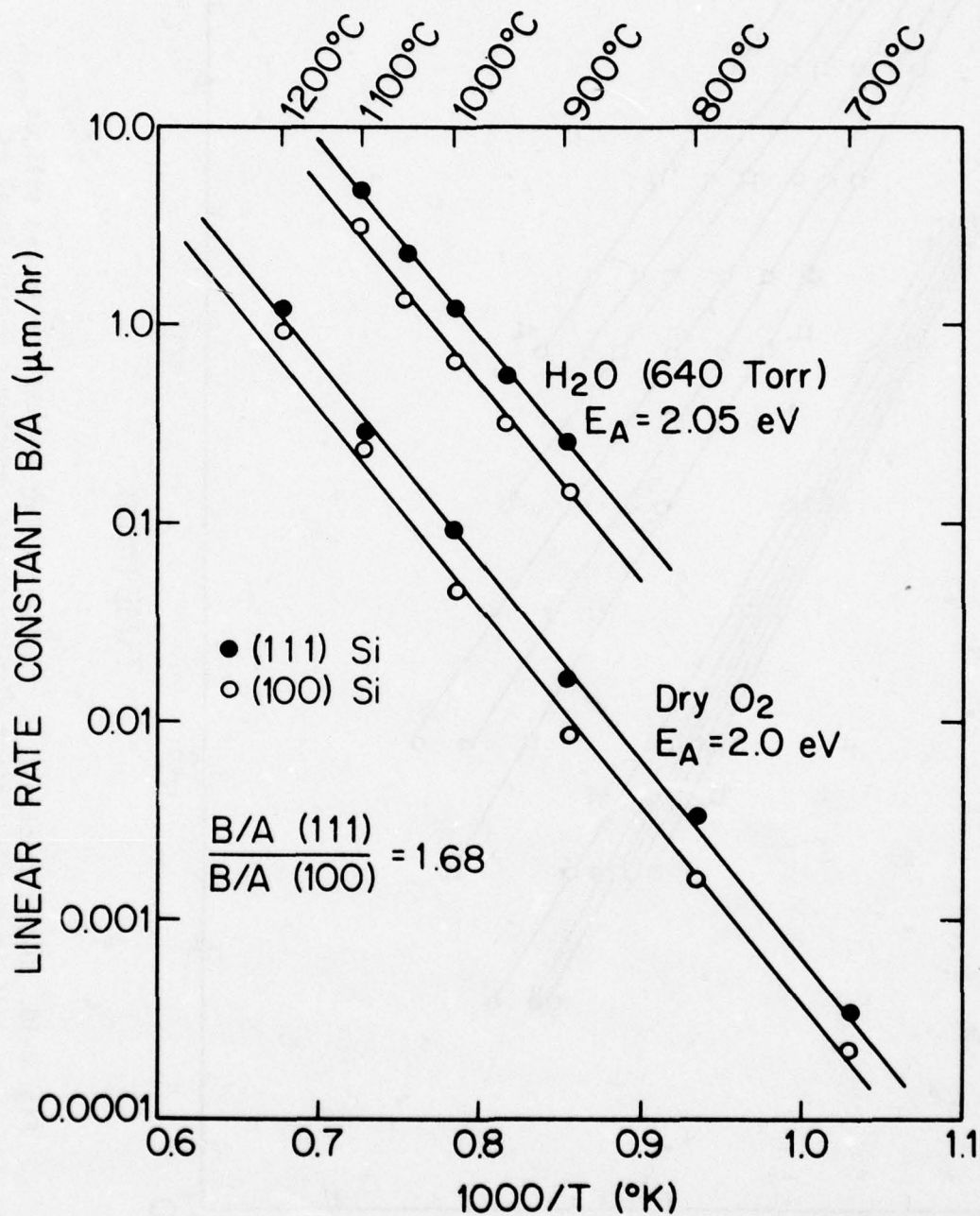


Fig. 2-9. Dependence of linear rate constant  $B/A$  on temperature for the thermal oxidation of silicon in pyrogenic  $\text{H}_2\text{O}$  (640 Torr) or dry  $\text{O}_2$ .

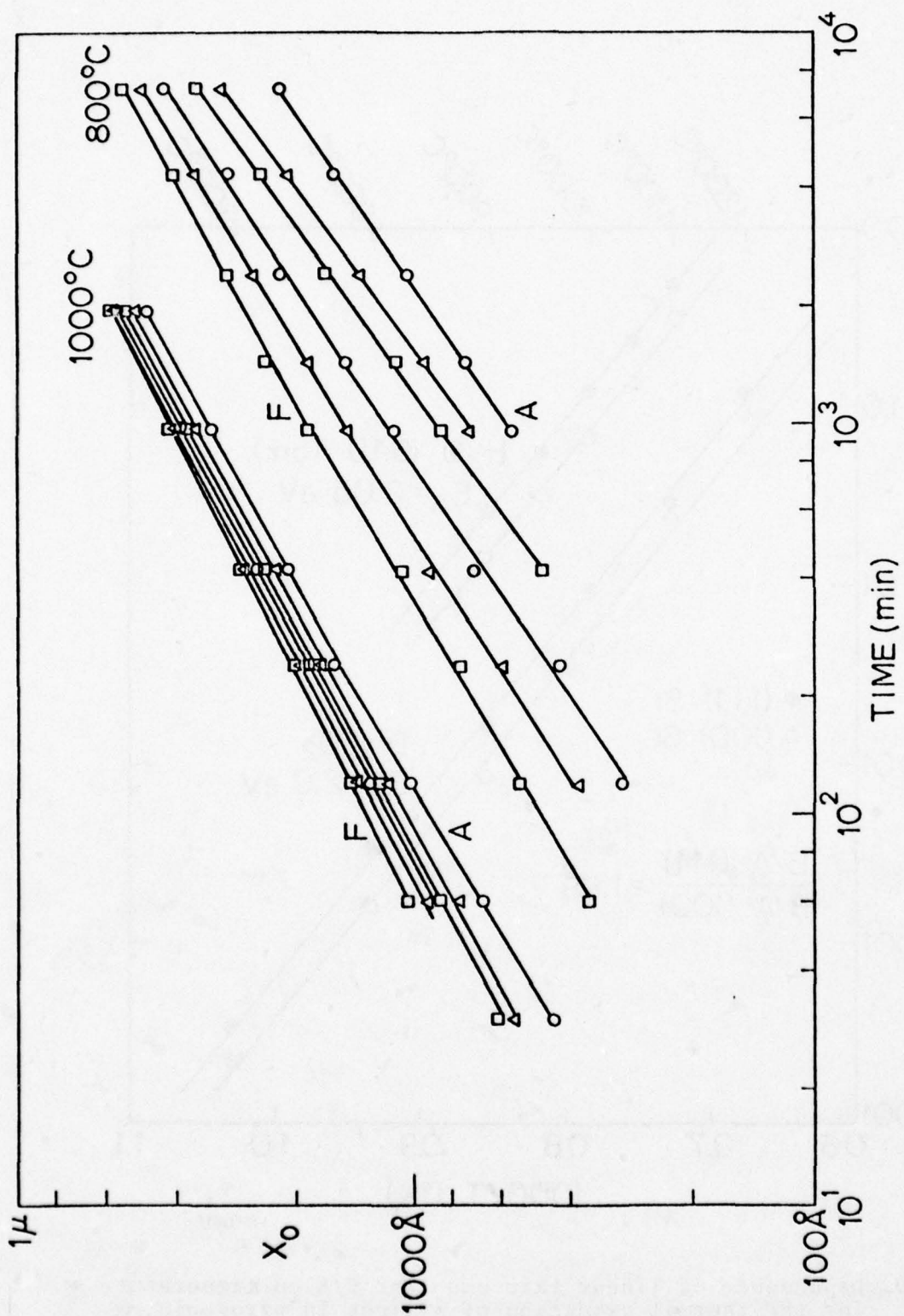


Fig. 2-10. Oxide thickness vs. oxidation time for  $\langle 111 \rangle$  oriented silicon in dry  $\text{O}_2$  ambient with substrate phosphorus doping level as parameter, at  $800$  and  $1000^\circ\text{C}$ .

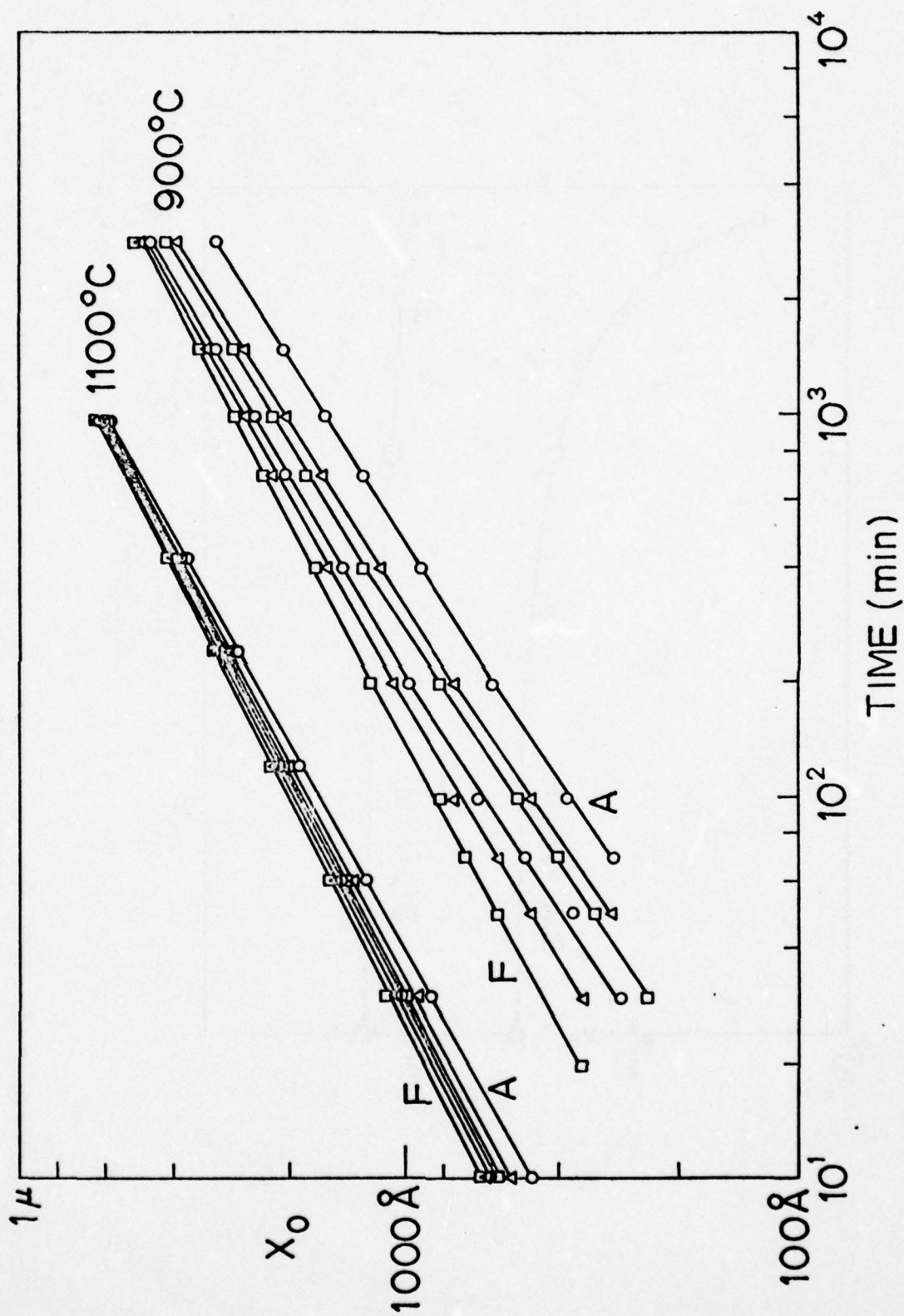


Fig. 2-11. Oxide thickness vs. oxidation time for <111> oriented silicon in dry  $\text{O}_2$  ambient with substrate phosphorus doping level as parameter, at  $900$  and  $1100^\circ\text{C}$ .

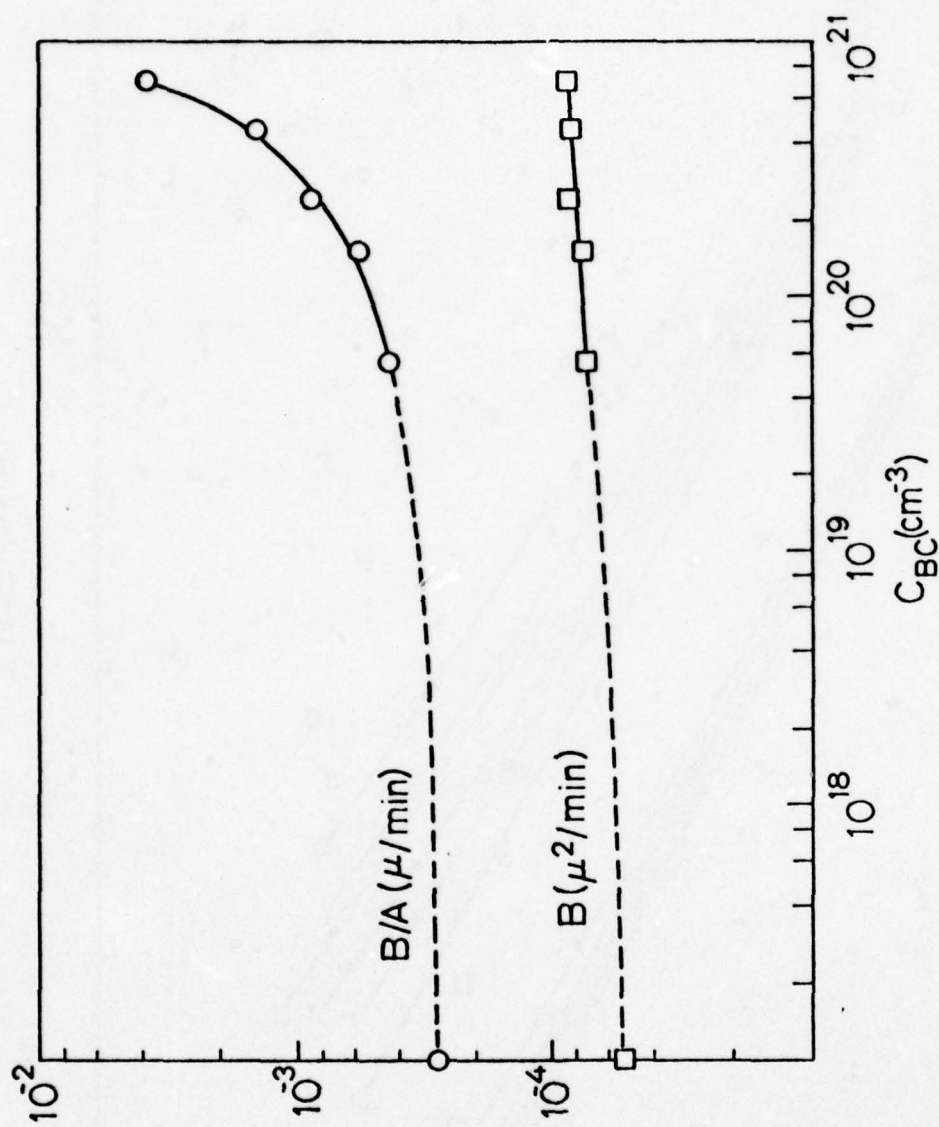


Fig. 2-12. Oxidation rate constants vs. initial substrate chemical phosphorus doping level at  $900^\circ\text{C}$ .

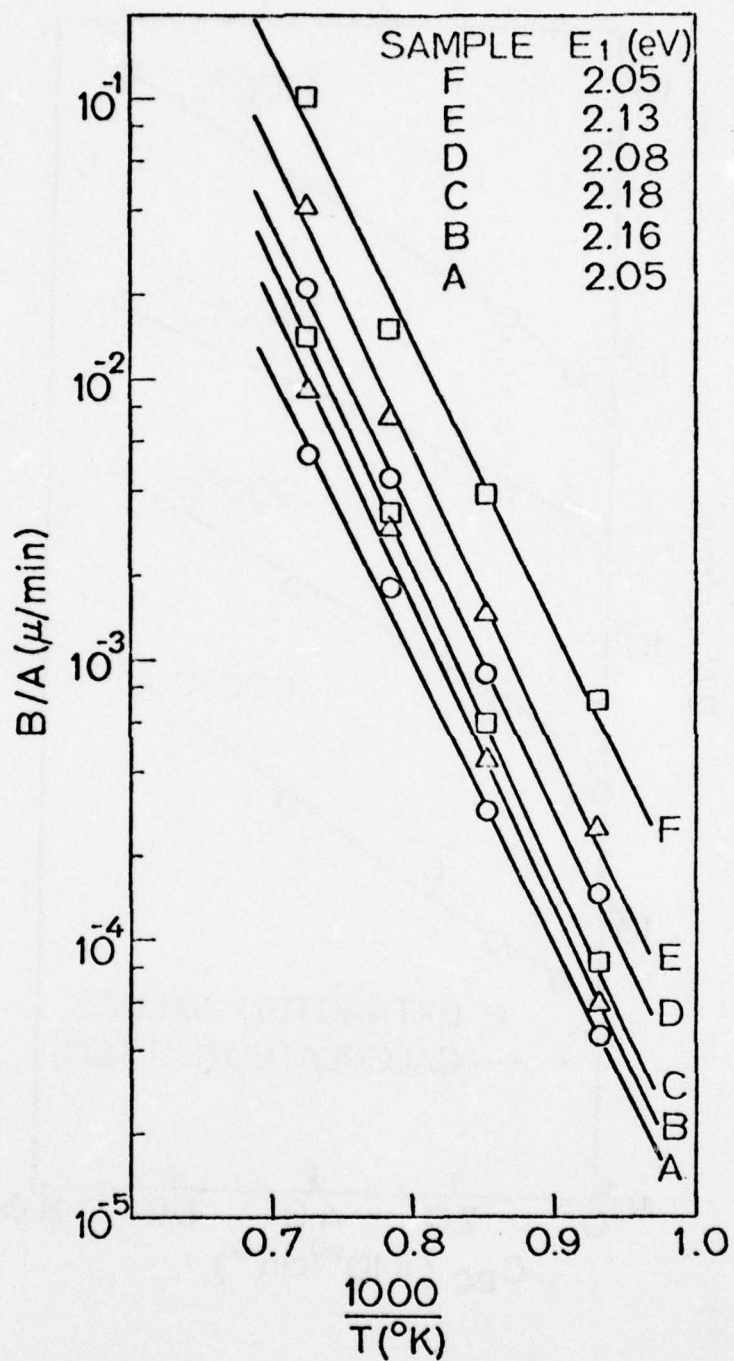


Fig. 2-13. Linear rate constant temperature dependence and effective activation energies with substrate phosphorus doping level as parameter.

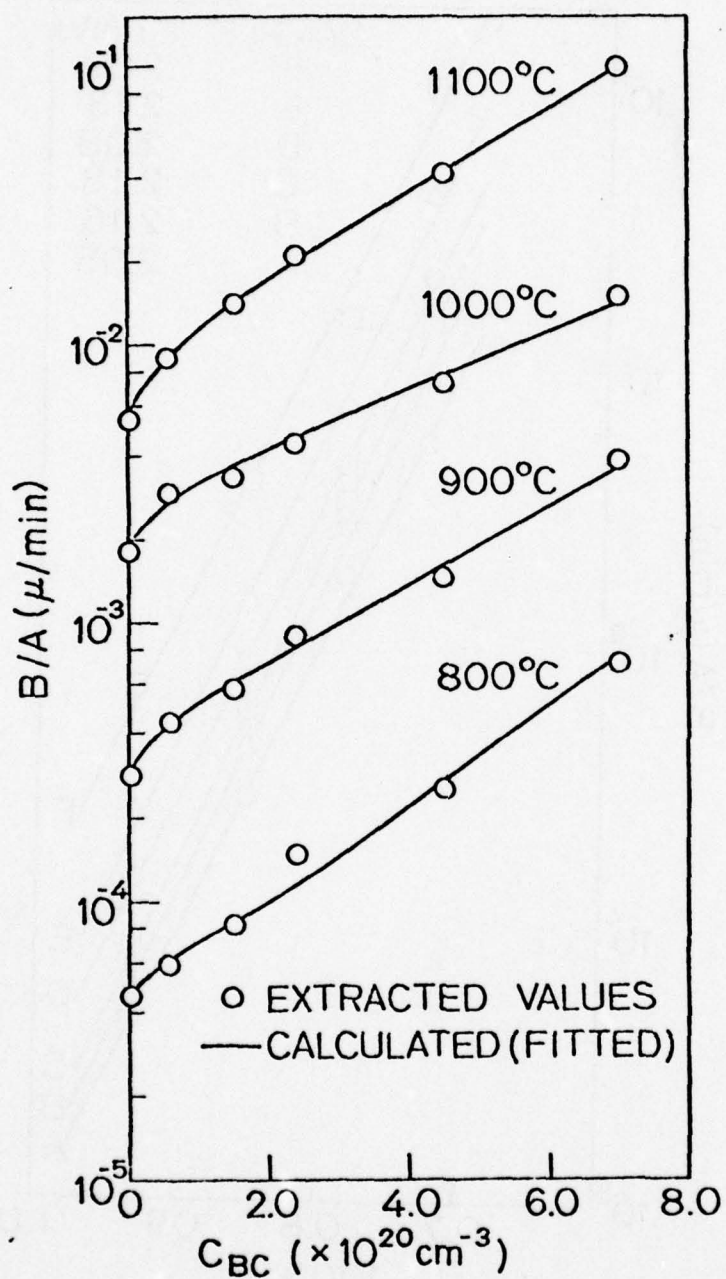


Fig. 2-14. Linear rate constant vs. initial substrate chemical phosphorus doping level with oxidation temperature as parameter.

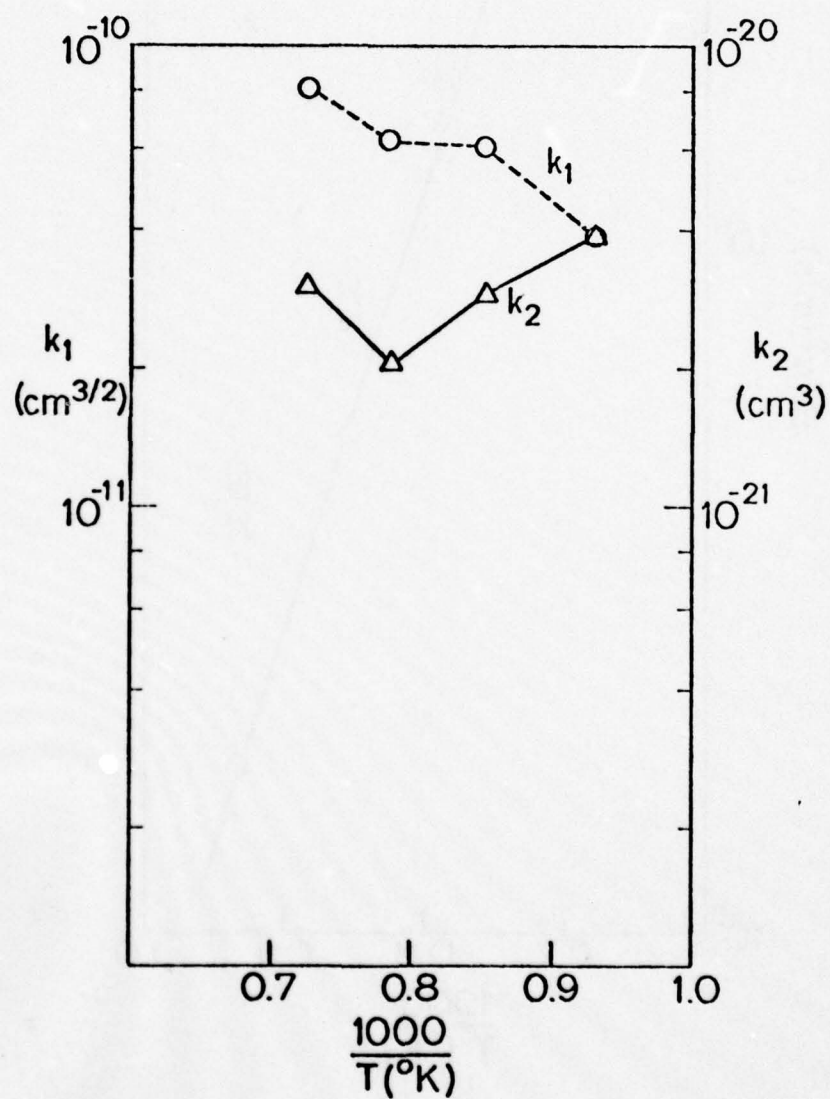


Fig. 2-15. Fitted parameters vs.  $1/T$  for linear rate constant dependence on initial substrate chemical phosphorus doping level.

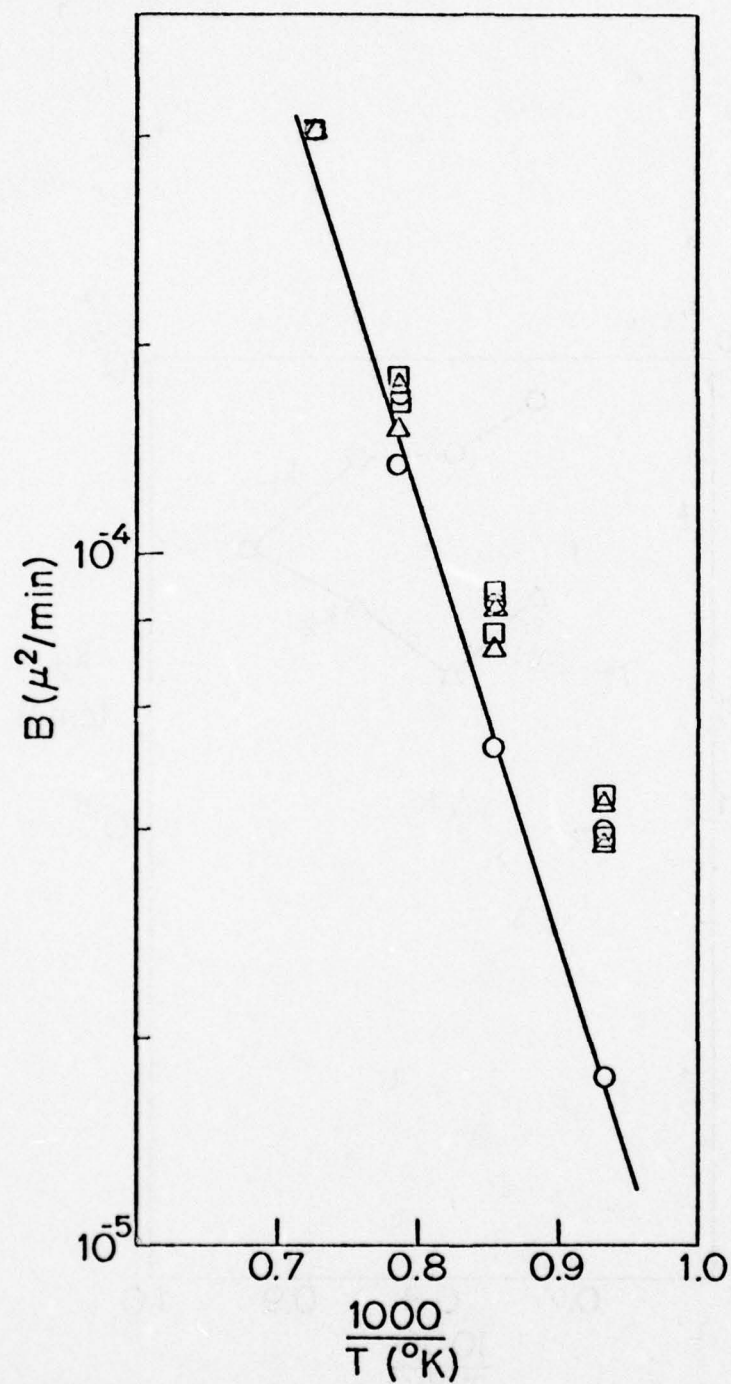


Fig. 2-16. Parabolic rate constant temperature dependence with substrate phosphorus doping level as parameter.

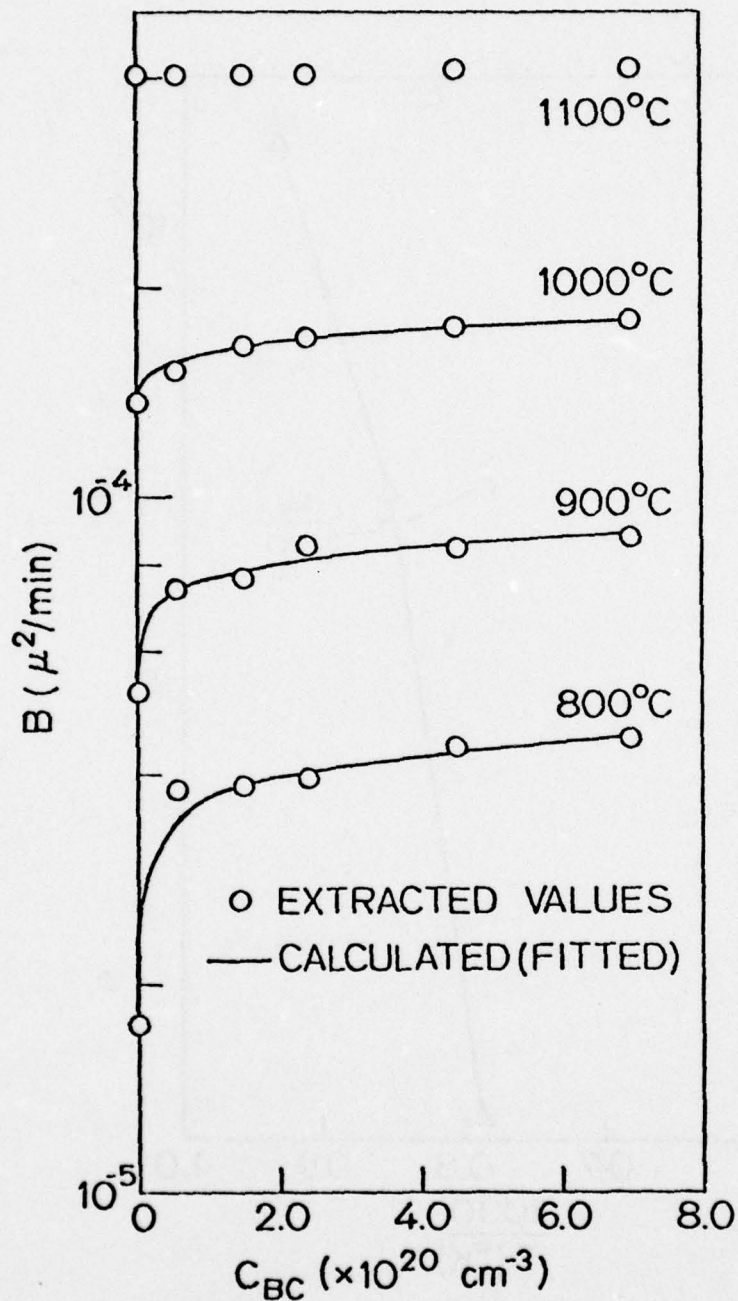


Fig. 2-17. Parabolic rate constant vs. initial substrate chemical phosphorus doping level with oxidation temperature as parameter.

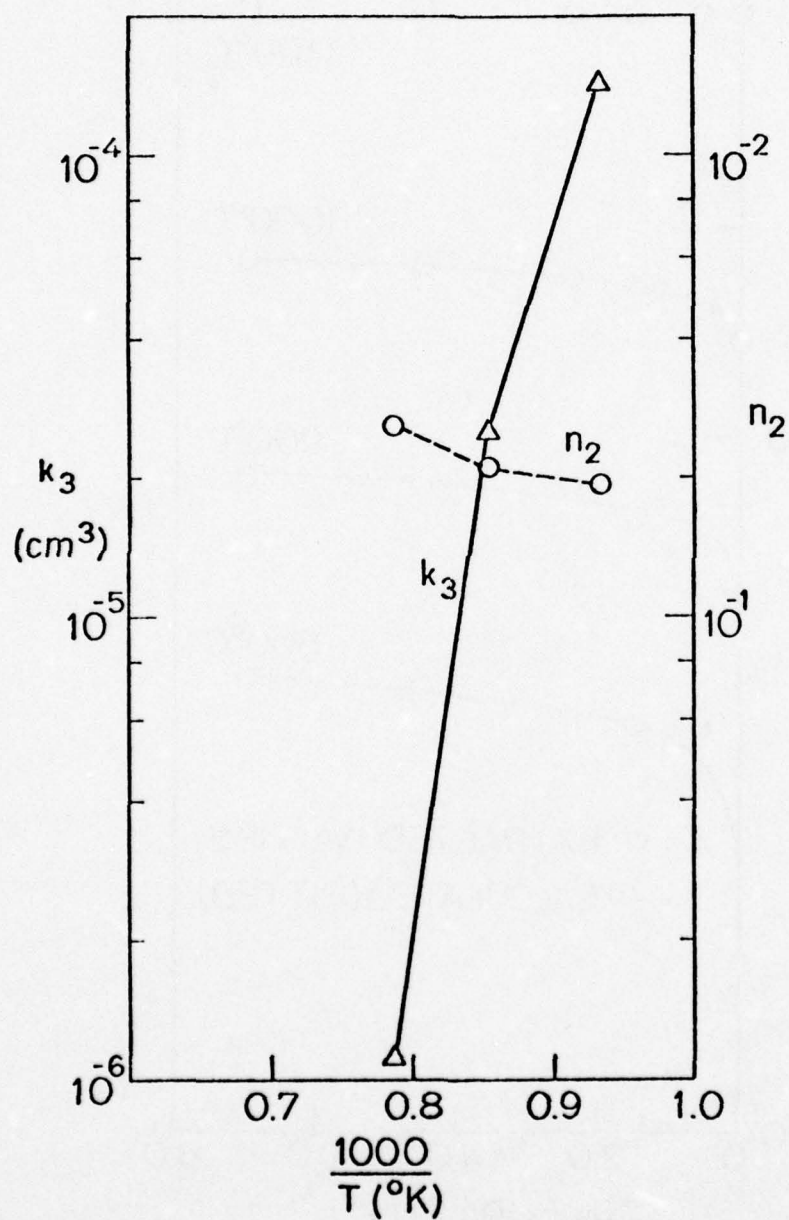


Fig. 2-18. Fitted parameters vs.  $1/T$  for parabolic rate constant dependence on initial substrate chemical phosphorus doping level.

POSSIBLE Si VACANCY AND INTERSTITIAL MECHANISMS  
INVOLVED IN INTERFACE OXIDATION REACTION

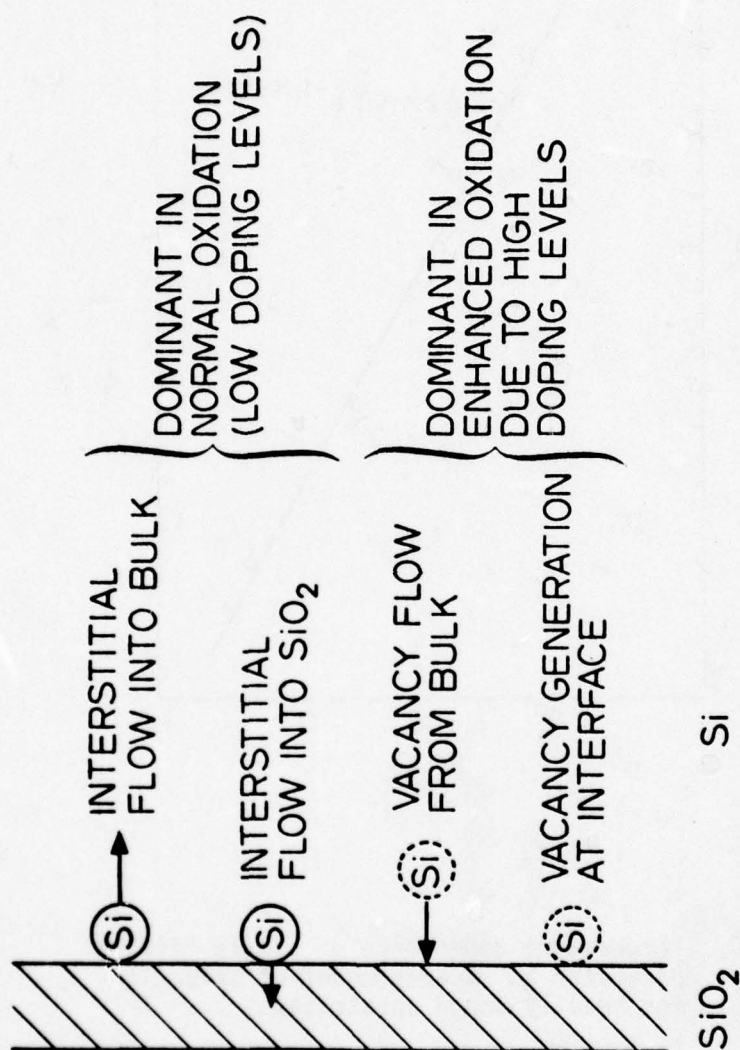


Fig. 2-19.

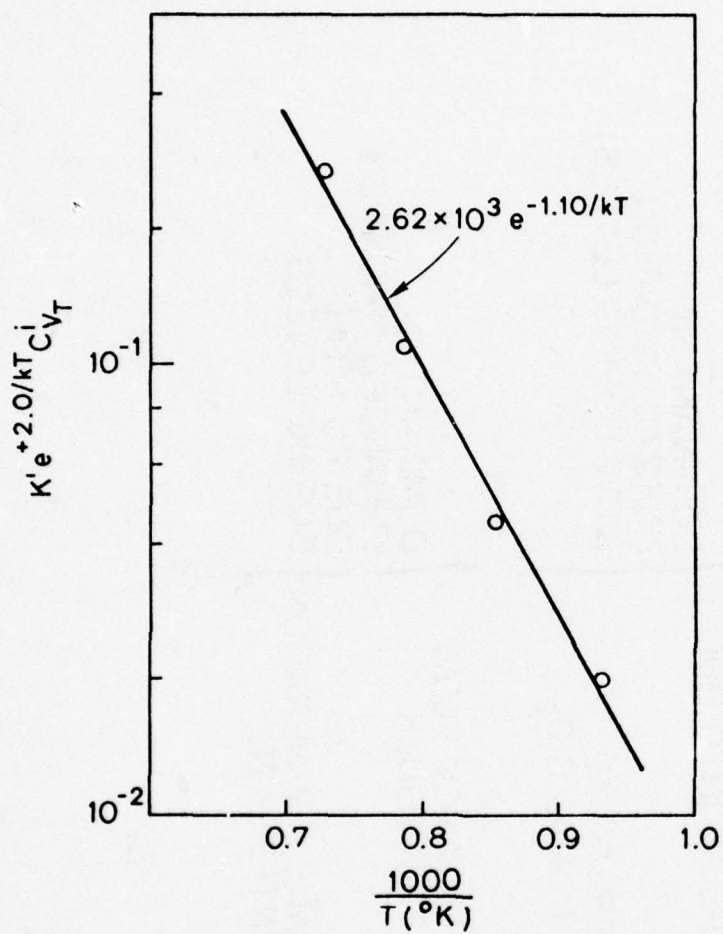


Fig. 2-20. Temperature dependence of single "fitted" parameter in vacancy model of oxidation for heavily doped substrates.

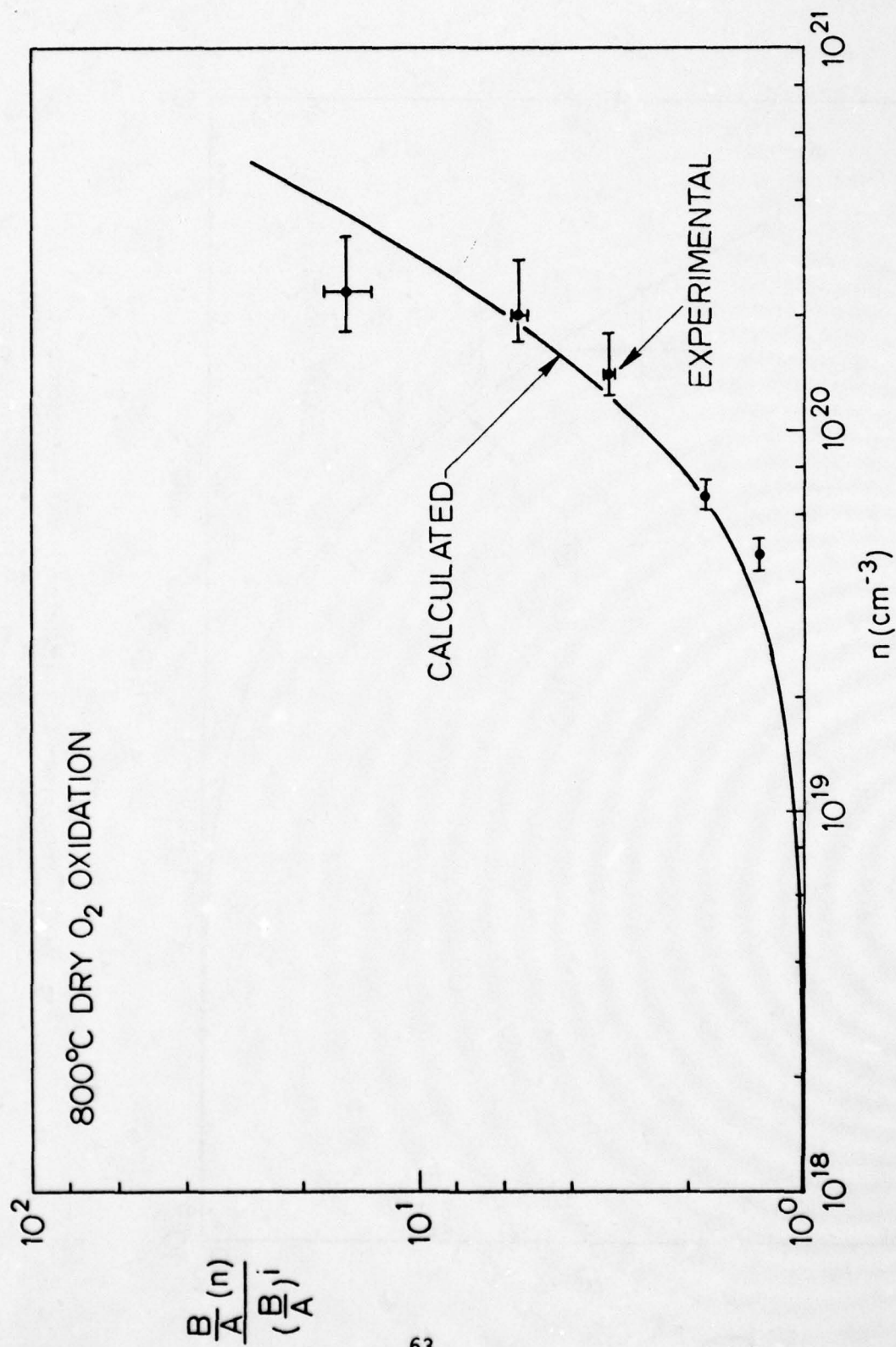


Fig. 2-21. Comparison of calculated linear rate constant based on vacancy model and experimental results. 800°C dry O<sub>2</sub> oxidation, <111> phosphorus doped substrates.

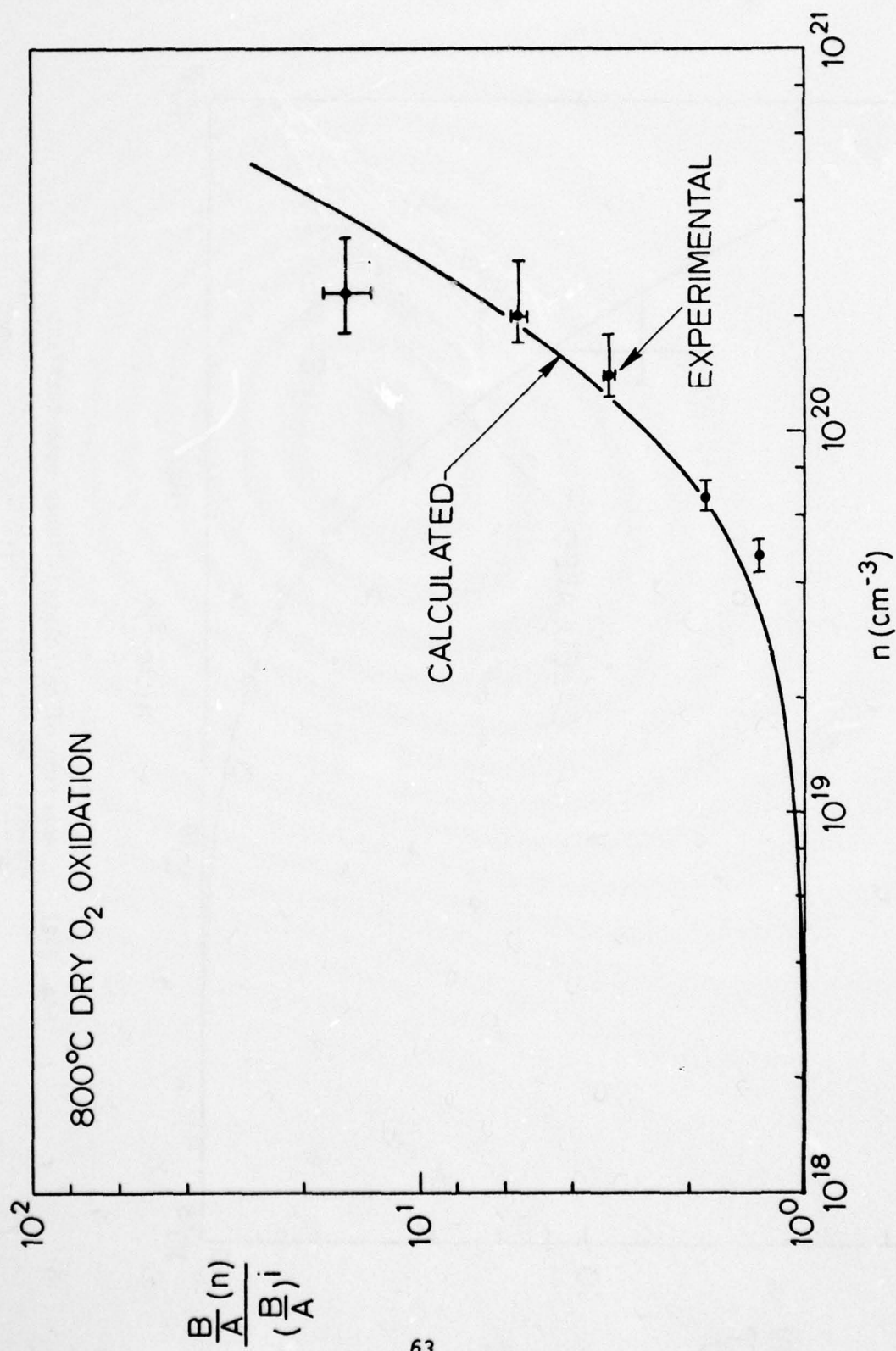


Fig. 2-21. Comparison of calculated linear rate constant based on vacancy model and experimental results. 800°C dry O<sub>2</sub> oxidation, <111> phosphorus doped substrates.

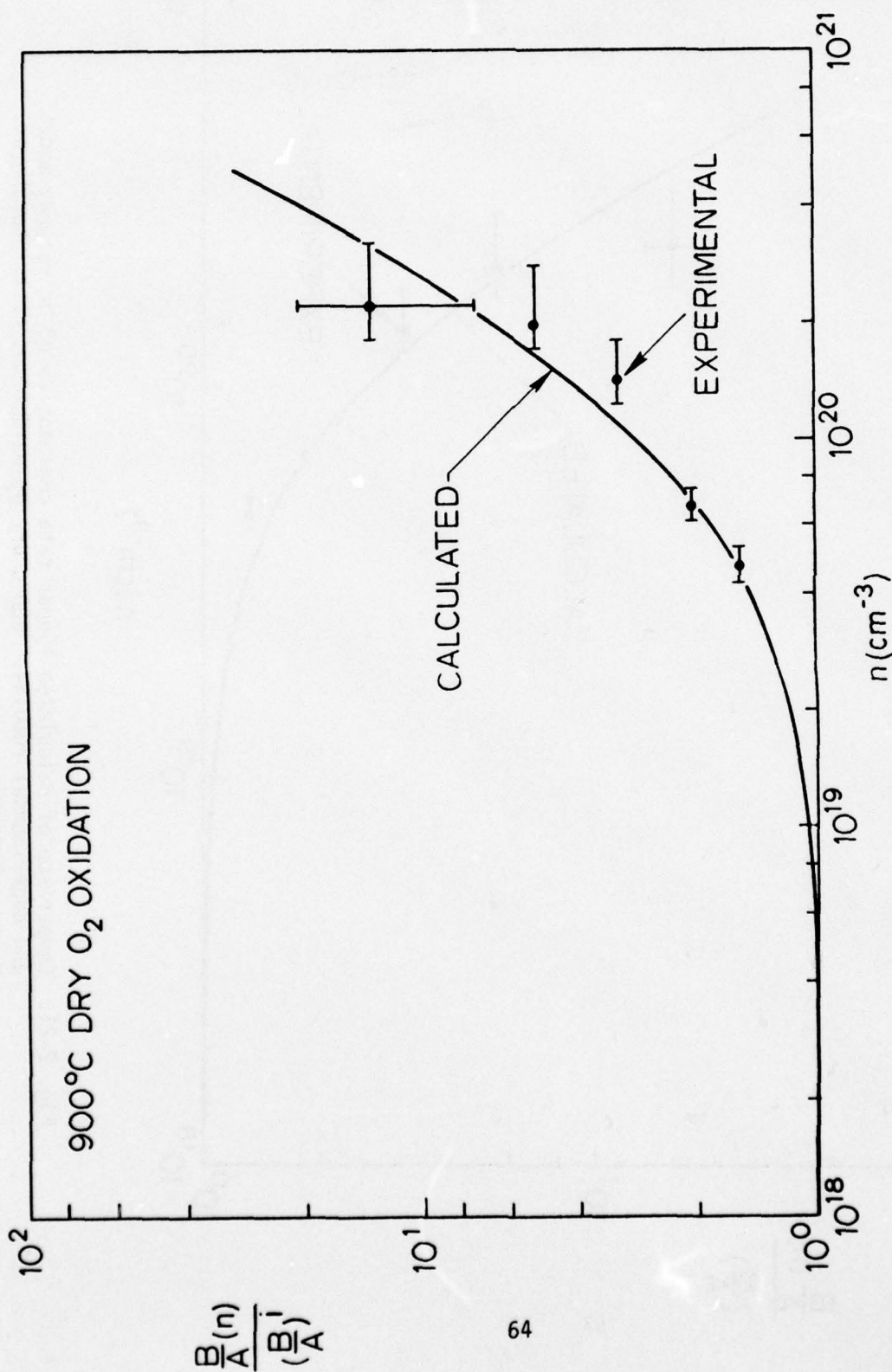


Fig. 2-22. Comparison of calculated linear rate constant based on vacancy model and experimental results; 900°C dry O<sub>2</sub> oxidation, <111> phosphorus doped substrates.

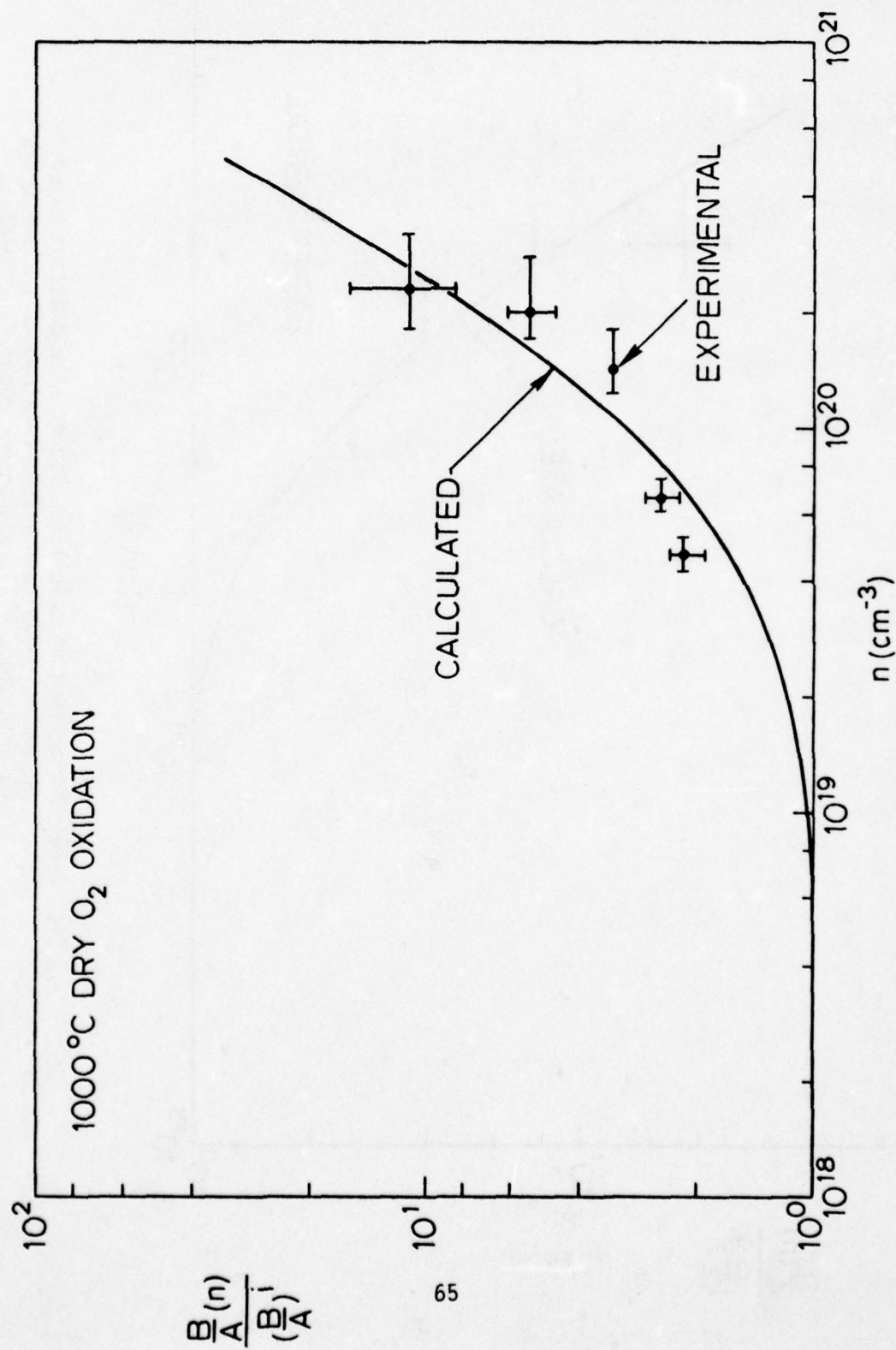


Fig. 2-23. Comparison of calculated linear rate constant based on vacancy model and experimental results; 1000°C dry O<sub>2</sub> oxidation, <111> phosphorus doped substrates.

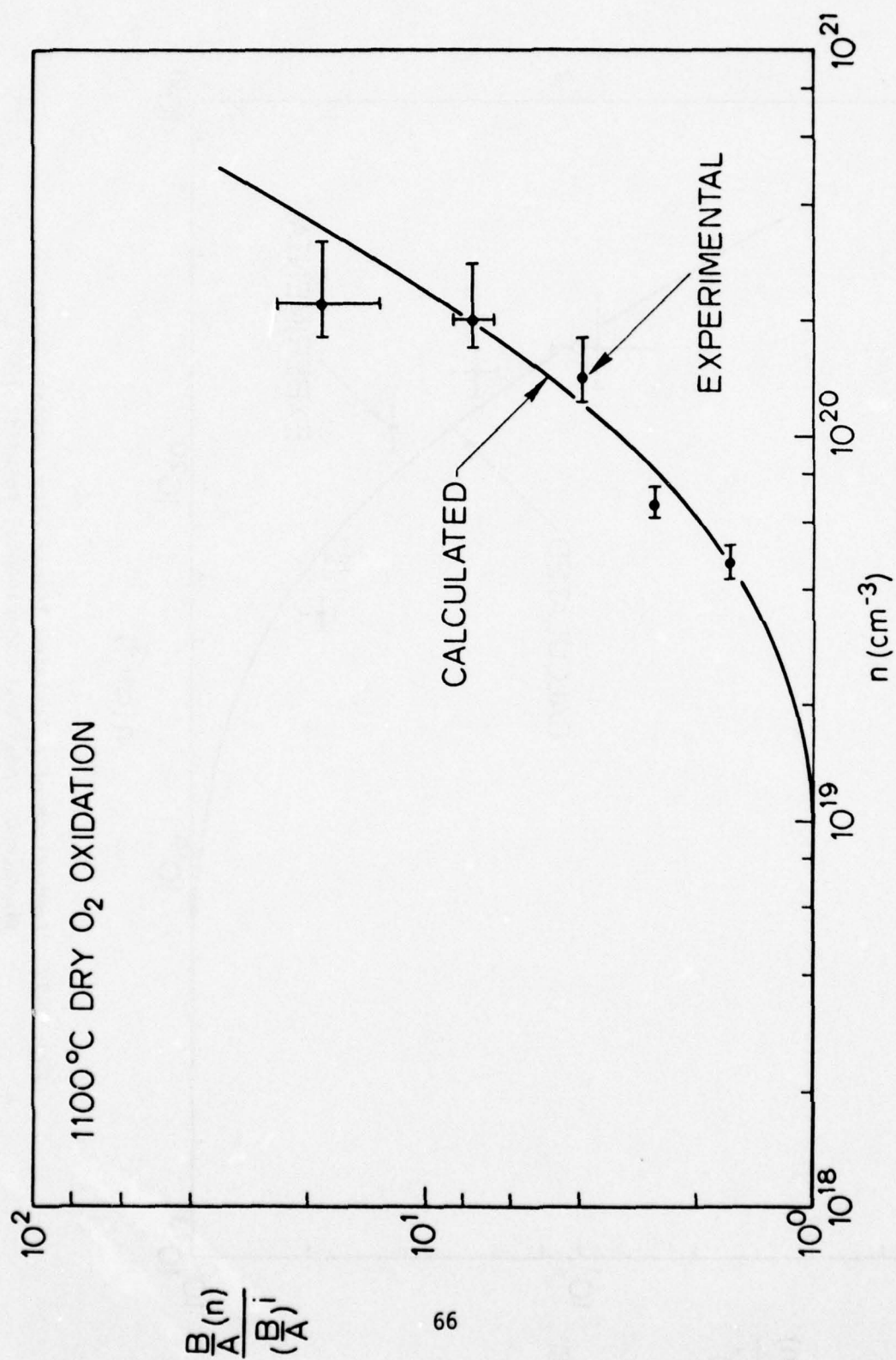


Fig. 2-24. Comparison of calculated linear rate constant based on vacancy model and experimental results; 1100°C dry O<sub>2</sub> oxidation, <111> phosphorus doped substrates.

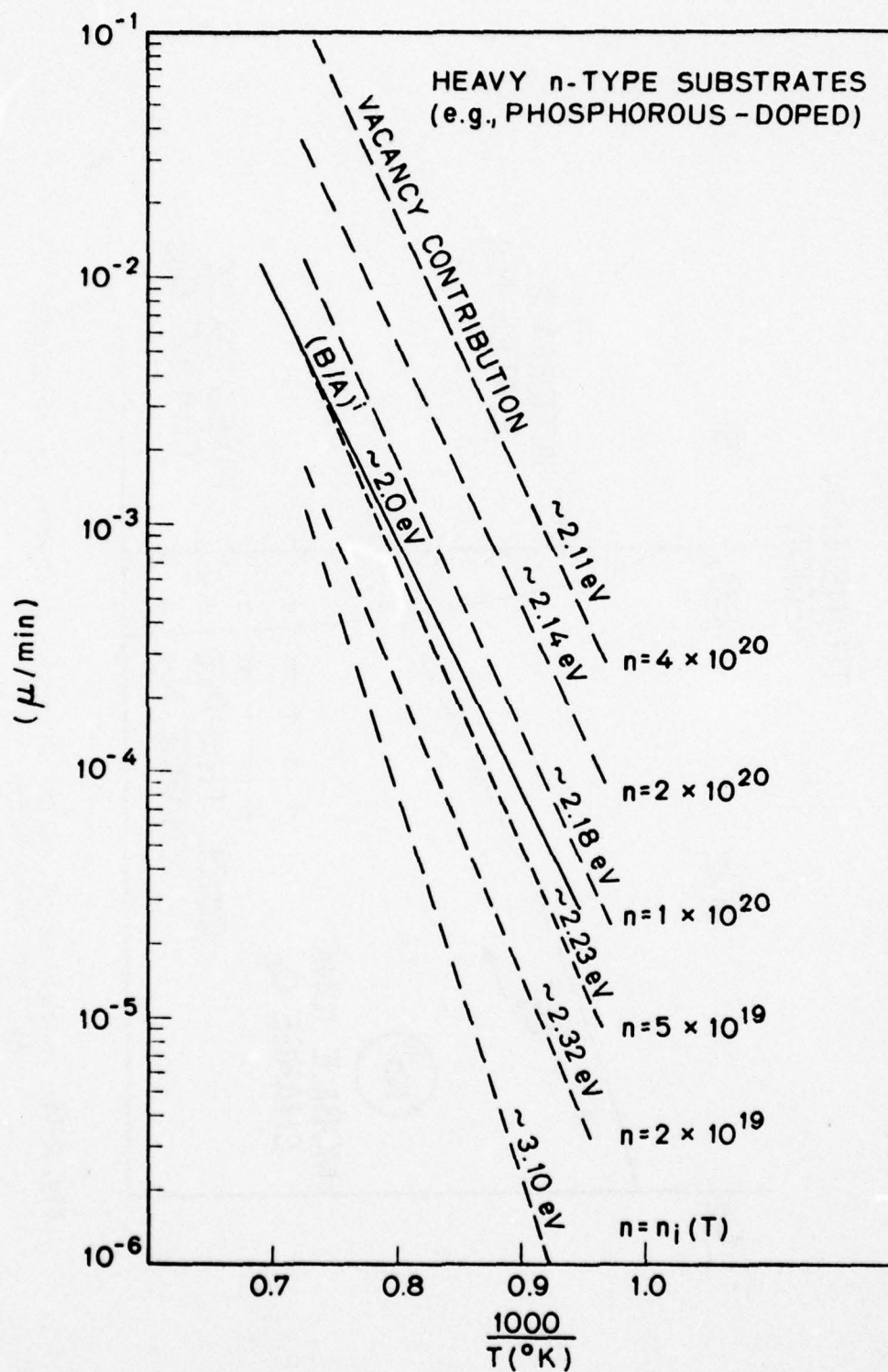


Fig. 2-25. Contributions to overall effective linear rate constant of  $(B/A)^1$  and vacancies.<sup>67</sup>

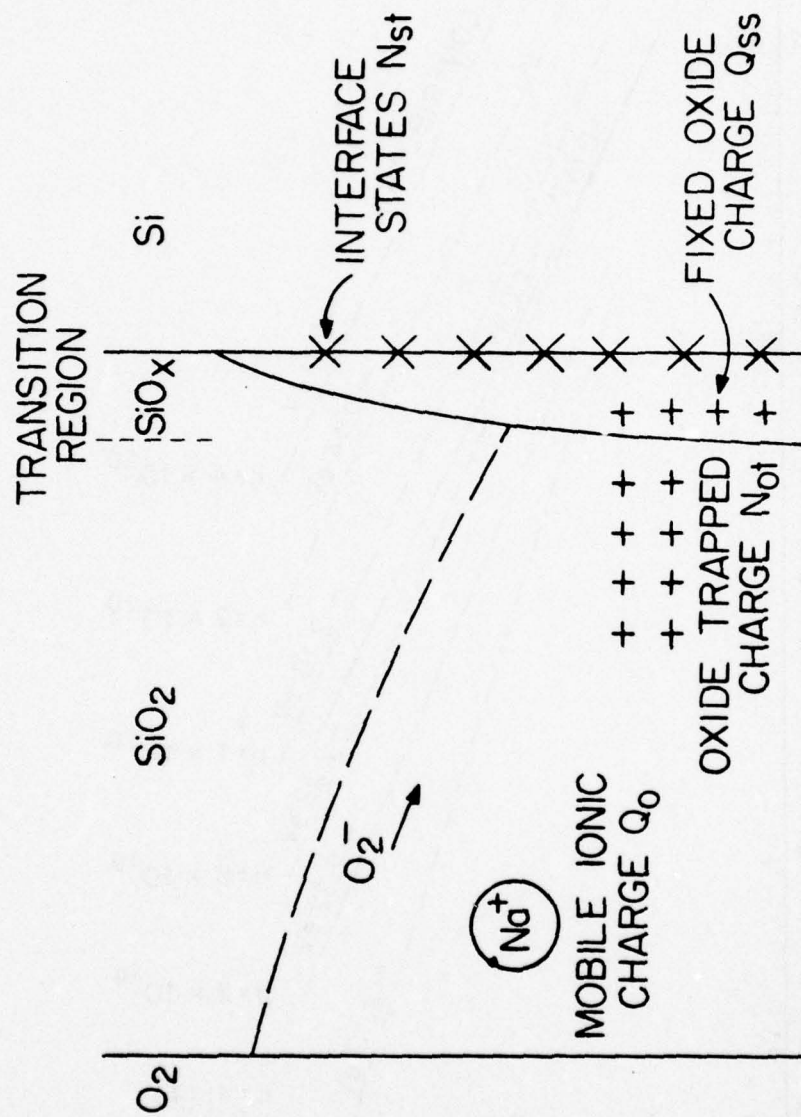
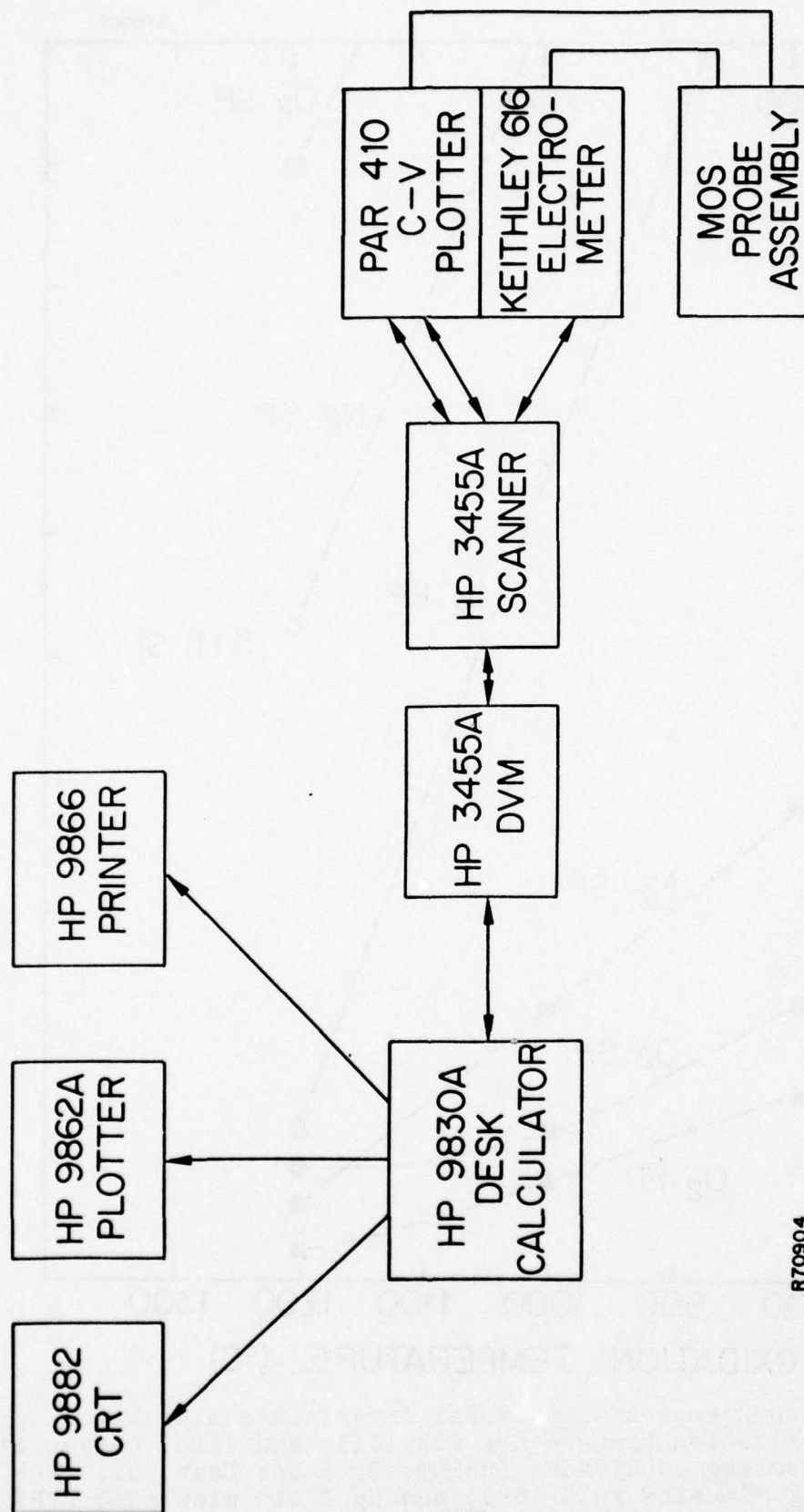


Fig. 2-26. Location of oxide charges in thermally oxidized silicon structure.



R70904

Fig. 2-27. Diagram of computerized quasistatic C-V system.

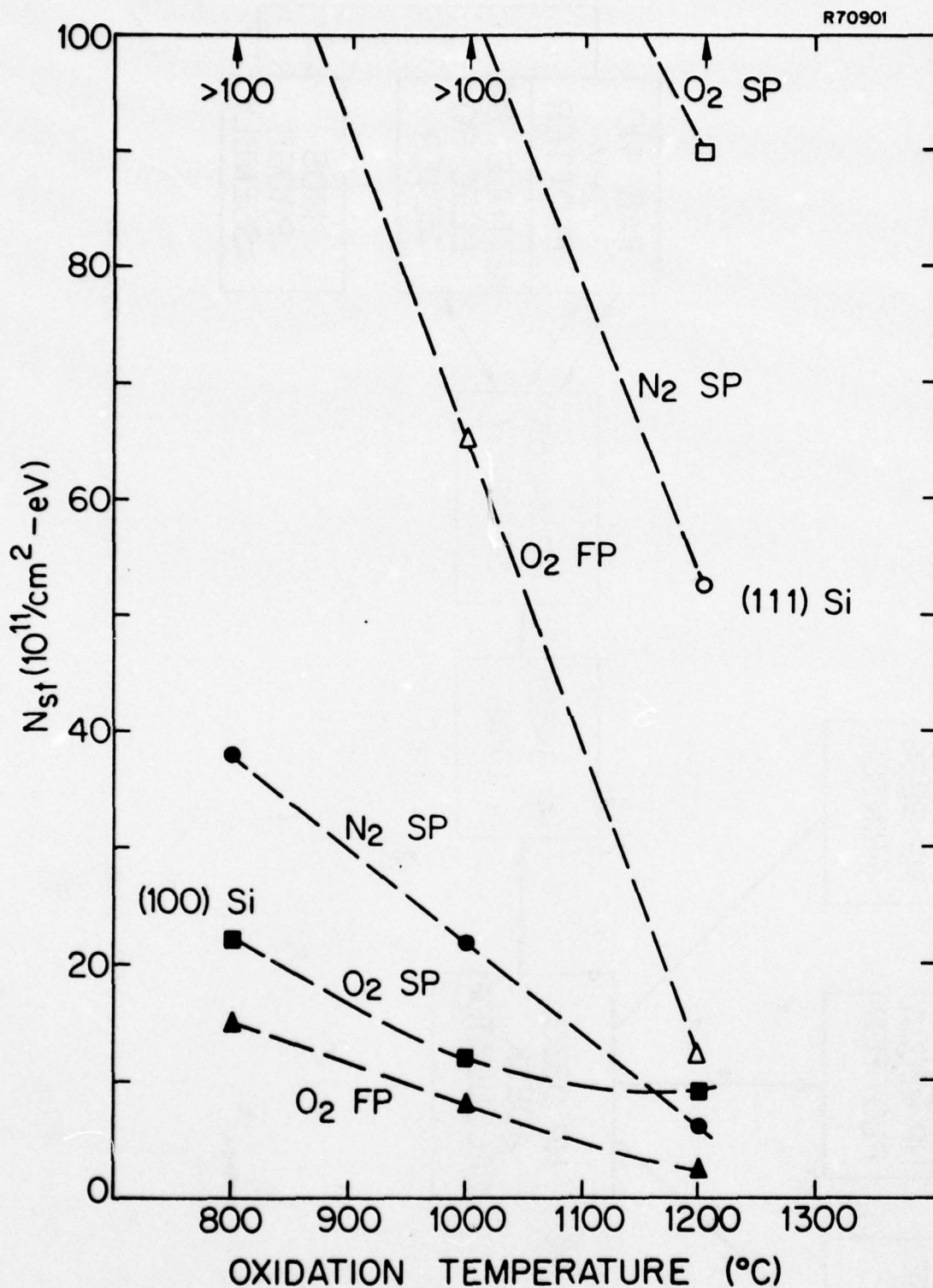


Fig. 2-28. Dependence of structural interface states  $N_{st}$  on dry  $O_2$  oxidation temperature for (111) and (100) n-type silicon. Cooling conditions include  $O_2$  3 sec fast pull (FP),  $O_2$  10 min slow pull (SP), and  $N_2$  2 min slow pull (SP). All reported values of  $N_{st}$  are at midgap.

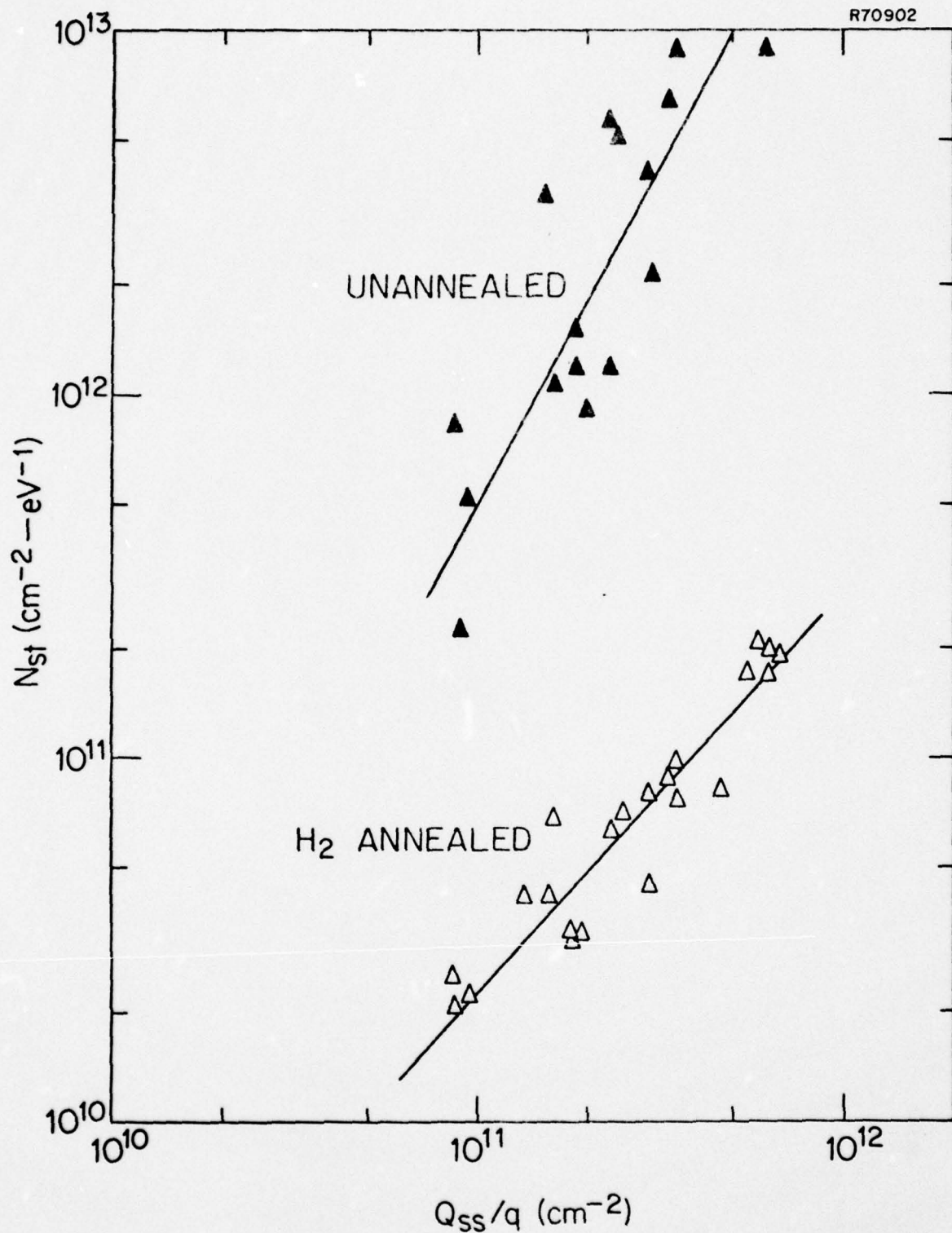


Fig. 2-29.  $N_{st}$  vs  $Q_{ss}/q$  for H<sub>2</sub> annealed (10% H<sub>2</sub>/N<sub>2</sub>, 10 min, 500°C) and unannealed n-type dry O<sub>2</sub> thermally oxidized silicon.

## Part 3

### CHEMICAL VAPOR DEPOSITION OF SILICON

K.C. Saraswat, R. Reif, T.I. Kamins and M. Mandurah

#### 3.1 INTRODUCTION

Chemical-vapor-deposition of silicon is one of the most important processes used for fabrication of integrated circuits. Epitaxial deposition of crystalline silicon on single crystal substrates is heavily used in integrated circuit technologies, such as bipolar,  $I^2L$ , DMOS, VMOS, oxide isolation and silicon on sapphire. Deposition of polycrystalline silicon has been the single most important factor in the success of silicon-gate MOS technology. Thus the control and predictability of chemical-vapor-deposition of single crystal and polycrystalline silicon is of utmost importance to the electronics industry.

One of the major areas in silicon epitaxy, which has been so far relatively poorly understood, is dopant inclusion. A model for the dopant inclusion into silicon epitaxial films is being developed at the Stanford Integrated Circuits Laboratory [3.1, 3.2, 3.3]. The feasibility of determination of transfer function of the dopant system of a horizontal, atmospheric-pressure, epitaxial reactor, by transient characterization was reported in the last year's annual report [3.4] of this program. The growth rate dependence of the transient and steady state response of the dopant system and a physico-chemical model for the dopant incorporation into silicon epitaxial films is presented here (section 3.2).

The transient and steady-state response of the dopant system were studied at different growth rates to learn the effect of the growth rate on the parameters entering into the transfer function. These experiments showed

the presence of a kinetic region of operation in which the rate-limiting step seems to be related to the growing surface. In the physicochemical model developed the different mechanisms entering into the doping process and their relative importance is analyzed using the model. The results which were obtained from the transient and steady-state study are used to confirm the model. It is shown that the transient and steady-state studies provide insights into different aspects of the dopant-incorporation process. The transfer function  $H(s)$  obtained experimentally in the previous paper, together with the growth-rate dependence of its parameters  $K$  and  $\tau$ , are derived using the model.

The second major area of our investigation is chemical-vapor-deposition of silicon. The structure of silicon films deposited by low-pressure, chemical vapor deposition in the 600°C temperature range has been investigated by x-ray diffraction and transmission electron microscopy. There is a critical temperature near 600°C, above which the deposited films are polycrystalline and below which amorphous films are obtained. This temperature is close to that used to deposit films for integrated-circuit applications. When the films are polycrystalline, the 110 texture dominates. The polycrystalline films are reasonably stable upon annealing to temperatures up to approximately 1100°C. The initially amorphous films, however, easily crystallize. Crystallization has been observed to be well advanced after annealing at 800°C. Large stresses are built into the amorphous films, while the stresses in the polycrystalline films are lower. The results of this work are described in Section 3.3.

### 3.2 EPITAXY

#### 3.2.1 TRANSIENT AND STEADY-STATE STUDY OF THE DOPANT SYSTEM

##### A. TRANSIENT STUDY

In order to relate the spatial variation of the doping concentration in the epitaxial layer  $N(x)$  to the time variation of the gas stream composition  $c(t)$ , the epitaxial reactor can be viewed as a "black-box" with  $c(t)$  as the input and  $N(x)$  as the output (Figure 3.1). If the black-box behaves linearly (within certain operation conditions), an expression  $h(t)$  characterizing the input-output relation of the reactor can be found experimentally by studying the step response of the reactor [3.1,3.4]. With that expression, using standard linear systems techniques, the response  $N(x)$  of the system to an arbitrary input  $c(t)$  can be easily computed and vice versa [3.4].

In addition to providing a method of fabricating a desired dopant profile, this transient response study provides basic information concerning the various mechanisms involved in the dopant incorporation process. As indicated by Kobayashi and Kobayshi [3.5], transient studies reveal the importance of various mechanisms which may not be apparent in steady-state studies.

All the experiments presented here were carried out in a commercially available (Unicorp Model HIER II) horizontal, water-cooled, rf-heated epitaxial reactor operating at atmospheric pressure. A schematic of this reactor is shown in Figure 3.2. The quartz reactor tube has the dimensions  $5.1 \times 8.3 \times 91.4 \text{ cm}^3$ . It has an effective cross section of  $27 \text{ cm}^2$  above the susceptor. The dimensions of the silicon-carbide-coated graphite susceptor were of  $0.64 \times 6.7 \times 22.8 \text{ cm}^3$ . A quartz susceptor cradle was used to tilt the susceptor to  $2^\circ$ . Dopant gases are delivered to the reactor tube through a double-dilution dopant system.

Hydrogen was used as the carrier gas at a velocity of 34 cm/sec (at room temperature). The source of silicon was silane obtained from Precision Gas Products, Inc. The doping source was approximately 70 ppm arsine in hydrogen obtained from the Matheson Gas Company, Inc.

Before each run, the susceptor was vapor phase etched with HCl and then coated with approximately 5  $\mu\text{m}$  of high resistivity silicon by the hydrogen reduction of  $\text{SiCl}_4$ . In a typical run, the susceptor and wafer are heated in hydrogen, vapor phase etched for two minutes by 1% HCl and deposited by the decomposition of  $\text{AsH}_3/\text{SiH}_4$ . The composition of the gas mixture was monitored and controlled through calibrated Brooks flowmeters. Temperature measurements were made during the etching and deposition reactions using a calibrated Leeds and Northrup optical pyrometer, and corrected for the emissivity of silicon [3.6] and for the absorption of the reactor tube walls. The corrected wafer surface temperature during etching and deposition were approximately 1180°C and 1070°C respectively. The substrates were chem-mechanically polished on one side, Czochralsky-grown, phosphorus doped, silicon wafers, with (100) orientation. The purpose of this experiment was to study the dopant distribution  $N(x)$  resulting from a step change in dopant gas flow, i.e. to determine the step response, and then to study the growth rate dependence of the step response of the dopant system of the reactor.

This experiment can be easily described with the help of Figure 3.3. At  $t = 0$  the deposition cycle started and silane and arsine were metered into the reactor tube. The silane flow was kept constant during the whole deposition cycle which ended at  $t = T_D$ . At  $t = T_D$  the arsine flow was abruptly changed to a lower value simulating a step change. This was accomplished by abruptly changing the flow setting on the flowmeter labeled "inject" in

Figure 3.2, since it is the nearest to the reactor tube. Hydrogen was flowing into the reactor before, during, and after the deposition cycle. The experiment was repeated four times, each time at a different growth rate. The silane partial pressure was adjusted for each experiment in the  $10^{-4}$  -  $10^{-3}$  atm. range to produce growth rates of 0.14, 0.32, 0.6 and 1.3  $\mu\text{m}/\text{min}$ . The dopant partial pressure was adjusted accordingly in the  $10^{-10}$  -  $10^{-9}$  atm. range to compensate for the difference in growth rate and keep the doping level changes in each experiment between  $1 \cdot 10^{15}$  and  $3 \cdot 10^{15} \text{ cm}^{-3}$ . The resulting impurity profiles in the epitaxial layers were determined by capacitance-voltage measurements on planar p-n junctions, mesa p-n junctions and deep-depletion MOS structures [3.7].

Typical results from the transient experiments are shown in Figure 3.4 together with the dopant gas flow input and a table indicating the values of  $T_0$  and  $T_D$  in each case where the measured dopant concentration is plotted as a function of distance from the surface of the epitaxial film for a decreasing step change in the dopant gas flow during the deposition [1]. The impurity profiles obtained for growth rates of 0.6 and 1.3  $\mu\text{m}/\text{min}$  are indistinguishable (solid curve), and both differ strongly from the one obtained at 0.14  $\mu\text{m}/\text{min}$ , which changes much more abruptly with distance (dashed curve).

An excellent fit to the data can be obtained by using the expression [3.3]

$$N(x) = N_I + (N_F - N_I) \left[ 1 - \exp \left( - \frac{x-x_0}{L(g)} \right) \right] \quad \text{for } x \geq x_0 \quad (3.1)$$

where:  $N(x)$  = dopant concentration at a distance  $x$  from the substrate

$N_I$  = initial doping level for  $x < x_0$

$N_F$  = final doping level

$L(g)$  = decay length (a function of the growth rate  $g$ )

$x_0$  = distance from the substrate at which the transient begins  
( $x_0 = g T_0$ )

The same expression also fits the doping profile corresponding to an increasing step change in the dopant gas flow [3.1].

The impulse response characterizing the input-output relation of the dopant system can be obtained from eq. (3.1) using elementary systems theory to be [3.8]

$$h(t) = \frac{K}{\tau} \exp\left(-\frac{t}{\tau}\right) \quad (3.2a)$$

$$H(s) = \frac{K}{\tau} \frac{1}{s + 1/\tau} \quad (3.2b)$$

$\tau \equiv L/g$  is the decay time of the dopant system: it corresponds physically to the time it takes to grow a thickness of epitaxial layer equal to one decay length.  $K$  is the proportionality factor relating the dopant concentration in the epitaxial layer ( $N$ ) to the gas phase concentration ( $c$ ) during growth under steady-state conditions (no transient effects, uniform doping distribution):  $N \equiv K \cdot c$ .  $K^{-1}$  represents what has sometimes been called the "effective segregation coefficient" [3.9].

Figures 3.5a and 3.5b show the decay length and decay time respectively as a function of growth rate. The dashed line in Figure 10b corresponds to a slope of -1 which in this log-log plot indicates the decay time values that are inversely proportional to the growth rate. At 0.6 and 1.3  $\mu\text{m}/\text{min}$ , the

decay lengths are equal (see Figure 3.4) and the decay times are proportional to  $g^{-1}$  - they fall exactly on the dashed line. At lower growth rates, the decay length decreases with decreasing growth rate and the decay time varies less rapidly than  $g^{-1}$  showing a trend to become constant at very low growth rates. An expression fitting the experimental points can be found to be:

$$L = \frac{K_0}{K_1 + K_2/g} \quad (3.3a)$$

$$\tau = \frac{K_0}{g(K_1 + K_2/g)} \quad (3.3b)$$

where  $g$  is the growth rate and  $K_0$ ,  $K_1$ ,  $K_2$  are constants.

#### B. STEADY-STATE STUDY

The steady-state experiments involved studying the effect of the silicon deposition rate on the impurity concentration of uniformly doped epitaxial layers. The arsine partial pressure was kept at  $6.2 \times 10^{-10}$  atm., and the silane partial pressure was adjusted to produce growth rates varying from 0.13  $\mu\text{m}/\text{min}$  to 1.2  $\mu\text{m}/\text{min}$  ( $2.7 \times 10^{-4}$  -  $2.3 \times 10^{-3}$  atm.). The substrates were boron-doped with resistivities ranging from 1-4 ohm-cm. The thicknesses of the epitaxial layers were kept between 5.5 and 8.1  $\mu\text{m}$  and were measured by a groove-and-stain technique. A four-point probe was used to determine the resistivity of the layers. Carrier concentrations were obtained from Irvin's resistivity data [3.10] and assumed to be equal to the arsenic concentration in the epitaxial layer.

The results from these experiments are shown in Figure 3.6, where the arsenic concentration of uniformly doped epitaxial layers is plotted versus silicon growth rate. At growth rates greater than approximately 0.6  $\mu\text{m}/\text{min}$ , the doping density becomes inversely proportional to the silicon deposition rate, as indicated by a slope of -1 on the log-log plot. At lower growth rates, the doping density varies less rapidly than  $g^{-1}$  and shows a trend toward becoming constant at very low growth rates. A very similar behavior has been observed by Shepherd [3.11], Bloem [3.9] and more recently by Duchemin [3.12]. An expression fitting the experimental data can be found to be:

$$N = \frac{1}{g(K_1' + K_2'/g)} \quad (3.4)$$

However, comparing Figure 3.5b and 3.6, we see that  $\tau$  vs.  $g$  and  $N$  vs.  $g$  curves have the same shape and more important the same slope for higher  $g$ . Therefore it is easy to visualize that  $K_1' = K_1$  and  $K_2' = K_2$ . Thus equation (3.4) becomes

$$K = \frac{N}{c} = \frac{1}{g(K_1 + K_2/g)} \quad (3.5)$$

The fact that at growth rates  $\geq 0.6 \mu\text{m}/\text{min}$  the decay time is proportional to  $g^{-1}$ , indicates that the transient dies out faster at higher growth rates. This in turn implies that the mechanisms responsible for the transient behavior must be associated with the growing surface. On the other hand, the fact that at  $g \geq 0.6 \mu\text{m}/\text{min}$  the doping density is proportional to  $g^{-1}$  indicates that the dopant incorporation process in this region of operation is kinetically controlled [3.13] by one or more rate-limiting steps.

It is thus possible that these rate-limiting steps are responsible for the transient behavior and are therefore related to the growing surface. This is in agreement with the fact that at lower growth rates the doping density tends to depart from the kinetic region and the decay time tends to become independent of the growth rate.

The temperature dependence of the As concentration in the Si epitaxial film is shown in Figure . The points marked with the same symbol (e.g. ) correspond to layers grown on the same day. Different symbols indicate different days separated by several months. Notice how a very slight increase in the deposition temperature (e.g. 1025°C to 1075°C) results in a strong decrease in the epitaxial As concentration. In all cases the epitaxial growth rate was the same ( $\sim 1.1 \mu\text{m}/\text{min}$ ) as expected, since the silicon deposition takes place under mass transport controlled conditions where the growth rate is almost unaffected by temperature changes. The slope in the figure correspond to approximately 30 kcal/mole. The implications of this experiment will be discussed later.

A physicochemical model, from where equations (3.2), (3.3) and (3.5) can be derived, will be the subject of the next section.

### 3.2.2 PHYSICOCHEMICAL MODEL OF THE DOPANT SYSTEM

In the previous section, transient and steady-state experimental studies of the dopant system of a horizontal, atmospheric-pressure, epitaxial reactor were presented. The purpose of that section was to find a transfer function that relates the time-variation of the gas-phase dopant ( $\text{AsH}_3$ ) concentration to the spatial variation of the epitaxial layer dopant (As) concentration. In this section, a model is presented that physically explains the experimental results of the previous section. It is shown that the transient and steady-state studies complement each other by revealing different aspects of the dopant-incorporation process.

The model considers processes occurring both in the gas phase and at the surface. The sequence of steps in the gas phase is shown in Figure 3.8: (1) Mass transport of the dopant compound ( $\text{AsH}_3$ ) from the reactor-tube entrance to the deposition region. (2) Mass transport of  $\text{AsH}_3$  from the well-mixed main gas stream through the boundary layer to the growing surface. (3) Gas-phase chemical reactions, in which  $\text{AsH}_3$  may dissociate into several different As-containing compounds, particularly  $\text{AsH}_2$ . The sequence of steps occurring at the surface is shown in Figure 3.9. (4) Adsorption of the As-containing compound on the growing surface. (5) Chemical dissociation into As and H in the adsorbed layer. (6) Surface diffusion and incorporation of adsorbed As at atomic steps and kink sites on the surface. (7) "Burying" of the incorporated As atoms by subsequently arriving Si atoms during epitaxial growth. (8) Desorption of hydrogen from the surface.

By analyzing the sequence of steps listed above, a model can be derived to describe mathematically the doping process. Under steady-state conditions all of the steps occur at the same rate. Under this condition the epitaxial-layer dopant distribution is uniform. However, when the dopant gas flow is

a function of time, the doping process may be in a transient state. During this transient, all of the steps involved in the doping process no longer occur at the same rate, and the correct physical picture is properly described by considering mass-balance of the As-containing compounds at each of the steps in the process.

1. Mass balance of AsH<sub>3</sub> within the deposition region:

$$\left[ \begin{array}{l} \text{rate at which} \\ \text{AsH}_3 \text{ enters} \\ \text{the deposition} \\ \text{volume} \end{array} \right] - \left[ \begin{array}{l} \text{rate at which} \\ \text{AsH}_3 \text{ leaves} \\ \text{the deposition} \\ \text{volume} \end{array} \right] - \left[ \begin{array}{l} \text{rate at which} \\ \text{AsH}_3 \text{ leaves} \\ \text{the main gas} \\ \text{stream towards} \\ \text{the wafer sur-} \\ \text{face} \end{array} \right] - \left[ \begin{array}{l} \text{rate of change of} \\ \text{AsH}_3 \text{ concentration} \\ \text{in the main gas} \\ \text{stream within the} \\ \text{deposition volume} \end{array} \right]$$

which can be mathematically expressed by:

$$\begin{aligned} N_{300} \cdot f_{H_2} \cdot x_{AsH_3}^i(t) - N_{300} \cdot f_{H_2} \cdot x_{AsH_3}^o(t) - k_m \cdot [x_{AsH_3}^g(x,t) - x_{AsH_3}^s(x,t)] \\ = V \cdot N_{T_G} \cdot \frac{\delta x_{AsH_3}^g(x,t)}{\delta t} \end{aligned} \quad (3.6)$$

where:

$x_{AsH_3}^i(x_{AsH_3}^o)$  is the AsH<sub>3</sub> molar fraction in the reactor tube before entering (after leaving) the deposition region

$N_{300}$  is the total gas phase concentration at 300 K

$f_{H_2}$  is the hydrogen flow at 300 K

$k_m$  is the boundary layer mass transport coefficient of AsH<sub>3</sub> in H<sub>2</sub>

$x_{AsH_3}^g$  is the AsH<sub>3</sub> molar fraction in the main gas stream within the deposition region. It is a function of position due to gas stream depletion of AsH<sub>3</sub> above the susceptor

$x_{\text{AsH}_3}^s$  is the gas phase  $\text{AsH}_3$  molar fraction above the gas-solid interface

$V$  is the volume of the deposition region

$N_{T_g}$  is the total gas phase concentration inside the deposition region.  
 $T_g$  is the temperature of the well-mixed gas stream within the deposition region.

Equation (3.6) can be simplified by assuming that  $\text{AsH}_3$  is a slow function of position within the deposition region. With this assumption:

$$N_{300} \cdot f_{\text{H}_2} \cdot \left[ x_{\text{AsH}_3}^i(t) - x_{\text{AsH}_3}^o(t) \right] - k_m \cdot \left[ \bar{x}_{\text{AsH}_3}(t) - x_{\text{AsH}_3}^s(t) \right] = V \cdot N_{T_g} \cdot \frac{d \bar{x}_{\text{AsH}_3}(t)}{dt} \quad (3.7)$$

where  $x_{\text{AsH}_3}^g(x,t)$  is replaced by the average value  $\bar{x}_{\text{AsH}_3}(t)$ .

This assumption will not cause serious errors because the deposition conditions were such that  $x_{\text{AsH}_3}^o \geq 0.95 x_{\text{AsH}_3}^i$ , i.e. less than 5% of the incoming  $\text{AsH}_3$  molecules take part in the doping process. Using the same argument, Eq. (3.7) can be further simplified to:

$$N_{300} \cdot f_{\text{H}_2} \cdot \left[ x_{\text{AsH}_3}^i(t) - \bar{x}_{\text{AsH}_3}(t) \right] - k_m \cdot \left[ \bar{x}_{\text{AsH}_3}(t) - x_{\text{AsH}_3}^s(t) \right] = V \cdot N_{T_g} \cdot \frac{d \bar{x}_{\text{AsH}_3}(t)}{dt} \quad (3.8)$$

where  $x_{\text{AsH}_3}^o$  is approximated by  $\bar{x}_{\text{AsH}_3}$ .

## 2. Mass balance of AsH<sub>3</sub> above the gas-crystal interface

$$\begin{aligned}
 & \left[ \begin{array}{l} \text{rate at which} \\ \text{AsH}_3 \text{ arrives} \\ \text{at the gas-} \\ \text{crystal inter-} \\ \text{face} \end{array} \right] - \left[ \begin{array}{l} \text{net rate of AsH}_3 \\ \text{adsorption on the} \\ \text{growing surface} \end{array} \right] - \left[ \begin{array}{l} \text{net rate of gas} \\ \text{phase chemical} \\ \text{reaction} \end{array} \right] = \left[ \begin{array}{l} \text{rate of change of} \\ \text{gas phase AsH}_3 \\ \text{concentration above} \\ \text{the gas-crystal} \\ \text{interface} \end{array} \right] \\
 & r_m - r_l - r_5 = V' \cdot N_{T_s} \cdot \frac{d x_{\text{AsH}_3}^s(t)}{dt} \\
 & \hspace{25em} (3.9)
 \end{aligned}$$

where  $V' \cdot N_{T_s}$  is the total number of gas molecules in a thin layer of volume  $V'$  above the gas-crystal interface which is at a temperature  $T_s$ .

$$r_m = k_m \cdot [\bar{x}_{\text{AsH}_3}(t) - x_{\text{AsH}_3}^s(t)] \quad (3.10)$$

The adsorption process is analyzed as follows:

$$\text{AsH}_3(g) + s \xrightleftharpoons[k_{r1}]{k_{f1}} \text{AsH}_3-s \quad K_1 = \frac{\theta_{\text{AsH}_3}}{x_{\text{AsH}_3}^s \cdot p_{\text{H}_2} \cdot \theta} = \frac{k_{f1}}{k_{r1}} \quad (2.3)$$

where

$s$  represents a free adsorption site on the surface

$\text{AsH}_3-s$  represents an  $\text{AsH}_3$  molecule adsorbed on the surface, i.e. occupying an adsorption site

$K_1$  is the equilibrium constant for the reaction

$\theta_{\text{AsH}_3}$  is the fraction of the total density of adsorption sites occupied by  $\text{AsH}_3$  molecules

$\theta$  is the fraction of the total density of adsorption sites which are vacant

$P_{H_2}$  is the hydrogen pressure (1 atm)

$k_{f1}$  ( $k_{r1}$ ) is the forward (reverse) rate constant for the adsorption reaction

The net rate of adsorption of  $AsH_3$  on the surface is given by:

$$r_1 = k_{f1} \cdot \theta \cdot P_{H_2} \cdot x_{AsH_3}^s(t) - k_{r1} \cdot \theta_{AsH_3}(t)$$

$$r_1 = k_{f1} \cdot \theta \cdot x_{AsH_3}^s(t) - k_{r1} \cdot \theta_{AsH_3}(t) \quad (3.12)$$

where  $\theta$  is assumed to be constant and equal to its equilibrium value, and

$P_{H_2}$  is replaced by 1 atm. (see Section 8).

$$r_1 = k_{f1} \cdot \theta \cdot \left[ x_{AsH_3}^s(t) - \frac{k_{r1}}{k_{f1}} \cdot \frac{\theta_{AsH_3}(t)}{\theta} \right]$$

$$r_1 = k_{f1} \cdot \theta \cdot \left[ x_{AsH_3}^s(t) - \frac{1}{K_1} \cdot \frac{\theta_{AsH_3}(t)}{\theta} \right]$$

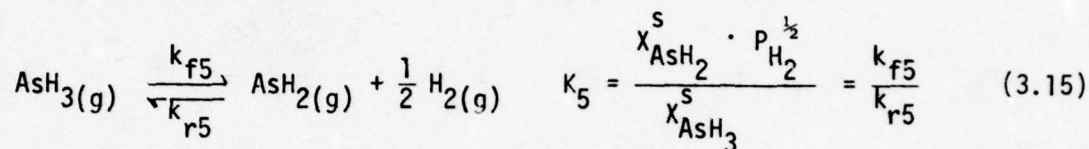
$$r_1 = k_{f1} \cdot \theta \cdot \left[ x_{AsH_3}^s(t) - x_{\theta_{AsH_3}}(t) \right] \quad (2.5)$$

where

$$x_{\theta_{AsH_3}}(t) \equiv \frac{1}{K_1} \cdot \frac{\theta_{AsH_3}(t)}{\theta} \quad (2.6)$$

is defined as the gas phase  $\text{AsH}_3$  molar fraction that would exist in instantaneous equilibrium with  $\theta_{\text{AsH}}(t)$ . The expression within brackets in Eq. (3.13) represents the driving force for the adsorption process. When  $x_{\text{AsH}_3}^s = x_{\theta_{\text{AsH}_3}}$ , then  $r_1 = 0$  and the adsorption process is in thermodynamic equilibrium.

The gas phase chemical reaction is analyzed analogously:



$$r_5 = k_{f5} \cdot x_{\text{AsH}_3}^s(t) - k_{r5} \cdot x_{\text{AsH}_2}^s(t)$$

$$r_5 = k_{f5} \cdot \left[ x_{\text{AsH}_3}^s(t) - \frac{1}{K_5} \cdot x_{\text{AsH}_2}^s(t) \right]$$

$$r_5 = k_{f5} \cdot \left[ x_{\text{AsH}_3}^s(t) - x_{x_{\text{AsH}_2}}(t) \right] \quad (3.16)$$

where

$$x_{x_{\text{AsH}_2}}(t) \equiv \frac{x_{\text{AsH}_2}^s(t)}{K_5} \quad (3.17)$$

is defined as the gas phase  $\text{AsH}_3$  molar fraction that would exist in equilibrium with  $x_{\text{AsH}_2}^s$ .

Substituting (3.10), (3.13), and (3.16) into (3.9), the following mass balance equation results:

$$\begin{aligned} k_m \left[ \bar{x}_{\text{AsH}_3}(t) - x_{\text{AsH}_3}^s(t) \right] - k_{f1} \cdot \theta \cdot \left[ x_{\text{AsH}_3}^s(t) - x_{\theta_{\text{AsH}_3}}(t) \right] - k_{f5} \cdot \left[ x_{\text{AsH}_3}^s(t) - x_{x_{\text{AsH}_2}}(t) \right] \\ = V \cdot N_{T_s} \cdot \frac{d x_{\text{AsH}_3}^s(t)}{d t} \end{aligned} \quad (3.18)$$

3. Mass balance of AsH<sub>2</sub> above the gas crystal interface.

$$\left[ \begin{array}{l} \text{net rate of} \\ \text{formation of} \\ \text{AsH}_2 \end{array} \right] - \left[ \begin{array}{l} \text{net rate of} \\ \text{adsorption of} \\ \text{AsH}_2 \text{ on the} \\ \text{surface} \end{array} \right] = \left[ \begin{array}{l} \text{rate of change of gas phase} \\ \text{AsH}_2 \text{ concentration above the} \\ \text{gas-crystal interface} \end{array} \right]$$

$$r_5 - r_6 = V' \cdot N_{T_s} \cdot \frac{d x_{\text{AsH}_2}^s(t)}{d t} \quad (3.19)$$

Adsorption of AsH<sub>2</sub>:

$$\text{AsH}_2(g) + s \xrightleftharpoons[k_{r6}]{k_{f6}} \text{AsH}_2\text{-s} \quad K_6 = \frac{\theta_{\text{AsH}_2}}{x_{\text{AsH}_2}^s \cdot p_{\text{H}_2} \cdot \theta} = \frac{k_{f6}}{k_{r6}} \quad (3.20)$$

$$r_6 = k_{f6} \cdot \theta \cdot x_{\text{AsH}_2}^s(t) - k_{r6} \cdot \theta_{\text{AsH}_2}(t)$$

$$r_6 = k_{f6} \cdot \theta \cdot [x_{\text{AsH}_2}^s(t) - x_{\text{AsH}_2}^{e6}(t)] \quad (3.3)$$

where

$$x_{\text{AsH}_2}^{e6}(t) \equiv \frac{1}{K_6} \cdot \frac{\theta_{\text{AsH}_2}(t)}{\theta} \quad (3.22)$$

is gas phase AsH<sub>2</sub> molar fraction that would exist in equilibrium with  $\theta_{\text{AsH}_2}(t)$ .

Equation (3.21) can also be expressed in terms of  $x_{\text{AsH}_3}$  by using Eq. (3.17) together with

$$x_{\theta_{\text{AsH}_2}}(t) \equiv \frac{1}{K_5} \cdot x_{\text{AsH}_2}^{e6}(t) \quad (3.23)$$

$$\left[ x_{\theta_{\text{AsH}_2}}(t) = \frac{\theta_{\text{AsH}_2}(t)}{K_5 \cdot K_6 \cdot \theta} \right] \quad (3.24)$$

$$r_6 = k_{f6} \cdot K_5 \cdot \theta \cdot \left[ x_{x_{\text{AsH}_2}}(t) - x_{\theta_{\text{AsH}_2}}(t) \right] \quad (3.25)$$

From (3.19), (3.16), (3.25), and (3.17):

$$\begin{aligned} k_{f5} \cdot \left[ x_{\text{AsH}_3}^s(t) - x_{x_{\text{AsH}_2}}(t) \right] - k_{f6} \cdot K_5 \cdot \theta \cdot \left[ x_{x_{\text{AsH}_2}}(t) - x_{\theta_{\text{AsH}_2}}(t) \right] \\ = V' \cdot N_{T_s} \cdot K_5 \cdot \frac{d x_{x_{\text{AsH}_2}}(t)}{d t} \end{aligned} \quad (3.26)$$

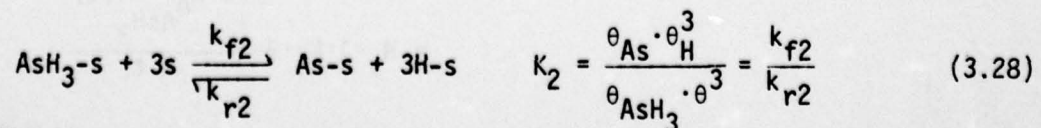
4. Mass balance of  $\text{AsH}_3$ -s ( $\text{AsH}_3$  adsorbed on the surface):

$$\left[ \begin{array}{l} \text{net rate of} \\ \text{adsorption} \\ \text{of } \text{AsH}_3 \text{ on} \\ \text{the surface} \end{array} \right] - \left[ \begin{array}{l} \text{net rate of} \\ \text{chemical} \\ \text{dissociation} \\ \text{of } \text{AsH}_3\text{-s} \end{array} \right] = \left[ \begin{array}{l} \text{rate of change of the} \\ \text{surface density of} \\ \text{AsH}_3\text{-s} \end{array} \right]$$

$$r_1 - r_2 = N_s \cdot A \cdot \frac{d \theta_{\text{AsH}_3}(t)}{d t} \quad (3.27)$$

where  $N_s$  is the total surface density of adsorption sites and  $A$  is the total deposition area.

The chemical reaction of  $\text{AsH}_3$ -s is:



$$r_2 = k_{f2} \cdot \theta^3 \cdot \theta_{AsH_3}(t) - k_{r2} \cdot \theta_H^3 \cdot \theta_{As}(t)$$

where  $\theta_H$  is assumed constant and equal to its equilibrium value (see Section 8).

$$r_2 = k_{f2} \cdot \theta^3 \cdot \left[ \theta_{AsH_3}(t) - \theta_{AsH_3}^{e2}(t) \right] \quad (3.29)$$

where

$$\theta_{AsH_3}^{e2} \equiv \frac{\theta_H^3 \cdot \theta_{As}(t)}{K_2 \cdot \theta^3} \quad (3.30)$$

Using Eq. (3.14) and

$$x_{\theta_{As}}(t) = \frac{1}{K_1} \cdot \frac{\theta_{AsH_3}^{e2}(t)}{\theta} \quad (3.40)$$

$$\left[ x_{\theta_{As}}(t) = \frac{\theta_H^3}{K_1 \cdot K_2 \cdot \theta^4} \cdot \theta_{As}(t) \right] \quad (3.41)$$

$$r_2 = k_{f2} \cdot K_1 \cdot \theta^4 \cdot \left[ x_{\theta_{AsH_3}}(t) - x_{\theta_{As}}(t) \right] \quad (3.42)$$

From Eqs. (3.27), (3.13), (3.42), and (3.14):

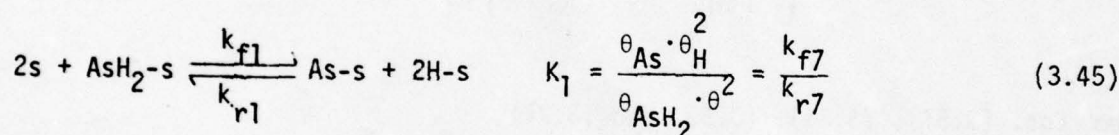
$$\begin{aligned} k_{f1} \cdot \theta \cdot \left[ x_{AsH_3}^s(t) - x_{\theta_{AsH_3}}(t) \right] - k_{f2} \cdot K_1 \cdot \theta^4 \cdot \left[ x_{\theta_{AsH_3}}(t) - x_{\theta_{As}}(t) \right] \\ = N_s \cdot A \cdot K_1 \cdot \theta \cdot \frac{d x_{\theta_{AsH_3}}(t)}{d t} \end{aligned} \quad (3.43)$$

5. Mass balance of AsH<sub>2</sub>-s (AsH<sub>2</sub> adsorbed on the surface)

$$\left[ \begin{array}{l} \text{net rate of adsorption} \\ \text{of AsH}_2 \text{ on the surface} \end{array} \right] - \left[ \begin{array}{l} \text{net rate of chemical} \\ \text{dissociation of AsH}_2\text{-s} \end{array} \right] = \left[ \begin{array}{l} \text{rate of change of the} \\ \text{surface density of} \\ \text{AsH}_2\text{-s} \end{array} \right]$$

$$r_6 - r_7 = N_s \cdot A \cdot \frac{d \theta_{\text{AsH}_2}}{d t} \quad (3.44)$$

The chemical reaction of AsH<sub>2</sub>-s is:



$$r_7 = k_{f7} \cdot \theta^2 \cdot \theta_{\text{AsH}_2}(t) - k_{r7} \cdot \theta_{\text{H}}^2 \cdot \theta_{\text{As}}(t)$$

$$r_7 = k_{f7} \cdot \theta^2 \cdot \left[ \theta_{\text{AsH}_2}(t) - \theta_{\text{AsH}_2}^{e7}(t) \right] \quad (3.46)$$

where

$$\theta_{\text{AsH}_2}^{e7}(t) \equiv \frac{\theta_{\text{H}}^2 \cdot \theta_{\text{As}}(t)}{K_7 \cdot \theta^2} \quad (3.47)$$

Using Eq. (3.22) and  $x_{\text{AsH}_2}^{e7}(t) \equiv \frac{\theta_{\text{AsH}_2}^{e7}(t)}{K_6 \cdot \theta}$  (3.48)

$$\left[ x_{\text{AsH}_2}^{e7}(t) = \frac{\theta_{\text{H}}^2}{K_6 \cdot K_7 \cdot \theta^3} \cdot \theta_{\text{As}}(t) \right] \quad (3.49)$$

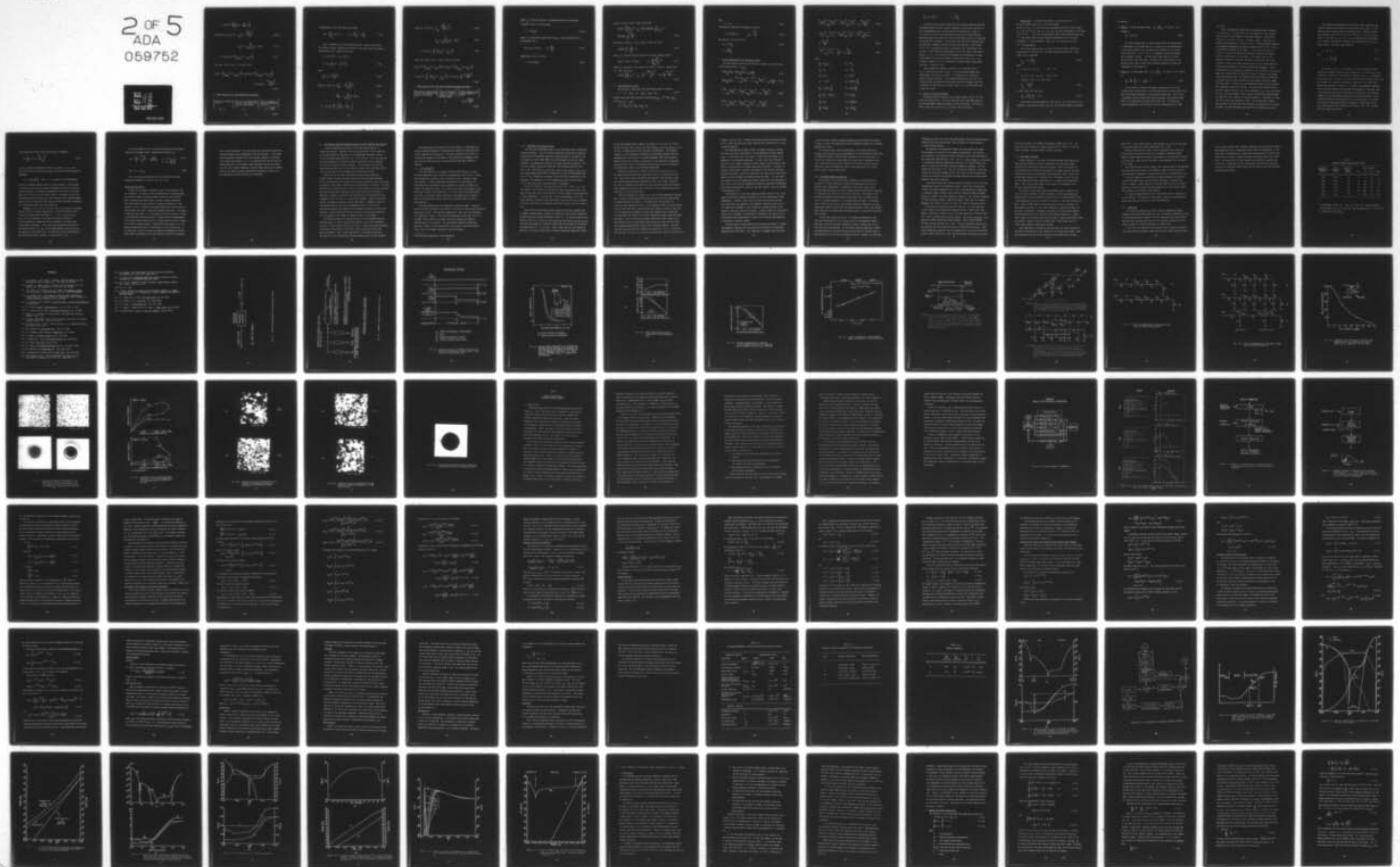
AD-A059 752

STANFORD UNIV CALIF INTEGRATED CIRCUITS LAB  
COMPUTER AIDED ENGINEERING OF SEMICONDUCTOR INTEGRATED CIRCUITS--ETC(U)  
JUL 78 J D MEINDL, K C SARASWAT, R W DUTTON DAAB07-77-C-2684  
DELET-TR-77-2684-2 NL

F/G 9/5

UNCLASSIFIED

2 OF 5  
ADA  
059752



$$r_7 = k_{f7} \cdot K_6 \cdot \theta^3 \cdot \left[ x_{AsH_2}^{e6}(t) - x_{AsH_2}^{e7}(t) \right]$$

And using Eq. (3.23) and  $x_{\theta_{As}}(t) \equiv \frac{x_{AsH_2}^{e.7}(t)}{K_5}$  (3.50)

$$x_{\theta_{As}}(t) = \frac{\theta_H^2}{K_5 \cdot K_6 \cdot K_7 \cdot \theta^3} \cdot \theta_{As}(t) \quad (3.51)$$

$$r_7 = k_{f7} \cdot K_6 \cdot K_5 \cdot \theta^3 \cdot \left[ x_{\theta_{AsH_2}}(t) - x_{\theta_{As}}(t) \right] \quad (3.52)$$

From Eqs. (3.51), (3.24), (3.53) and (3.24),

$$\begin{aligned} k_{f6} \cdot K_5 \cdot \theta \cdot \left[ x_{AsH_2}(t) - x_{\theta_{AsH_2}}(t) \right] - k_{f7} \cdot K_6 \cdot K_5 \cdot \theta^3 \cdot \left[ x_{\theta_{AsH_2}}(t) - x_{\theta_{As}}(t) \right] \\ = N_s \cdot A \cdot K_5 \cdot K_6 \cdot \theta \cdot \frac{d x_{\theta_{AsH_2}}(t)}{d t} \end{aligned} \quad (3.53)$$

6. Mass balance of As-s (As adsorbed on the surface):

$$\left[ \begin{array}{c} \text{net rate of formation} \\ \text{of As-s} \\ r_2 + r_7 \end{array} \right] - \left[ \begin{array}{c} \text{net rate of incorporation} \\ \text{of As-s into step or kink} \\ \text{sites on the surface} \\ r_3 \end{array} \right] = \left[ \begin{array}{c} \text{rate of change of} \\ \text{the surface density} \\ \text{of As-s} \\ N_s \cdot A \cdot \frac{d \theta_{As}(t)}{d t} \end{array} \right] \quad (3.54)$$

Incorporation of As-s into step or kink sites:

$$\text{As-s} \xrightleftharpoons[k_{r3}]{k_{f3}} \text{As-s}^i + s \quad K_3 = \frac{\theta_{\text{As}}^i \cdot \theta}{\theta_{\text{As}}} = \frac{k_{f3}}{k_{r3}} \quad (3.55)$$

$\text{As-s}^i$  represents an As atom incorporated into a step or kink site on the surface, and  $\theta_{\text{As}}^i$  represents the fraction of the total density of surface incorporation sites occupied by As atoms.

$$r_3 = k_{f3} \cdot \theta_{\text{As}}(t) - k_{r3} \cdot \theta \cdot \theta_{\text{As}}^i(t)$$

$$r_3 = k_{f3} \cdot \left[ \theta_{\text{As}}(t) - \theta_{\text{As}}^{e2}(t) \right] \quad (3.56)$$

where

$$\theta_{\text{As}}^{e2}(t) \equiv \frac{\theta \cdot \theta_{\text{As}}^i(t)}{K_3} \quad (3.57)$$

Using Eq. (3.30) and  $\theta_{\text{AsH}_3}^{e3} \equiv \frac{\theta_{\text{H}}^3 \cdot \theta_{\text{As}}^{e2}(t)}{K_2 \cdot \theta^3} \quad (3.58)$

$$\theta_{\text{AsH}_3}^{e3} = \frac{\theta_{\text{H}}^3}{K_2 \cdot K_3 \cdot \theta^2} \cdot \theta_{\text{As}}^i(t) \quad (3.59)$$

$$r_3 = k_{f3} \cdot K_2 \cdot \frac{\theta^3}{\theta_{\text{H}}^3} \cdot \left[ \theta_{\text{AsH}_3}^{e2} - \theta_{\text{AsH}_3}^{e3} \right] \quad (3.60)$$

Using Eq. (3.40) and 
$$x_{\theta_{As}^i} \equiv \frac{\theta_{AsH_3}^3(t)}{K_1 \cdot \theta} \quad (3.61)$$

$$x_{\theta_{As}^i} = \frac{\theta_H^3}{K_1 \cdot K_2 \cdot K_3 \cdot \theta^3} \cdot \theta_{As}^i(t) \quad (3.62)$$

$$r_3 = k_{f3} \cdot K_2 \cdot K_1 \cdot \frac{\theta^4}{\theta_H^3} \left[ x_{\theta_{As}}(t) - x_{\theta_{As}^i}(t) \right] \quad (3.63)$$

From Eqs. (3.54), (3.42), (3.52), (3.63), and (3.41):

$$\begin{aligned} & k_{f2} \cdot K_1 \cdot \theta^4 \cdot \left[ x_{\theta_{AsH_3}}(t) - x_{\theta_{As}}(t) \right] + k_{f7} \cdot K_6 \cdot K_5 \cdot \theta^3 \cdot \left[ x_{\theta_{AsH_2}}(t) - x_{\theta_{As}}(t) \right] \\ & - k_{f3} \cdot K_2 \cdot K_1 \cdot \frac{\theta^4}{\theta_H^3} \cdot \left[ x_{\theta_{As}}(t) - x_{\theta_{As}^i}(t) \right] = N_s \cdot A \cdot K_2 \cdot K_1 \cdot \frac{\theta^4}{\theta_H^3} \cdot \frac{d x_{\theta_{As}}(t)}{d t} \end{aligned} \quad (3.64)$$

7. Mass balance of As-s<sup>i</sup> (As atoms occupying incorporation sites)

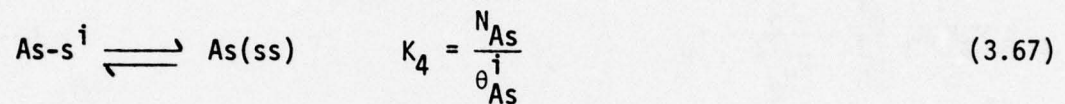
$$\begin{aligned} & \left[ \begin{array}{l} \text{net rate of incorporation} \\ \text{of As-s into step or kink} \\ \text{sites on the surface} \end{array} \right] - \left[ \begin{array}{l} \text{rate of "burying"} \\ \text{As-s}^i \text{ by silicon} \\ \text{atoms, i.e. epi-} \\ \text{taxial growth} \end{array} \right] = \left[ \begin{array}{l} \text{rate of change of the} \\ \text{surface density of} \\ \text{As-s}^i \end{array} \right] \\ & r_3 \quad \quad \quad - \quad \quad \quad r_4 \quad \quad \quad = \quad \quad \quad N_s^i \cdot A \cdot \frac{d \theta_{As}^i(t)}{d t} \end{aligned} \quad (3.65)$$

where  $N_{s^i}$  is the total density of incorporation sites on the surface.

"Burying" of  $As-s^i$  by silicon atoms:

$$r = g \cdot A \cdot N_{As}(t) \quad (3.66)$$

where  $g$  is the epitaxial growth rate and  $N_{As}$  is the As concentration in the epitaxial film.



Substituting (3.67) in (3.66):

$$r = g \cdot A \cdot K_4 \cdot \theta_{As}^i(t) \quad (3.68)$$

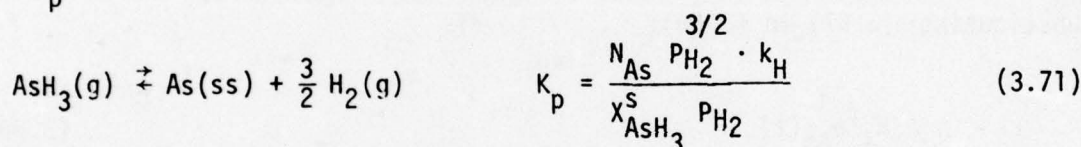
From Eqs. (3.65), (3.63), (3.68), and (3.62):

$$k_{f3}K_2K_1 \frac{\theta^4}{\theta_H^3} \left[ x_{\theta_{As}}(t) - x_{\theta_{As}^i}(t) \right] - gAK_4K_3K_2K_1 \frac{\theta^3}{\theta_H^3} x_{\theta_{As}^i}(t) = N_s iAK_3K_2K_1 \frac{\theta^3}{\theta_H^3} \frac{dx_{\theta_{As}^i}}{dt} \quad (3.69)$$

Notice that, from Eqs. (3.11), (3.28), (3.55), and (3.67):

$$K_4K_3K_2K_1 \frac{\theta^3}{\theta_H^3} = \frac{K_p}{p_{H_2}^{3/2}} = K_p \quad (3.70)$$

where  $K_p$  is the equilibrium constant for the overall doping reaction:



where  $k_H$  is the Henry's law constant for arsenic in silicon. Substituting

Eq. (3.70) into (3.69):

$$k_{f3}K_2K_1 \frac{\theta^4}{\theta_H^3} \left[ x_{\theta_{As}}(t) - x_{\theta_{As}^i}(t) \right] - \frac{gAK_p x_{\theta_{As}^i}(t)}{k_H} = N_s iA \frac{K_p}{K_4} \frac{dx_{\theta_{As}^i}}{dt} \quad (3.72)$$

#### 8. Determination of $\theta$ and $\theta_H$

The fraction of adsorption sites that remains vacant is given by:

$$\theta = 1 - \theta_H - \theta_{SiH_4} - \theta_{Si} - \theta_{AsH_3} - \theta_{AsH_2} - \theta_{As} \quad (3.73)$$

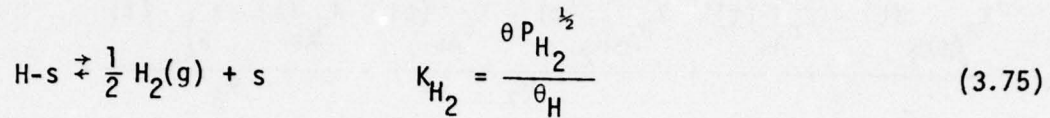
Assuming that under normal operation conditions ( $x_{SiH_4} \approx 10^{-3}$  atm,  $x_{AsH_3} \approx 10^{-10}$  atm,  $P_{H_2} = 1$  atm)

$$\theta_H \gg \theta_{SiH_4}, \theta_{Si}, \theta_{AsH_3}, \theta_{AsH_2}, \theta_{As}$$

Then

$$\theta = 1 - \theta_H \quad (3.74)$$

The adsorption reaction for hydrogen is given by:



and from Eqs. (3.74) and (3.75):

$$\theta_H = \frac{1}{1 + K_{H_2}} \quad (3.76)$$

$$\theta = \frac{K_{H_2}}{1 + K_{H_2}}$$

#### 9. Circuit Representation for the Dopant System

The final equation in each of the sections 1 through 7 may be rewritten in the following form ( $X \equiv X_{AsH_3}$ )

$$\frac{X^1(t) - \bar{X}(t)}{R_M} - \frac{\bar{X}(t) - X^S(t)}{R_M} = C_M \frac{d\bar{X}(t)}{dt} \quad (3.78)$$

$$\frac{\bar{X}(t) - X^S(t)}{R_M} - \frac{X^S(t) - X_{\theta_{AsH_3}}(t)}{R_1} - \frac{X^S(t) - X_{X_{AsH_2}}(t)}{R_5} = C_M \frac{dX^S(t)}{dt} \quad (3.79)$$

$$\frac{X^S(t) - X_{X_{AsH_2}}(t)}{R_5} - \frac{X_{X_{AsH_2}}(t) - X_{\theta_{AsH_2}}(t)}{R_6} = C_5 \frac{dX_{X_{AsH_2}}(t)}{dt} \quad (3.80)$$

$$\frac{X^S(t) - X_{\theta_{AsH_3}}(t)}{R_1} - \frac{X_{\theta_{AsH_3}}(t) - X_{\theta_{As}}(t)}{R_2} = C_1 \frac{dX_{\theta_{AsH_3}}(t)}{dt} \quad (3.81)$$

$$\frac{x_{x_{AsH_2}}(t) - x_{\theta_{AsH_2}}(t)}{R_6} - \frac{x_{\theta_{AsH_2}}(t) - x_{\theta_{As}}(t)}{R_7} = C_6 \frac{dx_{\theta_{AsH_2}}(t)}{dt} \quad (3.82)$$

$$\frac{x_{\theta_{AsH_3}}(t) - x_{\theta_{As}}(t)}{R_2} + \frac{x_{\theta_{AsH_2}}(t) - x_{\theta_{As}}(t)}{R_7} - \frac{x_{\theta_{As}}(t) - x_{\theta_{As}^i}(t)}{R_3} = C_2 \frac{dx_{\theta_{As}}(t)}{dt} \quad (3.83)$$

$$\frac{x_{\theta_{As}}(t) - x_{\theta_{As}^i}(t)}{R_3} - \frac{x_{\theta_{As}^i}}{R_p} = C_3 \frac{dx_{\theta_{As}^i}}{dt} \quad (3.84)$$

where:

$$\frac{1}{R_M} = N_{300} f_{H_2}$$

$$C_M = VN_{T_g}$$

$$\frac{1}{R_m} = k_M$$

$$C_m = V' N_{T_s}$$

$$\frac{1}{R_1} = k_{f1} \theta$$

$$C_1 = N_s A K_1 \theta$$

$$\frac{1}{R_2} = k_{f2} K_1 \theta^4$$

$$C_2 = N_s A K_1 K_2 \frac{\theta^4}{\theta_H^3}$$

$$\frac{1}{R_3} = k_{f3} K_2 K_1 \frac{\theta^4}{\theta_H^3}$$

$$C_3 = N_s i A \frac{K_p}{K_4 K_H}$$

$$\frac{1}{R_p} = \frac{g}{R_p} = g A K_p / k_H$$

$$C_5 = V' N_{T_s} K_5$$

$$\frac{1}{R_5} = k_{f5}$$

$$C_6 = N_s A K_5 K_6 \theta$$

$$\frac{1}{R_6} = k_{f6} K_5 \theta$$

$$\theta_H = \frac{1}{1 + K_{H_2}}$$

$$\frac{1}{R_7} = k_{f7} K_6 K_5 \theta^3$$

$$\theta = \frac{K_{H_2}}{1 + K_{H_2}}$$

In order to have a better insight into the different mechanisms entering the doping process and their relative importance, an equivalent electric circuit corresponding to Eqs. (3.78)-(3.84) can be derived and is shown in Fig. 3.10. This circuit can be considered as the circuit representation of the dopant system since both, the circuit and the dopant system, are described by the same set of equations. On the other hand, the circuit representation also provides a method for solving the system of equations. The Rs and Cs in Fig. 3.10 correspond to electric "resistances" and "capacitances" respectively. Each resistance R correspond to each of the steps in the doping process, i.e.  $R_1$  is the resistance corresponding to the adsorption of  $AsH_3$ ,  $R_7$  corresponds to the surface chemical dissociation of  $AsH_2$ -s, etc. The "current"  $r$  shown in Fig. 3.10 represents the actual dopant incorporation rate into the epitaxial film.

Under steady-state operation conditions, the right-hand side of Eqs. (3.78)-(3.84) are equal to zero, i.e. the capacitance becomes zero and disappear from the circuit model. The capacitors are needed only during transient conditions. They represent the physical fact that, in a transition from one steady-state operating condition to another, some time is required for the densities of  $AsH_3(g)$ ,  $AsH_3$ -s, etc. to attain their new steady-state values.

#### 10. Analysis of the Circuit Model

The steady-state and transient circuit models shown in Figs. 3.10 and 3.10b are analyzed below. It will be shown that the circuit model explains all the experimental results presented in the previous paper. We first consider steady-state and then the more general time varying case.

Steady-State: To simplify the analysis, two limiting cases of the circuit model shown in Fig. 3.10 are considered:

(i)  $R_5 + R_6 + R_7 \gg R_1 + R_2$ , with the corresponding simplified circuit shown in Fig. 3.11a and (ii)  $R_5 + R_6 + R_7 \ll R_1 + R_2$ , with the corresponding circuit shown in Fig. 3.11b.  $R_M$  is not included because under normal operation conditions it is much smaller than the value obtained experimentally for the overall resistance, i.e.  $(R_M)$  calculated  $\ll [R_M + R_m + (R_1 + R_2)/(R_5 + R_6 + R_7) + R_3 + R_p]_{\text{experimental}}$ .

The circuits shown in Figs. 3.11a and 3.11b can be used to derive the doping density in the epitaxial film under steady-state conditions. Using common circuit techniques:

$$X_{\theta_{As}}^i = X^i \frac{R_p}{R + R_p} \quad (3.85)$$

where:

$$R \equiv R_m + R_1 + R_2 + R_3 \quad (\text{Fig. 3.11a})$$

or

$$R \equiv R_m + R_5 + R_6 + R_7 + R_3 \quad (\text{Fig. 3.11b})$$

From Eqs. (3.41), (7.3), and (3.70)

$$X_{\theta_{As}}^i = \frac{N_{As} k_H}{K_p} \quad (3.86)$$

so that, from (3.85) and (3.86)

$$N_{As} = \frac{R_p}{R + R_p} \frac{K_p}{k_H} X^i = KX^i \quad (3.87)$$

Notice the similarity between Eq. (3.87) and Eq. (3.5) from section 3.2.1. Depending on the epitaxial growth rate used, two limiting regions of operation

are apparent.

- a. Region I: at very low growth rates  $R_p = \frac{k_H}{g \cdot A \cdot K_p} \gg R$  and Eq. (3.87)

reduces to:

$$N_{As} \approx K_p \cdot X^i / k_H \quad (3.88)$$

Eq. (3.88) indicates that at very low growth rates the doping process is independent of the growth rate and is controlled by the thermodynamics of the doping reaction ( $K_p$  is the equilibrium constant for the overall doping reaction, Eq. (3.71)). This is in agreement with the experimental data presented in Figure of the previous paper, where it is shown that at growth rates lower than  $\sim 0.5 \mu\text{m}/\text{min}$  the arsenic density in the epitaxial layer shows a trend towards becoming constant and growth rate independent of the growth rate.

- b. Region II: at high growth rates  $R_p = \frac{k_H}{g \cdot A \cdot K_p} \ll R$  and Eq. (3.87) reduces to

$$N_{As} = \frac{R_p}{R} \cdot \frac{K_p}{k_H} \cdot X^i = \frac{1}{g \cdot A \cdot R} \cdot X^i \quad (3.89)$$

In this region of operation the dopant incorporation rate is controlled by the reaction kinetics, and the doping density in the epitaxial film must be inversely proportional to the epitaxial growth rate. This is also in agreement with the steady-state results presented in the previous paper, where it was shown that for growth rates higher than  $\sim 0.5 \mu\text{m}/\text{min}$  the arsenic concentration in the epitaxial film was proportional to  $g^{-1}$  (see

Fig. 3.6).

So far, the model has agreed with the steady-state data presented in section 3.2.1. The next step is to find whether the rate-limiting step in region II corresponds to a gas phase mechanism, in which case using Fig. 3.11b (Fig. 3.11a):  $R_m \gg R_1 + R_2 + R_3$  ( $R_m + R_5 \gg R_6 + R_7 + R_3$ ), or a surface related mechanism, in which case  $R_m \ll R_1 + R_2 + R_3$  ( $R_m + R_5 \ll R_6 + R_7 + R_3$ ). The temperature dependence experiments presented in section 3.2.1 allow us to differentiate between the two cases. It was shown in section 3.2.1 (Figure 3.7) that as the deposition temperature increases, the doping density in the epitaxial film decreases. This implies that, as the deposition temperature increases, the dopant incorporation rate or the "current" in the circuit model decreases, which in turn implies that the resistance corresponding to the rate-limiting step increases. A quick consideration of the temperature dependence of the resistances in the circuit model will indicate that the rate-limiting step is related to the surface rather than the gas phase. The boundary layer mass transport coefficient  $k_m$  usually increases with temperature with an apparent activation energy of 3-8 kcal/mole. Therefore, the corresponding resistance  $R_m$  will decrease with temperature rather than increase. The forward rate constant for the gas phase chemical reaction  $k_{f5}$  can be expressed as  $k_{f5} = k_{f0} \cdot \exp(-E_a/kT)$  with  $k_{f0}$  being the frequency factor and  $E_a$  the Arrhenius activation energy.  $E_a$  could be as low as zero but it can not be negative. Therefore,  $R_5 = 1/k_{f5}$  will not increase with temperature either. On the other hand, nothing that concrete can be said about the resistances corresponding to the surface reactions.  $R_3$ , the resistance associated with the incorporation of As-s

The transient study presented in the previous paper showed that the transient response was exponential with one single decay time, i.e., the dopant system using  $\text{AsH}_3$  contains one dominant pole. Therefore, either the capacitors at the left of  $R_6$  in Fig. 3.12C ( $C_g \equiv C_m + C_5$ ) or the capacitors at the right ( $C_s \equiv C_6 + C_2 + C_3$ ) are responsible for that dominant pole. However, the nature of the decay times associated with  $C_g$  and  $C_s$  are different. They can be approximated by

$$\tau_g \approx C_g \cdot R_m \quad (3.91)$$

and

$$\tau_s \approx C_s \cdot \frac{R_p \cdot R_6}{R_p + R_6} \quad (3.92)$$

It was shown in Fig. 3.5 of section 3.2.1 that at high growth rates the decay time depends strongly on the growth rate. This rules out  $C_g$  as the capacitance responsible for the dominant exponential since  $\tau_g$  is independent of the growth rate. Moreover, Eq. (3.92) looks very much the same as Eq. (3.3b) from section 3.2.1, which was an empirical expression fitting the experimental data presented in Figure 3.5. In summary, the exponential character of the transient response and the growth rate dependence of the decay time led to the conclusion that the capacitances responsible for the transient response are the capacitances associated with surface mechanisms. These surface capacitances correspond physically to the fact that, in a transition from one steady-state condition to another, it takes some time for the surface density of the adsorbed species,  $\text{AsH}_3$ -s, As-s, etc., to reach their new steady-state values.

into atomic step or kink sites, can be taken as an example.

$$R_3 = \left[ k_{f3} \cdot K_2 \cdot K_1 \cdot \frac{K_{H_2}^4}{1 + K_{H_2}} \right]^{-1} \quad (3.90)$$

$k_{f3}$  has a temperature dependence similar to  $k_{f5}$  above.  $K_1$ ,  $K_2$ , and  $K_{H_2}$ , being reaction equilibrium constants, have the following temperature dependence:

$$K = K_0 \exp \left( - \frac{\Delta H}{RT} \right) \quad \text{where } \Delta H \text{ is the heat of the corresponding}$$

reaction at constant pressure and  $R$  is the gas constant. Since the heat of reactions and activation energies corresponding to most of the doping steps are unknown, the temperature dependence of expressions of the type shown in Eq. (3.90) can not be stated a priori. In summary, the fact that the doping density in the epitaxial layer decreases with increasing temperatures, led to the conclusion that the rate-limiting resistance corresponds to a surface step rather than a gas phase step.

Transient: Figs. 3.12a and 3.12b show the circuit models corresponding to cases (i) and (ii) above, respectively. If one of the kinetic resistances is much larger than the others, e.g. if  $R_6 \gg R_m, R_5, R_7, R_1, R_2$ , (Fig. 3.12b) the "potential" drop across the smaller resistances will be negligible in comparison with the "potential" drop across the larger kinetic resistance. In this case, the capacitors at the left of the larger resistance, e.g.  $R_6$ , can be lumped together, and similarly for the capacitor at the right of  $R_6$ . The simplified circuit, assuming  $R_6$  as the rate-limiting step in region II, is shown in Fig. 3.12c.

The circuit model of Fig. 3.11c can be used to derive the transfer function of the dopant system. Neglecting the effect of  $C_g$ :

$$H(s) = \frac{N_{As}}{X_i} = \frac{K_p X_{\theta As}^i}{k_H X_i} = \frac{K_p R_p}{k_H (R + R_p)} \cdot \frac{1}{1 + s C_s \cdot \frac{R_p \cdot R_p}{R_p + R_s}} \quad (3.93)$$

$$H(s) = K \cdot \frac{1}{1 + s \tau_s} \quad (3.94)$$

This is exactly the same expression for the transfer function obtained experimentally in section 3.2.1 (Eq. 3.2b).

#### Summary and Conclusions

A model for the dopant incorporation into silicon epitaxial films was introduced. An electric circuit representation of the doping model was derived in order to provide a better insight into the different steps intervening the doping process and their relative importance. The circuit model was used to derive the doping concentration in the epitaxial film as a function of gas-phase dopant molar fraction and epitaxial growth rates under steady-state operation conditions. Two regions of operation were found: (i) a low-growth rate region (region I) in which it was shown that the doping process is controlled by the thermodynamics of the overall doping reaction and (ii) a high-growth rate region (region II) in which the doping process is controlled by the kinetics, i.e. the dopant incorporation process is controlled by a rate-limiting step. It was shown that in order to explain the temperature dependence of the epitaxial doping concentrations, the rate-limiting step must be associated

with a surface mechanism. The circuit model was also used to explain the transient-response results presented in the previous paper. It was shown that the mechanism responsible for the transient response is associated with surface "capacitances," i.e. it is associated with the fact that the surface densities of the different doping compounds covering the surface take some time to adjust themselves from one steady-state value to another. Finally, the transfer function experimentally obtained in section 3.2.1 was theoretically derived with the aid of the model.

### 3.3 LOW-PRESSURE CHEMICAL-VAPOR-DEPOSITION OF SILICON: STRUCTURE AND STABILITY

In the past decade polycrystalline silicon has become important in several applications. Submicron films of polycrystalline silicon, especially, are of great commercial importance in silicon-gate MOS integrated circuits [3.14] and charge-coupled devices [3.15]. Until recently, these films have generally been deposited in cold-wall reactors in which the silicon substrates lie flat on an externally heated susceptor. The low capacity and the high capital and operating costs of these reactors, however, may contribute significantly to the cost of the integrated-circuit fabrication process.

Within the last two years, low-pressure, chemical-vapor-deposition (LPCVD) systems for depositing polycrystalline-silicon have been developed [3.16]. The high capacity and lower costs of these systems have led to their rapid acceptance in high-volume, integrated-circuit manufacturing facilities. Since the deposition rate, temperature and pressure in these reactors are markedly different from those conventionally employed, some characterization of the material deposited is needed to ensure that the characteristics and reliability of the integrated circuit in which it is used are not degraded. Because low-pressure reactors are generally operated slightly above 600°C, a temperature close to the amorphous-crystalline transition temperature seen in silicon films deposited by chemical vapor deposition at atmospheric pressure [3.17,3.18], the structure in the as-deposited film and its stability upon further processing of the integrated-circuit wafer are important topics to investigate.

The detailed properties of the polycrystalline silicon become especially important when it is used in critical applications, such as for high-valued resistors in static memory circuits [3.19,3.20]. In image-sensing CCDs dependence of the optical transmission of the films on the structure will affect the device performance. Even in more conventional, silicon-gate applications, the stability of the structure may influence properties such as step coverage.

This paper reports the results of the first phase of a study being conducted at Stanford designed to investigate the properties of polycrystalline silicon deposited at low pressures. The crystal structure of the films is discussed and compared to that found in films deposited at atmospheric pressure, and the stability of the structure during further heat treatment is reported.

### 3.3.1 FILM PREPARATION

Films were deposited in a Tempress (Unicorp) LPCVD reactor at several different temperatures and a pressure of approximately 0.35-0.5 torr.\* Silane was the deposition source gas, and no diluent was used. Although a temperature gradient is normally used along the length of an LPCVD reactor, for these depositions the temperature was adjusted to be uniform throughout the length of the deposition zone. A full load of 137, three-inch-diameter silicon wafers was included in each deposition. Six of the wafers were sample wafers to be used in subsequent studies; the majority were dummy wafers included in order to avoid perturbing the gas flow with a different number of wafers in each deposition.

Films were deposited over the temperature range 580 to 640°C. Samples of several different thicknesses were studied at the typically used, nominal deposition temperature of 620°C. The deposition temperatures, rates, and film thicknesses are summarized in Table I. The films were deposited on both <100>- and <111>-oriented, lightly doped silicon wafers which were covered with 1000 Å of thermally grown silicon dioxide. The two different substrate orientations were used in order to allow investigation of the various crystallite orientations in the films without interference from the substrate.

---

\* The films were deposited by Intel Corporation.

### 3.3.2. STRUCTURE OF AS-DEPOSITED FILMS

The films were investigated both by x-ray diffraction and by transmission electron microscopy. The x-ray texture (preferred orientation) was measured by observing the diffracted intensity at twice the angle of incidence of the x-ray beam in a Picker Model 3488K x-ray diffractometer with 20 keV copper radiation. The samples were tilted  $2^\circ$  to reduce substrate reflections. This tilt only slightly reduced the reflections from the polycrystalline films (Fig. 3.13). The intensity of the signal from the {220} planes in the  $1.05\text{ }\mu\text{m}$ -thick sample deposited at  $620^\circ\text{C}$  was reduced by a factor of approximately two for a  $5^\circ$  tilt, indicating a variation in the crystallite orientations of this magnitude. For comparison, a  $2^\circ$  tilt reduced the signal from the single-crystal substrate by more than three orders of magnitude.

Resolvable reflections were observed from the {111}, {220}, {311}, and {331} planes in the thickest polycrystalline samples deposited at  $620^\circ\text{C}$ , but some of these peaks could not be observed in thinner samples or those deposited at lower temperatures. In no case was a signal corresponding to the {400} planes observed, indicating either the absence of grains with  $\langle 100 \rangle$  orientation or the low sensitivity of the measuring technique to grains with this orientation.

After normalizing the measured peak heights by the signal expected from a randomly oriented sample, we obtain an indication of the relative importance of crystallites with various orientations (Table 3.1). The standard normalization factors [3.21] for an infinitely thick sample have been modified [3.22] for this case where the samples are very much thinner than the reciprocal of the absorption coefficient ( $\mu^{-1} = 71\text{ }\mu\text{m}$  [10]). Table I shows that the  $\langle 110 \rangle$  texture is dominant in all three of the films of different thicknesses deposited at  $620^\circ\text{C}$ .

As the films become thicker, however, the amounts of  $\langle 110 \rangle$  and  $\langle 331 \rangle$  texture increase much more than linearly with film thickness, while the amounts of  $\langle 111 \rangle$  - and  $\langle 311 \rangle$  - oriented grains do not increase as significantly. The dramatic increase in  $\langle 110 \rangle$  texture with increasing film thickness indicates that the preference for  $\langle 110 \rangle$  texture is a growth phenomenon rather than nucleation behavior [3.24] and is similar to that seen in films deposited at atmospheric pressure [3.25]. Table I also indicates that no texture could be resolved in films deposited at 580°C in two different depositions.

Samples were prepared for transmission electron microscopy by etching the supporting substrate and the oxide from the back of the polycrystalline film. The film was usually further thinned chemically from the back so that the electron beam could easily penetrate the film; in all cases, therefore, the results correspond to the portion of the film farthest from the substrate. After preparation the samples were examined in a Philips EM200 electron microscope with a 100 keV electron beam.

Typical micrographs are shown in Fig. 3.14 for films deposited at 580 and 620°C, and the corresponding transmission-electron-diffraction (TED) patterns are shown below the micrographs. Films deposited at 600 and 640°C are similar to those deposited at 620°C. Films deposited at 600°C and above exhibit a more-or-less equi-axed, polycrystalline grain structure similar to that seen in films deposited at atmospheric pressure and somewhat higher temperatures in conventional CVD reactors [3.17,3.25]. Numerous twin lamella are seen within the grains. Films of different thicknesses deposited at 620°C appear to be qualitatively similar to each other, with the grain size near the top of the film increasing approximately linearly with increasing thickness. The grain size near the top of the film increases from about 0.05 - 0.1  $\mu\text{m}$  in the 0.26  $\mu\text{m}$ -thick films to 0.15-0.2  $\mu\text{m}$  in the 0.47  $\mu\text{m}$ -thick films, and to 0.3-0.4  $\mu\text{m}$  in the

thickest (1.05  $\mu\text{m}$ ) films. Transmission-electron-diffraction patterns (bottom of Fig. 3.14b) show the typical sharp rings and spots characteristic of polycrystalline material.

The films deposited at 580°C exhibit a different structure, although the results are not as consistent as in films deposited at higher temperatures. In some cases (Fig. 3.14a, left), a few crystallites appear to be embedded in a structureless background. In other cases some structure is seen (Fig. 3.14a, right), although the grains appear to be much smaller than those in the polycrystalline samples deposited at 600-640°C. Variations in contrast as the sample is rotated a few degrees in the electron microscope indicate that there is crystalline character in at least some of these grains. However, no fine structure was observed within the grains. The less consistent results in the films deposited at 580°C suggest that this temperature is very close to the transition temperature between the deposition of amorphous silicon and polycrystalline silicon so that some regions of each are included in the deposited films.

The TED patterns of the films deposited at 580°C (bottom of Fig. 3.14a) appear qualitatively different from those of the films deposited at higher temperatures. Instead of sharp rings, only very diffuse halos are seen. Since these halos are suggestive of an amorphous structure [3.26], we will call these films "amorphous" in our discussion, although portions of the samples do show some crystalline character. Further evidence for classifying these films as amorphous is the absence of detectable x-ray texture in the as-deposited films and the dramatic change in the structure upon annealing, as considered in the next section.

From the results discussed above we may conclude that there is a transition between an amorphous and a polycrystalline structure at a deposition temperature very near 580°C. This temperature is somewhat lower than that

at which a similar transition between amorphous and polycrystalline structure is seen in silicon films deposited by CVD at atmospheric pressure in a nitrogen ambient [3.17,3.18].

The somewhat higher transition temperature in the latter case may be related to the reduction of the surface mobility of the depositing silicon atoms by adsorbed nitrogen or impurity atoms contained in the nitrogen [3.27]. It may also be related to the higher deposition rates used at atmospheric pressure, rather than being directly related to the different pressures during deposition; deposition temperature and rate have been shown to be related over at least a limited range [3.28].

### 3.3.3 STRUCTURAL CHANGES ON ANNEALING

The presence of a transition from an amorphous to a polycrystalline structure for slight differences in deposition temperature and the use of markedly higher temperatures in subsequent IC fabrication steps lead to questions about the stability of the as-grown structure upon further processing. To investigate the stability of the various structures, films grown at the different temperatures were annealed at 800, 1000, 1100, and 1200°C for one hour in a nitrogen atmosphere in a standard diffusion furnace. A different piece of the film was used for each different annealing temperature, and the samples were rapidly inserted into the annealing furnace (within a few seconds). After annealing, the samples were investigated both by x-ray diffraction and by TEM, as before.

In some cases, especially at the higher annealing temperatures, the films were overcoated with a 0.5  $\mu\text{m}$ -thick layer of low-temperature (480°C) deposited silicon dioxide before annealing in order to protect the silicon films from the furnace ambient. At the highest annealing temperature (1200°C) some deterioration of the optical quality of the films was observed after annealing when the films were not overcoated with oxide. However, no significant

differences in the x-ray results were seen between bare and overcoated samples, indicating that the oxide cap does little to enhance or retard changes in structure during annealing.

The amorphous films deposited at 580°C were very unstable and showed marked changes in structure for all annealing temperatures. No structure was revealed by x-ray diffraction before annealing, while significant amounts were seen after annealing (Fig. 3.15a). The  $\langle 311 \rangle$  texture appears to be dominant at intermediate annealing temperatures, while the  $\langle 111 \rangle$  texture shows a tendency to increase at the highest annealing temperature employed. This preference for the growth of  $\langle 311 \rangle$  and  $\langle 111 \rangle$  textures on annealing is to be contrasted with the strong tendency of the  $\langle 110 \rangle$  texture to develop during deposition, and indicates that markedly different mechanisms may dominate during deposition and during annealing.

X-ray results taken after similar annealing are shown in Fig. 3b for the intermediate-thickness film deposited at 620°C. Unlike the film deposited at 580°C, the higher-temperature film, which is polycrystalline as deposited, is reasonably stable, showing little structural change for annealing temperatures up to 1000°C; only some tendency for growth of  $\langle 331 \rangle$  texture is observed. At 1100°C and above, however, significant change is seen; the  $\langle 110 \rangle$  texture decreases significantly, and the  $\langle 111 \rangle$  and  $\langle 331 \rangle$  textures increase slightly.

Films were also observed by TEM after annealing. The films deposited at 620°C showed little change after annealing at 800 or 1000°C, while they showed a significant increase in grain size after annealing at 1100 and 1200°C (Fig. 3.16), consistent with the x-ray results. The initially amorphous films deposited at 580°C showed more dramatic changes. After an 800°C anneal, definite structure was seen (Fig. 3.17a). The grain boundaries were not very well defined, but fine structure was easily visible within the grains. After higher-temperature annealing, the films appeared more crystalline, with better-defined, larger grains (Fig. 3.17b). The rapid change in structure can be seen

from the TED pattern of the 580°C film annealed at 800°C (Fig. 3.18). The transition from a diffuse halo pattern (bottom of Fig. 3.14a) to a ring-spot pattern indicates the rapid growth of crystal structure.

#### 3.3.4 ADDITIONAL DISCUSSION

Further evidence of a qualitative difference between films deposited at 580°C and those deposited at higher temperatures was seen during sample preparation for transmission electron microscopy. After the substrate and oxide were chemically etched and the samples were removed from the wax which protected the surface, the unannealed films deposited at 580°C curled, indicating large stresses built into these films. No tendency to curl was seen in films deposited at higher temperatures or in annealed films deposited at 580°C. Thus, large stresses appear to be present in the amorphous films, but not in polycrystalline samples.

The results of the present annealing experiments may be compared to results of similar studies of initially amorphous silicon films deposited by evaporation [3.17] or by atmospheric-pressure CVD in a nitrogen ambient [3.29]. In the evaporated films [3.17] a dendritic structure is seen after annealing at 650°C. After an 850°C anneal an equi-axed grain structure is dominant, but some dendritic structure is still seen, indicating a competition between the two types of nucleation. Presumably, the details of the nucleation behavior are influenced by the rate of heating to the annealing temperature. After a 1040°C anneal, only the equi-axed structure appears. Nagasima and Kubota [3.29] also observe a needle-like grain structure after a 700°C anneal, while an 1100°C anneal produces an equi-axed structure.

These observations are generally consistent with the results observed in the present investigation for the annealing of films deposited at 580°C. Both equi-axed grains and long, narrow structures are observed after the 800°C

anneal (Fig. 3.17a), while primarily a well-defined, equi-axed grain structure is seen after annealing at higher temperatures (Fig. 3.17b).

Anderson states [4] that stress in the as-deposited film provides the driving force for dendritic growth, while presumably the greater thermal energy at higher temperatures leads to the formation of the equi-axed structure. As we have seen, large stresses are present in the amorphous films considered in this study.

The structure which initially appears upon crystallization of the amorphous films may possibly be related to the anomalous, dendritic structure seen in films deposited at atmospheric pressure and relatively low temperatures [3.25].

From this comparison, we see that the annealing behavior of amorphous silicon films deposited by several different techniques is qualitatively similar. However, residual impurities contained within the films may impede annealing, causing differing transition temperatures for the various types of films studied in the different investigations.

It should be emphasized that all of these results refer to annealing in an inert ambient. The presence of other gases or dopant sources during heat cycling may affect the structure of the film differently.

### 3.3.5 CONCLUSIONS

This study has shown that a critical transition temperature between amorphous and polycrystalline deposits exists for deposition temperatures close to those typically used to deposit films for integrated-circuit applications. When the films are polycrystalline, the  $\langle 110 \rangle$  texture is dominant, and this texture becomes of increasing importance in thicker films.

If silicon films deposited by low-pressure CVD are initially polycrystalline, they should be reasonably stable and should not change markedly because

of heat cycles normally seen in modern integrated circuit fabrication; however some changes may occur if temperatures above 1100°C are encountered. On the other hand, films deposited at slightly lower temperatures are initially amorphous and will crystallize during the thermal processing likely to be encountered. The implications of these changes on the electrical properties and reliability of integrated circuits incorporating these initially amorphous films must be considered further before the films can be used with confidence for device applications.

Table 3.1  
DEPOSITION CONDITIONS AND X-RAY TEXTURE

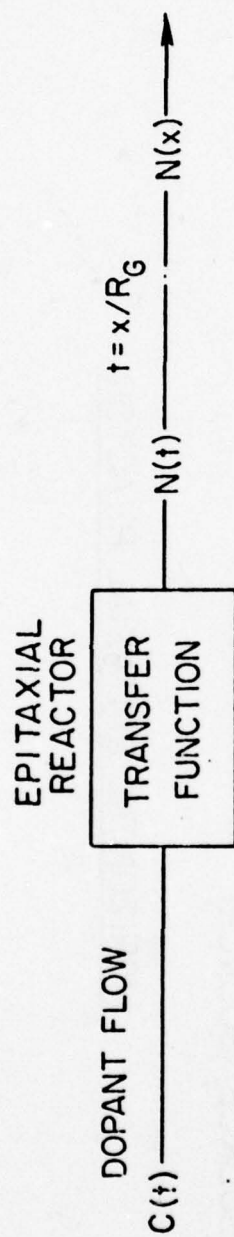
Deposition Temperature (°C)	Film Thickness ( $\mu\text{m}$ )	Deposition Rate ( $\text{\AA}/\text{min}$ )	X-Ray Texture <sup>a</sup>			
			<111>	<110>	<311>	<331>
580	0.32	70	0	0	0	0
600	0.50	73	8	324	19	29
620	0.26	110	10	102	21	0
620	0.47	110	12	422	33	19
620	1.05	110	12	2000	56	221
640	0.45	99	11	259	21	19

<sup>a</sup> The magnitudes of the <111> , <220>, <311> and <331> x-ray peak heights were divided by 1.00, 0.37, 0.18 and 0.054, respectively [3.21, 3.22, 3.23] to obtain the x-ray texture.

### References

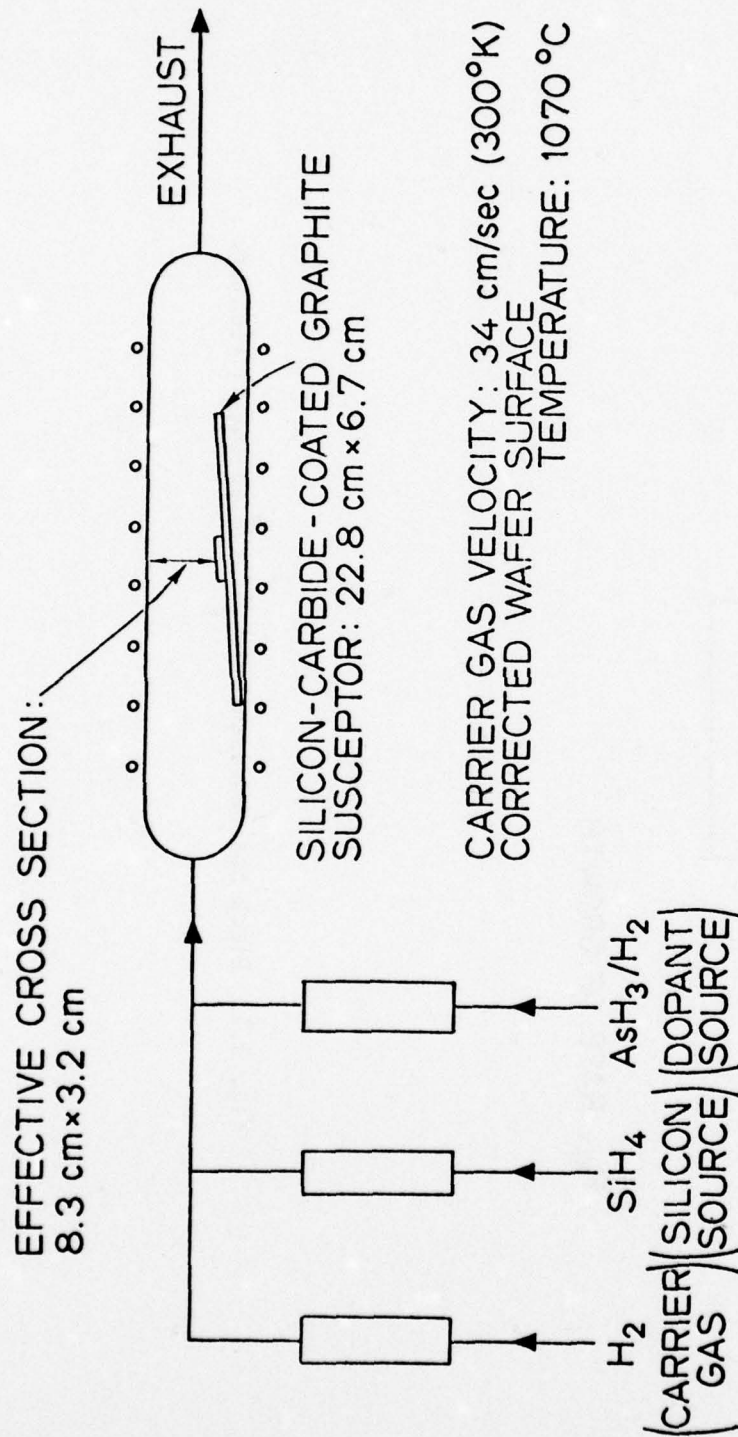
- 3.1 T.I. Kamins, R. Reif, and K.C. Saraswat, 1976 Electrochem. Soc. Fall Meeting, Abs. 230, Las Vegas, Oct. 17-22, 1976, pp. 601-603.
- 3.2 R. Reif, T.I. Kamins, and K.C. Saraswat, 1977 Electrochem. Soc. Fall Meeting, Abs. 350, Atlanta, Oct. 9-14, 1977, pp. 921-923.
- 3.3 J.D. Meindl, K.C. Saraswat, and J.D. Plummer, Semiconductor Silicon 1977, Princeton, NJ, The Electrochem. Soc. Inc., 1977, pp. 894-909.
- 3.4 J.D. Meindl, et al., "Final Report on Computer-Aided Semiconductor Process Modeling," Stanford Electronics Laboratories report TR-4969-73-F, Stanford University, Stanford, Calif., Oct 1976.
- 3.5 H. Kobayashi and M. Kobayashi, Catalysis Reviews - Science and Engineering, 10, 139 (1974).
- 3.6 F.G. Allen, Journal of Applied Physics, Vol. 28, 1957, p. 1510.
- 3.7 R.F. Pierret and D.W. Small, Solid-State Electronics, 18, 79 (1975).
- 3.8 Cheng, D.K., "Analysis of Linear Systems," Addison-Wesley Publishing Company, 1959, p. 244.
- 3.9 J. Bloem, Semiconductor Silicon 1973, Princeton, New Jersey, The Electrochemical Society, Inc., 1973, pp. 213-226.
- 3.10 R.S. Muller and T.I. Kamins, "Device Electronics for Integrated Circuits," John Wiley & Sons, 1977.
- 3.11 W.H. Shepherd, J. Electrochem. Soc., 115, 541 (1968).
- 3.12 J.P. Duchemin, Revue Technique, Thomson-CSF, 9, 411 (1977).
- 3.13 J. Bloem, J. of Crystal Growth, 13/14, 302 (1972).
- 3.14 F. Faggin and T. Klein, Solid-State Electron. 13, 1125 (1970).
- 3.15 D.F. Barbe, Proc. IEEE, 63, 38 (1975).
- 3.16 R.S. Rosler, Solid State Technology, 20, No. 4, 63 (April 1977).
- 3.17 R.M. Anderson, J. Electrochem. Soc., 120, 1540 (1973).
- 3.18 N. Nagasima and N. Kubota, Japan J. Appl. Phys., 14, 1105 (1975).
- 3.19 T.R. O'Connell, et al., IEEE International Solid State Circuits Conference, Philadelphia, Feb. 16-18, 1977, paper WAM 1.2.

- 3.20 V.G. McKenny, IEEE International Solid State Circuits Conference, Philadelphia, Feb. 16-18, 1977, paper WAM 1.3.
- 3.21 J.V. Smith (ed.), X-Ray Power Data File, American Society for Testing and Materials, Philadelphia, 1960, card 5-0565.
- 3.22 B.D. Cullity, Elements of X-Ray Diffraction, Addison-Wesley, Reading Mass., 1956, p. 270, Eq. (9-4).
- 3.23 Ref. 9, p. 466.
- 3.24 E. Bauer, "Growth of Oriented Films on Amorphous Surfaces," in Single Crystal Films (ed. M.H. Francombe and H. Sato), Pergamon Press, New York, pp. 43-67 (1964).
- 3.25 T.I. Kamins and T.R. Cass, Thin Solid Films, 16, 147 (1973).
- 3.26 M.H. Brodsky, et al., Phys. Rev., B-1, 2632 (1970).
- 3.27 T.I. Kamins, J. Electrochem. Soc., 121, 681 (1974).
- 3.28 T.I. Kamins, J. Manoliu, and R.N. Tucker, J. Appl. Phys., 43, 83 (1972).
- 3.29 N. Nagasima and N. Kubota, J. Vac. Sci. Technol., 14, 54 (1977).



$R_G$ : RATE OF GROWTH

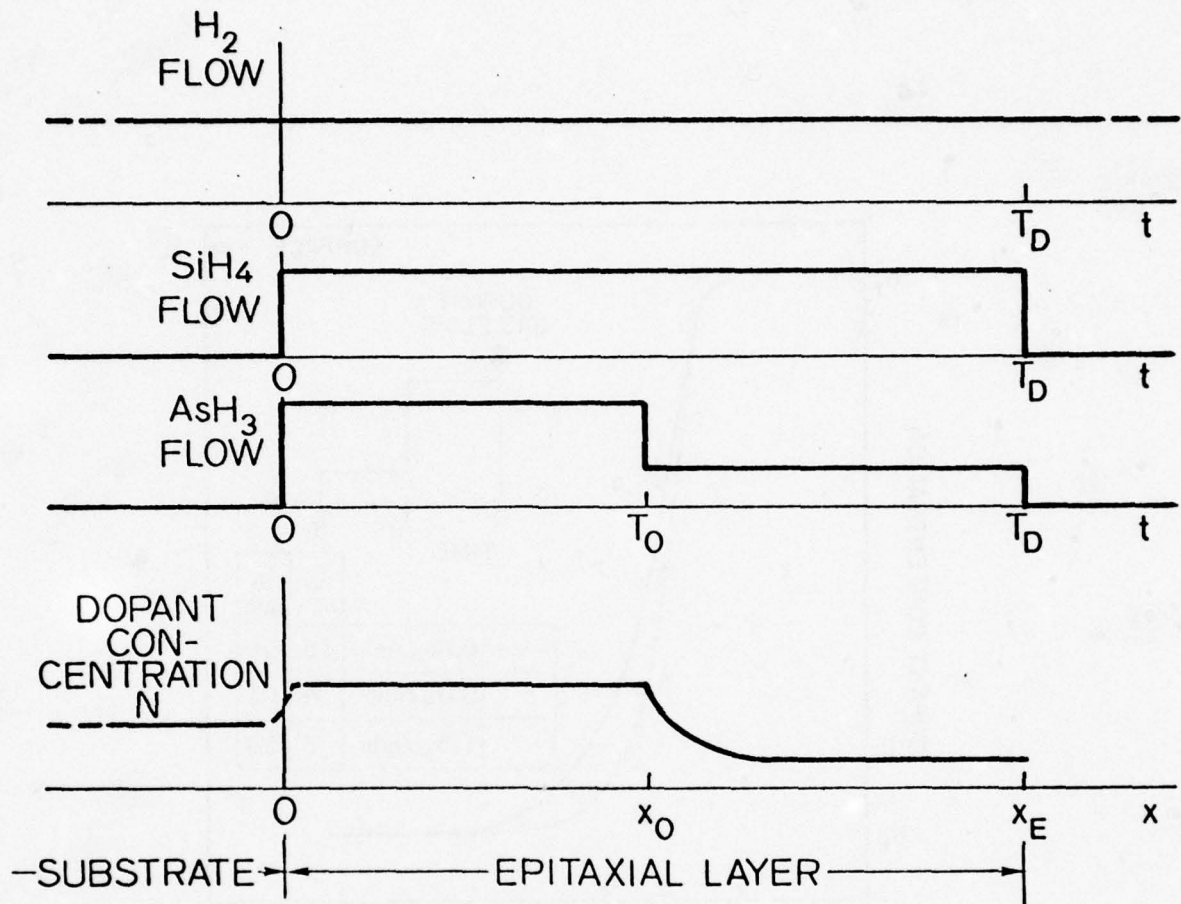
Fig. 3.1. Black box representation of the epitaxial reactor.



### HORIZONTAL EPITAXIAL REACTOR

Fig. 3.2. Schematic diagram of the epitaxial reactor.

# TRANSIENT STUDY



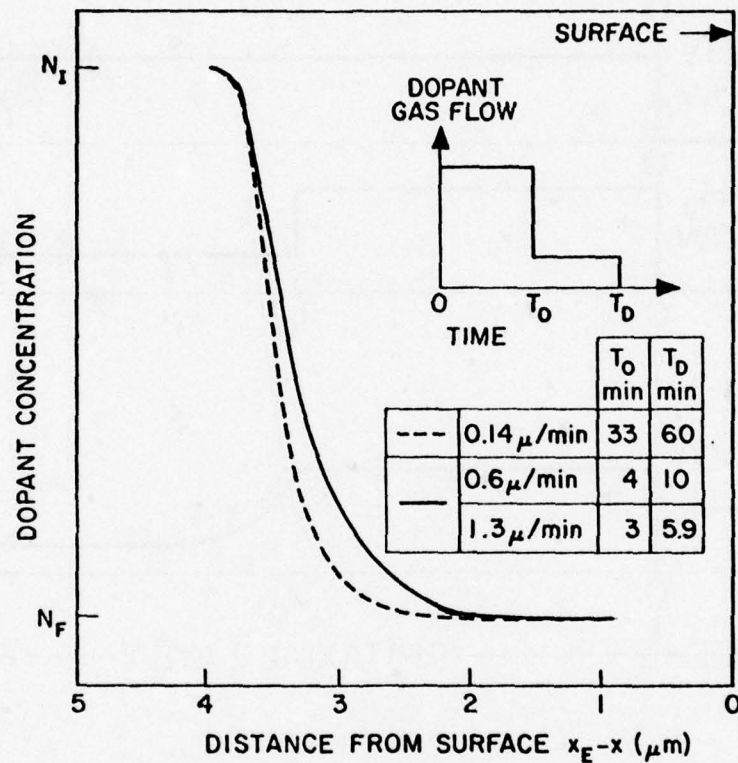
$x_E$ : TOTAL EPITAXIAL THICKNESS

$$x_E = g \cdot T_D$$

$g$ : SILICON GROWTH RATE

$T_D$ : TOTAL DEPOSITION TIME

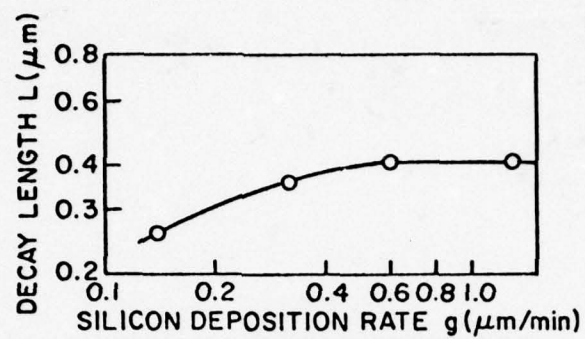
Fig. 3.3. Various gas flows as a function of time in the transient study and the resulting dopant concentration in the epitaxial layer.



$x_E$ : TOTAL EPITAXIAL THICKNESS  
 $x$ : DISTANCE FROM THE SUBSTRATE

Fig. 3.4. Measured dopant concentration as a function of distance from the surface of the epitaxial film for a decreasing step change in the dopant gas flow, as indicated in the inset.  $x_E$ : total epitaxial thickness ( $gT_D$ );  $x$ : distance from the substrate.

(a)



(b)

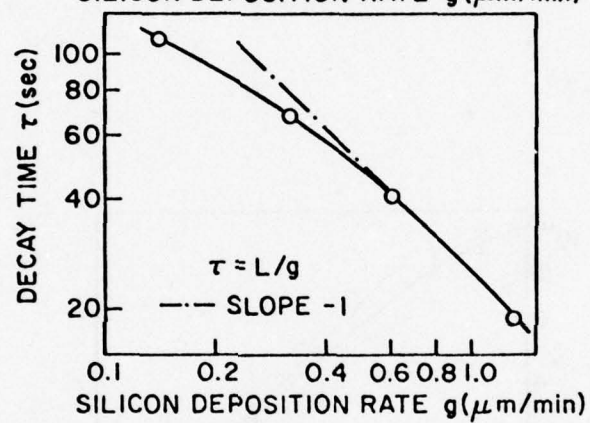


Fig. 3.5. Decay length and decay time as a function of silicon deposition rate.

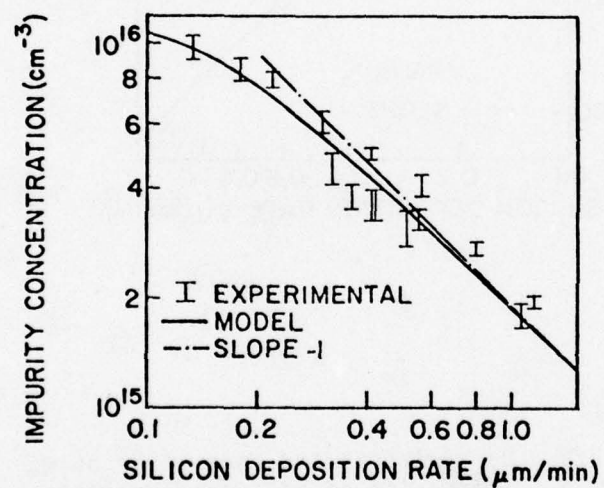


Fig. 3.6. Impurity concentration as a function of silicon deposition rate, for a constant partial pressure of  $\text{AsH}_3 = 6.2 \times 10^{-10}$  atm.

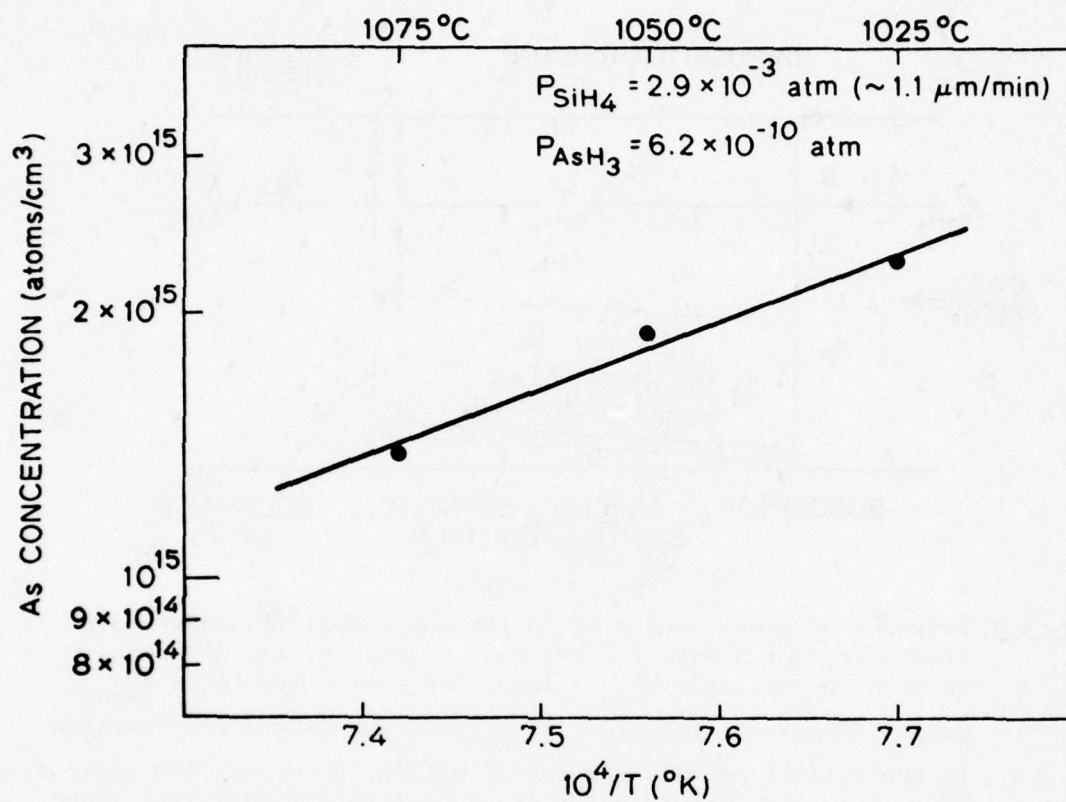


Fig. 3.7. Arsenic concentration in the epitaxial layer as a function of growth temperature.

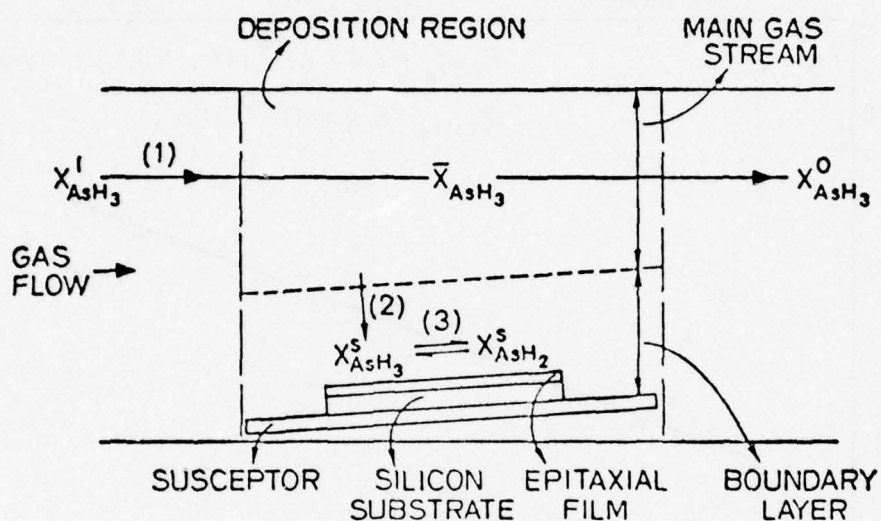


Fig. 3.8. Sequence of steps occurring in the gas phase: (1) input mass transport, (2) boundary-layer mass transport, (3) gas-phase chemical reactions.  $X_{AsH_3}^i$ : input  $AsH_3$  molar fraction;  $X_{AsH_3}^o$ : output  $AsH_3$  molar fraction;  $\bar{X}_{AsH_3}$ : average  $AsH_3$  molar fraction in the well-mixed main gas stream within the deposition region;  $X_{AsH_3}^s(AsH_2)$ : gas-phase molar fraction of  $AsH_3(AsH_2)$  just above the gas-solid interface.

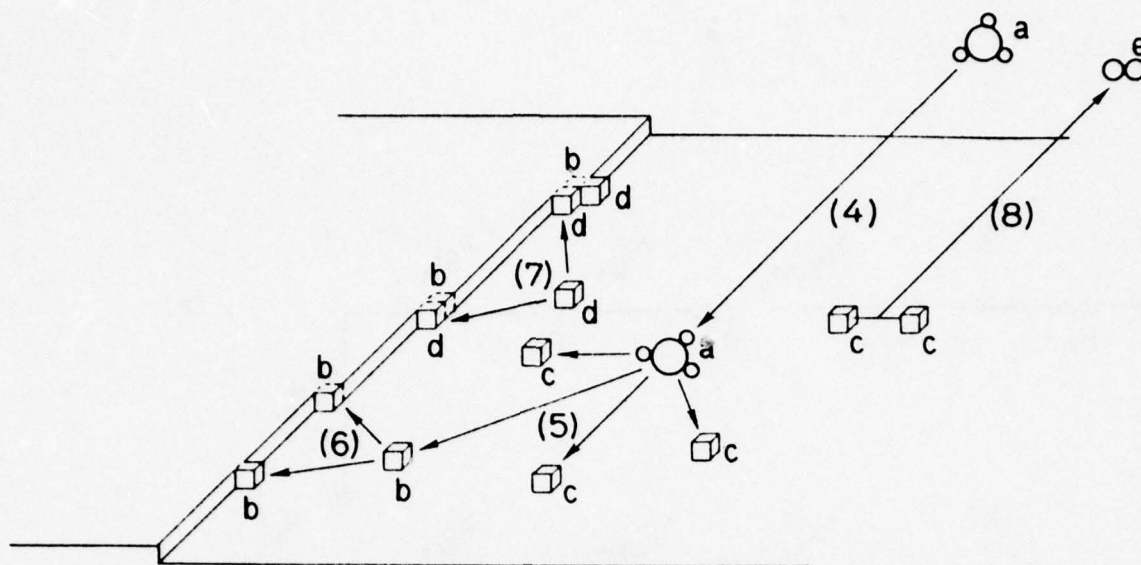


Fig. 3.9. Sequence of steps occurring on the surface: (4) adsorption of the As-containing compound; (5) surface chemical dissociation; (6) surface diffusion and site incorporation; (7) "burying" of As by subsequently arriving Si atoms; (8) desorption of hydrogen. a.  $\text{AsH}_3$ , b. As, c. H, d. Si, e.  $\text{H}_2$ .

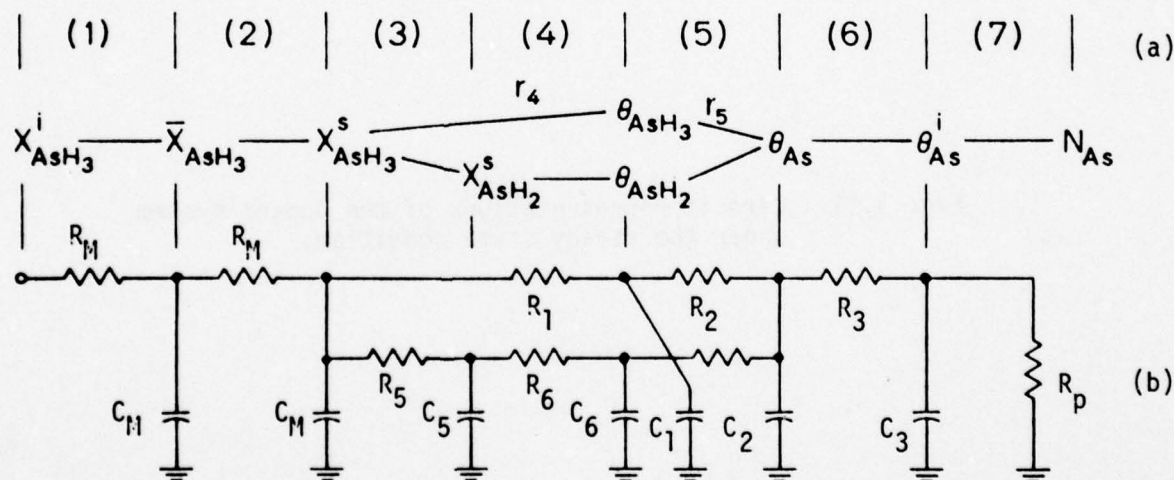


Fig. 3.10. Circuit representation of the dopant system. Each resistance corresponds to one of the steps in the doping process.

$\theta_{\text{AsH}_3}(\text{AsH}_2)(\text{As})$ : fraction of adsorption sites occupied by  $\text{AsH}_3(\text{AsH}_2)(\text{As})$ .  $\theta_{\text{As}}^i$ : fraction of incorporation sites occupied by As.  $\bar{N}_{\text{As}}$ : dopant concentration in the epitaxial film. Processes (1)-(7) correspond to the mechanisms shown in Figs. 1 and 2.

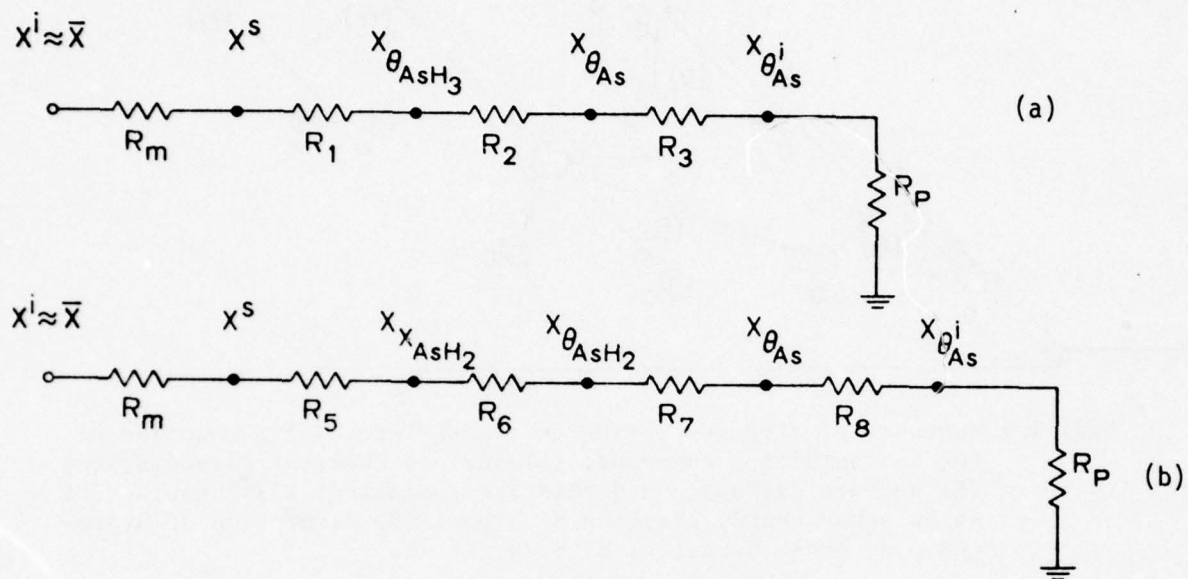


Fig. 3.11. Circuit representations of the dopant system under the steady state condition.

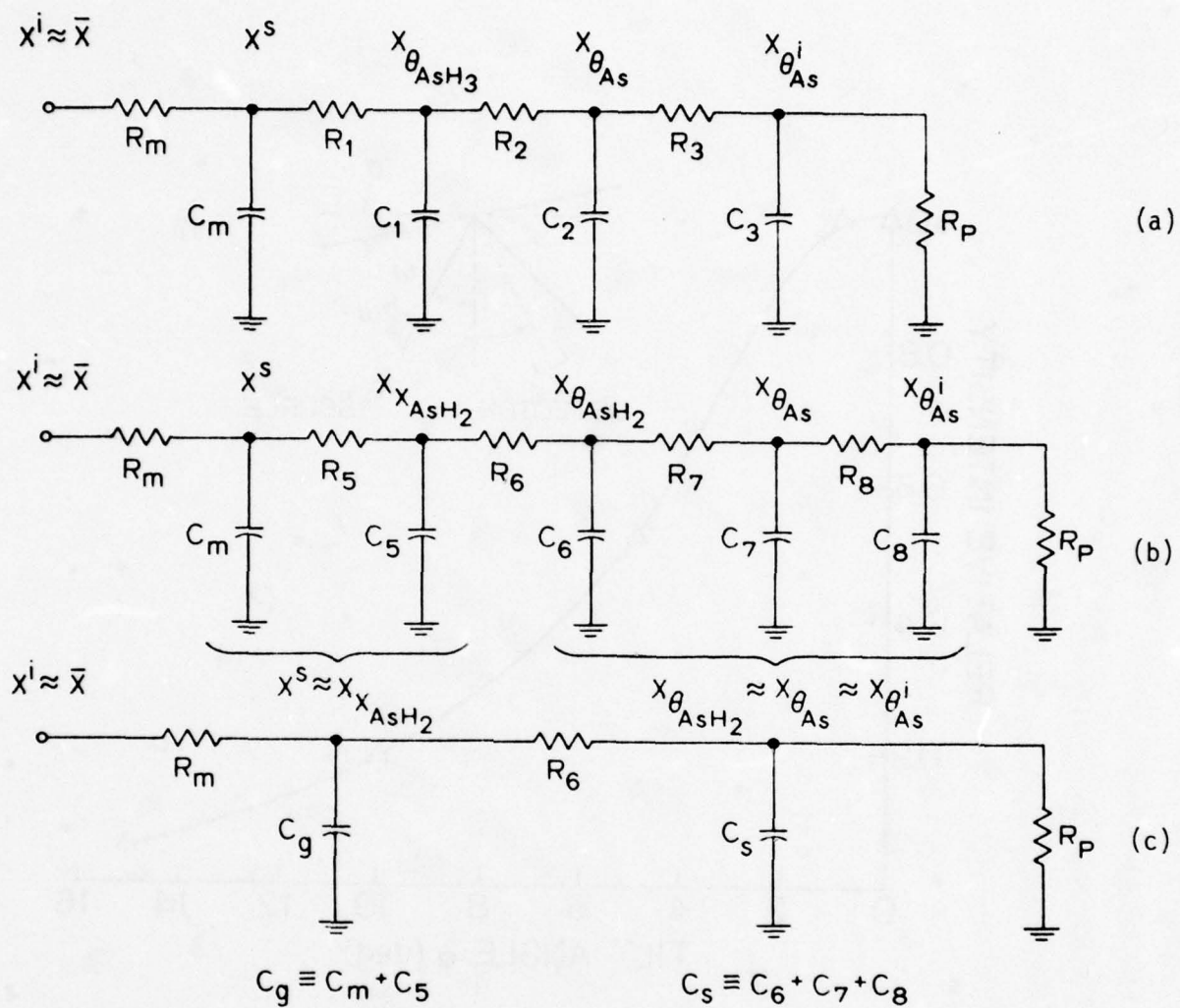


Fig. 3.12. Circuit representations of the dopant system under the transient condition.

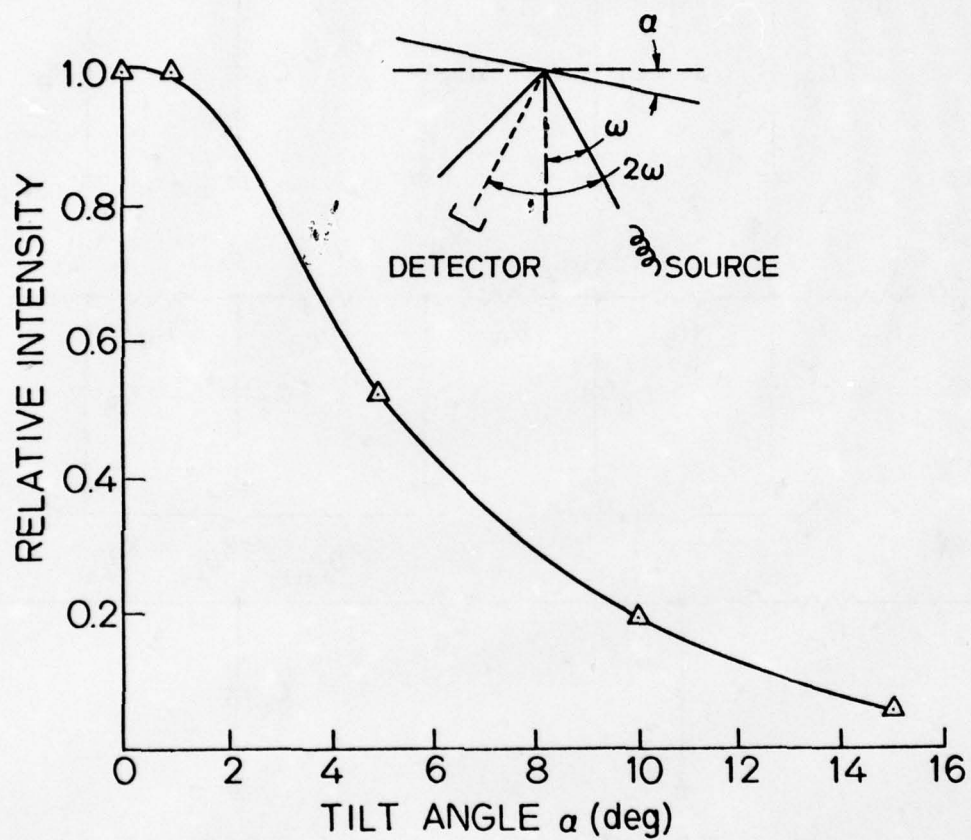
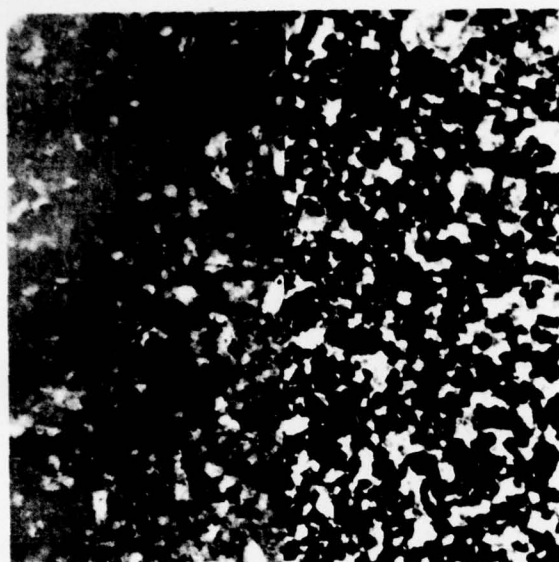
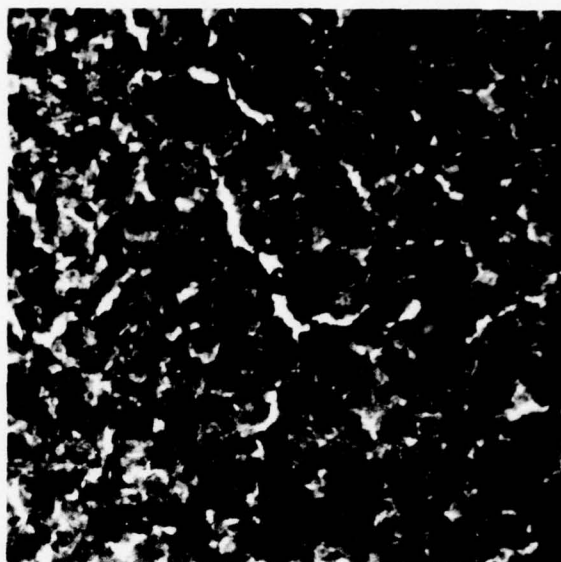


Fig. 3.13. Intensity of the diffracted x-ray signal intercepted from the  $\langle 220 \rangle$  planes of the  $1.05 \mu\text{m}$ ,  $620^\circ\text{C}$  film as a function of the tilt angle  $\alpha$ .



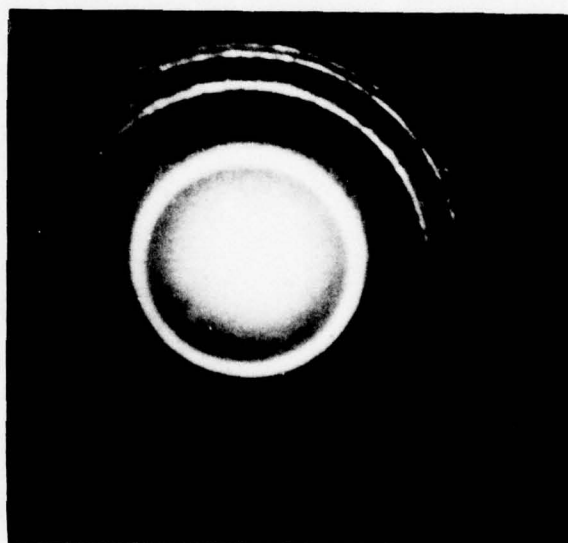
0.2  $\mu\text{m}$  → | | ←



0.2  $\mu\text{m}$  → | | ←



(a)



(b)

Fig. 3.14. Transmission electron micrographs of films deposited at (a) 580°C and (b) 620°C. The corresponding transmission-electron-diffraction patterns are shown below the micrographs.

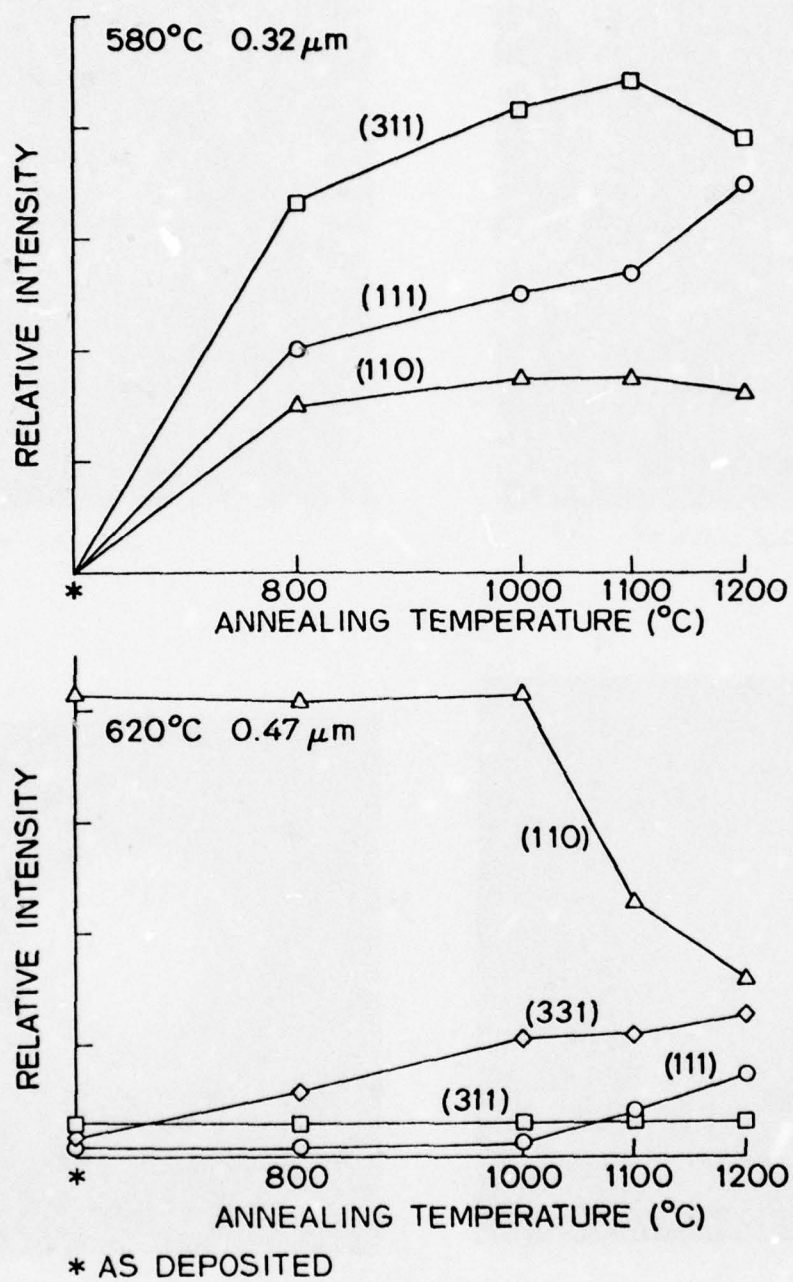


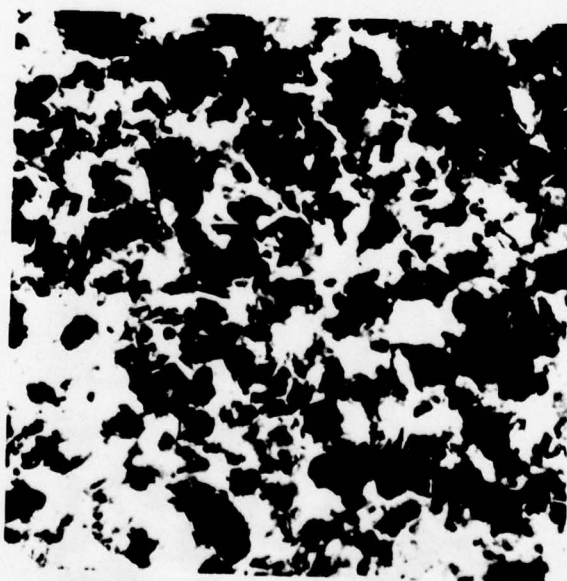
Fig. 3.15. Development of the x-ray texture after annealing at the indicated temperatures for films deposited at (a) 580°C and (b) 620°C.

(a)



(b)

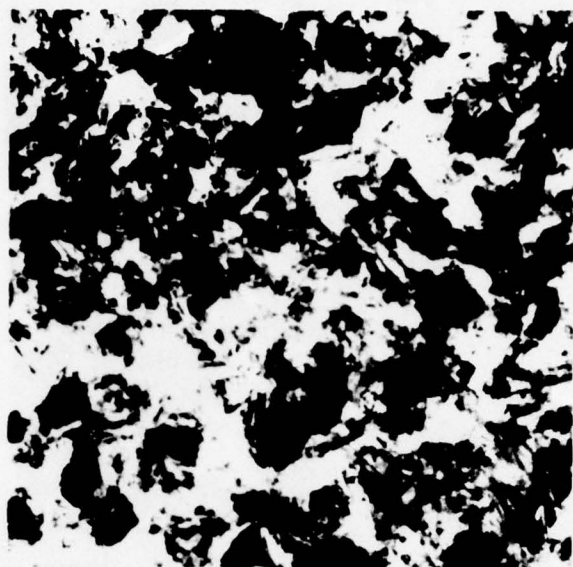
(b)



(a)

Fig. 3.16. Transmission electron micrographs of 0.47 μm-thick films deposited at 620°C and annealed at (a) 1100 and (b) 1200°C.

(a)



(A)

0.2  $\mu\text{m}$  → | | ←

(b)



(B)

0.2  $\mu\text{m}$  → | | ←

Fig. 3.17. Transmission electron micrographs of films deposited at 580°C and annealed at (a) 800 and (b) 1200°C.

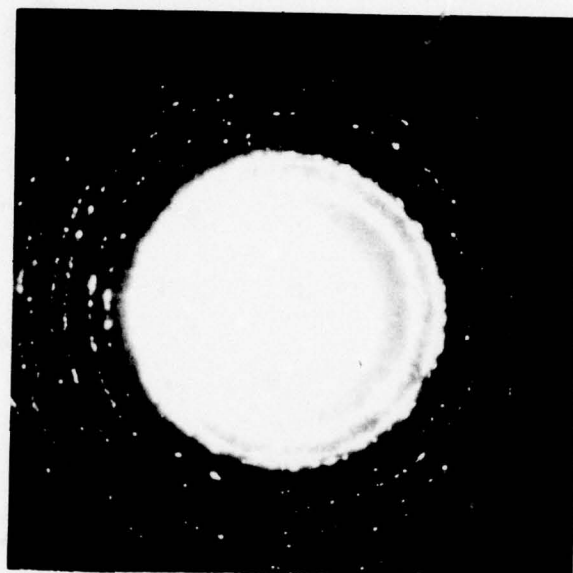


Fig. 3.18. Transmission-electron-diffraction pattern of film deposited at 580°C and annealed at 800°C.

## Part 4

### DEVICE SIMULATION AND STATISTICAL CIRCUIT MODELING

#### 4.1 Project Goals

The material discussed in the following subsections has two key objectives. First, fabrication process information is used directly as input for device simulation so that technology variables are correctly reflected in device characteristics. While the present examples of this process/device simulation coupling focus primarily on one-dimension, progress on the two-dimensional analysis programs is encouraging. Second, equivalent circuit and statistical analysis capabilities are being developed with emphasis on predicting geometry and process dependent effects. The impact of this work on both reliability and circuit yield will be discussed.

This report gives substantial technical detail concerning progress on specific tasks. It is the purpose of this introduction to consolidate the separate work units and provide background as needed. In particular, several overview figures are essential in understanding the discussions which follow. Figure 4.1.1a shows the block diagram for program SUPREM [4.1]. This program is a multi-step process simulator which generates impurity profiles, oxide thicknesses and epitaxial films as a result of sequential IC fabrication sequences. The efforts described in the previous sections involving oxidation, epitaxy and ion implantation are currently being incorporated into the respective subblocks shown in Figure 4.1.1a. Figure 4.1.1b shows a sequence of input/output files for the SUPREM program which use the implantation, oxidation and diffusion

subblocks to generate boron-arsenic profiles for a bipolar transistor. From the output data one can directly obtain information such as junction depths ( $x_j$ ), concentrations ( $N(x)$ ), oxide thickness ( $x_{ox}$ ) and sheet resistances ( $\rho \square$ ). The capabilities of SUPREM will be used directly in the work described in this section. The detailed discussion of the SUPREM program is given elsewhere [4.1].

Figure 4.1.2 shows in block diagram form how the SUPREM program relates to the research efforts to be discussed. SUPREM, based on fabrication process specifications, generates doping profiles and associated physical and electrical information. The objective of the work discussed in this section is to develop device and circuit simulation tools to use directly the SUPREM-generated data. Specifically, device simulation and device analysis based on SUPREM input can generate Poisson and transport solutions for one- and eventually two-dimensional device structures. In addition, the electrical device model parameters can be generated for circuit simulation. A key point to be emphasized here is that in addition to determining model parameters from the device simulation, the underlying process and geometry sensitivities can be explained using the SUPREM capabilities. The final block in Figure 4.1.2 indicates that circuit simulation based on device model equations is available. This report focuses on two aspects of circuit simulation. First, modeling problems associated with distributed device effects are discussed. CMOS latch up circuit models are described which relate both to multiple-device geometries and impurity profiles. A gate capacitance/charge model is discussed which is especially important for SOS floating bulk devices. Both these modeling efforts relate directly to reliability problems of high performance circuit technologies. Second, recent advances in

statistical circuit simulation are discussed. This capability is essential for understanding the distributions of circuit performance parameters -- propagation delay  $\tau_d$  for example -- which result from both process and device geometry variations. The ability to simulate and understand these process control variables has a direct relationship to yield and circuit reliability. Figure 4.1.3 shows the coupling of statistical circuit simulation, including parameter correlations (shown as dashed lines), with the underlying process control variables and device parameters.

The underlying assertion of the device simulation and statistical circuit modeling efforts is that for custom IC's the availability of computer tools will enhance reliability, procurement speed and technology documentation. Reliability depends on a precise understanding of technology limits and device sensitivities with process and geometry variations. These limits and sensitivities can be predicted using the approach shown in Figure 4.1.3. Improvements in procurement speed are possible owing to three factors:

- 1) The simulation tools allow easy cross-checks for multiple vendors.
- 2) The simulation results allow bounds to be established on both physical and electrical parameters
- 3) Many target-runs can be avoided by the use of simulation during process development.

A final outcome of this work which is novel is that process documentation is available for the first time. The availability of SUPREM

makes it feasible to require custom IC vendors to provide process documentation equivalent to existing requirements for circuit simulation.

Having stated the overall objectives of this work, the specific subsections will be described briefly. Section 4.2 defines the mathematics for a one-dimensional device simulator, SEDAN, which uses SUPREM output and generates steady-state Poisson and carrier transport solutions. Examples are given for both bipolar and MOS devices. Section 4.3 describes the results to-date on two-dimensional device analysis. The introduction of Section 4.3 describes the need to use a non-rectangular grid approach as well as the broad class of device examples which are to be studied. The results given in Section 4.3 show that quasi-one-dimensional examples give favorable results compared with SEDAN. In addition, the two-dimensional Poisson solutions for CCD and SOS devices show both program flexibility and potential for realistic device applications.

A key limitation in two-dimensional device modeling is precise specifications of the two-dimensional impurity profiles. This problem becomes severe as device minimum feature sizes shrink and devices are packed more densely. In addition to the need for precise specification of two-dimensional profiles, potential circuit malfunctions due to device interactions become more likely. Section 4.4 discusses profile measurement techniques and test structure results for a CMOS process. The results show that surface impurity profiles can be characterized by electrical device measurements. A proposed method for obtaining bulk profile information is also discussed. Section 4.5 combines profile and circuit modeling information in the prediction of latch up hazards in CMOS circuits. The latch up problem is a critical one in the context of small geometry structures and in the presence of radiation environments. The modeling

results show the need for a close coupling of technology (SUPREM) and device topology (SEDAN). Furthermore the circuit models needed to simulate latch up hazards must correctly reflect the artwork/geometry constraints.

Section 4.6 describes a gate charge/capacitance model which is of special importance for SOS/CMOS circuits. The floating bulk node of MOS devices fabricated on SOS can give rise to potential circuit malfunctions. However, to date the device models available for circuit simulation have been totally inadequate in modeling gate charge for SOS. The model discussed in Section 4.6 allows correct prediction of circuit performance. The next step in this work is to use the two dimensional process and device simulation programs as tools to define the charge equations.

Section 4.7 summarizes recent progress in statistical circuit modeling by means of ECL circuit example. A recent journal publication [4.2] which defines the statistical device model is included as an appendix to Section 4.7. The key contributions of this section are two fold. First, the development and use of a realistic device model is essential for correctly predicting circuit parameter distributions which in turn control circuit yield. Second, the computer program used to demonstrate the circuit simulations is an efficient, minicomputer program which brings such analysis capabilities into a practical range for user applications.

# SUPREM MULTI STEP PROCESS SIMULATOR

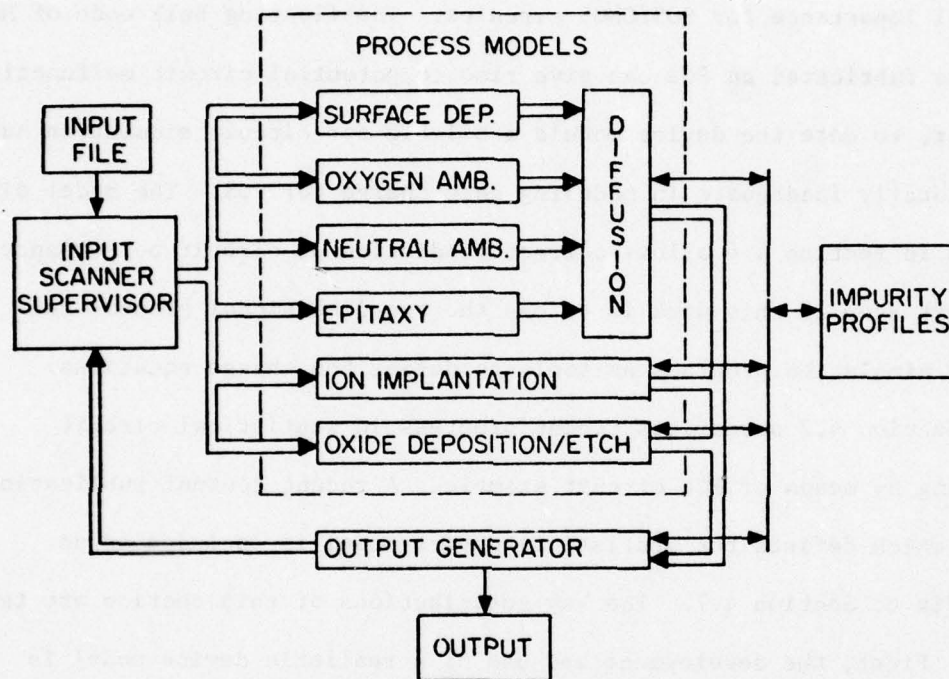


Figure 4.1.1a - Block diagram for SUPREM [4.1].

# INPUT :

# OUTPUT:

\*\*\* STANFORD UNIVERSITY PROCESS ENGINEERING MODELS PROGRAM \*\*\*

```

TITLE SUPREM TEST EXAMPLE #1
GRID URS10.005, OPTHR0.4, XMAXR0.8
SUBS ELEMAS, CONC02.0E15, JMNTR111
PLOT AYSKY, IDIVRY, TOTLRY, YMINR10, YMAXR7, XINDR0.8
PRINT HEADRY, IDIVRY, TOTLRY

MODEL NAMEBDF1, ELEMAS, BETAS0.0, NIFPR0.1E18
MODEL NAMEBDF2, ELEMAS, BETAS100.0, NIFPR0.1E18

COMM ION IMPLANT (BORON)
STEP TYPEIMPL, ELEMAS, DUSER1.0E16, AKEV50

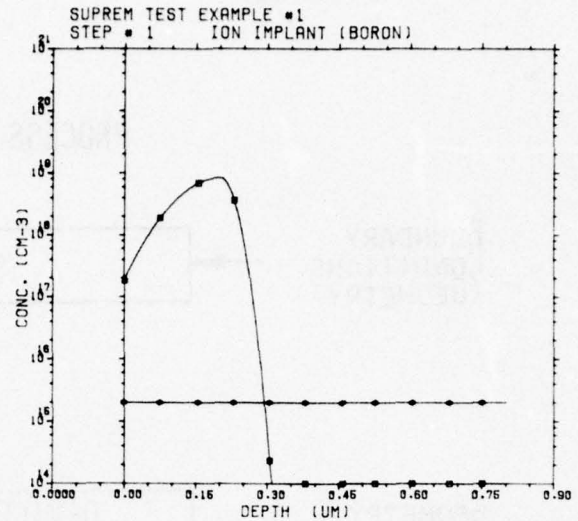
COMM OXIDATION (DRY/WET/DRY)
STEP TYPEOXID, TEMPS1000, TIME10, MOULDRHY0, MOULDRIF1
STEP TYPEOXID, TEMPS1000, TIME200, MOULDRHY0, MOULDRIF1
STEP TYPEOXID, TEMPS1000, TIME45, MOULDRHY0, MOULDRIF1

COMM REMOVE OXIDE
STEP TYPEETCH, TEMPR25

PRINT TOTLRY
PLOT TOTLRY

COMM CAPSULE DEPOSITION (ARSENIC)
STEP TYPEDEP, TEMPS1000, TIME20, ELEMAS, MOULDRIF1, MOULDRIF2
* CONC02.5E20

ENDS
  
```



\*\*\* STANFORD UNIVERSITY PROCESS ENGINEERING MODELS PROGRAM \*\*\*

```

TITLE SUPREM TEST EXAMPLE #1
GRID URS10.005, OPTHR0.4, XMAXR0.8
SUBS ELEMAS, CONC02.0E15, JMNTR111
PLOT AYSKY, IDIVRY, TOTLRY, YMINR10, YMAXR7, XINDR0.8
PRINT HEADRY, IDIVRY, TOTLRY

MODEL NAMEBDF1, ELEMAS, BETAS0.0, NIFPR0.1E18
MODEL NAMEBDF2, ELEMAS, BETAS100.0, NIFPR0.1E18

COMM ION IMPLANT (BORON)
STEP TYPEIMPL, ELEMAS, DUSER1.0E16, AKEV50

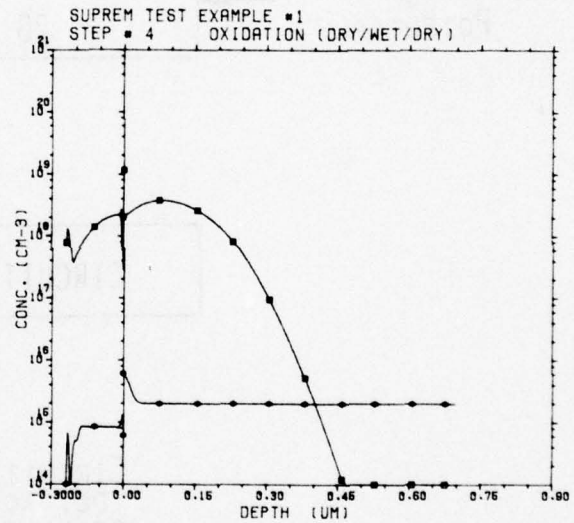
COMM OXIDATION (DRY/WET/DRY)
STEP TYPEOXID, TEMPS1000, TIME10, MOULDRHY0, MOULDRIF1
STEP TYPEOXID, TEMPS1000, TIME200, MOULDRHY0, MOULDRIF1
STEP TYPEOXID, TEMPS1000, TIME45, MOULDRHY0, MOULDRIF1

COMM REMOVE OXIDE
STEP TYPEETCH, TEMPR25

PRINT TOTLRY
PLOT TOTLRY

COMM CAPSULE DEPOSITION (ARSENIC)
STEP TYPEDEP, TEMPS1000, TIME20, ELEMAS, MOULDRIF1, MOULDRIF2
* CONC02.5E20

ENDS
  
```



\*\*\* STANFORD UNIVERSITY PROCESS ENGINEERING MODELS PROGRAM \*\*\*

```

TITLE SUPREM TEST EXAMPLE #1
GRID URS10.005, OPTHR0.4, XMAXR0.8
SUBS ELEMAS, CONC02.0E15, JMNTR111
PLOT AYSKY, IDIVRY, TOTLRY, YMINR10, YMAXR7, XINDR0.8
PRINT HEADRY, IDIVRY, TOTLRY

MODEL NAMEBDF1, ELEMAS, BETAS0.0, NIFPR0.1E18
MODEL NAMEBDF2, ELEMAS, BETAS100.0, NIFPR0.1E18

COMM ION IMPLANT (BORON)
STEP TYPEIMPL, ELEMAS, DUSER1.0E16, AKEV50

COMM OXIDATION (DRY/WET/DRY)
STEP TYPEOXID, TEMPS1000, TIME10, MOULDRHY0, MOULDRIF1
STEP TYPEOXID, TEMPS1000, TIME200, MOULDRHY0, MOULDRIF1
STEP TYPEOXID, TEMPS1000, TIME45, MOULDRHY0, MOULDRIF1

COMM REMOVE OXIDE
STEP TYPEETCH, TEMPR25

PRINT TOTLRY
PLOT TOTLRY

COMM CAPSULE DEPOSITION (ARSENIC)
STEP TYPEDEP, TEMPS1000, TIME20, ELEMAS, MOULDRIF1, MOULDRIF2
* CONC02.5E20

ENDS
  
```

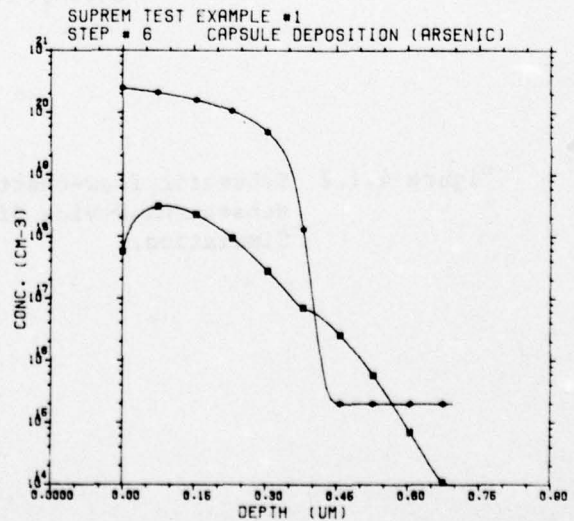


Figure 4.1.1b - Three input/output listings from the SUPREM process simulation of an As-B double-diffused bipolar process.

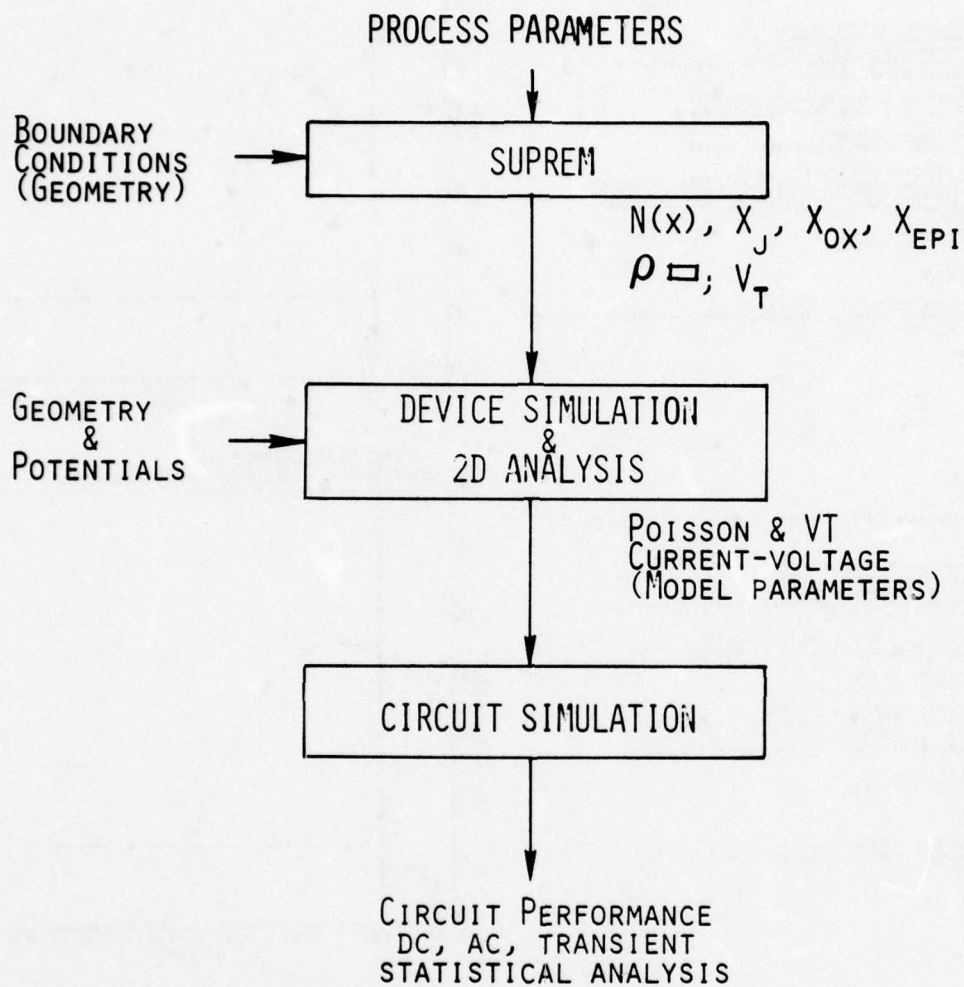


Figure 4.1.2 Schematic flow-chart showing how SUPREM is used in subsequent Device Simulation Analysis and Circuit Simulation.

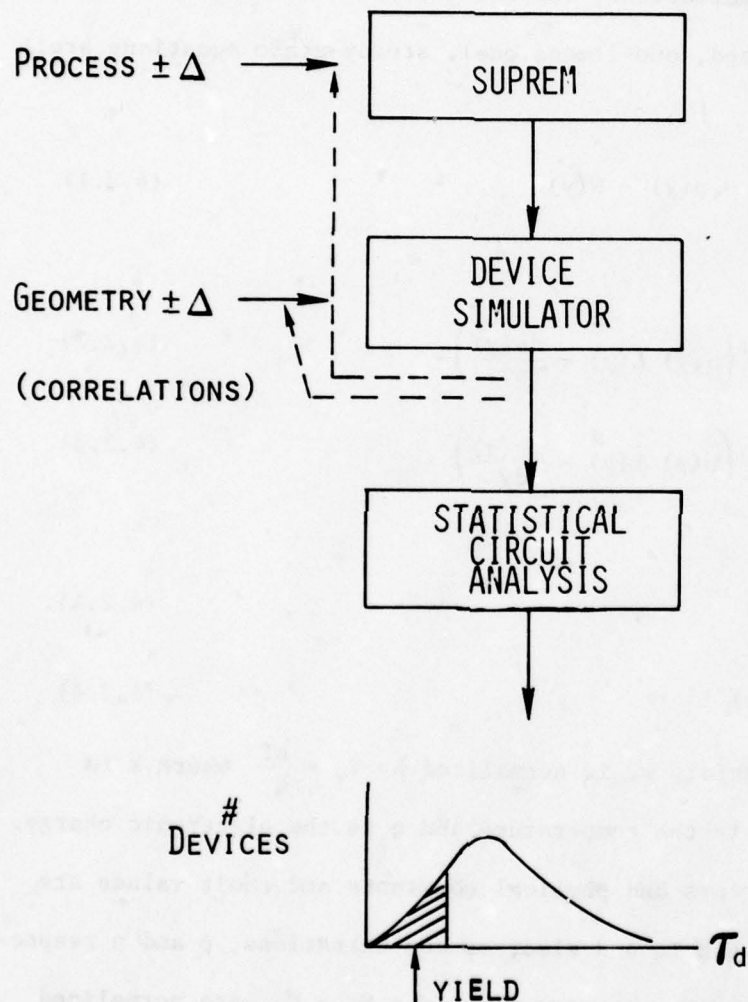


Figure 4.1.3 Schematic flow-chart showing how circuit parameter distributions (i.e.  $\tau_d$  -- delay time) can be traced back to geometry - and process-limiting contributions by means of parameter correlations.

## 4.2 One-Dimensional Semiconductor Device Analysis (SEDAN), (D.C.D'Avanzo)

### Introduction

The electrical properties of a semiconductor device can be completely specified by five physical relationships; Poisson's equation, electron and hole transport equations and electron and hole continuity equations. With the appropriate boundary conditions the coupled equations can be solved for carrier concentrations, current densities and the electrostatic potential. The normalized, one-dimensional, steady-state equations are:

Poisson

$$\frac{d^2 \psi(y)}{dy^2} = n(y) - p(y) - N(y) \quad (4.2.1)$$

Transport

$$J_n(y) = \frac{1}{\gamma_n(y)} \left( n(y) E(y) + \frac{dn(y)}{dy} \right) \quad (4.2.2)$$

$$J_p(y) = \frac{1}{\gamma_p(y)} \left( p(y) E(y) - \frac{dp(y)}{dy} \right) \quad (4.2.3)$$

Continuity

$$\frac{dJ_n(y)}{dy} = U(y) \quad (4.2.4)$$

$$\frac{dJ_p(y)}{dy} = -U(y) \quad (4.2.4)$$

The electrostatic potential,  $\psi$ , is normalized by  $V_T = \frac{kT}{q}$  where  $k$  is Boltzmann's constant,  $T$  is the temperature and  $q$  is the electronic charge. (The normalizing parameters and physical constants and their values are listed in Table 4.2.1. The hole and electron concentrations,  $p$  and  $n$  respectively, and the net impurity concentration,  $N = N_D - N_A$ , are normalized by the intrinsic electron density,  $n_{i0}$ , where the  $o$  subscript denotes the maximum band gap value, to facilitate the inclusion of band-gap narrowing effects. The inverse of the normalized hole and electron mobilities are

$\gamma_p$  and  $\gamma_n$  respectively. The electric field is defined as the negative gradient of the potential;  $E(y) = -\frac{d\psi(y)}{dy}$ . The normalized recombination rate,  $U(y)$ , includes single level Shockley-Read-Hall and Auger recombination mechanisms. The recombination current is defined as the spatial integral of the recombination rate,  $J_r(y) = \int_0^y U(y')dy'$ . The transport equations have been written assuming the applicability of the Einstein relation for non-degenerate semiconductors.

The discussion will be limited to the npn bipolar transistor structure in Figure 4.2.4a although the method can be applied to any number and combination of impurity layers with two or three contacts. For the structure shown the positions of the contacts are  $y = 0$  for the emitter,  $y = B$  for the base and  $y = L$  for the collector. The selection of  $B$  is not critical since the majority carrier (hole) quasi-fermi level is fairly constant in the base region under most operating conditions. Inclusion of the base current is accomplished by imposing a boundary condition on the majority carriers at  $B$  and dividing the calculation of hole concentrations between a collector region,  $B \leq y \leq L$ , and an emitter region,  $0 \leq y \leq B$ . All potentials are referenced to the majority carrier quasi-fermi level at  $B$ ,  $\phi_p(B)$ , which is set to zero. The electrostatic potential  $\psi$  corresponds to the potential associated with the intrinsic Fermi level as shown in Figure 4.2.4b.

#### Solutions to the Transport and Continuity Equations

The solution technique utilizes Gummel's iterative scheme [4.3] so that carrier concentrations can be written as explicit functions of the electrostatic potential, boundary conditions at the contacts and the carrier concentrations of the previous iteration. As DeMari has shown [4.4] the transport equations can be rearranged and treated as linear differential

equations in  $n(y)$  and  $p(y)$  with non-constant coefficients so that (4.2.2)

and (4.2.3) become;

$$\frac{dn(y)}{dy} + E(y) n(y) = \gamma_n(y) J_n(y) \quad (4.2.6)$$

$$\frac{dp(y)}{dy} - E(y) p(y) = -\gamma_p(y) J_p(y) \quad (4.2.7)$$

The analytical solutions for the carrier concentrations are [4.5] for electrons,

$$n(y) = e^{\psi(y)} \left\{ n(L) e^{-\psi(L)} - \int_y^L \gamma_n(y') J_n(y') e^{-\psi(y')} dy' \right\} \quad (4.2.8)$$

holes in the emitter region

$$p(y) = e^{-\psi(y)} \left\{ p(B) e^{\psi(B)} + \int_y^B \gamma_p(y') J_p(y') e^{\psi(y')} dy' \right\} \quad (4.2.9)$$

for  $0 \leq y < B$

and holes in the collector region,

$$p(y) = e^{-\psi(y)} \left\{ p(L) e^{\psi(L)} + \int_y^L \gamma_p(y') J_p(y') e^{\psi(y')} dy' \right\} \quad (4.2.10)$$

for  $B \leq y \leq L$

By integrating the continuity equations, expressions can be derived for the electron current density throughout the structure,

$$J_n(y) = J_r(y) + J_n(0) \quad 0 \leq y \leq L \quad (4.2.11)$$

The hole current in the emitter region

$$J_p(y) = -J_r(y) + J_p(0) \quad 0 \leq y < B \quad (4.2.12)$$

and the hole current in the collector region

$$J_p(y) = -J_r(y) + J_p(B) + J_r(B) \quad B \leq y \leq L \quad (4.2.13)$$

Expressions for  $J_n(0)$ ,  $J_p(0)$  and  $J_p(B) + J_r(B)$  can be derived by substituting (4.2.11), (4.2.12) and (4.2.3) into (4.2.8), (4.2.9) and (4.2.10) respectively and solving at  $y = 0$  for the first two cases and  $y = B$  for the third case.

The results are;

$$J_n(o) = \frac{n(L)e^{-\psi(L)} - n(o)e^{-\psi(o)} - \int_o^L \gamma_n(y') J_r(y') e^{-\psi(y')} dy'}{\int_o^L \gamma_n(y') e^{-\psi(y')} dy'} \quad (4.2.14)$$

$$J_p(o) = \frac{p(o)e^{\psi(o)} - p(B)e^{\psi(B)} + \int_o^B \gamma_p(y') J_r(y') e^{\psi(y')} dy'}{\int_o^B \gamma_p(y') e^{\psi(y')} dy'} \quad (4.2.15)$$

$$J_p(B) + J_r(B) = \frac{p(B)e^{\psi(B)} - p(L)e^{\psi(L)} + \int_B^L \gamma_p(y') J_r(y') e^{\psi(y')} dy'}{\int_o^L \gamma_p(y') e^{\psi(y')} dy'} \quad (4.2.16)$$

To simplify the notation the following definitions will be used;

$$F_{nL}(y) = \int_y^L \gamma_n(y') e^{-\psi(y')} dy'$$

$$FR_{nL}(y) = \int_y^L \gamma_n(y') J_r(y') e^{-\psi(y')} dy'$$

$$F_{pB}(y) = \int_y^B \gamma_p(y') e^{\psi(y')} dy'$$

$$FR_{pB}(y) = \int_y^B \gamma_p(y') J_r(y') e^{\psi(y')} dy'$$

$$F_{pL}(y) = \int_y^L \gamma_p(y') e^{\psi(y')} dy'$$

$$FR_{pL}(y) = \int_y^L \gamma_p(y') J_r(y') e^{\psi(y')} dy'$$

Equations (4.2.14), (4.2.15), and (4.2.15) become;

$$J_n(o) = \frac{n(L)e^{-\psi(L)} - n(o)e^{-\psi(o)} - FR_{nL}(o)}{F_{nL}(o)} \quad (4.2.17)$$

$$J_p(o) = \frac{p(o)e^{\psi(o)} - p(B)e^{\psi(B)} + FR_{pB}(o)}{F_{pB}(o)} \quad (4.2.18)$$

$$J_p(B) + J(B) = \frac{p(B)e^{\psi(B)} - p(L)e^{\psi(L)} + FR_{pL}(B)}{F_{pL}(B)} \quad (4.2.19)$$

Rewriting the carrier concentrations including the recombination and terminal currents results in;

$$n(y) = e^{\psi(y)} \left\{ n(L)e^{-\psi(L)} - n(L)e^{-\psi(L)} \frac{F_{nL}(y)}{F_{nL}(o)} + n(o)e^{-\psi(o)} \frac{F_{nL}(y)}{F_{nL}(o)} + FR_{nL}(o) \frac{F_{nL}(y)}{F_{nL}(o)} - FR_{nL}(y) \right\} \quad (4.2.20)$$

$$p(y) = e^{-\psi(y)} \left\{ p(B)e^{\psi(B)} + p(o)e^{\psi(o)} \frac{F_{pB}(y)}{F_{pB}(o)} - p(B)e^{\psi(B)} \frac{F_{pB}(y)}{F_{pB}(o)} + FR_{pB}(o) \frac{F_{pB}(y)}{F_{pB}(o)} - FR_{pB}(y) \right\} \text{ for } 0 \leq y < B \quad (4.2.21)$$

$$p(y) = e^{-\psi(y)} \left\{ p(L)e^{\psi(L)} + p(B)e^{\psi(B)} \frac{F_{pL}(y)}{F_{pL}(B)} - p(L)e^{\psi(L)} \frac{F_{pL}(y)}{F_{pL}(B)} + FR_{pL}(B) \frac{F_{pL}(y)}{F_{pL}(B)} - FR_{pL}(y) \right\} \text{ for } B \leq y < L \quad (4.2.22)$$

Except for numerical limitations which will be discussed in a later section, equations (4.2.17) through (4.2.22) in conjunction with (4.2.11), (4.2.12), and (4.2.13) completely describe the solutions of the transport and continuity equations for the one-dimensional steady state situation. Concentrations are expressed as explicit functions of the electrostatic potential,  $\psi(y)$  the recombination current,  $J_r(\psi(y), p(y), n(y))$ , and the boundary conditions,  $\psi$ ,  $p$  and  $n$  at  $y=0$ ,  $B$  and  $L$ .

#### Solution to the Poisson Equation

The solution to the normalized one-dimensional Poisson equation can be found by Newton-Raphson iteration. Equation (4.2.1) is discretized on a non-uniform grid and transformed to a set of non-linear difference equations which form a vector,  $F(\psi)$ , whose  $m$ 'th element is defined by,

$$\begin{aligned} \frac{2}{dy_{m+1}(dy_{m+1} + dy_m)} \psi_{m-1} - 2 \left( \frac{1}{dy_{m+1}} + \frac{1}{dy_m} \right) \left( \frac{1}{dy_{m+1} + dy_m} \right) \psi_m \\ + \frac{2}{dy_m(dy_{m+1} + dy_m)} \psi_{m+1} - n_m + p_m + N_m \end{aligned} \quad (4.2.23)$$

where  $dy_m = y_m - y_{m-1}$ . Letting  $\bar{\psi}^k$  represent the potential vector of the previous iteration then the potential vector of the next iteration  $\bar{\psi}^{k+1}$ , can be obtained by the Newton-Raphson method which in matrix form is [4.6];

$$F'(\bar{\psi}^k) \cdot (\bar{\psi}^{k+1} - \bar{\psi}^k) = -F(\bar{\psi}^k) \quad (4.2.24)$$

where  $F'$ , the Jacobian of  $F$ , contains the elements  $F'_{ij} = \frac{\partial f_i}{\partial \psi_j}$  for  $1 \leq i, j \leq \ell$  where  $\ell$  is the number of grid points and  $f_i$  is the  $i$ 'th element of  $F$ .

For purposes of calculating the Jacobian it is convenient to assume Boltzmann statistics for the carrier concentrations such that;

$$n_m = n_{iE,m} \exp(\psi_m - \phi_{n,m}) \quad (4.2.25)$$

$$p_m = n_{iE,m} \exp(\phi_{p,m} - \psi_m) \quad (4.2.26)$$

where  $\phi_n$  and  $\phi_p$  are the electron and hole quasi-fermi levels and  $n_{iE}$  is the effective intrinsic electron concentration. (As will be discussed in a later section the band gap and as a consequence the intrinsic electron concentration depend on the impurity concentration.) The assumption of Boltzmann statistics in the Jacobian does not preclude the use of Fermi-Dirac statistics since  $n$  and  $p$  appear explicitly in Poisson's equation. The tri-diagonal matrix  $F'$  is obtained by substituting (4.2.25) and (4.2.26) into (4.2.23) and differentiating. The  $m$ 'th row of  $F'$  has off diagonal elements.

$$\frac{2}{dy_{m+1}(dy_{m+1} + dy_m)}$$

and diagonal element,

$$\begin{aligned} & -2 \left( \frac{1}{dy_m} + \frac{1}{dy_m} \right) \left( \frac{1}{dy_{m+1} + dy_m} \right) - n_{iE,m} \exp(\psi_m^k - \phi_{n,m}) \\ & - n_{iE,m} \exp(\phi_{p,m} - \psi_m^k). \end{aligned}$$

The matrix equation 4.2.24 is readily inverted by LU decomposition and Gauss elimination techniques [4.5] and the improved potential values  $\psi^{-k+1}$  are obtained.

#### General Iteration

In the last two sections solutions were derived for carrier concentrations from the continuity and transport equations given the potential, and for the potential from Poisson's equation given the electron and hole densities. In this section a general iterative scheme will be outlined which couples the two solutions in a manner which results in convergence under most bias conditions. The iterative loop is diagrammed in the flow chart of Figure 4.2.5.

After specifying the impurity concentration profile the concentration dependent physical parameters,  $n_{iE}$ ,  $\gamma_n$ ,  $\gamma_p$  are calculated and the non-uniform grid is determined. The first step is to solve for the equilibrium case (zero-bias). Initial guesses for  $\psi(y)$ ,  $n(y)$ , and  $p(y)$  are determined from the neutrality condition,  $n-p = N$  or assuming Boltzmann statistics,

$$n_{iE} \exp(\psi - \phi_n) - n_{iE} \exp(\phi_p - \psi) = N \quad (4.2.27)$$

In equilibrium  $\phi_n(y) = \phi_p(y) = 0$  so that (4.2.27) becomes;

$$\exp(\psi) - \exp(-\psi) = \frac{N}{n_{iE}} \quad (4.2.28)$$

Multiplying both sides of (4.2.28) by  $\exp(\psi)$ , adding  $\frac{N^2}{4n_{iE}^2}$  and rearranging results in,

$$\exp(2\psi) - \frac{N}{n_{iE}} \exp(\psi) + \frac{N^2}{4n_{iE}^2} = 1 + \frac{N^2}{4n_{iE}^2} \quad (4.2.29)$$

$$\text{or} \\ \left( \exp(\psi) - \frac{N}{2n_{iE}} \right)^2 = 1 + \frac{N^2}{4n_{iE}^2}$$

and solving for  $\psi$ ,

$$\psi = \pm \ln \left\{ \sqrt{1 + \frac{N^2}{4n_{iE}^2}} \pm \frac{N}{2n_{iE}} \right\} \quad (4.2.30)$$

where the positive signs apply to  $N > 0$  and the negative signs to  $N < 0$ .

Equation (4.2.30) is solved at each grid point and the resulting values of  $\psi$  are used to calculate  $n$  and  $p$ . The initial estimates are substituted into the Newton-Raphson formulation of Poisson's equation to obtain improved values at  $\psi$  which are used to calculate new values of  $n$  and  $p$ , from Boltzmann statistics. The process is repeated until convergence is achieved. The loop required in equilibrium or for an MOS capacitor does not include the continuity and transport solutions since no current is flowing under either condition.

After convergence of the equilibrium solution, desired bias voltages are applied between the base-emitter junction,  $V_{BE}$ , and the collector-base junction,  $V_{CB}$ . The bias voltages affect the boundary conditions as shown in Figure 4.2.4b, assuming equilibrium at the end contact;

$$\phi_p(o) = \phi_n(o) = -V_{BE} \quad (4.2.31)$$

and

$$\phi_p(L) = \phi_n(L) = V_{CB} \quad (4.2.32)$$

If charge neutrality and Boltzmann statistics are also assumed then

$$\psi(o) = -V_{BE} + \ln \left\{ \sqrt{1 + \frac{N(o)^2}{4n_{iE}(o)^2}} + \frac{N(o)}{2n_{iE}(o)} \right\} \quad (4.2.33)$$

$$\psi(L) = V_{CB} + \ln \left\{ \sqrt{1 + \frac{N(L)^2}{4n_{iE}(L)^2}} + \frac{N(L)}{2n_{iE}(L)} \right\} \quad (4.2.34)$$

and

$$n(o) = n_{iE}(o) \exp \left\{ \psi(o) + V_{BE} \right\} \quad (4.2.35)$$

$$n(L) = n_{iE}(L) \exp \left\{ \psi(L) - V_{CB} \right\} \quad (4.2.36)$$

$$p(o) = n_{iE}(o) \exp \left\{ -V_{BE} - \psi(o) \right\} \quad (4.2.37)$$

$$p(L) = n_{iE}(L) \exp \left\{ V_{CB} - \psi(L) \right\} \quad (4.2.38)$$

Equations (4.2.33) through (4.2.38) constitute a complete set of boundary conditions at the emitter and collector contacts while the assumption of Boltzmann statistics and the restriction that  $\phi_p(B) = 0$  represent a complete set of boundary conditions at the base contact. However, all carrier concentrations and current densities are written in terms of general boundary conditions and are not necessarily restricted to the preceding assumptions.

Poisson's equation is solved subject to the new boundary conditions and the values of  $n$ ,  $p$  and  $\psi$  from the previous bias or equilibrium solution. For the bipolar transistor or diode the electric field is calculated from the spatial derivative of the improved potential values,  $\psi^{k+1}$ , the normalized hole and electron mobilities are determined as a functions of the field. The recombination rate,  $U$ , is determined as a function of  $\psi^{k+1}$  and the hole and electron concentrations from the previous iteration,  $n^k$  and  $p^k$ . The recombination current,  $J_r^{k+1}$ , is calculated by integrating  $U$ . Hole and electron concentrations and current densities are derived from the solutions to the continuity and transport equations as functions of  $\psi^{k+1}$ ,  $J_r^{k+1}$ ,  $\gamma_n^{k+1}$  and  $\gamma_p^{k+1}$  and the boundary conditions. The new values of  $n$  and  $p$  are substituted into Poisson's equation and improved potential values are calculated. The loop continues until the convergence criterion is satisfied and new bias conditions can be imposed.

The total current densities are calculated from the hole and electron current densities at the contact using the conventional polarities;

$$J_C = - \left\{ J_n(L) + J_p(L) \right\} = - \left\{ J_n(o) + J_r(B) + J_p(B) \right\} \quad (4.2.39)$$

$$J_E = - \left\{ J_n(o) + J_p(o) \right\} \quad (4.2.40)$$

$$J_B = J_E - J_C = J_r(B) + J_p(B) - J_p(o) \quad (4.2.41)$$

The highest degree of non-linearity is introduced through the recombination current  $J_r$  since it depends on the values of  $n$  and  $p$  from the previous iteration. As a result, the number of iterations required for convergence increases with increasing recombination currents (The recombination rate calculation will be discussed in a later section.) This effect is intensified at high forward bias and limits the practical range of  $V_{BE}$  to approximately 0.9 volts. However, the limiting value is well beyond

the threshold for high level injection as will be shown in the examples.

The preceding sections have outlined a solution method which in principle can determine the electrical properties of one-dimensional semiconductor structures in steady-state. However, as De Mari has demonstrated [4.4] two numerical features of the formulation limit the usefulness of the solution. In the next two sections methods will be presented to avoid these limitations.

#### Reformulation to Avoid the Differences Between Nearly Equal Numbers

Under high forward bias conditions intolerable errors are introduced because certain terms in the expressions for carrier concentrations become nearly equal.

For the electron concentration, equation (4.2.20), when  $y$  is close to 0 and  $F_{nL}(y) \approx F_{nL}(0)$ , the 1st and 2nd terms and the 4th and 5th terms within the brackets become nearly equal. If their differences are comparable in magnitude to the 3rd term loss of significant digits and large errors in the concentration calculation result.

This problem can be avoided by defining the integrals [4.4],

$$F_{no}(y) \equiv \int_0^y \gamma_n(y') e^{-\psi(y')} dy'$$

$$FR_{no}(y) \equiv \int_0^y \gamma_n(y') J(y') e^{-\psi(y')} dy'$$

and observing that;

$$F_{nL}(0) = F_{nL}(y) + F_{no}(y)$$

$$FR_{nL}(0) = FR_{nL}(y) + FR_{no}(y)$$

Substituting these expressions into equation (4.2.20) and rearranging yields,

$$n(y) = \frac{e^{\psi(y)}}{F_{nL}(0)} \left\{ n(L)e^{-\psi(L)}F_{no}(y) + n(0)e^{-\psi(0)}F_{nL}(y) + FR_{no}(y)F_{nL}(y) - F_{no}(y)FR_{nL}(y) \right\} \quad (4.2.42)$$

which is immune to the problem of small differences between nearly equal numbers.

An analogous situation exists for holes in the emitter region, equation (4.2.21), where the 1st and 3rd terms and the 4th and 5th terms tend to cancel when  $y \approx 0$ . In this case the following integrals are defined,

$$F_{p0}(y) \equiv \int_0^y \gamma_p(y') e^{\psi(y')} dy'$$

$$FR_{p0}(y) \equiv \int_0^y \gamma_p(y') J_r(y') e^{\psi(y')} dy'$$

and the substitutions

$$F_{pB}(0) = F_{pB}(y) = F_{p0}(y)$$

$$FR_{pB}(0) = FR_{pB}(y) + FR_{p0}(y)$$

are made in equation (4.2.21). The resulting expression for holes in the emitter region is;

$$p(y) = \frac{e^{-\psi(y)}}{F_{pB}(0)} \left\{ p(B)e^{\psi(B)}F_{p0}(y) + p(0)e^{\psi(0)}F_{pB}(y) + FR_{p0}(y)F_{pB}(y) - FR_{pB}(y)F_{p0}(y) \right\} \quad (4.2.43)$$

for  $0 \leq y < B$

In a similar manner integrals can be defined and substituted into the expression for holes in the collector region, equation (4.2.22);

$$F_{pC}(y) \equiv \int_B^y \gamma_p(y') e^{\psi(y')} dy'$$

$$FR_{pC}(y) \equiv \int_B^y \gamma_p(y') J_r(y') e^{\psi(y')} dy'$$

and

$$F_{pL}(B) = F_{pC}(y) + F_{pL}(y)$$

$$FR_{pL}(B) = FR_{pC}(y) + FR_{pL}(y)$$

and the resulting expression for holes is;

$$p(y) = \frac{e^{-\psi(y)}}{F_{pL}(B)} \left\{ p(L)e^{\psi(L)} F_{pC}(y) + p(B)e^{\psi(B)} F_{pL}(y) + FR_{pC}(y) F_{pL}(y) - FR_{pL}(y) F_{pC}(y) \right\} \quad (4.2.44)$$

for  $B \leq y \leq L$

#### Potential Scaling to Avoid Overflow

The formulation in the preceding sections is general in principle but limited in practice by the maximum representable number in the computer. In the case of HP 2100 minicomputers the maximum number is on the order of  $1 \times 10^{39}$  which limits the bias range to approximately two volts, since  $\exp(V/(kt/q)) \approx 1 \times 10^{39}$  when  $V = 2.0$  volts. To avoid this problem De Mari has shown [4.4] that the potential distribution can be divided into a number of cells such that a unique scaling voltage is defined within each cell. The scaling voltages are subtracted from the actual potentials so that the exponential terms never overflow.

To implement this method the potential distribution is divided into  $k$  cells as shown in Figure 4.2.26. If  $\exp(R)$  is the maximum representable number then the cell potential height is  $2R$  (except for the  $k$ 'th cell whose height is  $R$  and the first cell which does not require scaling under active bias conditions). The scaling potentials in each cell is defined as the average of the cell boundary potentials;

$$\psi_{oj} = (\psi_c(j) + \psi_c(j-1))/2 \quad (4.2.45)$$

where  $j$  denotes the cell number. ( $\psi_{ok} = \psi(L)$ ). The boundary potentials and coordinants are defined in Table 4.2.2.

The procedure requires defining new integrals so that all  $\exp(\psi)$  terms are transformed to  $\exp(\psi - \psi_{oj})$ . The expressions for carrier concentration are then reformulated in terms of the new integrals and are independent of the scaling voltages. The electron integrals are;

$$F_{nj}(y) = \int_y^L \gamma_n(y') \exp(\psi_{oj} - \psi(y')) dy' \quad (4.2.46)$$

$$FR_{nj}(y) = \int_y^L \gamma_n(y') J_r(y') \exp(\psi_{oj} - \psi(y')) dy' \quad (4.2.47)$$

If  $y$  is in the  $j$ th cell then the upper limit of integration becomes  $y_c(j+1)$  since for  $y > y_c(j+1)$ ,  $\psi_{oj} - \psi(y)$  will be large and negative so that contributions to the integrals are negligible.  $F_{nj}(y) \cdot \exp(-\psi_{oj})$  and  $FR_{nj}(y) \cdot \exp(-\psi_{oj})$  can be substituted for  $F_{nL}$  and  $FR_{nL}$  in equations (4.2.20) and (4.2.17) resulting in;

$$\begin{aligned} n(y) = & \frac{e^{\psi(y) - \psi_{oj}}}{F_{nl}(0)e^{\psi(0) - \psi_{01}}} \left\{ \left( n(0) - n(L) / (e^{\psi(L) - \psi(0)} F_{nj}(y)) \right) \right. \\ & + \frac{n(L)e^{\psi(0) - \psi_{01}}}{e^{\psi(L) - \psi_{oj}}} F_{nl} + e^{\psi(0) - \psi_{01}} (F_{rnl}(0)F_{nj}(y) \\ & \left. - F_{nl}(0)FR_{nj}(y)) \right\} \end{aligned} \quad (4.2.48)$$

and

$$J_n(0) = \left\{ n(L)e^{\psi_{01} - \psi(L)} - n(0)e^{\psi_{01} - \psi(0)} - FR_{nl}(0) \right\} / F_{nl}(0) \quad (4.2.49)$$

The terms containing the  $\exp(-\psi(L))$  are negligible when  $\psi(L)$  is large and can be set to zero.

For holes in the collector region the corresponding integrals are;

$$F_{pj} = \int_B^y \gamma_p(y') e^{\psi(y') - \psi_{oj}} dy' \quad (4.2.50)$$

$$FR_{pj} = \int_B^y \gamma_p(y') J_r(y') e^{\psi(y') - \psi_{oj}} dy' \quad (4.2.51)$$

In this case the integration is from B to y so that contributions to the integral when  $|\psi(y') - \psi_{oj}|$  is large can be neglected.

The non-scaled integrals become;

$$F_{pL}(y) = e^{\psi_{ok}} F_{pk}(L) - e^{\psi_{oj}} F_{pj}(y) \quad (4.2.52)$$

$$FR_{pL}(y) = e^{\psi_{ok}} FR_{pk}(L) - e^{\psi_{oj}} FR_{pj}(y) \quad (4.2.53)$$

Substituting into equations (4.2.22) and (4.2.19) with the condition that  $\psi_{ok} = \psi(L)$  results in;

$$p(y) = \frac{e^{\psi_{oj} - \psi(y)}}{F_{pk}(L)} \left\{ \left( p(L) - p(B) e^{\psi(B) - \psi(L)} \right) F_{pj}(y) + p(B) e^{\psi(B) - \psi_{oj}} F_{pk}(L) + \left( FR_{pj}(y) F_{pk}(L) - FR_{pk}(L) F_{pj}(y) \right) \right\} \quad (4.2.54)$$

and

$$J_p(B) + J_r(B) = \frac{p(B) e^{\psi(B) - \psi(L)} - p(L) + FR_{pk}(L)}{F_{pk}(L)} \quad (4.2.55)$$

Again the terms involving  $\exp(-\psi(L))$  become negligible for large  $\psi(L)$ .

Incorporating potential scaling in the collector region allows large reverse biases across the collector base junction. Large forward bias on the base-

emitter junction can be maintained simultaneously since the expression for hole density in the emitter region (4.2.43) has been rearranged to avoid small differences between nearly equal numbers. The following section completes the program description with a discussion of mobility, recombination and band-gap narrowing.

### Physical Models

#### Mobility

Hole and electron mobilities are expressed as empirical functions of impurity concentration and electric field. In general;

$$\mu(y) = \left( \mu_{\min} + \frac{\mu_{\max} - \mu_{\min}}{1 + \left( \frac{N(y)}{N^*} \right)^k} \right) \frac{1}{(1 + E(y)/E_c)} \quad (4.2.56)$$

Values of the empirical constants for electrons and holes are listed in Table 4.2.3.

#### Band-Gap Narrowing

When the impurity concentration is greater than  $10^{17} \text{ cm}^{-3}$  electron wave functions associated with the impurity energy levels begin to overlap forming bands which in turn overlap the intrinsic conduction and valence band edges. The spread of energy levels causes localized band gap narrowing and as a result an increase in the effective intrinsic electron concentration,  $n_{iE}$ . Slotboom has shown [4.8] that the band gap narrowing effect can be accounted for by defining an effective intrinsic electron concentration;

$$n_{iE}(y) = n_{i0} \exp \left\{ \frac{V_1}{2kt/q} \left( \ln \frac{N(y)}{N_0} + \sqrt{\ln^2 \frac{N(y)}{N_0} + C} \right) \right\} \quad (4.2.58)$$

where  $n_{i0}$  is the intrinsic electron concentration without band gap narrowing,  $V_1 = 9 \text{ mV}$ ,  $N_0 = 10^{17} \text{ cm}^{-3}$  and  $C = 0.5$ . The mathematical model derived in the previous sections facilitates incorporation of  $n_{iE}(y)$  since the independent

variables are  $n$  and  $p$ . As a result  $n_{iE}$  appears explicitly only at the boundaries and in the expression for recombination rate.

#### Recombination

The recombination rate is calculated assuming the hole and electron concentrations and the electrostatic potentials are known. Consequently any recombination term which depends on  $n$ ,  $p$  and  $\psi$  can be easily incorporated into the model. The present formulation includes single level Shockley-Read-Hall (SRH) and Auger recombination mechanisms. The unnormalized recombination rate is  $U(y) = U_{SRH} + U_A$ . The SRH component is;

$$U_{SRH}(y) = \frac{n_{i0} (n(y)p(y) - n_{iE}(y)^2)}{\tau_p (n(y) + n_1(y)) + \tau_n (p(y) + p_1(y))} \quad (4.2.58)$$

where  $\tau_p$  and  $\tau_n$  are the hole and electron lifetimes respectively in seconds and  $n_2(y) = n_{iE}(y) \exp(E_T/kt - \psi(y))$  and  $p_1(y) = n_{iE}(y) \exp(\psi(y) - E_T/kt)$  where  $E_T$  is the trap energy level measured in electron volts from the intrinsic fermi level. The Auger component is;

$$U_A(y) = \{C_n (n^2 p - n n_{iE}^2) + C_p (p^2 n - p n_{iE}^2)\} n_{i0}^3$$

where  $C_n = 2.8 \times 10^{-31} \text{ cm}^6/\text{sec}$  and  $C_p = 9.9 \times 10^{-32} \text{ cm}^6/\text{sec}$ .

#### Applications

SEDAN is capable of analyzing a wide variety of one dimensional device structures and is limited only by the requirement of two or three contacts. The information obtained from the device analysis includes values of the independent variables  $p$ ,  $n$ ,  $\psi$ ,  $J_n$  and  $J_p$  over the specified bias range as well as any parameters which can be derived from the independent variables such as electron and hole quasi-fermi levels, terminal currents, junction capacitance, integrated charge, etc. The following

examples demonstrate calculations for several different device structures including a PIN diode, an NPN transistor and an MOS capacitor.

#### PIN Diode

The diode considered in this example is 2.0 microns in total length and is divided into 100 grid elements. The PIN impurity profile is constructed analytically using two Gaussian diffusions and a constant substrate. (Alternatively, measured or simulated profiles can be read directly from data files). Figure 4.2.7 shows the hole and electron concentrations under reverse bias, and moderate and high forward bias. For the reverse bias case hole and electron concentrations fall off exponentially through the depletion region while in forward bias, the exponential dependence is modified by recombination in the depletion region and the non-uniform profile. For high level injection the electron and hole concentrations rise above the donor and acceptor levels and are roughly equivalent throughout the lightly doped portion of the device.

Figure 4.2.8 shows the effects of recombination and band gap narrowing on the forward characteristics of the PIN diode. If recombination and band gap narrowing are neglected then the current density displays the familiar exponential dependence on the applied bias voltage. When recombination is included the recombination current in the space charge region dominates at low bias levels, increasing the current density and increasing the slope of the exponential dependence. Band gap narrowing tends to increase the current without changing the functional dependence on applied bias since the current density is approximately proportional to  $n_{iE}$ .

#### NPN Transistor

Figure 4.2.9a shows the impurity profile and hole and electron concentrations for a typical epitaxial bipolar transistor operating in the normal

active mode. The impurity profile is constructed analytically using three Gaussian diffusions and a constant epitaxial layer and is divided into 100 grid elements. The electrostatic potential,  $\psi$ , and the electron and hole quasi-fermi levels  $\phi_n$  and  $\phi_p$  are plotted in Figure 4.2.9a. The hole quasi-fermi level is roughly constant throughout the base region confirming the assumption that the choice of the base contact position is non-critical. The kink in the hole quasi-fermi level near the end of the collector depletion region is due to the large generation rate in the space charge layer.

Similar information is plotted for high level injection in Figures 4.2.10 (a) and (b). In this example  $V_{BE}=0.8$  volts and  $V_{CB}=0.5$  volts. The hole quasi-fermi level remains constant throughout the base region even under high level injection. The hole and electron concentrations now exceed the donor and acceptor concentrations resulting in base "push-out" and increased integrated base conductivity. Both of these effects tend to decrease  $\beta$  and impede the rise of collector current,  $J_c$ , at high forward bias as can be seen in Figures 4.2.11(a) and (b). Another second order effect is apparent at low bias where recombination in the base-emitter space charge region increases the base current,  $J_B$ , and decreases  $\beta$ .

#### MOS Capacitor

Analysis of an MOS capacitor consists of solving Poisson's equation in the direction perpendicular to the oxide interface since steady state current can be neglected. The dissimilarity in dielectric constants across the oxide-silicon interface is accounted for by including a normalized relative permittivity,  $\epsilon_r$ , in Poisson's equation. The matrix

F' of equation (4.2.24) is multiplied by the vector  $E_r$  whose elements are defined by;

$$E_{r,i} = \begin{cases} \frac{\epsilon_{ox}}{\epsilon_{si}} & \text{for } i < I_t \\ 1 & \text{for } i \geq I_t \end{cases}$$

where  $I_t$  is the grid node corresponding to the oxide thickness, and  $\epsilon_{ox}$  and  $\epsilon_{si}$  are the permittivities of the oxide and silicon respectively. Metal semiconductor work functions and oxide charges are incorporated by offsetting the applied bias by a flat-band voltage.

Figure 4.2.12 shows the electron and hole concentrations for several gate voltages in a surface implanted, p-substrate device. The total electron charge,  $Q_n$ , and the total net charge,  $Q_{net}$ , ( $Q_{net}$  is the integral of  $|N_A + n-p|$  throughout the structure) are plotted as functions of the surface potential in Figure 4.2.13. Three distinct operational regions, accumulation, depletion and strong inversion, are evident. Other applications to MOS capacitors include the effects of back-gate bias and the presence of one or more junctions beneath the surface.

### Conclusion

A detailed description of a one-dimensional steady-steady semiconductor analysis program has been presented. Fundamental equations were outlined, numerical procedures were discussed and several applications to one dimensional structures were presented.

Future work will emphasize unique applications of the one-dimensional solution to two-dimensional problems by coupling the numerical solution in one dimension with analytical or numerical solutions in the other dimension.

This quasi-two dimensional approach is especially useful for VMOS and DMOS transistors since channel impurity profiles vary in a direction parallel to the surface while current perpendicular to the surface is usually negligible under most operating conditions.

Two important objectives of numerical device simulation are to understand the dominant physical mechanisms determining device performance and to apply this knowledge to analytical models for use in circuit simulation. The one-dimensional analysis program will contribute to these objectives standing alone in some cases and coupled with additional analysis techniques in other cases.

Table 4.2.1

Normalized parameters, normalizing factors and physical contacts

Normalized quantity		Normalization factor		
Description	Symbol	Symbol	Value	Units
Position coordinant	y	$L_I \equiv \sqrt{V_T \epsilon_{si}/q n_{i0}}$	$3.405 \times 10^{-3}$	cm
Electrostatic potential	$\psi$	$V_T \equiv kT/q$	.02586	volts
Quasi-fermi levels	$\phi_n, \phi_p$	$V_T$	.02586	volts
Electric field	E	$V_T/L_I$	7.595	V/cm
Carrier densities and effective intrinsic electron concentration	$n, p, n_{iE}$	$n_{i0}$	$1.45 \times 10^{10}$	$\text{cm}^{-3}$
Net, donor and acceptor densities	$N, N_A, N_D$	$n_{i0}$	$1.45 \times 10^{10}$	$\text{cm}^{-3}$
Carrier mobilities	$\gamma_n^{-1}, \gamma_p^{-1}$	$\mu_0$	1.0	$\text{cm}^2/\text{V-sec}$
Recombination, electron and hole current densities	$J_r, J_n, J_p$	$J_0 \equiv q \mu_0 n_{i0} V_T/L_I$	$1.762 \times 10^{-8}$	$\frac{\text{coul}}{\text{sec-cm}^2}$
Recombination rate	U	$U_0 \equiv \mu_0 V_T n_{i0}/L_I^2$	$3.234 \times 10^{13}$	$1/\text{sec-cm}^3$

## Physical Constants

Boltzmann's constant	k	$8.62 \times 10^{-5}$	ev/°K
Temperature	T	300	°K
Electronic charge	q	$1.6 \times 10^{-19}$	coul.
Si permittivity	$\epsilon_{si}$	$1.04 \times 10^{-12}$	Farad/cm
SiO <sub>2</sub> permittivity	$\epsilon_{ox}$	$3.3 \times 10^{-12}$	Farad/cm

Table 4.2.2

Potential and Spatial Boundaries for Potential Scaling Cells

Cell #	Potential Boundaries	Spatial Boundaries
1	$\psi_c(1) \geq \psi(y) > \psi_c(2)$	$0=y_c(1) < y < y_c(2) = B$
2	$\psi_c(2) \leq \psi(y) < \psi_c(3)$	$y_c(2) \leq y < y_c(3)$
$\vdots$	$\vdots$	$\vdots$
j	$\psi_c(j) \leq \psi(y) < \psi_c(j+1)$	$y_c(j) \leq y < y_c(j+1)$
$\vdots$	$\vdots$	$\vdots$
k-1	$\psi_c(k-1) \leq \psi(y) < \psi_c(k)$	$y_c(k-1) \leq y < y_c(k)$
k	$\psi_c(k) \leq \psi(y) < \psi_c(k+1)=\psi(L)$	$y_c(k) \leq y \leq y_c(k+1) = L$

Table 4.2.3  
Mobility Parameters

	$\mu_{\max}$ $\text{cm}^2/\text{V-sec}$	$\mu_{\min}$ $\text{cm}^2/\text{V-sec}$	$N^*$ $\text{cm}^{-3}$	$k$ -	$E_c$ $\text{V/cm}$
n	1350	130	$5 \times 10^{17}$	0.72	>396
p	475	90	$3 \times 10^{16}$	0.76	20,000

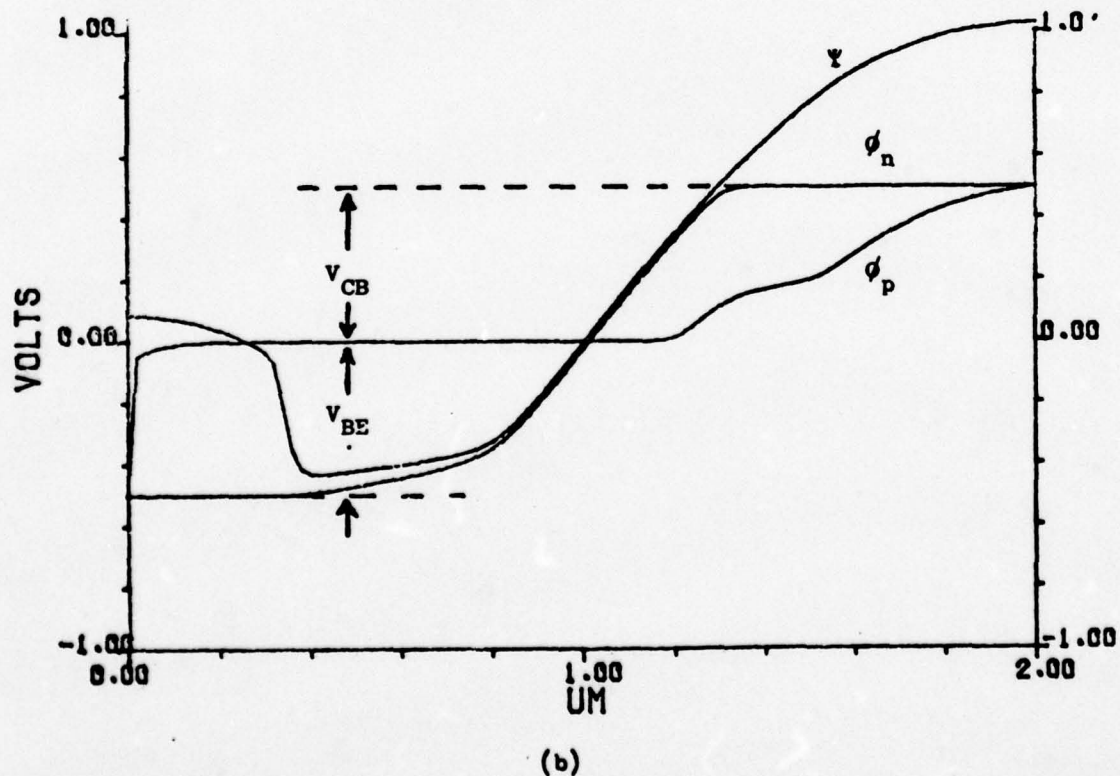
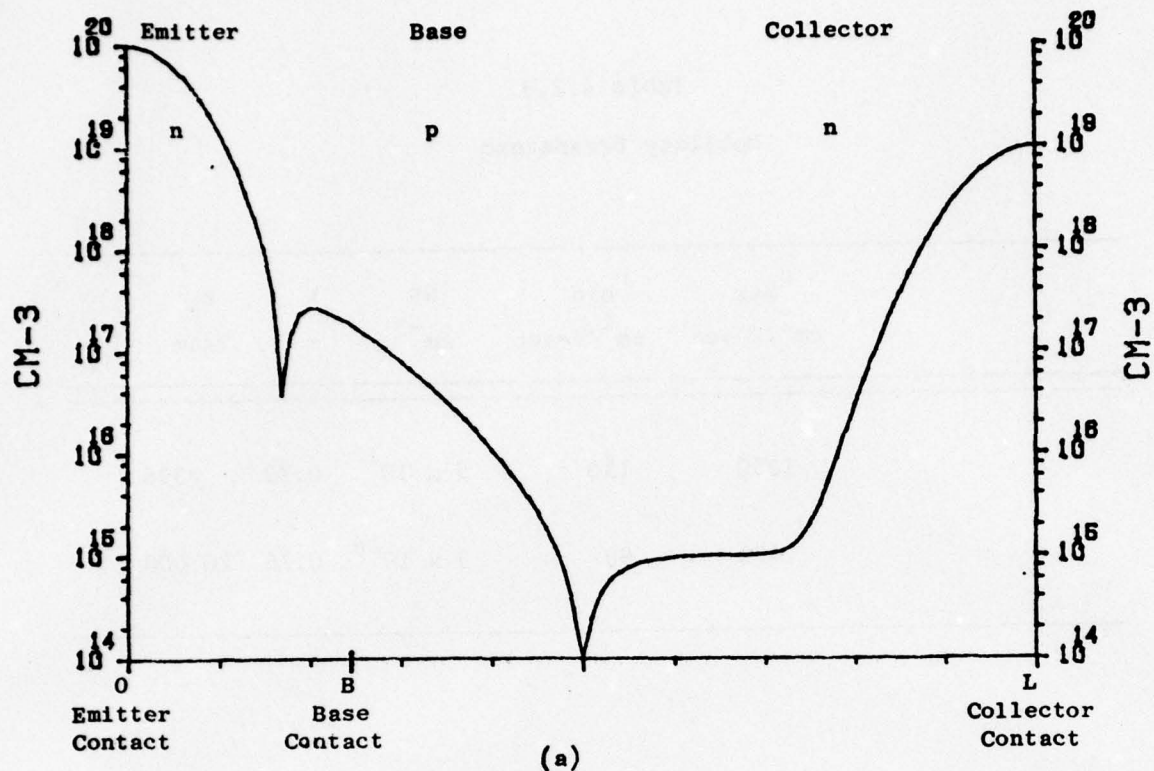


Figure 4.2.4 - Impurity profile of a typical npn bipolar transistor.  
 (a) Electrostatic potential,  $\psi$ , electron,  $\phi_n$ , and hole,  $\phi_p$ , quasi-fermi potentials and bias potentials,  $V_{BE}$  and  $V_{CB}$ , for an actively biased npn transistor.

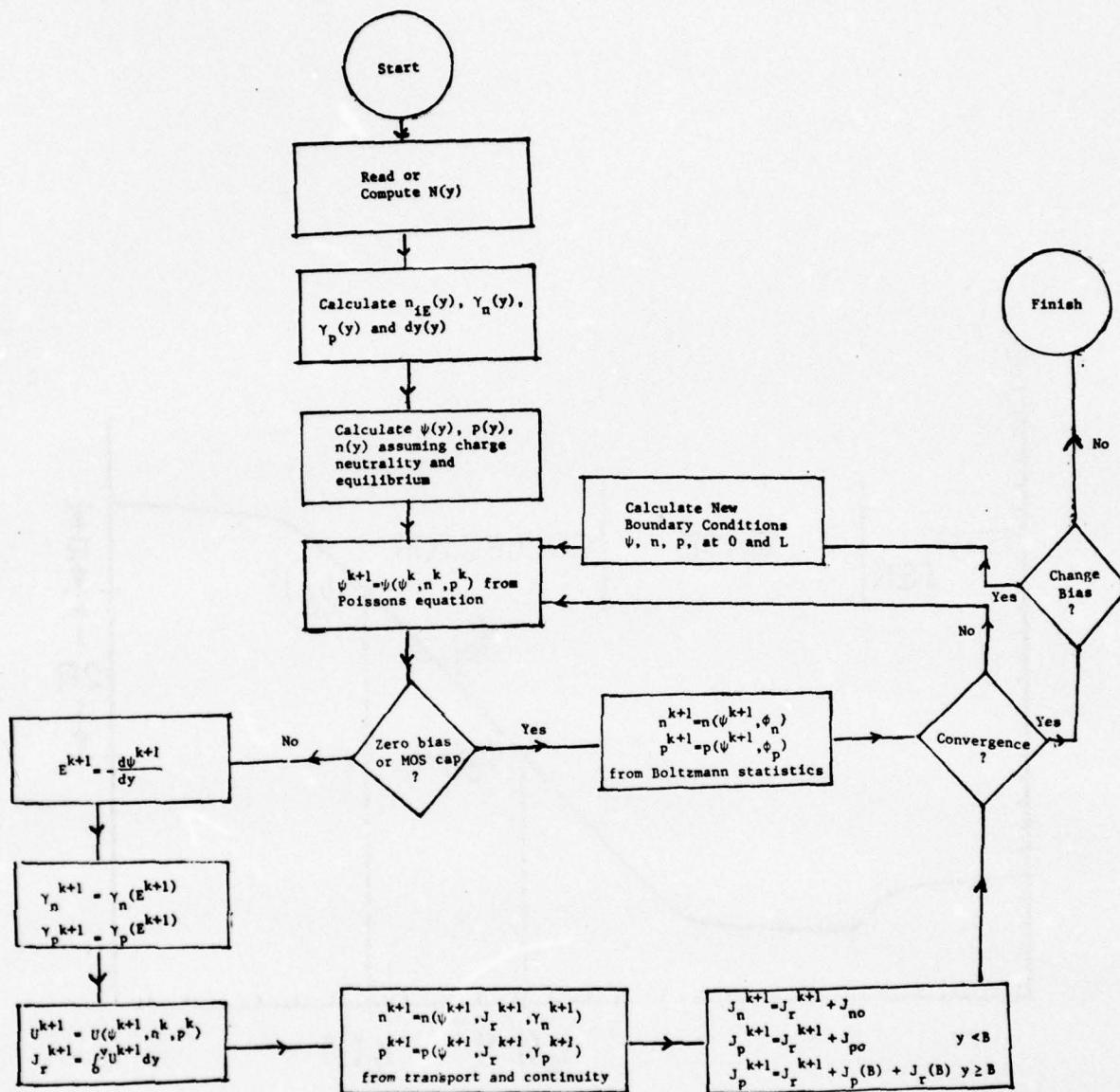


Figure 4.2.5 - Flow diagram of the general iteration procedure.

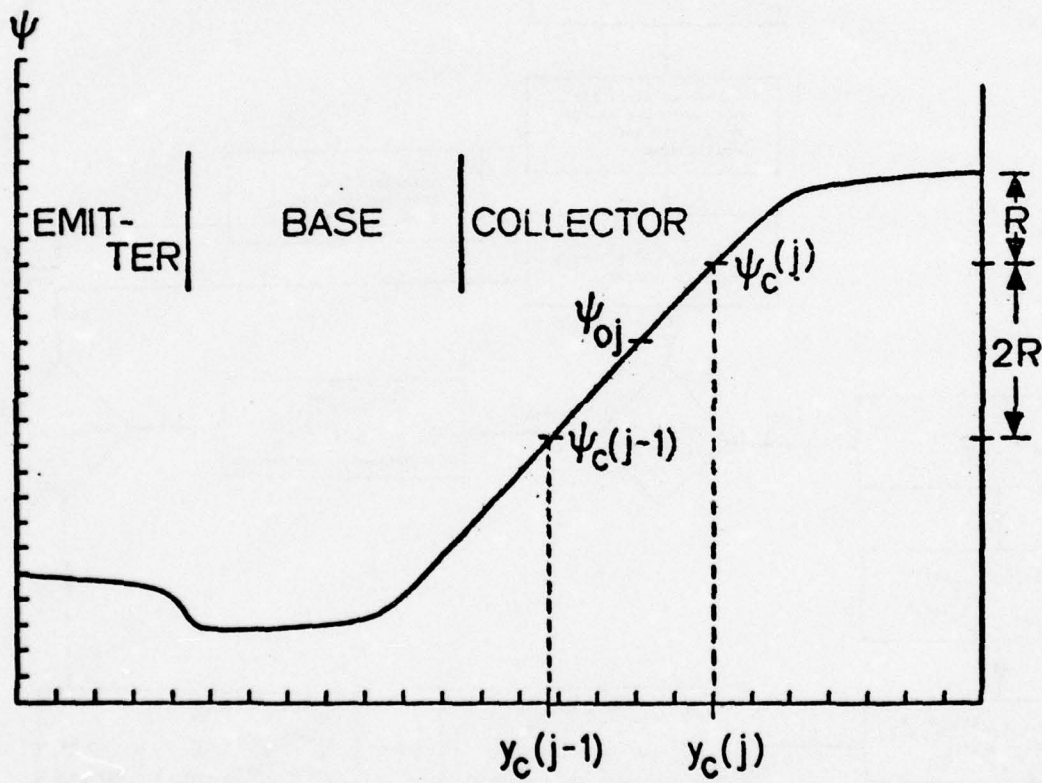


Figure 4.2.6 - Potential scaling for an npn transistor.  $\psi_{oj}$  is the scaling potential for cell  $j$ ,  $2R$  is the nominal cell width, and  $y_c$  and  $\psi_c$  are the spatial and potential cell boundaries.

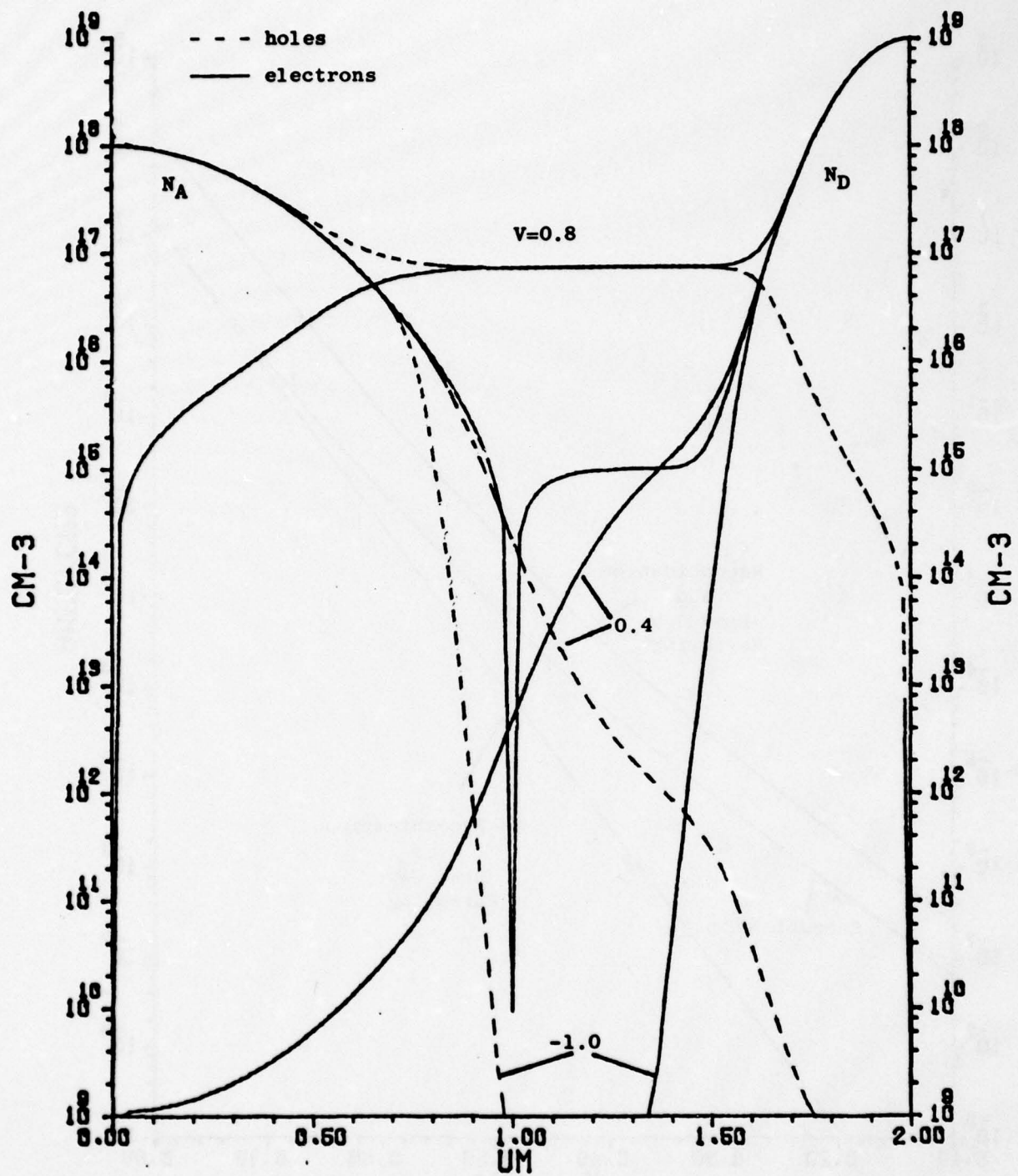


Figure 4.2.7 - Hole (---) and electron (—) densities in a PIN diode for three bias voltages, V.

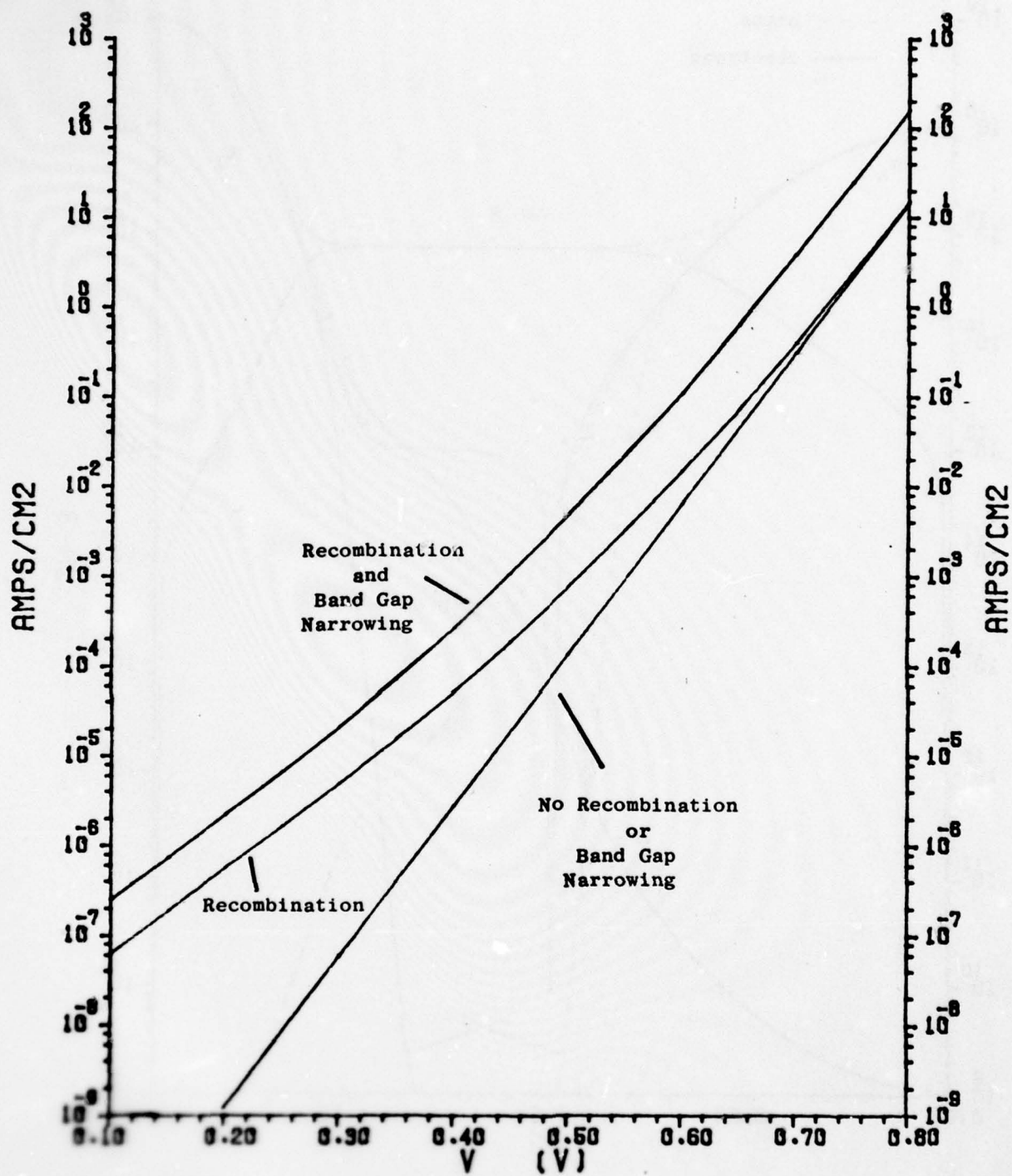


Figure 4.2.8 - PIN diode current versus bias voltage for recombination and band gap narrowing, recombination alone and no recombination on band gap narrowing.

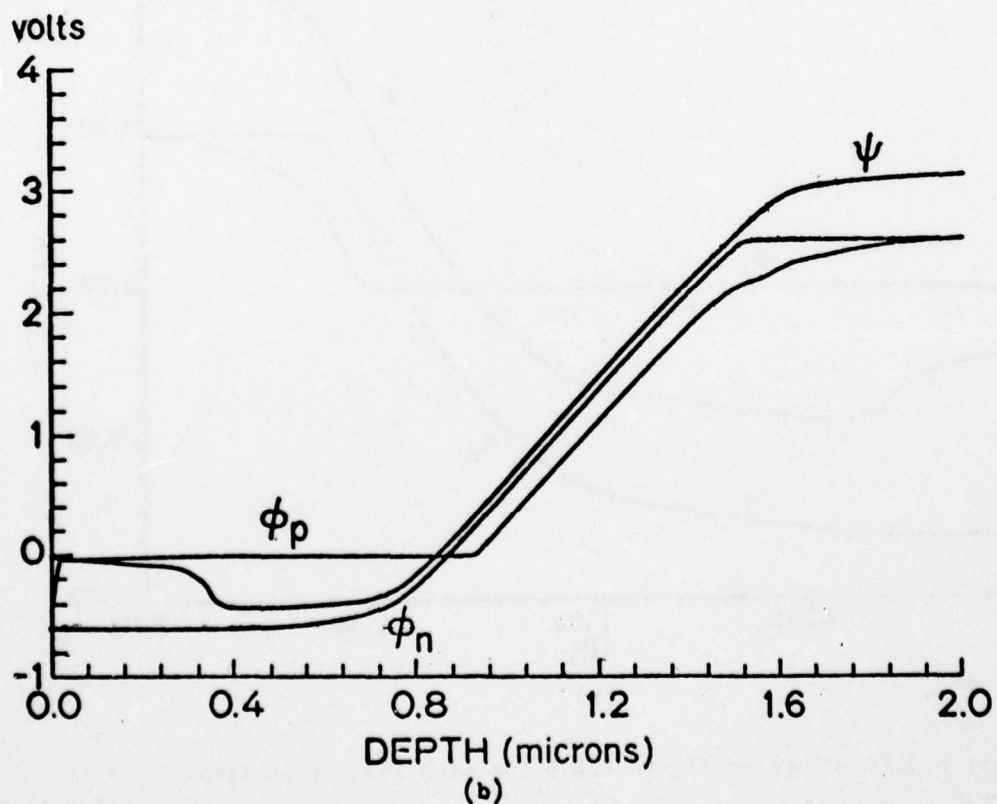
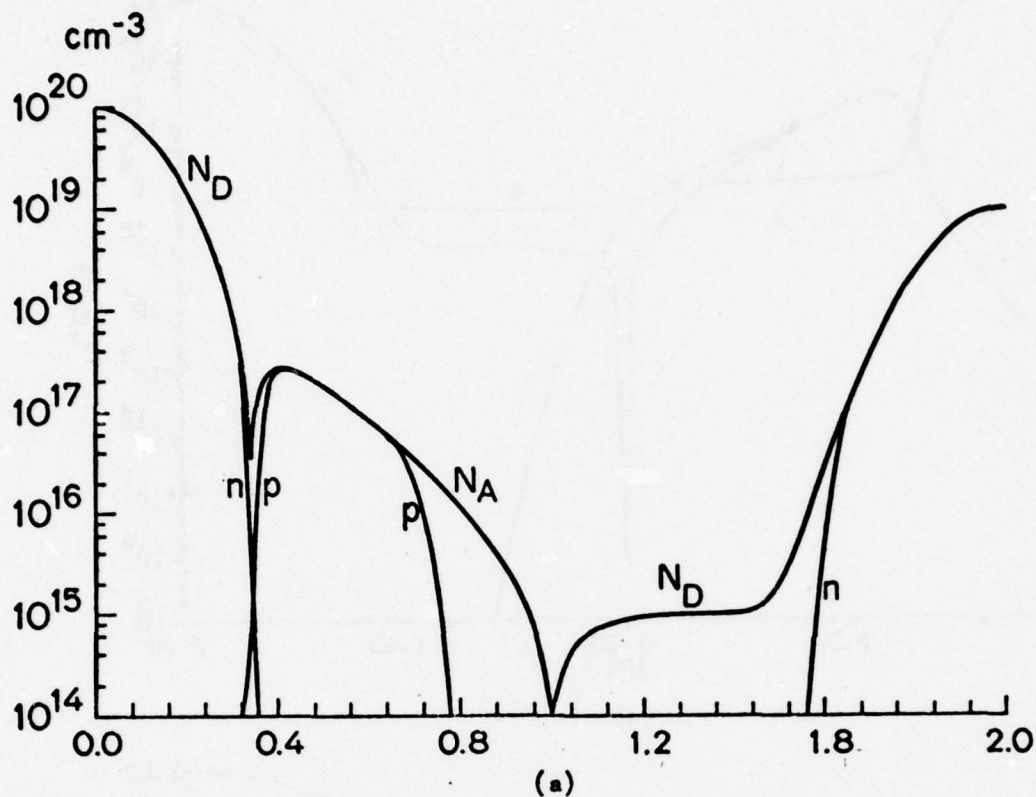


Figure 4.2.9 - Electron,  $n$ , hole,  $p$ , and impurity concentrations  $N_A$ ,  $N_D$  versus depth (a) and electrostatic potential, and hole quasi-Fermi potentials,  $\phi_n$  and  $\phi_p$ , versus depth (b) for an actively biased npn transistor under low level injection.

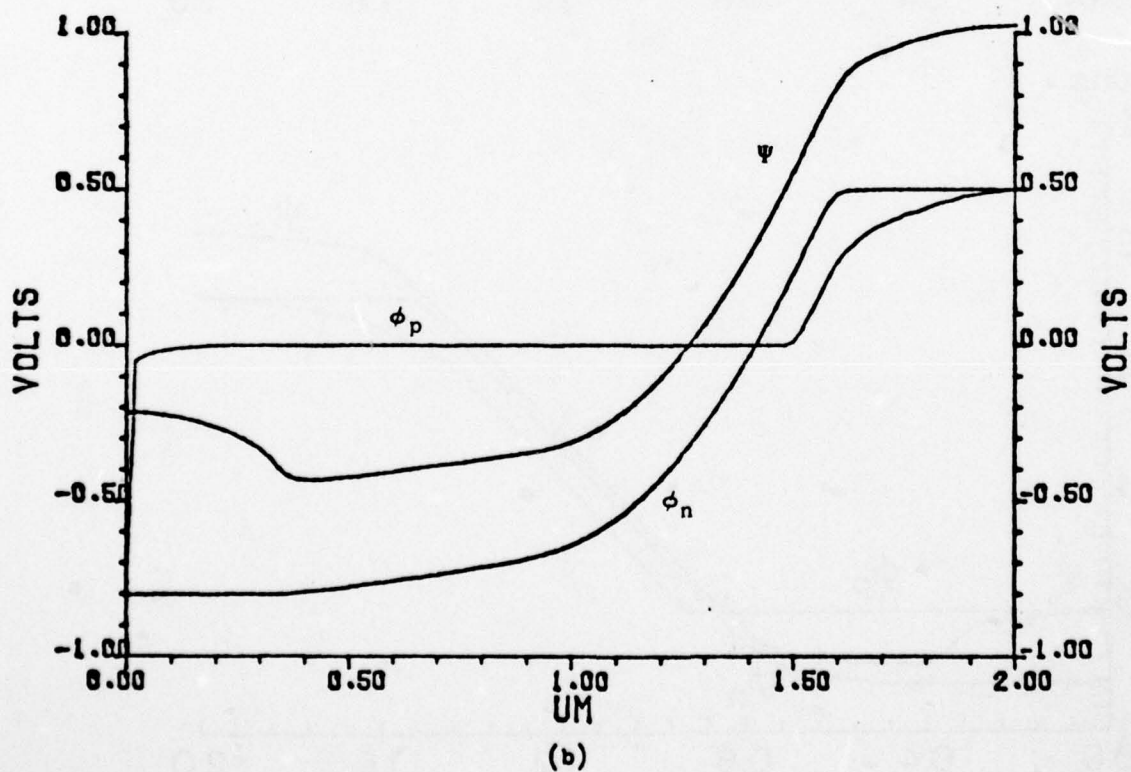
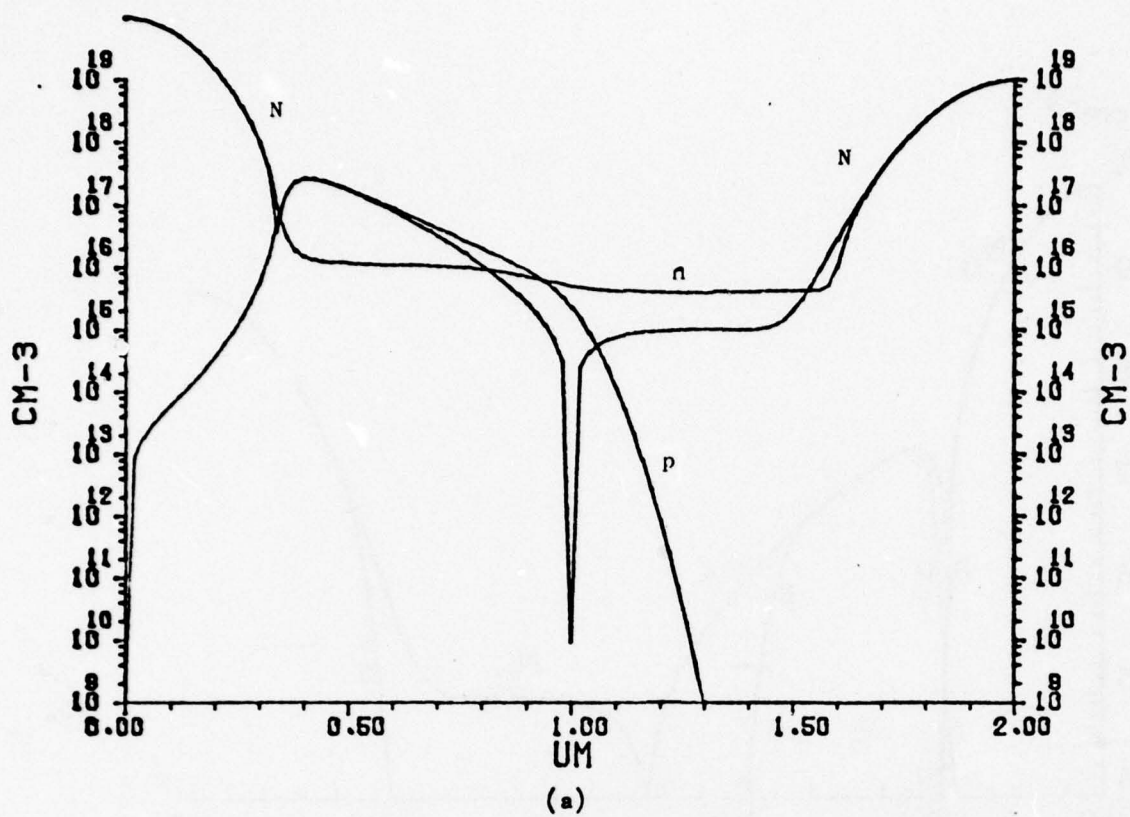
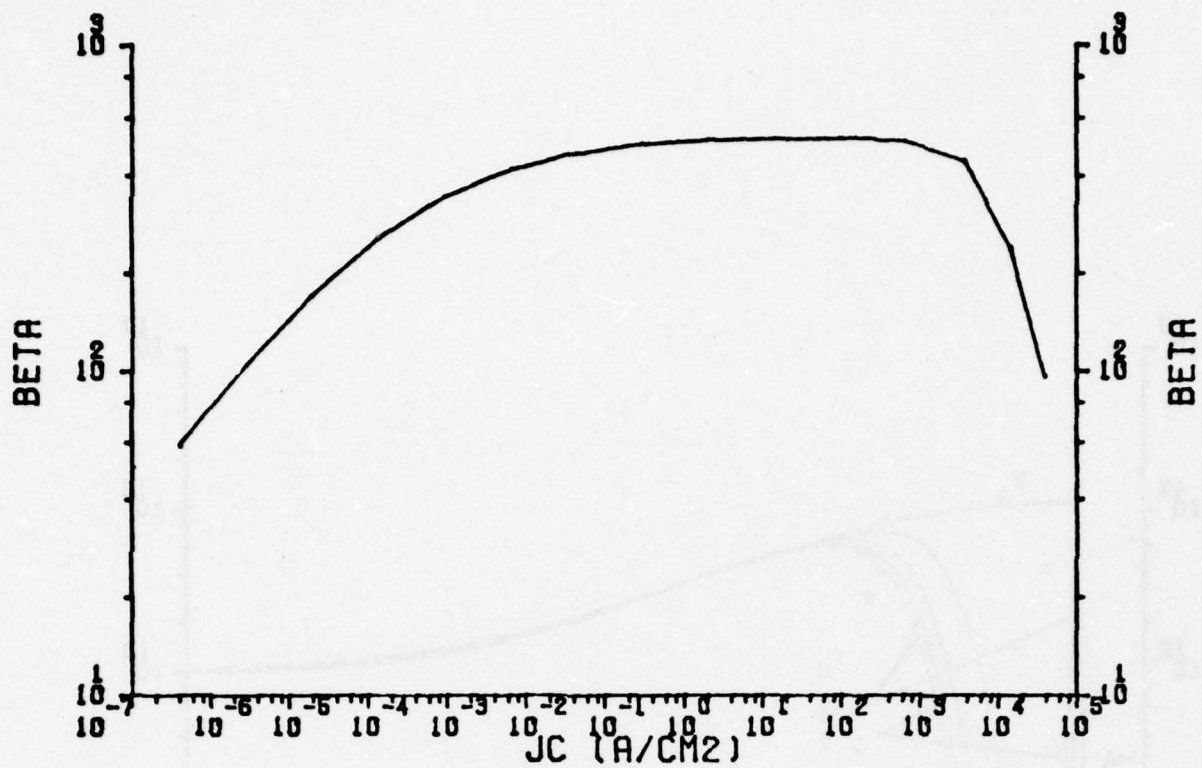
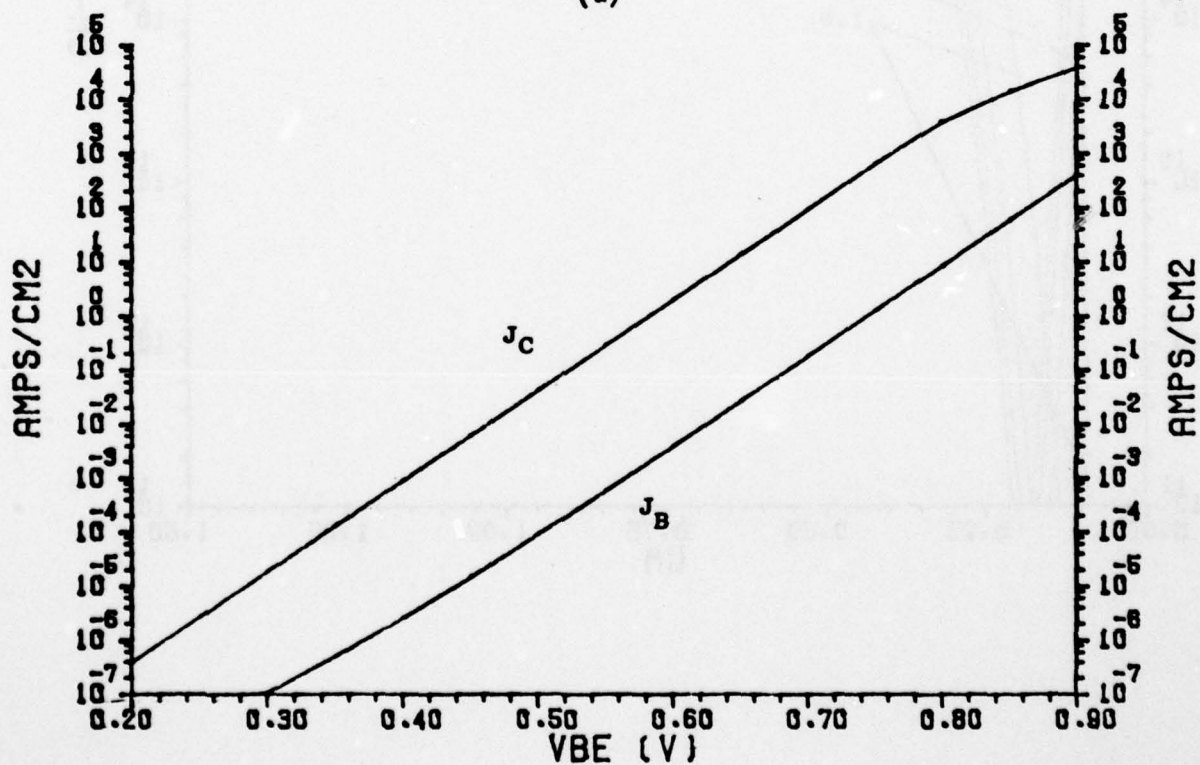


Figure 4.2.10 - Same as Figure 4.2.9 for high level injection.



(a)



(b)

Figure 4.2.11 -  $\beta$  versus collector current density (a) and collector current density  $J_C$ , and base current density,  $J_B$ , versus base emitter voltage,  $V_{BE}$ , (b) for the npn transistor in Figures 4.2.9 and 4.2.10.

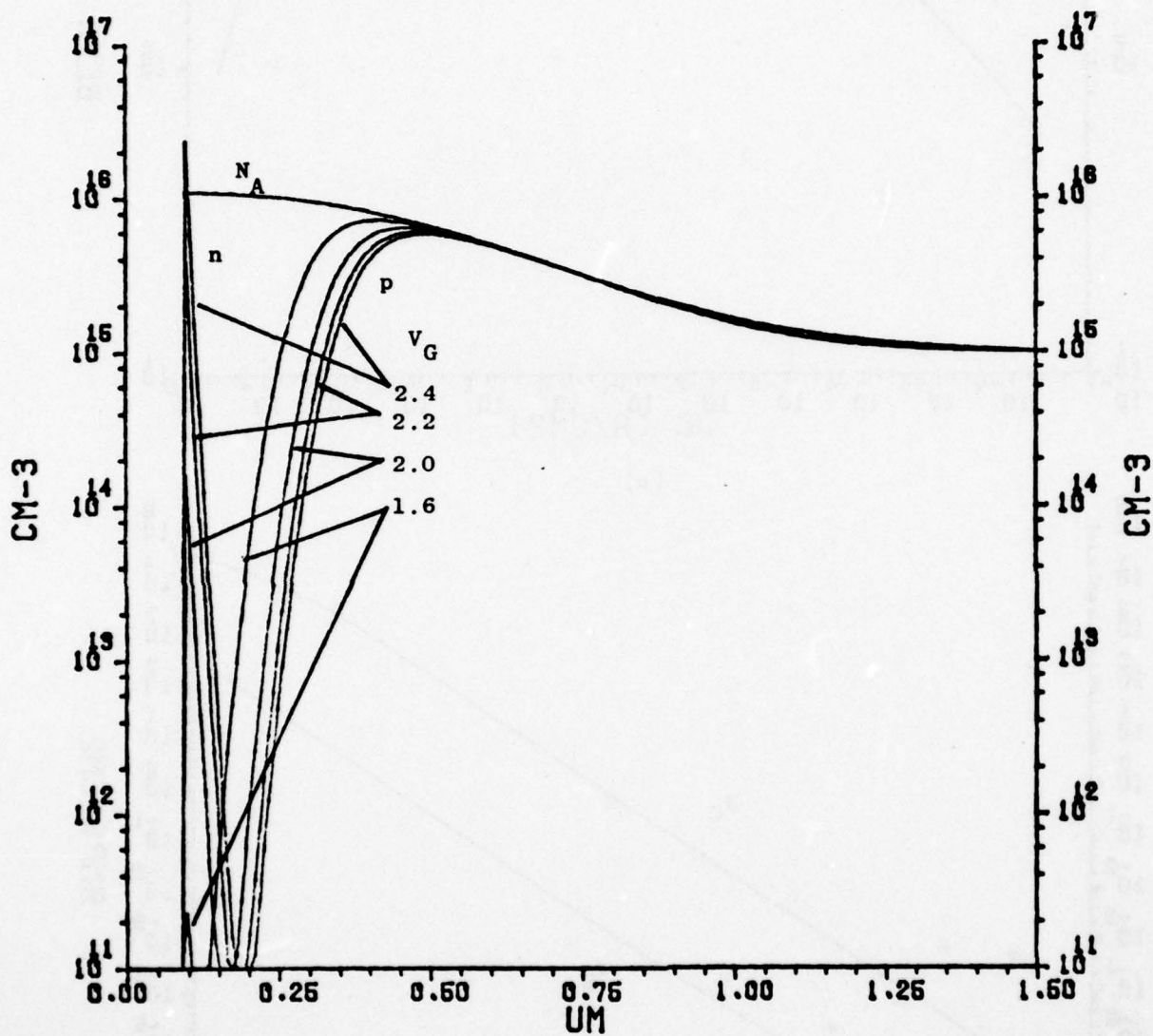


Figure 4.2.12 - Electron,  $n$ , hole,  $p$ , and impurity,  $N_A$ , concentration for an implanted MOS capacitor with varying gate voltage,  $V_G$ .

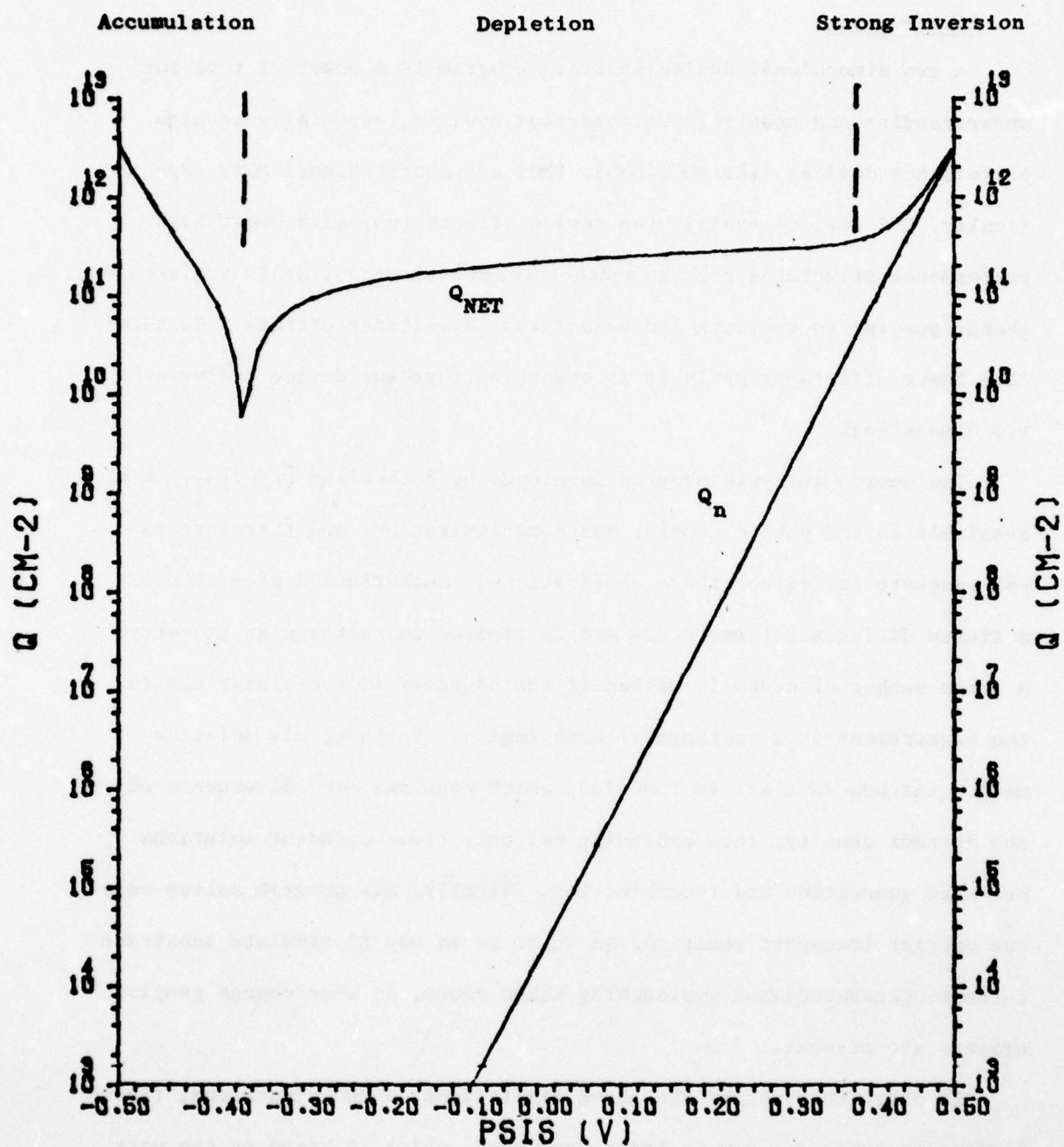


Figure 4.2.13 - Total net charge,  $Q_{NET}$ , and total electron charge,  $Q_n$ , versus surface potential,  $PSIS$ , for the MOS capacitor of Figure 4.2.12.

#### 4.3 Finite Elements for Semiconductor Device Simulation (S.Y. Oh, R. J. Lomax)

##### 1. Introduction

A two dimensional device analysis program is a powerful tool for understanding and modeling semiconductor devices, especially in high performance devices like SOS, DMOS, VMOS and short channel MOS. Specifically, SOS devices exhibit the device effects typical at most high performance structures such as punch-through saturation, drain avalanching, charge pumping to the bulk and associated capacitance effects. To simulate these effects properly it is essential that the device analysis be two dimensional.

The device analysis program developed by Sutherland [4.15] which is available in the public domain, has some limitations and therefore is not adequate for all of these applications. Sutherland's program uses a finite difference formulation and is limited to rectangular geometry. A large number of nodes is wasted if the boundary is non-planar due to the requirement of a rectangular mesh region. Further, his solution method introduces a stream function, which requires zero divergence of the current density, thus excluding not only time-dependent solutions but also generation and recombination. Finally, his program solves only one carrier transport equation, so there is no way to simulate substrate currents generated when avalanching takes place, or when charge pumping effects are present.

In order to overcome the above limitations, a two dimensional finite element analysis program is being developed, which is based on the work of Barnes and Lomax [4.9], [4.10], and [4.11]. The advantages and potential of this program are:

- 1) Due to use of the finite element method, the mesh shape is not limited to rectangular. It is therefore suitable for simulating devices which have non-planar geometry.
- 2) Due to the natural boundary condition property [4.11] of the finite element method, it is easy to implement the boundary conditions. In particular, it is very straightforward to simulate the insulating substrate boundaries of SOS and GaAs devices.
- 3) It allows both steady state and time dependent simulation, therefore it is possible to simulate transient effects like charge pumping.
- 4) It solves both the hole and electron transport equations, therefore it is possible to simulate the substrate current arising when avalanche takes place, and the effects of charge pumping.

The basic formulation of the finite element method is given in reference [4.11]. The current conservative properties are discussed in Section 2 and the implementation in Section 3. Several improvements on the original program of Barnes and Lomax are necessary for simulation of devices having realistic doping levels and dimensions for a reasonable cost.

- 1) The time scheme used previously was not fully implicit but evaluated some terms in past time. In this time scheme, the time step is limited by the dielectric relaxation time  $\tau$ .  $\tau$  is extremely small in the high doping region or strongly inverted channel (for example; if  $N_d = 10^{20} \text{ cm}^{-3}$  then  $\tau = 3 \times 10^{-16} \text{ sec}$ ), therefore, it takes many time steps to simulate a reasonable time period. In order to overcome this

time step limitation, a fully implicit time scheme in which Poisson's equation and the current continuity equations are solved simultaneously, and which has no time step limitation [4.23], is incorporated into the program. The details of the fully implicit time scheme is given in Appendix A. With the new fully implicit time scheme, up to  $5 \times 10^{-10}$  sec time step has been used without numerical divergences.

2) The current density is not continuous across the element boundaries when linear shape functions are used as in this finite element program. Therefore the terminal current calculated from the flux of current density at the contacts is not conserved exactly (i.e. the sum of the total terminal current is not zero). This can cause difficulties in comparing the currents of the simulation with those of the real devices and this is evidence that conservative schemes tend to give more physically meaningful results. However it is possible to compute currents in a way which is conservative. Details of this are given in Section 2. The new method gives the current conservation up to the numerical accuracy of the computation.

3) In many applications, it is sufficient to be able to solve only Poisson's equation for given quasi-Fermi levels. When appropriate this can be done in much less computation time than a full solution, therefore, a Poisson solution program has been implemented separately by taking the Poisson's equation solution part from the main program.

Several devices have been simulated with the new program. A one dimensional p-n junction diode was first simulated to check the numerical accuracy of the program against the available one dimensional finite difference program [4.19] based on the Gummel [4.20] and De Mari [4.21] algorithm.

Secondly, a charge-coupled device with multiple gate structure has been simulated to check the program in the two dimensional case against a two dimensional finite difference Poisson's equation solution program. In this case, the simplified version of the finite element program (Poisson's equation solution program) has been used for comparison. Close agreements was observed between the finite element solution and its corresponding finite difference solution despite the relatively coarse mesh in the finite element case compared to the finite difference case. Finally, an SOS MOSFET has been simulated to show the flexibility of the finite element approach in the simulation of non-planar geometry and insulating substrate boundary conditions. The simplified version was also used in this case. More details of the device simulation are discussed in Chapter 4.

## 2. Charge and Current Conservation

The equations to be solved within the semiconductor device are

$$\nabla \cdot (\epsilon \nabla V) + q (p - n + N_d) = 0 \quad (4.3.59)$$

$$\frac{\partial p}{\partial t} + \nabla \cdot \frac{\vec{J}_p}{q} - G = 0 \quad (4.3.60)$$

$$\frac{\partial n}{\partial t} + \nabla \cdot \frac{\vec{J}_n}{-q} - G = 0 \quad (4.3.61)$$

where

$V$  = the potential,

$p, n$  = hole and electron concentrations,

$N_d$  = net doping concentration,

$G$  = electron-hole pair generation rate,

$\vec{J}_p, \vec{J}_n$  = hole and electron current densities,

$q$  = electronic charge, and

$t$  = time

The finite element equations are obtained [4.11] by multiplying Eqs. (4.3.59) - (4.3.61) through by a shape function  $\phi_1(k,y)$  (in two dimensions) and integrated over the region of the device. However, it is instructive in considering conservation properties to perform integrals over individual elements  $e$  as follows

$$\int_e \phi_1 \left[ \nabla \cdot (\epsilon \nabla V) + q (p-n + N_d) \right] dS = 0 \quad (4.3.62)$$

$$\int_e \phi_1 \left[ q \frac{\partial p}{\partial t} + \nabla \cdot (\vec{J}_p) - qG \right] dS = 0 \quad (4.3.63)$$

$$\int_e \phi_1 \left[ -q \frac{\partial n}{\partial t} + \nabla \cdot (\vec{J}_n) + qG \right] dS = 0 \quad (4.3.64)$$

These are transformed by Gauss' theorem to

$$\begin{aligned} & \int_e \left[ \epsilon \nabla \phi_1 \cdot \nabla V - q \phi_1 (p-n + N_d) \right] dS \\ &= \oint_e \phi_1 \epsilon \nabla V \cdot \vec{n} d\ell \triangleq Q_1^e \end{aligned} \quad (4.3.65)$$

and

$$\begin{aligned} & \int_e \left( q \phi_1 \frac{\partial p}{\partial t} - \nabla \phi_1 \cdot \vec{J}_p - q \phi_1 G \right) dS \\ &= \oint_e \phi_1 \vec{J}_p \cdot \vec{n} d\ell \triangleq I_{p1}^e \end{aligned} \quad (4.3.66)$$

where the line integrals are around the edge of the element. A similar expression to Eq. (4.3.66) is obtained for the electrons defining  $I_{n1}^e$ . The quantity  $Q_1^e$  may be interpreted as the charge (per unit length in the two-dimensional case) associated with node 1 of element  $e$ , and  $I_{p1}^e$ ,  $I_{n1}^e$  are the outflowing hole and electron currents (per unit length). Although it is convenient to associate  $Q_1^e$  and  $I_{p1}^e$  with nodes, the defining integrals are in fact weighted fluxes over the sides of the element.

It is in the definitions of charges and currents by Eqs. (4.3.65) and (4.3.66) that the present approach differs from that of references [4.16], [4.13] and [4.14]. In the work of Hachtel et. al, current is defined as the flux of current density across the sides of the element. Unless the shape functions  $\phi_i$  possess continuous derivatives at these interfaces, a discontinuity in current will arise. Buturla et al. resolve this problem by defining an auxiliary mesh so that currents are evaluated as the flux through lines internal to the element (for triangles these are lines from the mid point of each side to the intersection of the perpendicular bisectors of the triangle). Because current density is continuous internally, exact current conservation is obtained. As will be shown below, currents and charges defined by [4.15] and [4.16] preserve charge and current continuity.

Consider the sum of the  $Q_i^e$  over all elements which contain node  $i$ :

$$\sum_{i \in e} Q_i^e = \sum_{i \in e} \int_e \phi_i \epsilon \nabla V \cdot \vec{n} \, d\ell \quad (4.3.67)$$

Figure 4.3.14 shows a typical arrangement of elements. For simplicity triangular elements are shown but the new argument to follow does not depend upon this. At an interior node such as 6 in Figure 4.3.14, the integrals on the right hand side of Eq. (4.3.67) will sum to zero for the following reasons. Along sides of adjacent elements such as the line joining nodes 6 and 7,  $\phi_i$  and  $\nabla V$  are continuous but the outward normal  $\vec{n}$  is oppositely directed in the two adjacent elements. The contributions to the integrals therefore cancel. Along the edges joining nodes 2, 3, 7, 9, 8 and 5,  $\phi_i = 0$  and so the remaining contributions are zero, giving at an interior node

$$\sum_{i \in e} Q_i^e = 0 \quad (4.3.68)$$

In practice, the  $Q_i^e$  do not have to be evaluated explicitly at interior nodes since the usual assembly process to produce finite element equations corresponds to the imposition of Eq. (4.3.68). At a boundary node such as 2, two possibilities arise. If the node belongs to an insulating boundary and there is no surface charge, then  $\nabla V \cdot \vec{n} = 0$  on the boundary. Thus along the edge joining nodes 1, 2 and 3, the integrand of Eq. (4.3.67) is zero. The remaining contributions cancel along 2, 6 and 2, 5 and are zero along 1, 5, 6, 3 for the same reasons as for interior nodes. Equation (4.3.68) is therefore still valid. This in turn gives a finite element equation when  $p$ ,  $n$  and  $V$  are inserted. If the potential is specified at node 2 (Dirichlet condition), no equation corresponding to this node is required for the potential solution. Equation (4.3.68) can still be applied consistently if an induced charge  $-\sum_{i \in e} Q_i^e$  is associated with the node. This interpretation is readily shown to be correct in the limit of infinitesimal element size from the definition, Eq. (4.3.67). Again in practice explicit evaluation of the  $Q_i^e$  can be avoided by generating an "equation" for the node at which a Dirichlet condition applies in the same manner as for all other nodes. The residual (right hand side minus left hand side) gives the net charge associated with the node.

Similarly

$$\sum_{i \in e} I_{pi}^e = 0 \quad (4.3.69)$$

at interior and insulating boundary nodes, whereas  $-\sum_e I_{pi}^e$  represents the current associated with node  $i$  which is entering the device. By summing over all nodes and elements it follows that

$$\sum_i \sum_e \left( I_{pi}^e + I_{ni}^e + \frac{dQ_i^e}{dt} \right) = - \sum_i \int_{\Omega} \nabla \phi_i \cdot \left( \vec{J}_p + \vec{J}_n - \epsilon \frac{\partial}{\partial t} (\nabla v) \right) dS, \quad (4.3.70)$$

where the integral is over the whole device region  $\Omega$ . With the usual definition of shape functions

$$\sum_i \phi_i = 1, \quad (4.3.71)$$

and it follows that the right hand side of Eq. (4.3.70) is zero. Since this arises from the vanishing of  $\nabla \sum_i \phi_i$  rather than the current, it is true for both the exact currents and the finite-element approximation to the current. (In approximations which also specify derivatives at nodes, a linear combination of the  $\phi_i$  is found which sum to a constant, leading to the same result.) On the left hand side of Eq. (4.3.70), sums over elements vanish at interior nodes and insulating boundary nodes because of Eqs. (4.3.68) and (4.3.69) leaving only a summation over contacts:

$$\sum_{\substack{\text{contact} \\ \text{nodes } i}} I_{tot} = 0 \quad (4.3.72)$$

where

$$I_{tot \ i} = \sum_e \left( I_{pi}^e + I_{ni}^e + \frac{dQ_i^e}{dt} \right) \quad (4.3.73)$$

which represents the total current, particle and displacement associated with node  $i$ . Equation (4.3.72) represents the conservation of current at the contacts. Several points may be noted. (1) By carrying out a similar argument over just the element rather than region  $\Omega$  it can be shown that current is conserved over the nodes of the element. (2) It is straightforward to show that currents computed by summing  $I_{tot \ i}$  over

AD-A059 752

STANFORD UNIV CALIF INTEGRATED CIRCUITS LAB  
COMPUTER AIDED ENGINEERING OF SEMICONDUCTOR INTEGRATED CIRCUITS--ETC(U)  
JUL 78 J D MEINDL, K C SARASWAT, R W DUTTON DAAB07-77-C-2684  
DELET-TR-77-2684-2 NL

UNCLASSIFIED

3 OF 5  
ADA  
059752



nodes belonging to a specific contact give the correct physical current in the limit of infinitesimal element size. (3) By considering sums of  $Q_i^e$ ,  $I_{pi}^e$  or  $I_{ni}^e$  individually, conservation of charge, and conservation of hole and electron current can be shown to be satisfied exactly.

### 3. Practical Implementation

Implementation of these finite-element equation has been described previously [4.11]. Apart from some preliminary work [4.17] these did not incorporate the Scharfetter method of current computation which is needed if severe restrictions on element size are to be avoided. Although this technique was originally developed in the context of one-dimensional solution it has been extended to rectangular finite-difference solutions [4.18] but there is no obvious generalization to finite-element schemes which in general have no preferred directions of integration. One approach has been given by Buturla and Cottrell [4.12] which is appropriate to their method of computation. An alternative suggested here is to replace  $\vec{J}_p$  in the continuity equation by a constant current  $\vec{J}_p'$  computed within an element from

$$\vec{J}_p' = \left( \int_e \vec{J}_p' \cdot e^{qV/kT} dS \right) / \left( \int_e e^{qV/kT} dS \right) \quad (4.3.74)$$

or less generally components of  $\vec{J}_p'$  may be computed by line integrals in two perpendicular directions  $\vec{v}_1$  and  $\vec{v}_2$

$$\vec{J}_p' \cdot \vec{v}_1 = \left( \int \vec{J}_p' \cdot \vec{v}_1 e^{qV/kT} dl \right) / \int e^{qV/kT} dl \quad (4.3.75)$$

The second method has been used together with a finite-element implementation of Gummel's method of integrating Poisson's Equation, i.e. applying Newton's method to solve

$$\nabla \cdot (\epsilon \nabla V) = -qn_i \left( e^{q(E_p - V)/kT} - e^{-q(E_n - V)/kT} + N_d/n_i \right) \quad (4.3.76)$$

where  $E_p$  and  $E_n$  are quasi-Fermi levels assumed to be constant within the Newton iteration. The calculation is made fully implicit by iteration between Poisson's equation and the two continuity equations until convergence is obtained at each time step.

#### 4. Evaluation of the Numerical Accuracy of the Program

In order to check the numerical accuracy of the solution, different simulation programs with known accuracy are necessary. Two finite difference programs are available for comparison. One is the one dimensional Poisson's equation and transport equation solution program [4.19] based on Gummel's [4.20] and De Mari's algorithms [4.21]. The other is the two-dimensional Poisson's solution program [4.22].

A one dimensional p-n junction diode was first simulated and compared with the one dimensional finite difference program. The p-n junction diode was chosen because it has a simple and one dimensional geometry but it is a basic structure in semiconductor devices. In order to ensure the same conditions for both simulations, the same mobility equation and recombination equations are used for both simulations. The input data for both simulations are listed in Table 4.3.4. The mesh used in the two dimensional program is shown in Figure 4.3.14a. The total length of the diode is 2.5  $\mu\text{m}$ . The p-type region is 1.5  $\mu\text{m}$  long and uniformly doped at  $4 \times 10^{15} \text{ cm}^{-3}$ . The n-type region is 1.0  $\mu\text{m}$  long and uniformly doped at  $10^{16} \text{ cm}^{-3}$ . The total number of nodes is 250 (50 x 5) for the two dimensional simulation, and 101 for the one dimensional simulation.

The boundary conditions imposed at the contacts for both simulations are:

1) Electrostatic potentials are specified

2) Majority carrier concentration =  $N_d$

Minority carrier concentration =  $N_i^2/N_d$ .

where  $N_d$  is the doping concentration and  $N_i$  is the intrinsic carrier concentration.

Figure 4.3.14b shows the real projection of the hole distribution simulated by the two-dimensional program. Figure 4.3.15a shows the comparison at the hole and electron concentrations from the finite difference and finite element simulations at a reverse bias at  $-0.128V$ . In this reverse bias case, the decrease of the minority carrier near the depletion region is clear. The potential distribution is compared in Figure 4.3.15b. The agreement is within 1%. The comparison for the forward bias case is shown in Figure 4.3.16. There is a discrepancy of the minority carrier concentration near the contact. In this short diode, the diffusion length is comparable to the length of the neutral region, therefore some of the injected minority carriers are collected at the contacts. The mesh used in this region of rapid change was coarser in the two dimensional analysis than in the one dimensional simulation. This is believed to be a reason for the discrepancy. Secondly, in order to check the two dimensional capabilities of the program, a charge coupled device with a multigate structure was simulated. The device is  $33 \mu m$  long and  $10 \mu m$  thick. The gate oxide is  $1000 \text{ \AA}$  thick. The substrate is n type, and uniformly doped at  $5 \times 10^{14} \text{ cm}^{-3}$ . In this simulation, the simplified version of the program (Poisson's solution) was used. The minority carriers were suppressed in order to obtain the electrostatic potential

distribution in deep depletion. The input material parameters were the same as those of the diode. Figure 4.3.18a shows a two-dimensional altitude plot of the electrostatic potential distribution. A contour mapping of the same results is given in Figure 4.3.18b. This solution has also been compared with a two dimensional finite difference solution [4.22]. The comparison shows about 50mV shift in the potential distribution between the two simulations. This discrepancy is thought to arise from the different ways of specifying the doping at the Si-SiO<sub>2</sub> interface. Except for the shift, the equipotential contours match very closely. Finally, an SOS MOSFET was simulated to show the flexibility of the finite element approach in the simulations of non-planar geometry and insulating substrate boundary conditions. The simplified version was also used but both carriers were present. Figure 4.3.19a shows the finite element mesh for the SOS MOSFET. The mask channel length is 6  $\mu\text{m}$ , the effective channel length is 4  $\mu\text{m}$ , and the lateral diffusion is 1  $\mu\text{m}$ . The thickness of the epi-layer is .65  $\mu\text{m}$  and the oxide thickness is 1000 $\text{\AA}$ . The source and drain are uniformly doped at  $10^{20}\text{cm}^{-3}$  and the substrate is uniformly doped at  $10^{16}\text{cm}^{-3}$ . Figure 4.3.19b shows a two dimensional altitude plot of the electrostatic potential distribution in the device for  $V_{\text{DS}} = 0\text{V}$  and gate voltage 1.38V above the flat band voltage. The substrate is floating. The device is in the subthreshold region.

## 5. Conclusion

A two dimensional finite element program is being developed in order to simulate non planar high performance devices such as VMOS, DMOS, and SOS, which cannot be simulated by the program [4.15] available in the public domain. In order to bench mark the program performance, a one dimensional

p-n junction diode, a charge-coupled device and SOS MOSFET have been simulated and compared with the results of the corresponding finite different programs.

It is planned to simulate several examples of devices with the program which solves two dimensional Poisson's equation and transport equations. They will be checked against the results of Sutherland's program and other available two dimensional analysis programs.

A simplified quasi two-dimensional analysis will be implemented which will combine a one dimensional Poisson's equation and transport solution program with two dimensional Poisson's solution program. Electron and hole quasi-Fermi levels will be obtained from the one dimensional program and assumed constant in the direction perpendicular to Si-SiO<sub>2</sub> interface. With these quasi Fermi levels, the two dimensional distributions at hole and electron concentration, and electrostatic potentials will be obtained from the two dimensional Poisson's equation solution program.

TABLE 4.3.4 - INPUT MATERIAL PARAMETER

$\epsilon_{si}$	11.8
temperature	300 C
saturation velocity	$10^7$ cm/sec
$\mu_n$	1350 cm <sup>2</sup> /v.sec
$\mu_p$	500 cm <sup>2</sup> /v.sec
$\tau_n$	$10^{-10}$ sec
$\tau_p$	$10^{-10}$ sec
$n_i$	$1.45 \times 10^{10}$ /cm <sup>3</sup>

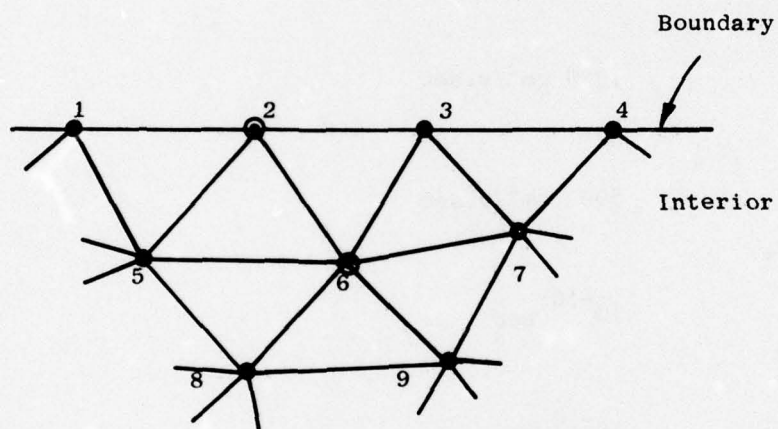
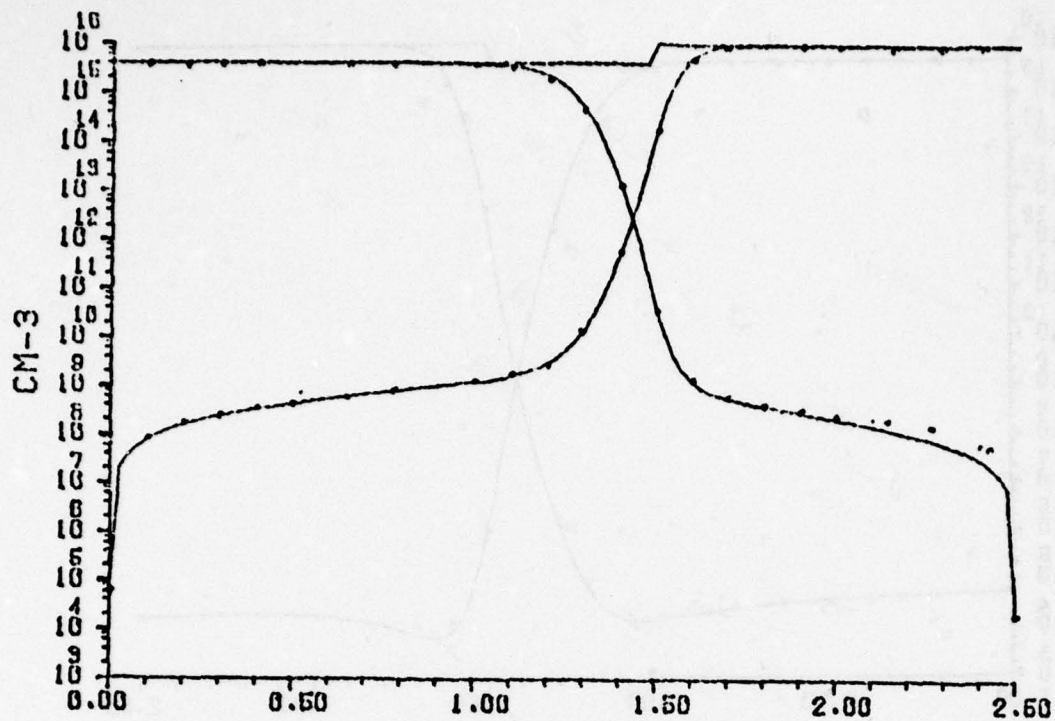
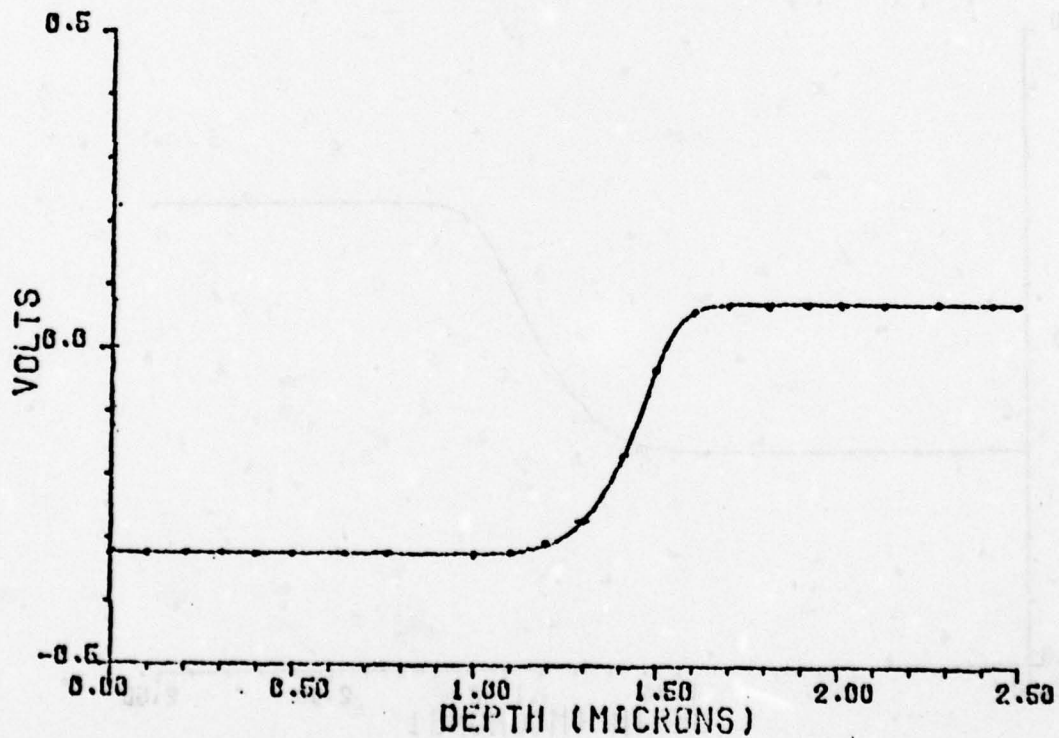


Figure 4.3.14 - Schematic of elements in the vicinity of a boundary node 2 and an interior node 6.

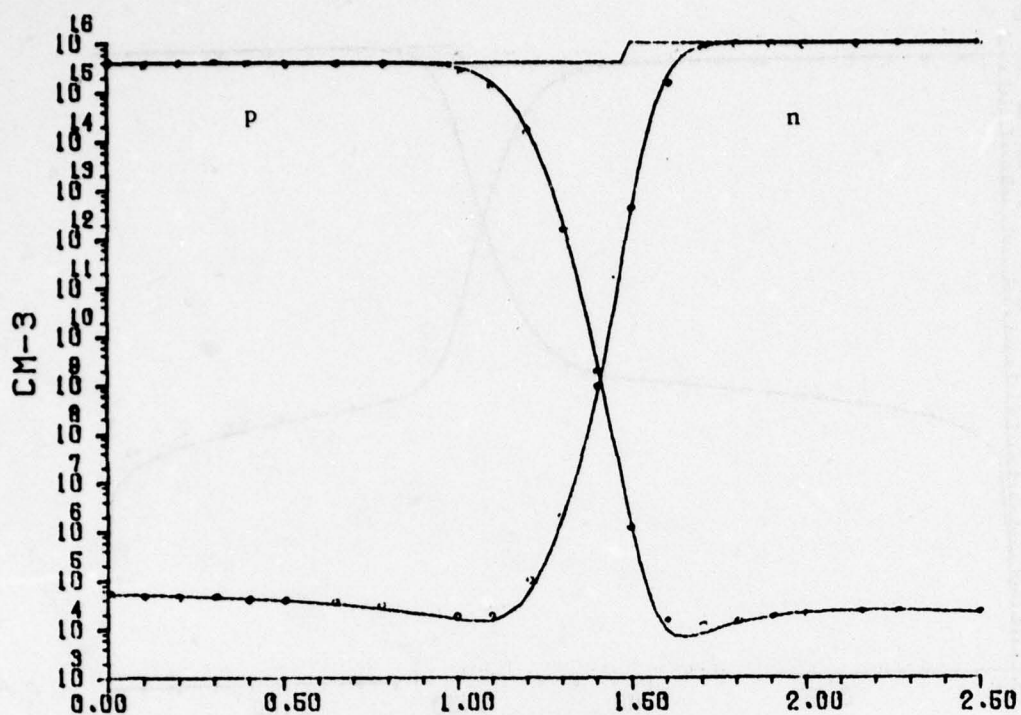


(a) Hole and electron distributions

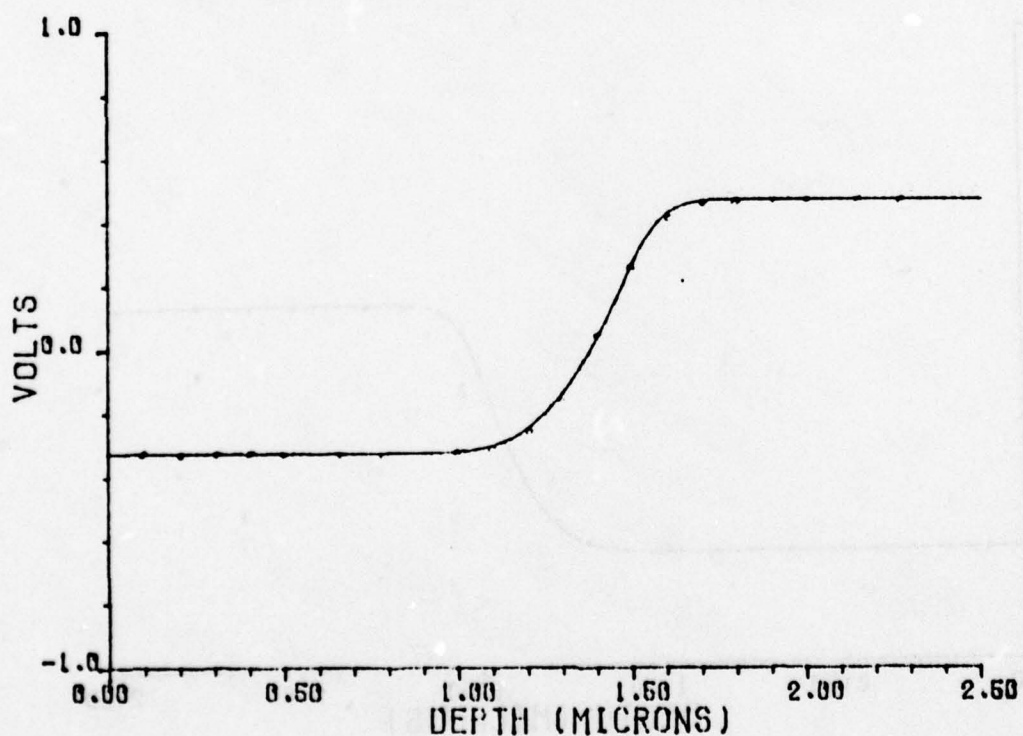


(b) Potential distribution

Figure 4.3.16a - Hole and electron distributions, and  
 4.3.16b - potential distribution of a P-N junction diode at 0.272V forward bias. (Finite element solution: . . . , finite difference solution: \_\_\_\_\_.)



(a) Hole and electron distribution



(b) Potential distribution

Figure 4.3.17a - Hole and electron distributions, and  
 4.3.17b - potential distribution of a P-N junction diode at 0.128V  
 forward bias. (Finite element solution: ... , finite  
 difference solution: \_\_\_\_\_.)

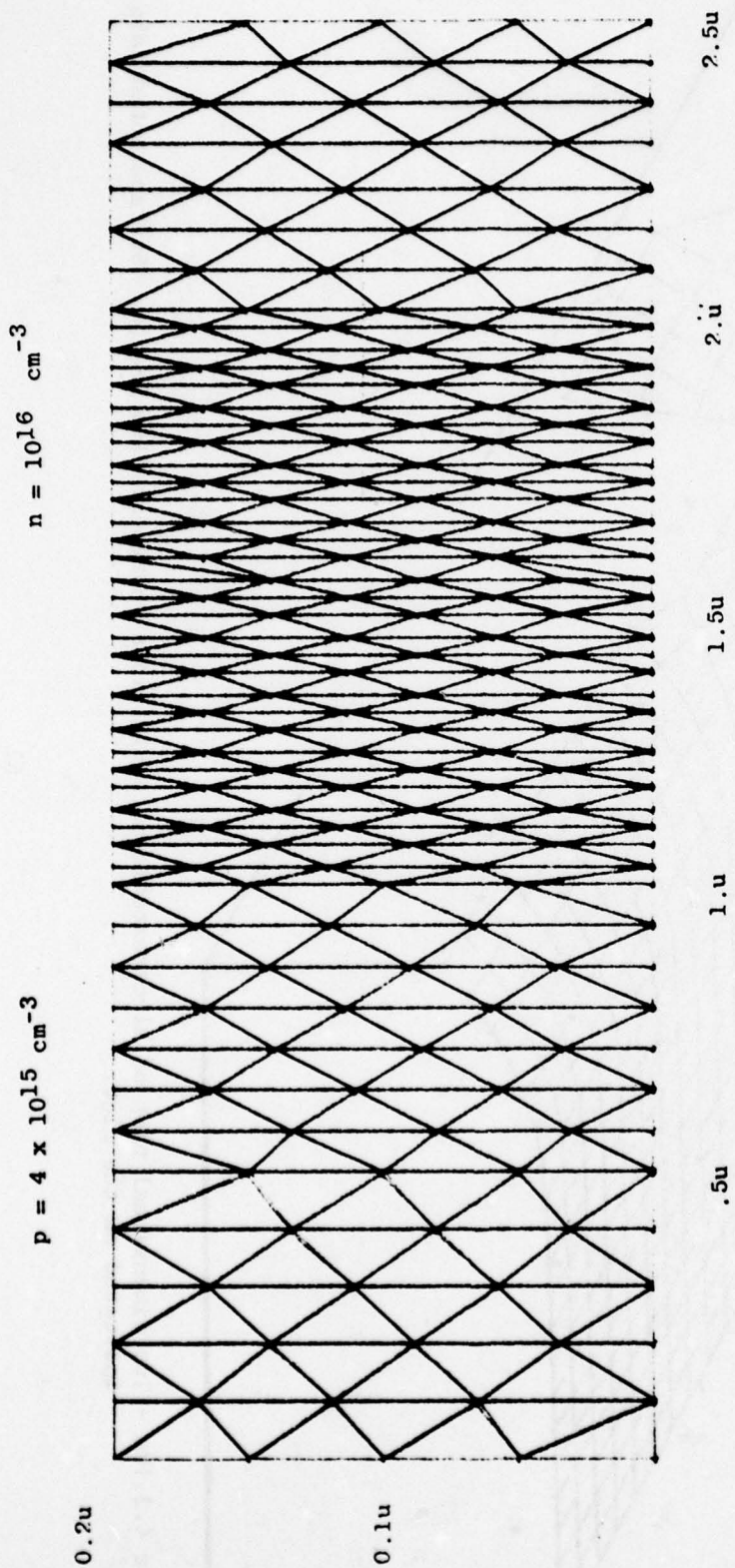
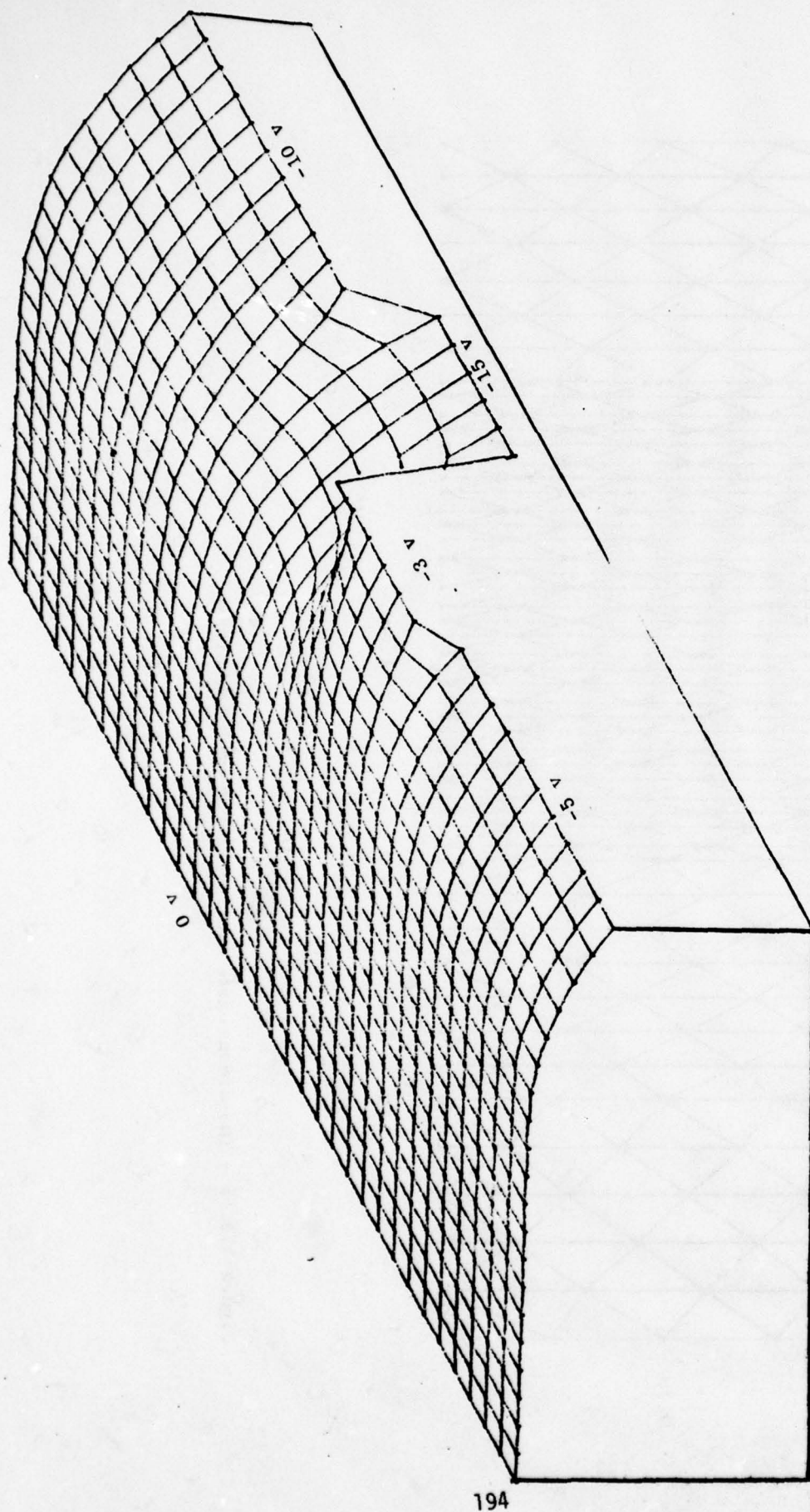
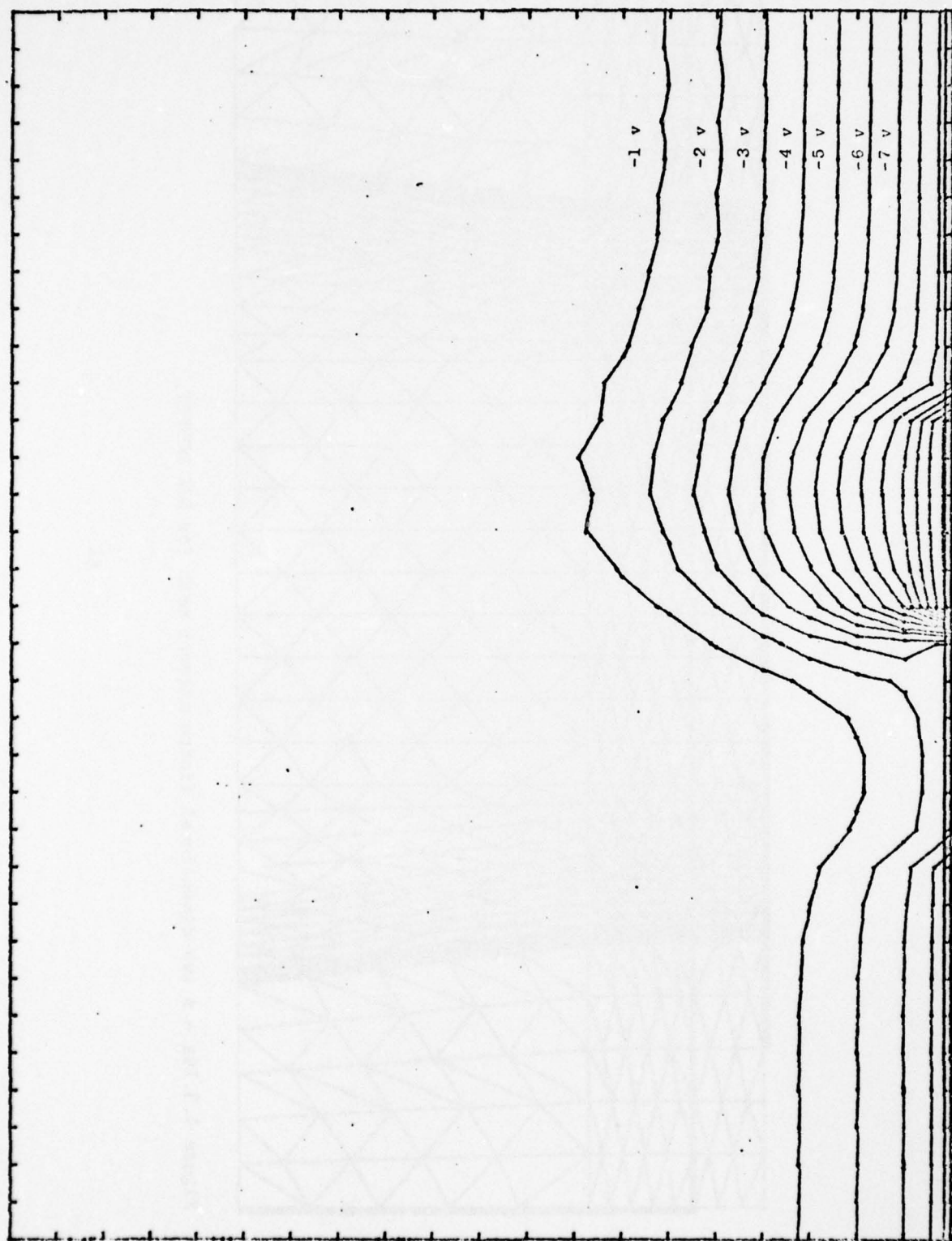


Figure 4.3.15 - Two-dimensional finite-element mesh for diode.





195

Figure 4.3.18b - Corresponding contour plot of potential.

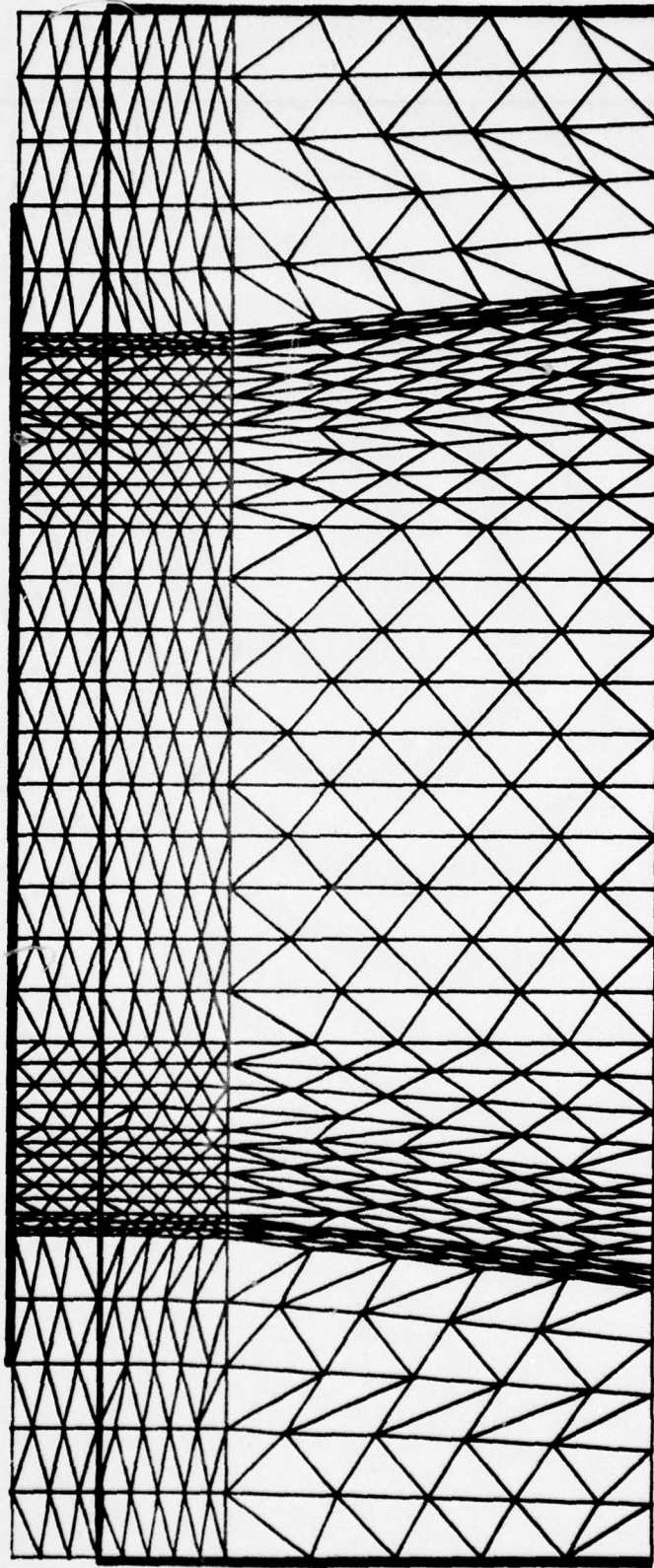


Figure 4.3.19a - A two-dimensional finite element mesh for SOS MOSFET.

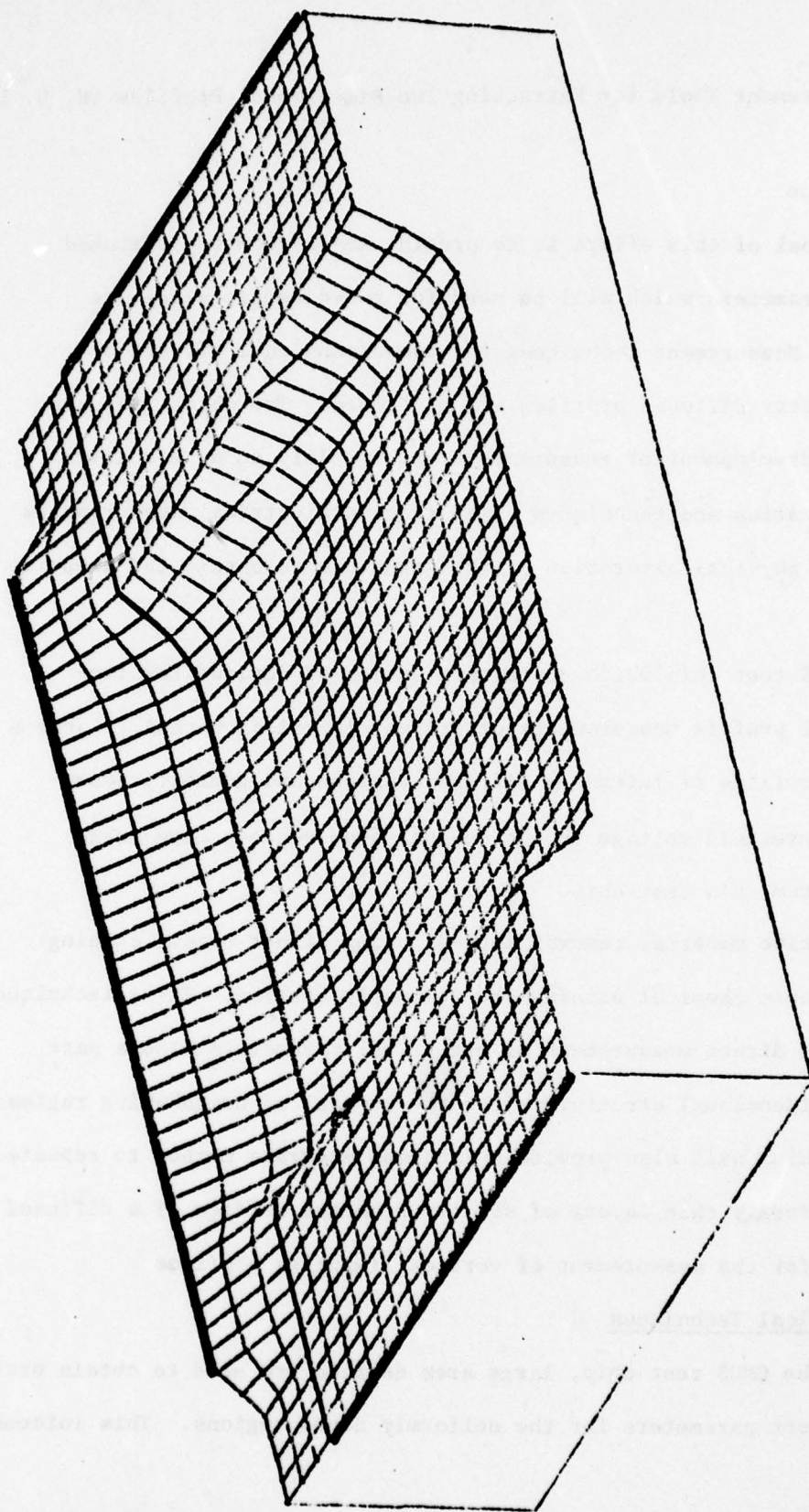


Figure 4.3.19b - Two-dimensional plot of electrostatic potential in a SOS MOSFET. Surface potentials are indicated on the plot.

#### 4.4 Measurement Tools for Extracting Two-Dimensional Profiles (H. G. Lee)

##### Introduction

The goal of this effort is to provide small geometry diffused profile parameters which will be used for two-dimensional device modeling. Measurement techniques for two-dimensional effects of small geometry diffused profiles are developed. Two objectives are defined: development of measurements based solely on an electrical characterization and techniques which require electrical measurements as well as physical alteration of the structure to obtain the impurity profiles.

A CMOS test chip which contains a series of devices for two-dimensional profile measurements offers an electrical method. Surface impurity profiles of laterally diffused regions and geometry dependence of threshold voltage in the channel stop regions have been measured from this test chip.

Selective material removal methods using either plasma etching or anisotropic chemical etching are currently studied. These techniques will enable direct measurement of electrical parameters from a part of a two-dimensional structure after the removal of neighboring regions. Plasma etching will also provide a fast and accurate method to repeatedly remove uniformly thin layers of silicon from the surface of a diffused structure for the measurement of vertical impurity profiles

##### A. Electrical Techniques

For the CMOS test chip, large area devices are used to obtain profile and transport parameters for the uniformly doped regions. This information

gives the limiting case values to be compared with the two-dimensional measurement techniques. Several test structures provide MOS capacitance and p-n junction capacitance to obtain vertical doping profiles. Others provide large area threshold and mobility data. A series of devices named PCS and LTA are special devices which test several approaches for two-dimensional profile measurements. Figure 4.4.20 shows a plan view of the test chip. The design and fabrication of test structures and some measurement results will be reviewed.

#### 1. Fabrication of Test Structures

The test chip has been fabricated with a CMOS process using boron ion-implanted p-well and lateral channel stop (LCS) regions. The p-well is implanted through a nitride layer with an energy of 180 keV and dose of  $4.5 \times 10^{12}$  atoms/cm<sup>2</sup>. The LCS is implanted with an energy of 25 keV and dose of  $3 \times 10^{13}$  atoms/cm<sup>2</sup>. The LCS regions are subjected to a subsequent drive-in diffusion and field oxidation, while p-well regions are protected by the nitride layer. The drive-in is 19 hours at 1100°C in 5% O<sub>2</sub> in N<sub>2</sub>, while the field oxidation is 9 hours wet O<sub>2</sub> at 1000°C. After the field oxidation, nitride and field oxide are stripped and a 1000Å gate oxide is grown. An n<sup>+</sup> poly-silicon gate is deposited and phosphorus source and drain are diffused.

#### 2. Doping Profile Measurement.

MOS capacitors and p-n junction capacitors are used to profile the substrate p-well and LCS regions. All devices use p-n junction guardrings or metal-gate guardrings. Phosphorus pile-up and boron redistribution at the surface are observed from MOS capacitors. Deeper profiles are measured using p-n junction capacitors. However, profiles for p-well and LCS regions obtained from either capacitor structures are limited in

depth due to the breakdown. Spreading Resistance technique is used to obtain the LCS impurity profile and it is compared to the result of a process simulator SUPREM in Figure 4.4.21.

### 3. Parallel Channel Structures (PCS)

Three bulk n-channel MOS transistors for the measurement of surface impurity profiles of laterally diffused regions are fabricated. Each transistor has 32 parallel channels and each channel is composed of the indicated combinations of substrate, p-well and LCS regions as shown in Figure 4.4.22a. The  $I_D$  vs.  $V_G$  characteristics of these devices at a small drain potential are shown in Figure 4.4.22b and are markedly different from the linear region characteristics of a conventional device due to the nonuniform doping across the width of the channel. The transistors have threshold  $V_T$  variations in Z direction only. For these transistors, the transconductance  $g_m$  at a small drain potential  $V_D$  is given as follows [4.24]

$$g_m = \left. \frac{\partial I_D}{\partial V_G} \right|_{V_D = \text{const}}$$

$$= \frac{I_D}{\mu(V_G, V_B)} \cdot \frac{\partial \mu(V_G, V_B)}{\partial V_G} + \frac{2\mu(V_G, V_B)}{L} C_{ox} V_D Z(V_G) \quad (4.4.47)$$

where  $\mu(V_G, V_B)$  is the mobility of carriers in the n-channel,  $Z(V_G)$  is the location which turns on at  $V_G$ , and other symbols have their usual meanings.

Four large area n-channel transistors are used to measure threshold voltage and electron mobility for p-type substrates which did (I) or did not (II) experience a long field oxidation and for p-well (III) and

LCS (IV) regions, respectively. The mobility dependence on gate potential for each channel doping has been measured at  $V_{SB} = 0$  and  $-1$  volt;  $V_{SB} = 0$  volt case is shown in Figure 4.4.23.

Measured mobilities are fit to an empirical equation

$$\mu = \frac{\mu_o}{1 + \theta(V_G - V_T)} \quad (4.4.78)$$

at each substrate bias. The transconductance  $g_m$  is calculated from the measured  $I_D$  vs.  $V_G$  data and we obtain  $Z(V_G)$  from equations (4.4.77) and (4.4.78). Given  $Z(V_G)$ , we know the threshold  $V_T(Z)$  at  $Z$ , since  $V_T\{Z(V_G)\} = V_G$ .

The threshold voltage of an n-channel structure with an  $n^+$  - dope poly-silicon gate is

$$V_T = -\left(\frac{E_G}{2q} + \frac{\psi_s}{2} + \frac{qN_{ox}}{C_{ox}}\right) + \psi_s + \frac{1}{C_{ox}} \sqrt{2qE_s N_A (V_{SB} + \psi_s)} \quad (4.4.79)$$

Measuring the threshold voltages at two substrate biases,

$$V_{T1}(Z) - V_{T2}(Z) = \frac{1}{C_{ox}} \sqrt{2qE_s N_A(Z)} \left( \sqrt{V_{SB1} + \psi_s(Z)} - \sqrt{V_{SB2} + \psi_s(Z)} \right) \quad (4.4.80)$$

The surface concentration at  $Z$  is given by

$$N_A(Z) = \frac{C_{ox}^2}{2qE_s} \cdot \frac{\left\{ V_{T1}(Z) - V_{T2}(Z) \right\}^2}{\left\{ \sqrt{V_{SB1} + \psi_s(Z)} - \sqrt{V_{SB2} + \psi_s(Z)} \right\}^2} \quad (4.4.81)$$

$N_A(Z)$  is obtained from this equation by an iterative technique.

Surface profiles near the edges of CMOS p-well (structure B) and LCS (structure C) regions obtained using the algorithm are shown in Figures 4.4.24 and 4.4.25. Theoretical lateral profiles [4.24] generated using an intrinsic diffusion coefficient for boron  $D = 8.2 \times 10^{-4} \mu m^2/min$  at  $1100^\circ C$  are shown and give reasonable fits to the measured data.

However, theoretical profiles with  $D = 5.0 \times 10^{-4} \mu\text{m}^2/\text{min}$  for the p-well and  $D = 1.0 \times 10^{-3} \mu\text{m}^2/\text{min}$  for the LCS seem to make better fits to the measured profiles. It has to be noted that LCS drive-in was under a 5% oxygen environment while the p-well was separated from oxygen by a nitride layer.  $D = 1.0 \times 10^{-3} \mu\text{m}^2/\text{min}$  at  $1100^\circ\text{C}$  is in agreement with a reported value for a boron diffusion coefficient under 100% oxygen [4.25]; other work [4.26] suggests that even a trace amount of oxygen results in a similarly enhanced diffusion coefficient.

The surface impurity concentration of LCS obtained from a Spreading Resistance technique agrees well with the lateral profile measurement. The total number of boron impurity atoms per unit area in the LCS predicted by the Spreading Resistance technique is also in a good agreement with a value obtained from the theoretical lateral profile when the non-Gaussian vertical profile near the surface due to the boron depletion is taken into account.

The lateral profile for structure A has also been calculated and is shown in Figure 4.4.26. In this case, the structure is more complicated than the B or C structures. Figure 4.4.26 was calculated using the basic algorithm up until the p-well turned on. For higher gate voltages, the proper mobility value to use is uncertain which leads to inaccuracies in  $V_T(Z)$ . For these higher gate voltages slightly better results were obtained using  $V_T(Z)$  at 0 substrate bias only and assuming constant flat-band voltage across the entire device. The curve of Figure 4.4.26 shows the expected features of the substrate doping followed by the p-well and finally rising to the LCS doping level. Naturally the curve does not reflect the physical placement of the LCS region since it actually lies between the substrate and p-well regions.

#### 4. LTA Devices

The LTA devices are constructed using a field oxide window to define a narrow channel-stop to be used as the intrinsic W/L for an n-channel field effect transistor. The devices are fabricated in a p-well on an n-substrate. The W dimension, as determined by two poly-silicon diffusion mask is 50  $\mu\text{m}$  and the window widths are 1,2,3 and 5  $\mu\text{m}$ . A metal gate is used for all devices.

A matrix of four process variations is utilized to obtain various structures as shown in Figure 4.4.27. The key parameters of interest in this experiment are threshold and conduction parameters as a function of bias and process variations.

The  $I_D$  vs.  $V_G$  characteristics of (A) and (B) devices at a small drain voltage are measured and shown in Figure 4.4.28. Device (A) which use the field oxide as gate oxide show very high threshold voltages ranging from 23 to 30 volts for channel lengths in the range of 3.5 to 7.5  $\mu\text{m}$ . Devices (B) with uniform and thin gate oxide thickness show lower thresholds. Both groups of devices show subthreshold characteristics due to the non uniform doping along the channel. It is more apparent in devices (A) where the non uniform oxide thickness also adds the subthreshold characteristics. The drain current ratios in the linear region for (B) devices are shown in Table 1. It is noted that the current ratios do not track their mask W/L ratios. This is mostly due to the so called "bird's beak" oxidation [4.28] which occurs at the edge of  $\text{Si}_3\text{N}_4$  which is used as a oxidation barrier. For the fabrication process of this test chip, the length of a bird's beak will be more than a micron on each side. This will result in the expected channel lengths shown in Table 4.4.4.

The (A) and (B) devices give a measure of the threshold near the  $n^+$  channel stop region. The thick oxide and  $n^+$  directly up against the oxide represent the device conditions typically used. The (A-) and (B-) devices give a useful contrast since the  $n^+$  diffusions do not affect the LCS profile. Effective bulk doping for (B) and (B-) devices are calculated from back gate bias measurements and are shown in Table 4.4.5. Effective bulk doping for (B) devices are lower than (B-) devices as expected. Also effective doping of devices with shorter channel lengths are lower than devices with longer channel lengths. This is an example of two-dimensional effects in a small geometry device. The decrease of effective bulk doping with the decrease of the channel length as in (B) devices will be more prominent for devices with lower bulk doping.

In conclusion, PCS and LTA devices provide methods of measuring two-dimensional effects on impurity profile and transport parameters for a two-dimensional device modeling.

#### B. Plasma Etching and V-Groove Etching

Impurity atom distribution near the diffusion mask edge has been theoretically predicted by several authors [4.24], [4.28]. The Parallel Conductance Structure described in the preceding section provides one experimental method to obtain information on the laterally diffused regions. A selective material removal technique which will be described in this section offers another method of testing the validity of the two-dimensional diffusion models. The conductance of laterally diffused regions in a diffused resistor can be measured using this technique. Idealized section-views of the laterally diffused regions after removing

the center part are shown in Figure 4.4.29. Three possible selective removal techniques will be reviewed and compared.

Plasma Etching can be used to remove the center part of the diffused resistor as shown in Figure 4.4.29a. The oxide diffusion mask also serves as an etching mask to protect the laterally diffused regions while the center part is etched. Etching parameters have to be optimized in order to minimize undercutting.

Ion Milling has the advantage of smaller undercutting compared to Plasma Etching. However, Ion Milling is a momentum transfer technique. The etch rates of most materials used in silicon integrated circuit structures fall in the same range. Therefore, the difficulty to find a good etching mask sets a limit to the depth that a structure can be profiled.

The advantage of V-Groove Etching for a selective removal of silicon results from straightforward masking.  $\text{SiO}_2$  is a good etching mask. However, aluminum cannot be used as a contact pad to measure the resistance of the diffused resistor since it is easily attacked by the chemicals used. Chromium-Gold can be used to protect the contact region from being etched and also serve as a contact pad. The resulting structure after V-Groove Etching of the center part is different from the structure obtained by Plasma Etching or Ion Milling. A combination of the above techniques -- e.g., Plasma Etching after V-Groove Etching -- also will be possible.

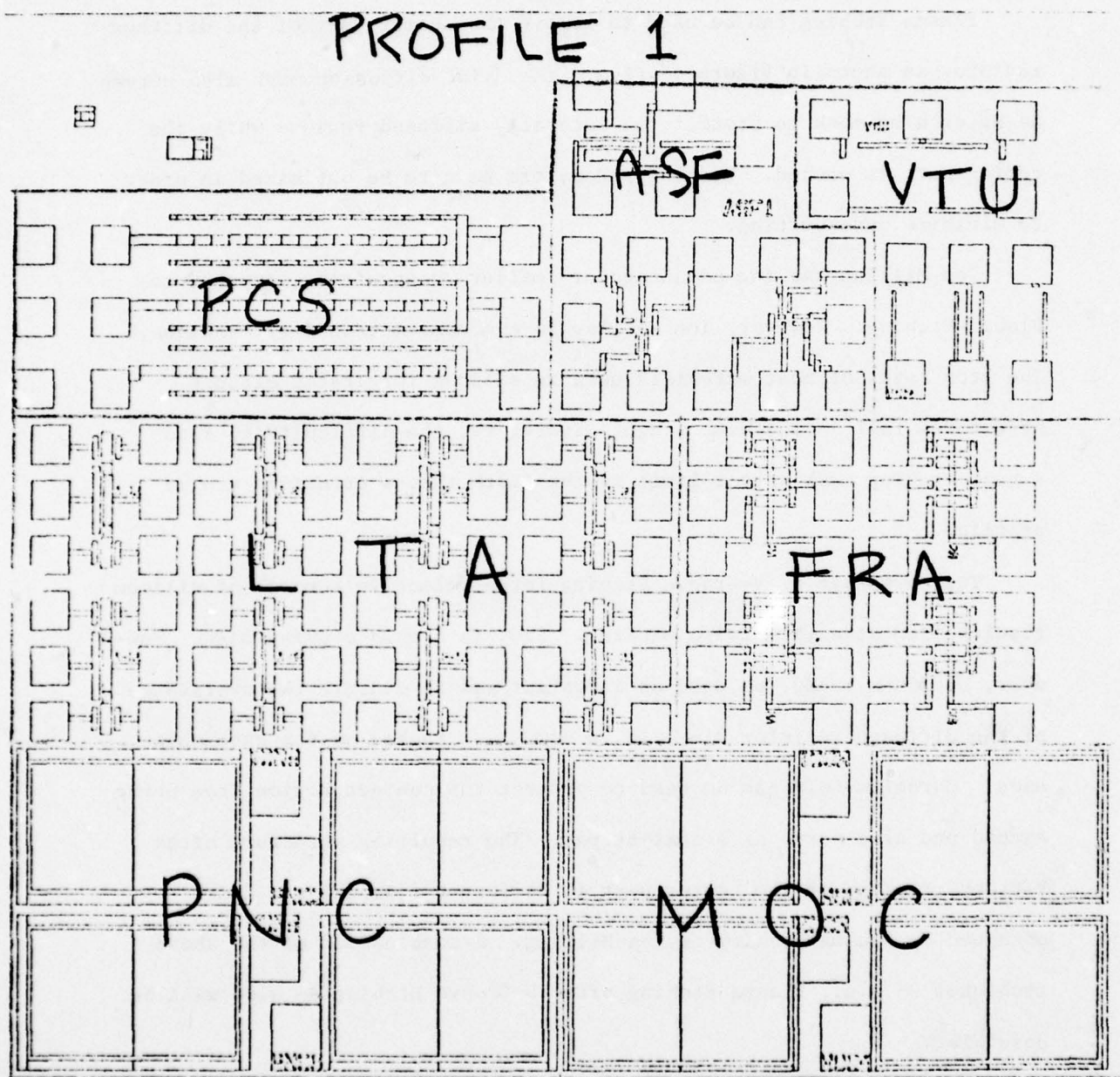


Figure 4.4.20 - Plan view of a CMOS test chip for an electrical measurement technique of two-dimensional profiles.

# PROFILE1-LCS : SUPREM SIMULATION VS. SPREADING RESISTANCE

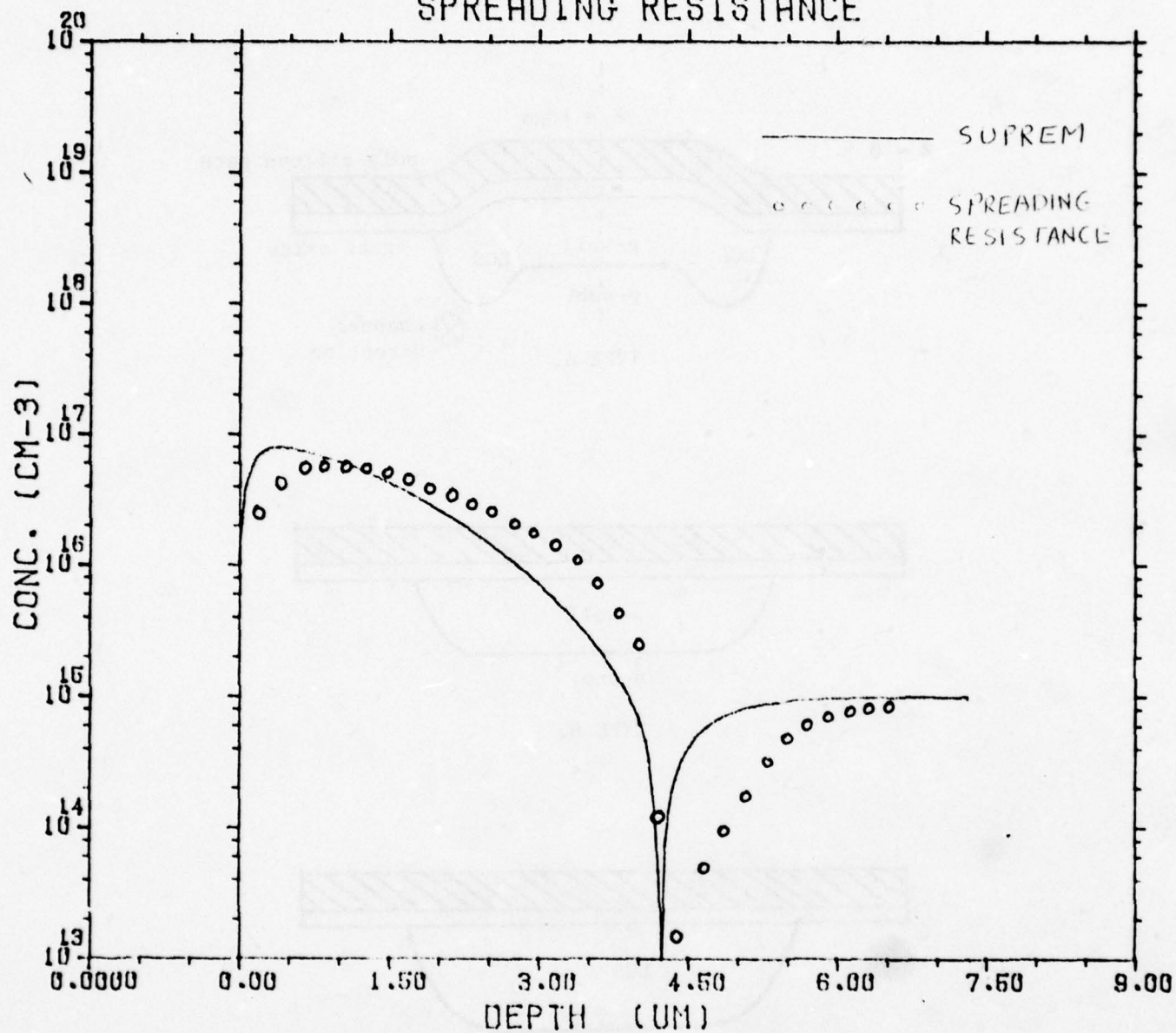
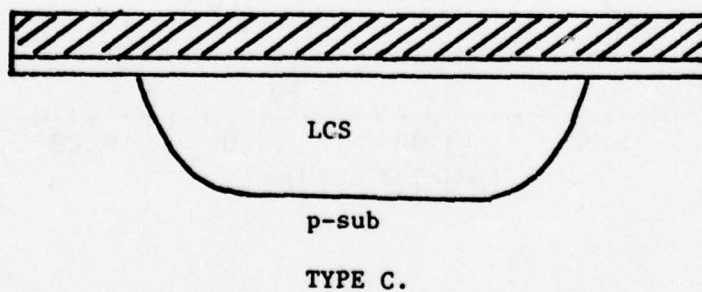
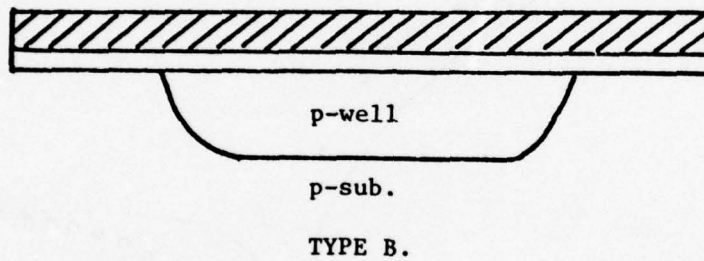
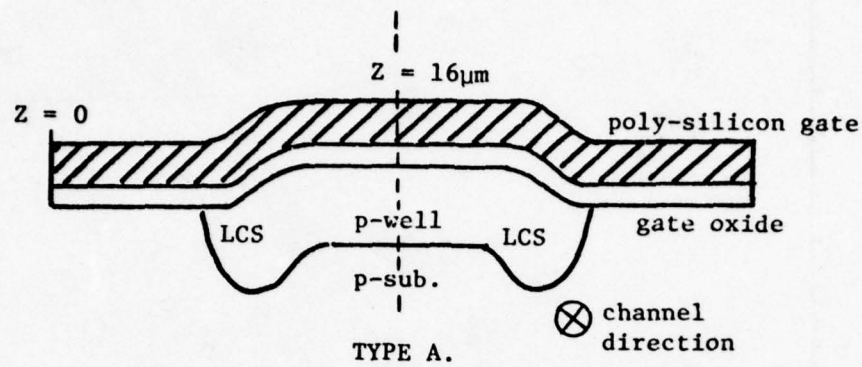


Figure 4.4.21 - Vertical impurity profile of the Lateral Channel Stop in the CMOS test chip.



(a)

Figure 4.4.22 - (a) Three types of n-channel elements with different combinations of substrate, p-well and LCS. Parallel connections of 32 elements for each type form three large MOSFET's A, B and C.

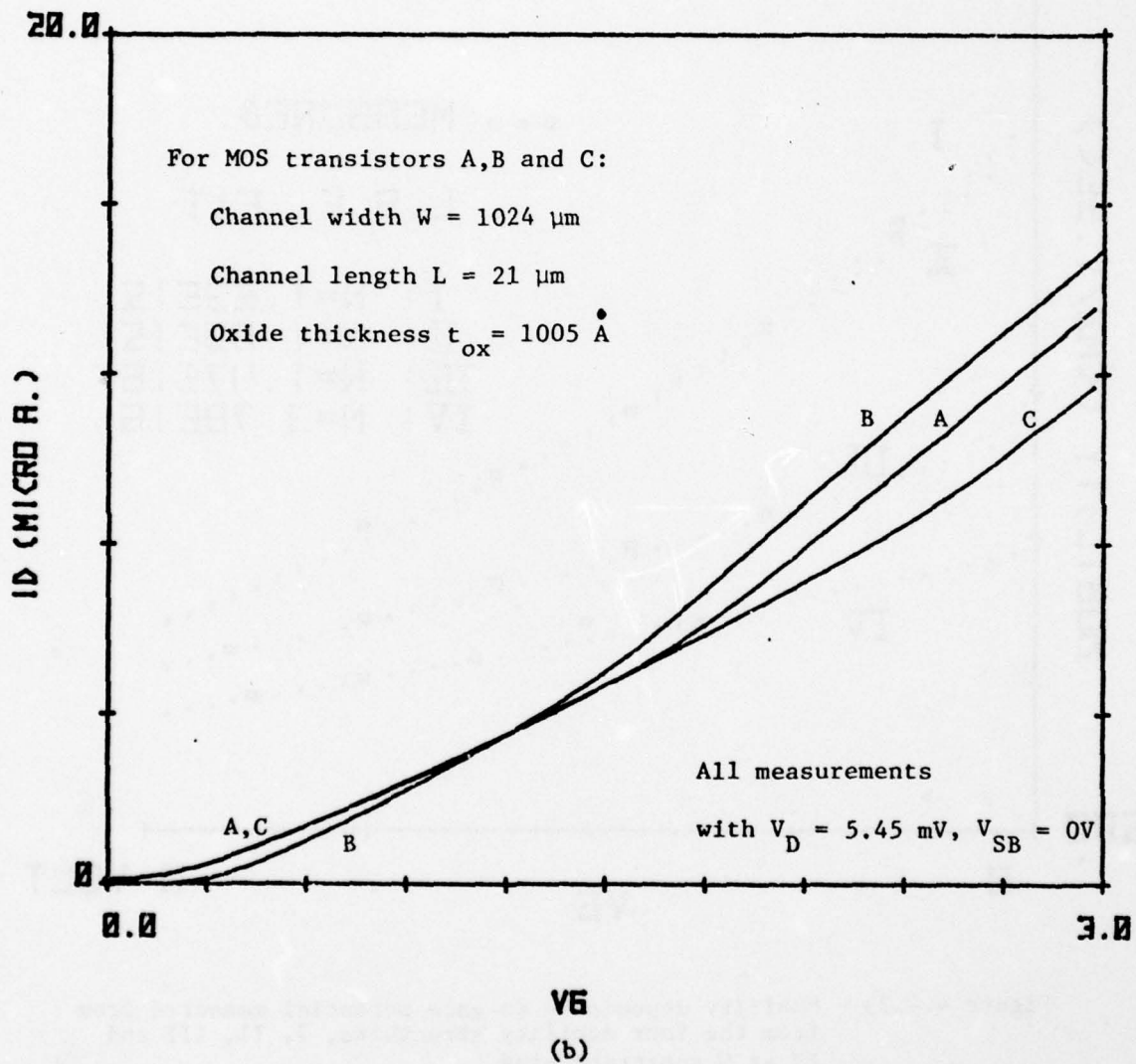


Figure 4.4.22b -  $I_D$  vs.  $V_G$  characteristics of A, B and C at a small drain voltage. All curves are concave upward due to the increasing channel width with gate voltage increase.

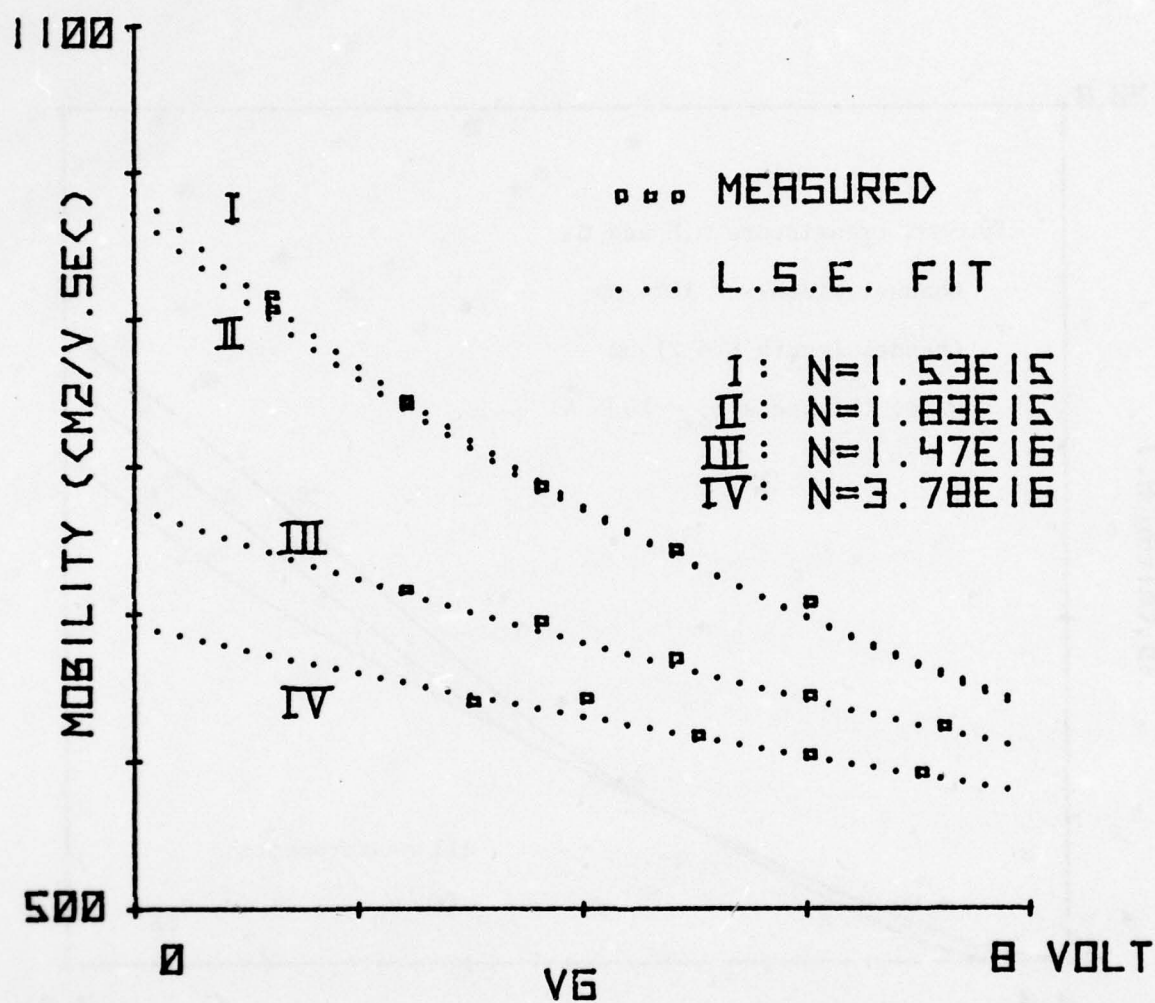


Figure 4.4.23 - Mobility dependence on gate potential measured from the four mobility structures, I, II, III and IV at 0 substrate bias.

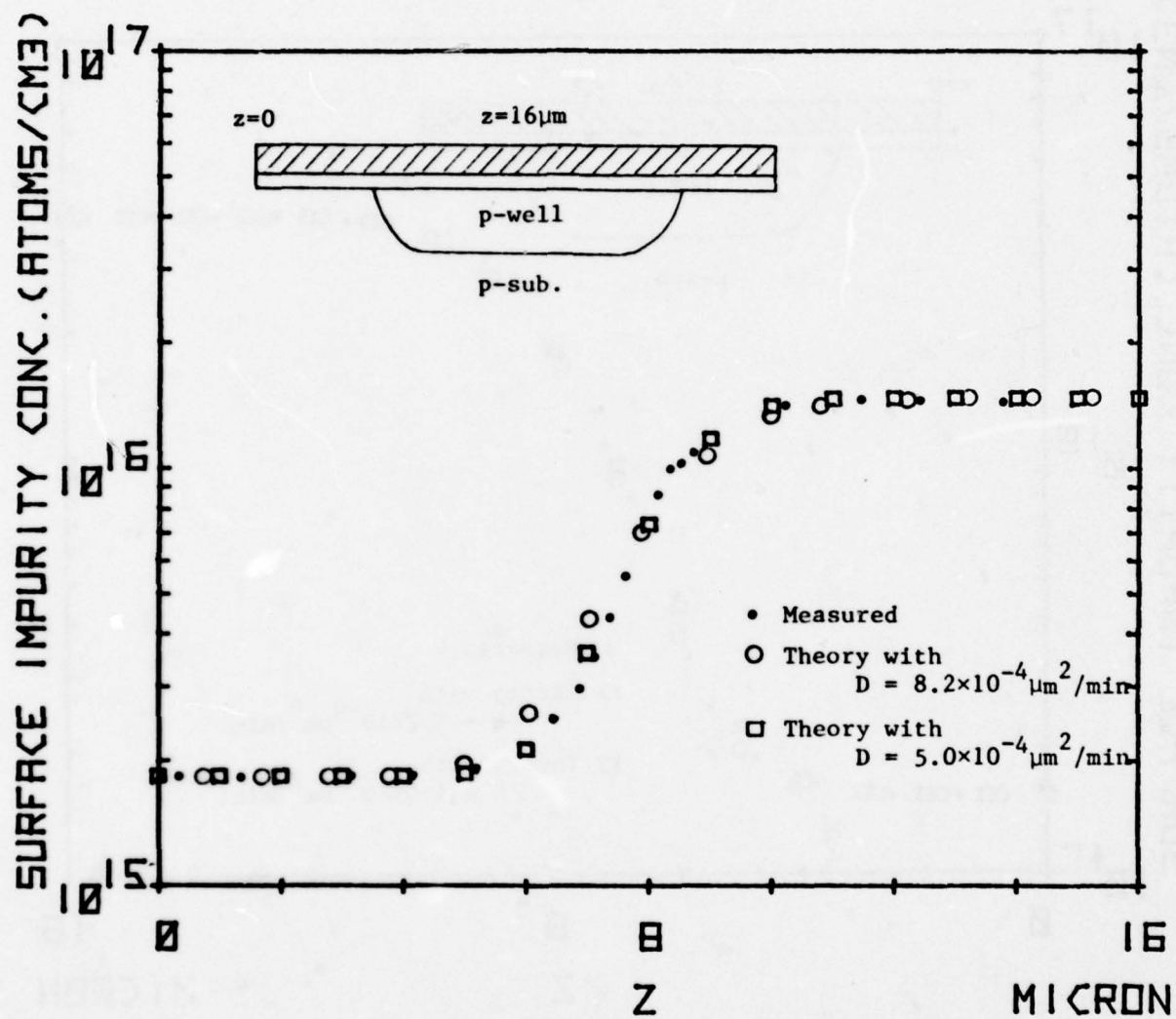


Figure 4.4.24 - Surface impurity profile across the channel for structure B.

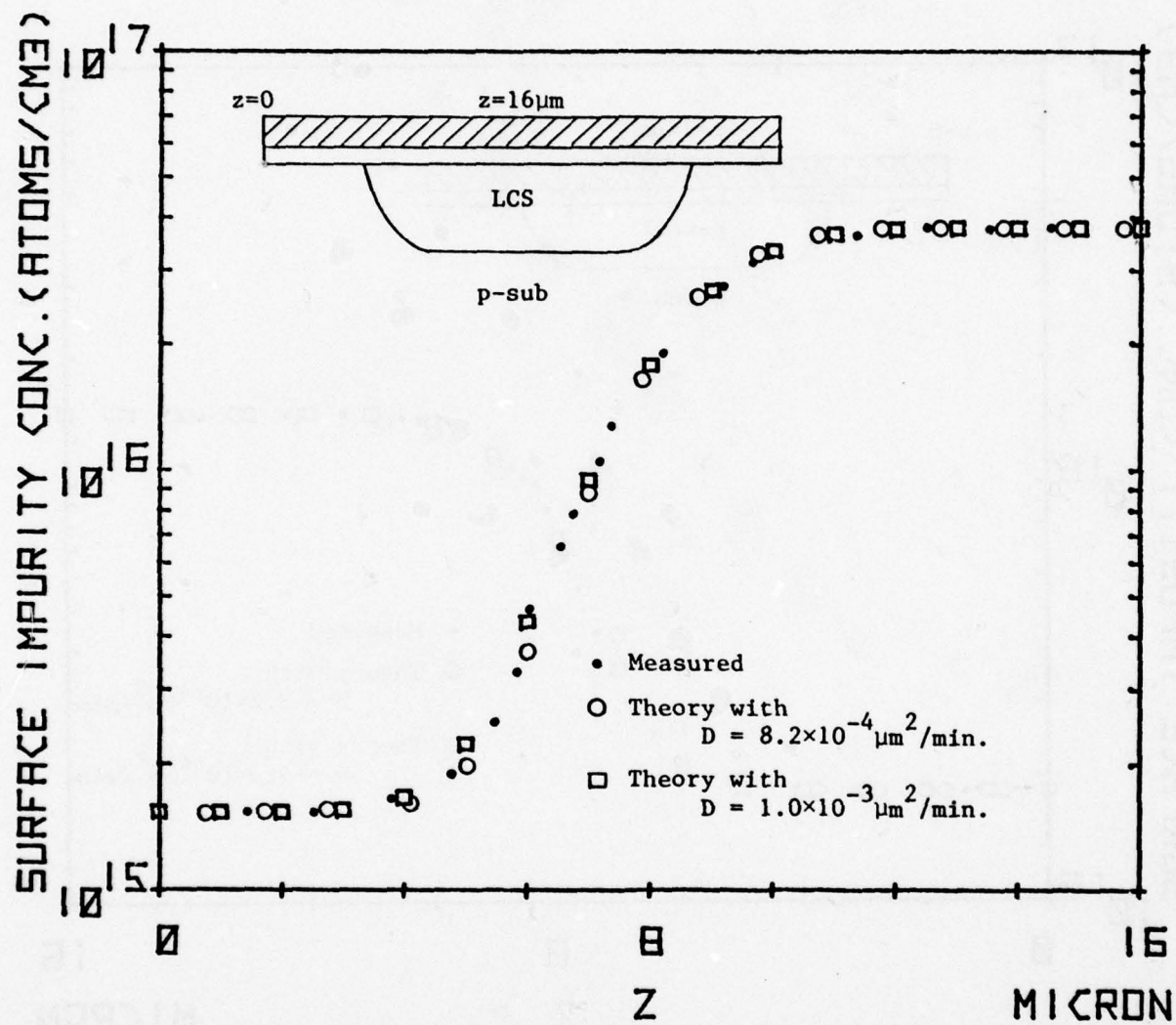


Figure 4.4.25 - Surface impurity profile across the channel width for structure C.

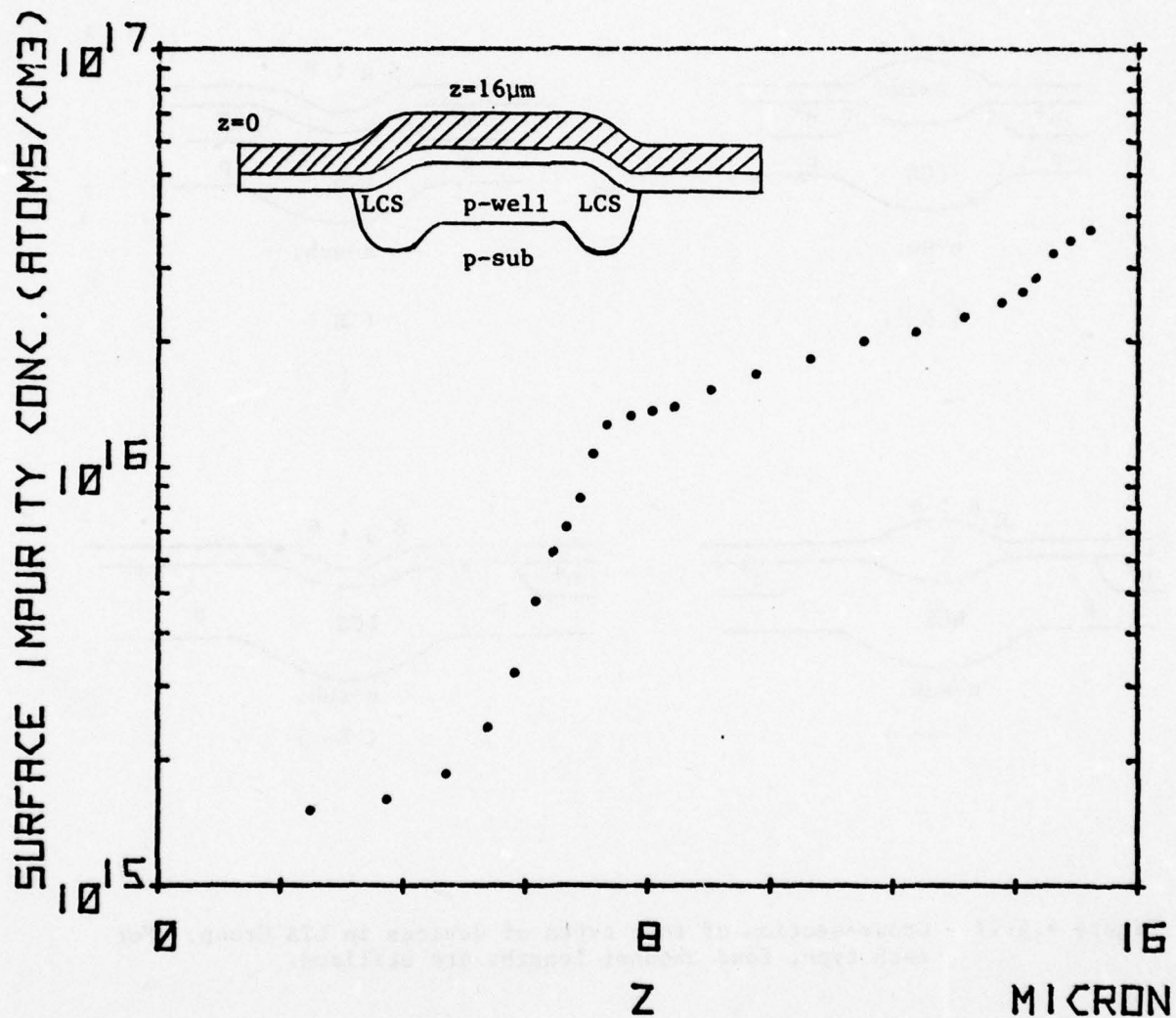
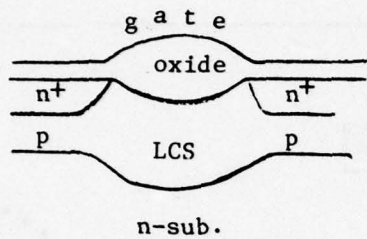
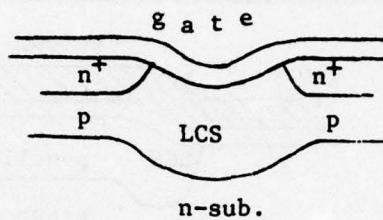


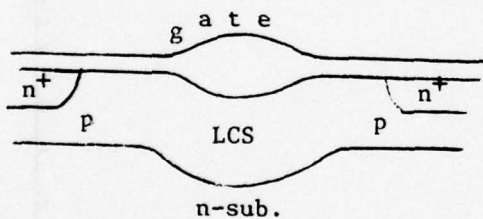
Figure 4.4.26 - Surface impurity profile across the channel width for structure C.



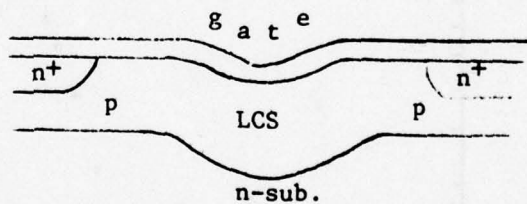
( A )



( B )



( A- )



( B- )

Figure 4.4.27 - Cross-section of four types of devices in LTA Group. For each type, four channel lengths are utilized.

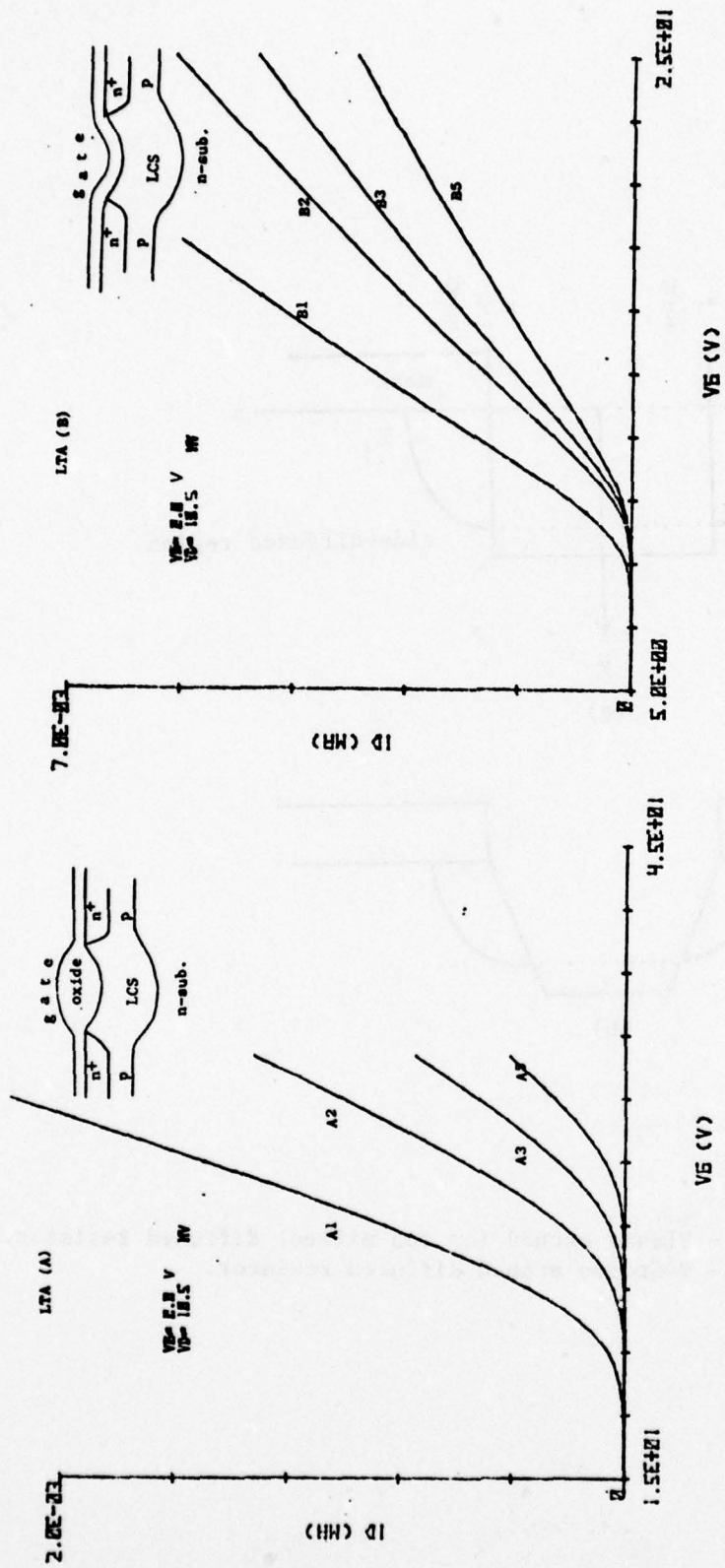


Figure 4.4.28 -  $I_D$  vs.  $V_G$  characteristics of devices LTA (A) and LTA (B)

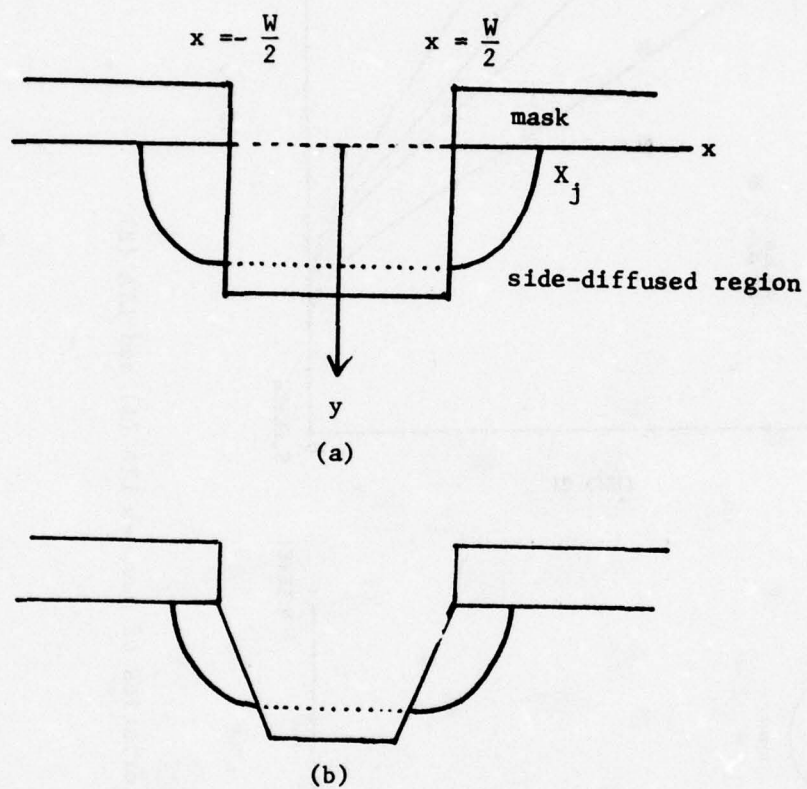


Figure 4.4.29a - Plasma etched (or ion milled) diffused resistor.  
 4.4.29b - V-Groove etched diffused resistor.

Table 4.4.4  
Current Ratio of LTA (B) Devices at a Small Drain Voltage.  
( $V_D = 10.5$  mV)

Device	$I_D$ ( $\mu A$ ) (at $V_G - V_T = 5V$ )	$I_D$ ratio	Mask ( $\mu m$ ) channel length	Expected channel length ( $\mu m$ )
B1	2.44	2.32	1	3.58
B2	1.72	1.63	2	4.58
B3	1.44	1.37	3	5.58
B5	1.06	1.00	5	7.58

Bird's beak of  $1.29 \mu m$  on each side is assumed in the calculation of expected channel lengths. This value is obtained from the current ratio of devices B3 and B5.

Table 4.4.5

Devices	$V_T$ (Volts)			Effective Bulk Doping <sub>-3</sub> $N_B$ (cm <sup>-3</sup> )	
	$V_{SB}=0^V$	$V_{SB}=0.5^V$	$V_{SV}=1.0^V$		
LTA (B)	B1	9.68	13.70	17.02	$2.75 \times 10^{16}$
	B2	10.47	14.75	18.29	$3.13 \times 10^{16}$
	B3	10.52	14.86	18.44	$3.22 \times 10^{16}$
	B5	10.61	14.96	18.59	$3.24 \times 10^{16}$
LTA(B-)	B-1	9.18	13.98	18.02	$3.79 \times 10^{16}$
	B-2	9.82	14.88	19.10	$4.23 \times 10^{16}$
	B-3	10.37	15.46	19.81	$4.28 \times 10^{16}$
	B-5	10.58	15.57	19.89	$4.11 \times 10^{16}$

Calculation of effective LCS doping using back-gate bias measurement

#### 4.5 Latch-Up in CMOS Integrated Circuits (D. B. Estreich)

##### Introduction

"Latch-up" in integrated circuits may be defined as a high-current state accompanied by a collapsing or low-voltage condition. Upon application of a radiation transient or an electrical excitation meeting certain requirements, the latched or high-current state can be triggered. Three regenerative mechanisms are known which can initiate latch-up [4.39]. They are (a) four layer (SCR) regenerative switching action [4.30] - [4.32], (b) secondary breakdown [4.33], and (c) sustaining voltage breakdown [4.34]. In CMOS and related integrated circuits, the four-layer regenerative switching action is the most troublesome. Hence in this study the term "latch-up" will be confined to mean four-layer regenerative switching.

Complementary MOS integrated circuits are particularly susceptible to latch-up [4.35] - [4.37]. The objective of the research described below is to develop the methods and tools to analyze and predict the threshold of latch-up, starting from impurity profile and geometrical layout data. The results of such work should be especially valuable for analyzing latch-up susceptibility of new CMOS processes and layout rules for custom CMOS integrated circuits. However, the procedures developed for CMOS analysis can be applied to other integrated circuit families, for example, triple-diffused bipolar integrated circuits are latch-up prone and some linear integrated circuit processes have shown latch-up problems.

In the next section the nature of latch-up in CMOS integrated circuits is discussed. The various ways in which latch-up can be initiated are

described. Following this description, a procedure is given which allows the analysis of latch-up. Factors influencing the current gains of both the parasitic lateral PNP and vertical NPN transistors are considered with regard to their importance to latch-up analysis. Finally, the last section gives an example of latch-up in a CMOS integrated circuit and compares experimental results with the results of an analysis of the principal latch-up path on this integrated circuit.

#### The Problem of Latch-Up in CMOS

CMOS integrated circuits use two fundamental configurations for circuit design. The inverter gate, as shown in Figure 4.5.30a, is the most basic build block for CMOS [4.38]. The substrate of the P-channel transistor is at a positive potential  $V_{DD}$ , while the substrate (P-well) of the N-channel transistor is at a negative potential (or ground)  $V_{SS}$ . Note that the sources of both the P-channel and N-channel MOS transistors are tied to their respective substrates.

The other fundamental block is the transmission gate or analog switch [4.38], shown in Figure 4.5.30b. The transmission gate is a single-pole, single-throw switch formed by the parallel connection of a P-channel transistor and an N channel transistor. In this case, the substrate of the N-channel transistor is at  $V_{SS}$  (negative potential or ground), and the substrate of the P-channel transistor is at  $V_{DD}$  (positive potential), but the sources and drains of both MOS transistors are allowed to freely swing. Normally, inverter gates are used in conjunction with transmission gates so that when the N-channel gate potential  $V_{gn}$  is high, the P-channel gate potential  $V_{gp}$  is low, and vice-versa. This arrangement overcomes the premature-cutoff problem associated with the single MOS transistor transmission gate because one of the two channels is always being operated as a drain-loaded (low

resistance) stage regardless of the states of the analog input or output.

Conventional CMOS integrated circuits contain parasitic PNP devices\*. A commonly used analog for the PNP device is a pair of complementary bipolar junction transistors. Figure 4.5.31 illustrates a typical CMOS structure with one possible PNP path shown (between the source regions of the two MOS transistors).

For latch-up (SCR action) to occur between the source regions indicated in Figure 4.5.31, three conditions must be met. First, the bias conditions, regardless of how achieved, must allow both emitter-base junctions ( $p^+$  source-to-substrate and  $N^+$  source-to-P-well junctions) of the parasitic transistors  $Q_1$  and  $Q_2$  to become forward biased. The substrate-to-P-well junction is normally reverse-biased because  $V_{DD}$  is at a higher potential than  $V_{SS}$ . Secondly, the loop gain of the two parasitic transistors must be large enough to produce regeneration. Regeneration results when the total loop gain equals or exceeds unity. Normally, it is stated that this condition is fulfilled when

$$\beta_{NPN} \cdot \beta_{PNP} \geq 1 \quad (4.5.82)$$

where  $\beta_{NPN}$  is the common-emitter current gain ratio of the parasitic vertical NPN transistor, and  $\beta_{PNP}$  is the identical parameter of the parasitic lateral PNP transistor [4.35]. This is exactly equivalent to

$$\alpha_{NPN} + \alpha_{PNP} \geq 1 \quad (4.5.83)$$

where the  $\alpha$ 's are the common-base current transfer ratios ( $\alpha = \frac{\beta}{\beta + 1}$ ). The third condition is that the circuits or networks connected to the regions forming the end layers of the PNP structure must be capable

---

\*Dielectric isolation is excluded from this discussion.

of sourcing or sinking a current greater than the holding current of the PNP device. If these three conditions are met, then the latch-up threshold can be achieved.

To be more specific, consider the inverter gate shown in cross-section in Figure 4.5.32.  $V_{DD}$  is always at a higher potential than  $V_{SS}$ ; for standard commercial CMOS the  $V_{DD}$ -to- $V_{SS}$  voltage range is typically specified at +3 to +18 volts (sometimes to 15 volts). Exceeding the upper value of this voltage range can initiate latch-up, provided the three conditions listed above are satisfied.

Suppose that  $V_{SS}$  is grounded and  $V_{DD}$  is increased slowly. Increasing  $V_{DD}$  increases the reverse-bias junction voltage appearing across the substrate-to-P-well junction. At higher reverse-bias voltages, avalanche multiplication [4.39] becomes important. Increased current multiplication causes a corresponding increase in the current through the  $V_{DD}$  and  $V_{SS}$  terminals.

This has important consequences for the inverter gate connection because of the bulk resistance of both the substrate and P-well. Consider the effect of the lateral current  $I$  flowing laterally in the P-well as shown in Figure 4.5.33. It is assumed that the potential at the ohmic contact surface B-B' of the P-well is at ground. The potential at cross section A-A' is higher than ground potential because of the IR voltage drop across the P-well bulk resistance. The source region of the N-channel transistor is at ground potential. The potential difference between B-B' and cross section A-A' is such as to forward bias the N+ source-to-P-well junction. Note that the forward bias will be greatest at the edge of the source region most distant from the ohmic contact to the P-well.

For sufficiently large forward-bias, a substantial number of minority carriers may be injected into the P-well, hence, further increasing the current crossing the substrate-to-P-well junction. This turns on the parasitic vertical NPN transistor in the CMOS structure. Analogous behavior occurs in the substrate, where the  $P^+$  source-to-substrate junction becomes forward-biased. This causes the parasitic lateral PNP transistor to become active and can enhance its current gain.

Figure 4.5.34 shows a schematic of the equivalent circuit of the latch-up path. Resistors  $RS_1$  and  $RS_2$  represent the substrate and P-well bulk resistances, respectively. Two emitters are shown on each parasitic transistor to represent the separate source and drain regions (the drain regions are connected to form " $V_{out}$ "). From the equivalent circuit it is easily seen that the collector current which each parasitic transistor must supply includes not only the base current of the companion parasitic transistor, but also the current through the resistance shunting the emitter-base junction of the companion transistor. Hence, for the above described manner for the initiation of latch-up, the  $\beta_{NPN} \cdot \beta_{PNP}$  product must be greater than unity. In fact, the smaller the magnitude of  $R_{S1}$  and  $RS_2$ , the larger the required  $\beta_{NPN} \cdot \beta_{PNP}$  product.

In the above discussion, a slowly increasing voltage  $V_{DD}$  was assumed. avalanche multiplication within the substrate-to-P-well junction was responsible for establishing sufficient lateral current, causing the source junctions to become forward-biased, therefore, initiating latch-up. Now suppose a rapidly increasing voltage is applied at the  $V_{DD}$  terminal (or, equivalently, a rapidly decreasing voltage at the  $V_{SS}$  terminal). The potential across the depletion layer capacitances of the substrate-to-P-well

and source/drain junctions must follow the voltage excursion\*. Thus, lateral current can flow because of the shifting charge produced by the voltage transient. This lateral current, assuming it to be of sufficient magnitude, forward-biases the source junctions, with latch-up resulting in the manner explained previously. In practice, such voltage transients can originate from power supply spikes, motor and switch sparking, corona, and radio frequency interference (RFI) from sources too numerous to mention [4.40].

In general, given a PNP structure such that unity loop gain is attainable, the injection of sufficient minority carriers into the substrate and/or P-well can establish the necessary lateral current to trigger latch-up. Several other ways exist in which such minority carrier injection can be accomplished. If the network which loads the output is capable of sinking or sourcing a current exceeding the holding current of the PNP path, then

$$\begin{aligned} V_{OUT} &\geq V_{DD} + V_{BE} \\ \text{or} & \\ V_{OUT} &\leq V_{SS} - V_{BE} \end{aligned} \tag{4.5.84}$$

leads to latch-up, where  $V_{BE}$  is the forward-bias voltage required to inject sufficient current for regeneration. Furthermore, if gate protection diodes are included, then

$$\begin{aligned} V_{IN} &\geq V_{DD} + V'_{BE} \\ \text{or} & \\ V_{IN} &\leq V_{SS} - V'_{BE} \end{aligned} \tag{4.5.85}$$

---

\*This is simply the  $C(\Delta V/\Delta t)$  current, where  $C$  is the effective capacitance.

can initiate latch-up. In this case,  $V_{BE}$  is the forward-bias voltage of the gate protection diodes, which are connected from the input gates of the MOS transistors to the substrate and P-well separately. If  $V_{IN}$  meets the conditions given in (4.5.85), the forward-bias on one of the diodes causes minority carriers to be directly injected into the PNP path. Of course, the physical location of the gate protection diodes with respect to the PNP path is an important consideration in whether latch-up can result.

In addition, avalanching the source or drain junctions of either MOS transistor can establish a lateral current flow. If any source or drain junction executes punch-through to the substrate-to-P-well junction, latch-up conditions are possible. However, punch-through occurrences are controllable by layout factors and should rarely present a problem. Finally, radiation (both photons and neutrons) produces minority carrier pairs. The photocurrents generated by transient ionizing radiation induce latch-up by altering the internal bias conditions presented to the parasitic lateral PNP and vertical NPN transistors [4.35]. The photocurrent flows between the  $V_{DD}$  and  $V_{SS}$  power supplies via the large P-well-to-substrate diode. Of course, with the photocurrent established from the transient radiation, the emitter-base junctions become forward biased in the same way as described above.

Next consider the transmission gate structure. The transmission gate is unlike the inverter gate in that  $V_{DD}$  is not connected to the P-channel transistor's source. Figure 4.5.35 shows a cross-section of a typical CMOS structure in the proper terminal connection for the transmission gate.

Latch-up can occur in the transmission gate in an analogous manner to that described for the inverter gate where a PN junction becomes forward-biased. Suppose the voltages on the analog input and analog output are

denoted by  $V_{IN}^{(A)}$  and  $V_{OUT}^{(A)}$ , respectively. Then any one of the following conditions will cause either a source or drain junction to become forward-biased and inject minority carriers.

$$\left. \begin{aligned} V_{IN}^{(A)} &\leq V_{SS} - V_{BE} \\ V_{OUT}^{(A)} &\leq V_{SS} - V_{BE} \end{aligned} \right\} \quad (4.5.86)$$

$$\left. \begin{aligned} V_{IN}^{(A)} &\geq V_{DD} + V_{BE} \\ V_{OUT}^{(A)} &\geq V_{DD} - V_{BE} \end{aligned} \right\} \quad (4.5.87)$$

As before, the minority carriers establish a current flow. If sufficient loop gain around the two parasitic transistors (PNPN path) can be generated, latch-up is likely. Of course, the same three conditions listed above in the inverter gate discussion must be satisfied for the latched state to be on.

Conditions (4.5.86) and (4.5.87) can be fulfilled by either a transient spike on the power supply ( $V_{DD}$  or  $V_{SS}$ ) or by either the analog input or output exceeding the power supply range. The latter possibility imposes restrictions upon the loading of the transmission gate. Carelessness in selecting the loading network connected to the analog terminals has been responsible for giving the transmission gate a poor latch-up reputation.

Allowing the total applied voltage  $|V_{DD} - V_{SS}|$  across the substrate-to-P-well junction to exceed the avalanche breakdown voltage can also lead to latch-up. However, the loading (and attendant voltage state) on the analog terminals must be favorable to latch-up. This can be seen by examining latch-up equivalent circuit for the transmission gate in Fig. 4.5.36.

Generally, gate protection diodes are not connected to the gating inputs of the transmission gate because of the buffering with inverter gates. If gate protection diodes are used on the buffering inverter gates, and if these diodes are physically close to the MOS transistors forming the switch itself, then forward-biasing these diodes may initiate latch-up. This is not usually a problem in typical commercially available CMOS because of the layout separation. Also, radiation can initiate latch-up in transmission gates.

#### Analysis of CMOS Latch-Up

The general approach taken in latch-up prediction for an integrated circuit can be summarized as follows:

- (1) Data on impurity levels, impurity profiles, and minority carrier lifetimes is collected.
- (2) Principal latch-up paths are identified using the layout of the integrated circuit (or postulated if the analysis is conducted before or during layout).
- (3) Bulk resistances and current flow paths calculated in both substrate and P-well.
- (4) Calculate the appropriate current gain for the parasitic vertical NPN transistor.
- (5) Calculate the appropriate current gain for the parasitic lateral PNP transistor including field-aiding effects.
- (6) Finally, form the product of the current gains and test (equation 4.5.82) to check for latch-up occurrence.

Geometry in CMOS integrated circuits plays a crucial role in determining latch-up behavior. From the discussion in the previous section,

it is clear that reducing the parasitic bulk resistances (resistors  $R_{S1}$  and  $R_{S2}$  in Figure 4.5.34) in order to minimize the voltage drop across a source region, and maximizing the lateral PNP transistor's base width to reduce its current gain will reduce the susceptibility of the integrated circuit to latch-up. Furthermore, reducing the bulk resistances also reduces the lateral field-aiding enhancement of the PNP transistor's current gain. Of course, these factors are strong functions of layout. To reduce the magnitude of the bulk parasitic resistances, it is necessary to distribute  $V_{DD}$  and  $V_{SS}$  via metal interconnections to many points across the chip (unfortunately, it is not always compatible with layout efficiency). Furthermore, placing  $V_{DD}$  contacts as close to the P-well, and  $V_{SS}$  contacts as close to the substrate as practical, helps in this regard.

The orientation of the source regions relative to the latch-up current path is important in determining the forward-bias lateral voltage differential across the source junctions. It can be of some advantage to place the lengthwise direction of the source perpendicular to the latch-up current path (often this is approximately parallel to the edge of the most adjacent P-well). Another factor of considerable importance is the P-well-to-source spacing relative to the  $V_{DD}$  contact-to-P-well spacing. To reduce latch-up susceptibility, this ratio should be as large as feasible. From the above discussion, it is clear that geometrical factors are critical in the consideration of latch-up. Efforts to increase the density of CMOS integrated circuits by scaling down the geometrical features increases latch-up susceptibility. Unfortunately, control of geometry alone is not always adequate to prevent latch-up.

Minority carrier lifetime is an important parameter influencing latch-up. Consider the vertical NPN transistor's current gain -- some CMOS

integrated circuits (particularly high voltage custom CMOS integrated circuits) have deep P-well diffusions resulting in wide transistor base widths. The base transport factor becomes important in wide base transistors which means that minority carrier lifetime can strongly influence the current gain. To analyze the NPN current gain, the P-well and source diffusion profiles must be known. The impurity profile data can either be determined by measurement or from the process simulator SUPREM [4.41]. Using a one-dimensional numerical semi-conductor device analysis program such as SEDAN [4.42], the current gain of the vertical NPN transistor may be determined.

The role of lifetime is even more important in the operation of the parasitic lateral PNP transistor where base widths can be of the order of a diffusion length or more. In fact, the lateral PNP structures commonly encountered along latch-up paths have current gains which are dominated by the base transport efficiency. An additional factor must be considered when analyzing the lateral PNP transistor's current gain. An electric field accompanies the lateral current flow in the bulk regions. This current-induced electric field (a) enhances the minority carrier transport in the base, and (b) concentrates the minority carrier injection of the forward-biased source-substrate junction at the edge closest the P-well (collector). Both effects act to increase the PNP transistor's current gain. Typical current-induced electric field strengths in CMOS structures can range from approximately 20 to 100 volts/cm at the threshold of latch-up. Figure 4.5.37 shows the calculated current gain of the lateral PNP transistor, which has unity emitter efficiency, as a function of base width normalized to diffusion length and for lateral electric field strength. Clearly, the lateral current-induced field strongly enhances the effective

current gain and must be accounted for in the analysis.

By reducing the minority carrier lifetime to small enough values, latch-up can be eliminated. In fact, the use of gold doping to reduce lifetime in CMOS integrated circuits have been investigated by Dawes and Derbenwick [4.43] — — they found that with sufficient introduction of gold that latch-up can be eliminated. The reduction of current gain from decreasing lifetime is evident in Figure 4.5.37 if one recalls that the diffusion length,  $L$ , is proportional to the square root of the lifetime. Hence, being able to equate effective current gain for both the NPN and lateral PNP parasitic transistors with bulk lifetime is crucial in the analysis of latch-up threshold for a given CMOS process and geometry.

Example: Latch-Up in Siliconix DG 515

An example of the analysis of latch-up susceptibility in a CMOS integrated circuit is presented in this section. The Siliconix DG 515 is a four-bit D/A converter switch (SPDT) with CMOS switch drivers included on chip. Figure 4.5.38 shows a section of the DG 515 chip containing one of the input CMOS inverters. Latch-up can be induced in the DG 515 if sufficient current flows between the  $V_{DD}$  and  $V_{SS}$  contacts along the latch-up path shown in Figure 4.5.38.

A detailed analysis along this latch-up path predicts that a lateral current of approximately 4.5 mA must be present to generate sufficient forward-bias to turn-on the parasitic transistors. This is consistent with measured results as shown in Figure 4.5.39 where a P-well-to-substrate avalanche current of 4.15 mA triggers the latch-up mode. A sampling of twenty DG 515 integrated circuits gave latch-up threshold currents of 3.8 to 4.9 mA.

The bulk resistance in the substrate between the  $V_{DD}$  contact and the P-well is approximately 1050 ohms, whereas, the lightly doped P-well resistance is of the order of 3000 to 4000 ohms from  $V_{SS}$  contact to the far P-well edge. As the current along the latch-up path increases, the NPN transistor turns on before the lateral PNP. Measured NPN current gains ranged from 40 to 115 for near identical conditions. At 4.5 mA of lateral current along the latch-up path, about 0.6 volt is developed between the  $V_{DD}$  contact and the  $P^+$  source of the P-channel MOS transistor. This allows the parasitic lateral PNP to turn on. For the lateral PNP, the base width is close to one and one-half times the diffusion length in the substrate. The calculated current-induced lateral aiding field is 45 volts/cm, which considerably enhances the current gain of the lateral PNP. The estimated peak lateral PNP current gain is five, however, this can not be verified by measurements because individual measurement of the PNP current gain does not allow the lateral electric field to be applied. The product of the current gains of both the NPN and lateral PNP transistors considerably exceed unity, hence, latch-up is predicted. In the case selected for the DG 515, the latch-up threshold current is determined by the lateral current needed to bias the transistors in the "on" state (sufficient forward voltage on emitter-base junctions). Latch-up was experimentally achieved for both  $C \frac{dv}{dt}$  currents from pulses on the  $V_{DD}$  supply line and from voltages high enough to breakdown the P-well-to-substrate junction allowing avalanche current to flow.

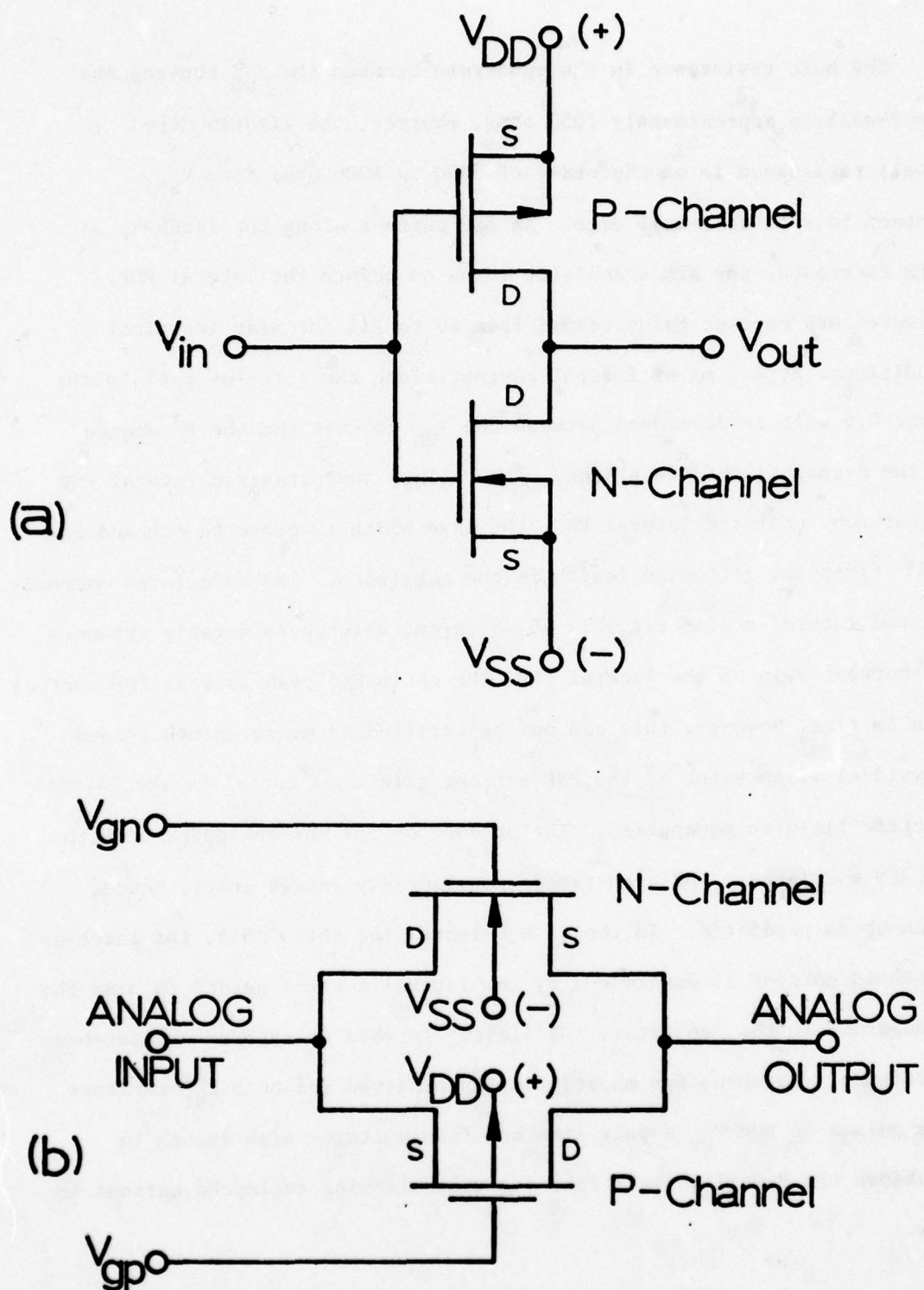
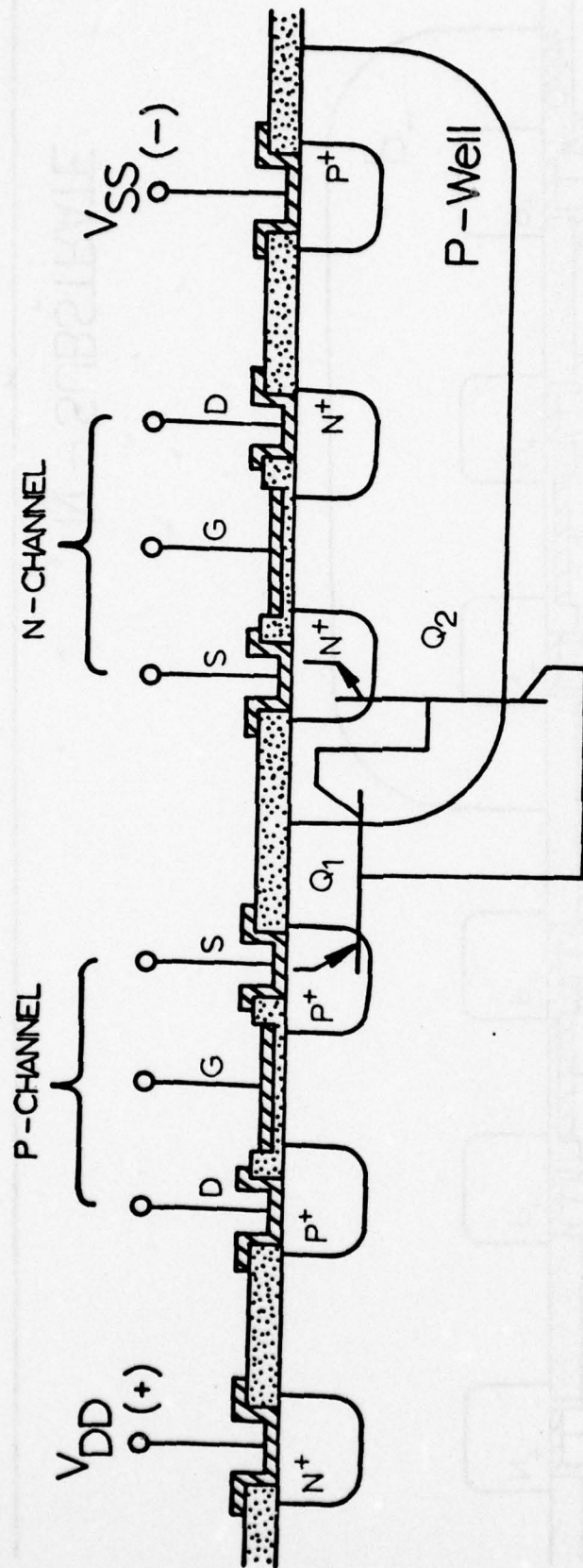
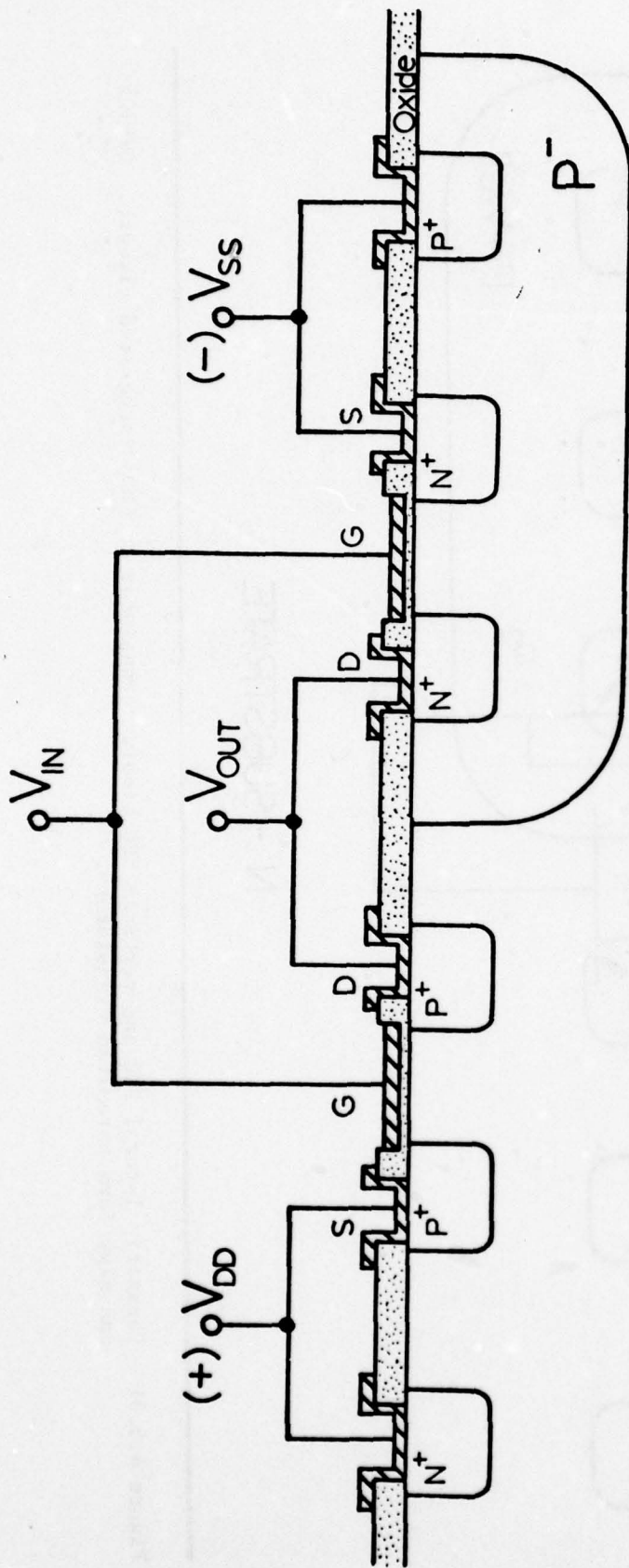


Figure 4.5.30. a) CMOS inverter connection, and  
b) CMOS transmission gate connection.



N - SUBSTRATE

Figure 4.5.31 - Parasitic lateral PNP and vertical NPN bipolar transistor in CMOS integrated circuit. Drains can also form parasitic transistors.



N - SUBSTRATE

Figure 4.5.32 - Cross-section of CMOS inverter connection.

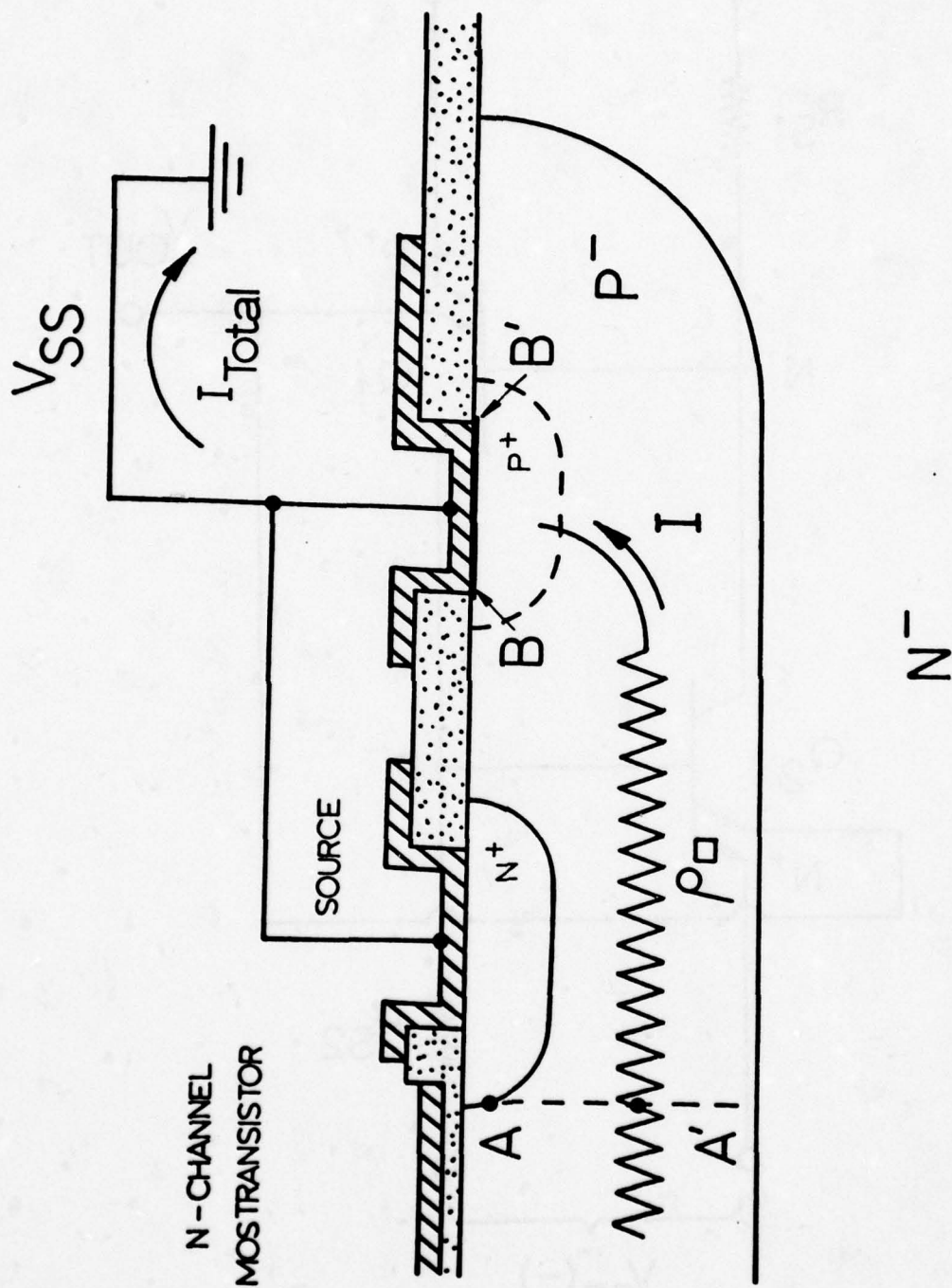


Figure 4.5.33. Effect of lateral current in P-well.

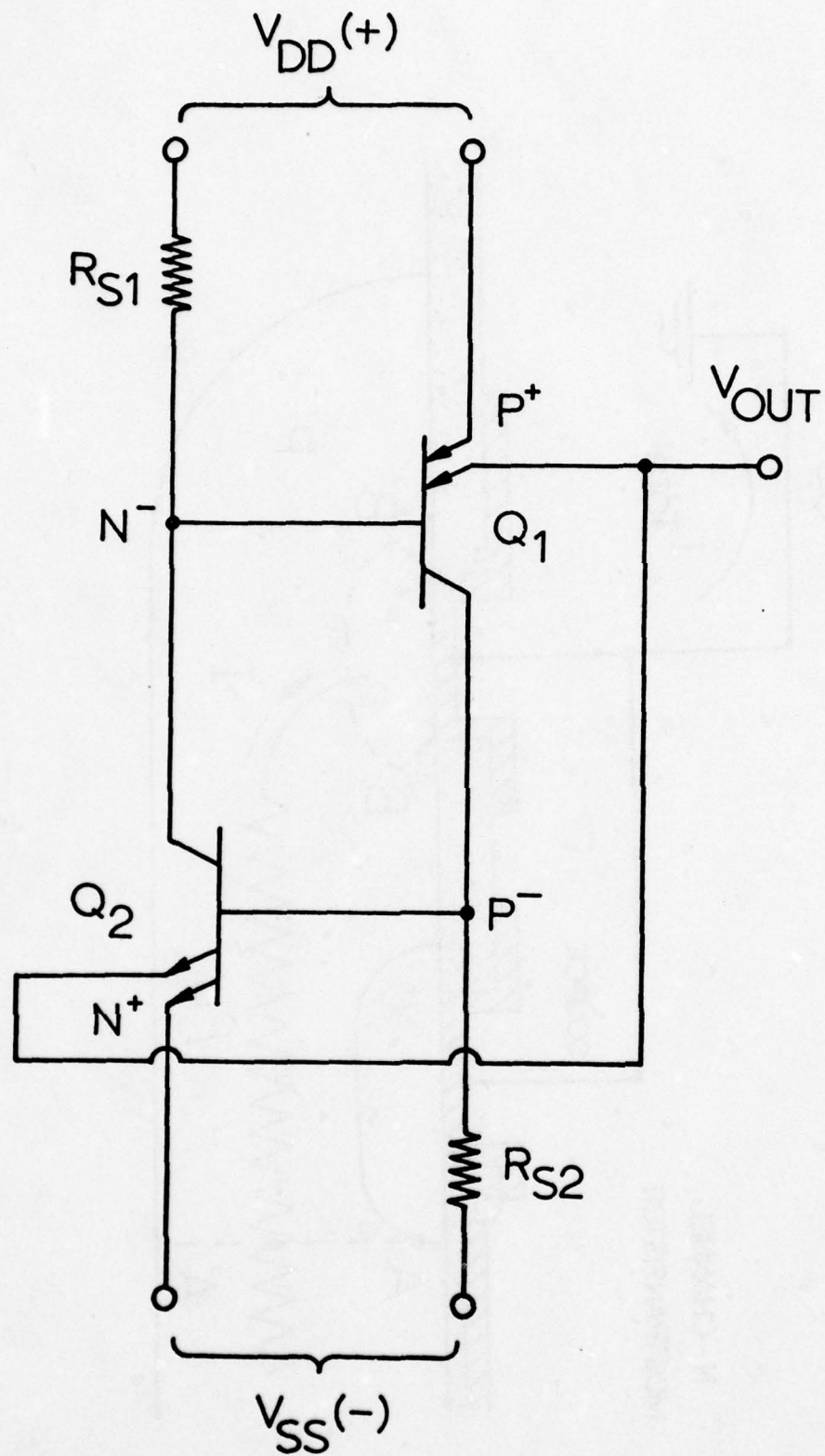


Figure 4.5.34 - Latch-up equivalent circuit for CMOS inverter.

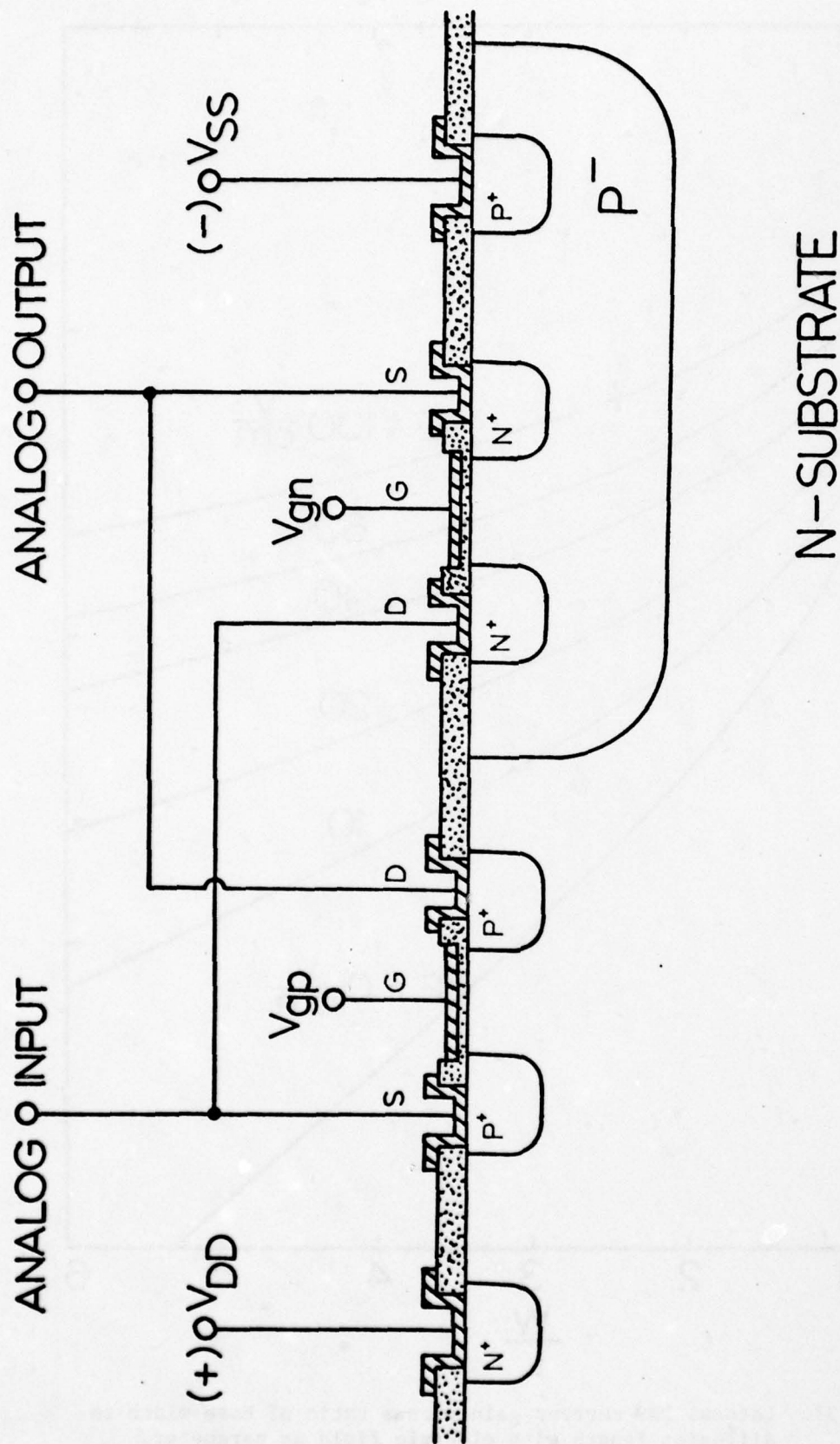


Figure 4.5.35. Cross-section of CMOS transmission gate connection.

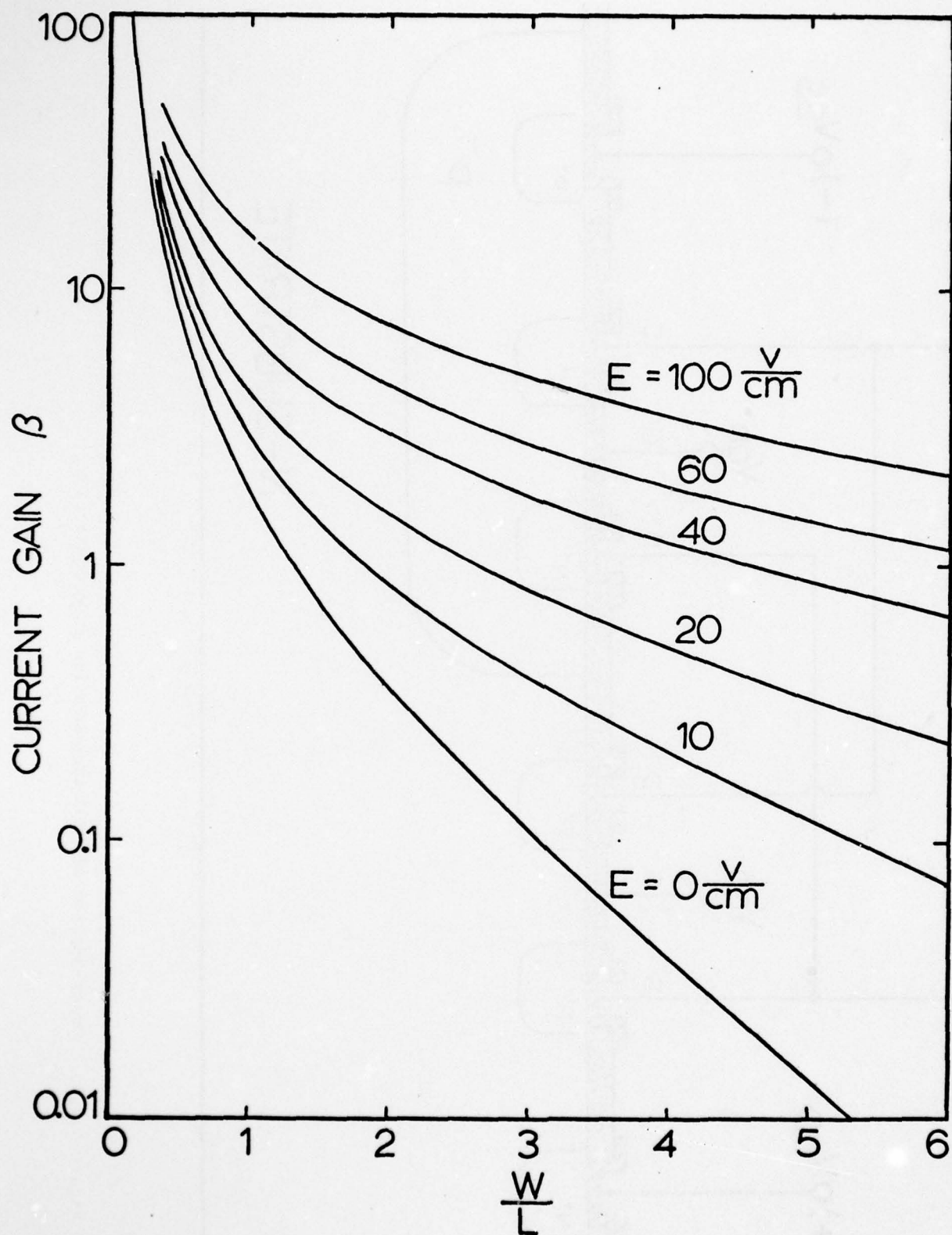


Figure 4.5.37. Lateral PNP current gain versus ratio of base width to diffusion length with electric field as parameter.

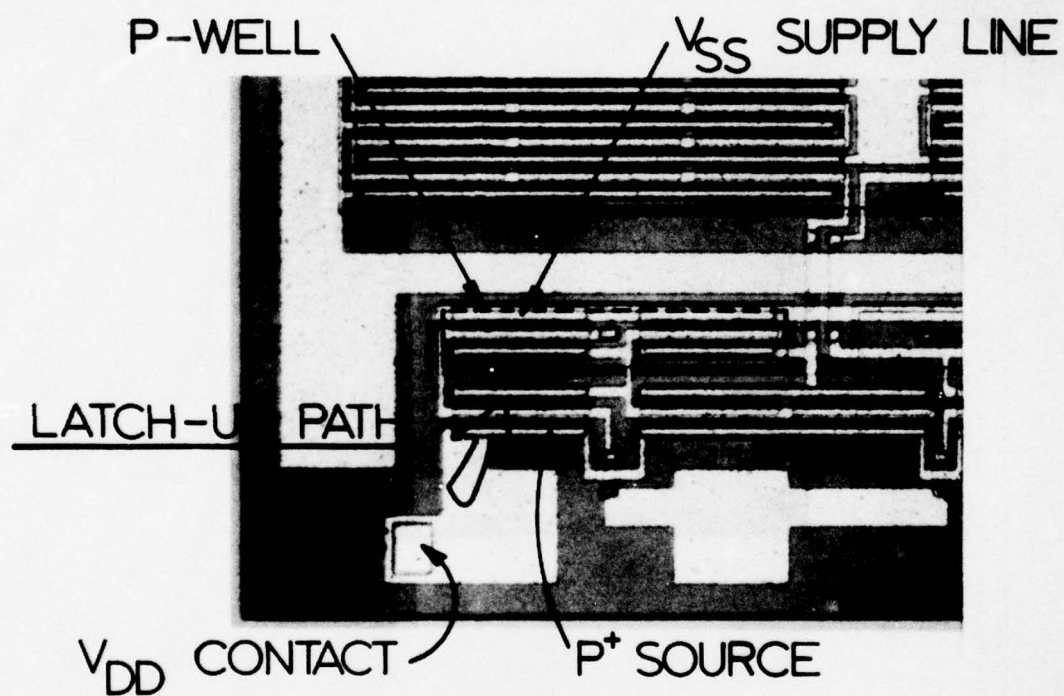


Figure 4.5.38. Section of silicon DG 515 CMOS IC with principal latch-up path shown.

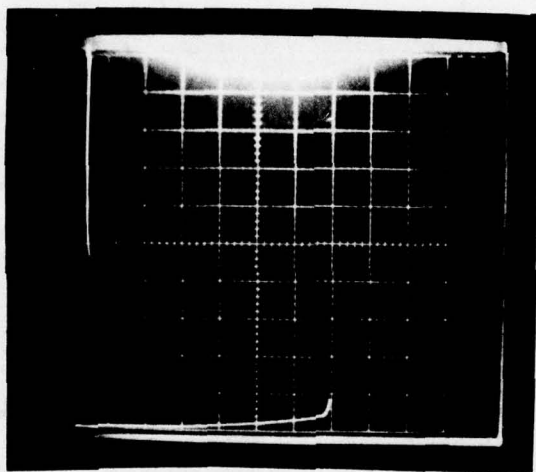


Figure 4.5.39. Latch up in siliconix DG 515 IC (abscissa: 5 volts/  
division ordinate: 5mA/division).

#### 4.6 A Charge-Oriented Model for MOS and Transistor Capacitances (D.E. Ward)

##### Introduction

The successful computer simulation of MOS circuits requires an accurate model for transistor capacitances. While use of average capacitance values may suffice for some devices or circuits, it is usually necessary to consider the variation of capacitance with voltage. A model which does this was developed by Meyer [4.44], and is used in many modern circuit simulators. While this model works well for most cases, it is inadequate for use with some newer device and circuit technologies. In particular, it fails for circuits in which charge storage is important. Such is the case for many dynamic and silicon-on-sapphire (SOS) circuits. A model to handle circuits in which charge is more important than capacitance will be presented here.

##### The Conventional Model

Meyer's model is shown in Figure 4.6.40. Three non-linear capacitors are defined in terms of the total gate charge  $Q_G$ :

$$C_{GD} \triangleq \frac{\partial Q_G}{\partial V_D} \quad C_{GB} \triangleq \frac{\partial Q_G}{\partial V_B} \quad C_{GS} \triangleq \frac{\partial Q_G}{\partial V_S} \quad (4.6.88)$$

The current through each capacitor is computed from

$$i = C(V_O) \frac{dV}{dt} \quad (4.6.89)$$

where the capacitance has been evaluated at some appropriate voltage  $V_O$ .

Several problems can occur with this model, the most important being the omission of source-bulk and drain-bulk capacitances. These problems lead to a non-conservation of charge (charge-pumping) in which the charge stored in a node is not equal to the integrated net current flowing into the node. Discontinuities in the capacitance functions can also cause instabilities in the Newton-Raphson iteration procedure.

### The Charge-Oriented Model

The proposed model is based on the actual charge distribution in the MOS structure (Figure 4.6.41). For any region of space we can write

$$i = \frac{dQ}{dt}$$

where  $i$  is the net current flowing into the region and  $Q$  is the total charge contained in the region. Thus we can write

$$i_G = \frac{dQ_G}{dt} \quad i_B = \frac{dQ_B}{dt} \quad i_S + i_D = \frac{d(Q_S + Q_D)}{dt} \quad (4.6.90)$$

For use in a circuit simulator we integrate these equations:

$$\int_{t_0}^{t_1} i \, dt = Q(t_1) - Q(t_0) \quad (4.6.91)$$

In general  $Q$  is a complex function of time. . The problem is simplified by assuming that the charge at any time is determined by the terminal voltages at that instant. Then  $Q$  can be determined from steady-state conditions.

Any theory of MOS transistor operation which predicts the total gate and bulk charges can be used to find  $Q_G$ ,  $Q_B$ , and  $Q_S + Q_D$ . The results given here are based on the simple theory of Ihantola and Moll [4.45]. Gate and bulk charges are calculated from the one-dimensional Poisson equation applied perpendicular to the surface. Channel charge is computed from

$$Q_C = - (Q_G + Q_B) \quad (4.6.92)$$

and is related to the source and drain charges:

$$Q_C = Q_S + Q_D \quad (4.6.93)$$

Unfortunately, the drain and source charges are not as well-defined as the gate and bulk charges and must be obtained by partitioning the channel charge. The present model uses

$$Q_S = Q_D = \frac{1}{2} Q_C \quad (4.6.94)$$

The partitioning of channel charge will be considered in more detail later.

Equations (4.6.90) and (4.6.91) are used to relate voltage and current as follows. Let subscripts denote timepoints and superscripts denote Newton-Raphson iteration numbers. Thus we have

$V_0$  = Voltage at last timepoint (known)

$V_1^0$  = Voltage at previous iteration, this timepoint (known)

$V_1^1$  = Voltage at next iteration, this timepoint (unknown)

From (4.6.91)

$$\frac{h}{2} (i_1^1 + i_0) = Q_1^1 - Q_0 \quad (4.6.95)$$

where the integral of current has been approximated by a trapezoidal integration formula.

Expanding  $Q_1^1(V)$  about  $V_1^0$ :

$$Q_1^1(V) \approx Q_1^0 + \sum_x \left. \frac{\partial Q}{\partial V_x} \right|_{V_x = V_{x1}^0} (V_{x1}^1 - V_{x1}^0) \quad (4.6.96)$$

The subscript  $x$  takes the values "D", "G", "S", and "B", denoting one of the terminals. Thus

$$\frac{h}{2} (i_1^1 + i_0) = (Q_1^0 - Q_0) + \sum_x \left. \frac{\partial Q}{\partial V_x} \right|_{V_x = V_{x1}^0} (V_{x1}^1 - V_{x1}^0) \quad (4.6.97)$$

This equation for  $i_1^1$  can be substituted into the nodal admittance matrix to obtain a solution  $V_{x1}^1$ .

It is clear that charge is conserved in this model since it is computed directly from the voltages. Convergence problems are minimized by complete linearization of (4.6.91). The inclusion of an equation for the bulk insures that capacitance effects associated with the bulk will be modeled.

It is convenient to define the capacitances

$$C_{yx} \triangleq \frac{\partial Q_y}{\partial V_x} \quad (4.6.98)$$

Note that there are two capacitances between each pair of terminals. Thus, for example we have  $C_{GB} = \frac{\partial Q_G}{\partial V_B}$  and  $C_{BG} = \frac{\partial Q_B}{\partial V_G}$  between gate and bulk. These cannot be represented by a normal, two-terminal, reciprocal capacitor since in general  $C_{yx} \neq C_{xy}$ . As an example,  $C_{GB}$  and  $C_{BG}$  are plotted as functions of gate voltage in Figure 4.6.42. It is apparent that the present model differs substantially from that of Meyer.

The Meyer model defines  $C_{GD}$ ,  $C_{GB}$ , and  $C_{GS}$  in the same manner as the present model, but assumes that  $C_{DG} = C_{GD}$ ,  $C_{BG} = C_{GB}$ , and  $C_{SG} = C_{GS}$ . Also, a simpler form for bulk charge is assumed. Thus, as shown in Figure 4.6.42, the gate-bulk capacitance for the Meyer model is zero above  $V_T$  while it can be seen that the charge model gives capacitances which are significant.

Figure 4.6.43 compared  $C_{GD}$  and  $C_{DG}$  for the charge model and that of Meyer. Here we can readily see a physical basis for the difference between  $C_{GD}$  and  $C_{DG}$  in saturation.  $C_{GD}$  describes the effect of the drain on the gate (a feedback effect). In saturation, the drain voltage is isolated from the channel by the pinch-off condition and cannot affect the gate charge. Thus  $C_{GD}$  is zero. A change in gate voltage, however will produce a change in channel charge. Some of this change in charge will come about through a drain current. Thus  $C_{DG}$ , which describes the effect of

gate voltage on drain charge (a feed forward effect) will not be zero.

Figure 4.6.43 also shows  $C_{GD}$  for the Meyer model. Although similar to  $C_{GD}$  of the charge model, the threshold voltage at the drain is computed from the bulk charge at the source.

In order to find the drain and source currents from (4.6.90), we must have an algorithm for partitioning  $Q_C$  into  $Q_D$  and  $Q_S$ . This splitting may be done in several ways:

1) Divide the channel physically at some  $y_0 = aL$ , where  $L$  is the channel length. Then take

$$Q_S = \int_0^{y_0} \frac{dQ_C}{dy} dy \text{ and } Q_D = \int_{y_0}^L \frac{dQ_C}{dy} dy \quad (4.6.99)$$

Thus the charge to the source side of  $y_0$  goes into  $Q_S$  and the charge on the drain side goes into  $Q_D$ . Then  $y_0 = aL$  can be found by

- a) Take  $a = \text{constant}$
- b) Take  $y_0$  as the point where the surface potential is some constant fraction of the drain-to-source voltage.
- c) Calculate the transient current in the channel  $\delta I(y)$  due to a change in a terminal voltage  $V_x$ . Take  $y_0$  so that  $\delta I(y_0) = 0$ . This gives the exact terminal currents. The point  $y_0$  may vary with bias and may depend on which voltage  $V_x$  is changed.
- d) Take  $a = \frac{y_0}{L}$  as any empirical function of the terminal voltages.

2) Divide the channel charge mathematically, take  $Q_D = b Q_C$ ,  $Q_S = (1-b) Q_C$ , and  $0 \leq b \leq 1$ . In general,  $b$  may be a function of the terminal voltages.

In this case  $\frac{\partial Q_D}{\partial V_x} = b \frac{\partial Q_C}{\partial V_x} + Q_C \frac{\partial b}{\partial V_x}$ . Thus we must take derivatives of  $b$ .

The method chosen was method 2 with  $b = \frac{1}{2}$ .

Although model 1(c) gives the exact capacitances it is difficult analytically. This method was used in a numerical analysis to find the capacitances  $C_{DG}$  and  $C_{SG}$ . These are compared with the results using method 2,  $b = \frac{1}{2}$ , and with the Meyer model in Figure 4.6.44. Thus the charge model assigns half the channel charge in saturation to the source and half to the drain while the Meyer model assigns all the charge to the source. The exact result assigns  $\frac{5}{8}$  of the channel charge to the source and  $\frac{3}{8}$  to the drain.

#### Examples

Several examples which illustrate the importance of the charge-oriented model applied in circuit simulation are now considered. Figure 4.6.45a shows a non-linear capacitance driven by the voltage waveform of Figure 4.6.45b. Figure 4.6.45c shows the capacitance as a function of time. The Meyer model approximates this capacitance by the stair-step shown in the dotted line. The size of the step depends on the timestep  $h$  used in the simulation. The current entering the capacitor is shown in Figure 4.6.45d. Note that in the simulated (dotted) waveform more current flows out of the capacitor than flows in. This represents a charge loss, as shown in Figure 4.6.45e. In many practical circuits this charge loss would result in a voltage error.

Figure 4.6.46a shows a more realistic version of the previous example. In this bootstrap circuit the variable capacitor has been replaced by the gate source and gate-drain capacitance of a MOS transistor and a

load capacitance was added. The simulated output using the Meyer model is shown in Figure 4.6.46c. Note that the DC levels are in error by several volts. Also, the result depends on the timestep used. Even with 64 timesteps in the risetime of the input, the output is in error by .5 volt after two cycles. As seen in Figure 4.6.46d, the charge oriented model gives accurate DC levels even for a timestep equal to the risetime of the input. Thus we can greatly reduce simulation time while maintaining increased accuracy.

Figure 4.6.47 is the circuit of a D-type latch fabricated with CMOS-on-sapphire technology. When the clock goes high, M2 turns off breaking the feedback path, and the input data is connected to the inverter pair through M1, in an n-channel, floating-bulk device. When the clock again goes low M1 turns off and M2 turns on, latching the data.

Figure 4.6.48c shows the output of a simulation for the inputs of Figures 4.6.48a and 4.6.48b. According the old model the output never goes high. The results predicted by the new model are correct.

The discrepancy is due to the difference in capacitance models during the rising clock. Figure 4.6.49a shows the Meyer model for M1 at this time. The bulk is coupled to node "S" through a capacitive divider chain consisting of the junction capacitances  $C_{JSB}$  and  $C_{JDB}$ . Figure 4.6.48d shows that while the bulk of M1 follows node "S" to some extent, a back-bias of 5V still develops to turn off the device. An approximate equivalent circuit using the new model, Figure 4.6.49b, has two more capacitances in the divider network. The bulk-gate capacitance  $C_{BG}$  couples the rising clock signal to the bulk, while the bulk-source capacitance  $C_{BS}$  couples

the bulk to node "S". The result, seen in Figure 4.6.48e, is that only 1V of back-bias is produced and node "S" rises to a voltage capable of setting the latch.

#### CONCLUSIONS

A model for MOS capacitance which is based on charge has been presented. The model is especially suited to circuits where charge-conservation is important, such as in dynamic and SOS circuits. Examples have been given for which the charge-oriented model gives correct results while the conventional model is inadequate.

#### ACKNOWLEDGEMENT

Initial support through Hewlett-Packard Corporate Engineering is gratefully acknowledged. Continuing research support from Advanced Research Projects Agency DAA-B07-C-1344 is also acknowledged. One author acknowledges his NSF Fellowship.

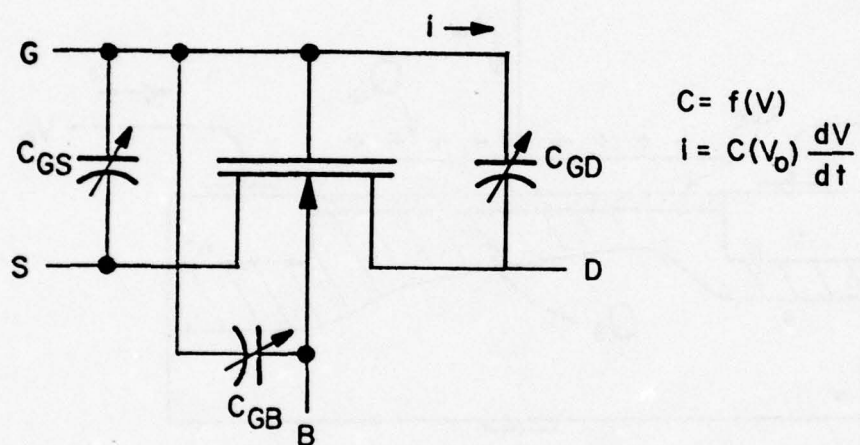


Figure 4.6.40 - Meyer Model

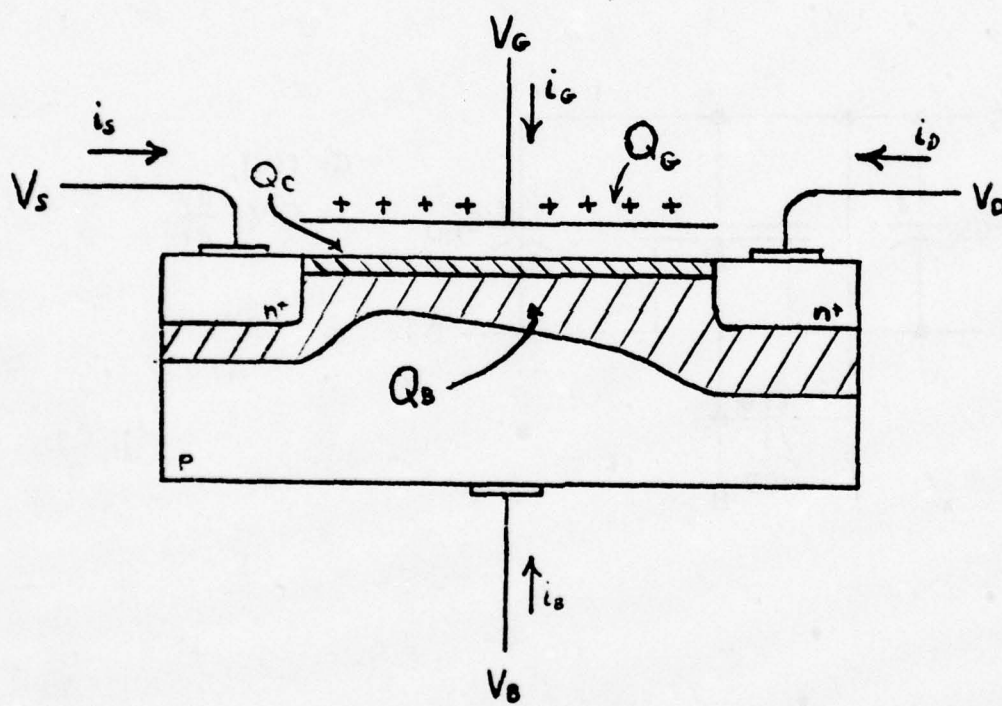


Figure 4.6.41 - Charge-oriented Model

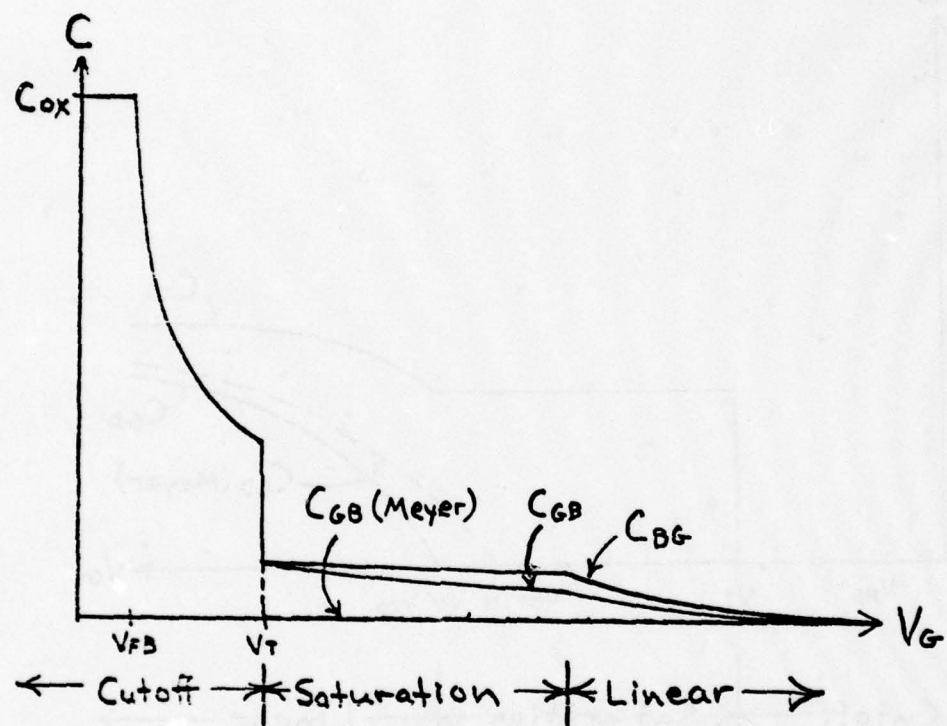


Figure 4.6.42 - Gate-bulk capacitances

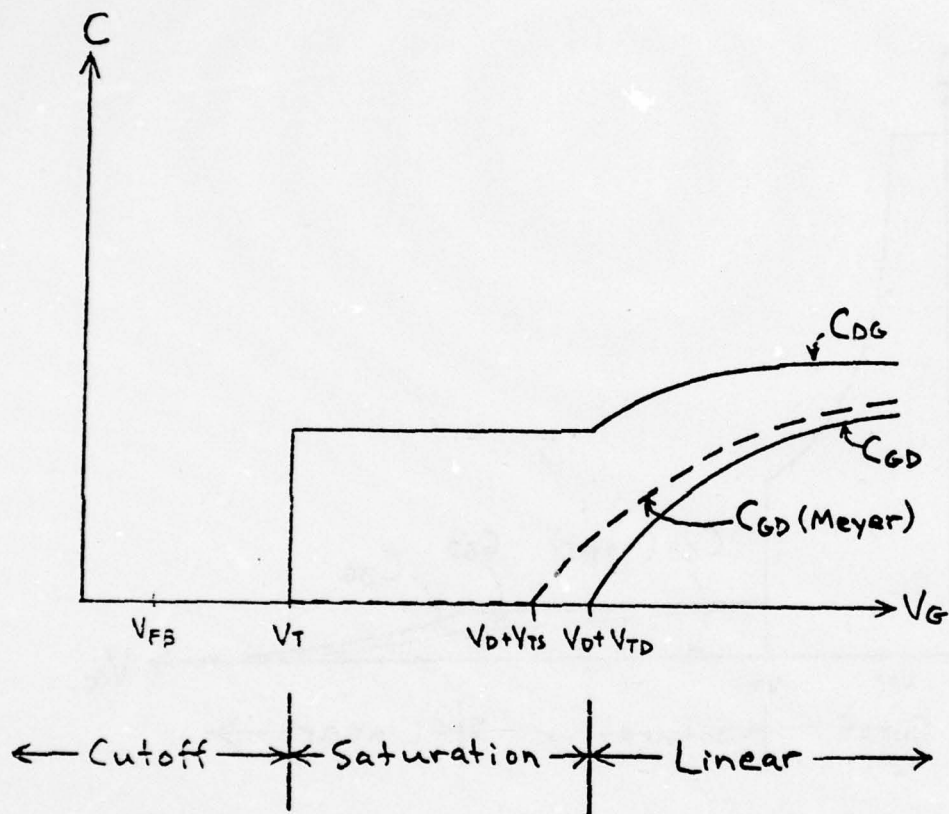
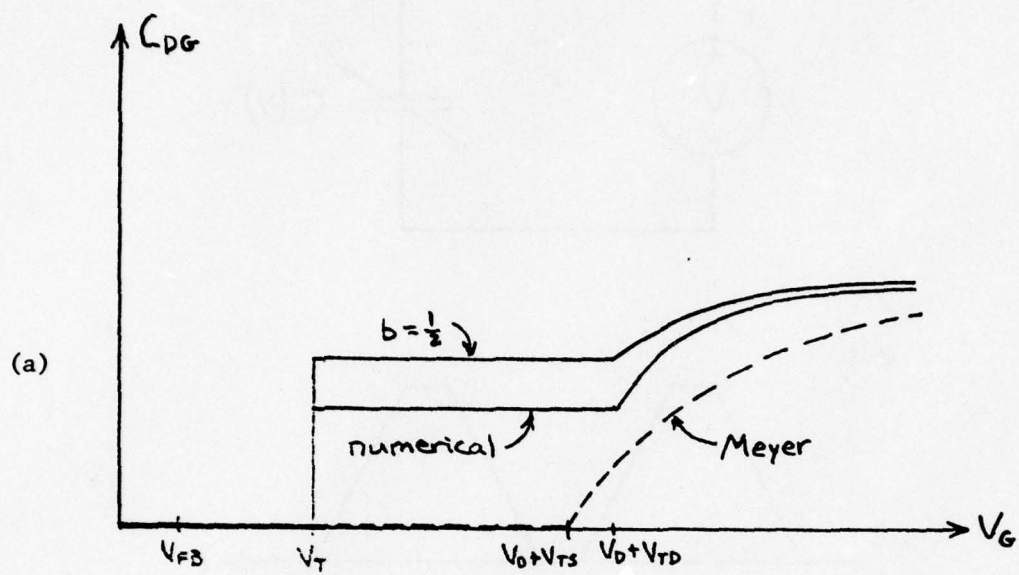


Figure 4.6.43 - Gate-drain capacitances



← Cutoff → Saturation → Linear →

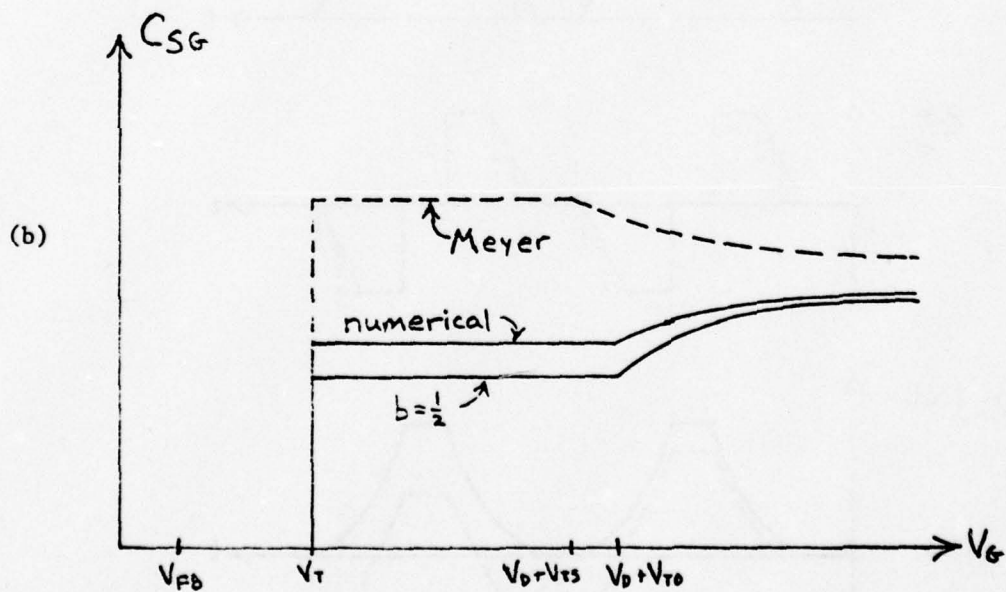


Figure 4.6.44a - Drain-gate and

4.6.44b - Source-gate capacitances

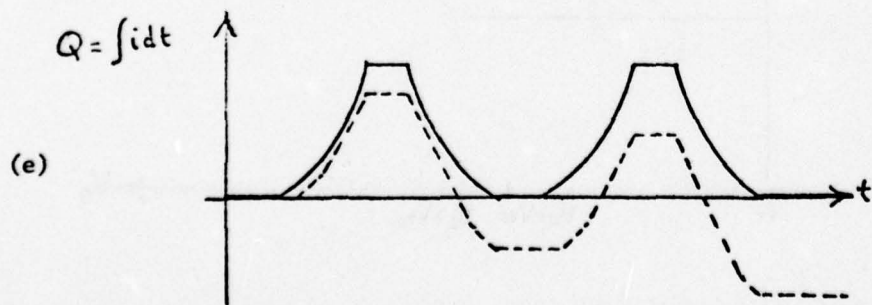
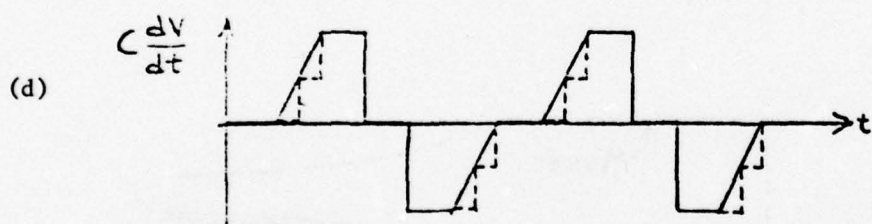
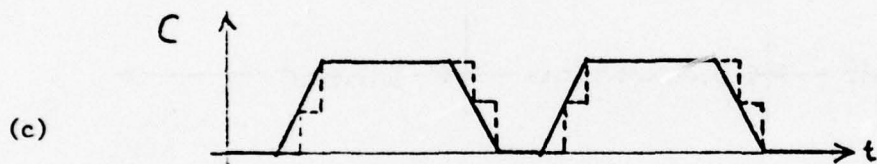
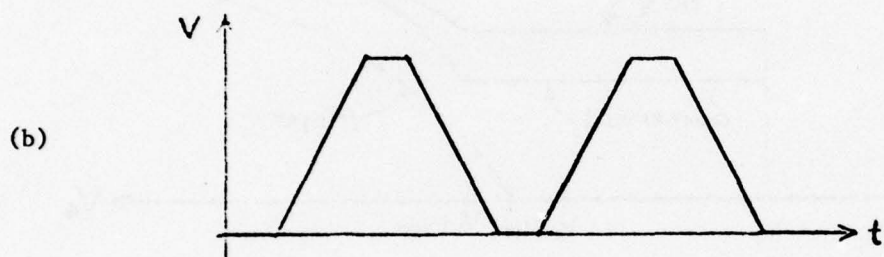
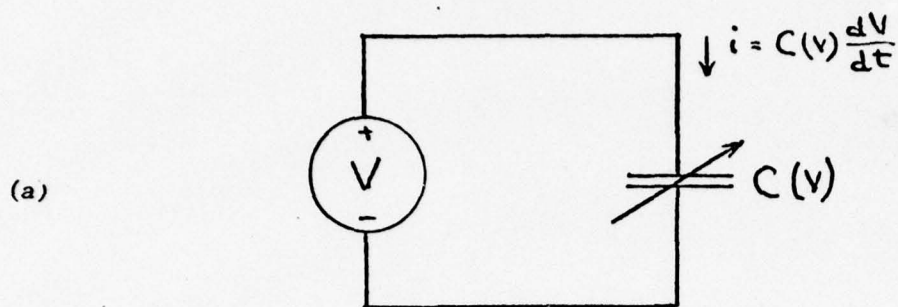


Figure 4.6.45 - Circuit showing non-conservation of charge

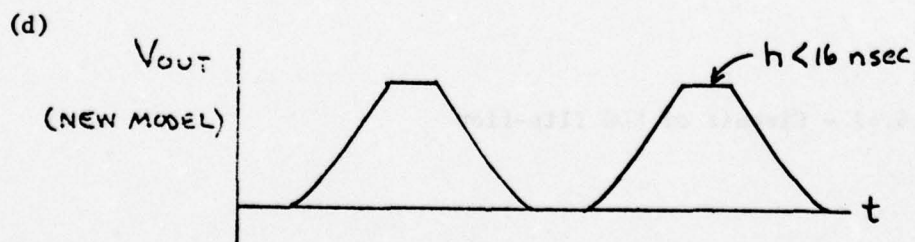
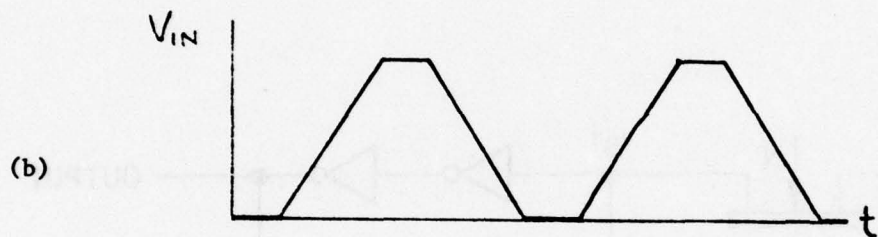
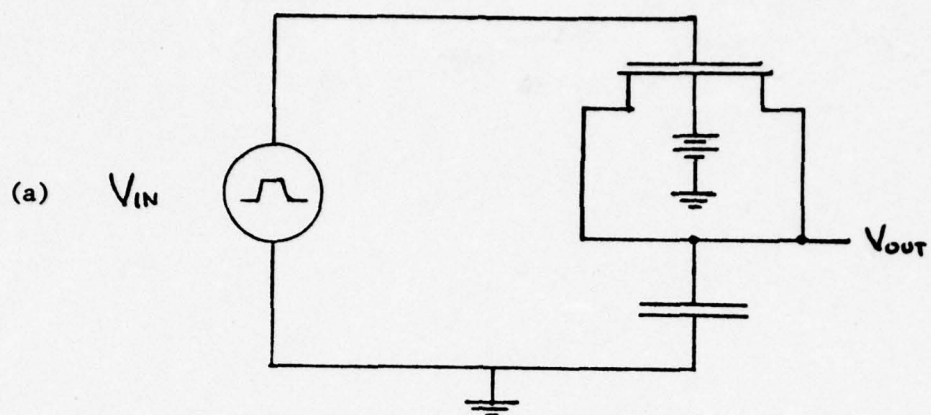


Figure 4.6.46 - Bootstrap circuit

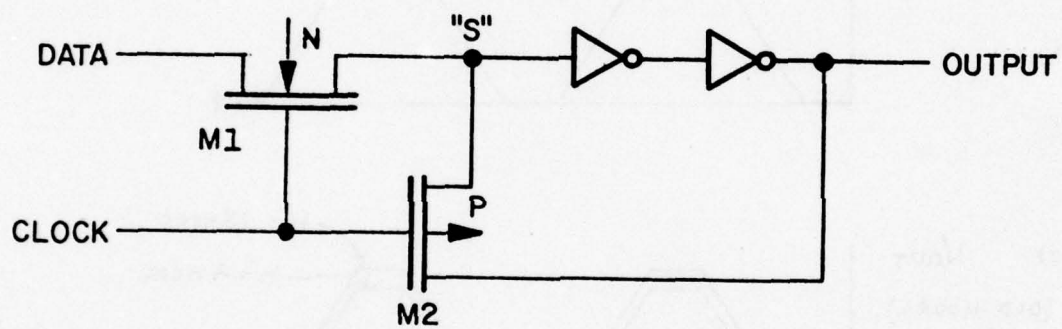


Figure 4.6.47 - Circuit of SOS flip-flop

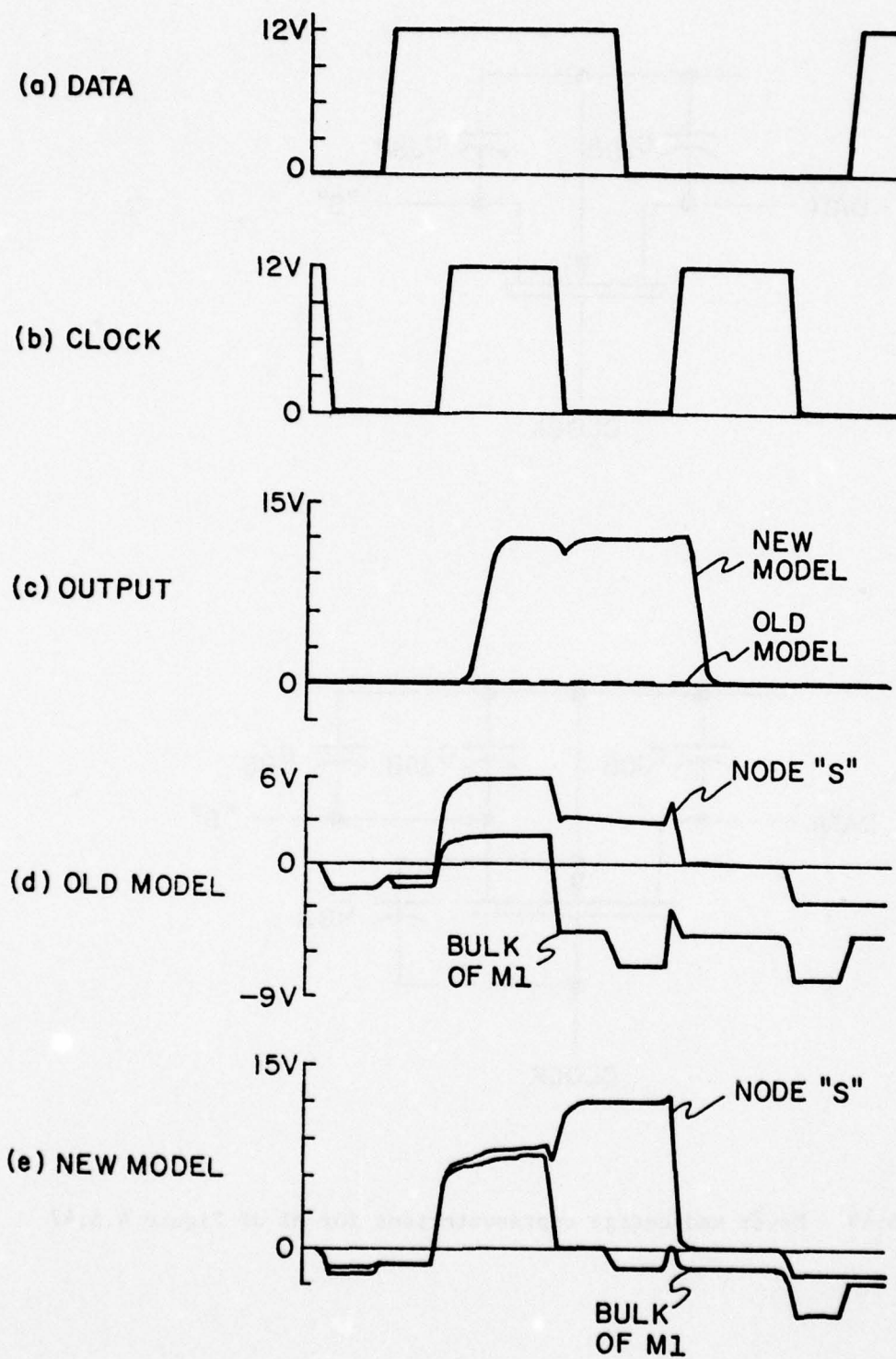


Figure 4.6.48 - Waveforms for circuit of Figure 4.6.47

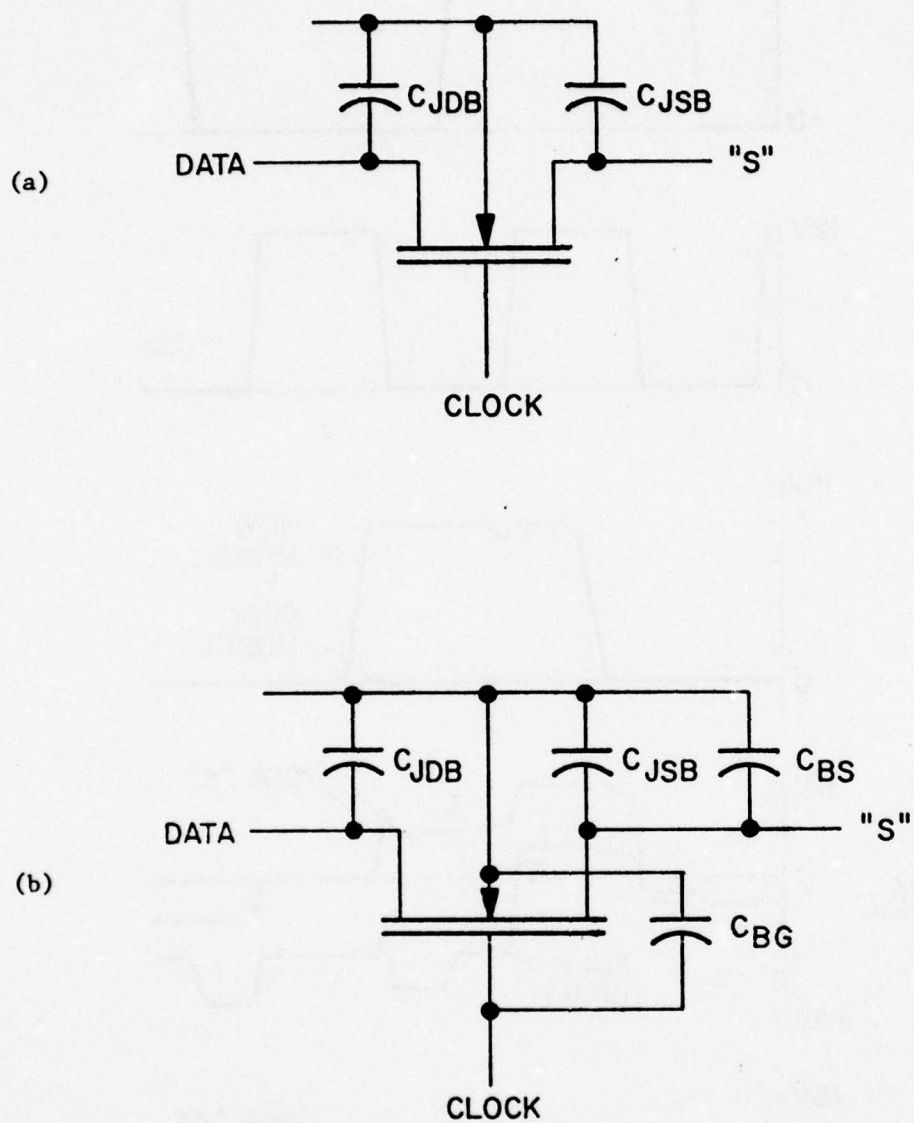


Figure 4.6.49 - Meyer and charge representations for MI of Figure 4.6.47

#### 4.7 Statistical Circuit Analysis -- An Example (D. A. Divekar, W. J. McCalla)

##### Introduction

The procedure of statistical circuit analysis is illustrated with the help of a simple circuit example. The circuit consists of two transistors connected in the form of an emitter coupled pair which can be considered as a portion of an emitter coupled logic gate. The circuit is intended for micro-power applications [4.46].

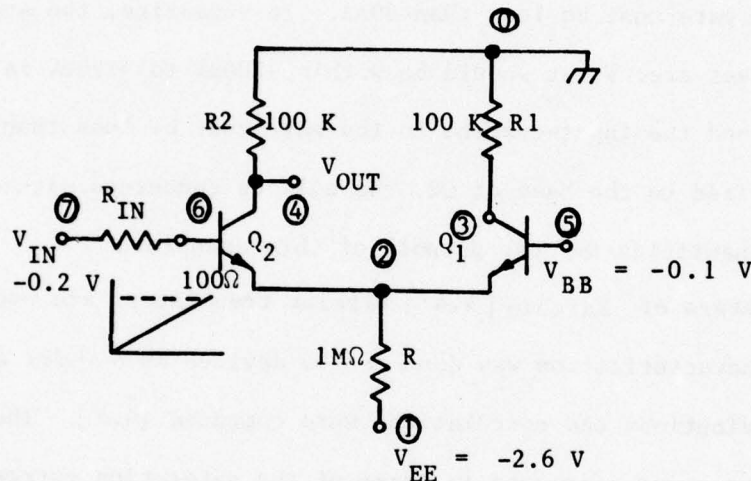


Figure 4.7.50 - Basic circuit schematic for a micropower ECL gate.

Figure 4.7.50 shows the circuit along with the component and power supply values and the node numbers used in the simulation program.  $R_{IN}$  can be considered as a part of the power supply impedance and is included only to monitor the input current of the gate. The voltage  $V_{BB}$  is fixed at  $-0.1V$  and the input voltage is varied from 0 to  $-0.2V$ . Current thru  $R$  is about  $2 \mu A$  and it is switched from  $Q_2$  to  $Q_1$  as the voltage applied to the input changes from 0 to  $-0.2V$ . The circuit is intended

to operate between the logic levels of 0V and -0.2V. The circuit has to have a fan-out of at least 2. The logic levels should have a tolerance of  $\pm 5\%$ . Since the output voltage is likely to have more variation when Q2 is on, we will consider only that case. When Q2 is on, a current of 2  $\mu\text{A}$  flows thru R2 and the output voltage is -0.2V. With +5% tolerance, the maximum limit is -190mV. Also, if we want the zero level output voltage to be less than -10mV, then this allows a current of 100nA to flow thru R2 when Q2 is off. Therefore, for a fan-out of 2, the input current of the gate must be less than 50nA. To summarize, the specifications of interest are: V out should be within -200mV to -190mV range when Q2 is on and the input-current to the gate must be less than 50nA when 0V is applied to the base of Q2. We will be concerned with only these two dc quantities for the purpose of this example.

The parameters of Kitchip [4.47] bipolar transistors are used in this study. Characterization was done for 35 devices on a wafer and the parameter distributions and correlations were computed [4.2]. Then, all the parameters were expressed in terms of the saturation current  $I_s$  as the independent parameter. Only the dc parameters  $\beta_{Fm}$ ,  $I_s$ ,  $C_2$  and  $n_e$  play an important role for the above circuit since these parameters govern the dc low current behavior of the circuit.

#### Nominal Analysis

The first step in the analysis is to use the mean values of all the parameters from their distributions and model the circuit to check if it functions as desired. The input deck for the nominal analysis is shown in Figure 4.7.51 and the corresponding output voltage and the voltage at the collector of Q1 is shown in Figure 4.7.52 as a function of input voltage.

The input voltage is swept as a function of time and hence the values of time in mili-seconds correspond to the magnitude of  $V_{in}$  in mili-volts. It is to be noted that the voltage is varied from 0 to -200mV. These transfer curves show that the output voltage is within desired limits when  $V_{in}$  is 0 and -200mV and the cross-over takes place at  $V_{in} = V_{BB} = -0.1V$  as expected. The input current to the gate is 40nA.

#### Worst Case Analysis

The next step is to analyze the circuit under worst case conditions of the device parameters to check if the performance still remains within the desired limits. For the circuit under consideration, when  $V_{in} = 0$  and Q2 is on, the output voltage will have limiting values under following conditions.

	$I_s$	$\beta$	$n_e$	$C_2$	$V_{out}$	$I_{in}$
Case 1	max	min	min	max	-50mV	1500nA
Case 2	min	max	max	min	-197mV	10nA

The circuit behavior is well within the desired limits for case 2 but its performance for case 1 is not at all satisfactory.

One drawback of performing this worst case analysis is that it just tells within what limits the performance may vary but it does not give any idea for how many devices on a wafer will this extreme limits be observed. Therefore this gives a pessimistic picture of the circuit since theoretically the probability of occurrence of these worst case conditions may be negligible.

#### Statistical Analysis Without Correlations

To get an idea of the distributions of output voltage and input current to the gate, it is necessary to perform a statistical analysis of the circuit. In this analysis, a number of cases are analyzed by choosing

samples from the probability distribution functions of various device parameters. The distributions obtained from the measurements of the kitchip devices were used to analyze 100 cases. Corresponding input deck is shown in Figure 4.7.53. Figure 4.7.54 shows the histograms of  $I_s$ , as an example, generated for this analysis which is compared with the measured histogram of  $I_s$ . The cumulative probabilities are to be compared in the two cases since the actual number of devices, listed in the second column from right will be different depending upon the number of cases analyzed. The agreement between the two distribution confirms the fact that the distributions generated by the program are indeed similar to that the distributions generated by the program are indeed similar to the measured ones. Figure 4.7.55 shows the envelope plot of the output voltage of the output voltage for the desired number of cases are plotted at each of the values of the input voltage. The spread in output voltage is more when Q2 is on, i.e., when  $V_{in} = 0$  than when Q2 is off ( $V_{in} = -200\text{mV}$ ) as expected. This verifies the assumption made in the previous section of circuit description. Since we are interested in the output voltage when  $V_{in} = 0$ , we can observe the histogram of the output voltage at that  $V_{in}$ , which is shown in Figure 4.7.56. The spread in the voltage output is much less compared to the extreme values suggested by the worst case analysis. This is because of the fact that the particular combinations used for worst case analysis do not occur in this analysis. From the histogram we can also see that for 75% of the circuits, the output voltage is less than  $-190\text{V}$  as desired. Thus we may conclude that about 75% of the circuits will meet the output voltage specifications. From the histogram of input current, shown in Figure 4.7.57, it can be seen that 62% of the circuits have

input current lower than 50nA as desired. (It is to be noted that the program computes all currents in nA. Therefore when the program prints a prefix of mico (micro) for the current, the actual current is a milli-micro amps or nA.) Similar to the output voltage, the spread in input current is less than that for the worst-case analysis.

During this analysis mode, all the device parameter values were chosen independently from their respective distributions. But for actual devices fabricated on a wafer using a particular fabrication process, the device parameters will not be completely independent. Therefore it is necessary to take into account this interdependency of the parameters.

#### Statistical Analysis with Parameter Extractions

One way of taking into account the parameter correlations is to select one parameter as independent parameter and express the remaining parameters in terms of the independent parameter. The independent parameter is selected randomly from its distributions and the other parameter values are then computed from the corresponding expressions.

A study of the measured device parameters showed that the saturation current  $I_S$  is a good choice for the independent parameter. First order expressions for the remaining parameters suggest that it may be adequate to express these parameters in terms of  $I_S$  with the help of simple linear equations. This is done as the next step of this statistical simulation. Figures 4.7.58 to 4.7.61 show the input, the envelope plot and the histograms of output voltage and input current respectively. The spreads in these two performance parameters of interest are even less than those without correlations. The histograms show that all the circuits satisfy the output voltage requirements are satisfied by all the circuits and 98% of the circuits satisfy the input current requirement.

### Statistical Analysis with Measured Parameters

To verify the simulation results, measured parameters of the experimental devices were used as the model parameters and the circuit was analyzed for those 35 cases. The resulting envelope plot and the histograms are shown in Figures 4.7.62 to 4.7.64. Here all the circuits satisfy both the output voltage as well as the input current requirements.

### Discussion

The worst case analysis of the circuit gives large variations in the circuit performance because even if it is assumed that the device parameters are independent, the probability of occurrence of the particular combinations used for the worst-case analysis is negligibly small. Moreover, in reality, the parameters are not independent and hence the particular combinations giving rise to worst values will never exist. For instance, the measured parameters  $\beta$  and  $I_S$  show positive correlation. Therefore it is not possible to obtain maximum value of  $I_S$  with a minimum value of  $\beta$ . Similarly, the correlation between  $n_e$  and  $C_2$  is positive making the combination of minimum  $n_e$  and maximum  $C_2$  unrealistic. The simulations making use of the parameter distributions give better results but still in this case the physical inter-relationships between various parameters are not taken into account. Considerations of these parameter correlations gives more realistic results which agree with the circuit performance obtained by using the measured device parameters. This indicates the usefulness of statistical simulations and the improvements achieved by accounting for the physical correlations between the various device parameters.

- M S I N C - VER. 85.01

# MICROPOWER ECL GATE (NOMINAL ANALYSIS)

JOB : DILIP

DATE : NOV/15/77

TIME IS 0:56:13

XX

```

*
VEE 1 0 -2.6
VBB 5 0 -.1
VIN 7 0 0 0 -.2 .2
*
R1 3 0 100
R2 4 0 100
*
R 2 1 1000
*
RIN 7 6 .1
*
Q1 3 5 2 QMOD
Q2 4 6 2 QMOD
*
MODEL QMOD NPN IS=5.667E-16 BFM=174.71 NE=1.54 C2=37
*
TIME .004 .2
*
PLOT 4 3
*
END

```

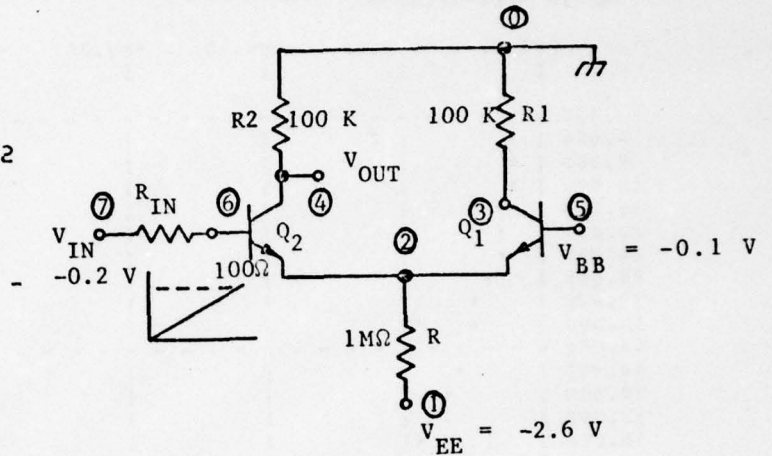


Figure 4.7.51 - Circuit simulator input for the nominal case ECL circuit shown.

- M S I N C - VER. B5.01

MICROPOWER ECL GATE (NOMINAL ANALYSIS)

+ : 4 0  
\* : 3 0

TIME IN MILLI-SECONDS

	-200.00	-160.00	-120.00	-80.00	-40.00	.00	MILI	
	I	I	I	I	I	I		
.000	-	-	-	-	-	-	-	-
4.000	I +	I	I	I	I	* I	-194.516	-4.064
8.000	I +	I	I	I	I	* I	-193.463	-4.716
12.000	I +	I	I	I	I	* I	-192.249	-5.553
16.000	I +	I	I	I	I	* I	-191.034	-6.349
20.000	I +	I	I	I	I	* I	-189.379	-7.607
24.000	I +	I	I	I	I	* I	-187.723	-8.865
28.000	I +	I	I	I	I	* I	-186.068	-10.123
32.000	I +	I	I	I	I	* I	-184.412	-11.381
36.000	I +	I	I	I	I	* I	-181.675	-13.529
40.000	-	-	-	-	-	-	-179.338	-15.676
44.000	I	I	I	I	I	* I	-176.800	-17.824
48.000	I	I	I	I	I	* I	-174.263	-19.972
52.000	I	I	I	I	I	* I	-170.430	-23.435
56.000	I	I	I	I	I	* I	-166.597	-26.898
60.000	I	I	I	I	I	* I	-162.763	-30.361
64.000	I	I	I	I	I	* I	-158.930	-33.824
68.000	I	I	I	I	I	* I	-153.498	-38.924
72.000	I	I	I	I	I	* I	-148.066	-44.024
76.000	I	I	I	I	I	* I	-142.634	-49.124
80.000	I	I	I	I	I	* I	-137.202	-54.224
84.000	-	-	-	-	-	-	-130.346	-60.810
88.000	I	I	I	I	I	* I	-123.490	-67.395
92.000	I	I	I	I	I	* I	-116.633	-73.980
96.000	I	I	I	I	I	* I	-109.777	-80.566
100.000	I	I	I	I	I	* I	-102.390	-87.759
104.000	I	I	I	I	I	* I	-95.003	-94.953
108.000	I	I	I	I	I	* I	-87.616	-102.146
112.000	I	I	I	I	I	* I	-80.229	-109.340
116.000	I	I	I	I	I	* I	-73.561	-115.898
120.000	-	-	-	-	-	-	-66.894	-122.442
124.000	I	I	I	I	I	* I	-60.226	-128.993
128.000	I	I	I	I	I	* I	-53.559	-135.545
132.000	I	I	I	I	I	* I	-48.454	-140.594
136.000	I	I	I	I	I	* I	-43.349	-145.643
140.000	I	I	I	I	I	* I	-38.244	-150.692
144.000	I	I	I	I	I	* I	-33.139	-155.741
148.000	I	I	I	I	I	* I	-29.707	-159.155
152.000	I	I	I	I	I	* I	-26.275	-162.570
156.000	I	I	I	I	I	* I	-22.843	-165.984
160.000	-	-	-	-	-	-	-19.410	-169.398
164.000	I	I	I	I	I	* I	-17.301	-171.508
168.000	I	I	I	I	I	* I	-15.192	-173.619
172.000	I	I	I	I	I	* I	-13.083	-175.729
176.000	I	I	I	I	I	* I	-10.973	-177.840
180.000	I	I	I	I	I	* I	-9.748	-179.073
184.000	I	I	I	I	I	* I	-8.523	-180.307
188.000	I	I	I	I	I	* I	-7.298	-181.541
192.000	I	I	I	I	I	* I	-6.073	-182.775
196.000	I	I	I	I	I	* I	-5.337	-183.521
200.000	-	-	-	-	-	-	-4.601	-184.268
	-	-	-	-	-	-	-3.864	-185.014

ELAPSED TIME IS 35 SECONDS

Figure 4.7.52 - Simulated output voltage waveforms at nodes 4 and 3 with the "time" axis representing input voltage (in milli-volts) at node 7.

- M S I N C - VER. 85.01

MICROPOWER ECL GATE (STATISTICAL ANALYSIS WITHOUT CORRELATIONS)

JOB : DILIP DATE : NOV/15/77 TIME IS 1: 0: 8

XX

```
*
VEE 1 0 -2.6
VBB 5 0 -.1
VIN 7 0 0 0 -.2 .2
*
R1 3 0 100
R2 4 0 100
*
R 2 1 1000
*
RJN 7 6 .1
*
Q1 3 5 2 QMOD
Q2 4 6 2 QMOD
*
MODEL QMOD NPN BFM=174.71 NE=1.54 C2=37
+ IS=5.667E-16 EQUATION EQN1 (PIS)
PIS DISTRIBUTION TABLE TPIS
DISTRIBUTION QMOD:BFM TABLE TBFM
DISTRIBUTION QMOD:NE TABLE TNE
DISTRIBUTION QMOD:C2 TABLE TC2
*
EQUATION EQN1 (X) = X * 1E-16
*
TABLE TPIS CUMULATIVE 4.00,0 4.60,5 5.20,16 5.80,23
+ 6.40,26 7.00,30 7.60,30 8.20,33
+ 8.80,33 9.40,35
TABLE TNE CUMULATIVE 1.28,0 1.34,3 1.40,9 1.46,9
+ 1.52,13 1.58,22 1.64,25 1.70,32
+ 1.76,32 1.82,34 1.88,35
TABLE TC2 CUMULATIVE 0.00,0 25.5,22 51.0,27 76.5,30
+ 102,32 127.5,33 153,34 178.5,34
+ 204,34 229.5,34 255,35
TABLE TBFM CUMULATIVE 150,0 156,2 162,6 168,13
+ 174,20 180,25 186,29 192,30
+ 198,31 204,33 210,35
*
CASES 100
*
TIME .004 .2
*
SAMPLE 0
*
PLOT 4 3
*
STATISTICAL PLOT 4 3 J:RJN J:R
HISTOGRAM 4 (-201.25E-3,-101.25E-3,40) 3 (-3.975E-3,-1.975E-3,40)
HISTOGRAM J:RJN (-10.0E-6,790.0E-6,40)
HISTOGRAM J:R (1.8975E-3,2.0975E-3,40)
HISTOGRAM PIS (4,10,10) QMOD:BFM (150,210,10)
HISTOGRAM QMOD:NE (1.28,1.88,10) QMOD:C2 (0,255,10)
*
END
```

Figure 4.7.53 - Circuit simulator input for a worst case analysis without correlations for device model parameters. Values are picked randomly from the four tables and 100 transfer curves which are generated.

MICROPOWER EUL GATE (STATISTICAL ANALYSIS WITHOUT CORRELATIONS)

PIS	I	I	I	I	I	I NO.	CUM.PROB.
4.300	XXXXXXXXXX	XXXXXXXXXXXX	XXXXXXXXXXXX			22	.2200
4.900	XXXXXXXXXX	XXXXXXXXXXXX	XXXXXXXXXXXX			27	.4900
5.500	XXXXXXXXXX	XXXXXXXXXXXX	XXXXXXXXXXXX			20	.6900
6.100	XXXXXXX					7	.7600
6.700	XXXXXXX					7	.8300
7.300						0	.8300
7.900	XXXXXXX					8	.9100
8.500						0	.9100
9.100	XXXXXXXXXX					9	1.0000
9.700						0	1.0000

SIMULATED

PIS

MIN.	MAX.	MEAN	STD.
4.0051	9.2613	5.7259	1.4374

PIS

PIS	I	I	I	I	I	I NO.	CUM.PROB.
4.300	XXXXXXXXXXXXXXXXXXXXXXXXXXXXXXXXXXXX					6	.1714
4.900	XXXXXXXXXX	XXXXXXXXXXXXXXXXXXXXXXXXXXXXXXXXXXXX				10	.4571
5.500	XXXXXXXXXXXXXXXXXXXXXXXXXXXXXXXXXXXX					7	.6571
6.100	XXXXXXXXXXXXXXXXXX					3	.7429
6.700	XXXXXXXXXXXXXXXXXXXX					4	.8571
7.300						0	.8571
7.900	XXXXXXXXXXXXXXXXXX					3	.9429
8.500						0	.9429
9.100	XXXXXXXXXXXX					2	1.0000
9.700						0	1.0000

MEASURED

PIS

MIN.	MAX.	MEAN	STD.
4.0192	9.3615	5.6662	1.3446

Figure 4.7.54 - Simulated histograms showing the simulated and measured distributions of parameter I (ie PIS)

MICROPOWER FUL GATE (STATISTICAL ANALYSIS WITHOUT CORRELATIONS)

\* : 4 : 0 = MIN  
 \* : 4 : 0 = MAX  
 # : 4 : 0 = MEAN

TIME IS MILLI- SECONDS

* :	-200.00	-160.00	-120.00	-80.00	-40.00	.00	MILI
* :	-200.00	-160.00	-120.00	-80.00	-40.00	.00	MILI
# :	-200.00	-160.00	-120.00	-80.00	-40.00	.00	MILI
	1	1	1	1	1	1	
0.000	+	-	-	-	-	-	-199.222 -140.029
4.000	+	#	I	*	I	I	-198.167 -139.108
8.000	1	#	I	*	I	I	-196.949 -138.054
12.000	1	#	I	*	I	I	-195.730 -137.000
16.000	1	#	I	*	I	I	-194.064 -135.598
20.000	1	+	I	*	I	I	-192.397 -134.195
24.000	1	+	I	*	I	I	-190.730 -132.793
28.000	1	+	I	*	I	I	-189.064 -131.391
32.000	1	+	I	*	I	I	-186.496 -129.329
36.000	1	+	I	*	I	I	-183.928 -127.267
40.000	-	+	-	-	-	-	-181.360 -125.205
44.000	1	+	I	*	I	I	-178.792 -123.144
48.000	1	+	I	*	I	I	-174.693 -120.175
52.000	1	+	I	*	I	I	-170.993 -117.207
56.000	1	+	I	*	I	I	-167.094 -114.238
60.000	1	+	I	*	I	I	-163.194 -111.270
64.000	1	+	I	*	I	I	-157.643 -107.258
68.000	1	+	I	*	I	I	-152.092 -103.247
72.000	1	+	I	*	I	I	-146.541 -99.236
76.000	1	+	I	*	I	I	-140.990 -95.225
80.000	-	-	-	-	-	-	-133.958 -90.360
84.000	1	+	I	*	I	I	-126.926 -85.496
88.000	1	+	I	*	I	I	-119.894 -80.632
92.000	1	+	I	*	I	I	-112.862 -75.767
96.000	1	+	I	*	I	I	-105.830 -70.903
100.000	1	+	I	*	I	I	-97.675 -65.561
104.000	1	+	I	*	I	I	-90.062 -60.459
108.000	1	+	I	*	I	I	-82.488 -55.356
112.000	1	+	I	*	I	I	-75.628 -50.401
116.000	1	+	I	*	I	I	-68.767 -45.247
120.000	-	-	-	-	-	-	-61.907 -41.092
124.000	1	+	I	*	I	I	-55.046 -37.138
128.000	1	+	I	*	I	I	-49.794 -33.645
132.000	1	+	I	*	I	I	-44.542 -30.152
136.000	1	+	I	*	I	I	-39.290 -26.659
140.000	1	+	I	*	I	I	-34.037 -23.167
144.000	1	+	I	*	I	I	-30.509 -20.797
148.000	1	+	I	*	I	I	-26.980 -18.428
152.000	1	+	I	*	I	I	-23.451 -16.058
156.000	1	+	I	*	I	I	-19.922 -13.689
160.000	-	-	-	-	-	-	-17.755 -12.216
164.000	1	+	I	*	I	I	-15.589 -10.744
168.000	1	+	I	*	I	I	-13.422 -9.271
172.000	1	+	I	*	I	I	-11.255 -7.799
176.000	1	+	I	*	I	I	-9.948 -6.935
180.000	1	+	I	*	I	I	-8.741 -6.071
184.000	1	+	I	*	I	I	-7.483 -5.207
188.000	1	+	I	*	I	I	-6.226 -4.342
192.000	1	+	I	*	I	I	-5.471 -3.519
196.000	1	+	I	*	I	I	-4.715 -3.296
200.000	-	-	-	-	-	-	-3.960 -2.773

Figure 4.7.55 - The simulated output voltage transfer plot at node 4 for the mean, minimum and maximum simulations. The maximum plot represents a case where the output voltage (-140 mv) would cause a circuit malfunction.

- M S I M C - VER. 00101 HISTOGRAM - SAMPLE TIME .000 MILLI SECONDS  
MICROPOWER EOL GATE (STATISTICAL ANALYSIS WITHOUT CORRELATIONS)

4 : 0 MILLI		I I I I I					I NO.	CUM. PROB.
-200.00	XXXX						4	.0400
-197.50	XX						42	.4600
-195.00	XXXXXXXXXXXXXXXXXXXX						16	.6200
-192.50	XXXXXXX						7	.6900
-190.00	XXXXXX						6	.7500
-187.50	XXXXXX						6	.8100
-185.00	XXXXXX						6	.8700
-182.50	XX						2	.8900
-180.00							0	.8900
-177.50	XXX						3	.9200
-175.00							0	.9200
-172.50	XXX						3	.9500
-170.00							0	.9500
-167.50							0	.9500
-165.00							0	.9500
-162.50	XX						2	.9700
-160.00							0	.9700
-157.50							0	.9700
-155.00							0	.9700
-152.50							0	.9700
-150.00							0	.9700
-147.50	X						1	.9800
-145.00							0	.9800
-142.50	X						1	.9900
-140.00	X						1	1.0000
-137.50							0	1.0000
-135.00							0	1.0000
-132.50							0	1.0000
-130.00							0	1.0000
-127.50							0	1.0000
-125.00							0	1.0000
-122.50							0	1.0000
-120.00							0	1.0000
-117.50							0	1.0000
-115.00							0	1.0000
-112.50							0	1.0000
-110.00							0	1.0000
-107.50							0	1.0000
-105.00							0	1.0000
-102.50							0	1.0000

4 : 0 MILLI			
MIN.	MAX.	MEAN	STD.
-199.2220	-140.0293	-190.9948	11.3691

Figure 4.7.56 - Simulated histograms of output-low voltages for the 100 examples in Figure 4.7.53. Circuits with output-low between -190.mv and -140.mv can be considered as malfunctioning.

- M S I N C - VER. 0401 HISTOGRAM - SAMPLE TIME .000 MILLI SECONDS

MICROPROCESSOR ECU DATA (STATISTICAL ANALYSIS WITHOUT CORRELATIONS)

J-RIN	1	1	1	1	1	I NO.	CUM.PROB.
-0.000	x					1	.0100
20.000	XX					51	.5200
40.000	XXXXXXXXXX					10	.6200
60.000	XXXXXXX					7	.6900
80.000	XXXXXX					5	.7400
100.000	XXX					3	.7700
120.000	XXXXX					5	.8200
140.000	XXXXX					5	.8700
160.000	XX					2	.8900
180.000						0	.8900
200.000	XX					2	.9100
220.000	X					1	.9200
240.000						0	.9200
260.000	XXX					3	.9500
280.000						0	.9500
300.000						0	.9500
320.000						0	.9500
340.000	X					1	.9600
360.000	X					1	.9700
380.000						0	.9700
400.000						0	.9700
420.000						0	.9700
440.000						0	.9700
460.000						0	.9700
480.000						0	.9700
500.000	X					1	.9800
520.000						0	.9800
540.000						0	.9800
560.000	X					1	.9900
580.000	X					1	1.0000
600.000						0	1.0000
620.000						0	1.0000
640.000						0	1.0000
660.000						0	1.0000
680.000						0	1.0000
700.000						0	1.0000
720.000						0	1.0000
740.000						0	1.0000
760.000						0	1.0000
780.000						0	1.0000

J-RIN	MIN.	MAX.	MEAN	STD.
	9.5816	577.0969	73.2932	111.5033

Figure 4.7.57 - Simulated histogram of input current for the 100 examples from Figure 4.7.53. Currents greater than 50 nA (J-RIN axis) indicate circuit malfunctioning.

- M S I N C - VER. 85.01

MICROPOWER ECL GATE (STATISTICAL ANALYSIS WITH PARAMETER EQUATIONS)

JOB : DILJP DATE : NOV/15/77 TIME IS : 1:17:47

XX

\*  
VEE 1 0 -2.0  
VRN 5 0 -1.1  
VIN 7 0 0 0 -1.2 .2

\*  
R1 3 0 100  
R2 4 0 100

\*  
R 2 1 1000

\*  
RIN 7 6 .1

\*  
Q1 3 5 2 QMOD  
Q2 4 6 2 QMOD

\*  
MODEL QMOD NPN IS=5.007E-15 EQUATION EQN1 (PIS)  
+ GPM=174.71 EQUATION EQBF (PIS)  
+ ME=1.59 EQUATION EQBE (PIS)  
+ C2=37 EQUATION EQC2 (PIS)  
\*

EQUATION EQN1 (X) = X \* 1E-16  
EQUATION EQBF (X) = 5.96\*X + 159.99  
EQUATION EQBE (X) = 0.06\*X + 1.2  
EQUATION EQC2 (X) = 30.55\*X - 150.55

} EQUATIONS  
AS DISCUSSED

\*  
PIS DISTRIBUTION TABLE TPIS

\*  
TABLE TPIS CUMULATIVE 4.00,0 4.60,5 5.20,15 5.80,23  
+ 6.40,28 7.00,30 7.60,30 8.20,35  
+ 8.80,35 9.40,35  
\*

\*  
CASES 100

\*  
TIME .004 .2

\*  
SAMPLE 0

\*  
PLOT 4 3

\*  
STATISTICAL PLOT 4 3 J:RIN J:R

HISTOGRAM 4 (-201.00E-3,-101.00E-3,40) 5 (-3.975E-3,-1.975E-3,40)

HISTOGRAM J:RIN (-10.00E-3,790.00E-3,40)

HISTOGRAM J:R (1.0071E-3,2.0075E-3,40)

HISTOGRAM PIS (0,10,10) QMOD:Q1 (150,210,10)

HISTOGRAM QMOD:Q2 (1.20,1.20,10) QMOD:Q2 (0,255,10)

\*  
END

Figure 4.7.58 - Circuit simulator input for a statistical analysis of 100 cases using parameter correlations [4.2]. The equation give explicit correlations as discussed in ref [4.3].

- M S I N C - VER. 65:01

# STATISTICAL ANALYSIS

MICROFOMER COLL RATE (STATISTICAL ANALYSIS WITH PARAMETER EQUATIONS)

+ : 4 : 0- MIN  
\* : 4 : 0- MAX  
# : 4 : 0- MEAN

TIME IN MILLI- SECONDS

	-200.00	-160.00	-120.00	-80.00	-40.00	.00	MILLI
	-200.00	-160.00	-120.00	-80.00	-40.00	.00	MILLI
	-200.00	-160.00	-120.00	-80.00	-40.00	.00	MILLI
0.000	1	1	1	1	1	1	-200.546 -193.935
4.000	1	1	1	1	1	1	-199.499 -192.881
8.000	1	1	1	1	1	1	-198.289 -191.669
12.000	1	1	1	1	1	1	-197.079 -190.457
16.000	1	1	1	1	1	1	-195.421 -188.805
20.000	1	1	1	1	1	1	-193.763 -187.154
24.000	1	1	1	1	1	1	-192.105 -185.502
28.000	1	1	1	1	1	1	-190.448 -183.850
32.000	1	1	1	1	1	1	-187.886 -181.519
36.000	1	1	1	1	1	1	-185.323 -178.769
40.000	1	1	1	1	1	1	-182.761 -176.258
44.000	1	1	1	1	1	1	-180.199 -173.727
48.000	1	1	1	1	1	1	-176.294 -169.905
52.000	1	1	1	1	1	1	-172.389 -166.083
56.000	1	1	1	1	1	1	-168.485 -162.260
60.000	1	1	1	1	1	1	-164.580 -158.438
64.000	1	1	1	1	1	1	-159.002 -153.022
68.000	1	1	1	1	1	1	-153.424 -147.607
72.000	1	1	1	1	1	1	-147.846 -142.191
76.000	1	1	1	1	1	1	-142.268 -136.776
80.000	1	1	1	1	1	1	-135.183 -129.940
84.000	1	1	1	1	1	1	-128.097 -123.105
88.000	1	1	1	1	1	1	-121.011 -116.269
92.000	1	1	1	1	1	1	-113.926 -109.434
96.000	1	1	1	1	1	1	-106.841 -102.069
100.000	1	1	1	1	1	1	-98.595 -94.705
104.000	1	1	1	1	1	1	-90.350 -87.341
108.000	1	1	1	1	1	1	-83.265 -79.977
112.000	1	1	1	1	1	1	-76.335 -73.530
116.000	1	1	1	1	1	1	-69.404 -66.683
120.000	1	1	1	1	1	1	-62.474 -60.056
124.000	1	1	1	1	1	1	-55.544 -53.390
128.000	1	1	1	1	1	1	-50.259 -48.501
132.000	1	1	1	1	1	1	-44.934 -43.212
136.000	1	1	1	1	1	1	-39.629 -38.123
140.000	1	1	1	1	1	1	-34.324 -33.034
144.000	1	1	1	1	1	1	-30.762 -29.613
148.000	1	1	1	1	1	1	-27.201 -26.191
152.000	1	1	1	1	1	1	-23.639 -22.770
156.000	1	1	1	1	1	1	-20.077 -19.349
160.000	1	1	1	1	1	1	-17.692 -17.246
164.000	1	1	1	1	1	1	-15.707 -15.144
168.000	1	1	1	1	1	1	-13.521 -13.041
172.000	1	1	1	1	1	1	-11.336 -10.936
176.000	1	1	1	1	1	1	-10.069 -9.717
180.000	1	1	1	1	1	1	-8.602 -8.446
184.000	1	1	1	1	1	1	-7.535 -7.275
188.000	1	1	1	1	1	1	-6.268 -6.054
192.000	1	1	1	1	1	1	-5.507 -5.320
196.000	1	1	1	1	1	1	-4.746 -4.586
200.000	1	1	1	1	1	1	-3.986 -3.852

Figure 4.7.59 - Simulation output voltage transfer curves for mean, maximum and minimum -- similar to figure 4.7.55 -- using parameter correlation equations.

- M S I N C - VER. 85:01 HISTOGRAM - SAMPLE TIME .000 MILI SECONDS

MICROPOWER ECL GATE (STATISTICAL ANALYSIS WITH PARAMETER EQUATIONS)

4 :	0	MILI	I	I	I	I	I	NO.	CUM. PROB.
-200.00	xxxxxxx							7	.0700
-197.50	xxxxxxxxxxxxxxxxxxxxxxxx							23	.3000
-195.00	xx							70	1.0000
-192.50								0	1.0000
-190.00								0	1.0000
-187.50								0	1.0000
-185.00								0	1.0000
-182.50								0	1.0000
-180.00								0	1.0000
-177.50								0	1.0000
-175.00								0	1.0000
-172.50								0	1.0000
-170.00								0	1.0000
-167.50								0	1.0000
-165.00								0	1.0000
-162.50								0	1.0000
-160.00								0	1.0000
-157.50								0	1.0000
-155.00								0	1.0000
-152.50								0	1.0000
-150.00								0	1.0000
-147.50								0	1.0000
-145.00								0	1.0000
-142.50								0	1.0000
-140.00								0	1.0000
-137.50								0	1.0000
-135.00								0	1.0000
-132.50								0	1.0000
-130.00								0	1.0000
-127.50								0	1.0000
-125.00								0	1.0000
-122.50								0	1.0000
-120.00								0	1.0000
-117.50								0	1.0000
-115.00								0	1.0000
-112.50								0	1.0000
-110.00								0	1.0000
-107.50								0	1.0000
-105.00								0	1.0000
-102.50								0	1.0000

4 : 0 MILI

MIN.	MAX.	MEAN	STD.
-200.5461	-193.9332	-195.8592	1.5714

Figure 4.7.60 - Simulated histogram of output-low voltages for the 100 examples given in Figure 4.7.58 and using correlations.

- M S I N C - VER. B5:01 HISTOGRAM - SAMPLE TIME .000 MILI SECONDS

MICROPOWER LCL GATE (STATISTICAL ANALYSIS WITH PARAMETER EQUATIONS)

J-RIN	MICO					I NO.	CUM.PROB.
	I	I	I	I	I		
-.000	XXXXXXXXXX					9	.0900
20.000	XXXXXXXXXXXXXXXXXXXXXXXXXXXX					23	.3200
40.000	XX					63	.9500
60.000	xxx					3	.9800
80.000						0	.9800
100.000						0	.9800
120.000						0	.9800
140.000						0	.9800
160.000						0	.9800
180.000						0	.9800
200.000						0	.9800
220.000						0	.9800
240.000						0	.9800
260.000						0	.9800
280.000						0	.9800
300.000						0	.9800
320.000						0	.9800
340.000						0	.9800
360.000						0	.9800
380.000						0	.9800
400.000						0	.9800
420.000						0	.9800
440.000						0	.9800
460.000						0	.9800
480.000						0	.9800
500.000						0	.9800
520.000						0	.9800
540.000						0	.9800
560.000						0	.9800
580.000						0	.9800
600.000						0	.9800
620.000						0	.9800
640.000						0	.9800
660.000						0	.9800
680.000						0	.9800
700.000						0	.9800
720.000						0	.9800
740.000						0	.9800
760.000						0	.9800
780.000						0	.9800

J-RIN	MICO			
	MIN.	MAX.	MEAN	STD.
	-19.5050	52.8288	30.4473	15.3115

Figure 4.7.61 - Simulated histogram of input current for the 100 examples given in Figure 4.7.58 and using correlations.

TIME IN MILI- SECONDS

Figure 4.7.62 - Simulated output voltage transfer curves for mean, maximum and minimum gates based on measured parameters. (Compare with Figure 4.7.59)

4 : 0 MILI						I NO.	CUM.PROB.
	I	I	I	I	I		
-200.00						0	.0000
-197.50	XXXXXXXXXXXXXXXXXXXXXXXXXXXXXXXXXXXX					18	.5143
-195.00	XXXXXXXXXXXXXXXXXXXXXXXXXXXXXXXXXXXX					17	1.0000
-192.50						0	1.0000
-190.00						0	1.0000
-187.50						0	1.0000
-185.00						0	1.0000
-182.50						0	1.0000
-180.00						0	1.0000
-177.50						0	1.0000
-175.00						0	1.0000
-172.50						0	1.0000
-170.00						0	1.0000
-167.50						0	1.0000
-165.00						0	1.0000
-162.50						0	1.0000
-160.00						0	1.0000
-157.50						0	1.0000
-155.00						0	1.0000
-152.50						0	1.0000
-150.00						0	1.0000
-147.50						0	1.0000
-145.00						0	1.0000
-142.50						0	1.0000
-140.00						0	1.0000
-137.50						0	1.0000
-135.00						0	1.0000
-132.50						0	1.0000
-130.00						0	1.0000
-127.50						0	1.0000
-125.00						0	1.0000
-122.50						0	1.0000
-120.00						0	1.0000
-117.50						0	1.0000
-115.00						0	1.0000
-112.50						0	1.0000
-110.00						0	1.0000
-107.50						0	1.0000
-105.00						0	1.0000
-102.50						0	1.0000

4 : 0 MILI

MIN.	MAX.	MEAN	STD.
-197.8236	-194.9568	-196.2563	.6909

Figure 4.7.63 - Simulated histogram of output-low using measured parameters.  
(Compare with Figure 4.7.60)

J-RIN	I	MICU	I	I	I	I	NO.	CUM.PROB.
-.000							0	.0000
20.000	XX						24	.6857
40.000	XXXXXXXXXXXXXXXXXXXX						11	1.0000
60.000							0	1.0000
80.000							0	1.0000
100.000							0	1.0000
120.000							0	1.0000
140.000							0	1.0000
160.000							0	1.0000
180.000							0	1.0000
200.000							0	1.0000
220.000							0	1.0000
240.000							0	1.0000
260.000							0	1.0000
280.000							0	1.0000
300.000							0	1.0000
320.000							0	1.0000
340.000							0	1.0000
360.000							0	1.0000
380.000							0	1.0000
400.000							0	1.0000
420.000							0	1.0000
440.000							0	1.0000
460.000							0	1.0000
480.000							0	1.0000
500.000							0	1.0000
520.000							0	1.0000
540.000							0	1.0000
560.000							0	1.0000
580.000							0	1.0000
600.000							0	1.0000
620.000							0	1.0000
640.000							0	1.0000
660.000							0	1.0000
680.000							0	1.0000
700.000							0	1.0000
720.000							0	1.0000
740.000							0	1.0000
760.000							0	1.0000
780.000							0	1.0000

J-RIN	MIN.	MAX.	MEAN	STD.
	18.5156	44.0733	26.5884	6.6839

Figure 4.7.64 - Simulated histogram of input current using measured parameters.  
Compare with Figure 4.7.61)

# References:

- [4.1] D. A. Antoniadis, S. E. Hansen, R. W. Dutton, and A. G. Gonzalez, "SUPREM 1 -- A Program for IC Process Modeling and Simulation", Technical Report No. 5019-1, Stanford Electronics Laboratories, Stanford University, May 1977.
- [4.2] D. A. Divekar, R. W. Dutton and W. J. McCalla, "Experimental Study of Gummel-Poon Model Parameter Correlations for Bipolar Junction Transistors", IEEE J. of Solid State Circuits, Vol. SC-12, No. 5, pp. 552-559, October 1977.
- [4.3] H. K. Gummel, "A Self Consistent Iterative Scheme for One-Dimensional Steady State Transistor Calculations", IEEE Trans. on Electron Devices, pp. 455-465, October 1964.
- [4.4] A. De Mari, "An Accurate Numerical Steady-State One-Dimensional Solution of the P-N Junction", Solid-State Electronics, vol. 11, pp. 33-58, 1968.
- [4.5] S. L. Ross, Differential Equations, Balisdell Publishing Co., NY, 1967.
- [4.6] C. Dahlquist and A. Bjorck, Numerical Methods, Prentice Hall, NJ, 1974.
- [4.7] G. Forsythe and C. B. Moler, Computer Solution of Linear Algebraic Systems, Prentice Hall, New Jersey, 1967.
- [4.8] J. M. Slotboom, "The pn-Product in Silicon", Solid State Electronics, vol. 20, pp. 279-283, 1977.
- [4.9] J. J. Barnes and R. J. Lomax, "Two-dimensional Finite Element Simulation of Semiconductor Devices", Electron Lett., Vol. 10, pp. 341-343, August 8, 1974.
- [4.10] J. J. Barnes and R. J. Lomax, "Finite-Element Simulation of GaAs MESFETs with Lateral Doping Profiles and Submicron Gates", IEEE Trans. Electron Devices, vol. ED-23, pp. 1042-1048, September 1976.
- [4.11] J. J. Barnes and R. J. Lomax, "Finite-Element Methods in Semiconductor Device Simulation", IEEE Trans. Electron Devices, vol. ED-24, pp. 1082-1089, August 1977.
- [4.12] E. M. Buturla and P. E. Cottrell, "Two-Dimensional Finite Element Analysis of Semiconductor Transport Phenomena", Proc. Int. Conf. On Numerical Methods in Electric and Magnetic Field Problems, Italy, June 1976.
- [4.13] G. D. Hachtel, M. H. Mack and R. R. O'Brien, "Semiconductor Device Analysis via Finite Elements", Conference Record, Eight Asilomar Conference on Circuits, Systems and Computers (Pacific Grove, CA), pp. 332-338, December 1974.

AD-A059 752

STANFORD UNIV CALIF INTEGRATED CIRCUITS LAB  
COMPUTER AIDED ENGINEERING OF SEMICONDUCTOR INTEGRATED CIRCUITS--ETC(U)  
JUL 78 J D MEINDL, K C SARASWAT, R W DUTTON DAAB07-77-C-2684  
DELET-TR-77-2684-2

F/G 9/5

UNCLASSIFIED

NL

4 OF 5  
ADA  
059752



- [4.14] G. D. Hachtel, M. H. Mack and R. R. O'Brien and B. Speelpenning, "Computational Aspects of Nonlinear Finite Element Analysis", IBM Research Report RC 6555 (#28177), May 1977.
- [4.15] A. D. Sutherland, "A Two-Dimensional Model for MOSFET Operation", Final Report ECOM-75-1344F, Computer Aided Engineering of Semiconductor Integrated Circuits, U. S. Army Electronics Command, Ft. Monmouth, NJ, Chapter VI, pp. 216-256, August 1977.
- [4.16] D. C. Mayer, N. A. Masnari and R. J. Lomax, "A Submicron Channel Vertical Junction Field-Effect Transistor", Conference Digest, International Electronic Device Meeting, Washington D.C., December 1977.
- [4.17] R. J. Lomax, "Transverse Effects in Avalanche Transit-Time Devices", Final Report on NSF Grant No. GK-37581, Electron Physics Laboratory, The University of Michigan, Ann Arbor, August 1975.
- [4.18] M. Reiser, "A Two-Dimensional Numerical FET Model for DC, AC and Large-Signal Analysis, IEEE Trans. Electron Devices, vol. ED-20, pp. 35-45, January 1973.
- [4.19] D. D'Avanzo, Private Communication.
- [4.20] M. K. Gummel, "A Self-Consistent Iterative Scheme for One Dimensional Steady State Transistor Calculations", IEEE Trans. Electron Devices, vol. 11, pp. 455-465, 1964.
- [4.21] A. De Mari, "An Accurate Numerical Steady-State One-Dimensional Solution of the P-N Junction", Solid State Electronics, vol. 11 pp. 33-58, 1968.
- [4.22] J. Greenfield, Private Communication.
- [4.23] M. Reiser, "On the Stability of Finite Difference Schemes in Transient Semiconductor Problems", Computer Meth. in Appl. Mech. and Eng. 1 (1973), pp. 65-68.
- [4.24] J. Sansbury, J. Moll and H. G. Lee, "On Measurement of Surface Impurity Profiles of Laterally Diffused Regions," 1977 IEDM Technical Digest.
- [4.25] A. G. Gonzalez, D. A. Antoniadis and R. W. Dutton, "Boron in Near-Intrinsic <100> and <111> Silicon Under Inert and Oxidizing Ambients -- Diffusion and Segregation Coefficients," to be published.
- [4.26] G. Masetti, S. Solmi and G. Soncini, "Temperature Dependence of Boron Diffusion in <111>, <110> and <100> Silicon, " Solid State Electronics, 1976, vol. 19, pp. 545-546.
- [4.27] E. Bassons, H. N. Yu, and V. Maniscalco, "Topology of Silicon Structures with Recessed SiO<sub>2</sub>," J. of the Electrochem. Soc., vol. 123, no. 11, November 1976.

- [4.28] D. P. Kennedy and R. R. O'Brien, "Analysis of the Impurity Atom Distribution Near the Diffusion Mask for a Planar p-n Junction," IBM Journal, pp. 179-186, May 1965.
- [4.29] L. W. Ricketts, Fundamentals of Nuclear Hardening of Electronic Equipment, Wiley-Interscience, New York, 1972.
- [4.30] J. L. Moll, M. Tannenbaum, J. M. Goldey, and N. Holonyak, "P-N-P-N Transistor Switches," Proc. IRE, vol. 44, pp. 1174-1182, September 1956.
- [4.31] A. K. Jonscher, "P-N-P-N Switching Diodes," J. Elect. and Control, vol. 3, pp. 573-586, 1957.
- [4.32] F. E. Gentry, F. W. Gutzwiller, N. Holonyak, and E. E. von Zastrow, Semiconductor Controlled Rectifiers: Principles and Applications of p-n-p-n Devices, Prentice-Hall, Inc., Englewood Cliffs, NJ, 1964.
- [4.33] H. A. Schafft, "Second Breakdown -- A Comprehensive Review," Proc. IEEE, vol. 55, pp. 1272-1288, August 1967.
- [4.34] W. D. Raburn and W. H. Causey, "Calculations of Sustaining Voltage in Silicon Bipolar Transistors," Microelectronics, vol. 6, pp. 4-6, 1975.
- [4.35] C. E. Barnes, et al., "Latch-Up Prevention in CMOS," Sandia Laboratories Report SAND 76-0048, Albuquerque, New Mexico, 1976.
- [4.36] B. L. Gregory and B. D. Shafer, "Latch-Up in CMOS Integrated Circuits," IEEE Trans. Nuc. Sci., vol. NS-20, pp. 293-299, December 1973.
- [4.37] W. J. Dennehy, A. G. Holmes-Siedle, and W. F. Leopold, "Transient Radiation Response of Complementary-Symmetry MOS Integrated Circuits," IEEE Trans. Nuc. Sci., Vol. NS-16, pp. 114-119, December 1969.
- [4.38] McMOS Handbook, Motorola, Inc., Geneva, Switzerland, 1974.
- [4.39] K. G. McKay, "Avalanche Breakdown in Silicon," Phys. Rev., vol. 94, pp. 877-884, May 1954.
- [4.40] R. E. Taylor (Ed.), Radio Frequency Interference Handbook, NASA Special Publication 3067, Washington, D.C., 1971.
- [4.41] D. A. Antoniadis, S. E. Hansen, R. W. Dutton, and A. G. Gonzalez, "SUPREM 1 - A Program for IC Process Modeling and Simulation," Stanford Electronics Laboratories Technical Report 5019-1, Stanford University, Stanford, California, May 1977.
- [4.42] Refer to Don D'Avanzo's section on SEDAN.
- [4.43] W. R. Dawes, and G. F. Derbenwick, "Prevention of CMOS Latch-Up by Gold Doping," IEEE Trans. Nuc. Sci., vol. NS-24, pp. 2027-2030, December 1976.

- [4.44] J. E. Meyer, "MOS Models and Circuit Simulation", RCA Review, Volume 32, pp. 42-63, March 1971.
- [4.45] H. K. J. Ihantola and J. M. Moll, "Design Theory of a Surface Field-Effect Transistor", Solid State Electronics, Vol. 7 pp. 423-430, June 1964.
- [4.46] J. D. Meindl, Micropower Circuits, Chapter 11, John Wiley and Sons, Inc., 1969.
- [4.47] S. R. Combs and J. D. Meindl, "Kitchip - A Generalized Integrated Circuit for Biomedical System Design", presented at the 3rd Int. Symposium on Biotelemetry, Asilomar, CA, May 1976.

## APPENDIX A

### PARTIAL LIST OF DISTRIBUTED COPIES OF SUPREM (OCTOBER 15, 1977)

#### Government

- |                                 |                 |
|---------------------------------|-----------------|
| 1. ECOM, Fort Monmouth, NJ      | Randy Reitmeyer |
| 2. National Bureau of Standards | Tom Leedy       |
| 3. National Security Agency     | Bill Bundy      |
| 4. Harry Diamond Laboratories   | Brian Biehl     |

#### DOD Contract Holders

- |  |                    |
|--|--------------------|
| 1. TRW Defense and Space Systems Group                           | John Choma         |
| 2. Hughes Aircraft Co., Calsbad Research Center                  | Michael Jack       |
| 3. Sandia Laboratories   | Chuck Gwyn         |
| 4. Northrop Corporation, Northrop Research and Technology Center | F. W. Pfeiffer     |
| 5. Questron Corporation, El Segundo, CA                          | James P. Spratt    |
| 6. General Electric, Syracuse, NY                                | John R. Debolt     |
| 7. Rockwell International, Anaheim, CA                           | Dr. R. R. August   |
| 8. General Dynamics, Pomona                                      | Dr. V. A. Twaddell |

#### Industry U.S.A.

- |  |                       |
|--|-----------------------|
| 1. RCA Solid State Division Somerville, NJ               | Chris Davis           |
| 2. Bell Laboratories                                     |                       |
| A. Allentown, PA   | Paul Langer           |
| B. Murray Hill, NJ                                       | Dr. Jacques Ruch      |
| C. Holmdel, NJ   | Alexander Voshchenkov |
| 3. Intel, Santa Clara, CA                                | Chris Martensen       |
| 4. Prime Computer Inc., Framingham, MS                   | Mike Payne            |
| 5. Texas Instruments, Dallas, TX                         | Dr. William Doughton  |
| 6. Tektronix, Beaverton, OR                              | Dr. Doug Ritchie      |
| 7. Signetics, Santa Clara, CA                            | Tak Young             |
| 8. Litronix: Advanced LSI Technology Inc., Cupertino, CA |                       |
| 9. Control Data Corporation, Minneapolis, MN             | Molz B. Khambaty      |
| 10. Bell Northern Research                               | Chuck Naber           |
| 11. National C.S.S., Santa Clara, CA                     | Michael Coughney      |
| 12. National Semiconductor, Los Altos, CA                | Mr. Wong              |
| 13. Xerox, El Segundo, CA                                | Darrell Erb           |
| 14. Philips Laboratories, Briarcliff Manor, NY           | Keming W. Yeh         |
| 15. Solid State Scientific, Montgomeryville, PA          | Jerry S. Sullivan     |
| 16. Hewlett-Packard, Corporate Engineering, Palo Alto    | Jeff Steinwedel       |
|  | Hal Daseking          |

- |  |                        |
|--|------------------------|
| A. Loveland Instruments Division                 | Dick Toftness          |
| B. Microwave Semiconductor Division              | Craig Snapp            |
| C. Solid-State Laboratory                        | Ken Lisiak             |
| D. Integrated Circuits Laboratory                | Skip Rung              |
| E. Data Systems Division                         | Wei Wu                 |
| F. Colorado Springs Division                     | Grant Sommers          |
| 17. Lawrence Livermore Laboratories              | Ken Harmon             |
| 18. Amdahl Corporation, Sunnyvale, CA            | John Foggiats          |
| 19. Hitachi Ltd., Mountain View, CA              | Tsugio Makimoto        |
| 20. IBM, Essex Junction, Vermont                 | A. Bhattacharyya       |
| 21. American Microsystems, Inc., Santa Clara, CA | Shi Ping Fan           |
| 22. Eastman Kodak Co., Rochester, NY             | Dr. Rajinder P. Khosla |
| 23. Fairchild, Palo Alto, CA                     | Bruce Deal             |
| 24. Motorola, Inc. Phoenix, AZ                   | S. V. Pabbisetty       |
| 29. Xerox Park, Palo Alto, CA                    | Bob Tremain            |

#### Industry Foreign

- |  |                    |
|--|--------------------|
| 1. Centre Electronique Horloger, Switzerland | Heinz W. Luginbuhl |
|--|--------------------|

#### Educational Institutions

- |  |                            |
|--|----------------------------|
| 1. University of Maryland  | Professor H. C. Lin        |
| 2. University of California, Berkeley  | David Angst                |
| 3. University of Toronto   | Professor C. A. T. Salama  |
| 4. Laboratory for Semiconductor Technology,<br>The Technical University of Denmark | Jens Guldberg              |
| 5. Technische Universitat Wien, Vienna   | Prof. Dr. Phil H. W. Potzl |
| 6. Twente University of Technology, Netherlands                                    | Ben Spaanenburg            |

## APPENDIX B

### PUBLICATIONS RESULTING FROM WORK DONE UNDER THIS PROGRAM

#### ION IMPLANTATION

1. A. Chu, "A Theoretical Approach to the Calculation of Annealed Impurity Profiles of Ion Implanted Boron into Silicon," Ph.D. dissertation, SEL TR 4969-2, Stanford University, Stanford, CA, May 1977.
2. D. Smith and J. Gibbons, "Application of the Boltzmann Transport Equation to the Calculation of Range Profiles and Recoil Implantation in Multi-layer Media," Ion Implantation Conf., Boulder, CO, Aug. 1976.
3. A. Goetzberger, D.J. Bartelink, J.P. McVittie and J.F. Gibbons, Appl. Phys. Lett. 29(4):259-261, 1976.
4. A. Chu and J. Gibbons, "A Theoretical Approach to the Calculation of Impurity Profiles for Annealed, Ion Implanted B in Si," Ion Implantation Conf., Boulder, CO, Aug. 1976.

## OXIDATION

1. D.W. Hess and B.E. Deal, "Kinetics of the Thermal Oxidation of Silicon in  $O_2/HCl$  Mixtures," J. Electrochem Soc., Vol. 124, No. 5, May 1977, pp. 735-739.
2. D.W. Hess, "Effect of Chlorine in the Negative Bias Instability in MOS Structures," J. Electrochem. Soc., Vol. 124, No. 5, pp. 740-743.
3. B.E. Deal, D.W. Hess, J.D. Plummer and C.P. Ho, "Kinetics of the Thermal Oxidation of Silicon in  $O_2/H_2O$  and  $O_2/Cl_2$  Mixtures," accepted for publication in J. Electrochem. Soc.
4. C.P. Ho, J.D. Plummer, B.E. Deal and J.D. Meindl, "Thermal Oxidation of Heavily Phosphorus Doped Silicon," submitted for publication in J. Electrochem. Soc.
5. J.S. Johannessen, W.E. Spicer, J.F. Gibbons, J.D. Plummer and N.J. Taylor, "Observation of Phosphorus Pile-up at the  $SiO_2-Si$  Interface," submitted for publication to J. Appl. Phys.

## CHEMICAL VAPOR DEPOSITION OF SILICON

1. R. Reif, T.I. Kamins and K.C. Saraswat, "Transient and Steady-State Response of the Dopant System of an Epitaxial Reactor: Growth Rate Dependence," Electrochemical Society Fall Meeting, Abstract 350, Atlanta, Oct. 9-14, 1977, pp. 921-923.
2. T.I. Kamins, R. Reif and K.C. Saraswat, "Transient Response of Dopant Incorporation into Si Epitaxial Films," Electrochemical Society Fall Meeting, Abstract 230, Las Vegas, Oct. 17-22, 1976, pp. 601-603.
3. J.D. Meindl, K.C. Saraswat and J.D. Plummer, "The Need for Process Models in a Ubiquitous Technology," Semiconductor Silicon 1977, Princeton, New Jersey, The Electrochemical Society Inc., 1977, pp. 894-909.
4. K.C. Saraswat and J.D. Meindl, "Epitaxial Si Growth on Ion Implanted Si," Electrochemical Society Spring Meeting, Abstract 116, Philadelphia, Oct. 8-13, 1977.
5. T.I. Kamins, M.M. Mandurah and K.C. Saraswat, "Structure and Stability of Low-Pressure Chemically-Vapor-Deposited Si Films," submitted to the J. of Electrochem. for publication.

## DEVICE SIMULATION AND STATISTICAL CIRCUIT MODELING

### PUBLICATIONS FUNDED UNDER ARPA (5021)

1. R. W. Dutton, et. al. "Oxidation and Epitaxy", Stanford Electronics Laboratory Technical Report, Technical Report No. 5021-1, May 1977.
2. R. W. Dutton, D. A. Divekar, "Statistical Modeling", Stanford Electronics Laboratory Technical Report, Technical Report No. 5021-1, May 1977.
3. R. W. Dutton, et. al, "NATO Advanced Study Institute on Process and Device Modeling for Integrating Circuit Design, Louvain-la-Neuve, Belgium, July 19-29, 1977.
4. R. W. Dutton, et. al. "Correlation of Fabrication Process and Electrical Device Parameter Variations", IEEE Journal of Solid-State Circuits, Volume SC-12, No. 4, pp. 349-355, August 1977.
5. D. C. D'Avanzo, S. R. Combs, and R. W. Dutton, "Effects of the Diffused Impurity Profile on the DC Characteristics of VMOS and DMOS Devices", IEEE Journal of Solid-State Circuits, Volume SC-12, No. 4, pp.356-362, August, 1977.

### ARPA and ARO

1. D. A. Antoniadis, S. E. Hansen, R. W. Dutton, and A. G. Gonzalez, "SUPREM 1 -- A Program for IC Process Modeling and Simulation", Stanford Electronics Laboratory Technical Report, SEL 77-006, May 1977.
2. R. W. Dutton, D. A. Antoniadis, "Modeling of Moving Boundaries During Semiconductor Fabrication Processes", Moving Boundary Problems Symposium, Gatlinburg, Tennessee, September 26-28, 1977.
3. R. W. Dutton, D. A. Antoniadis, "Technology Modeling for IC Fabrication", Modeling Semiconductor Devices (Journées D'Electronique 1977) Lausanne, Switzerland, October 18-20, 1977.
4. M. Rodoni, D. A. Antoniadis, and R. W. Dutton, "Impurity Redistribution in  $\text{SiO}_2$ -Si During Oxidation A Numerical Solution Including Interfacial Fluxes", Electrochemical Society, Las Vegas, Nevada, October 1976.
5. D. A. Antoniadis, A. G. Gonzalez, and R. W. Dutton, "Boron in Near-Intrinsic  $\langle 100 \rangle$  and  $\langle 111 \rangle$  Silicon Under Inert and Oxidizing Ambients -- Diffusion and Segregation", Electrochemical Society, October 1977.

APPENDIX C

A THEORETICAL APPROACH TO THE CALCULATION OF ANNEALED  
IMPURITY PROFILES OF ION IMPLANTED BORON INTO SILICON

by

Alejandro Chu

May 1977

Technical Report No. 4969-2

Prepared under

Defense Advanced Research Projects Agency  
Contract DAA-B07-75-C-1344

and

National Science Foundation  
Grant GH-31999

Solid-State Electronics Laboratory  
Stanford Electronics Laboratories  
Stanford University                      Stanford, California

© Copyright 1977

by

Alejandro Chu

Reproduction or use, in whole or in part, is permitted for any  
purpose of the United States Government.

# ABSTRACT

A multi-stream diffusion model is proposed for the calculation of the annealing behavior of boron that is ion implanted into silicon at room temperature and subsequently annealed. This model is capable of predicting both the redistribution and the electrical activation of boron during the anneal, as a realistic model should. The calculated results compare very well with extensive experimental data reported in the literature. The comparison includes samples that are implanted at room temperature with boron in the dose range from  $10^{14}$  to  $10^{16}$  ions/cm<sup>2</sup> and subsequently annealed in the temperature range from 800°C to 1000°C. This range of dose and annealing conditions includes both the typical applications of ion implantation as it is applied in the fabrication of devices and the unconventional cases of high dose implants and low temperature annealing.

The annealing model is in essence a diffusion model extended to include the following situations:

- (1) precipitation of boron, when the boron concentration level exceeds the solid solubility limit, in high dose implantation cases
- (2) trapping of boron by the strain fields associated with dislocation dipoles that form during annealing at low temperature

In both cases, the presence of this immobile and electrically inactive boron alters significantly the redistribution and electrical activation behavior of boron during the anneal.

The presence of boron precipitates makes it necessary to include four species in the annealing model. These species are substitutional (electrically active) boron, boron-vacancy pairs (electrically inactive), positively charged vacancies, and the aforementioned immobile boron. The electrically active boron is assumed to diffuse substitutionally by means of random encounters with neutral vacancies. The boron-vacancy pair is assumed to diffuse much more rapidly. The principal interaction among the species is the reaction of active boron with positive vacancies to form BV-pairs.

The parameters in the model are a set of diffusivities and lifetimes for various species and interaction. These parameters are estimated from the examination of each diffusion and each interaction. The values of the most important parameters obey simple activation energy relations. In other cases, the modelling was either not carried to the extent necessary as to make the temperature dependence apparent, or else the parameters represent the composite effects of very complex interactions. In all cases, the mathematical model and the parameter set are universal in the sense that the same equations and parameters can be used for the prediction of ordinary diffusion, proton enhanced diffusion, and the annealing behavior of ion implanted boron at room temperature under conditions that include precipitation effects and low annealing temperature anomalies. Furthermore, in most cases of practical importance, high dose and low annealing temperature conditions are of limited interest and, as a result, the three stream diffusion model with an appropriate subset of parameters is sufficient. This reduced model is still very important and attractive because, once the parameters associated with high dose and/or low temperature anomalies are deleted, the remaining parameters have simple activation energies and are determined by the specification of a single variable: the temperature.

#### ACKNOWLEDGMENT

I would like to express my sincere gratitude to Professor James F. Gibbons, my research advisor, for providing his guidance in an atmosphere that awakened my interest in many areas, for formulating questions that sharpened my judgment, and for being critical in a way that encouraged my self-improvement. For these reasons, my research under his supervision has been a most meaningful academic and educational experience.

I am indebted to Dr. T. J. Magee of Stanford Research Institute for his considerable assistance with the transmission electron microscopy experiments in this thesis. I thank Dr. A. Hindmarsh of the Lawrence Livermore Laboratory and Professor O. Buneman for their advice in the area of numerical analysis. I am grateful to Dr. K. Saraswat and my colleagues, E. Ammar, A. Lidow, T. Herman, A. Gat, and F. Wu, for their assistance or comments on this work. In particular, I am much obliged to Dr. J. R. Anderson for his valuable discussions on the diffusion of boron in silicon.

Finally, I would like to thank my family. I am especially grateful to the following members: my parents from whom I learned perseverance, my sister Anna who provided the financial support that made possible my first studies in the United States, and my wife Cira who gives me constant encouragement.

The financial support of the Santa Rosa Division of the Hewlett-Packard Company is gratefully acknowledged. This work was supported jointly by the Defense Advanced Research Projects Agency under Contract No. DAA-B07-75-C-1344 and the National Science Foundation under Contract No. GH-31999.

## CONTENTS

	<u>Page</u>
I. THE ANNEALING OF ION IMPLANTED BORON INTO SILICON AT ROOM TEMPERATURE . . . . .	1
A. Introduction . . . . .	1
1. The Problem . . . . .	1
2. The Implantation of Ions . . . . .	1
3. The Anneal . . . . .	2
4. The Spatial Redistribution of Impurities During Annealing . . . . .	2
5. The Need for an Annealing Model . . . . .	4
6. Cases to be Studied . . . . .	4
B. A Summary of Relevant Experimental Data . . . . .	5
1. Experiments on Diffusion . . . . .	6
2. Experiments on the Lattice Location of Boron . . . . .	15
3. Transmission Electron Microscopy . . . . .	18
C. The Annealing Model . . . . .	24
1. Choice of Diffusion Model . . . . .	25
2. The Immobile and Nonsubstitutional Boron . . . . .	27
D. Development of the Model . . . . .	27
1. The Typical Annealing Cases . . . . .	29
2. The Spontaneous Conversion of BV-Pairs . . . . .	31
3. The 'Boron-Boron Vacancy Pair' Reaction . . . . .	32
4. The Positively Charged Vacancies . . . . .	34
5. Summary of the Typical Annealing Cases . . . . .	38
6. High Dose Cases . . . . .	39
7. Low Temperature Annealing . . . . .	43
8. Summary . . . . .	47
II. THE ANNEALING MODEL . . . . .	49
A. The Mathematical Model . . . . .	51
B. The Selection of Parameters . . . . .	55
1. Diffusion Coefficients--Only Functions of Temperature . . . . .	57

## CONTENTS (Cont)

	<u>Page</u>
2. The Equilibrium Constant in the Thermo- dynamic Reaction . . . . .	60
3. Equilibrium Concentration of Positively Charged Vacancies . . . . .	60
4. $\tau$ , The Lifetime of BV-Pairs . . . . .	61
5. The Lifetime of Vacancies . . . . .	62
6. $\tau_{DAM}$ , Damage Annealing Time Constant . . . . .	63
7. Solid Solubility Limit (SSL) . . . . .	63
8. Threshold Concentration Level for the Formation of Dislocation Dipoles . . . . .	64
9. Time Constants Associated with Precip- itation and the Trapping of Boron by Dislocation Dipoles . . . . .	64
10. Time Constant Associated with the Dis- solution of Precipitates and the Release of Boron from Dislocation Dipoles . . . . .	65
C. The Initial Conditions . . . . .	65
III. COMPARISON OF CALCULATED AND EXPERIMENTAL RESULTS . . . . .	69
A. Typical Annealing Cases . . . . .	69
B. High Dose Cases . . . . .	75
C. Low Annealing Temperature Cases . . . . .	78
IV. SUMMARY AND CONCLUSIONS . . . . .	83
A. The Three Stream Diffusion Model . . . . .	83
B. The Relation between Diffusion and Electrical Activity . . . . .	84
C. High Dose and Low Annealing Temperature Anomalies . . . . .	85
D. The Model and the Parameters . . . . .	85
E. The Initial Conditions . . . . .	87
F. Discussion . . . . .	88
G. Conclusion . . . . .	90
H. Suggestions for Future Work . . . . .	91

CONTENTS (Cont)

	<u>Page</u>
Appendix A. THE NUMERICAL INTEGRATION OF THE COUPLED DIFFUSION EQUATIONS . . . . .	93
Appendix B. CALCULATION OF AN EFFECTIVE DIFFUSION COEFFICIENT . . . . .	127
REFERENCES . . . . .	131

# TABLES

<u>Number</u>	<u>Page</u>
1. A comparison of diffusion coefficients at various temperatures obtained under different conditions, after Hofker et al [2] . . . . .	9
2. Isochronal annealing results . . . . .	28
3. The annealing cases . . . . .	39
4. Key attributes in the annealing problem . . . . .	50
5. The temperature dependent parameters . . . . .	56
6. The relation of the parameters to the implantation dose and annealing temperature . . . . .	58
7. The estimation of $D_{BV}$ . . . . .	59
8. The estimation of the lifetime of BV-pairs . . . . .	62
9. Models for annealing or diffusion . . . . .	89
A1. Definition of the vector $\vec{y} = (y_1 \dots y_{99})$ . . . . .	96
A2. Nonzero elements of the Jacobian . . . . .	99

## ILLUSTRATIONS

<u>Figure</u>	<u>Page</u>
1. As-implanted B profile and the annealed profile at 900°C for 35 min, after Hofker et al [2] . . . . .	3
2. The high concentration anomaly--comparison of experimental diffusion profile with the calculated profile using the diffusion coefficients determined in low concentration experiments, after Nicholas [7] . . . . .	8
3. A comparison of total boron profiled determined experiments using SIMS with the electrical carrier profile that result after two hours of irradiation with 10 KeV proton, after Anderson et al [12] . . . . .	12
4. Concentration profile of boron and the corresponding charge carrier profiles obtained after annealing at different temperatures for 35 min, after Hofker et al [14] . . . . .	13
5. Concentration profiles of a boron implantation with a dose of (a) $10^{14}$ ions/cm <sup>2</sup> , (b) $10^{15}$ ions/cm <sup>2</sup> , (c) $10^{16}$ ions/cm <sup>2</sup> , and at an energy of 70 KeV before and after annealing (annealing duration: 35 min); after Hofker et al [2] . . . . .	14
6. Effect of dose on the fraction of ion implanted boron on substitutional location during annealing . . . . .	17
7. Schematic summary of results and their interpretation, after Bicknell [17] . . . . .	19
8. Transmission electron micrographs of 70 keV boron implanted into 100 silicon and subsequently annealed for 5, 10, 15, and 35 min at (a) 900°C and (b) 800°C; implanted dose = $10^{14}$ ions/cm <sup>2</sup> . . . . .	20
9. Transmission electron micrographs of 70 keV boron implanted into 100 silicon and subsequently annealed for 5, 10, 15, and 35 min at (a) 900°C and (b) 800°C; implanted dose = $10^{15}$ ions/cm <sup>2</sup> . . . . .	21
10. The electrical activation and redistribution behavior of boron in typical annealing cases . . . . .	30
11. The calculated vacancy concentration profile produced by the implantation of boron . . . . .	36

# ILLUSTRATIONS (Cont)

<u>Figure</u>	<u>Page</u>
12. The electrical activation and redistribution behavior of boron in high dose cases . . . . .	40
13. The dissolution rate of precipitates . . . . .	42
14. The electrical activation and redistribution behavior of boron in low annealing temperature cases . . . . .	43
15. The annealing of a $10^{14}$ ions/cm <sup>2</sup> dose B implant at 900°C . . . . .	70
16. The annealing of a $10^{15}$ ions/cm <sup>2</sup> dose B implant at 900°C . . . . .	71
17. The annealing of a $10^{14}$ ions/cm <sup>2</sup> dose B implant at 1000°C . . . . .	72
18. The annealing of a $10^{15}$ ions/cm <sup>2</sup> dose B implant at 1000°C . . . . .	73
19. The comparison of calculated electrical activity versus time with experimental isothermal results by Seidel and MacRae . . . . .	74
20. The annealing of a $10^{16}$ ions/cm <sup>2</sup> dose B implant at 900°C . . . . .	76
21. The annealing of a $10^{16}$ ions/cm <sup>2</sup> dose B implant in the temperature range of 800°C to 1000°C . . . . .	77
22. The annealing of a $10^{14}$ ions/cm <sup>2</sup> dose B implant at 800°C . . . . .	78
23. The comparison of calculated electrical activity versus time with the experimental isothermal result by Seidel and MacRae . . . . .	79
24. The annealing of a $10^{15}$ ions/cm <sup>2</sup> dose B implant in the temperature range of 800°C to 1000°C . . . . .	80
25. The temperature dependence of parameters . . . . .	86

# SYMBOLS

$B^-$	Ionized boron
$B^-V^+$	Boron vacancy pair
$B_{\text{prec}}$	Boron precipitate
$B_I$	Immobile boron
$B_{\text{trapped}}$	Boron trapped by dislocation dipoles
c	Superscript denoting center
C	Concentration in $\#/\text{cm}^3$
$C_B$	Concentration of electrically active boron in $\#/\text{cm}^3$
$C_{BI}$	Concentration of immobile boron
$C_{B_{\text{prec}}}$	Concentration of boron precipitates
$C_{B_{\text{total}}}$	Total boron concentration
$C_{B_{\text{trapped}}}$	Concentration of boron trapped by dislocation dipoles
$C_{BV}$	Concentration of boron-vacancy pairs
$C_{dd}$	Threshold concentration level of boron for the formation of dislocation dipoles
$C_{SSL}$	Concentration at the solid solubility limit
$C_{V^+}$	Concentration of positively charged vacancies
$C_{V^+_{eq}}$	Equilibrium concentration of positively charged vacancies
D	Diffusion coefficient in units of $\text{cm}^2/\text{sec}$
$D_i$	Diffusion coefficient under intrinsic conditions
$D_B$	Diffusion coefficient of electrically active boron
$D_{BV}$	Diffusion coefficient of boron-vacancy pairs
$D_{\text{exp}}$	Diffusion coefficient measured in an experiment
$D_V$	Diffusion coefficient of vacancies
Damage(x)	Damage profile computed from the distribution of energy deposited into atomic processes in ion implanted silicon

EA	Electrical activity, fraction of ionized impurities to the total number of implanted impurities
$E_F$	Fermi energy level in the band gap
$E_{V+}$	Energy level of the positive vacancies in the band gap
$f_i$	$i^{\text{th}}$ function
i	Integer index
j	Integer index
J	Jacobian matrix
$J_{ij}$	Element in the Jacobian matrix
k	Constant
$k_o$	Equilibrium constant in the B-BV-pair reaction
K	Boltzmann's constant, $8.62 \times 10^{-5}$ eV/°K
$K_1, K_2, K_3, \left. \begin{matrix} K, K', K_V, K'_V \end{matrix} \right\}$	Scaled parameters
l	Superscript denoting left
p	Hole concentration in hole/cm <sup>-3</sup>
$p_i$	Hole concentration under intrinsic conditions
r	Superscript denoting right
SSL	Solid solubility limit
T	Temperature in degrees kelvin
$\tau$	Lifetime of BV-pairs
$\tau_{\text{DAM}}$	Time constant associated with the release of vacancies from the primary implantation damage
$\tau_{\text{dd}}$	Time constant associated with the trapping of boron by dislocation dipoles
$\tau_{\text{diss}}$	Time constant associated with the dissolution of boron precipitates
$\tau_{\text{prec}}$	Time constant associated with the precipitate of boron
$\tau_{\text{rel}}$	Time constant associated with the release of boron from the annealing dislocation dipoles

$\tau_v$	Lifetime of vacancies
$v^+$	Positively charged vacancies
$v^0$	Neutral vacancy
$x$	Space
$\Delta x$	Spatial increment
$\vec{y}$	Vector
$y_i, y_j$	The $i^{\text{th}}$ and $j^{\text{th}}$ components of vector $\vec{y}$
$\dot{y}_i$	The time derivative of the $i^{\text{th}}$ component of $\vec{y}$

## Chapter I

### THE ANNEALING OF ION IMPLANTED BORON INTO SILICON AT ROOM TEMPERATURE

#### A. Introduction

##### 1. The Problem

Ion implantation is a technique [1] for introducing selected impurities into a substrate material in a controlled fashion. It is based on the generation of a mass analyzed ion beam followed by the acceleration of these ions in an electric field directed toward the substrate material. This scheme is easily controlled with electronic instrumentation. As a result, it is possible to achieve repeatably high purity ion beams, to implant ions to an accurate dose, and to impart precise kinetic energy to the ions, thus controlling reproducibly their stopping points in the substrate. These advantages are complemented by the availability of a theoretical model from which one can compute accurately the as-implanted distribution of impurity atoms. However, this latter advantage is somewhat fictitious, because the implanted ions may produce substantial damage in the (crystalline) substrate as they come to rest. To repair this damage, an anneal has to follow the implantation. During this anneal, a diffusive redistribution of the implanted impurities will occur and, as a result, the actual impurity profile may differ substantially from the as-implanted profile. The quantitative prediction of this redistribution problem is the principal subject of this thesis.

##### 2. The Implantation of Ions

To elaborate on the nature of this problem, it is first useful to remark that the distribution of implanted ions in the solid substrate depends on both the acceleration voltage and mass relations between the implanted ion and the atoms of the target. Stopping of an energetic ion occurs as a result of collisions between the ion and the electrons and atoms of the target. If these collisions are sufficiently energetic, host atoms will be displaced from lattice sites, thus leaving vacancies behind. These displaced atoms may in turn displace other atoms in the

lattice, forming as a result a disorder cluster around the ion track. Furthermore, since the process just described is far away from thermal equilibrium, only some of the implanted impurities will be located on substitutional sites, after the implantation. In general, a larger fraction will be found in interstitial positions and still other impurity atoms will form complexes with simple lattice defects (lattice vacancies and interstitials). Furthermore, the doping characteristics of the impurity may be overwhelmed by the damage. As a result, the as-implanted substrate will usually exhibit an electrical carrier concentration far below that which would be predicted simply from the implanted impurity concentration profile. In other words, only a small percentage of the implanted impurities contribute to electrical carriers.

### 3. The Anneal

In order to obtain the expected electrical properties, it is necessary to anneal the implanted material at an elevated temperature. During annealing, some vacancies will be annihilated by silicon interstitials, divancies will anneal out, stress created by the damage clusters will be relieved by the formation of dislocation loops and vacancy clusters, there will be migration of defects, transformation of complexes, etc., and, most importantly, a relocation of impurities on substitutional sites accompanied by spatial redistribution. After the anneal, the substrate will still retain residual dislocation networks, but for silicon at least, the mobility and electrical activity (ration of electrically active to the totality of implanted impurities) are comparable to bulk-doped samples, and hence this process is adequate for device fabrication.

### 4. The Spatial Redistribution of Impurities During Annealing

In order to examine further the spatial redistribution of Boron during the anneal, we observe that, at the outset of the anneal, the implanted Boron distribution is in the presence of an abnormally high concentration of lattice defects, mostly vacancies. Consequently, as annealing begins, the defects migrate and transform, and the redistribution of boron is occurring simultaneously under conditions far away from

thermal equilibrium. Therefore, it is not surprising to find that the redistribution of boron during annealing cannot be predicted with a simple diffusion model that utilizes diffusion coefficients derived from ordinary diffusion experiments under thermal equilibrium conditions. For instance, Fig. 1 shows an as-implanted profile for boron in silicon together with this same profile after 35 minutes of annealing at 900°C. Both profiles were determined experimentally by Hofker et al [2]. These authors show that, to fit the annealed profile with the calculated profile that result from the diffusion of the as-implanted boron distribution, the diffusion coefficient should be set equal to  $1.4 \times 10^{-14} \text{ cm}^2/\text{sec}$ . This value is an order of magnitude higher than  $1.3 \times 10^{-15} \text{ cm}^2/\text{sec}$ , the diffusion coefficient determined from ordinary diffusion experiments extrapolated to 900°C. Further annealing

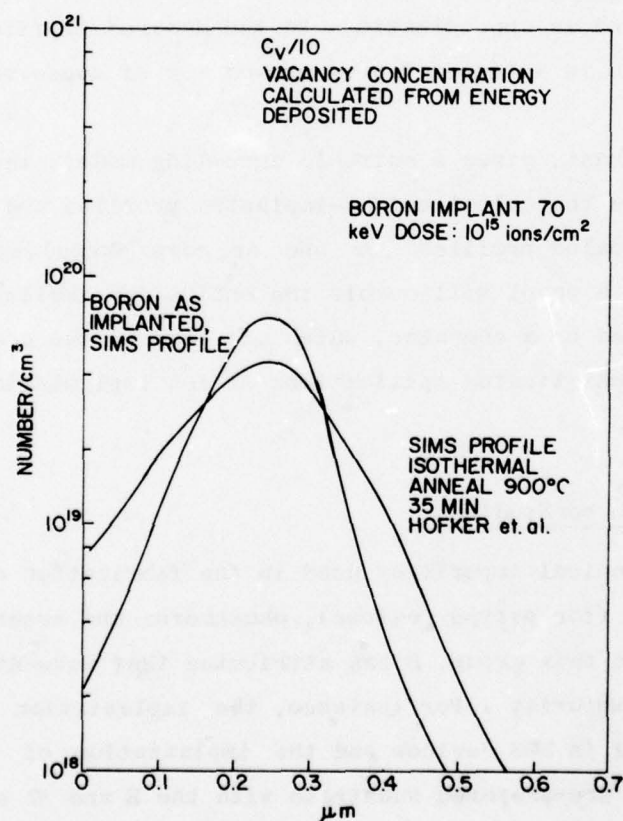


Fig. 1. AS-IMPLANTED B PROFILE AND THE ANNEALED PROFILE AT 900°C FOR 35 MIN, AFTER HOFKER ET AL [2].

shows that this enhancement in diffusion is a transient and that eventually, as the electrical activity approaches 100%, diffusion will gradually slow down and the ordinary thermal diffusion rate of  $1.3 \times 10^{-15} \text{ cm}^2/\text{sec}$  will be obtained.

#### 5. The Need for an Annealing Model

The example in the preceding section is from a common industrial application. It serves the purpose of showing the need for a realistic annealing model. Such a model should provide not only reasonable predictions of the annealed boron profile, but also a reasonable prediction of the evolution of electrical activity versus time. At present, empirical procedures are used to arrive at the implantation conditions and annealing schedule that will achieve the desired profiles. In this empirical process, the accurately calculated as-implanted profiles are only used as approximations to the desired profiles. And the annealing schedule is selected from a proven set of conservative schedules.

In contrast, given a suitable annealing model, the device designer can utilize the calculated as-implanted profiles and from these determine the annealed profiles for one or more annealing schedules. Furthermore, such a model will enable the entire ion implantation process to be modelled on a computer, which may lead to the eventual development of more sophisticated applications of ion implantation in device fabrication.

#### 6. Cases to be Studied

The principal impurities used in the fabrication of silicon devices are boron (for p-type regions), phosphorus and arsenic (for n-type regions). In this group, B has attributes that make it the most widely implanted impurity. For instance, the implantation of B for threshold shifting in MOS devices and the implantation of the boron doped base into a pre-prepared substrate with the E and C structures are possible because of the light damage and the long range characteristics of ion implanted boron. We chose in the present work to study the annealing behavior of ion-implanted boron into silicon at room

temperature under conditions that include the most relevant cases in device fabrication; i.e., dose range of  $10^{14}$  to  $10^{15}$  ions/cm<sup>2</sup> and annealing temperature range between 900°C to 1000°C. The primary input to the annealing model is the history of the substrate summarized by two distributions: the as-implanted boron profile (either computed or determined experimentally) and the distribution of energy deposited into nuclear processes by the boron ions. Damage is a product of this energy distribution. Our goal is to use this basic information (which is available for various combinations of projectiles and targets with acceleration voltage as a parameter) to predict the isothermal annealing of boron implanted into Si at room temperature (the most common application). Specifically, we wish to determine the evolution of the electrically-active boron in both time and space. A realistic annealing model should predict ordinary diffusion, proton enhanced diffusion, and naturally be consistent with the collection of experiments that we will review hereafter.

#### B. A Summary of Relevant Experimental Data

The purpose of reviewing relevant experiments is to establish that, despite the complexity of the actual situation, a model containing only four interacting species is capable of explaining the major features of the annealing behavior. These species are: substitutional boron, boron vacancy pairs, positively charged vacancies, and immobile boron (B trapped by defects or B precipitate). In what follows, we will show that with these four species we can model both the diffusive redistribution of ion implanted boron and the electrical activation of the implanted boron during annealing.

The experiments we will review can be grouped in three major areas: diffusion, electrical activation, and implantation damage. In the first area, we will examine diffusion anomalies, proton enhanced diffusion, and the redistribution of profiles during annealing. A vacancy mechanism is likely to account for the global features in these experiments. However, other features will require additional explanations. This is the case for the abnormal structures in low-temperature and short-time anneals.

Next, we will examine the experiments on the lattice location of ion-implanted boron. These experiments reveal that at the initial stages of annealing only a small fraction of boron is on substitutional sites. This fraction gradually increases to 100% toward the end of the anneal. Then, we review experiments on the electrical activity of the implanted Boron and show that this data is in good agreement with the channeling data.

It is evident from these experiments that there is a nonsubstitutional fraction of boron during annealing. Naturally, this inactive boron need not be in a single type of defect or complex. Whereas, in many cases it does seem that a single type of defect is responsible for the electrical inactivity, in other cases it is apparent that more than one form of inactive boron is required. To study this possibility, we performed a group of experiments on the evolution of implantation damage during an isothermal annealing to elucidate this issue. The global transmission electron microscopy results indicate that, when the presence of more than one form of inactive boron is evident, the second form is either boron trapped by defects formed during annealing or boron precipitate, if the solid solubility limit was exceeded by the boron concentration.

#### 1. Experiments on Diffusion

The study of diffusion depends heavily on the determination of concentration profiles. Whereas some profiling techniques are based on the identification of the species chemically present, others are based on the electrical effect of the ionized specie present in the substrate. In the first category, we find the use of radiotracers, secondary ion mass spectrometry, Auger, backscattering, and ESCA. In the second category, the techniques are two point or four point resistance measurements, CV profiling, and Hall-mobility measurements. In general, these methods do not give the depth information unless they are used in conjunction with a layer removal technique such as anodic oxidation and oxide stripping or sputtering with an argon ion beam. The data that we will review were obtained using SIMS for the determination of total boron concentration profiles in the substrate and Hall-mobility measurement to determine the ionized, electrically active boron profiles. For moderate

concentrations under thermal equilibrium conditions, the electrically active Boron concentration approaches the total boron concentration. In contrast, under nonequilibrium thermodynamic conditions such as at the completion of a boron implant or a proton irradiation or before the completion of an anneal, the active boron concentration will differ substantially from the total boron concentration, as we will see.

a. Ordinary Diffusion

At low concentrations, the diffusion of impurities into near intrinsic silicon substrates obeys Fick's laws, hence the diffused profile from a constant concentration source is represented by a complementary error function. At high concentrations, boron and many Group III and Group V impurities diffuse abnormally fast. This high concentration anomaly [3-7] is depicted in Fig. 2; after Nicholas [5]. Another anomaly is the effect of substrate background doping. If the substrate is doped a-priori with arsenic or phosphorus, the a-posteriori diffusion of boron is greatly reduced [6,7]. These diffusion anomalies can be represented by the following equation, after Crowder et al [8].

$$D/D_i = p/p_i \quad (1)$$

where  $D$  and  $p$  symbolize diffusion coefficient and hole concentration, respectively, and the subscript  $i$  denotes intrinsic condition. This equation can be derived [8] assuming that the diffusion of boron is proportional to the total vacancy concentration, which is in turn Fermi level dependent. An alternate derivation by Anderson and Gibbons [9] has also been published and is, in fact, consistent with the annealing model we will develop here.

There are other anomalies, such as the enhancement in diffusion in mechanically polished substrates and diffusion in the presence of oxidation. These cases require an alternative mechanism to explain the enhanced diffusion, for instance, Nicholas [7] and Parker [10] propose that vacancies are generated from the nonconservative motion of dislocation.

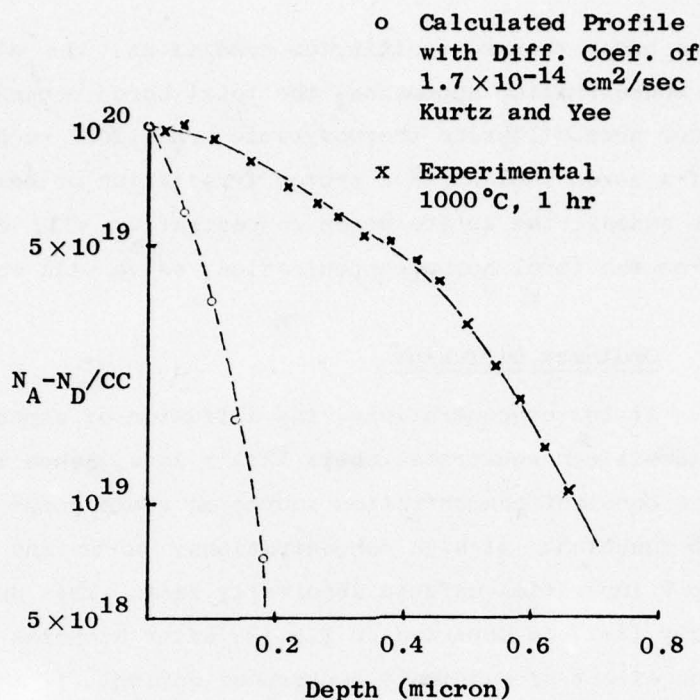


Fig. 2. THE HIGH CONCENTRATION ANOMALY--COMPARISON OF EXPERIMENTAL DIFFUSION PROFILE WITH THE CALCULATED PROFILE USING THE DIFFUSION COEFFICIENTS DETERMINED IN LOW CONCENTRATION EXPERIMENTS, AFTER NICHOLAS [7].

During annealing, the redistribution of boron is anomalous. At the beginning, the diffusion rate is high. However, as the annealing proceeds, the diffusion rate decreases to values obtained in ordinary diffusion experiments [2]. The relative importance of this transient effect is shown in Table 1, after Hofker et al [2]. The diffusion coefficients in the second and third columns are obtained from curve fitting the experimental profiles after 35 min of annealing with calculated profiles originated from the as-implanted profiles. The values in the fourth column are obtained from fitting experimental profiles at longer annealing times with calculated profiles originated from annealed profiles. Agreement of the values in the fourth column with the diffusion coefficients in column five, obtained in ordinary diffusions, indicate that, once the ion implanted impurities are on substitutional sites, the diffusion mechanism is indistinguishable from ordinary diffusion.

Table 1

A COMPARISON OF DIFFUSION COEFFICIENTS AT VARIOUS TEMPERATURES  
OBTAINED UNDER DIFFERENT CONDITIONS, AFTER HOFKER ET AL [2]

Anneal- ing Temp. (°C)	$D \text{ (cm}^2 \text{ s}^{-1}\text{)}$			
	$N(\xi,0)$ : Not Annealed Distribution		$N(\xi,0)$ : Annealed Distribution	from Kurtz
	$10^{14}$ dose: ions $\text{cm}^{-2}$	$10^{15}$ dose: ions $\text{cm}^{-2}$		
800	---	---	$1.5 \cdot 10^{-15}$	$5.2 \cdot 10^{-16}$ (extrapol.)
900	$1.7 \cdot 10^{-14}$	$1.4 \cdot 10^{-14}$	$1.4 \cdot 10^{-15}$	$1.3 \cdot 10^{-15}$ (extrapol.)
1000	$4.8 \cdot 10^{-14}$	$5.2 \cdot 10^{-14}$	$1.8 \cdot 10^{-14}$	$1.7 \cdot 10^{-14}$
1100	$1.9 \cdot 10^{-13}$	$1.5 \cdot 10^{-13}$	---	$1.7 \cdot 10^{-13}$

#### b. Proton Irradiation

In the preceding review, we have examined situations in which the boron-silicon system is near thermal equilibrium conditions. In other words, equilibrium has been achieved with respect to temperature and all possible chemical reactions in the system. We purposely exclude the attainment of equilibrium with respect to the distribution of matter within the system in this definition. In what follows, we turn the attention to the perturbation of the equilibrium condition. First, we discuss the use of protons to create an excess vacancy concentration, and then we compare the differences between a proton enhanced diffusion and the annealing problem with respect to thermal equilibrium.

The purpose of perturbing a system at equilibrium with an excitation is to observe the subsequent response. Generally, a system under perturbed condition will expose the driving forces that will enable the system to return to equilibrium, hence elucidating physical mechanisms hidden under thermal equilibrium conditions. In the boron-silicon

system, the equilibrium condition can be altered by an excess vacancy concentration produced by proton irradiation. Since the production of vacancies that result from collision is a complicated problem, it is pertinent to elaborate upon the conditions under which excess vacancies are produced. Obviously, we want to avoid producing severe damage to the crystal, since in this case the recovery of equilibrium will be a much more complicated matter.

Energetic light ions such as protons or boron produce diffuse disorder clusters. These clusters are isolated because, even at room temperature, there is a certain amount of annealing that prevent the overlapping of individual disorder clusters. In contrast, if the implantation is performed at liquid nitrogen temperature, then the disorder clusters will overlap and an amorphous layer will form. This is a direct consequence of the negligible annealing at low temperature. An amorphous layer is also observed if the implanted ion is heavy. In this case, even if the implantation is carried out at room temperature and the implanted dose is moderate, the size of the disorder clusters are so extended that they will overlap.

In a Proton Enhanced Diffusion (PED), generally the substrate is held at an elevated temperature and the diffusion occurs under a steady proton bombardment. In view of this continuous excitation and the criterion of thermal equilibrium, we can classify the PED as a non-equilibrium-steady state problem. We shall see that the annealing of ion-implanted boron bears some resemblance and some differences with this case. As in the proton case, vacancies produced by the light boron damage give rise to an initial nonequilibrium condition; and, in contrast with the PED case, the perturbation is not at steady state. Hence, annealing of ion-implanted boron is a transient problem with a nonequilibrium initial condition. In this analysis, the simplest case is the ordinary diffusion occurring under thermal equilibrium, then in increasing order of difficulty: PED, a steady state nonequilibrium problem, and finally the annealing of ion-implanted Boron, a transient problem.

This analysis provides a natural way of conceiving how the enhanced diffusion at the outset of the anneal can turn into ordinary diffusion at a later time. In this interpretation, it is simply a transient problem reducing to the thermal equilibrium condition.

Furthermore, it is possible that ordinary diffusion, proton enhanced diffusion, and the annealing of boron are indeed the same problem with different excitation and initial condition. With this preliminary discussion, we turn the attention back to the consequences of a perturbation of the boron-silicon system at equilibrium with proton bombardment.

Fladda et al [11] have shown that substitutional boron in a diffused sample can be rapidly removed from their lattice sites by proton bombardment at room temperature. This same result can be achieved if the diffused sample is replaced by an ion implanted boron doped sample that was fully annealed. However, if an unannealed ion-implanted sample is used, no change in the fraction of substitutional boron can be detected even for proton doses as high as  $10^{17}$  protons/cm<sup>2</sup>. Similar results can be obtained at higher temperatures. Figure 3 shows profiles from a boron diffused sample irradiated by 10 KeV protons at 550°C for two hours, as determined by SIMS and electrical resistivity measurement [12]. The impurity distribution is characterized by the presence of a dip in the electrical carrier profile near the proton range and by some diffusion of the tail of the profile. This dip is not observed in the total boron concentration. The enhanced diffusion of the tail is more pronounced at higher temperatures such as 850°C or 900°C. If the proton dose is increased, then a peak starts to emerge from the bottom of the dip. This peak is attributed [13] to pileup of immobile boron (complexes, precipitates, dislocation trapping, etc.). To elucidate this issue, we analyze the annealing of damage produced by the room temperature irradiation of a  $5 \times 10^{15}$  protons/cm<sup>2</sup> dose on an annealed sample. The transmission electron micrograph shows the formation of lineated defects, that we identify as dislocation dipoles [19].

### c. Profiling Measurements

Figure 4 shows a collection of isochronally annealed Boron profiles (35 min) at 800°C to 1000°C and the corresponding electrical carrier profiles for implantation doses\* of  $10^{14}$  to  $10^{16}$  ions/cm<sup>2</sup>, after

---

\*The calculation based on the integration of the SIMS profiles shows that the actual implanted doses are ~ 30%, ~ 16%, and 30% higher than the nominal doses of  $10^{14}$ ,  $10^{15}$ , and  $10^{16}$  ions/cm<sup>2</sup>.

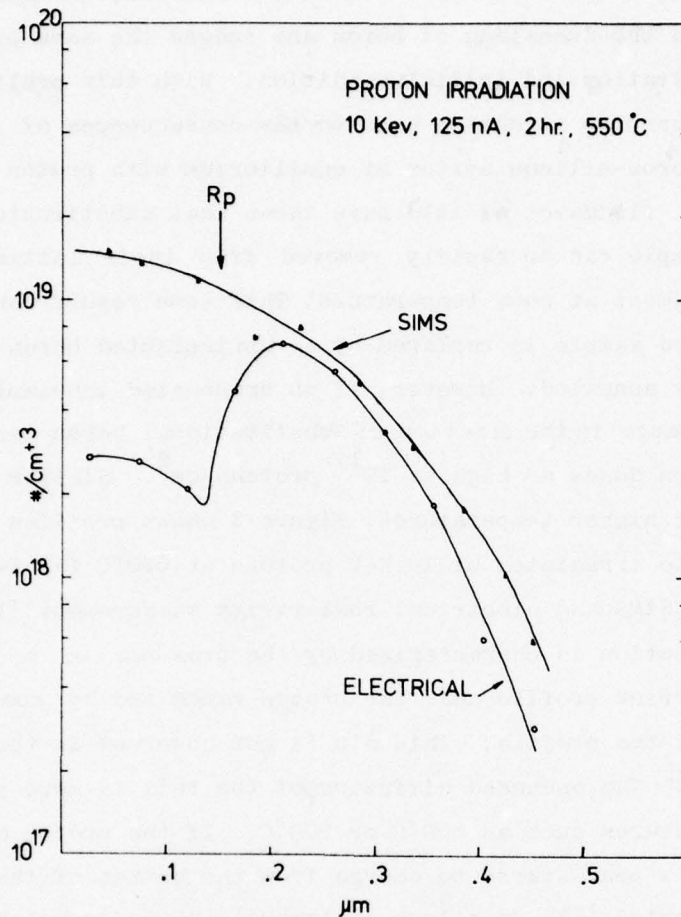


Fig. 3. A COMPARISON OF TOTAL BORON PROFILE DETERMINED EXPERIMENTALLY USING SIMS WITH THE ELECTRICAL CARRIER PROFILE THAT RESULT AFTER TWO HOURS OF IRRADIATION WITH 10 KeV PROTON, AFTER ANDERSON ET AL [12].

Hofker et al [2,14]. Figure 5 displays the juxtaposition of the annealed profiles with the as-implanted boron profiles for each dose, permitting the comparison of the profiles as the annealing temperature is varied (after Hofker et al).

Inspection of these figures indicates that:

- (1) 100% electrical activity is attained after 35 minutes of annealing a temperature of 900 °C or higher and for implanted doses of  $10^{15}$  ions/cm<sup>2</sup> or lower.

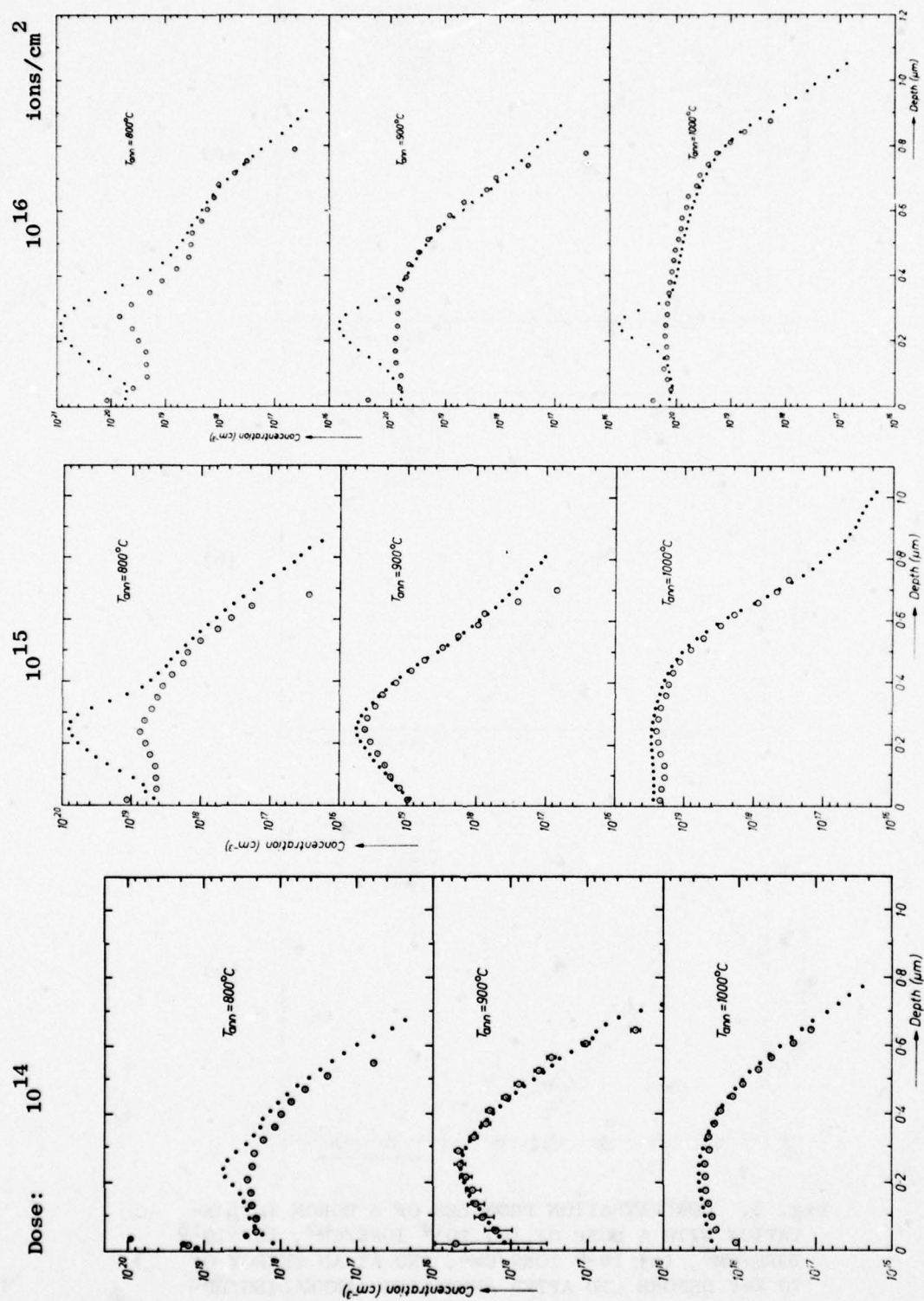
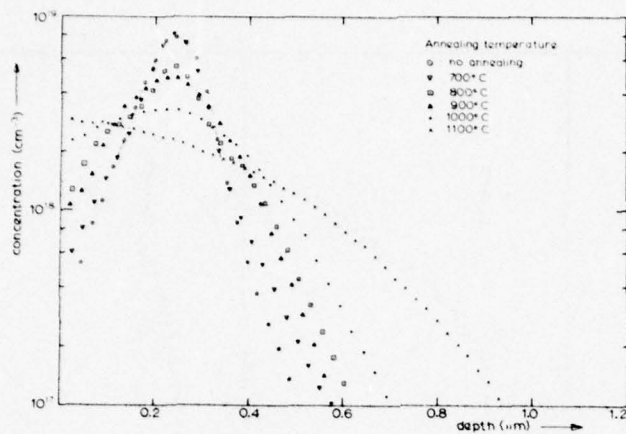
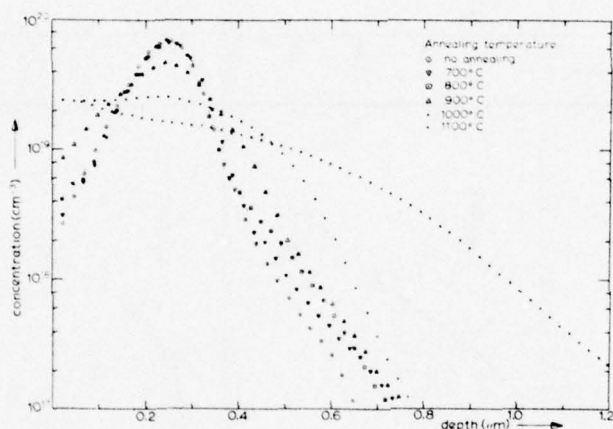


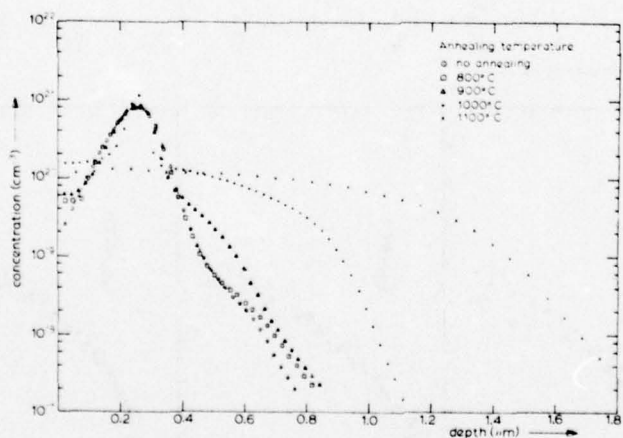
Fig. 4. CONCENTRATION PROFILE OF BORON AND THE CORRESPONDING CHARGE CARRIER PROFILES OBTAINED AFTER ANNEALING AT DIFFERENT TEMPERATURES FOR 35 MIN, AFTER HOFKER ET AL [14].



(a)



(b)



(c)

Fig. 5. CONCENTRATION PROFILES OF A BORON IMPLANTATION WITH A DOSE OF (a)  $10^{14}$  IONS/ $\text{CM}^2$ , (b)  $10^{15}$  IONS/ $\text{CM}^2$ , (c)  $10^{16}$  IONS/ $\text{CM}^2$ , AND AT AN ENERGY OF 70 KeV BEFORE AND AFTER ANNEALING (ANNEALING DURATION: 35 MIN); AFTER HOFKER ET AL [2].

- (2) In the  $10^{16}$  ions/cm<sup>2</sup> cases, the boron peak concentration exceeds solid solubility. Therefore, there will be precipitation of boron.
- (3) In the lower dose cases, when the anneal is carried out at 800°C, there is a fraction of boron that is electrically inactive and does not diffuse, hence similar to a precipitate. However, the boron concentration is below the solid solubility limit for these cases.

## 2. Experiments on the Lattice Location of Boron

The techniques used in the experiments that we will review are really indirect measurements that permit the inference that a fraction of boron is on substitutional sites. For instance, the carriers observed in an electrical resistance measurement are assumed to arise from the ionization of impurity atoms located on substitutional sites. However, substitutionality can also be measured independently by the channeling technique.

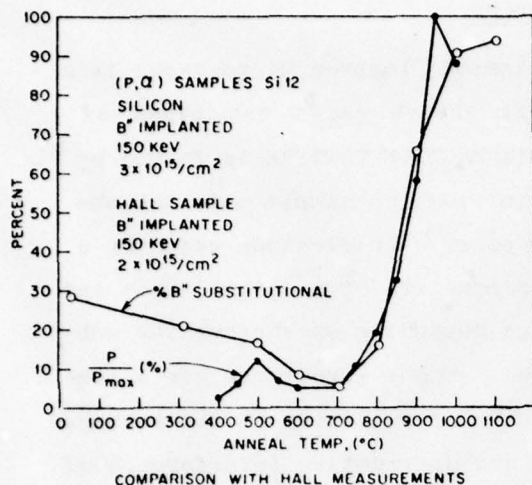
This method is based on the interactions of a low dose proton or Helium ion beam with the crystal lattice. This choice of ions is important because light mass ions at low doses produce negligible damage to the crystal. As a result, the probing ion will contribute with little error to the measurement. The quantitative measurement is based on the detection of backscattered ions with a solid state detector. These backscattered ions are the result of wide angle collisions of the light incident ions with heavier atoms in the substrate. During the measurement, the incident beam is directed along the channels of the crystal, hence the interactions with the substrate come primarily from (low impact parameter) collisions with off-lattice-site atoms (nonsubstitutional atoms). The calculation of the fraction of nonsubstitutional atoms is based on the comparison of the detector yield under channelled condition with the random yield, when the crystal is oriented randomly with respect to the incident beam. The substitutional fraction of atoms is the complementary fraction to unity. There are complicating factors that make the interpretation more difficult. For instance, the presence of lattice damage and flux peaking effects [15] can result in errors that are significant.

#### a. Channeling Experiments

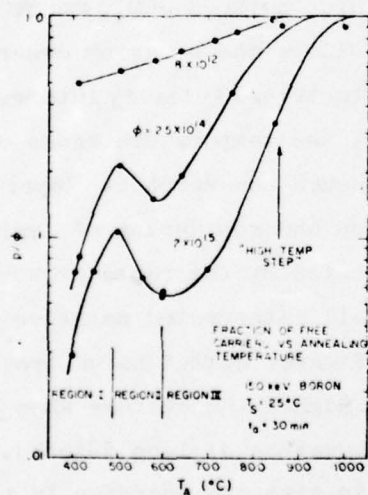
Figure 6a shows the results of a channeling experiment by North and Gibson [16] on the lattice location of ion implanted boron in silicon. They determined that upon isochronal annealing at a sequence of monotonically increasing temperatures, the substitutional fraction of boron decreases first to a small fraction at temperatures between 500°C and 700°C and then it increases smoothly to near 90%, at higher annealing temperatures. Also, in Fig. 6a the fraction of substitutional boron can be compared with the percentage of electrical carriers produced by the implanted impurity dose. The agreement between the two curves is excellent above 700°C. The difference at lower temperatures is attributed by the authors to the compensation effect of intrinsic damage produced by the implantation. Although such an explanation is reasonable and transmission electron micrographs on samples of equivalent preparation do show [17] the presence of a high concentration of vacancy clusters and dislocation loops, there is perhaps insufficient attention given to the consequences of dechanneling of the probing beam by said defects. Certainly, a correction of the data to include this effect will result in a lower fraction of substitutional boron in this region.

Basically, this experiment indicates that annealing proceeds with the conversion of nonsubstitutional, electrically inactive boron into Boron that is electrically active and located on substitutional sites. A more detailed inspection of Fig. 6a reveals that between 500°C and 700°C the electrical activity as well as the concentration of substitutional boron decreases to a minimum. This phenomenon is known as negative or reverse annealing, and occurs near the recrystallization temperature of Silicon for boron implanted in the dose range of  $10^{14}$  to  $10^{15}$  ions/cm<sup>2</sup>. Transmission Electron Microscopy (TEM) work by Bicknell [17] indicates that negative annealing is accompanied by the formation of lineated defects.

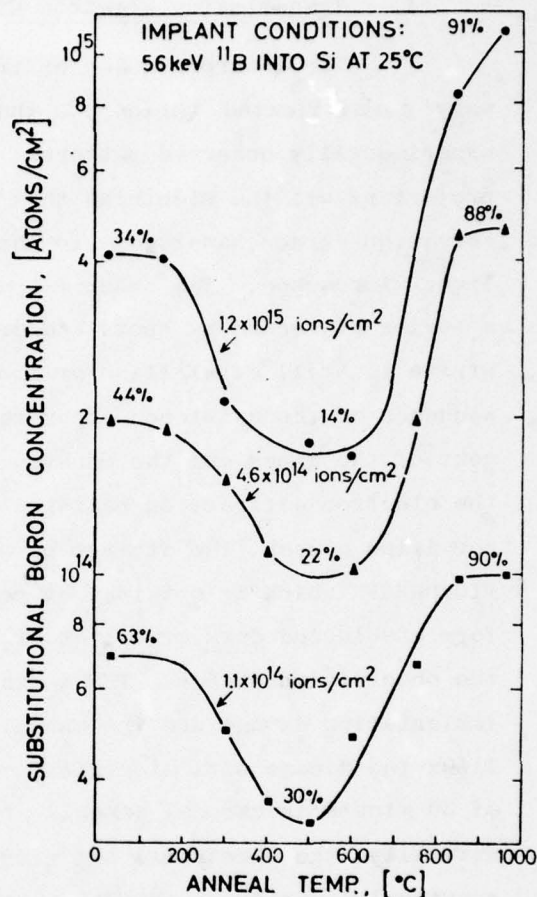
The effect of an increase in dose is a decrease in the fraction of substitutional boron and a lower initial electrical activity. This result is depicted in Fig. 6b after Fladda et al [11] and in Fig. 6c after Seidel and McRae [18].



- a. The percentage of the boron atoms which occupy substitutional lattice sites as a function of annealing temperature. Also shown is the carrier concentration expressed as a percentage of the maximum number of observed carriers determined from Hall measurements on a sample implanted to a fluence of  $2 \times 10^{15}/\text{cm}^2$ . After North and Gibson [15].



- c. Isochronal data in reduced form. The ratio of the free carrier content from Hall measurements to the dose is plotted against the annealing temperature for three doses. The maximum free carrier content is nearly equal to the measured dose  $p_m \approx \phi$ . After Seidel and MacRae [18].



- b. Anneal behavior of 56-keV room-temperature boron implants in silicon. The variation of the substitutional concentration with anneal temperature is shown for three different boron doses:  $\bullet$   $1.2 \times 10^{15}$  ions/cm<sup>2</sup>,  $\blacktriangle$   $4.6 \times 10^{14}$  ions/cm<sup>2</sup>, and  $\blacksquare$   $1.1 \times 10^{14}$  ions/cm<sup>2</sup>. At a few selected temperatures, the substitutional concentration is also given in percent of the implanted dose. After Fladda et al [11].

Fig. 6. EFFECT OF DOSE ON THE FRACTION OF ION IMPLANTED BORON ON SUBSTITUTIONAL LOCATION DURING ANNEALING.

### 3. Transmission Electron Microscopy

The interpretation of transmission electron micrographs is a very sophisticated topic. A thumbnail sketch shows two types of experimentally observed patterns. A DIFFRACTION PATTERN is formed by projecting all the electrons that emerge from the sample onto the observation screen, analogous to the low power magnification case in a light microscope. The observed pattern consists of a central spot and a series of secondary spots and/or rings depending on whether the substrate is still crystalline or amorphous. These structures are a consequence of the existence of or the lack of periodicity in the arrangement of the atoms and the constructive and destructive interference of the electron diffraction patterns from the individual atoms on the observation screen. The other type of pattern is the DARK or BRIGHT FIELD MICROGRAPH which is obtained by permitting only those electrons that form a selected dark or bright area of the DIFFRACTION pattern to reach the observation screen. TEM is an effective technique for the study of implantation damage and the annealing behavior. Bicknell [17] correlated the damage with electrical activity resulting from a succession of 30 minute isochronal anneals at temperatures between 300°C and 1100°C. Naturally, the electrical activity result follows the behavior described previously, namely, a general increase in electrical activity interrupted by reverse annealing between 500°C to 600°C, the temperature range over which amorphous silicon recrystallizes. Although no amorphous layer is produced in this experiment, severe migration and reordering of implantation induced defects occur. This is indicated by the rapid growth of lineated defects in the micrographs. Bicknell interpreted negative annealing as precipitation of boron and the lineated defect as a product of the precipitation. Further annealing at higher temperature show the disappearance of lineated defects and the emergence of loop defects. At even higher temperatures, these loops grow in size and decrease in number. Figure 7, after Bicknell, shows a schematic summary of the result and the interpretation. As mentioned previously, we are interested in the correlation of implantation damage with electrical activity in an isothermal anneal. In particular, we speculate whether the lineated defects will be present in isothermal annealing at 800°C and 900°C for

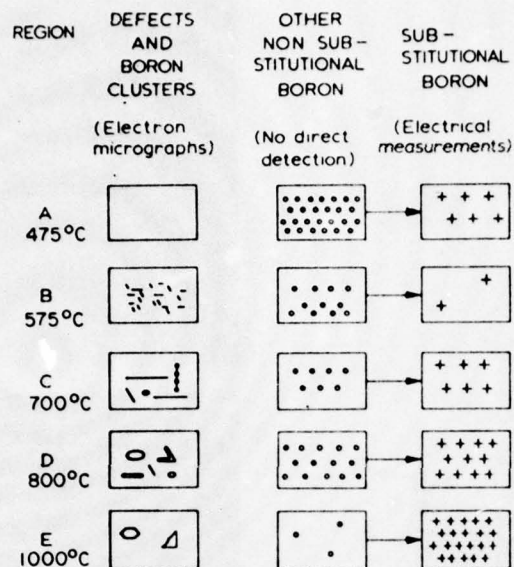
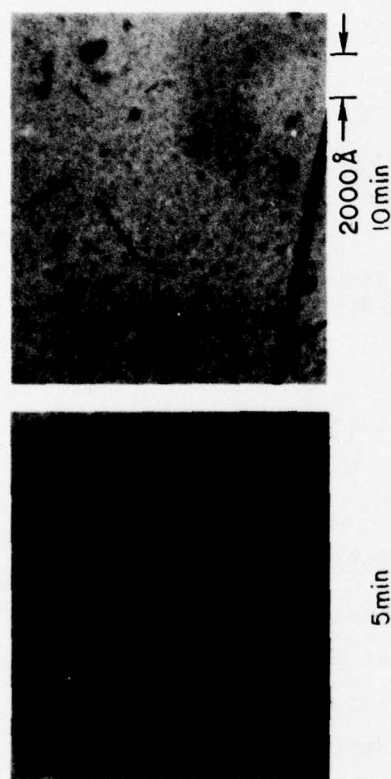


Fig. 7. SCHEMATIC SUMMARY OF RESULTS AND THEIR INTERPRETATION, AFTER BICKNELL [17].

length of time consistent with the electrical activation of boron. Next, we will present the isothermal annealing results.

#### a. The Isothermal Annealing of Implantation Damage

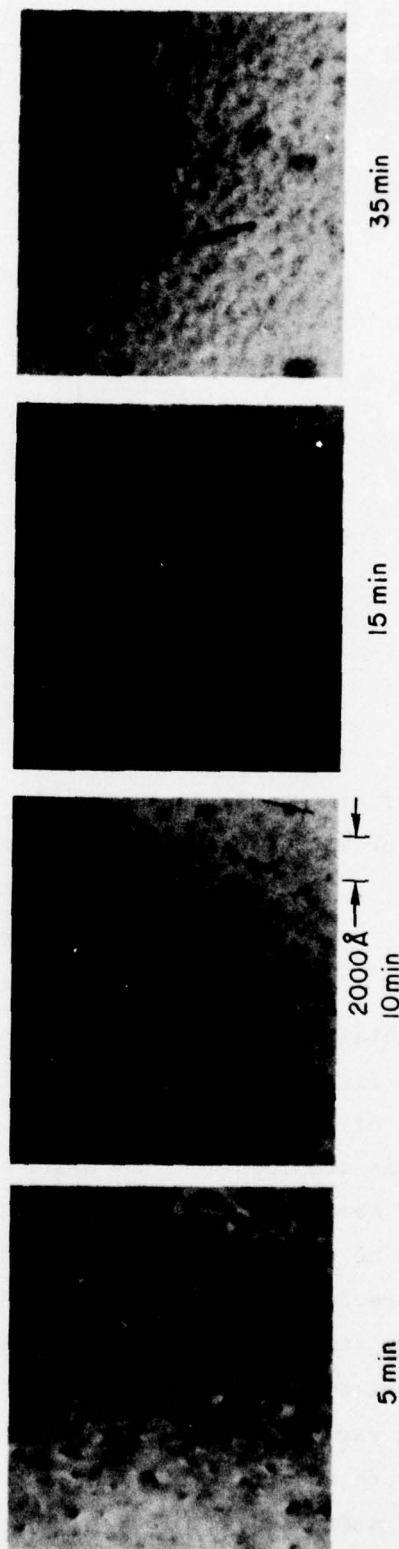
Representative bright field transmission electron micrographs obtained on isothermally annealed samples at 800°C and 900°C are shown in Figs. 8 and 9. The samples were implanted with 70 keV boron to doses of  $10^{14}$  and  $10^{15}$  ions/cm<sup>2</sup>. These implantation and annealing conditions are identical to those of Hofker et al [2,14] and close to those of Seidel and MacRae [18]. Consequently, the present TEM study [19] can be correlated with the electrical activation and profiling work by the previously cited authors. We can identify two distinct damage annealing stages in the 800°C isothermal anneals. The first stage is characterized by the appearance of a high concentration of 150 to 200 Å diameter vacancy dislocation loops inclined to the (100) plane, as shown in Figs. 8b and 9b, at 5 minutes. The maximum loop density occurs at a depth of approximately 1800 Å, in agreement with calculations of the location of the primary loops is estimated to be approximately  $10^{19}$  and  $10^{20}$



5 min

None observable defects at 15 and 35 min

(a)



5 min

15 min

35 min

(b)

Fig. 8. TRANSMISSION ELECTRON MICROGRAPHS OF 70 keV BORON IMPLANTED INTO 100 SILICON AND SUBSEQUENTLY ANNEALED FOR 5, 10, 15, AND 35 MIN AT (a) 900°C AND (b) 800°C; IMPLANTED DOSE =  $10^{14}$  IONS/CM<sup>2</sup>.

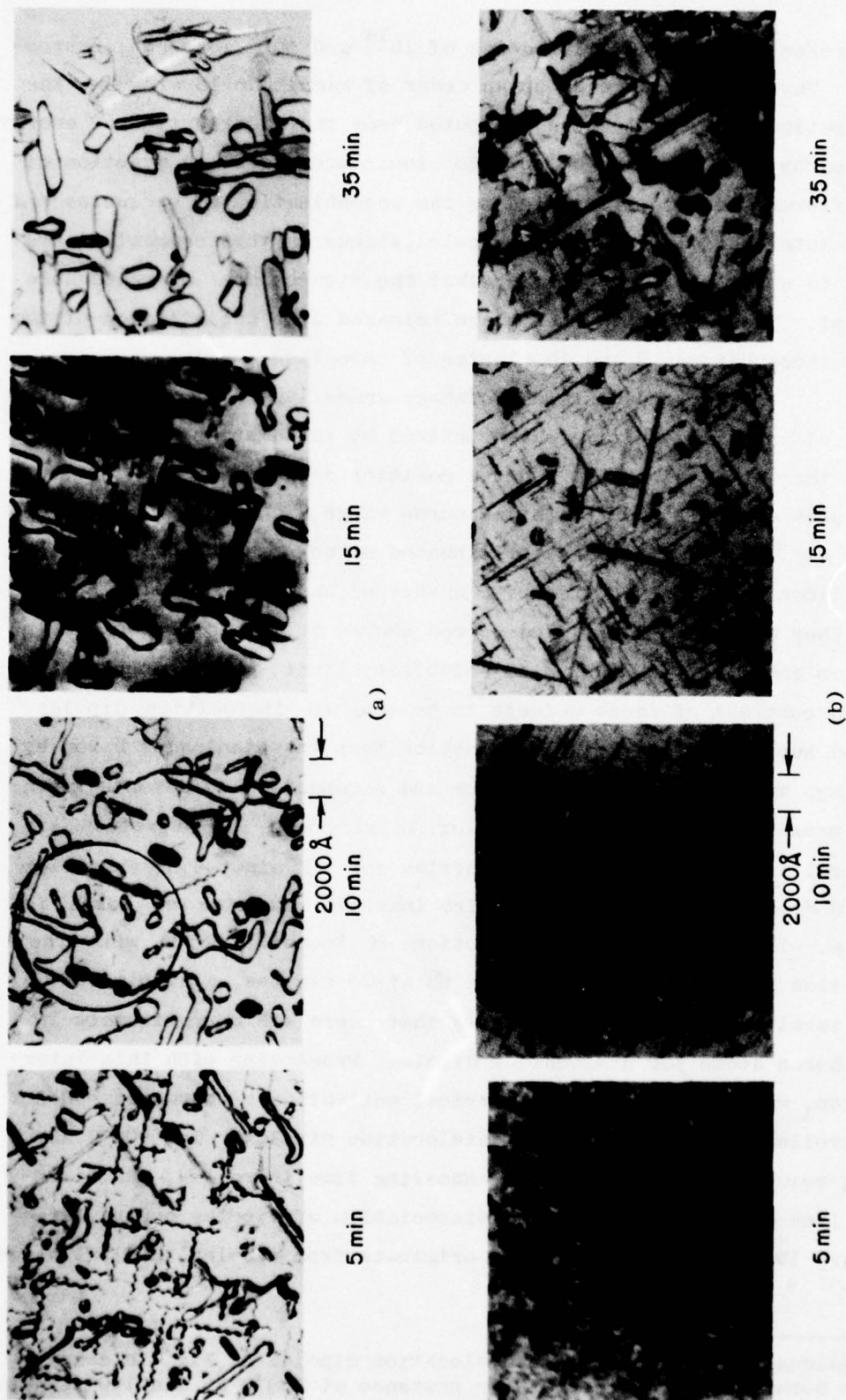


Fig. 9. TRANSMISSION ELECTRON MICROGRAPHS OF 70 keV BORON IMPLANTED INTO 100 SILICON AND SUBSEQUENTLY ANNEALED FOR 5, 10, 15, AND 35 MIN AT (a) 900 °C AND (b) 800 °C; IMPLANTED DOSE =  $10^{15}$  IONS/CM<sup>2</sup>.

vacancies/cm<sup>3</sup> for implantation doses of 10<sup>14</sup> and 10<sup>15</sup> ions/cm<sup>2</sup>, respectively. These figures are about an order of magnitude lower than the concentration of Frenkel Pairs, computed from the distribution of energy deposited by the implanted boron into atomic processes. A fraction of this difference can be attributed to the recombination of vacancies and silicon interstitials. Since both calculations in this comparison are subject to some error, we consider that the figures are in reasonable agreement. These bound vacancies are released upon annihilation of the primary loops between 5 and 10 minutes of annealing.

The second stage of damage annealing appears within 10 minutes of annealing. It is characterized by the emergence of lineated defects that are distributed about a position deeper than the primary damage peak and coincident with the boron range, in agreement with Pelous et al [20]. The presence of lineated structures in boron implanted into silicon has been reported by a number of authors [21-24]. Previously, they have been identified as rod shaped defects or boron precipitates in conflict with the solid solubility limit. We interpret the observed contrast of these defects to be due to dislocation dipoles [25] and support Pelous's [20] suggestion that the pinning of boron by long range interactions between boron and secondary line defects is a likely possibility. The comparison of total boron concentration and electrical carrier concentration profiles for 35 minutes of annealing at 800°C does indicate that the entire inactive fraction of boron is immobile. If we associate this fraction of immobile boron with the dislocation dipoles\* in Figs. 8b and 9b at 35 minutes, a simple calculation involving defect density shows that there are approximately 10<sup>4</sup> pinned boron atoms per dislocation dipole. Proceeding with this interpretation, we reason that the electrical activation of boron at 800°C is controlled by the annealing of dislocation dipoles. The 900°C annealing results indicate that, as annealing time increases, the dislocation line density decreases and dissociation of dipoles occur. Large secondary loops have been shown to originate from dipoles, as illustrated

---

\* The residual damage other than dislocation dipoles in Fig. 2b does not retain boron, as inferred by their presence at 900°C 35 min 100% elect.

(circled region in Fig. 9a). Many of the secondary loops, dislocation ring structures, and arrays remain in the lattice as residual damage after 35 minutes. At this time, the electrical activity is near 100%, therefore, this residual damage does not trap boron. Presumably, at 900°C, the two stages of annealing apparent in the 800°C cases occurred at earlier points in time.

The experimental evidence on hand does not permit a detailed explanation on the exact nature of how these dislocation dipoles trap boron atoms. There are, however, strong indications that the formation of dislocation dipoles require the presence of both a high concentration of Boron and a high concentration of vacancies. For instance, the existence of dislocation dipoles in high concentration diffusions [26] indicates that the formation mechanism requires a boron concentration above a certain level. We can also infer that, in addition to the boron, a large concentration of vacancies is required to form the dislocation dipoles. This deduction follows from the observation that the dislocation dipole density is much higher in the implanted case than in the diffused case. To give further support to this point, we recourse to a micrograph in which various dislocation dipoles are emerging, each one from a vacancy cluster. Furthermore, we performed [19] another irradiation experiment in which an annealed ion implanted sample was subsequently irradiated with protons followed by a short 10 minute anneal at 800°C. The transmission electron micrograph of this sample shows that, prior to the proton bombardment, as described previously, dislocation dipoles formed and annealed out at 900°C. After the  $5 \times 10^{15}$  protons/cm<sup>2</sup> bombardment at room temperature, the micrograph shows that dislocation dipoles were formed again, presumably when the vacancy concentration was greatly increased by the proton irradiation.

Given the number of boron atoms to be associated with a dislocation dipole (approximately  $10^4$  boron/dd), we visualize the impurities as being located in a cloud imbedded in the strain field of the dislocation dipole. Upon annealing, the dislocation dipoles dissociate, releasing the boron atoms. As mentioned in a previous section, as annealing proceeds, some dislocation dipoles produce secondary defect loops and the residual damage that remains in the crystal is ineffective for trapping boron atoms.

### C. The Annealing Model

In the preceding section, we reviewed a group of experiments that encompassed electrical behavior and redistribution of boron under conditions of ordinary diffusion, proton irradiation, and boron introduced in the substrate by ion implantation. Before we develop our annealing model, it is pertinent to highlight some of the models proposed to explain some of these experiments.

As mentioned previously, there is not an unanimous agreement on the nature of the diffusion of boron in silicon. Details of this interstitial-vacancy-controversy are well documented in the literature. Some arguments in favor of an interstitial mechanism can be found in an excellent review article by Seeger and Chick [27], and numerous quantitative models based on the monovacancy mechanism extended to cover different diffusion anomalies are available [28-30]. Basically, a monovacancy mechanism is a single stream diffusion model where the impurity diffusion coefficient is linearly dependent upon the total vacancy concentration. Therefore, substitution of the expression for the variation of the positive vacancy concentration with the Fermi level in the bandgap by Longini and Green [31] yield an impurity diffusion coefficient dependent on the Fermi level, hence on the impurity concentration and/or substrate doping.

Also based on vacancies but in a different manner, recently Anderson and Gibbons [9] proposed a two stream model for the diffusion of boron in silicon. The two species are: substitutional boron and boron vacancy pair.

In this formulation, the diffusion of boron is a weighted process with contributions from a slow and a fast diffusing species, substitutional boron and boron vacancy pair, respectively. And, the charged monovacancies come into play through the following chemical reaction:



For instance, an increase in the positive vacancy concentration with the position of the Fermi level approaching to the valence band edge manifest as a shift of the reaction to the right, hence increasing the population

of BV-pairs, the fast diffusant. This increase, in turn, causes an increase in the overall diffusion. As we can see, this approach can also predict the doping anomalies, and it is possible to derive from this formulation the basic expression in Eq. (1):

$$D/D_1 = P/P_1$$

This two stream diffusion model has also been shown to give reasonable predictions of proton enhanced diffusion. This result is important for two reasons. First, one would expect that a realistic model should apply to both ordinary diffusion and proton enhanced diffusion. Second, because there are many similarities between the PED case and the annealing problem, that it is likely that the basic two stream approach may be applicable to the annealing behavior of ion-implanted boron.

We should also mention at this point that Baruch et al [32] proposed an interstitial counterpart of the two stream diffusion model for the prediction of proton enhanced diffusion. For ordinary diffusion, they propose a shift from the interstitial diffusion mechanism to a vacancy mechanism. Thus far, maybe all three approaches appear to be nearly equivalent, however, when we examine them in regard to the ion-implantation related experiments, it will be apparent that extending the basic two stream model with boron vacancy pairs to include positive vacancies may result in an annealing model capable of predicting the diffusive redistribution of boron during annealing.

#### 1. Choice of Diffusion Model

The single species approach is incapable of accounting for both the substitutional and nonsubstitutional form of boron. In the two stream diffusion approach, the BV-pair or boron interstitial are naturally associated with the nonsubstitutional boron. However, internal friction [33] and photoconductivity experiments [34] have indicated that boron interstitials anneal out near 300°C; therefore, it is unlikely that they are present at 600°C. Recently, Watkins [35] reported the experimental evidence of an Electron Paramagnetic Resonance (EPR) peak that he tentatively identified as related to BV-pairs. However, in his experiments, this peak is only stable up to 260°K.

We are faced with a difficult decision. Until more evidence on the stability and positive identification of the BV-pair is available, we proceed with the examination of the boron-BV-pair two stream diffusion models extended to include the diffusion of vacancies. This extension is necessary because, in general, the migration of vacancies during annealing cannot be safely neglected. In this three-stream diffusion model, the electrical activity becomes the ratio of substitutional boron to the sum of BV-pairs and B substitutional. The stoichiometry of the reaction, namely, one substitutional to boron and one vacancy to form one BV-pair can correspond to the fixed proportion of boron removed from substitutional sites per unit dose of proton irradiation in the experiments by Fladda et al [11]. Furthermore, let us examine qualitatively if the diffusion attributes of the substitutional boron and BV-pair are consistent with the redistribution of ion-implanted boron during annealing. The small fraction of substitutional boron at the outset of the anneal implies a large fraction of BV-pairs, the fast diffusant. Annealing proceeds then with the conversion of nonsubstitutional boron or BV-pairs into substitutional boron as indicated by the experiments on the lattice location of boron. Therefore, the redistribution during annealing is characterized by an initial fast diffusion caused by a large fraction of BV-pairs reducing gradually to a slow diffusion when the population of substitutional boron predominates. This prediction is in agreement with the anomalous transient diffusion observed in annealing experiments. Qualitatively, there is an obvious relation between the overall diffusion coefficient and the electrical activity. Furthermore, if the chemical reaction in Eq. (2) is the dominant annealing mechanism, then it is possible to relate the lifetime of the BV-pairs to the annealing time at a particular temperature. This is the kind of reasoning that we use to determine the values of the parameters in the model; some of them not determined previously, others we will obtain by alternative means.

In summary, the three stream diffusion model appears to contain the global features for explaining the annealing behavior of ion implanted boron into silicon. We shall see later that it will be necessary to extend this model to include other forms of nonsubstitutional boron

in order to predict the annealing behavior under all the annealing temperature and implantation dose ranges that we are interested in.

## 2. The Immobile and Nonsubstitutional Boron

A comparison of the electrical carrier concentration profiles and the total boron profiles for various implantation doses and annealing temperatures is depicted in Fig. 4. It is apparent from the inspection of these cases that, in the high dose and/or low annealing temperature cases, there is a fraction of electrically active boron that is IMMOBILE. This new fraction is present near the peak of the boron profile. In the high dose,  $10^{16}$  ions/cm<sup>2</sup> cases, the boron peak exceeds the solid solubility limit; therefore, the immobile boron is a precipitate. However, in the moderate dose cases, the peak boron concentration does not exceed the solid solubility limit; hence, this immobile boron is not a precipitate in the conventional sense. We propose that this immobile boron consists of boron atoms trapped by dislocation dipoles that form during the annealing.

### D. Development of the Model

In the preceding sections, we reviewed a group of experiments related to ion-implantation and our interpretation of these experiments. In this section, we will use the four species inferred previously (substitutional boron, boron-vacancy pairs, positive vacancies, and immobile boron) to formulate a model capable of describing the overall annealing behavior of boron implanted into silicon at room temperature. Specifically, we wish to explain the redistribution and the electrical activation of the implanted boron. In the course of this discussion, the key attributes in the annealing will be apparent and the global features that result, when the implantation dose and anneal temperature are varied, will also follow naturally.

The cases to be studied are shown schematically in Table 2. In the horizontal direction, we show boron implantation doses varying from  $10^{14}$  to  $10^{16}$  ions/cm<sup>2</sup>. For a 70 keV boron implant, this dose range will lead to peak concentrations between  $10^{19}$  to  $10^{21}$  atoms/cm<sup>3</sup>. In the vertical direction, we show annealing temperature ranging between 800°C to 1000°C.

Table 2

## ISOCHRONAL ANNEALING RESULTS

Annealing Time = 35 min

		Dose: ions/cm <sup>2</sup>		
		10 <sup>14</sup>	10 <sup>15</sup>	10 <sup>16</sup>
Annealing Temperature °C	800	Boron Adsorption Near Profile Peak ~25% Activity		Boron < 16%
	900	Three Stream Diffusion Model Applies		Precipitates when 40%
	1000	(B <sup>-</sup> , V <sup>+</sup> , B <sup>-</sup> V <sup>+</sup> ) 100% Activity		C <sub>B</sub> > C <sub>SS</sub> 65%

When the annealing is performed isochronally for 35 min, in this range of temperatures the electrical activity (at the completion of the anneal) will vary from a small fraction to near 100%, depending on the particular implantation dose and annealing temperature. In other words, the ratio of implanted boron that contribute electrical carriers (holes) to the totality of implanted boron ions is a function of implantation dose, annealing temperature, and time. The understanding of these relationships is one of our principal objectives.

This collection of implantation doses and annealing temperatures illustrated in Table 2 covers a very wide range of conditions. For instance, most applications of ion implantation in device fabrication are performed under conditions represented in the lower left-hand corner of this table. These cases are very relevant because the electrical activities approach to near 100% after 35 minutes of annealing. Among the remaining cases in this table, we can distinguish two groups. The first group is composed of high dose implants represented by the right-hand column of the table. In these cases, the peak impurity concentration

produced by the  $10^{16}$  ions/cm<sup>2</sup> doses exceed the solid solubility limit at all the annealing temperatures in the table. Therefore, boron will precipitate. And, the precipitated phase is characteristic of the high dose implantation cases. The remaining cases are represented in the upper left-hand corner of the table and they are characterized by the trapping of boron atoms by dislocation dipoles that form during the early stages of annealing. At 800°C, these dislocation dipoles do not anneal out completely in 35 minutes. Therefore, they are incapable of releasing the boron atoms trapped in the associated strain fields.

These three groups have distinct characteristics that will manifest in the electrical activation as well as in the redistribution of the implanted boron. In the discussions that will follow, we will select canonical cases representative of each of the aforementioned groups. Our exposition will concentrate on each of the three canonical cases and on the global features in the anneal when implantation dose and annealing temperature are varied.

#### 1. The Typical Annealing Cases

We first examine the  $10^{14}$  ions/cm<sup>2</sup> dose, 70 keV boron implant annealed at 900°C for 35 minutes. This is a relatively simple case. In the insert in Fig. 10a, we depict the silicon surface coincident with the origin of the horizontal axis representing depth in tenth of microns into the substrate material. The 70 keV boron beam is directed toward the surface from left to right. As these energetic ions penetrate the target, their stopping in the substrate is produced by collisions with electrons and host atoms. In this process, some collisions are sufficiently energetic that host atoms are displaced from their lattice sites leaving vacancies behind; the displaced atoms may in turn displace other atoms. This process leaves a disorder cluster around the ion track. The insert in Fig. 10a represents one disorder cluster. Since this collision process is random in nature, not all the implanted boron ions will stop at the same depth. Instead, the ions will come to rest at different depths with different probabilities. Thus, after the implant, the distribution of implanted ions is represented by the impurity concentration profile shown in Fig. 10a. The peak concentration is  $8 \times 10^{18}$  atoms/cm<sup>2</sup> for the  $10^{14}$  ions/cm<sup>2</sup> dose implant in this example.

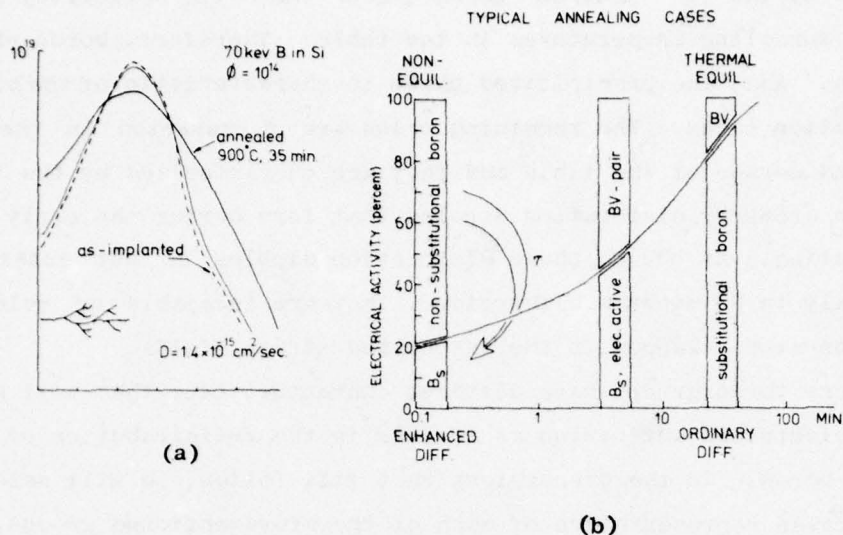


Fig. 10. THE ELECTRICAL ACTIVATION AND REDISTRIBUTION BEHAVIOR OF BORON IN TYPICAL ANNEALING CASES.

The process we just described is far away from thermal equilibrium. Therefore, only a small fraction of boron atoms will be located on substitutional sites, a larger fraction will be on interstitial sites, and other boron atoms will form complexes with simple defects, i.e., vacancies and silicon interstitials. Consequently, the electrical activity at the completion of the implant is far below what one would expect from the implanted dose. This situation is depicted in Fig. 10b at the origin of the time axis, in the horizontal direction. The electrical activity is represented on the vertical axis. At any instant in time, the fraction of boron that contributes to electrical carriers is represented by the ordinate of the electrical activity curve. On the other hand, the nonelectrically active boron is represented above the curve by the distance between the 100% activity line and the ordinate of the curve. Therefore, we can also interpret Fig. 10b as a bar graph describing the relative concentrations of active and inactive boron. In general, the nonelectrically-active boron need not be in a single form; however, in

this particular case, it does appear that all the inactive boron is in the form of boron-vacancy pairs. During annealing, as we can appreciate from observing the monotonic nature of the electrical activity versus time curve, it is possible to relocate the nonactive boron on substitutional sites, hence increasing the electrical activity to near 100% in 35 min. During annealing, a succession of events take place: there is annihilation of vacancies by interstitials, annealing of divacancies, formation of vacancy clusters and vacancy dislocation loops as a means of releasing stress created by the vacancy clusters in the crystal lattice, and, most importantly, there is relocation of inactive boron on substitutional sites accompanied by redistribution. This conversion of electrically inactive boron to electrically active boron is represented in Fig. 10b by the arrow crossing the electrical activity curve which is the boundary between the two forms of boron. As the annealing proceeds, the fraction of electrically active boron increases gradually while the impurity atoms diffuse in the crystalline substrate. Finally, at the end of the 35 min, we find that the implanted distribution has displaced significantly and it is now represented by the deeper boron profile in Fig. 10a. An attempt to predict this diffusive redistribution would be to take the diffusion coefficient of boron in silicon at the annealing temperature of 900°C, which is  $1.4 \cdot 10^{-15} \text{ cm}^2/\text{sec}$ , and use this number to calculate where the implanted profile will diffuse to after 35 minutes have elapsed. This calculation shows that the profile would move only very slightly. Hofker et al [2] show that, in order to fit the experimental profile obtained after the annealing, the diffusion coefficient in the aforementioned calculation has to be increased to  $1.7 \cdot 10^{-14} \text{ cm}^2/\text{sec}$ , which is one order of magnitude higher than the ordinary diffusion rate. These calculations clearly indicate the presence of enhanced diffusion during annealing. Further annealing indicates that the enhanced diffusion is only transitory because, as the electrical activity approaches to 100%, the enhanced diffusion reduces to ordinary diffusion.

## 2. The Spontaneous Conversion of BV-Pairs

At the outset of the anneal, we encounter a nonequilibrium situation characterized by low electrical activity, a large population

of BV-pairs, and enhanced diffusion, see Fig. 10b. On the other hand, at the completion of the anneal, we find a thermal equilibrium situation characterized by high electrical activity, a large population of substitutional boron, and ordinary diffusion. We insert these dichotomous attributes in the figure as mnemonics for our next argument. By inspection of Fig. 10b, we can interpret annealing as a transient process going from a nonequilibrium state toward an equilibrium state in which a large initial population of BV-pairs transform into electrically active substitutional boron. The comparison of the diffusive attributes with the population of BV-pairs and substitutional boron at the outset and end of the anneal lead us to infer that BV-pairs are fast diffusants and substitutional boron are slow diffusants. With this interpretation, the diffusive behavior during annealing becomes a weighted process with contributions from a fast and electrically inactive species, the BV-pair, and a slow and electrically active fraction, the substitutional boron. Hence, a large population of BV-pairs lead to enhanced diffusion, whereas a large population of substitutional boron produces ordinary diffusion.

In summary, annealing is governed by the driving forces that arise from a nonequilibrium state. These driving forces produce the spontaneous conversion of BV-pairs into substitutional boron. And, the electrical activation and diffusive behavior are consequences of the dichotomous attributes of BV-pairs and substitutional boron with respect to electrical activity and diffusion.

### 3. The 'Boron-Boron Vacancy Pair' Reaction

In the preceding section, we concluded that the spontaneous conversion of BV-pairs into substitutional boron governed the annealing behavior. Now, we will examine this conversion problem in greater detail. The transformation of BV-pairs into substitutional boron comes gradually to an end as the equilibrium conditions are attained. We can now address the question whether it is possible to perturb the equilibrium condition and force the transformation in the reverse direction? The answer is yes. It is possible to perturb the equilibrium by implanting protons. Protons are light ions. Therefore, the damage they produce is also light, consisting mainly of simple defects that raise the vacancy

concentration above the equilibrium level. Fladda et al [11] observed that a given dose of protons removes a fixed amount of boron from substitutional sites, rendering the boron electrically inactive. Furthermore, they observed that doubling the proton dose will, in turn, double the number of boron atoms removed from substitutional sites. This correspondence between the number of boron atoms rendered inactive with the proton dose or indirectly with the number of vacancies produced, leads us to infer the existence of a chemical reaction between a substitutional boron and a vacancy. Since BV-pairs are the inactive boron, it is apparent that a substitutional boron reacts with a (positive) lattice vacancy to form a BV-pair. Because the BV-pair is electrically neutral and the substitutional boron is ionized negatively, the presence of the positive vacancy is necessary in order to preserve the conservation of charge in the proposed reaction:



Let us elaborate on the implications of this reaction. We just saw that a proton implant drives the vacancy concentration above the equilibrium level forcing the reaction in Eq. (3) to the right. And, we recall that during annealing the high BV-pair concentration forces the reaction in Eq. (3) to the left. When the reactions in opposing directions cancel each other, the reaction is at equilibrium. Under this special circumstance, a simple algebraic expression exists relating the concentrations of reactants and product:

$$C_{BV} = k_o C_B C_{V+} \quad (4)$$

where  $k_o$  is the equation constant, a function of temperature. Whereas the equality of the members in this equation is indicative of equilibrium, the inequality is a measure of the departure from thermodynamic equilibrium. Consequently, the kinetics of this reaction can be modelled by the driving force represented by the departure from equilibrium and a time constant  $\tau$ , as indicated in Eq. (5):

$$\text{Reaction Rate} = \frac{C_{BV} - k_o C_B C_V}{\tau} \quad (5)$$

This term will be used in the mathematical formulation of the annealing model. The time constant  $\tau$  determines the rate of the BV-pair-substitutional boron reaction. Therefore, indirectly it also determines the rate of the anneal and the diffusive redistribution.

#### 4. The Positively Charged Vacancies

The presence of positive vacancies in this model has important implications. For instance, rearranging Eq. (4), we obtain:

$$\frac{C_{BV}}{C_B} = k_o C_{V^+} \quad (6)$$

In this expression, we can appreciate that the concentration of positive vacancies determines at equilibrium the relative concentrations of active boron and BV-pairs, hence the overall diffusion.

Vacancies exist in the silicon lattice in various charged states. The neutral vacancy is a nonionized flaw; therefore, according to the analysis by Shockley and Moll [36], its equilibrium concentration is a function of the temperature only. We use the expression in Eq. (7), after Seidel and MacRae [37]

$$C_{V_o}^o = 5 \cdot 10^{25} \exp(-1.7 \text{ eV}/KT) \quad (7)$$

The positive vacancy is, on the other hand, an ionized flaw. Consequently, its equilibrium concentration is a function of both temperature and the Fermi level in the bandgap:

$$C_{V_{eq}^+} = C_{V_o}^o(T) \exp\left(\frac{E_{V^+} - E_F}{kT}\right) \quad (8)$$

where

$C_{V_o}^o$  = concentration of neutral vacancies [Eq. (7)]

$E_{V^+}$  = energy level of positive vacancies, 0.35 eV above the valence band edge

$E_F$  = Fermi level

$K$  = Boltzmann constant

$T$  = temperature in degrees Kelvin

The Fermi level is, in turn, dependent on the concentration of active boron through the Fermi-Dirac statistics. It is apparent now that the Fermi level dependence of the concentration of positive vacancies is the mechanism responsible for the high-concentration and substrate-doping anomalies observed in ordinary diffusions under thermal equilibrium conditions.

Under nonequilibrium conditions, if the perturbation is small, the bulk and the surface of the semiconductor will absorb or generate vacancies to restore the equilibrium vacancy concentration. We model the rate for the attainment of equilibrium using the departure from equilibrium as the driving force and a time constant  $\tau_V$ , see Eq. (9):

$$\text{Rate for the Attainment of Equilibrium} = \frac{C_{V^+} - C_{V^+eq}}{\tau_V}$$

where  $\tau_V$  is the vacancy lifetime. The values that  $\tau_V$  take are small compared to other time constants associated with diffusion. Consequently, in those cases where the vacancies are only slightly perturbed, it is possible to approximate that the vacancy concentration is the equilibrium concentration.

Naturally, when the perturbation is large, the aforementioned approximation may no longer be adequate. For instance, Fig. 11 shows the vacancy concentration produced by the implantation of boron ions at 70 keV into silicon. This profile is computed from the number of Frenkel-pairs produced by the implantation; which is, in turn, calculated from the distribution of energy deposited into atomic processes by the energetic ions [38] and by assuming that 12 eV are required to produce a Frenkel-pair. The calculated vacancy profile is many orders of magnitude

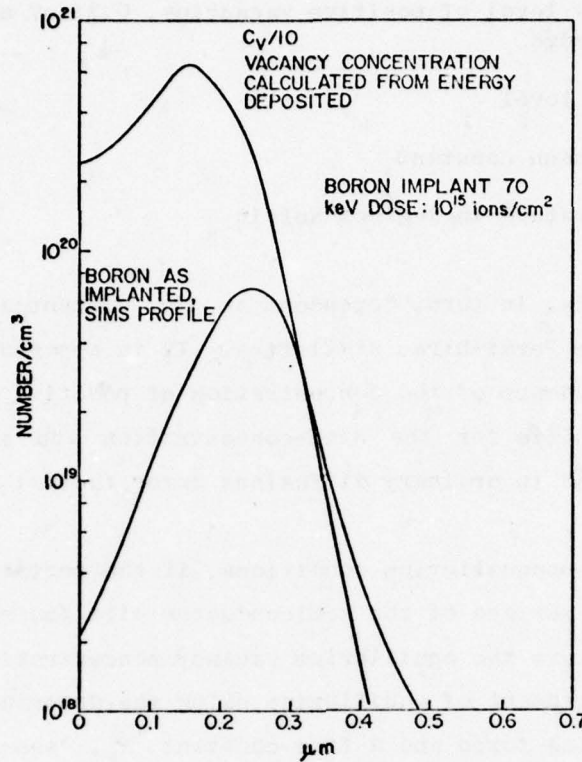


Fig. 11. THE CALCULATED VACANCY CON-  
CENTRATION PROFILE PRODUCED BY THE  
IMPLANTATION OF BORON.

above the equilibrium vacancy concentration. Consequently, the substrate is severely stressed and it is incapable of sustaining such an extraordinary excess vacancy concentration. As a result, the vacancies coalesce in vacancy clusters and vacancy loops to relieve the stress in the lattice. Transmission electron micrographs reveal that bound vacancies will be released from the vacancy clusters and vacancy loops as these defects anneal out and that the background vacancy concentration will reach thermal equilibrium very rapidly. This result is in agreement with the backscattering work by Westmoreland et al [39]. The process we just described can be modelled with the vacancy generation pulse in Eq. (10), that we propose.

$$\text{Vacancy Generation Rate} = k \text{ Damage}(x) \exp(-t/\tau_{\text{DAM}}) \quad (10)$$

In this expression,  $\text{Damage}(x)$  is the vacancy distribution computed from the distribution of energy deposited into nuclear processes,  $k$  is a constant adjusted to produce the total number of vacancies calculated in Fig. 11, and  $\tau_{\text{dam}}$  in the exponential factor determines the duration of the generation of vacancies.

In this section, we modelled three processes that take place during the annealing of room temperature implantation of boron into silicon. These processes are: the release of vacancies from vacancy clusters and vacancy loops, the absorption of vacancies by the bulk and the surface to restore the equilibrium vacancy concentration and the spontaneous breakup of BV-pairs. During the anneal, the great majority of vacancies generated are absorbed by the substrate and the smaller remaining fraction may increase the population of BV-pairs only if the time constant associated with the generation of vacancies is comparable to the lifetime of BV-pairs. At annealing temperatures below  $1000^{\circ}\text{C}$ , the lifetime of BV-pairs is long compared to the duration of the generation of vacancies. Consequently, the boron-BV-pair reaction finds essentially the concentration of positive vacancies at equilibrium. At  $1000^{\circ}\text{C}$  and above, the lifetime of BV-pairs is short; therefore, there is some overlap between the generation of vacancies and the breaking up of BV-pairs. For this reason, the shape of the annealed profile is modified by the localized enhancement in diffusion caused by the vacancies that arise from the annealing of vacancy clusters and loops. This effect is only observable at short annealing times. At longer annealing times, it is masked by ordinary diffusion which is more important at  $1000^{\circ}\text{C}$  and above. It is appropriate to emphasize that this description pertains to the annealing of a silicon substrate implanted with boron ions at room temperature. The behavior of vacancies under implantation conditions that produce an amorphous layer will certainly be different.

The major results in this section can be summarized as:

- (a) Under thermal equilibrium, the concentration of neutral vacancies is a function of temperature only [36].
- (b) Under thermal equilibrium, the concentration of positive vacancies is a function of temperature and the Fermi-level in the bandgap [36].

- (c) Under thermal equilibrium, because the lifetime of vacancies is short compared to other time constants in the diffusion process, it is possible to approximate that the vacancy concentration is the thermal equilibrium concentration.
- (d) During the annealing of room temperature boron implants, it is possible to model the vacancy perturbation arising from the implantation as a vacancy pulse superimposed on a background vacancy concentration at equilibrium with the substrate.
- (e) In many instances, the effect of the vacancy pulse (arising from the annealing of vacancy clusters and vacancy loops) on the overall annealing is not significant. This effect is only apparent in short anneals at high annealing temperature.
- (f) This description of vacancies does not apply to the annealing of boron that is implanted at liquid nitrogen temperature or the case of the implantation of a heavy ion.

#### 5. Summary of the Typical Annealing Cases

Within the group represented by this canonical case, annealing will proceed as described with the following trends as temperature and implantation dose are varied. An increase in annealing temperature will result in a decrease in the reaction time constant. Consequently, annealing will be faster (a shorter transient is equivalent to a faster attainment of equilibrium conditions). An increase in implantation dose produces proportionally higher boron concentrations but lower initial electrical activity as observed by Fladda et al [11] and Seidel and Mac Rae [18]. Therefore, annealing time will be longer than for a lower dose case annealed at the same temperature. This situation holds true until the increased dose causes a peak boron concentration to exceed the solid solubility limit at the annealing temperature. Under these circumstances, annealing will no longer obey the description given above, instead it will follow the global features of high dose cases represented in the left-hand column in Table 2.

We conclude the discussion of the first canonical case which is representative of the cases in the lower left-hand corner of Table 3 by summarizing that:

Table 3  
THE ANNEALING CASES

		Dose: ions/cm <sup>2</sup>		
		10 <sup>14</sup>	10 <sup>15</sup>	10 <sup>16</sup>
Temperature °C	800	Low Annealing Temperature Cases		High
	900	Typical Annealing		Dose
	1000	Cases		Cases

- (a) The species are: substitutional boron, electrically active and a slow diffusant; BV-pair, electrically inactive and a fast diffusant, and positive vacancies.
- (b) A reaction exists between B, BV-pairs, and positive vacancies. The kinetics of this reaction governs the time evolution of the populations of active boron and BV-pairs. Therefore, it also governs the electrical activation and indirectly the redistribution.
- (c) The diffusion of boron is a weighted process with contributions of BV-pairs, the fast diffusant, and substitutional boron, the slow diffusant.
- (d) Under thermal equilibrium, the concentration of positive vacancies is a function of the temperature and the Fermi level in the bandgap.

#### 6. High Dose Cases

The high dose cases are represented in the left-hand column in Table 3. The canonical case representing this group is the 10<sup>16</sup> ions/cm<sup>2</sup> dose implant, annealed at 900°C. In this case, the peak boron concentration is  $8 \times 10^{20}$  atoms/cm<sup>3</sup> and the solid solubility limit at 900°C is  $1.1 \times 10^{20}$  atoms/cm<sup>3</sup>; therefore, we expect the boron atoms to precipitate. The

experimental annealing result shows in Fig. 12a that there is diffusion of the tail in the impurity concentration profile, but the central portion near the peak remained unchanged. Furthermore, in the same figure we can appreciate from the inspection of the annealed electrical carrier profile that the immobile boron is also electrically inactive. At the outset of the anneal, especially at this high dose, the electrical activity is quite low ( $\approx 12\%$ ); therefore, nearly all the implanted boron is electrically inactive. From these facts, we conclude that the composition of the inactive boron is mostly boron precipitate and a much smaller fraction of BV-pairs. The experimental evidence on hand does not indicate whether the boron precipitate is formed directly from the implanted boron once the solid solubility limit is exceeded or whether BV-pairs are first formed and then followed by precipitation. We choose the second possibility for the sake of convenience in our mathematical model. This arbitrary choice does not modify the end result because precipitation takes place very rapidly regardless of the boron source. Consequently, in this interpretation, annealing of this canonical case will proceed as follows. At the outset, the low activity is due to a large fraction of BV-pairs, from which the fraction above the solid

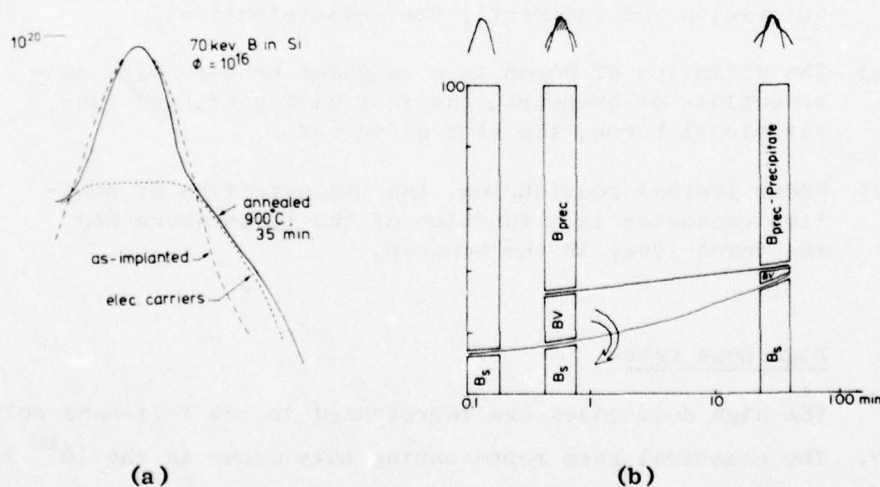


Fig. 12. THE ELECTRICAL ACTIVATION AND REDISTRIBUTION BEHAVIOR OF BORON IN HIGH DOSE CASES.

solubility limit precipitates very rapidly. After a short time, we find the situation depicted in the insert in Fig. 12b: the annealing profile at this time differs very slightly from the implanted profile. Near the profile peak, the boron has precipitated and it is immobile. The remaining boron, which is composed mainly of BV-pairs, has diffused very slightly in this short time. Later in time, annealing proceeds with two mechanisms. One mechanism is the conversion of BV-pairs into electrically active boron accompanied by redistribution as described in the first canonical case. The other mechanism is the dissolution of precipitated boron. The dissolution takes place because the redistribution of boron removes boron from the areas of high concentration, thus upsetting the equilibrium concentrations of precipitated and nonprecipitated boron with respect to solid solubility. This nonequilibrium situation is, in turn, corrected by the dissolution of precipitates. Whereas the B-BV pair reaction reaches equilibrium conditions in the course of annealing, dissolution is a slow process at 900°C and, after 35 min of annealing, there is still a large fraction of boron precipitates. This situation is depicted in the insert to the left in Fig. 12b. The boron precipitate remains essentially unchanged, however, the fraction of BV-pairs diffused as they converted into substitutional boron. Hence, the total boron concentration profile exhibits a shoulder-like structure in agreement with the experiment. Furthermore, we can also predict that subsequent annealing will produce diffusion of the tail of the profile at ordinary diffusion rate because the B-BV pair reaction reached equilibrium conditions, and the electrical activation will be extremely slow because equilibrium with respect to solid solubility is only slightly perturbed by the slow diffusion at 900°C. To elaborate further on this subject, we can contrast this case with a higher annealing temperature case. As the annealing temperature is increased, the solid solubility limit increases and diffusion becomes more important. Consequently, the dissolution of boron precipitates will occur more readily and a higher rate of electrical activation results. For instance, at 1100°C, the electrical activity approaches 100% after 35 minutes of annealing. In summary, annealing of high dose implants occur as a result of two mechanisms. The boron-BV pair reaction governing the redistribution behavior and the dissolution

of boron precipitates governing the annealing time. We model the precipitation and dissolution kinetics by assuming again a rate proportional to the departure from equilibrium as the driving force and a time constant. Thus, the precipitation rate becomes:

$$\text{Precipitation Rate} = + \frac{C_{BV} - \text{Solid Solubility Limit (SSL)}}{\tau_{\text{prec}}} \quad (11)$$

and likewise the dissolution rate results in a more complicated relation:

$$\text{Dissolution Rate} = \begin{cases} C_{B_{\text{total}}} > \text{SSL} & - \frac{\text{SSL} - (C_{BV} + C_B)}{\tau_{\text{diss}}} \\ C_{B_{\text{total}}} \leq \text{SSL} & - \frac{C_{B_{\text{prec}}}}{\tau_{\text{diss}}} \end{cases} \quad (12)$$

The upper branch accounts for the situation depicted in Fig. 13a, in which the fraction of precipitates below the solid solubility limit (SSL) indicated by the bracket should decay to zero. Similarly, the

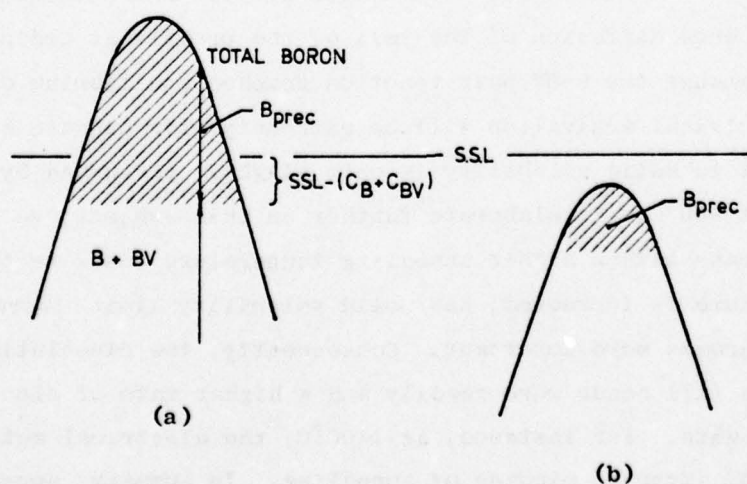


Fig. 13. THE DISSOLUTION RATE OF PRECIPITATES.

lower branch represents the case in Fig. 13b when the total boron concentration is below the solid solubility limit. In this case, if there is a precipitate, it should decay spontaneously to zero.

By inspection of these equations, we can verify that the rates reduce to zero at equilibrium.

## 7. Low Temperature Annealing

We will examine now the low temperature annealing cases in which 'metastable boron precipitates' form as a result of the trapping of boron by dislocation dipoles. The canonical case representative of this group is the  $10^{14}$  ions/cm<sup>2</sup> dose implant annealed at 800°C. In this example, the boron peak concentration is  $8 \times 10^{18}$  atoms/cm<sup>3</sup>, which is below  $10^{19}$  atoms/cm<sup>3</sup>, the solid solubility limit at 800°C. However, the experimental profile that results after 35 minutes of annealing shows again the shoulder-like structure in Fig. 14a. The electrical carrier profile shows a behavior very similar to the high dose cases with the presence of true precipitates. In essence, it appears that there is again a threshold level of concentration, resembling a solid solubility

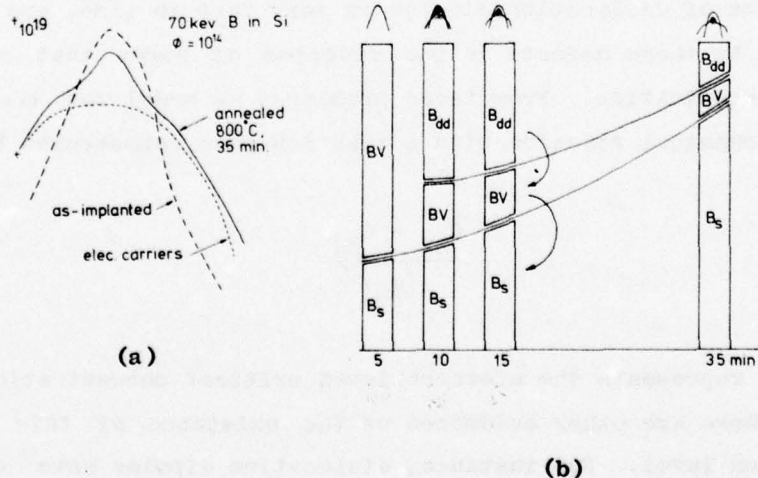


Fig. 14. THE ELECTRICAL ACTIVATION AND REDISTRIBUTION BEHAVIOR OF BORON IN LOW ANNEALING TEMPERATURE CASES.

limit, above which concentration the boron becomes immobile and electrically inactive. The boron in this case is certainly not a precipitate in the conventional sense. An analysis of transmission electron micrographs and electrical activation results indicate that this boron is trapped by dislocation dipoles that form and evolve during annealing. A more detailed description of this issue was given in a previous section. Our objective here is to describe the role and participation of the trapped boron in the low temperature annealing. At the outset of the anneal, the large concentration of vacancies generated by the implantation coalesce into vacancy clusters and loops, as indicated by the 5 minute transmission electron micrograph in Fig. 9b. We assume that the low electrical activity is due to a large concentration of BV-pairs, as shown in Fig. 14b. As annealing proceeds, the micrograph corresponding to 10 minutes of annealing (Fig. 9b) indicates that the vacancy clusters break up and two events take place. One is the migration of vacancies in the bulk and to the surface. The other is the formation of dislocation dipoles in the substrate. The consequences of this annealing stage is the attainment of equilibrium concentration for the vacancies and the trapping of boron atoms by the dislocation dipoles. This is depicted in Fig. 14b, and we can see that the trapped boron, immobile and electrically inactive, is formed at the expense of the BV-pairs. Apparently, the formation of dislocation dipoles is very fast in time, and the boron immobilized by these defects is the fraction of boron that exceeds a critical concentration. From these premises, we model the trapping of boron as a chemical reaction with a reaction rate represented by:

$$\frac{C_{BV} - C_{dd}}{\tau_{dd}} \quad (13)$$

where  $C_{dd}$  represents the aforementioned critical concentration.

There are other evidences of the existence of this critical concentration level. For instance, dislocation dipoles have only been observed in high concentration diffusions and not at lower concentrations. Furthermore, since dislocation dipoles form when they are about 100 Å long (Bicknell et al [17]), we can estimate the concentration

level for which two boron atoms are  $100 \text{ \AA}$  apart. Such a calculation yields a boron concentration of  $10^{18} \text{ atoms/cm}^3$ , which is consistent with the observed threshold.

Once the boron has been trapped by the dislocation dipoles, further annealing proceeds with two distinct mechanisms. One is the B-BV pair reaction, as in the other cases that we already examined. The other mechanism is the release of trapped boron atoms from the dislocation dipoles as they anneal out. The transmission electron micrograph at 15 minutes of annealing indicates that the dislocation dipoles have decreased in number and increased somewhat in length. Hence, we would expect a release of trapped boron atoms. We do not have clear evidence of how the trapped boron becomes active. However, the faster diffusion, inferred from Table 2 on the behavior of the annealed distribution, appears to indicate that the trapped boron becomes a BV-pair, the fast diffusant. It is conceivable that a vacancy migrates to the neighborhood of a boron atom imbedded in the strain field of a dislocation dipole. When the dislocation dipole is annealing out, the strain field is weakened and the vacancy may approach the boron atom to form a boron vacancy pair. It is also possible that the dislocation dipoles emit vacancies as they anneal out, hence increasing locally the probability for the formation of BV-pairs. The global features characteristic of this case are depicted in Fig. 14b. The inserts below the graph represent schematically the evolution of defects, among which are the dislocation dipoles, capable of trapping boron atoms in their strain fields. In the electrical activity graph, we show, using a bar graph representation, the fractions of immobile boron, BV-pairs, and electrically active boron. The arrows connecting these fractions represent the continuous release of trapped boron from the dislocation dipoles as they anneal out and the conversion of BV-pairs into active boron. The inserts above the electrical activation graph indicate the evolution of the redistribution behavior that results from the presence of immobile boron, BV-pairs (fast diffusant), and substitutional boron (slow diffusant). The shoulder-like structure at annealing times of 15 and 35 minutes are consequences of the immobility of the trapped boron near the profile peak and the mobility of the BV-pairs responsible for the faster diffusion of

the profile's tail. We can appreciate at this point that the major difference between this present case and the high dose case originates from the fact that, whereas the dissolution of boron precipitates in the high dose case is a consequence of the removal of boron from the areas of high concentration, in the low annealing temperature case the release of boron is the result of the annealing of dislocation dipoles. The release of boron from the strain fields associated with the dislocation dipoles is a complicated matter. The individual strain fields may overlap and produce a nonlinear relation between the number of boron atoms associated with a dislocation dipole and the dislocation dipole density. However, as we will see, despite the complexity in the real situation, the simple exponential release rate in Eq. (14) is capable of capturing the key features under consideration:

$$\text{B Release Rate} = \frac{C_{\text{B trapped}}}{\tau_{\text{dd}}} \quad (14)$$

This equation is mathematically identical to the expression for the dissolution of the precipitate when the boron concentration is below the solid solubility limit. Therefore, Eq. (12) can be used in the high dose as well as in the low annealing temperature cases, provided the appropriate parameters are substituted.

Let us examine now the global features of the anneal when implantation dose or annealing temperature are increased with respect to the canonical case that we just studied. An increase in dose produces a proportional increase in the dislocation dipole density. The time evolution of the defects is depicted in Fig. 9b. The principal difference with the canonical case is the formation of residual damage from the annealing of the dislocation dipoles. In contrast with the dipoles, the residual damage does not trap boron atoms. Annealing of the higher dose case at the same annealing temperature of 800°C requires a longer annealing time because a larger fraction of boron is trapped by the defects. The other situation of interest is when the annealing temperature is increased. At a higher temperature, annealing becomes more rapid. For instance, Fig. 8 shows that the dislocation dipole density

after 5 minutes of annealing at 900°C is equivalent to 35 minutes of annealing at 800°C. Presumably, at higher temperature, the sequence of events in the 800°C anneal depicted in the micrographs in Fig. 8b at 5, 10, and 15 minutes occur at earlier times in the 900°C anneal. Consequently, annealing in this case is not dominated by the time required to release the trapped boron but, instead, is governed by the B-BV pair reaction time constant. This is indeed the situation idealized by the first canonical case in which the presence of boron trapped by the dislocation dipoles is assumed to be negligible.

## 8. Summary

We describe in this chapter the annealing behavior of boron that is ion implanted at room temperature into silicon, in the dose range of  $10^{14}$  to  $10^{16}$  ions/cm<sup>2</sup> and annealed in the temperature range of 800°C to 1000°C. This wide range of implantation dose and annealing temperatures include from the typical annealing cases of ion implantation in the fabrication of devices to the unconventional situations in which the annealing is dominated by boron precipitates (high dose implantation) and/or boron trapped by dislocation dipoles (low temperature annealing).

To model the redistribution and electrical activation of boron, we propose a model composed of substitutional boron (electrically active and slow diffusant), boron-vacancy pair (electrically inactive and fast diffusant), and the positively charged vacancy. The overall diffusion of boron is then composed of a slow and electrically active fraction, the substitutional boron, and a fast and electrically inactive fraction, the boron vacancy pair. The diffusive and electrical attributes of boron and the BV-pair enable the overall diffusion of boron to assume the dichotomous characteristics that pertain to the prevalent specie in the diffusion. For instance, the implanted boron react with nearby vacancies to form BV-pairs. This dominant population of BV-pairs is responsible for the low electrical activity and enhanced diffusion at the outset of the anneal. During the anneal, the BV-pairs break up spontaneously into its constituents until the thermodynamic equilibrium is reached. At equilibrium, the opposing rates in the reaction cancel and the remaining

fraction of BV-pairs is small compared to the population of substitutional boron. For this reason, the diffusion is slow and the electrical activity is high at the completion of the anneal. This annealing behavior is characteristic of the typical annealing cases. In order to include the precipitation effects of high dose implants, and the low annealing temperature anomalies caused by the trapping of boron by dislocation dipoles, it is necessary to expand this basic model to include the immobile boron and additional reaction-kinetic terms. In the next chapter, we will utilize these premises to formulate a mathematical model for the annealing of ion implanted boron at room temperature, under the described conditions of implantation dose and annealing temperature.

## Chapter II

### THE ANNEALING MODEL

In this chapter, we will develop the mathematical model for predicting the annealing behavior of ion implanted boron into silicon. Because annealing is a very complex problem, the first chapter was devoted to the description and definition of the problem, to the analysis of relevant experiments pertinent to annealing. From these experiments, we inferred the key attributes of the annealing problem. The results of these inferences are summarized in Table 4. In the left-hand side of the table, we show the species and their electrical and diffusive characteristics. To the right, we indicate the reactions the species participate in, which annealing behavior a particular reaction determines, and when this reaction prevails. It is apparent that the kinetics of the dominant reaction and the electrical and diffusive attributes of reactants and products determine the electrical activation and the redistribution features, respectively. For this reason, it is important to relate the reaction that prevails with the corresponding implantation and annealing conditions. This cross-reference is provided by Table 3, which is repeated here from the preceding chapter.

Table 3

#### THE ANNEALING CASES

		Dose: ions/cm <sup>2</sup>		
		10 <sup>14</sup>	10 <sup>15</sup>	10 <sup>16</sup>
T e m p e r a t u r e  °C	800	Low Annealing Temperature Cases		High
	900	Typical Annealing		Dose
	1000	Cases		Cases

Table 4

## KEY ATTRIBUTES IN THE ANNEALING PROBLEM

Species	Symbol	Diffusant	Electrically	Reaction	Determines	Dominant
Substitutional Boron	B	slow	active	$B^- + V^+ = B^- V^+$	Redistribution behavior and electrical activation of mobile boron	ORD DIFF ENH DIFF Annealing in the absence of precipitates and disl. dip.
Positive Vacancies	$V^+$	fast	active			
Boron Vacancy Pair	BV	fast	inactive			
B Precipitate	$B_{PREC}$	immobile	inactive	Precipitation dissolution	Equilibrium of high dose implements	Ann. in the presence of precp.
Trapped Boron	$B_{DD}$	immobile	inactive	Trapping and release of B by disl. dip.	Equilibrium of low annealing temperature	Ann. in the pres. of disl. dip.

### A. The Mathematical Model

The quantitative description of the ideas summarized in Table 4 is represented below by Eq. (15). In essence, this set of equations performs the bookkeeping of each of the species in time and space with regard to entries such as diffusion, chemical reactions, etc.

RATE OF CHANGE IN CONC.	DIFFUSION	REACTIONS	
$\frac{\partial C_B}{\partial t}$	$= D_B \frac{\partial^2 C_B}{\partial x^2}$	$- \text{REAC}$	(15a)

$\frac{\partial C_{V^+}}{\partial t}$	$= D_V \frac{\partial^2 C_{V^+}}{\partial x^2}$	$- \text{REAC}$	$- \left\{ \begin{smallmatrix} \text{DISS} \\ \text{REL} \end{smallmatrix} \right\} + \text{GEN} - \text{EQ}$	(15b)
---------------------------------------	---	-----------------	---	-------

$\frac{\partial C_{BV}}{\partial t}$	$= D_{BV} \frac{\partial^2 C_{BV}}{\partial x^2}$	$+ \text{REAC} - \left\{ \begin{smallmatrix} \text{PREC} \\ \text{TRAP} \end{smallmatrix} \right\} + \left\{ \begin{smallmatrix} \text{DISS} \\ \text{REL} \end{smallmatrix} \right\}$	(15c)
--------------------------------------	---	--	-------

$\frac{\partial C_{Bi}}{\partial t}$	$=$	$+ \left\{ \begin{smallmatrix} \text{PREC} \\ \text{TRAP} \end{smallmatrix} \right\} - \left\{ \begin{smallmatrix} \text{DISS} \\ \text{REL} \end{smallmatrix} \right\}$	(15d)
--------------------------------------	-----	--	-------

where

$C$  = atomic concentration in  $\#/\text{cm}^2$

$D$  = diffusion coefficient in  $\text{cm}^2/\text{sec}$

and the subscripts denote

$B$  = substitutional boron, electrically active

$V^+$  = positively charged vacancy

$BV$  = boron vacancy pair

$Bi$  = immobile boron, a boron precipitate in the high dose implantation cases or a boron trapped by dislocation dipoles in the low temperature annealing cases

The brackets in Eq. (12) denote alternative choices. The upper selection in the brackets corresponds to high dose implantation cases, and the lower selection pertains to low annealing temperatures. The analytical expression of the various reactions in Eq. (15) are summarized in Eq. (16).

$$\text{REAC} = - \frac{C_{BV} - k_o C_B C_{V^+}}{\tau} \quad (16a)$$

$$\text{PREC} = \frac{C_{BV} - C_{SSL}}{\tau_{\text{PREC}}} \quad (16b)$$

$$\text{TRAP} = \frac{C_{BV} - C_{DD}}{\tau_{DD}} \quad (16c)$$

$$\text{DISS} = \begin{cases} C_{B_{\text{TOTAL}}} > C_{SSL} & - \frac{C_{SSL} - (C_{BV} + C_B)}{\tau_{\text{DISS}}} \\ C_{B_{\text{TOTAL}}} \leq C_{SSL} & - \frac{C_{Bi}}{\tau_{\text{DISS}}} \end{cases} \quad (16d)$$

$$\text{REL} = - \frac{C_{Bi}}{\tau_{\text{REL}}} \quad C_{B_{\text{TOTAL}}} < C_{SSL} \quad (16e)$$

$$\text{GEN} = \frac{\text{Damage}(x)}{\tau_{\text{DAM}}} \exp(-t/\tau_{\text{DAM}}) \quad (16f)$$

$$\text{EQ} = \frac{C_{V^+} - C_{V_{\text{eq}}^+}}{\tau} \quad C_{V_{\text{eq}}^+} = C_{V_o} \exp\left(\frac{E_{V^+} - E_F}{kT}\right) \quad (16g)$$

where

$k_o$  = equilibrium constant, a function of temperature only ( $\text{cm}^3$ )

$\tau$  = reaction time constant

$C_{SSL}$  = solid solubility limit, function of temperature

$C_{DD}$  = concentration threshold for the formation of dislocation dipoles

$\tau_{PREC}$  = precipitation time constant

$\tau_{DD}$  = time constant for the trapping of boron by dislocation dipoles

$\tau_{DISS}$  = time constant for the dissolution of B precipitate

$\tau_{REL}$  = time constant for the release of boron from the dislocation dipoles that anneal out

Damage(x) = primary damage profile computed from the energy deposited into nuclear processes

$\tau_{DAM}$  = time constant for the release of vacancies from vacancy clusters

$C_{V+eq}$  = equilibrium concentration of positive vacancies

$\tau_V$  = lifetime of vacancies

$C_{V^0}$  = equilibrium concentration of neutral vacancies

$E_{V+}$  = energy level of positive vacancy in the band gap

$E_F$  = Fermi energy level

$K$  = Boltzmann constant

$T$  = temperature in degree Kelvin

The reasons for representing boron precipitates (high dose implants) and boron trapped by dislocation dipoles (low annealing temperatures) as one single species in Eq. (15) are threefold. First, we recall that boron precipitates and trapped boron are both electrically inactive and immobile. Second, a comparison of Eq. (16b) with (16c) and Eq. (16d) with (16e) reveals that, with the exception of the parameters, the analytical expressions are respectively identical. Third, the only case in which boron precipitate and trapped boron are simultaneously present is when the  $10^{16}$  ions/cm<sup>2</sup> dose boron implant is annealed at 800°C. In this case, the electrical activation of boron due to the release of boron trapped by dislocation dipoles is so slow that the distinction between the two forms of boron becomes unnecessary. In this case also, the diffusion is so slight

that the dissolution of boron precipitates is negligible (see Fig. 5). In other cases, either boron precipitate or trapped boron is present. Consequently, by defining the immobile boron to represent either boron precipitate or trapped boron, we do not lose generality and we do gain simplicity in the mathematical formulation of the model.

In summary, we propose a mathematical model for predicting the redistribution and electrical activation of ion implanted boron that is subsequently annealed. The general model in Eq. (15) is aimed toward solving the annealing problem under the implantation and annealing conditions in Table 3. These conditions are by no means too restrictive; in fact, most applications fall into the subcategory of "typical annealing cases" in Table 3. To solve the simple annealing cases, as discussed in Chapter I, only three species are required. Consequently, Eq. (15) can be simplified by dropping the last equation and the associated coupling terms from the remaining equations. The importance of this simpler case is threefold. First, the annealing mechanism in this simpler case is also present in more complicated cases. Second, in these cases, after 35 minutes of isothermal annealing, the enhanced diffusion reduces to ordinary diffusion. Hence, this set of equations should also apply to ordinary diffusion if appropriate initial conditions are used. Third, the enhanced diffusion mechanism at the outset of the anneal is also responsible for the enhancement in diffusion produced by proton implants. Consequently, the three species model should be capable of predicting ordinary diffusion, proton enhanced diffusion, and the simpler annealing cases in Table 3. And, if the three species model is extended to include boron precipitate and boron trapped by dislocation dipoles, then the more general model in Eq. (12) can also predict the high dose implant and low annealing temperature cases in Table 3.

Let us outline now the necessary steps for solving the equations of the annealing model. First of all, a set of parameters is to be estimated based on thermodynamic considerations and experimental data. Then we will recall the discussions in Chapter I and establish the initial conditions for the annealing problem. With these elements, we can now integrate the set of coupled partial differential equations. This is an initial value problem, and the solution is implemented using numerical analysis methods

on a digital computer. The results of the integration are concentrations of each of the species as functions of time and space. Details concerning the solution are given in Appendix A. In order to evaluate the effectiveness of the model, we have to compare the calculated results with experimental data. In this respect, while the electrical carrier concentration profile can be compared directly with the calculated active boron profile at corresponding times, the comparison with other experimental data requires some algebraic manipulations. For instance, the total boron concentration determined experimentally using Secondary Ion Mass Spectrometry (SIMS) is to be compared with the summation in Eq. (17).

$$C_{B_{\text{total}}}(x,t) = C_B(x,t) + C_{BV}(x,t) + C_{BI}(x,t) \quad (17)$$

And, the electrical activation curve is to be compared with the spatial integration of the calculated active boron profile in Eq. (18).

$$ea(t) = \int_0^{+\infty} C_B(x,t) dx$$

#### B. The Selection of Parameters

The mathematical model presented in the preceding section is the result of inferences drawn from the discussions in Chapter I. Basically, the complex annealing problem is broken into three simpler cases. Then, the reactions dominant in each of the aforementioned cases are identified. The kinetics of these reactions are then modelled by first order approximations involving parameters with physical interpretations. Our objective in this section is to estimate the numerical values of these parameters.

In typical annealing cases, the problem is less complicated and the experimental data is more abundant. Consequently, it is possible to apply thermodynamic and physical considerations in the estimation of the parameters. Table 5 gives a summary of the estimated values of the parameters, which are functions of temperature only. The last two columns

Table 5

## THE TEMPERATURE DEPENDENT PARAMETERS

Parameter	800 °C	900 °C	1000 °C	D	Q (eV)	Source
$D_B^2$ cm <sup>2</sup> /sec	$7.35 \times 10^{-21}$	$8.32 \times 10^{-19}$	$4.477 \times 10^{-19}$	9000	-5.13	Fairfield et al [40]
$D_V^2$ cm <sup>2</sup> /sec	$9.4 \times 10^{-8}$	$4.5 \times 10^{-7}$	$1.68 \times 10^{-6}$	9	-1.7	Seidel and MacRae [37]
$D_{BV}^2$ cm <sup>2</sup> /sec	$10^{-14}$	$7 \times 10^{-14}$	$3.56 \times 10^{-13}$	$6.65 \times 10^{-5}$	-2.09	
$k_o$ cm <sup>3</sup>	$3.025 \times 10^{-12}$	$1.34 \times 10^{-13}$	$9.68 \times 10^{-15}$	$4 \times 10^{-28}$	+3.3817	
$\tau$ sec	2782	550	140	$1.515 \times 10^{-5}$	+1.76	
$\tau_V$ sec	$10^{-4}$	$10^{-4}$	$10^{-4}$			
$C_{V_o}^3$ #/cm <sup>3</sup>	$5.4 \times 10^9$	$1.25 \times 10^{11}$	$1.75 \times 10^{12}$	$5 \times 10^{25}$	-3.4	Seidel and MacRae [37]

contain the preexponential factors and the activation energies. This set of parameters is the backbone of the annealing model. These parameters control the redistribution and electrical activation of boron. They are the dominant parameters in the ordinary diffusion of boron and in the typical annealing cases of ion implanted boron into silicon. In high dose implantation and low annealing temperature cases, these parameters control the redistribution and electrical activation of the boron arising from the dissolution of boron precipitates or the boron released from the annealing of dislocation dipoles. As discussed previously, the modelling of precipitation and dissolution as well as the trapping of boron by dislocation dipoles and the subsequent release require additional parameters such as solid solubility limits, time constants, and so on. These parameters are generally obtained from more empirical considerations. A summary of all the parameters and their relation to implantation dose and annealing temperature is given in Table 6. In this manner, Table 6 displays mainly the parameters associated with anomalies, while Table 5 contains the parameters controlling the main diffusion mechanism. The data in Table 6 is arranged in six separate groups. Each group is a matrix displaying the behavior of the parameter as implantation dose (horizontal) and annealing temperature (vertical) are varied.

We shall now discuss the methods used in the estimation of the parameters in Tables 5 and 6.

#### 1. Diffusion Coefficients--Only Functions of Temperature

We assume that substitutional boron diffuses by the same mechanism as the self diffusion of silicon. Therefore, we use the self diffusion coefficient of silicon [40] for  $D_B$ . For positive vacancies, we use the diffusion coefficient proposed by Seidel and MacRae [37]. Finally, the diffusion coefficient for BV-pairs is estimated from various diffusion experiments. Hofker and coworkers measure the enhanced diffusion of ion implanted boron after 35 minutes of annealing. The enhanced diffusion coefficient they obtain is shown in the first column in Table 7. Since these are average values, they provide only lower limits for the value of  $D_{BV}$  at the respective temperatures. As an

Table 6

THE RELATION OF THE PARAMETERS TO THE  
IMPLANTATION DOSE AND ANNEALING TEMPERATURE

$$D_B, D_V, D_{BV}, k_O, \tau, \tau_V$$

800			
900			
1000			
	$10^{14}$	$10^{15}$	$10^{16}$

ions/cm<sup>2</sup>

(a)

$$\tau_{DAM} \text{ (sec)}$$

	40 sec	
40 sec	40 sec	40 sec

(b)

$$SSL \text{ (#/cm}^3\text{)}$$

$7 \times 10^{18}$	$7 \times 10^{18}$	$7 \times 10^{18}$
$1.1 \times 10^{20}$	$1.1 \times 10^{20}$	$1.1 \times 10^{20}$
$3.3 \times 10^{20}$	$3.3 \times 10^{20}$	$3.3 \times 10^{20}$

(c)

$$C_{DD} \text{ (#/cm}^3\text{)}$$

$4 \times 10^{18}$	$4 \times 10^{18}$	$4 \times 10^{18}$
	$5 \times 10^{19}$	$1.1 \times 10^{20}$ (SSL)
		$3.3 \times 10^{20}$ (SSL)

(d)

$$\tau_{PREC} - \tau_{DD} \text{ (sec)}$$

1 sec
-------

Arbitrarily small

(e)

$$\tau_{DISS} - \tau_{REL} \text{ (sec)}$$

$2.4 \times 10^4$	$3.6 \times 10^5$	$10^8^*$
	700	$10^8$
		$10^8$

\* Arbitrarily large

(f)

Table 7  
THE ESTIMATION OF  $D_{BV}$

	Enhanced Diffusion Coefficient by Hofker et al (cm <sup>2</sup> /sec)	$D_{BV}$ Estimated from the Dif- fusion of Annealed Profiles (cm <sup>2</sup> /sec)	$D_{BV}$ Estimated from the Ordinary Diffusion Coefficient (cm <sup>2</sup> /sec)	$D_{BV}$ Used (cm <sup>2</sup> /sec)
800°C		$7.5 \cdot 10^{-14}$	$2.51 \cdot 10^{-14}$	$10^{-14}$
900°C	$1.4 \cdot 10^{-14}$ $1.7 \cdot 10^{-14}$	$7 \cdot 10^{-14}$	$6.5 \cdot 10^{-14}$	$7 \times 10^{-14}$
1000°C	$1.5 \cdot 10^{-13}$	$9 \cdot 10^{-13}$	$8.5 \cdot 10^{-13}$	$3.56 \cdot 10^{-13}$

alternative, Anderson and Gibbons estimate the value of  $D_{BV}$  to be  $5.7 \times 10^{-14}$  cm<sup>2</sup>/sec at 750°C from proton enhanced diffusion experiments. Another alternative method of estimating the value of  $D_{BV}$  is based on the following relation between diffusion and electrical activity:

$$D_{\text{exp}} = D_{BV} (1 - \text{electrical activity}) \quad (19)$$

where  $D_{\text{exp}}$  is the diffusion coefficient measured in an experiment, hence the subindex.

The discussion and derivation of this relation is carried out in Appendix B. To estimate  $D_{BV}$ , we solve Eq. (19) under equilibrium conditions. For this reason, we assume that the electrical activity is 98% and we use for  $D_{\text{exp}}$  the experimental diffusion coefficients measured under equilibrium conditions by Hofker et al [2] and Kurtz (see Table 1). The values of  $D_{BV}$  thus estimated are shown in the second and third columns of Table 7, respectively. In the fourth column, we show the values used in the present work.

## 2. The Equilibrium Constant in the Thermodynamic Reaction

At thermal equilibrium, the concentrations of reactants and products of the boron-BV-pair reaction are given by the following thermodynamic equation:

$$C_{BV} = k_o C_B C_V \quad (4)$$

The equilibrium constant  $k_o$  of this reaction can be calculated from Eq. (4) as follows. Under equilibrium conditions, such as in an ordinary diffusion, the electrical activity is near 100%. Assuming again an electrical activity of 98% and rearranging Eq. (4), we obtain the following expression for  $k_o$ :

$$k_o = (C_{BV}/C_B) \left( 1/C_{V+} \right)_{\text{equil., intrinsic}} \quad (20)$$

where  $C_{V+}$  is the equilibrium concentration of positive vacancies under intrinsic conditions. The value of  $C_{V+}$  is obtained from Eq. (8) with the Fermi energy level at the middle of the energy band gap. Consequently,  $C_{V+}$  is a function of temperature only.

This choice of  $C_{V+}$  and the method for selecting  $D_{BV}$  insure that, when the electrical activity reaches 98%, the overall diffusion coefficient will approach to the value obtained from ordinary diffusion experiments under intrinsic conditions. From a different viewpoint, this choice of  $C_{V+}$  is responsible for the modelling of high dose and substrate doping effects by allowing the actual concentration of positive vacancies to alter the position of active to inactive boron [Eq. (6)].

## 3. Equilibrium Concentration of Positively Charged Vacancies

The equilibrium concentration of positive vacancies  $C_{V+}$  is dependent on the energy level  $E_{V+}$ , the Fermi energy level  $E_F$ ; <sup>eq</sup> the temperature  $T$  and the concentration of neutral vacancies  $C_{Vo}$ , which is a function of temperature only [36].

$$C_{V_{eq}^{+}} = C_{V^0} \exp\left(\frac{E_{V^{+}} - E_F}{kT}\right)$$

where  $E_{V^{+}} = 0.35$  eV above the valence band edge. The Fermi level is calculated using approximations to the Fermi-Dirac integral of order 1/2 (Blakemore [41]). Hence, doping degeneracies are accounted for. It is worthwhile to emphasize that the apparent concentration-dependent diffusion coefficient of boron is achieved in this model through the Fermi level. A high substitutional boron concentration shifts the Fermi level closer to the valence band edge, thus increasing the concentration of positive vacancies ( $E_V = 0.35$  eV above the valence band). This, in turn, increases the ratio of BV-pairs to substitutional boron, increasing the overall diffusion of boron.

#### 4. $\tau$ , The Lifetime of BV-Pairs

This parameter is estimated from the diffusion length associated with the BV-pairs, the fast diffusing specie of finite lifetime. If we assume that the distance  $x$  travelled by the profile tail is twice the diffusion length, then we can solve for  $\tau$  in the following expression:

$$x = 2\sqrt{D_{BV}\tau}$$

where the distance  $x$  is measured from the isochronal annealing profiles in Fig. 5a, after Hofker et al. The values of  $x$  at annealing temperatures in the range of 800°C to 1000°C are shown in the first column of Table 8. It is appropriate to comment that the values of  $x$  thus obtained are more representative of the enhanced diffusion at 800°C than at 1000°C. The reason for this is that, for a fixed annealing time of 35 minutes, the contribution of ordinary diffusion is less significant at lower temperatures than at higher temperatures. Consequently, the estimate of  $\tau$  at 1000°C is probably an upper limit. The values of  $\tau$  calculated in this manner using the values of  $D_{BV}$  estimated previously are shown in the second column of Table 8. As a comparison, we

Table 8

## THE ESTIMATION OF THE LIFETIME OF BV-PAIRS

	x Measured from the Annealing of $10^{14}$ Dose Implants ( $\mu\text{m}$ )	$\tau$ Estimated from $D_{BV}$ Used (sec)	$\tau$ Estimated from Enhanced Diffusion Coefficient (sec)	$\tau$ Used (sec)
800°C	0.110	3000	---	2780
900°C	0.079	230	1150	550
1000°C	0.180	270	540	140

repeat the calculation using the enhanced diffusion coefficient determined by Hofker et al; the results of this second estimation are shown in the third column. An alternative way to obtain the value of  $\tau$  is to solve the set of diffusion equations with initial conditions for an ordinary diffusion. Then, the values of  $\tau$  are chosen to fit experimental ordinary diffusion profiles. The values of  $\tau$  we use in the calculations are presented in the fourth column of Table 9.

#### 5. The Lifetime of Vacancies

The lifetime of vacancies is estimated from the diffusion length of vacancies. We use the diffusion length of  $1.78 \times 10^{-6}$  cm at 750°C, after Tsuchimoto et al [42]. The corresponding value of  $\tau_v$  computed from this diffusion length and the diffusion coefficient estimated previously is  $8.3 \times 10^{-5}$  sec, approximately  $10^{-4}$  sec. It is apparent that  $\tau_v$  is much smaller than  $\tau$ . Consequently, provided that this strong inequality is preserved, the annealing calculations will be rather insensitive to the actual value of  $\tau_v$ . For this reason, the lack of more data on the diffusion length of vacancies does not create a problem, and we can use the value of  $10^{-4}$  sec for  $\tau_v$  at all temperatures. It is evident that, if more data were available, then we could have estimated a vacancy lifetime that is temperature dependent.

In summary, with the exception of  $\tau_V$ , which is assumed to be constant, all the other parameters are functions of temperature only. To emphasize this dependence, we use the following representation. The dotted lines within the matrix (a) in Table 6 enclose sets of values that are invariant with implantation dose, but dependent on the annealing temperature. As mentioned previously, the parameters that follow hereafter are associated with anomalies arising from the annealing of implantation damage, high dose implants, and low annealing temperatures.

#### 6. $\tau_{DAM}$ , Damage Annealing Time Constant

This parameter characterizes the time evolution of vacancy clusters during annealing. Figures 9 and 10 show the presence of these vacancy sources in the transmission electron micrographs corresponding to 5 minutes of annealing at 800°C. At 800°C and 900°C, because of the longer lifetime of BV-pairs (> 10 min), the release of vacancies from vacancy clusters (< 10 min) does not alter the boron-BV-pair reaction significantly. On the other hand, at 1000°C the lifetime of BV-pairs is only 140 sec. Consequently, the simultaneous generation of vacancies slows down the conversion of BV-pairs into active boron, prolonging locally the enhanced diffusion. This effect is only observable at high temperatures and short annealing times because, at longer annealing times, it is masked by ordinary diffusion. In our calculations, we use the value of 40 sec for  $\tau_{DAM}$  at 1000°C (see Table 6b).

At lower temperatures, we can deduce from transmission electron micrographs and the lifetime of BV-pairs that the bounds of  $\tau_{DAM}$  are larger than 40 sec and smaller than 550 sec, respectively.

#### 7. Solid Solubility Limit (SSL)

The solid solubility limit is a function of temperature only. Table 6c shows the values we use in the calculation. These values are comparable to the experimental values by Vick et al [43].

#### 8. Threshold Concentration Level for the Formation of Dislocation Dipoles

We use this parameter to represent the trapping of boron by dislocation dipoles. It is obvious that, functionally, this threshold level will produce the desired fraction of electrically inactive and immobile boron that we propose to be trapped by dislocation dipoles. Physically, this parameter represents the composite effects of a sequence of complex events depicted by the transmission electron micrographs; viz., the formation of dislocation dipoles and the trapping of boron. As a consequence,  $C_{DD}$  cannot be obtained from simple physical arguments. The value of  $4 \times 10^{18} \text{ cm}^{-3}$  for  $C_{DD}$  at  $800^\circ\text{C}$  is first obtained from the inspection of Fig. 4 ( $10^{14}$  dose) and then varied to optimize the fit to experimental data. At higher temperatures, in the lower left-hand side of Table 6d, we can infer from the transmission electron micrographs at  $900^\circ\text{C}$  that the formation of dislocation dipoles and their subsequent annealing occurs so rapidly that the effects on annealing are not observable. It is for this reason that the corresponding values of  $C_{DD}$  are not estimated. At the right-hand side of Table 6d, we assume that all the immobile boron are precipitates that arise from exceeding the SSL. For this reason, we use the values of the solid solubility limit for  $C_{DD}$  in this region of the table. Lastly, TEM indicates the presence of dislocation dipoles during the  $900^\circ\text{C}$  annealing in the case of the  $10^{15}$  ions/ $\text{cm}^2$  dose implant. And, we find that, by incorporating the effects of dislocation dipoles in the conventional annealing model, we can improve slightly the fit between the calculated and the experimental profiles. We use the value of  $5 \times 10^{19} \text{ cm}^{-3}$  for  $C_{DD}$  in this case.

#### 9. Time Constants Associated with Precipitation and the Trapping of Boron by Dislocation Dipoles

In the low annealing temperature cases, the sequence of transmission electron micrographs show that the trapping of boron by dislocation dipoles occurs early during annealing. In the high dose implant cases, we assume that the precipitation of boron takes place rapidly.\*

---

\*It is possible that precipitation has occurred prior to annealing.

For these reasons, the only requirement for the value of this time constant is for it to be small. We choose both parameters to be 1 sec arbitrarily.

10. Time Constant Associated with the Dissolution of Precipitates and the Release of Boron from Dislocation Dipoles

In the high dose implant cases, the dissolution is so slow compared to the 35 minute anneal that  $\tau_{DISS}$  is chosen to be  $10^8$  sec, an arbitrarily large value. In the low annealing temperature cases, we estimate  $\tau_{REL}$  from the electrical activation data by Seidel and MacRae [18]. According to these authors, the time to reach 90% electrical activity at 800°C are  $6 \times 10^3$  and  $1.8 \times 10^5$  sec for implantation doses of  $10^{14}$  and  $10^{15}$  ions/cm<sup>2</sup>, respectively. We use the values of  $2.4 \times 10^4$  and  $3.6 \times 10^5$  sec in the calculation.

In summary, Table 6 presents the global features of the annealing problem by displaying the relation of implantation dose and annealing temperatures to the parameters in the model, hence to the various mechanisms that prevail during annealing. The parameters associated with the annealing of damage, high dose implants, and low annealing temperatures are estimated from a more limited amount of data. Functionally they account for the formation of the immobile and electrically inactive phase of boron and the subsequent transformation into BV-pairs. Hereafter, the behavior of the BV-pairs is governed by the set of parameters in Table 5. This other subset of parameters describe the redistribution and electrical activation of ion implanted boron. They describe ordinary diffusion with high dose anomalies. They describe the enhanced diffusion of boron and subsequent reduction to ordinary diffusion. And, they describe the enhancement in diffusion produced by proton implants. This subset of parameters in the model encompass the main issues in the annealing problem and their importance cannot be overstated.

C. The Initial Conditions

To solve the initial value problem described by the set of coupled partial differential equations, we need the following:

- (a) a set of parameters as estimated in the preceding section
- (b) a set of initial conditions, one for each of the independent variables:

$$\begin{aligned}
 &C_B(x,t) \\
 &C_{BV}(x,t) \\
 &C_{V^+}(x,t) \\
 &C_{BI}(x,t)
 \end{aligned}
 \quad \text{for } t = 0 \quad (22)$$

Naturally, the initial conditions are particular to a specific problem. In this section, our objective is to elaborate on those initial conditions pertinent to the annealing of B in Si.

The detailed discussion with regard to the overall annealing behavior can be found in Chapter I. In that discussion, special attention is devoted to the state of the boron-silicon system at the outset of the anneal. In particular, the initial state of the silicon substrate containing the as-implanted boron atoms is carefully analyzed. For this reason, we can formulate the initial conditions of interest by simply recalling the results in Chapter I.

The as-implanted profile as determined by secondary ion mass spectrometry is shown in Fig. 11. The vacancy concentration profile is calculated from the Frenkel-pairs produced by the 70 KeV incident boron ions as they deposit energy into atomic processes [38] along their trajectories. In what follows, we will make the conservative assumption that as the boron atoms come to rest they will all combine with nearby vacancies to form BV-pairs, which are electrically inactive. Hence, at the outset of the anneal, the electrical activity is zero. Although a nonzero activity is more reasonable, it will also require an initial profile for the electrically active boron. At present, we do not wish to introduce this unknown. In other words, the initial profiles of boron and BV-pair are the null and the as-implanted profiles, respectively. With regard to the immobile boron present in high dose implant and low annealing temperature cases, we assume that the initial concentration profile is identically zero. This is in agreement with the

transmission electron micrographs of samples annealed at low temperatures for short times (Figs. 9 and 10). However, for the case of the precipitates present in high dose implants, this is strictly an assumption. An alternative approach of assigning fractions of the as-implanted boron profiles to the BV-pairs and immobile boron could be as adequate. Transmission electron micrographs also indicate that the high vacancy concentration in Fig. 11 will condense first into vacancy clusters and vacancy dislocation loops imbedded in a background of vacancies at equilibrium concentration. Then, these defects will anneal, transform, and release vacancies very rapidly. For this reason, we use the equilibrium concentration of positive vacancies as the initial condition. In most instances, the release of vacancies from the annealing defects has little overlap in time with the boron-BV-pair reaction. Therefore, the effects are negligible. And, when the vacancies released from the vacancy clusters and dislocation loops do interact with the annealing, we use the generation term in the vacancy equation to model a pulse of vacancies that is distributed in space in accordance with the energy deposition profile.

In summary, the initial conditions are:

$$\begin{aligned}
 C_B(x,0) &= 0 \\
 C_{BV}(x,0) &= \text{As-Implanted Boron Profile} \\
 C_{V^+}(x,0) &= C_{V_{eq}^+}(E_F) \\
 C_{BI}(x,t) &= 0
 \end{aligned}
 \tag{23}$$

We recall that the primary input to the model is the history of the substrate summarized by two distributions: the as-implanted boron profile and the distribution of energy deposited into nuclear processes by the boron ions. We can appreciate now that, in this implementation of the annealing problem, the as-implanted B profile becomes an initial condition, while the energy deposition profile becomes the space dependence of the vacancy generation term.

### Chapter III

#### COMPARISON OF CALCULATED AND EXPERIMENTAL RESULTS

With the choice of parameters and initial conditions described in the preceding chapter, we can proceed to solve the annealing behavior of ion implanted boron into silicon. The results of the calculations corresponding to the cases in Table 3 can be structured in three canonical groups:

- (1) typical annealing cases
- (2) high dose cases
- (3) low annealing temperature cases

Each group has characteristic features that are manifest in the equations, reaction kinetic terms, and parameters. And, these characteristics features are consequences of special conditions present at certain implantation dose and/or annealing temperatures. For these reasons, we present the results of the calculations following the same organization.

##### A. Typical Annealing Cases

The result of the calculation with the initial condition corresponding to the  $10^{14}$  ions/cm<sup>2</sup> dose implant and the parameters for the 900°C anneal is shown in Fig. 15. The atomic concentration is represented on the vertical logarithmic scale, and the depth in microns into the silicon substrate is represented linearly on the horizontal axis. The as-implanted profile determined experimentally by Hofker et al [2] is represented by the dotted line. Upon annealing, the BV-pairs in this profile diffuse and convert into substitutional boron. Hence, a sequence of electrically active boron profiles will develop with time. Figure 15 shows calculated profiles after 1, 3, 10, and 35 minutes of annealing with corresponding electrical activities of 10, 28, 65, and 94 percent. The total boron concentration at 35 minutes is represented by triangles; the fit to the solid line representing the experimental SIMS profile is excellent. Since the ordinary diffusion of boron at 900°C would only

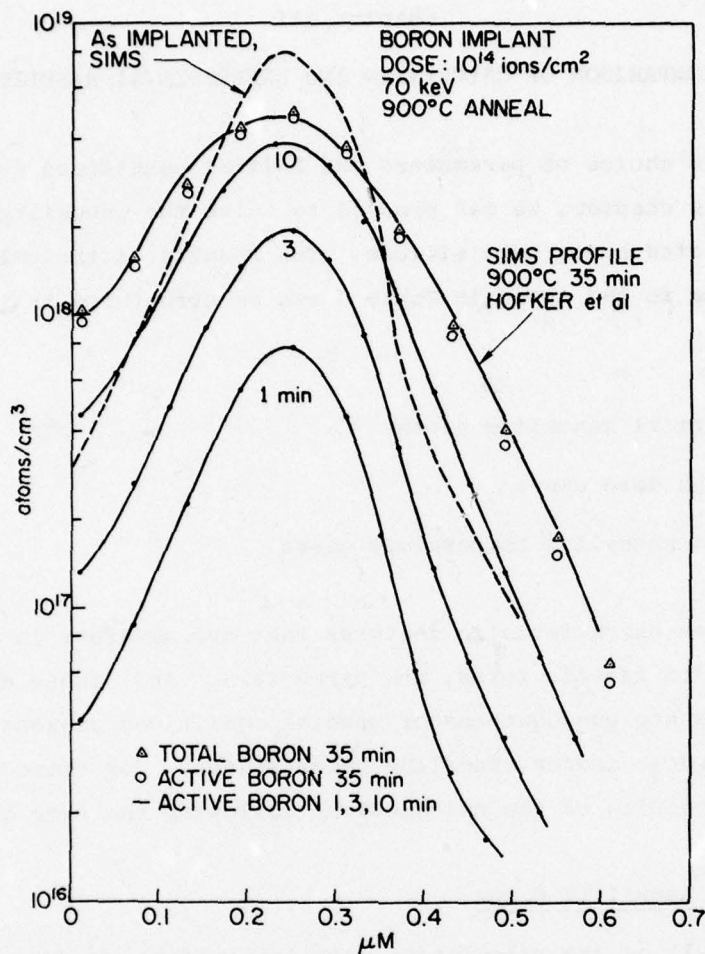


Fig. 15. THE ANNEALING OF A  $10^{14}$  IONS/CM<sup>2</sup> DOSE B IMPLANT AT 900°C. The comparison of calculated and experimental results.

modify the as-implanted profile very slightly, the fit between the calculated results and the deeper experimental profile is indicative of the existence of enhanced diffusion which progressively diminishes to the ordinary diffusion rate as the electrical activity approaches 100%. The calculated results are thus in good agreement with the experimental observations of Hofker and coworkers [2].

Figure 16 shows the results of the calculation for the  $10^{15}$  ions/cm<sup>2</sup> dose, which produces an order of magnitude increase in the impurity and damage profiles. We show again the evolution of the calculated

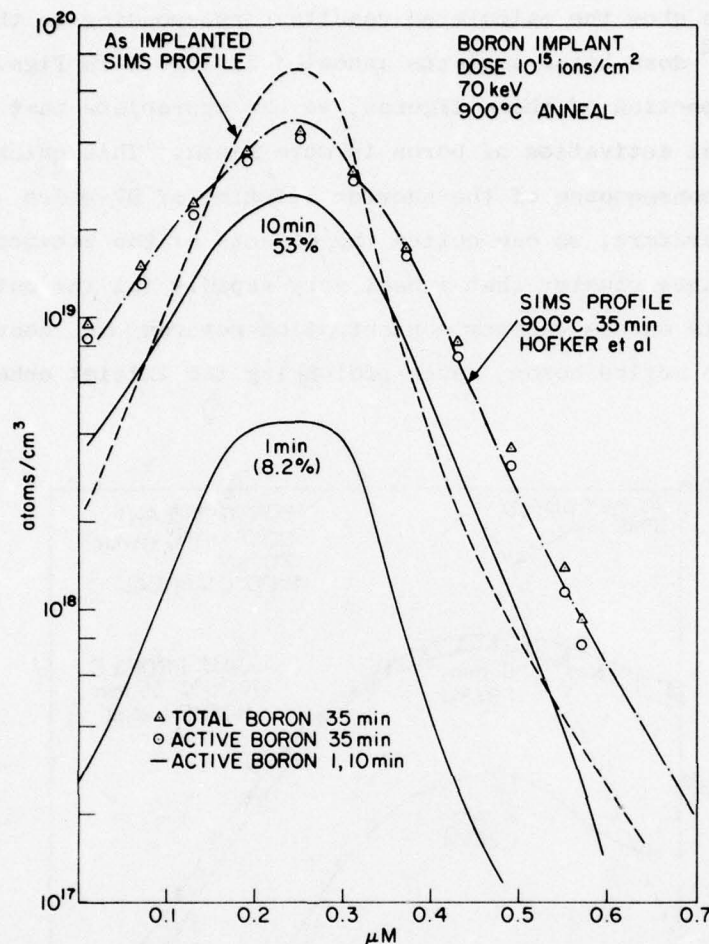


Fig. 16. THE ANNEALING OF A  $10^{15}$  IONS/CM<sup>2</sup> DOSE B IMPLANT AT 900°C. The comparison of calculated and experimental results.

active boron concentration with time, and we compare the calculated total boron concentration represented by triangles with the experimental SIMS profile represented by the solid line. Again, the fit is excellent. We wish to comment that this basic result can be obtained from two alternative calculations, by including or excluding the trapping effects of boron by dislocation dipoles, although there is a slight loss of accuracy if the effects of the dislocation dipoles are neglected. Figure 16 depicts the results of the calculation that includes the trapping of boron by defects.

Next, we show the calculated results corresponding to the  $10^{14}$  and  $10^{15}$  ions/cm<sup>2</sup> dose boron implants annealed at 1000°C in Figs. 17 and 18. From the inspection of these figures, we can appreciate that at 1000°C the electrical activation of boron is more rapid. This quicker activation is the consequence of the shorter lifetime of BV-pairs at 1000°C. At this temperature, we can notice the effects of the vacancies released from the vacancy cluster that anneal very rapidly (at the outset of the anneal). This excess vacancy concentration retards the conversion of BV-pairs into active boron, hence prolonging the initial enhancement in

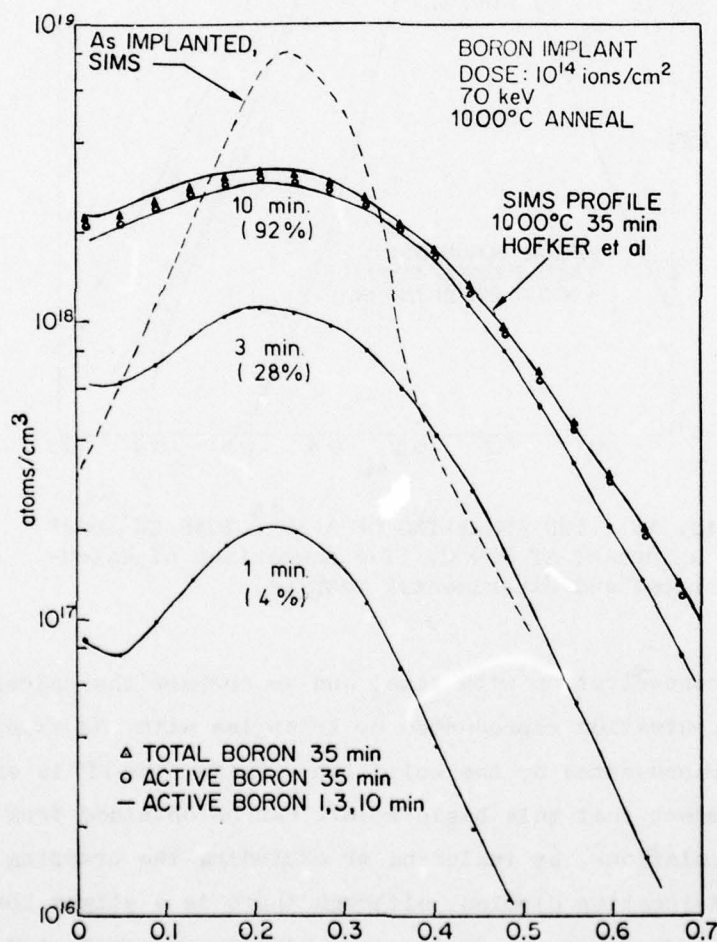


Fig. 17. THE ANNEALING OF A  $10^{14}$  IONS/CM<sup>2</sup> DOSE B IMPLANT AT 1000°C. The comparison of calculated and experimental results.

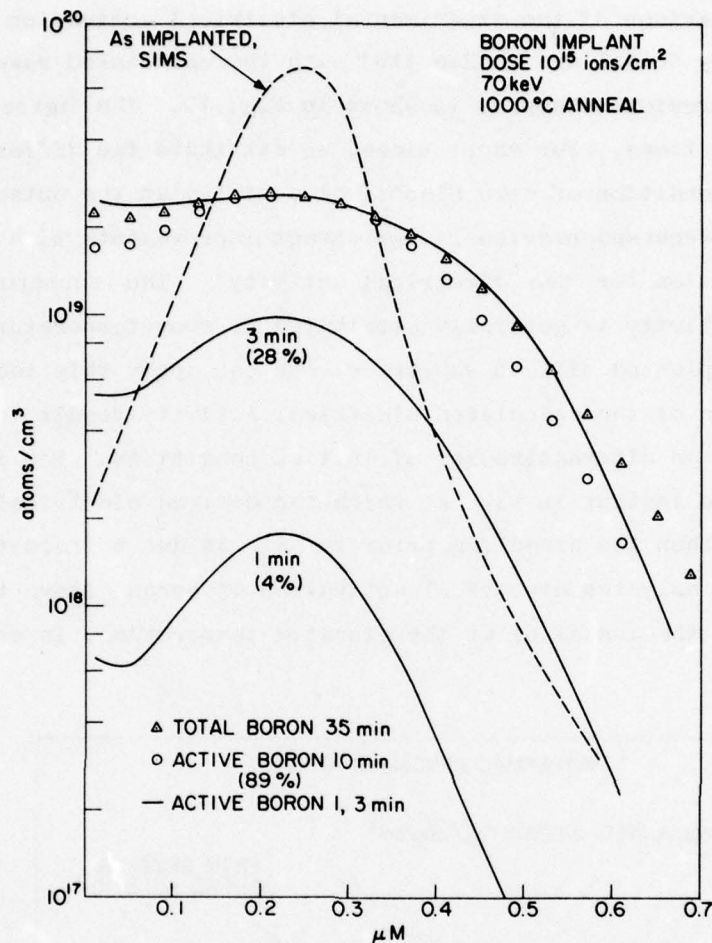


Fig. 18. THE ANNEALING OF A  $10^{15}$  IONS/CM<sup>2</sup> DOSE B IMPLANT AT 1000°C. The comparison of calculated and experimental results.

diffusion. It is for this reason that, for short annealing times, the inclusion of the generation term in the vacancy equation contributes to the improvement of the fit to the experimental data. Naturally, at longer annealing times, the enhanced diffusion is overwhelmed by the greater ordinary diffusion at higher temperatures and the aforementioned improvement becomes less noticeable. We can state from a different viewpoint that: for the case of a long annealing at high temperature, the neglect of the vacancy generation term in the calculation will not cause significant errors.

The comparison of the experimental electrical activation of boron versus time by Seidel and MacRae [18] with the calculated results from some of the previous examples is shown in Fig. 19. The agreement is good for long times. For short times, we attribute the difference to our initial condition of zero electrical activity at the outset of the anneal. As discussed previously, we expect improvements with a nonzero initial condition for the electrical activity. The nonzero initial electrical activity is generally attributed to room-temperature annealing of the implanted silicon substrate. We can apply this idea to the interpretation of the calculated electrical activity result in Fig. 19 and to obtain an alternative set of initial conditions. For instance, if  $t_0$  is the instant in time at which the desired electrical activity is attained, then the annealing prior to  $t_0$  is due to room-temperature annealing and only the electrical activation of boron after  $t_0$  is attributable to the annealing at the elevated temperature. In other words,

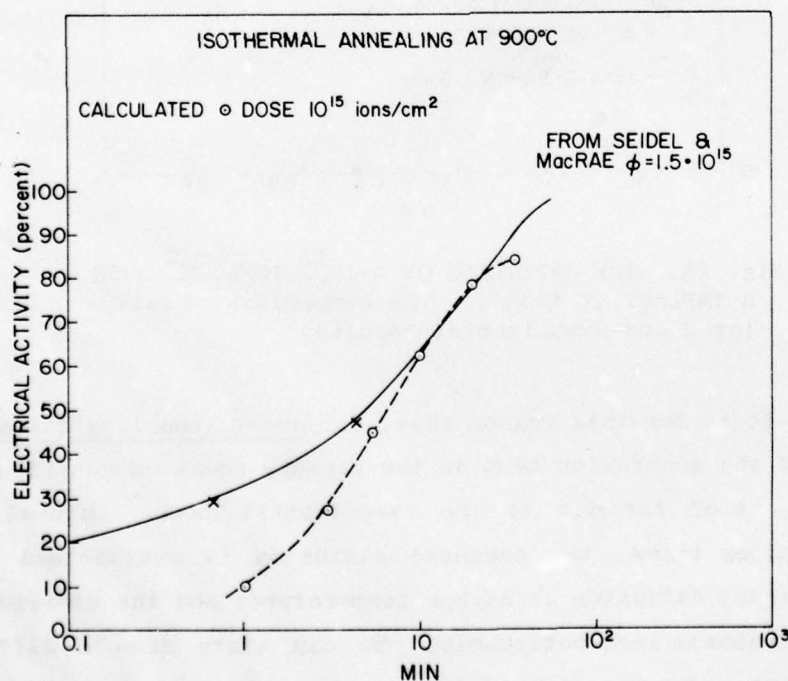


Fig. 19. THE COMPARISON OF CALCULATED ELECTRICAL ACTIVITY VERSUS TIME WITH EXPERIMENTAL ISOTHERMAL RESULTS BY SEIDEL AND MacRAE. Dose:  $10^{14}$  ions/cm<sup>2</sup>, 900°C.

AD-A059 752

STANFORD UNIV CALIF INTEGRATED CIRCUITS LAB  
COMPUTER AIDED ENGINEERING OF SEMICONDUCTOR INTEGRATED CIRCUITS--ETC(U)  
JUL 78 J D MEINDL, K C SARASWAT, R W DUTTON DAAB07-77-C-2684

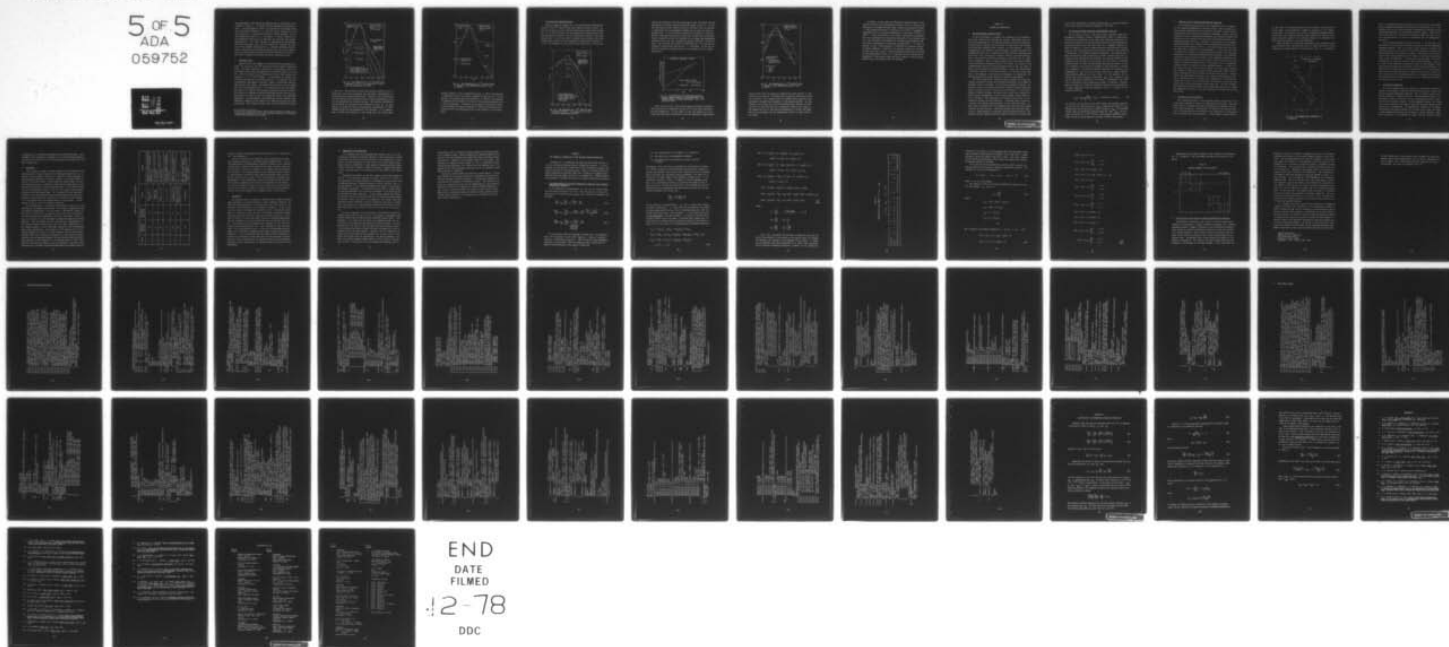
F/G 9/5

UNCLASSIFIED

DELET-TR-77-2684-2

NL

5 OF 5  
ADA  
059752



END  
DATE  
FILMED

12-78

DDC

the experimental result should be compared with the calculated result shifted in time by  $t_0$  to correct for room temperature annealing effects. Or, equivalently, a shift in time would not be required if the boron and BV-pair profiles at  $t_0$  were the initial conditions used in the calculation. To explore the validity of these arguments, we use the pertinent profiles at  $t_0 = 2.5$  minutes as initial conditions in the subsequent calculation. We find that the calculated data points represented by 'x's, thus obtained, do approximate the experimental electrical activation curve. We also verify that shifting the time axis of the original calculation by  $t_0$  produces equivalent results. Namely, subtraction of 2.5 minutes from the abscissa of each original data point (calculated using the zero initial electrical activity) moves the calculated data closely toward the experimental curve.

#### B. High Dose Cases

Figure 20 shows the comparison of calculated and experimental results\* for the case of the  $10^{16}$  ions/cm<sup>2</sup> dose boron implant annealed at 900°C. The slower electrical activation is a consequence of the small dissolution rate of boron precipitates and diffusion effects, as we will see. There are plateaus on the electrically active boron profiles calculated at 1, 3, 10, and 35 minutes. In particular, we compare the calculated electrically active boron profile at 35 minutes with the corresponding experimental electrical carrier concentration profile represented by the squares. The theoretical results are in good agreement with the experimental data. It is apparent that near the profile peak there is an immobile and electrically inactive fraction of boron. This fraction is composed of boron precipitates because the boron concentration is in excess of the solid solubility limit at the annealing temperature. Both theoretical and experimental results exhibit, upon annealing, a decrease in the width of the immobile fraction near the profile peak. This change of shape is due to the dissolution of boron

---

\* In the  $10^{16}$  ions/cm<sup>2</sup> dose cases, the annealed profiles by Hofker et al [2] have been corrected for the 30% ion yield increase in the precipitation area observed by the authors.

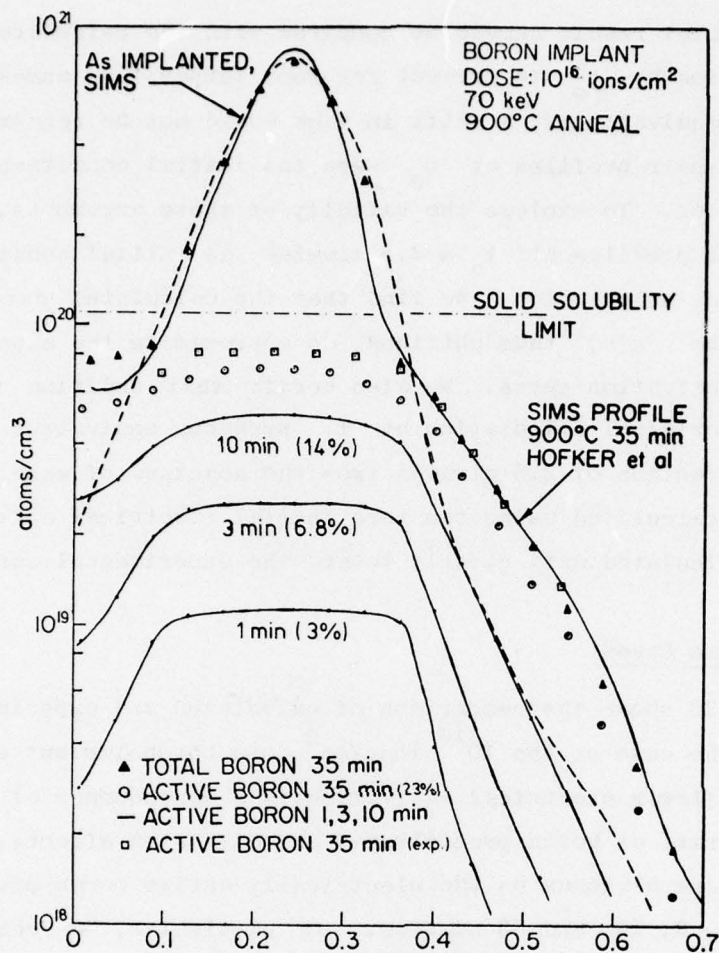


Fig. 20. THE ANNEALING OF A  $10^{16}$  IONS/CM<sup>2</sup> DOSE B IMPLANT AT 900°C. The comparison of calculated and experimental results.

in this area. The dissolution takes place because diffusion has depleted the mobile boron, upsetting the equilibrium concentrations of precipitated and nonprecipitated boron. Therefore, the dissolution is not only limited by the dissolution rate of boron precipitates, but it is also governed by the diffusion process. The relative importance of this diffusion can be assessed from inspection of Fig. 21. In this figure, we compare the total calculated boron concentration at 800°C through 1000°C with the experimental SIMS profiles. It is apparent that at 800°C the diffusion is very slight and the profile peak

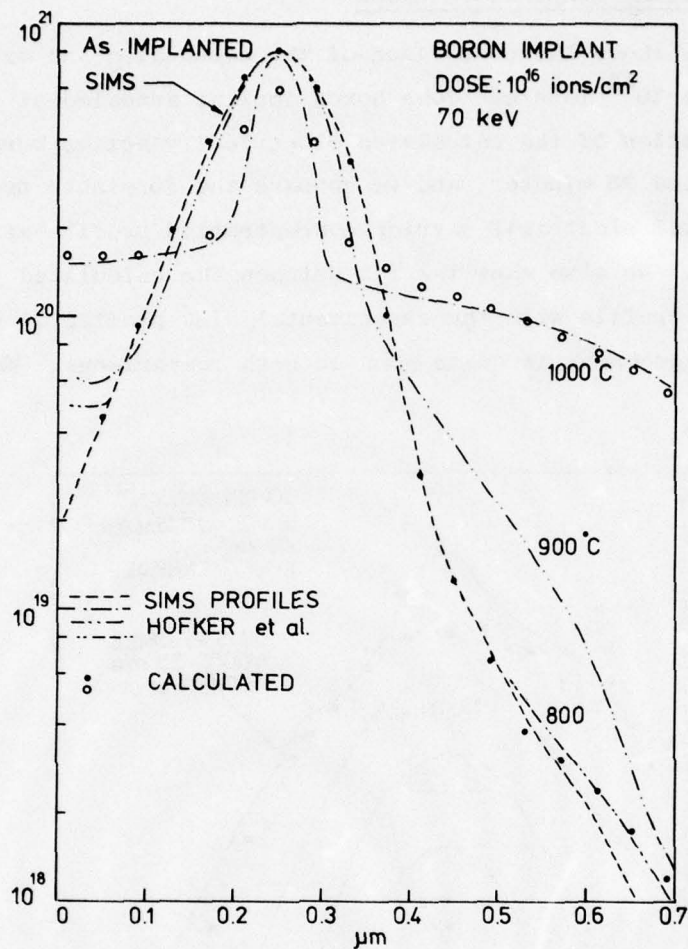


Fig. 21. THE ANNEALING OF A  $10^{16}$  IONS/CM<sup>2</sup> DOSE B IMPLANT IN THE TEMPERATURE RANGE OF 800°C TO 1000°C.

remains identical to the as-implanted profile. At 900°C, the diffusion is appreciable and we can observe a decrease in the width of the top portion of the profile peak upon annealing. At 1000°C, the diffusion is important and the removal of boron from the high concentration area is quite conspicuous. In summary, the electrical activation of boron in the annealing of high dose implants is controlled by both the dissolution rate of the precipitates and by the diffusion of the mobile boron.

### C. Low Annealing Temperature Cases

Figure 22 shows the comparison of the calculated and experimental results of the  $10^{14}$  ions/cm<sup>2</sup> dose boron implant annealed at 800°C. We show the evolution of the calculated electrically active boron profiles at 1, 3, 10, and 35 minutes, and we compare the 35 minute profile with the experimental electrical carrier concentration profile at the corresponding time. We also show the fit between the calculated total boron concentration profile with the experimental SIMS profile by Hofker et al [2]. The agreement is quite good in both comparisons. We can also

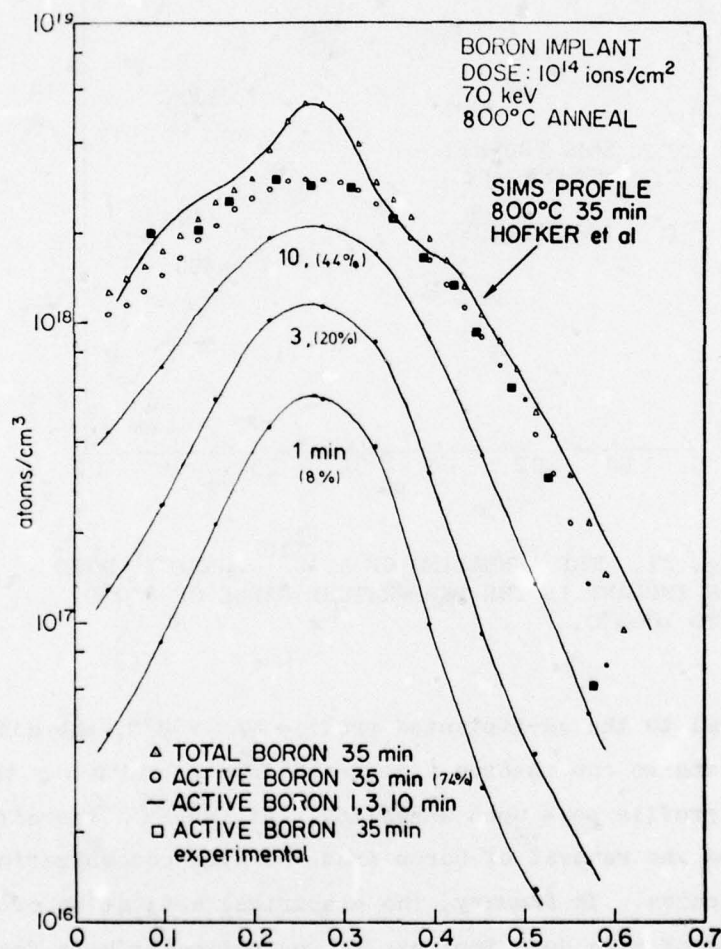


Fig. 22. THE ANNEALING OF A  $10^{14}$  IONS/CM<sup>2</sup> DOSE B IMPLANT AT 800°C. The comparison of calculated and experimental results.

compare the electrical activation predicted by this calculation with the experimental activation curve by Seidel and MacRae in Fig. 23. We can see that again the zero initial electrical activity in this calculation is responsible for the discrepancy between the two curves at short annealing times. As in the previous instance, we attribute to room-temperature annealing the electrical activation of boron until the desired initial electrical activity is attained, and we compare the experimental annealing curve with the corrected calculated electrical activation curve. The corrected data points are represented by 'x's and they are obtained by shifting the time axis by  $t_0 = 15$  minutes. We can see now that the corrected calculated points are in agreement with the experimental curve.

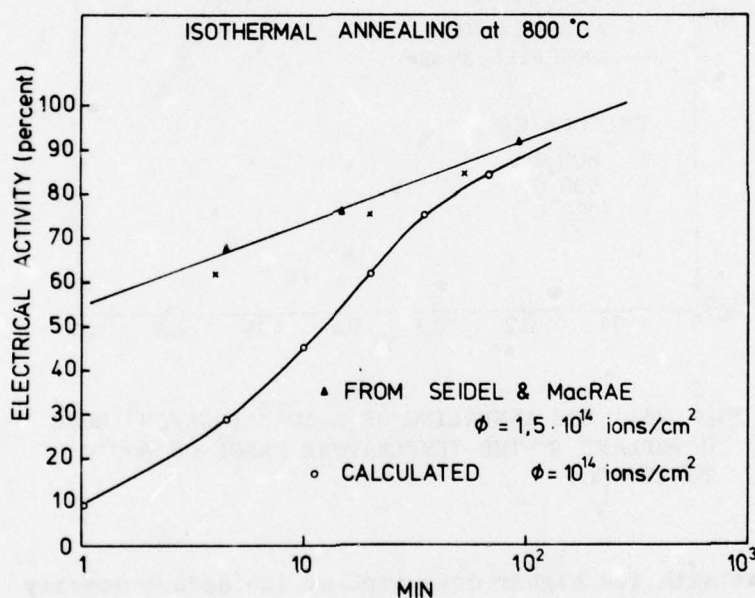


Fig. 23. THE COMPARISON OF CALCULATED ELECTRICAL ACTIVITY VERSUS TIME WITH THE EXPERIMENTAL ISOTHERMAL RESULT BY SEIDEL AND MacRAE. Dose:  $10^{14}$  ions/cm<sup>2</sup>, 800 °C.

Next, we show in Fig. 24 the result of the calculation performed with the same set of parameters for the  $10^{15}$  ions/cm<sup>2</sup> dose annealed at the same temperature. In this figure, we show the comparison of the calculated total boron concentration with the experimental SIMS profile.

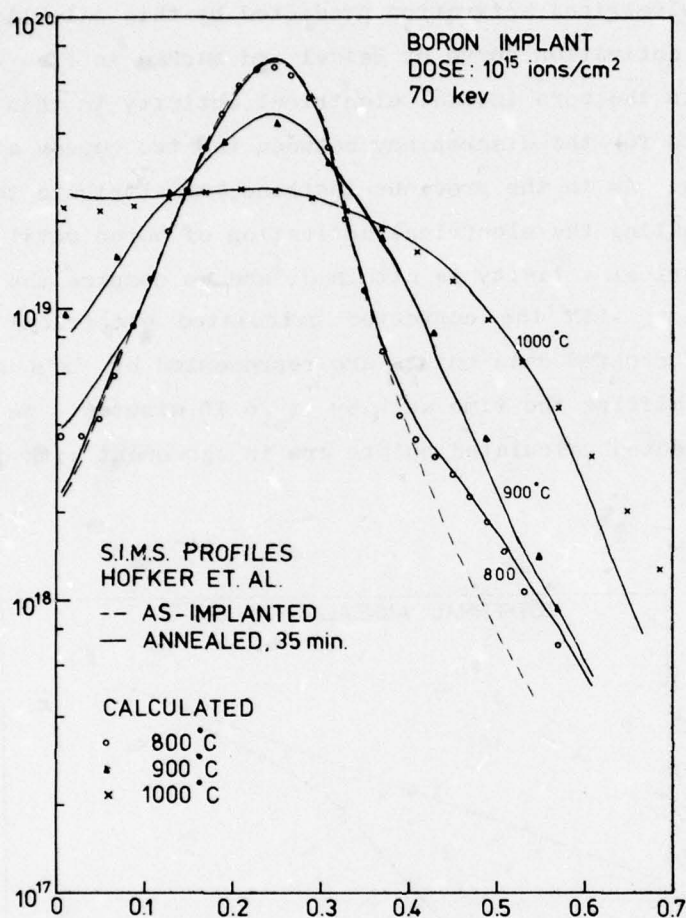


Fig. 24. THE ANNEALING OF A  $10^{15}$  IONS/CM<sup>2</sup> DOSE B IMPLANT IN THE TEMPERATURE RANGE OF 800°C TO 1000°C.

We recall that with the higher dose implant the defect density is also higher and the fraction of immobile boron trapped by dislocation dipoles also increases. This larger fraction of immobile boron produces a more pronounced 'shoulder-like structure' in the annealed profile. We also include in this figure the calculated annealed boron profiles for 900°C and 1000°C to show that there is a significant change in the shape of the annealed profile as the annealing temperature is varied. The agreement of the calculated with the experimental results is quite good in all cases.

In summary, we have used the mathematical annealing model in conjunction with the set of parameters in Tables 6 and 7 to calculate the annealing of ion-implanted boron under conditions summarized in Table 3. These conditions include a variation of two orders of magnitude in implantation dose and annealing temperature in the range of 800°C to 1000°C. In the calculations, we use initial conditions and parameters that are in agreement with experiments pertinent to the annealing problem. The main group of parameters are obtained using procedures that are based on thermodynamic and physical considerations. In other instances, we use a single parameter to represent the composite effects of several phenomena. Naturally, more detailed modelling is possible in these cases but, based on the good agreement between the calculated and the experimental results, it is apparent that the selected set of parameters is representing indeed the major elements in the annealing problem under the conditions that we described.

## Chapter IV

### SUMMARY AND CONCLUSIONS

#### A. The Three Stream Diffusion Model

In the first chapter, we studied the annealing of ion-implanted boron into silicon and we reviewed the relevant experiments that are of central importance for the annealing problem. With this background, we then discuss a general diffusion model in which boron atoms interact with positively charged silicon vacancies to form BV-pairs. In this interpretation, the diffusion of boron becomes a weighted diffusion with contributions from a slow, electrically active fraction (substitutional boron) and a fast, electrically inactive fraction (the boron-vacancy pair). The presence of positive vacancies in the model has two important consequences. First, a large concentration of vacancies in excess of the equilibrium concentration level will modify (by virtue of the aforementioned reaction) the relative populations of the two forms of boron, hence altering the overall diffusion. Second, the concentration of positive vacancies in the silicon lattice is a function of the Fermi level in the bandgap. This Fermi level dependence is responsible for high concentration anomalies observed in diffusion experiments.

This basic three stream diffusion model is capable of predicting ordinary diffusion of boron, proton enhanced diffusion, and a number of important cases of annealing. In the ordinary diffusion problem, the prevalent fraction of substitutional boron under equilibrium conditions results in high electrical activity and slow diffusion. In the proton enhanced diffusion problem, the steady state proton beam produces an excess vacancy concentration, which in turn creates a large concentration of BV-pairs. This predominance of BV-pairs results then in low electrical activity and fast diffusion. A somewhat similar situation is found in the typical annealing cases of ion implanted boron. In these cases, the majority of the implanted boron ions react with nearby vacancies and form BV-pairs. Annealing proceeds then with the conversion of a large population of BV-pairs into substitutional boron. Consequently, during annealing, the redistribution of boron is characterized

by an initial enhancement in diffusion that reduces to ordinary diffusion rates as the electrical activity increases to near 100%.

#### B. The Relation between Diffusion and Electrical Activity

The two forms of boron in this three stream diffusion model have dichotomous attributes. Namely, substitutional boron is electrically active and slow diffusing; on the other hand, the boron-vacancy pair is electrically inactive and fast diffusing. Because of this dichotomy and because the diffusion of the total boron is a weighted diffusion of these two species, a relation between diffusion and electrical activity ought to exist. We assume near 100% electrical activity in the selection of parameters to fit thermal diffusion experiments. This ensures that, when the abnormally high concentration of boron vacancy pairs that is produced by the implantation has annealed, the enhanced diffusion (associated with the initially low electrical act.) will relax to ordinary diffusion which is simply the near-thermal-equilibrium solution of the set of equations. The analytical analogue of this discussion is carried out in Appendix A. The boron and BV-pair equations are combined and the predominance of  $D_{BV}$  over  $D_B$  is used to arrive at a single approximated diffusion equation for total boron. In this equation, we can identify the overall diffusion coefficient  $D_{exp}$  with a product of  $D_{BV}$  and the fractional concentration of BV-pairs. Furthermore, the fractional concentration can be expressed in terms of electrical activity. Hence, we arrive at a diffusion coefficient (the only one accessible in an actual experiment, hence the subindex), which is a function of the electrical activity.

$$D_{exp} = D_{BV} \frac{C_{BV}}{C_{BV} + C_B} = D_{BV} (1 - \text{electrical activity}) \quad (6)$$

For instance, at the outset of the 900°C anneal, the assumed electrical activity is zero, and the value of  $D_{exp}$  is then initially equal to  $D_{BV}$ . During anneal, as the electrical activity increases,  $D_{exp}$  will decrease. Finally, when the electrical activity approaches 98%,  $D_{exp}$  will approach the value of  $1.4 \cdot 10^{-15} \text{ cm}^2/\text{sec}$ , the ordinary diffusion coefficient of boron at 900°C measured in thermal diffusion experiments.

### C. High Dose and Low Annealing Temperature Anomalies

In the typical annealing cases, the implantation dose is moderate and the annealing temperature is relatively high. These conditions ensure that the redistribution and electrical activation of boron evolves following the description in the preceding paragraph. However, when the implantation dose is increased sufficiently, the resultant impurity distribution in the substrate will exceed the solid solubility limit and a precipitated phase will form. Naturally, the presence of this immobile precipitated phase will strongly alter the redistribution and the electrical activation behavior of boron. A different situation arises when the annealing is performed at low temperature. In this case, many kinds of defects form, evolve, and interact during the anneal. The annealing temperature is an important parameter because processes have different activation energies and the selection of the temperature determines the duration and time sequence in the evolution of the defects and the likelihood of interactions between them. In particular, we are interested in defects that can interact with the implanted impurity. At 800°C, we have indications that the dislocation dipoles that form during annealing are capable of trapping boron atoms in their associated strain fields; hence, rendering the boron immobile and electrically inactive. For this reason, the redistribution profiles have special characteristics when the ion implanted boron is annealed at low temperature. The electrical activation in these cases is controlled by the release of boron from the strain fields as the dislocation dipoles anneal out. We wish to extend the three stream diffusion model to cover these high dose and low annealing temperature anomalies, since this constitutes a further test for the basic model.

### D. The Model and the Parameters

The mathematical model for the annealing problem is basically a diffusion model extended to include the aforementioned anomalies. The equations express in mathematical terms the diffusion and possible interactions among the species. Consequently, the essence of the overall model lies in the modelling of each diffusion, each interaction, and the parameters associated with each phenomenon. In this respect, these elements

are the links to the physical world and, in particular, the plausibility of the values of the parameters is indeed an indicator of the validity of the model. For instance, the values of temperature dependent parameters should obey simple activation energy relations and they should be invariant when we calculate the annealing behavior of different dose boron implants annealed at the same temperature.

Figure 25 shows the temperature dependence of the parameters in the basic diffusion model. The horizontal axis is linear in units of inverse temperature in degrees Kelvin, and the vertical axis is a logarithmic

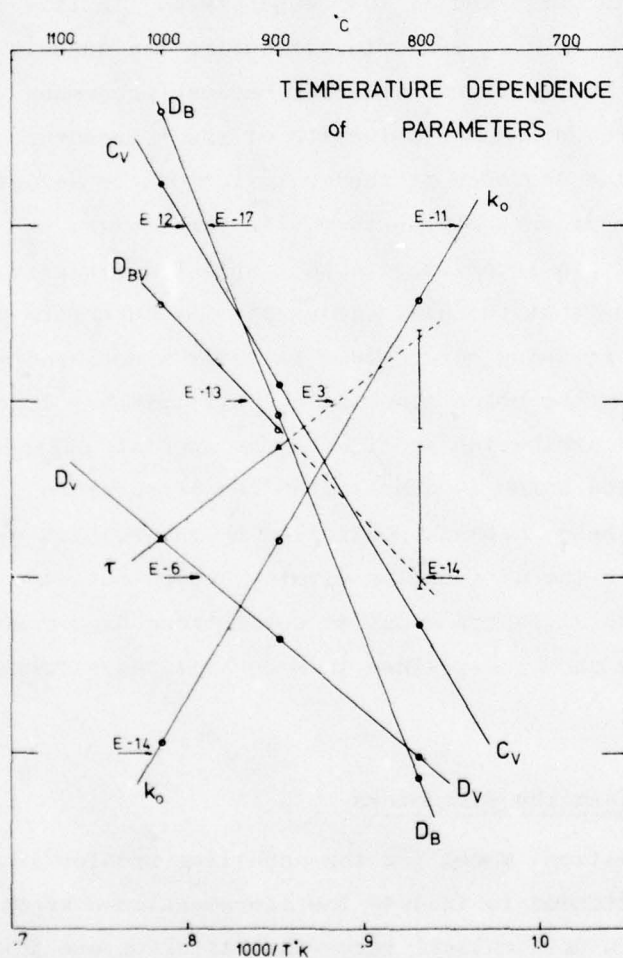


Fig. 25. THE TEMPERATURE DEPENDENCE OF PARAMETERS.

scale. The horizontal arrows adjacent to the lines give for each parameter the appropriate exponent to be read on the logarithmic scale. The straight lines in this semi-logarithmic representation indicate that the temperature dependence of the parameters follows indeed a simple activation energy relation. This result is extremely important, since it enables the determination of the set of parameters once the temperature is specified.

The remaining parameters are given in Table 7. In some cases, the modelling was not carried to the extent required to make the temperature dependence apparent. This is the case of the lifetime of vacancies, the vacancy generation time constant, and the time constants associated with the precipitation and dissolution of boron. For instance, the requirements on the latter parameters are for them to assume very small and very large values, respectively. In other cases, the parameters are chosen to represent the composite effects of very complex phenomena. Such is the case for the threshold concentration level for the trapping of boron by dislocation dipoles and the release of boron from these defects. In these cases, the representation is oversimplified and a more detailed model could be sought if necessary. However, based on the quality of the calculations in the preceding chapter, it is apparent that the present scheme captures the key features in the low annealing temperature and high dose cases as well.

#### E. The Initial Conditions

We wish to emphasize that the equations in conjunction with the parameter set constitute a diffusion model with provisions for high dose and low annealing temperature anomalies. But, to actually solve a particular problem, an ordinary diffusion, a proton-enhanced diffusion, or an anneal, we need, in addition, the set of appropriate initial conditions for the specific problem. In the preceding chapter, we solved nine cases of annealing with initial conditions for boron implanted into silicon at room temperature. The implantation condition is of importance because the damage produced by a low mass ion is light and there is room temperature annealing as the damage is being produced. Under these conditions, it is possible to assume that the initial vacancy

concentration is in thermal equilibrium in the silicon substrate. This assumption will certainly be inadequate for a liquid nitrogen implant or for the case of a heavy ion or a high dose implant that produces an amorphous damage layer.

#### F. Discussion

Let us examine a number of models reported in the literature. These models predict different aspects of the annealing problem that are included in our formulation. Table 9 is a summary of models proposed for the annealing or diffusion of boron in silicon. We list the number of species in the first column. In the second and third columns, we indicate whether the model is capable of predicting the redistribution or the electrical activation of boron during the anneal. In the fourth column, we list a representative source. And, the last column contains remarks pertinent to the particular model. It is apparent from the inspection of Table 9, that the proposed annealing model predicts both the redistribution and the electrical activation, as a realistic model should. It is also apparent that the proposed model is more complex. In this regard, we wish to offer the following discussion.

Our annealing model is devoted to the diffusion of boron and to the annealing of ion implanted boron under a wide range of implantation dose and annealing temperatures. For this reason, a substantial portion of this model is dedicated to the anomalies that arise when the implantation dose and annealing temperature vary over a wide range. In this regard, on one hand, it may be desirable to extend the model to cover other anomalies. And, the general nature of the numerical implementation of the solution enables additions to be made with minor modifications of the computer program. On the other hand, deletions could be appropriate under other circumstances. For instance, if the high dose and low annealing temperature cases are of little interest, then the three stream diffusion model with a subset of parameters will still predict ordinary diffusion, proton enhanced diffusion, and the typical annealing cases of boron implants at room temperature. This reduced model is still very important and attractive because, once the parameters associated with the anomalies are deleted, the remaining parameters have simple activation

Table 9

## MODELS FOR ANNEALING OR DIFFUSION

Species	Prediction of Annealing Profiles	Prediction of Electrical Activation	Authors	Remarks
1	Yes	No	Widely used for comparison	Nonphysical--diffusion coefficient dependent on dose--temperature--annealing time
2	No	Yes	Seidel and MacRae [18]	For the prediction of the electrical activation
2	Yes	No	Hofker et al [2]	To obtain the structure in $10^{16}$ dose annealings
1	Yes	No	Fair et al [29]	Background effects of substrate doping and impurity concentration on diffusion
2	Yes	No	W. Nuyts and Van Overstraeten [30]	Includes electric field effect and predicts ordinary diffusion
1	Yes	No	Longini & Green [31] Crowder et al [8]	$D/D_i = P/P_i$
4	Yes	Yes	Chu-Gibbons	Room temperature B implants Dose range: $10^{14} - 10^{16}$ ions/cm <sup>2</sup> Annealing temperature range: 800 °C - 1000 °C

energies and they are determined by the specification of a single variable: the temperature.

Lastly, we would like to elaborate on the boron-BV-pair reaction, the principal interaction in the three stream diffusion model. In the annealing problem, the spontaneous conversion of BV-pairs into substitutional boron is driven by the reaction rate, which is rather large during the anneal. From this viewpoint, it is apparent that the boron-BV-pair reaction is the dominant process in the annealing problem. However, in other problems, especially under thermal equilibrium when the boron-BV-pair reaction rate is small, it may be appropriate to reexamine the predominance of the boron-BV-pair reaction over other possible effects. For instance, depending on the nature of the problem and the features one wishes the model to predict, it may be necessary to consider effects such as the influence of internal electric fields or diffusion induced stresses due to the mismatch of the impurity atoms in the lattice.

#### G. Conclusion

The annealing model is capable of predicting boron impurity profiles under conditions of ordinary diffusion, proton enhanced diffusion, and radiation enhanced diffusion of the sort that occurs when boron is implanted at room temperature and subsequently annealed. In the latter case, the model also predicts the evolution of the electrically active boron as a function of space and time. In reference to practical implantation and annealing conditions, the model has been tested for all the cases in Table 2. In this wide range of dose and annealing temperatures, the most relevant case in device fabrication are in the lower left corner. The remaining cases are perhaps less important but not less interesting since the abnormalities are a real challenge to the annealing model. In calculating these cases, we show that by extending the basic approach it is possible to generalize the model to predict more complex situations. It is also remarked that this model and the associated parameter set are universal in the sense that the same equations and parameters are used in the prediction of ordinary diffusion, proton enhanced diffusion, and the annealing of ion-implanted boron into silicon at room temperature.

#### H. Suggestions for Future Work

It is apparent that this annealing model enables the use of the accurately calculated as-implanted profiles in the calculation of annealing profiles for the case of boron implants at room temperature. In this manner, the device designer can make a better use of the range calculations that are available for a large number of impurity-substrate combinations. From this viewpoint, it seems reasonable to suggest that perhaps similar annealing models can be developed for other commonly used impurities.

Phosphorus and arsenic are the most commonly used n-type dopants in silicon. It is generally accepted that their diffusion in silicon is also governed by a vacancy mechanism. Furthermore, a large body of work on ordinary diffusion, diffusion anomalies, lattice location, and annealing behavior of ion implanted phosphorus and arsenic is available in the technical literature. It is therefore likely that a careful review of relevant experiments will yield key attributes for the diffusion and the annealing of these impurities. In this regard, perhaps the subject of possible interactions between impurities and charged vacancies should be examined. Then, with some basic assumptions, the simplest model with the most essential attributes should be formulated and solved. Undoubtedly, many iterations of the described sequence will be necessary, and the availability of the 'diffusion solver' from this work will be useful.

We wish to highlight some similarities and differences between the suggested study and the case of boron. The diffusion of phosphorus and arsenic exhibit high concentration and background doping effects. Consequently, it is likely that the Fermi level dependence comes from interactions of the impurity with negatively charged vacancies. It is also possible that more than one kind of impurity-vacancy complexes coexist in the substrate and their different diffusive attributes give rise to anomalies in the diffusion profile. Certainly, the most important difference between the boron and the phosphorus or arsenic cases is the damage that results from the implantation. The heavy phosphorus or arsenic ions produce extended damage clusters in the lattice as the ions come to rest. In these cases, the room temperature annealing rate is

insufficient, and the individual damage clusters will overlap, producing an amorphous layer. During annealing, the implanted impurity will anneal in both the amorphous and crystalline regions following different behaviors. Meanwhile, the amorphous layer will also anneal. The regrowth of amorphous silicon layers is also a complicated matter. Backscattering experiments [44] indicate that the regrowth rate is dependent on the crystallographic direction, and it is modified by the doping effects of impurities.

Perhaps the problem should be addressed in three phases. A first phase devoted to the ordinary diffusion of phosphorus and arsenic and the most important diffusion anomalies. A second phase dedicated to the study of the regrowth of amorphous Si layers. The outcome of this study will certainly be useful for the understanding of the annealing behavior of boron that is implanted at liquid nitrogen temperature. And, lastly, in the third phase, the results of the first and second phases can be combined to develop an annealing model capable of predicting impurity profiles in the presence of an amorphous layer produced by the implantation.

## Appendix A

### THE NUMERICAL INTEGRATION OF THE COUPLED DIFFUSION EQUATIONS

In Chapter II, we formulated the annealing model which consists of a set of nonlinearly coupled partial differential equations. We will describe now the numerical integration of this mathematical problem. The solution consists of two distinct steps. First, we transform the set of Partial Differential Equations (PDE) into a larger set of Ordinary Differential Equations (ODE), and then we use GEARB [45], a FORTRAN subroutine package, to integrate the system of ordinary differential equations.

#### 1. The Transformation of Partial Differential Equations into Ordinary Differential Equations

To illustrate this transformation, we will use the three stream diffusion model described in Eq. (A1). This simpler case is chosen for the purpose of illustrating the problem with a minimum of algebraic complexities.

$$\frac{\partial C_B}{\partial t} = D_B \frac{\partial^2 C_B}{\partial x^2} - K_O \frac{C_B C_{V^+}}{\tau} + \frac{C_{BV}}{\tau} \quad (A1a)$$

$$\frac{\partial C_{V^+}}{\partial t} = D_{V^+} \frac{\partial^2 C_{V^+}}{\partial x^2} - K_O \frac{C_B C_{V^+}}{\tau} + \frac{C_{BV}}{\tau} - \frac{(C_{V^+} - C_{V^+}^{eq})}{\tau_V} \quad (A1b)$$

$$\frac{\partial C_{BV}}{\partial t} = D_{BV} \frac{\partial^2 C_{BV}}{\partial x^2} + \underbrace{K_O \frac{C_B C_{V^+}}{\tau}}_{\text{nonlinear coupling}} - \frac{C_{BV}}{\tau} \quad (A1c)$$

In this system of PDE, the dependent variables are: the concentrations of electrically active boron ( $C_B(x,t)$ ), positive vacancies ( $C_{V^+}(x,t)$ ), and BV-pairs ( $C_{BV}(x,t)$ ). Time and space are the independent variables in this problem. The transformation under consideration is based on the elimination of the spatial variable by:

- (a) the discretization of the space in  $N$  partitions
- (b) the definition of new dependent variables
- (c) the formulation of the problem in terms of the new variables

For example, first, the  $x$ -axis is divided into 33 partitions of width  $\Delta x$ . Second, we define the concentrations of active boron, positive vacancies, and BV-pairs in each one of the 33 partitions as new variables. Since 3 variables are associated with each partition, and there are 33 partitions, the total number of new dependent variables is 99. It is convenient to define a vector  $\vec{y}$  composed of the new dependent variables, as is illustrated in Table A1. We obtain the system of ODE in terms of the new variables by rewriting Eq. (A1) for each one of the 33 partitions and by approximating the second partial derivative with the central differences [46] in Eq. (A2).

$$\frac{\partial^2 C^c}{\partial x^2} \approx \frac{C^l - 2C^c + C^r}{\Delta x} \quad (A2)$$

In this equation, the superscripts  $l$ ,  $c$ , and  $r$  denote left, center, and right, respectively;  $\Delta x$  is the width of the partition. The central difference approximation in Eq. (A2) is indicating explicitly that the second partial derivative of the variable  $C$  at the central partition is only referenced to the same variable  $C$  at the same location and at adjacent locations (left and right). Following these instructions and using Table A1 to express the new variables in place of the old ones, we obtain Eq. (A3), the system of 99 coupled ordinary differential equations.

$$\begin{aligned} \dot{y}_{(1)} &= -2K_1 y_{(1)} + K_1 y_{(4)} - K y_{(1)} y_{(2)} + K' y_{(3)} \\ \dot{y}_{(2)} &= (-2K_2 - K_V) y_{(2)} + K_{(2)} y_{(5)} - K y_{(1)} y_{(2)} + K' y_{(3)} + K'_V \\ \dot{y}_{(3)} &= (-2K_3 - K') y_{(3)} + K_{(3)} y_{(6)} + K y_{(1)} y_{(2)} \\ i &= (1, 2, \dots, 31) \end{aligned} \quad (A3)$$

$$\dot{y}(31 + 1) = K_1 y(31 - 2) - 2K_1 y(31 + 1) + K_1 y(31 + 4)$$

$$- Ky(31 + 1) y(31 + 2) + K'y(31 + 3)$$

$$\dot{y}(31 + 2) = K_2 y(31 - 1) - (2K_2 + K_V) y(31 + 2) + K_2 y(31 + 5)$$

$$- Ky(31 + 1) y(31 + 2) + K'y(31 + 3) + K'_V$$

$$\dot{y}(31 + 3) = K_3 y(31) - (2K_3 + K') y(31 + 3) + K_3 y(31 + 6)$$

$$- Ky(31 + 1) y(31 + 2)$$

$$\dot{y}(97) = K_1 y(94) - 2K_1 y(97) - K_1 y(97) y(98) + K'y(99)$$

$$\dot{y}(98) = K_2 y(95) - (2K_2 + K_V) y(98) - Ky(97) y(98) + K'y(99) + K'_V$$

$$\dot{y}(99) = K_3 y(96) - (2K_3 + K') y(99) + Ky(97) y(98)$$

(A3)  
Cont.

where

$$K_1 = \frac{D_B}{\Delta x^2} \quad K = \frac{\text{Eq. Const.}}{\tau} \quad K' = \frac{1}{\tau}$$

$$K_2 = \frac{D_V}{\Delta x^2} \quad K_V = \frac{1}{\tau_V}$$

$$K_3 = \frac{D_{BV}}{\Delta x^2} \quad K'_V = \frac{C_{V+eq}}{\tau_V}$$

In Eq. (A3), we assumed, for the sake of simplicity, that the values of the variables is zero outside of the spatial range of interest. In principle, the ordering of the components in the vector  $\vec{y}$  (Table A1) is arbitrary, and other definitions of  $\vec{y}$  would yield equivalent sets of ordinary differential equations. However, as we analyze the

Table A1

DEFINITION OF THE VECTOR  $\vec{y} = (y_1 \dots y_{99})$

$$y_i = f(y_1 \dots y_{99}) \quad i = (1 \dots 99)$$

Partition	1			2			3			...			33		
Specie	B	V	BV	B	V	BV	B	V	BV	B	V	BV	B	V	BV
Concentration	$y_{(1)}$	$y_{(2)}$	$y_{(3)}$	$y_{(4)}$	$y_{(5)}$	$y_{(6)}$	$y_{(7)}$	$y_{(8)}$	$y_{(9)}$	$y_{(3i-2)}$	$y_{(3i-1)}$	$y_{(3i)}$	$y_{(98)}$	$y_{(99)}$	

Jacobian of the system, it will be apparent that this particular ordering of species in partitions does produce a set of ODE with a banded Jacobian in which the width of the band is small. And, such a system can be solved very efficiently since it does not require the storage of elements outside of the band.

It is more concise and convenient to use the vector notation in the description of the system of ordinary differential equations. For instance, Eq. (A3) can be expressed as:

$$\dot{y}_i = f_i(y_1, \dots, y_j, \dots, y_N) \quad i(1, \dots, N) \quad (A4)$$

where  $N$  is 99 in our example.

The Jacobian of the set of ordinary differential equations in Eq. (A4) has elements  $J_{ij}$  given by:

$$J_{ij} = \frac{\partial f_i}{\partial y_j} \quad (A5)$$

Hence,

$$J_{11} = -2K_1 - Ky(2) = \partial f_1 / \partial y_1$$

$$J_{12} = -Ky(1) = \partial f_1 / \partial y_2$$

$$J_{13} = K' = \partial f_1 / \partial y_3$$

$$J_{14} = K_1 = \partial f_1 / \partial y_4$$

$$\vdots \quad \text{etc.}$$

And, in general, the nonzero elements of  $J$  are for  $i = (0 \dots 32)$ :

$$J(3i + 1, 3i + 1) = -2K_1 - Ky(3i + 2)$$

$$J(3i + 1, 3i + 2) = -Ky(3i + 1) \quad (A6)$$

$$J(3i + 1, 3i + 3) = K'$$

$$J(3i + 1, 3i - 2) = \begin{cases} 0 & i = 0 \\ K_1 & i > 0 \end{cases}$$

$$J(3i + 2, 3i + 1) = -Ky(3i + 2)$$

$$J(3i + 2, 3i + 2) = -2K_2 - Ky(3i + 1) - K_V$$

$$J(3i + 2, 3i + 3) = K'$$

$$J(3i + 1, 3i + 4) = \begin{cases} K_1 & i = 32 \\ 0 & i < 32 \end{cases}$$

$$J(3i + 2, 3i + 5) = \begin{cases} K_2 & i < 32 \\ 0 & i = 32 \end{cases}$$

$$J(3i + 2, 3i - 1) = \begin{cases} K_2 & 0 < i \\ 0 & i = 0 \end{cases}$$

$$J(3i + 3, 3i + 1) = Ky(3i + 2)$$

$$J(3i + 3, 3i + 2) = Ky(3i + 1)$$

$$J(3i + 3, 3i + 3) = -2K_3 - K'$$

$$J(3i + 3, 3i + 6) = \begin{cases} K_3 & i < 32 \\ 0 & i = 32 \end{cases}$$

$$J(3i + 3, 3i) = \begin{cases} K_3 & i > 0 \\ 0 & i = 0 \end{cases}$$

(A6)  
Cont.



problems in which the stiffness is apparent, the use of the backward differentiation formula with the user supplied Jacobian is more efficient. The annealing problem falls into this category. In other problems, where the stiffness is only apparent in the later stage of the integration, it is possible to change the method of integration during the computation. The user need only to specify the initial step size of the integration. Thereafter, the package adjusts the step-size according to the error incurred in the integration. The communication with GEARB is performed through the subroutine DRIVEB by means of a CALL statement. The user supplies a MAIN PROGRAM and two subroutines: DIFFUN and PDB. The main program controls the input-output, initializes variables, selects the options, and performs the communication with DRIVEB. DIFFUN defines the system of ordinary differential equations [Eq. (A3)] and PDB is the Jacobian [Eq. (A6)] stored by diagonal lines. In the event that the Jacobian cannot be coded, it is possible to select an option that generates the Jacobian internally. The penalty associated with this option is, of course, a loss in efficiency. In our case, the sample codes that we list in the next section do contain the user supplied Jacobian.

It is apparent from this outline that the interface with GEARB has a modular structure. The definition of the mathematical problem is coded in DIFFUN and PDB, and the adaptation of the mathematical formulation to the particular problem is accomplished in the main program. For these reasons, the potential user will find that DIFFUN and PDB are of immediate use; however, he may wish to modify the main program, to alter the width of the partition, the step-size, the error control, etc., to suit his particular problem. In Section 3, we include the listing of the three stream diffusion model and the complete annealing model. GEARB is available in both single and double precision versions from:

Argonne Code Center  
Argonne National Laboratory  
9700 South Cass Avenue  
Argonne, Illinois 60439  
Telephone: (312) 739-7711, Ext. 4366

The user should send a blank magnetic tape, together with character, channel, and density specifications, and ask for the appropriate version of GEARB. For a complete description of GEARB and the user's instructions, the reader is referred to Ref. 45.

### 3. Three Stream Diffusion Model

C----- THIS IS A GENERAL PURPOSE VERSION OF THE 3-STREAM  
 C----- DIFFUSION MODEL FOR BORON IN SILICON. THE MODEL IS  
 C----- COMPOSED OF A MAIN PROGRAM AND 3 SUBROUTINES: DIFFUN,  
 C----- PDB AND SILS. DIFFUN IS THE SYSTEM OF ORDINARY DIFFE-  
 C----- RENTIAL EQUATIONS ASSOCIATED WITH THE DIFFUSION OF B.  
 C----- PDB CONTAINS THE NON-ZERO ELEMENTS OF THE JACOBIAN MA-  
 C----- TRIX. AND SILS IS A SUBROUTINE FOR THE CALCULATION OF  
 C----- THE FERMI-LEVEL AND CARRIER CONCENTRATIONS.  
 C----- THIS GROUP OF SUBROUTINES IS INTENDED TO BE USED IN  
 C----- CONJUNCTION WITH GEARB, A SUBROUTINE PACKAGE FOR THE  
 C----- SOLUTION OF SYSTEMS OF ORD.DIFFERENTIAL EQ. WITH BANDED  
 C----- JACOBIAN, BY A.C.HINDMARSH (LAWRENCE LIVERMORE LAB,  
 C----- U.C. LIVERMORE, CA. MARCH 1975).  
 C----- THE INPUTS TO THE DIFFUSION MODEL ARE: THE AS-  
 C----- IMPLANTED B PROFILE, A SIMS PROFILE THE USER WISHES  
 C----- TO APPROXIMATE, THE PARAMETERS AND THE TIMES AT WHICH  
 C----- THE OUTPUT ARE DESIRED. THE PRIMARY DAMAGE PROFILE IS  
 C----- ALSO REQUIRED IN THE DATA STATEMENT IN DIFFUN, IF THE  
 C----- PROBLEM IS AN ANNEAL OR A PROTON ENHANCED DIFFUSION.  
 C----- FOR THE CASE OF AN ORDINARY DIFFUSION THE DAMAGE  
 C----- PROFILE CAN BE REPLACED BY THE EQUILIBRIUM VACANCY  
 C----- CONCENTRATION OR ALTERNATIVELY, THE TIME CONSTANT  
 C----- ASSOCIATED WITH THE DAMAGE CAN BE SET TO A VERY LARGE  
 C----- VALUE, 1WD8 SECONDS.  
 C-----DECLARATIONS-----  
 C----- DOUBLE PRECISION B0(33),V0(33),BV0(33),  
 1 BT(33),Z0(132), DEPTH,XINC,X(8),Y0(99),PRN(8),TOUT,TIME,TLAST,  
 2 T0,H0,EPS,HUSED,DOSE,DOSEB,ACTIV,FVAL,SIMS(33),W0(99)  
 INTEGER MONTH,DAY,YEAR,  
 1 N,MF,INDEX,HL,MU,NQUSED,NSTEP,NFE,NJE

```

COMMON/GEAR9/HUSED,NQUSED,NSTEP,NFE,NJE
C-----INITIALIZATION-----
C----- XINC ----- SPATIAL INCREMENT IN CM.
C----- N ----- NUMBER OF POINTS = # SPECIES * # OF INCREMENTS
C----- T0 ----- INITIAL VALUE OF TIME T IN SECONDS
C----- MF ----- BACKWARD DIFFERENTIATION FORMULA METHOD
C----- FOR THE INTEGRATION.
C----- ML,MU ----- BAND-WIDTHS IN THE JACOBIAN MATRIX
C----- DEPTH ----- NUMBER OF PARTITIONS * XINC
C----- XINC= 2.0D-6
C----- N=55
C----- T0=0.000
C----- MF=21
C----- ML=3
C----- MU=3
C----- DEPTH = (33.0000) * (XINC)
C----- REAL DATE OF RUN -----
C----- READ(5,10) MONTH, DAY, YEAR
C----- FORMAT(12,1X,12,1X,14)
C-----EXAMPLE: START AT COL 1:03 12 1976
C----- LABELS -----
C----- WRITE(6,20) MONTH, DAY, YEAR
C----- FORMAT(39H BORON VACANCY PAIR DIFFUSIVE ANNEALING///
C----- 1 10X,10H RUN#-----,10X,7H DATE : ,12,1X,12,1X,14,
C----- 2 10X,20H 3-STREAM DIFF.MODEL///)
C----- READ INITIAL PROFILES-----
C----- THE INITIAL CONCENTRATION PROFILES ARE IN #/CM**3
C----- B0 ----- THE AS IMPLANTED BORON PROFILE, OR A
C----- DIFFUSED PROFILE
C----- SIMS ----- THE TOTAL BORON PROFILE WE WISH TO COMPARE WITH
C----- THE USER CAN INPUT THE INITIAL PROFILES FOR THE POS.
C----- VACANCIES AND THE SUBSTITUTIONAL BORON BY MODIFYING
C----- READ STATEMENT NUMBER 25.
C-----I WILL ALWAYS USE UNIFORM FORMAT D10.3 FOR ALL DOUBLE PRES.
C----- 25 READ(5,30) ( B0(I), I = 1,33), (SIMS(I), I=1,33)

```

```

30  FORMAT(3D10.3)
C--EXAMPLE: START AT COLUMN #1 >+1.000D+00 2.000D+00 3.000D+00 NEXT
C-----CONSTRUCT Y0, THE INPUT VECTOR FOR DRIVEN, IN GEARB
C----- DOSE, DOSEB ARE THE TOTAL BORON DOSE AND THE DOSE
C          OF ACTIVE BORON IN #/CM**2
C----- ACTIV IS THE ELECTRICAL ACTIVITY IN PERCENT
C----- FVAL - A COST FUNCTION CALCULATED FROM THE COMPARISON
C          OF THE CALCULATED TOTAL BORON PROFILE WITH THE DESIRED
C          PROFILE.
C----- H0 - STEP SIZE TO BE ATTEMPTED FOR THE FIRST TIME
C----- EPS - THE LOCAL ERROR TOLERANCE PARAMETER(SEE GEARB)
C----- INDEX - AN INTEGER FLAG. FOR THE FIRST CALL: INDEX=1
35  DOSE = 0.D00
    DOSEB = 0.D+00
    ACTIV = 0.D+00
    FVAL = 0.D+00
C----- CONSTRUCTION OF THE INPUT VECTOR Y0 FOR DRIVEN USING
C----- THE INITIAL CONDITIONS. THE VALUE ASSIGNED TO Y0(3*I-1)
C----- IS THE EQUILIBRIUM CONCENTRATION OF POSITIVE VACANCIES
C----- IN INTRINSIC SILICON AT 900 C.
    DO 40 I=1,33
      Y0(3*I-2)=0.D+00
      Y0(3*I-1) = 1.250D+11
      Y0(3*I)   = B0(I)
40  DOSE = DOSE + ( B0(I) + BV0(I) ) * XINC
    WRITE(6,145) DOSE, DOSEB, ACTIV
    H0=1.D-14
    EPS=1.D-4
    INDEX=1
C--ECHO INPUT TO OUTPUT -----Y0-----
    WRITE(6,50) (Y0(I), I=1,99)
50  FORMAT(10X,17H INITIAL PROFILES//
      2      3(5X,5HBORON,5X,7HVACANCY,5X,7HBV PAIR,5X)//
      3      11(1P3D12.3,1X,1P3D12.3,1X,1P3D12.3)//)
C-----READ PARAMETERS-----

```

```

C----- THE PARAMETERS ARE DESCRIBED IN THE FORMAT STATEMENT 80
60 READ(5,70)(X(I),I = 1,8)
70 FORMAT( 4D16.3)
C-START AT COL 1 >+4.000D+00 8.000D+00 1.200D+01 NEXT CARD
C--PARAMETERS 'ECUO INPUT PARAMETERS TO OUTPUT'
WRITE(6,80) (X(I),I = 1,8)
80 FORMAT(16X,11H PARAMETERS//
1 5X,23H DIFF.COEF.(BORON) = ,1PD10.3,10H CM**2/SEC/
2 5X,23H DIFF.COEF.(VACANCY) = ,1PD10.3,10H CM**2/SEC/
3 5X,23H DIFF.COEF.(BV PAIR) = ,1PD10.3,10H CM**2/SEC/
4 5X,23H EQUIL.CONST.(B+V=BV) = ,1PD10.3,6H CM**3/
5 5X,23H REACTION TIME CONST = ,1PD10.3,4H SEC/
6 5X,23H VACANCY LIFETIME = ,1PD10.3,4H SEC/
7 5X,23H TEMPERATURE = ,1PD10.3,6H DEG.C/
8 5X,23H DAMAGE TIME CONSTANT = ,1PD10.3,4H SEC///)

C-PARAMETER NORMALIZATION
DO 90 I = 1,3
90 PRN(I) = X(I) / ( XINC**2)
PRN(4) = X(4)/X(5)
PRN(5) = 1/ X(6)
PRN(6) = 1/ X(5)
PRN(7) = X(7)
PRN(8) = X(8)

C--OUTPUT THE MODIFIED PARAMETERS USED IN DIFFUN AND PDB
WRITE ( 6,100) (PRN(I),I = 1,8)
100 FORMAT(53H MODIFIED PARAM. OF DIM. 1/SEC USED IN PROGRAM PRN(7)//
1 1PD10.3///)

C----- READ TIMES -----
C--EXAMPLE: START AT COLUMN #1 >+1.000D+00 NEXT CARD
C--THE LAST TIME IS AN INTEGER FLAG:
C TOUT = 0 EXIT
C TOUT = 1 CHANGL PARAMETER SET
C TOUT = 2 CHANGL INITIAL PROFILES.
105 READ(5,110) TOUT
110 FORMAT (D10.3)

```

```

IF (TOUT.EQ.0.D00) GO TO 160
IF (TOUT.EQ.1.D00) GO TO 35
IF (TOUT.EQ.2.D00) GO TO 25
DOSE = 0.D00
  SEE = 0.D+00
  FVAL = 0.L+00
  CALL ERRSET(208,256,-1,1)
  CALL DRIVEB(N,T0,H0,Y0,TOUT,EPS,MF,INDEX,ML,MU,PRN)
  GEARB IS MODIFIED TO PASS THE PARAMETERS IN PRN TO THE
  SUBROUTINES DIFFUN AND PDB.
  THE MODIFICATIONS CONSIST IN THE ADDITION OF THE VECTOR
  PRN IN THE FOLLOWING SUBROUTINE, CALL AND DIMENSION
  STATEMENTS:
  SUBROUTINE DRIVEB(N,T0,H0,Y0,TOUT,EPS,MF,INDEX,ML,MU,PRN)
  DOUBLE PRECISION PRN(1)
  CALL STIFFB(Y, N0, PRN)
  SUBROUTINE STIFFB(Y, N0, PRN)
  DOUBLE PRECISION PRN(1)
  CALL DIFFUN (N,T,Y,SAVE1,PRN)
  CALL DIFFUN (N,T,Y,SAVE2,PRN)
  CALL PSETB(Y, N0, CON, MITER, IER, PRN)
  CALL DIFFUN (N,T,PW,SAVE1,PRN)
  CALL DIFFUN (N,T,SAVE1,SAVE2,PRN)
  SUBROUTINE PSETB(Y, N0, CON, MITER, IER, PRN)
  DOUBLE PRECISION PRN(1)
  CALL PDB (N,T,Y,PW,N0,ML,MU,PRN)
  CALL DIFFUN (N,T,Y,SAVE1,PRN)
  -----
  THE MAXIMUM VALUE OF N IS CURRENTLY SET TO 100.
  IF THIS NUMBER IS TO BE CHANGED TO A NUMBER NMX,
  THEN THE DECLARATIONS IN DRIVEB SHOULD READ AS
  AS FOLLOWS:
  COMMON /GEAR2/ YMAX(NMX)
  COMMON /GEAR3/ ERROR(NMX)
  COMMON /GEAR4/ SAVE1(NMX)
  -----

```

```

C ----- COMMON /GEAR5/ SAVE2(NMX)
C ----- COMMON /GEAR7/ IPIV(NMX)
C -----
C ----- DIMENSION Y(NMX,13)
C ----- THE DIMENSION IN COMMON BLOCK GEAR6 IS CURRENTLY
C ----- SET TO 3100 = (2 ML + MU + 1) * N , IF THIS NUMBER
C ----- IS TO BE CHANGED TO A NUMBER NMX, THEN THIS
C ----- DECLARATION SHOULD READ:
C ----- COMMON /GEAR6/ PW(NMX)
C -----
C ----- IF (INDEX.CL.D) GO TO 135
C ----- WRITE(6,130) INDEX
130 FORMAT(/26H ERROR RETURN WITH INDEX =,I3//)
C ----- GO TO 160
C -----
C ----- SORT Y0 -----
C ----- THE VECTOR Z0 CONTAINS THE CONCENTRATIONS OF SUBSTITU-
C ----- TIONAL BORON, POS. VACANCIES, BV-PAIRS AND TOTAL BORON.
135 DO 140 I = 1,33
      Z0(4*I-3) = Y0(3*I-2)
      Z0(4*I-2) = Y0(3*I-1)
      Z0(4*I-1) = Y0(3*I)
      Z0(4*I) = Z0(4*I-3) + Z0(4*I-1)
      W0(3*I-2) = Z0(4*I-1)/Z0(4*I)
      FVAL = FVAL + ((SINS(I)-Z0(4*I))/1.D+18)**2
      DOSEB = DOSEB + Z0(4*I-3) * XINC
140 DOSE = DOSE + Z0(4*I) * XINC
      ACTIV = (DOSEB/DOSE) * 100.D+00
C ----- THE VECTOR W0 CONTAINS AUXILIARY RESULTS. THE USER MAY
C ----- WISH TO MODIFY OR DELETE THEM.
      DO 142 I = 2,32
        W0(3*I-1) = ( W0(3*I+1) - W0(3*I-5) ) * Z0(4*I)
142 W0(3*I) = W0(3*I-2) * ( Z0(4*I+4) - Z0(4*I-4) )
      W0(2) = 0.D+00
      W0(3) = 0.D+00
      W0(98) = 0.D+00

```

```

W0(99) = 0.D+00
WRITE(6,145) DOSE, LOSEB, ACTIV, FVAL
145 FORMAT(5X,8H DOSE = ,1PD14.7,3X,14HBORON SUBS. = ,1PD14.7,
1 5X,14H % ACTIVITY = ,1PD10.3/
2 5X,8H FVAL = ,1PD23.16//)

C OUTPUT THE RESULT OF THE INTEGRATION
C----- THE OUTPUT LIST THE CONCENTRATIONS OF BORON, POSITIVE VACANCY
C----- BORON-VACANCY PAIR AND TOTAL BORON IN EACH PARTITION IN SPACE
C----- IN INCREASING ORDER FROM LEFT TO RIGHT .
WRITE(6,150) TOUT,XINC, DEPTH, (Z0(I), I = 1,132)
150 FORMAT(5X,8H TIME = ,1PD10.3,4H SEC,10X,13H INCREMENT = ,1PD10.3,
1 3H CH,10X,9H DEPTH = ,1PD12.3,3H CM//
2 3(3X,5HBORON,3X,7HVACANCY,3X,7HBV PAIR,3X,7HB TOTAL,4X)//
3 11(1P4D10.3,1X,1P4D10.3,1X,1P4D10.3)//)

WRITE(6,153) ( W0(I), I = 1,99)
153 FORMAT (3(3X,5H XI ,3X,7H SMALL ,3X,7H BIG )//
1 11(1P3D10.3,1X,1P3D10.3,1X,1P3D10.3)//)

GO TO 105
160 WRITE(6,170) NSTEP,NFE,NJE
170 FORMAT(//21H PROBLEM COMPLETED IN,15,6H STEPS/
1 21X,15,14H F EVALUATIONS/
2 21X,15,14H J EVALUATIONS//)

180 STOP
END

SUBROUTINE DIFFUN (M,T,Y,YDOT,K)
C USER SUPPLIED SUBROUTINE FOR GEAR B. K(1),K(2),K(3) ARE
C SCALED DIFFUSION COEFFICIENTS. K(5) IS THE 1/VAC.LIFETIME
C K(6)= 1/TIME CONSTANT, AND K(4) IS THE EQUILIBRIUM CONSTANT
C DIVIDED BY THE TIME CONSTANT. K(7) IS THE TEMPERATURE IN
C DEGRES CELCIUS AND K(8) IS THE TIME CONSTANT ASSOCIATED
C WITH THE RELEASE OF VACANCIES FROM THE DAMAGE REGION.
DOUBLE PRECISION T,Y,YDOT,K(1),DMG(33),TC,CA(33),CD(33),
1 ECI,EC(33),EF(33),CVEQ(33),DELVAC(33)
INTEGER N
DIMENSION Y(N),YDOT(N)

```

```

C----- DMG IS THE VACANCY CONCENTRATION PROFILE CALCULATED FROM
C-- THE DISTRIBUTION OF ENERGY DEPOSITED INTO ATOMIC PROCESSES.
C-- D.K.BRICE, PROC. OF THE 5TH INT.CONF. ON ION IMPL.,THOUSAND
C-- OAKS, CA. GORDON AND BREACH PUBLISHERS.
C-- THIS DISTRIBUTION CORRESPONDS TO A 10**15 DOSE, 70 KEV
C-- BORON IMPLANT.
DATA DMG/2.45D21,2.65D21,2.93D21,3.35D21,3.9D21,4.6D21,
1 5.6D21,6.3D21,6.2D21,5.4D21,4.5D21,3.55D21,
2 2.5D21,1.48D21,8.D20,4.5D20,2.3D20,1.D20,
3 4.9D19,2.3D19,1.12D19,5.4D18,2.5D18,1.2D18,
4 6.D17,2.9D17,1.4D17,6.7D16,3.1D16,1.4D16,
5 6.D15,3.D15,1.5D15/,CL/33*W.D+W0/
M = 33
C----- TC IS THE TEMPERATURE OF THE ANNEAL OR DIFFUSION IN DEG.C.
TC = K(7)
DO 5 I = 1,33
5 CA(I) = Y(3*I-2)
CALL SILS(M,TC,CA,CL,ECI,EC,EF,CVEQ,DELVAC)
C-----
YDOT(1) = -2.D0*K(1)*Y(1) + K(1)*Y(4) * 1.85D+00
1 - A(4)*Y(1)*Y(2) +Y(3)*K(6)
YDOT(2) = (-2.D0*K(2))*Y(2)+K(2)*Y(5)+K(2)*CVEQ(33)
1 -A(4)*Y(1)*Y(2)+Y(3)*K(6)
2 -K(5)* (Y(2)- CVEQ(1))
4 +DEXP(-T/K(8)) * DMG(1) / K(6)
YDOT(3) = -(2.D0*K(3)+K(6))*Y(3)+1.85D+00*K(3)*Y(6)+K(4)*Y(1)*Y(2)
DO 10 I= 1, 31
YDOT(3*I+1) = K(1)*Y(3*I-2)-2.D0*K(1)*Y(3*I+1)+K(1)*Y(3*I+4)
2 -K(4)*Y(3*I+1)*Y(3*I+2)+Y(3*I+3)*K(6)
YDOT(3*I+2) = K(2)*Y(3*I-1)-(2.D0*K(2))*Y(3*I+2)
1 +K(2) *Y(3*I+5) -K(4)*Y(3*I+1)*Y(3*I+2)+Y(3*I+3)*K(6)
2 -K(5) * ( Y(3*I+2) - CVEQ(I+1) )
4 +DEXP(-T/K(8)) * DMG(I+1) / K(8)
YDOT(3*I+3) = K(3)*Y(3*I)-(2.D0*K(3)+K(6))*Y(3*I+3)
1 + K(3)*Y(3*I+6) +K(4)*Y(3*I+1)*Y(3*I+2)

```

```

10 CONTINUE
YDOT(97) = K(1)*Y(94) - 2.D0*K(1)*Y(97) + K(1) * 5.D+16
1   -K(4)*Y(97)*Y(98)+Y(99)*K(6)
YDOT(98) = K(2)*Y(95) - (2.D0*K(2))*Y(98)+K(2)*CVEQ(33)
1   -K(4)*Y(97)*Y(98)+Y(99)*K(6)
2   -K(5) * ( Y(96) - CVEQ(33) )
4   +DEXP(-T/K(8)) * DMG(33) / K(8)
YDOT(99) = K(3)*Y(96) - (2.D0*K(3)+K(6))*Y(99) +K(3)*5.D+14
1   +K(4)*Y(97)*Y(98)
RETURN
END
SUBROUTINE PDB(N,T,Y,PD,N0,ML,MU,K)
C-----
C USER SUPPLIED SUBROUTINE FOR GEARB-ANALYTICAL JACOBIAN
C K(1),K(2),K(3),ARE SCALED DIFFUSION COEFFICIENTS.K(5) IS THE
C INVERSE OF THE VACANCY LIFETIME. K(6) IS THE INVERSE OF THE
C REACTION TIME CONSTANT. K(4) IS THE EQUILIBRIUM CONSTANT DIVIDED
C BY THE REACTION TIME CONSTANT. K(7) IS THE TEMPERATURE IN DEG.
C CELCIUS. K(8) IS THE TIME CONSTANT ASSOCIATED WITH THE RELEASE
C OF VACANCIES FROM THE DAMAGE REGION.
C-----
DOUBLE PRECISION T, Y, PL, K(1),TC,CA(33),CD(33),
1   ECI,EC(33),EF(33),CVEQ(33),DELVAC(33)
INTEGER N, N0,ML,MU
DIMENSION Y(N),PD(N0,7)
M = 33
C----- TC IS THE TEMPERATURE OF THE ANNEAL OR DIFFUSION IN DEG.C.
TC = K(7)
DO 5 I = 1,33
CA(I) = Y(3*I-2)
CALL SILS(M,TC,CA,CD,ECI,EC,EF,CVEQ,DELVAC)
DO 10 I = 1, 97, 3
PD(I,1) = K(1)
PD(I,2) = 0
PD(I,3) = 0
5

```

```

PD(I,4) = -2.D0*K(1)-K(4)*Y(I+1)
PD(I,5) = -K(4)*Y(I)
PD(I,6) = K(6)
PD(I,7) = K(1)

C THE ELEMENTS ABOVE WERE FOR THE FIRST SPECIE (BORON)

PD(I+1,1) = K(2)
PD(I+1,2) = 0
PD(I+1,3) = -K(4)*Y(I+1) -K(5)*DELVAC((I+2)/3)
PD(I+1,4) = -2.D0*K(2)-K(4)*Y(I)-K(5)
PD(I+1,5) = K(6)
PD(I+1,6) = 0
PD(I+1,7) = K(2)

C THE ELEMENTS ABOVE ARE FOR THE SECOND SPECIE (VACANCY)

PD(I+2,1) = K(3)
PD(I+2,2) = K(4)*Y(I+1)
PD(I+2,3) = K(4)*Y(I)
PD(I+2,4) = -2.D0*K(3)-K(6)
PD(I+2,5) = 0
PD(I+2,6) = 0
PD(I+2,7) = K(3)

C THE ELEMENTS ABOVE WERE FOR THE THIRD SPECIE (BV-PAIR)
10 CONTINUE
PD(1,7) = 1.85D+00 * K(1)
PD(2,7) = 1.D+00 * K(2)
PD(3,7) = 1.85D+00 * K(3)
RETURN
C RECALL THAT THE UNUSED LOCATIONS IN PD, GIVEN BY
C I - ML <= J <= 0 AND N < J <= I+MU, CAN BE FILLED
C ARBITRARILY. THIS SUBROUTINE IS TO BE USED WITH
C MITER = 1.
END
SUBROUTINE SILS(N,TC,CA,CD,ECI,EC,LF,CVEQ,DELVAC)
C-----THIS SUBROUTINE IS FOR SILICON, INPUT PARAMETERS ARE:
C-----N ----- # OF POINTS
C-----TC ----- TEMP. IN DEG.CELSIUS

```

```

C----- CA ----- ACCEPTOR IMPURITY CONCENTRATION
C----- CD ----- DONOR IMPURITY CONCENTRATION
C----- OUTPUT PARAMETERS ARE:
C----- ECI ----- INTRINSIC CARRIER CONC,
C----- EC ----- MAJORITY CARRIER CONC,
C----- EF ----- FERMİ LEVEL IN E.V. FROM THE
C----- MAJORITY BAND EDGE.
C----- CVEQ IS THE EQUILIBRIUM CONC OF SINGLY CHARGED VAC.
C----- DELVEQ IS THE PARTIAL DERIVATIVE OF CVEQ RESPECT TO THE
C----- IMPURITY CONCENTRATION
C----- IMPLICIT REAL*8(A-H,O-Z)
C----- DIMENSION CA(N),CD(N),EC(N),EF(N),CVEQ(N),DELVEQ(N)
C----- 'ED' AND 'EA' ARE THE ENERGY LEVELS OF DONORS AND ACCEPTORS
C----- ED = 0.046D+00
C----- EA = 0.045D+00
C----- TK IS THE TEMPERATURE IN DEGREES KELVIN.
C----- TK = TC + 2.7316D+02
C----- QVEQ IS THE ACTIVATION ENERGY OF FORMATION OF VACANCIES
C----- QVEQ = 3.4D+00
C----- PEX IS THE PRE-EXPONENTIAL FACTOR OF THE FORMATION OF VAC.
C----- PEX = 5.D+25
C----- THE FOLLOWING ARE THE ENERGY LEVELS OF THE SINGLY CHARGED
C----- VACANCIES IN THE BAND-GAP REFERRED TO THE RESPECTIVE BAND-
C----- EDGES. P AND N STAND FOR POSITIVE AND NEGATIVE CHARGE-STATES.
C----- EVP = 3.557D-01
C----- EVN = 5.557D-01
C----- ECI, FROM MORIN & MAITA
C----- ECI = 3.88D+16 * (TK ** 1.5D+00) * DEXP(-6.05D-01/(8.62D-05*TK))
C----- DO 10 I=1,N
C----- IF (CA(I).GE.CD(I)) GO TO 5
C----- PARAMETERS FOR N-TYPE
C----- EV = EVN
C----- DSC = 5.421978D+15 * ( TK**1.5D+00)
C----- ECT = 2.D+00 * DSC * (CD(I)-CA(I)) / ( DSC+2.7D-01
C----- * (CD(I)-CA(I)) + 5.D-01 *CA(I) *DEXP(ED/(8.62D-05
1

```

```

2      *TK)) + DSQRT((DSC - 2.7D-01 * (CD(I)-CA(I)) +
3      5.D-01 * CA(I) * DEXP( ED/ (8.62D-05 * TK))) **2.D+00
4      + 4.D+00 * 5.D-01 * (DSC-2.7D-01*CA(I)) * (CD(I)-CA(I))
5      * DEXP(ED/(8.62D-05*TK))))
      IF (CA(I).LE.CD(I)) GO TO 9
C----- PARAMETERS FOR P-TYPE
5      EV = EVP
      DSC = 2.0163964D+15 * (TK ** 1.5D+00)
      ECT = 2.D+00 * DSC * (CA(I)-CD(I)) / ( DSC+2.7D-01
1      * (CA(I)-CD(I)) + 2.D+00 * CD(I) * DEXP(EA/(8.62D-05
2      *TK)) + DSQRT((DSC - 2.7D-01 * (CA(I)-CD(I)) +
3      2.D+00 * CD(I) * DEXP( EA/ (8.62D-05 * TK))) **2.D+00
4      + 4.D+00 * 2.D+00 * (DSC-2.7D-01*CD(I)) * (CA(I)-CD(I))
5      * DEXP(EA/(8.62D-05*TK))))
9      EC(I) = ECT/ 2.D+00 + DSQRT( ((ECT)/2.D+00)**2.D+00
1     + (ECI**2.D+00) )
      EF(I) = + 8.62D-05 * TK * DLOG( (DSC/EC(I)) -2.7D-01)
      CVEQ(I) = PEX * DEXP( -QVEQ/ (8.62D-05*TK))
1     * DEXP( (EV-EF(I))/(8.62D-05*TK) )
10    DELVAC(I) = CVEQ(I) * DSC* (1 + ECT/DSQRT(
1     ( ECT/2.D+00)**2.D+00+(ECI**2.D+00)))
2     / ( 2.D+00 * EC(I)*EC(I) * ( DSC/EC(I) - 2.7D-01))
      RETURN
      END

```

#### 4. Four Species Model

```

C-- THIS IS A GENERAL PURPOSE VERSION OF THE FOUR SPECIES DIFFUSION
C-- MODEL. THIS MODEL IS IN ESSENCE THE THREE STREAM DIFFUSION
C-- MODEL EXTENDED TO INCLUDE THE ANOMALIES ASSOCIATED WITH HIGH
C-- DOSE IMPLANTS AND LOW ANNEALING TEMPERATURES. THE NEW SPECIES
C-- IS THE IMMOBILE BORON WHICH IS ELECTRICALLY INACTIVE. THIS
C-- MODEL IS COMPOSED OF A MAIN PROGRAM AND 3 SUBROUTINES: DIFFUN
C-- PDB AND SILS. THE STRUCTURE AND USAGE OF THIS CODE IS COMPLETELY
C-- ANALOGOUS TO THE PRECEEDING EXAMPLE. FOR THIS REASON WE ADVISE
C-- THE USER TO STUDY FIRST THE CODE FOR THE THREE STREAM DIFFUSION
C-- MODEL WHICH IS SIMPLER, AND THEN EXAMINE THIS CODE WHICH IS MORE
C-- COMPLEX BECAUSE OF THE ADDITIONAL INTERACTION TERMS AMONG THE
C-- SPECIES. THE NUMBER OF SPATIAL PARTITIONS IN THIS EXAMPLE IS 30,
C-- AND THERE ARE 4 SPECIES IN EACH PARTITION. CONSEQUENTLY THE NUMBER
C-- OF POINTS IS N=120. IN GEARB THE MAXIMUM NUMBER OF POINTS IS
C-- PRESET TO 100, THEREFORE IT IS NECESSARY TO PERFORM THE MODIFICATIONS
C-- TO GEARB INDICATED IN THE COMMENT CARDS IN THE PRECEEDING EXAMPLE.
C-----DECLARATIONS-----
C      IMPLICIT REAL*8(A-H,O-Z)
C      INTEGER MONTH, DAY, YEAR
C      DOUBLE PRECISION B0(30), V0(30), BV0(30),
C      1 Z0(120), Y0(120), SIMS(30), X(12), PRN(12)
C      COMMON/GEAR9/HUSED, NQUSED, NSTEP, NFE, NJE
C -- THIS IS THE SIMS PROFILE CORRESPONDING TO THE 70KEV BORON IMPLANTED
C -- TO THE DOSE OF 10D14 AND ANNEALED AT 800 C FOR 35MIN. (XINC=2.D-6CM)
C      DATA SIMS/1.2D18, 1.4D18, 1.7D18, 2.1D18, 2.5D18, 2.7D18,
C      1 2.8D18, 3.D18, 3.3D18, 3.9D18, 4.85D18, 5.2D18,
C      2 4.75D18, 4.15D18, 3.55D18, 3.D18, 2.5D18, 2.15D18,
C      3 1.87D18, 1.62D18, 1.43D18, 1.18D18, 9.2D17, 7.6D17,
C      4 6.1D17, 4.9D17, 3.85D17, 3.D17, 2.3D17, 1.7D17/

```

```

C-----INITIALIZATION-----
C -- THE LIST OF SYMBOLS IS GIVEN IN THE PRECEDING EXAMPLE.
XINC= 4.0D-6
N=120
T0=0.000
MF=21
ML=4
MU=4
DEPTH = (30.0D00) * (XINC)
C----- READ DATE OF RUN -----
READ(5,10) MONTH, DAY, YEAR
10 FORMAT(12,1X,12,1X,14)
C--EXAMPLE: START AT COL 1:03 12 1976
C----- LABELS -----
WRITE(6,20) MONTH, DAY, YEAR
20 FORMAT(39H BORON VACANCY PAIR DIFFUSIVE ANNEALING///
1 10X,10H RUN# ,10X,7H DATE : ,12,1X,12,1X,14,
2 10X,20H FOUR SPECIES MODEL ///)
C-----READ INITIAL PROFILES-----
C -- THE INITIAL CONCENTRATION PROFILES ARE IN #/CM**3
C -- IN THIS PARTICULAR EXAMPLE THE INPUT PROFILE REQUESTED IS EITHER
C -- THE AS-IMPLANTED BORON PROFILE OR A DIFFUSED PROFILE TO BE USED AS
C -- THE INITIAL BORON VACANCY PROFILE. IN GENERAL, THE USER MAY WISH
C -- TO INPUT THE INITIAL PROFILES FOR EACH OF THE SPECIES. IF THIS IS
C -- CASE, THE READ STATEMENT NUMBER 25 SHOULD BE MODIFIED.
C---I WILL ALWAYS USE UNIFORM FORMAT D10.3 FOR ALL DOUBLE PRES.
25 READ(5,30) ( B0(I), I = 1,30)
30 FORMAT(3D10.3)
C -- EXAMPLE: START AL COLUMN #1 >+1.000D+00 2.000D+00 3.000D+00
C-----MAKE Y0
35 DOSE = 0.000
DOSEB = 0.0D+00
ACTIV = 0.0D+00
FVAL = 0.0D+00
LO 40 I= 1,30

```

```

Y0(4*I-3) = 0.D+00
Y0(4*I-2)=1.25D+11
C -- THIS IS THE EQUILIBRIUM CONCENTRATION OF POSITIVE VACANCIES IN
C -- INTRINSIC SILICON.
Y0(4*I) = 0.D+00
IF (I.GE.16) GO TO 37
Y0(4*I-1) = B0(2*I-1)
GO TO 40
37 Y0(4*I-1) = 0.D+00
40 DOSE = DOSE + ( Y0(4*I) + Y0(4*I-1) + Y0(4*I-3)) * XINC
WRITE(6,145) DOSE,DOSEB,ACTIV
H0=1.D-13
EPS=1.D-4
INDEX=1
C---ECHO INPUT TO OUTPUT -----Y0-----
WRITE(6,50) (Y0(I),I=1,120)
50 FORMAT(10X,17H INITIAL PROFILES//
2 3(3X,5HBORON,3X,7HVACANCY,3X,7HBV PAIR,3X,7HBPRECIP)//
3 10(1P4D10.3,1X,1P4D10.3,1X,1P4D10.3)//)
C-----READ PARAMETERS-----
60 READ(5,70) (X(I),I = 1,12)
C -- THE PARAMETERS ARE DESCRIBED IN THE FORMAT STATEMENT 80
70 FORMAT( 3D10.3)
C-START AT COL 1 >+4.000D+00 8.000D+00 1.200D+01 NEXT CARD
C--PARAMETERS 'ECHO INPUT PARAMETERS TO OUTPUT'
WRITE(6,80) (X(I),I = 1,12)
80 FORMAT(10X,11H PARAMETERS//
1 5X,23H DIFF.COEF.(BORON) = ,1PD10.3,10H CM**2/SEC/
2 5X,23H DIFF.COEF.(VACANCY) = ,1PD10.3,10H CM**2/SEC/
3 5X,23H DIFF.COEF.(BV PAIR) = ,1PD10.3,10H CM**2/SEC/
4 5X,23H EQUIL.CONS.(B+V=BV) = ,1PD10.3,6H CM**3/
5 5X,23H REACTION TIME CONST = ,1PD10.3,4H SEC/
6 5X,23H VACANCY LIFETIME = ,1PD10.3,4H SEC/
7 5X,23H DAMAGE ANN. TIME CONS=,1PD10.3,4H SEC/
8 5X,23H DISS./B.REL.TIME CONS=,1PD10.3,4H SEC/

```

```

9      5X,23H ANNEAL TEMPERATURE  =,1PD10.3,8H CELSIUS/
1      5X,23H SOLID SOLUBILITY    =,1PD10.3,8H #/CM**3/
2      5X,23H PREC./B.TRAP. TIME CS=,1PD10.3,4H SEC/
3      5X,23H CONC.THRESHLD OF D.D.=,1PD10.3,8H #/CM**3///)

C-PARAMETER NORMALIZATION
DO 90 I = 1,3
90     PRN(I) = X(I) / ( XINC**2)
        PRN(4) = X(4)/X(5)
        PRN(5) = 1/ X(6)
        PRN(6) = 1/ X(5)
        PRN(7) = X(7)
        PRN(8) = 1/X(8)
        PRN(9) = X(9)
        PRN(10) = X(10)
        PRN(11) = 1/X(11)
        PRN(12) = X(12)

C--OUTPUT THE MOLIFIED PARAMETERS USED IN DIFFUN AND PDB
WRITE ( 6,100) (PRN(I),I = 1,12)
100  FORMAT(53H MODIFIED PARAM. OF DIM. 1/SEC USED IN PROGRAM PRN( )//
1      4(1P3D10.3)///)

C ----- READ TIMES -----
C -- EXAMPLE: START AT COLUMN #1 >+1.000D+00 NEXT CARD
C -- THE LAST TIME IS A FLAG:
C      TOUT = 0.000D+00 -----> EXIT
C      TOUT = 1.000D+00 -----> CHANGE PARAMETER SET
C      TOUT = 2.000D+00 -----> CHANGE INITIAL PROFILES
105  READ(5,110) TOUT
110  FORMAT (D10.3)
      IF (TOUT.EQ.0.D00) GO TO 160
      IF (TOUT.EQ.1.D00) GO TO 35
      IF (TOUT.EQ.2.D+00) GO TO 25
      DOSE = 0.D00
      DOSEB = 0.D+00
      FVAL = 0.D+00
      CALL ERRSET(208,256,-1,1)

```

```

C -- RECALL TO MODIFY DRIVES IN GEARB FOR N= 120 (NMN =120).
CALL DRIVEB(N,T0,H0,Y0,TOUT,EPS,MF,INDEX,ML,MU,PRN)
IF (INDEX.GE.0) GO TO 135
WRITE(6,130) INDEX
130 FORMAT(//26H ERROR RETURN WITH INDEX =,I3//)
GO TO 160

C-----SORT Y0 -----
135 DO 140 I = 1,30
C -- THE VECTOR Y0 CONTAINS THE SPECIES CORRESPONDING TO EACH OF
C -- THE 30 PARTITIONS. THE VECTOR Z0 IS AN AUXILIARY VECTOR
C -- CONTAINING THE DRIVING FORCES FOR THE BV-PAIR REACTION, THE
C -- PRECIPITATION, THE TOTAL BORON CONCENTRATION AND THE
C -- DIFFERENCE TO THE SIMS PROFILE. THE USER MAY WISH TO
C -- MODIFY OR DELETE THESE AUXILIARY RESULTS.
      Z0(4*I-3) = Y0(4*I-1) - Y0(4*I-3) * Y0(4*I-2) * X(4)
      Z0(4*I-2) = Y0(4*I-3) + Y0(4*I-1) - X(10)
      Z0(4*I-1) = Y0(4*I-3) + Y0(4*I-1) + Y0(4*I)
      Z0(4*I) = SIMS(I) - Z0(4*I-1)
      FVAL = FVAL + ( (SIMS(I)-Z0(4*I))/1.D+18)**2
      DOSEB = DOSEB + Y0(4*I-3) * XINC
140 DOSE = DOSE + Z0(4*I-1) * XINC
      ACTIV = ( DOSEB/DOSE ) * 100.D+00
      WRITE(6,145) DOSE, DOSEB,ACTIV,FVAL
145 FORMAT(5X,8H DOSE = ,1PD14.7,3X,14HBORON SUBS. = ,1PD14.7,
1      5X,14H % ACTIVITY = ,1PD16.3/
2      5X,8H FVAL = ,1PD23.16//)
C ----- OUTPUT THE RESULTS OF THE INTEGRATION -----
C ----- THE OUTPUT LIST THE CONCENTRATIONS OF BORON, POSITIVE VACANCY,
C ----- BORON-VACANCY PAIR AND IMMOBILE BORON IN EACH PARTITION IN SPACE
C ----- IN INCREASING ORDER FROM LEFT TO RIGHT.
C ----- THE AUXILIARY RESULTS ARE LISTED FOLLOWING THE SAME CRITERION.
      WRITE(6,150) TOUT,XINC, DEPTH, (Y0(I), I = 1,120), (Z0(I), I=1,120)
150 FORMAT(5X,8H TIME = ,1PD10.3,4H SEC,10X,13H INCREMENT = ,1PD10.3,
1      3H CM,10X,9H DEPTH = ,1PD12.3,3H CM//
2      3(3X,5HBORON,3X,7HVACANCY,3X,7HBV PAIR,3X,7HB PREC.,4X)//

```

```

3      16(1P4D10.3,1X,1P4D10.3,1X,1P4D10.3)/
2      3(3X,5HDR.FO,3X,7HPRC.FO,3X,7HB TOTAL,3X,7HB ERROR,4X)//
3      16(1P4D10.3,1X,1P4D10.3,1X,1P4D10.3)/
GO TO 105
160 WRITE(6,170) NSTEP,NFE,NJE
170 FORMAT(//21H PROBLEM COMPLETED IN,15,6H STEPS/
1      21X,15,14H F EVALUATIONS/
2      21X,15,14H J EVALUATIONS///)
180 STOP
END
SUBROUTINE DIFFUN (N,T,Y,YDOT,K)
C USER SUPPLIED SUBROUTINE FOR GEAR B. K(1),K(2),K(3) ARE
C SCALED DIFFUSION COEFFICIENTS. K(5) IS THE 1/VAC.LIFETIME
C K(6)= 1/TIME CONSTANT, AND K(4) IS THE EQUILIBRIUM CONSTANT
C DIVIDED BY THE TIME CONSTANT.
C K(7) IS THE DAMAGE TIME CONSTANT,K(8) IS 1/DISS. OR B.RELEASE TIME
C CONSTANT,K(9) IS THE ANNEALING TEMPERATURE,AND K(10) IS THE
C SOLID SOLUBILITY LIMIT FOR BORON IN SILICON. K(11) IS THE TIME
C CONSTANT ASSOCIATED WITH PRECIPITATION OR THE TRAPPING OF BORON
C BY DISLOCATION DIPOLES. K(12) IS THE THRESHOLD LEVEL FOR THE
C FORMATION OF DISLOCATION DIPOLES.
C DMG IS THE DAMAGE PROFILE USED FOR DISTRIBUTING THE VACANCY
C GENERATION SITES.
IMPLICIT REAL*8(A-H,O-Z)
DOUBLE PRECISION Y(N),YDOT(N),DMG(30),REAC(30),PREC(30),K(1)
1      ,LD(30),CA(30),CD(30),LC(30),EF(30),CVCQ(30),DELVAC(30)
C -- THIS DAMAGE PROFILE CORRESPONDS TO A 70 KEV B IMPLANT, LWD14 DOSE
DATA DMG/2.45D20,2.65D20,2.93D20,3.35D20,3.9D20,4.6D20,
1      5.6D20,6.3D20,6.2D20,5.4D20,4.5D20,3.55D20,
2      2.5D20,1.48D20,8.D19,4.5D19,2.3D19,1.D19,
3      4.9D18,2.3D18,1.12D18,5.4D17,2.5D17,1.2D17,
4      6.D16,2.9D16,1.4D16,6.7D15,3.1D15,1.4D15/,CD/30*0.D+00/
C -- TC IS THE ANNEALING TEMPERATURE IN DEGREES CELSIUS.
M = 30
TC = K(9)

```

```

5      DO 5 I = 1,30
      CA(I) = Y(4*I-3)
      CALL SILS(M,TC,CA,CD,ECI,EC,EF,CVEQ,DELVAC)
C-----
      REAC(1) = K(6)*Y(3) - K(4)*Y(1)*Y(2)
      PREC(1) = -K(8) * Y(4)
      LD(1) = 0.D+00
      IF (Y(3).GT.K(12)) LD(1) = K(11) * (Y(3) - K(12))
      IF (Y(3).GT.K(12)) LD(1) = K(11) * (Y(3)*Y(3) - K(12)*K(12))
C --- THE PRECEDING CARD CORRESPONDS TO AN OPTIONAL SECOND ORDER
C --- KINETIC TERM
      IF (Y(3).GE.K(10)) PREC(1) = K(8) * (Y(3)-K(10))
      YDOT(1) = - K(1)*2.D+00*Y(1) + K(1)*2.D+00*Y(5)
      1 + REAC(1)
      YDOT(2) = -K(2)*2.D+00*Y(2) + K(2)*2.D+00*Y(6)
      1 + REAC(1) + PREC(1) - K(5)*Y(2) - CVEQ(1)
      2 + (2.D-02/K(7)) *DMG(1) *DEXP(-T/K(7))
      YDOT(3) = -K(3)*2.D+00*Y(3) + K(3)*2.D+00*Y(7)
      1 -REAC(1) - PREC(1) -LD(1)
      YDOT(4) = PREC(1) +LD(1)
C-----
      DO 10 I = 8, 116, 4
      REAC(I/4) = K(6)*Y(I-1) - K(4)*Y(I-2)*Y(I-3)
      PREC(I/4) = -K(8) * Y(I)
      LD(I/4) = 0.D+00
      IF (Y(I-1).GT.K(12)) LD(I/4) = K(11) * (Y(I-1)-K(12))
      IF (Y(I-1).GT.K(12)) LD(I/4) = K(11) * (Y(I-1)*Y(I-1)-K(12)*K(12))
C --- THE PRECEDING CARD CORRESPONDS TO AN OPTIONAL SECOND ORDER
C --- KINETIC TERM
      IF (Y(I-1).GE.K(10)) PREC(I/4) = K(8) * (Y(I-1)-K(10))
      YDOT(I-3) = K(1) * ( Y(I-7) - 2.D+00*Y(I-3) + Y(I+1) )
      1 + REAC(I/4)
      YDOT(I-2) = K(2) * ( Y(I-6) - 2.D+00*Y(I-2) + Y(I+2) )
      1 + REAC(I/4) + PREC(I/4)
      2 + (2.D-02/K(7)) *DMG(I/4) *DEXP(-T/K(7))

```

```

3      YDOT(I-1) = K(3) * ( Y(I-2) - CVEQ(I/4) )
1      - K(3) * ( Y(I-5) - 2.D+00*Y(I-1) + Y(I+3) )
10     - REAC(I/4) - PREC(I/4) - LD(I/4)
      YDOT(I) = PREC(I/4) + LD(I/4)
C-----
      REAC(30) = K(6)*Y(119) - K(4)*Y(116)*Y(117)
      PREC(30) = -K(8) * Y(120)
      LD(30) = 0.D+00
      IF (Y(119).GT.K(12)) LD(30) = K(11) * (Y(119)-K(12))
      IF (Y(119).GT.K(12)) LD(30) = K(11) * (Y(119)*Y(119)-K(12)*K(12))
C -- THE PRECEDING CARD CORRESPONDS TO AN OPTIONAL SECOND ORDER
C -- KINETIC TERM
      IF (Y(119).GE.K(10)) PREC(30) = K(8) * (Y(119)-K(10))
      YDOT(117) = K(1) * ( Y(113) - 2.D+00*Y(117) + 1.D+15 )
      + REAC(30)
1      YDOT(118) = K(2) * ( Y(114) - 2.D+00*Y(118) + 1.D+12 )
      + REAC(30) + PREC(30)
1      + (2.D+02/K(7)) *DMG(30) *DEXP(-T/K(7))
2      - K(5) * ( Y(118) - CVEQ(30) )
3      YDOT(119) = K(3) * ( Y(115) - 2.D+00*Y(119) + 5.D+16 )
      - REAC(30) - PREC(30) - LD(30)
1      YDOT(120) = PREC(30) + LD(30)
      RETURN
      END
SUBROUTINE PDB(N,T,Y,PD,N0,ML,MU,K)
IMPLICIT REAL*8(A-H,O-Z)
DOUBLE PRECISION Y(N),PD(N0,9),K(1),LDF,
1      CA(30),CD(30),EC(30),EF(30),CVEQ(30),DELVAC(30)
      M = 30
      TC = K(9)
      DO 5 I = 1,30
      CA(I) = Y(4*I-3)
      CALL SILS(M,TC,CA,CD,ECI,EC,EF,CVEQ,DELVAC)
5
C-----
      DO 10 I = 1, 117, 4

```

```

SEL = 1.D+00
IF (Y(I+3).GE.K(10)) SEL = 0.D+00
LDF = 0.D+00
IF (Y(I+2).GT.K(12)) LDF = 1.D+00
C-----BORON SUBSTITUTIONAL -----
PD(I,1) = K(1)
PD(I,2) = 0.D+00
PD(I,3) = 0.D+00
PD(I,4) = 0.D+00
PD(I,5) = -2.D+00 * K(1) - K(4) * Y(I+1)
PD(I,6) = -K(4) * Y(I)
PD(I,7) = + K(6)
PD(I,8) = 0.D+00
PD(I,9) = K(1)
C-----V A C A N C Y -----
PD(I+1,1) = K(2)
PD(I+1,2) = 0.D+00
PD(I+1,3) = 0.D+00
PD(I+1,4) = -K(4) * Y(I+1) - K(5) * DELVAC((I+3)/4)
PD(I+1,5) = - 2.D+00 * K(2) - K(4) * Y(I) - K(5)
PD(I+1,6) = + K(6) + K(8) * (1.D+00 -SEL)
PD(I+1,7) = - K(8) *SEL
PD(I+1,8) = 0.D+00
PD(I+1,9) = K(2)
C-----BORON - VACANCY - PAIRS -----
PD(I+2,1) = K(3)
PD(I+2,2) = 0.D+00
PD(I+2,3) = + K(4) * Y(I+1)
PD(I+2,4) = + K(4) * Y(I)
PD(I+2,5) = - 2.D+00 * K(3) - K(6) - K(8) * (1.D+00 -SEL)
1
1
C 1
C 1 LDF *2.D+00 *K(11) *Y(I+2)
C --- THE PRECEDING CARD CORRESPONDS TO AN OPTIONAL SECOND ORDER
C --- KINETIC TERM
PD(I+2,6) = + K(8) *SEL

```

```

PD(I+2,7) = 0.D+00
PD(I+2,8) = 0.D+00
PD(I+2,9) = K(3)
C----- BORON IMMOBILE -----
PD(I+3,1) = 0.D+00
PD(I+3,2) = 0.D+00
PD(I+3,3) = 0.D+00
PD(I+3,4) = + K(8) * (1.D+00 -SEL) +LDF *K(11)
PD(I+3,4) = + K(8) * (1.D+00 -SEL) +LDF *2.D+00 *K(11) * Y(I+2)
C --- THE PRECEEDING CARD CORRESPONDS TO AN OPTIONAL SECOND ORDER
C -- KINETIC TERM
PD(I+3,5) = - K(6) *SEL
PD(I+3,6) = 0.D+00
PD(I+3,7) = 0.D+00
PD(I+3,8) = 0.D+00
PD(I+3,9) = 0.D+00
16 C-----
C-----
PD(1,9) = 2.D+00 * K(1)
PD(2,9) = 2.D+00 * K(2)
PD(3,9) = 2.D+00 * K(3)
RETURN
END
SUBROUTINE SILS(N,TC,CA,CD,ECI,EC,EF,CVEQ,DELVEQ)
THIS SUBROUTINE IS FOR SILICON, INPUT PARAMETERS ARE:
C----- N ----- # OF POINTS
C----- TC ----- TEMP. IN DEG.CELSIUS
C----- CA ----- ACCEPTOR IMPURITY CONCENTRATION
C----- CD ----- DONOR IMPURITY CONCENTRATION
C----- OUTPUT PARAMETERS ARE:
C----- ECI ----- INTRINSIC CARRIER CONC,
C----- EC ----- MAJORITY CARRIER CONC,
C----- EF ----- FERMI LEVEL IN E.V. FROM THE
C----- MAJORITY BAND EDGE.
C----- CVEQ IS THE EQUILIBRIUM CONC OF SINGLY CHARGED VAC.
C----- DELVEQ IS THE PARTIAL DERIVATIVE OF CVEQ RESPECT TO THE

```

```

C----- IMPURITY CONCENTRATION
      IMPLICIT REAL*8(A-H,O-Z)
      DIMENSION CA(N),CD(N),EC(N),EF(N),CVEQ(N),DELVAC(N)
C----- 'ED' AND 'EA' ARE THE ENERGY LEVELS OF DONORS AND ACCEPTORS
      ED = 0.046D+00
      EA = 0.045D+00
C-----TK IS THE TEMPERATURE IN DEGREES KELVIN.
      TK = TC + 2.7316D+02
C----- QVEQ IS THE ACTIVATION ENERGY OF FORMATION OF VACANCIES
      QVEQ = 3.4D+00
C----- PEX IS THE PRE-EXPONENTIAL FACTOR OF THE FORMATION OF VAC.
      PEX = 5.D+25
C----- THE FOLLOWING ARE THE ENERGY LEVELS OF THE SINGLY CHARGED
C----- VACANCIES IN THE BAND-GAP REFERRED TO THE RESPECTIVE BAND-
C----- EDGES. P AND N STAND FOR POSITIVE AND NEGATIVE CHARGE-STATES.
      EVP = 3.557D-01
      EVN = 5.557D-01
C-----ECI, FROM MORIN & MAITA
      ECI = 3.88D+16 * (TK ** 1.5D+00) * DEXP(-6.05D-01/(8.62D-05*TK))
      DO 10 I=1,N
      IF (CA(I).GE.CD(I)) GO TO 5
C----- PARAMETERS FOR N-TYPE
      EV = EVN
      LSC = 5.421978D+15 * (TK**1.5D+00)
      ECT = 2.D+00 * DSC * (CD(I)-CA(I)) / (DSC+2.7D-01
1          * (CD(I)-CA(I)) + 5.D-01 * CA(I) * DEXP(ED/(8.62D-05
2          * TK)) + DSQRT((DSC - 2.7D-01 * (CD(I)-CA(I)) +
3          5.D-01 * CA(I) * DEXP(ED/(8.62D-05 * TK))) ** 2.D+00
4          + 4.D+00 * 5.D-01 * (DSC-2.7D-01*CA(I)) * (CD(I)-CA(I))
5          * DEXP(ED/(8.62D-05*TK))))
      IF (CA(I).LE.CD(I)) GO TO 9
C----- PARAMETERS FOR P-TYPE
5      EV = EVP
      DSC = 2.0163964D+15 * (TK ** 1.5D+00)
      ECT = 2.D+00 * DSC * (CA(I)-CD(I)) / (DSC+2.7D-01

```

```

1      * (CA(I)-CD(I)) + 2.D+00 * CD(I) * DEXP(EA/(8.62D-05
2      *TK)) + DSQRT((DSC - 2.7D-01 * (CA(I)-CD(I)) +
3      2.D+00 * CD(I) * DEXP( EA/ (8.62D-05 * TK))) **2.D+00
4      + 4.D+00 * 2.D+00 * (DSC-2.7D-01*CD(I)) * (CA(I)-CD(I))
5      * DEXP(EA/(8.62D-05*TK))))
9      EC(I) = ECT/ 2.D+00 + DSQRT( ((ECT)/2.D+00)**2.D+00
1     + (ECI**2.D+00) )
      EF(I) = + 8.62D-05 * TK * DLOG( (DSC/EC(I)) -2.7D-01)
      CVEQ(I) = PEX * DEXP( -QVEQ/ (8.62D-05*TK))
1     * DEXP( (EV-EF(I))/(8.62D-05*TK) )
10    DELVAC(I) = CVEQ(I) * DSC* (1 + ECT/DSQRT(
1     ( ECT/2.D+00)**2.D+00+(ECI**2.D+00)))
2     / ( 2.D+00 * EC(I)*EC(I) * ( DSC/EC(I) - 2.7D-01))
      RETURN
      END

```

## Appendix B

### CALCULATION OF AN EFFECTIVE DIFFUSION COEFFICIENT

Equations (B1) and (B2) are equations (A1a) and (A1c) in Appendix A rewritten in terms of fluxes,  $J_B$  and  $J_{BV}$ .

$$\frac{dC_B}{dt} = \frac{dJ_B}{dx} + \left( \frac{C_{BV} - k_o C_B C_V}{\tau} \right) \quad (B1)$$

$$\frac{dC_{BV}}{dt} = \frac{dJ_{BV}}{dx} - \left( \frac{C_{BV} - k_o C_B C_V}{\tau} \right) \quad (B2)$$

Addition of Eqs. (B1) and (B2) yields:

$$\frac{d}{dt} (C_B + C_{BV}) = \frac{d}{dx} (J_B + J_{BV}) \quad (B3)$$

Expressing the fluxes in terms of concentration gradients and diffusion coefficients, we obtain Eq. (B4).

$$J_B + J_{BV} = D_B \frac{\partial C_B}{\partial x} + D_{BV} \frac{\partial C_{BV}}{\partial x} \quad (B4)$$

For this equation, we can show that the last term dominates as follows:  $D_{BV}$  is much greater than  $D_B$ , at 900°C; their values are  $7 \times 10^{-14}$  and  $1.6 \times 10^{-21}$  cm<sup>2</sup>/sec, respectively. At the outset of the anneal,  $C_{BV} > C_B$  and  $\partial C_{BV} / \partial x > \partial C_B / \partial x$ , hence we can neglect the first term. As the annealing proceeds, the diffusion of boron will approach ordinary diffusion conditions, namely,

$$\left( \frac{\partial C_{BV} / \partial x}{\partial C_B / \partial x} \right) \sim \frac{C_{BV}}{C_B} \sim 0.02$$

The inequality between gradients has reversed; however, because  $D_{BV}$  is much greater than  $D_B$ , the last term still overwhelms the first one. We can then approximate the total flux as in Eq. (5):

$$J_B + J_{BV} \approx D_{BV} \frac{\partial C_{BV}}{\partial x} \quad (B5)$$

We now let  $\xi$  be the fractional concentration of BV pairs, which is a function of the electrical activity:

$$\xi = \frac{C_{BV}}{C_{BV} + C_B} = 1 - \alpha \quad (B6)$$

Then,

$$C_{BV} = \xi (C_{BV} + C_B) \quad (B7)$$

and the gradient becomes:

$$\frac{\partial C_{BV}}{\partial x} = \frac{\partial \xi}{\partial x} (C_{BV} + C_B) + \xi \frac{\partial (C_{BV} + C_B)}{\partial x} \quad (B8)$$

We can now identify several situations in which the first term in Eq. (B8) is negligible in comparison with the last one. For instance, under equilibrium conditions, we can rewrite Eq. (3) in Section III as:

$$\frac{C_{BV}}{C_B} = k_o C_{V+}$$

Then, substitution of the above equation in the expression for  $1/\xi$  yields

$$\frac{1}{\xi} = 1 + \frac{C_B}{C_{BV}} = 1 + \frac{1}{k_o + C_{V+}}$$

where

$$C_{V+} = C_{V0}(T) \exp \frac{E_{V+} - E_F}{kT}$$

In general, the Fermi level, as a function of the acceptor concentration, will be a function of distance; however, for annealing temperatures

near 900°C and the boron concentration below  $\sim 10^{17}$  atoms/cm<sup>3</sup>, this dependence is very weak, hence  $C_{V+} \sim C_{Vo}$ ,  $\partial \xi / \partial x \sim 0$ , and the first term in Eq. (B8) is negligible. An analogous case arises when the annealing temperature is high, above 1100°C. In this case, the Fermi level is fixed in the middle of the bandgap.

Under nonequilibrium conditions, the comparison of the terms in Eq. (B8) can be performed numerically. For the typical annealing case in Table 3, the results of the calculation show that the approximation in Eq. (B8) is correct under nonequilibrium and equilibrium conditions, failing only under equilibrium conditions when the boron concentration is near and above  $10^{18}$  atoms/cm<sup>3</sup>. In other words, when the boron concentration is high and the Fermi level is a function of distance,  $\partial \xi / \partial x$  may no longer be small.

For cases in which  $d\xi/dx$  may be neglected, we may then simplify Eq. (B8) to

$$\frac{\partial C_{BV}}{\partial x} \approx \xi \frac{\partial (C_{BV} + C_B)}{\partial x} \quad (B9)$$

Substitution of Eq. (B9) in Eq. (B5) and Eq. (B5) in Eq. (B3) then yields

$$\frac{d(C_B + C_{BV})}{dt} = (D_{BV} \cdot \xi) \frac{d^2 (C_{BV} + C_B)}{dx^2} \quad (B10)$$

where  $(D_{BV} \cdot \xi)$  can be identified with the overall diffusion coefficient  $D_{exp}$ . Hence,

$$D_{exp} = D_{BV} \xi = D_{BV} (1 - \alpha) \quad (B11)$$

# REFERENCES

1. J. F. Gibbons, Proc. of the IEEE, 56, 3, March 1968, pp. 295-319; Proc. of the IEEE, 60, 9, Sep 1972, pp. 1062-1096.
2. W. K. Hofker, H. W. Werner, D. P. Oosthoek, and H. A. M. de Grefte, Appl. Phys., 2, Springer-Verlag, 1973, pp. 265-278.
3. E. Tanneu Baum, Solid State Electn., 2, 1961, p. 123.
4. P. A. Iles and B. Leibenhant, Solid State Electn., 5, 1962, p. 331.
5. V. K. Subashiev, A. P. Landsman, and A. A. Kukharskii, Sov. Phys. Solid State, 2, 1961, p. 2406.
6. S. Maekawa and T. Oshida, J. Phys. Soc. Japan, 19, 1964, p. 253.
7. K. H. Nicholas, Solid State Electn., 9, 1966, pp. 35-47.
8. B. L. Crowder, J. F. Ziegler, F. F. Morehead, and G. W. Cole, Proc. of the Third International Conf. on Ion Implantation in Semiconductors and Other Materials, edited by B. L. Crowder, Plenum Press, New York, 1973.
9. J. R. Anderson and J. F. Gibbons, Appl. Phys. Lett., 28, 4, 1976, p. 184.
10. T. J. Parker, J. Appl. Phys., 38, 9, 1967, pp. 3471-3477.
11. G. Fladda, K. Bjorkquist, L. Erikson, and D. Sigurd, Appl. Phys. Lett., 16, 8, Apr 1970.
12. J. R. Anderson and G. Thomas, private communication.
13. P. Baruch, J. Monnier, B. Blancherd, and C. Castaing, Proc. of the Third International Ion Implantation Conf., Yorktown Heights, edited by B. L. Crowder, Plenum Press, New York, 1973.
14. W. K. Hofker, H. W. Werner, D. P. Oosthoek, and N. J. Koeman, Appl. Phys., 4, Springer-Verlag, 1970, pp. 125-133.
15. J. V. Anderson, O. Andreasen, J. A. Davies, and E. Uggerhoj, Proc. of the First International Conf. on Ion Implantation in Semiconductors, Thousand Oaks, Calif., Gordon and Breach Pub., New York, 1970.
16. J. C. North and N. M. Gibson, Appl. Phys. Lett., 16, 3, Feb 1970.
17. R. W. Bicknell and R. M. Allen, Proc. of the First International Conf. on Ion Implantation in Semiconductors, Thousand Oaks, Calif., Gordon and Breach Pub., New York, 1970.

18. T. E. Seidel and A. U. MacRae, Proc. of the First International Conf. on Ion Implantation in Semiconductors, Thousand Oaks, Calif., Gordon and Breach Pub., New York, 1970.
19. To be published, jointly with T. Magee.
20. G. P. Pelous, D. P. Secrosnier, and P. Henoc, Ion Implantation in Semiconductors, edited by S. Namba, Plenum Press, New York, 1975.
21. R. W. Bicknell, Proc. Royal Soc. of London, Series A, 311, 1504, 1969.
22. L. T. Chadderton and F. H. Eisen, First International Conf. on Solid State in Semiconductors, Thousand Oaks, Calif., Gordon and Breach Pub., New York, 1970.
23. A. P. Karatsyuba, Vikurinny, Svrytchdova, T. P. Timashova, and V. V. Yudin, Proc. of the International Conf. at the U. of Reading, Jul 1972, published by Inst. of Physic, London, England.
24. M. Tamura, T. Ikeda, and N. Yoshikio, J. Appl. Phys. 40, 9, 1969.
25. L. J. Chen, K. Skshan, and G. Thomas, Phys. Stat. Solidi (A), 28, 1, 1975, p. 309.
26. E. Livine, J. Washburn, and G. Thomas, J. Appl. Phys., 38, 1, Jan 1967.
27. Seeger and Chick, Phys. Stat. Solidi, 29, 2, 1968, p. 455.
28. R. A. Swalin, J. Appl. Phys., 29, 4, 1958, p. 670.
29. R. B. Fair, J. Electrochem. Soc., 122, 6, Jun 1975.
30. W. Nuyts and Van Overstraeten, Phys. Stat. Solidi (A), 15, 1973, p. 329; 15, 1973, p. 455.
31. Longini and Greene, Phys. Rev., 102, 1956, p. 992.
32. C. Castaing, P. Baruch, J. P. Gailliard, G. Thomas, J. F. Gibbons, and J. R. Anderson, ESSDERC Conf., Grenoble, Sep 1975.
33. S. J. Tan, B. S. Berry, and W. F. J. Frank, Proc. of the International Conf. on Ion Implantation in Semiconductors and Other Materials, Yorktown Heights, Plenum Press, New York, Dec 1972.
34. B. Netange, M. Cherki, and P. Baruch, Appl. Phys. Lett., 20, 9, May 1972.
35. G. D. Watkins, Phys. Rev., 13, 6 Mar 1976.
36. W. Shockley and J. L. Moll, Phys. Rev., 119, 5, 1 Sep 1960.

37. T. E. Seidel and A. U. MacRae, Trans. of Metallurgical Soc. of AIME, 245, Mar 1969, pp. 491-498.
38. D. K. Brice, Proc. of the First International Conf. on Ion Implantation in Semiconductors, Thousand Oaks, Calif., Gordon and Breach Pub., New York, 1970.
39. J. E. Westmoreland, J. W. Meyer, F. H. Eisen, and B. Welch, Appl. Phys. Lett., 15, 9, Nov 1969.
40. J. M. Fairfield and B. J. Masters, J. Appl. Phys., 38, 5, Jul 1967.
41. J. S. Blakemore, Semiconductor Statistics, Mac Millan, New York, 1962.
42. T. Tsuchimoto and T. Tokuyama, Proc. of the First International Conf. on Ion Implantation in Semiconductors, Thousand Oaks, Calif., Gordon and Breach Pub., New York, 1970.
43. G. L. Vick and K. M. Whittle, J. Electrochem. Soc., 116, 8, 1969, p. 1142.
44. L. Csepregi, J. W. Mayer, and T. W. Sigmon, Phys. Lett., 54 A, 2, 25 Aug 1975; Appl. Phys. Lett., 29, 2, 15 Jul 1976; E. F. Kennedy, L. Csepregi, J. W. Meyer, and T. W. Sigmon, Proc. of the Fifth International Conf. on Ion Implantation in Semiconductors, Boulder, Colo., Aug 1976.
45. A. C. Hindmarsh, Report UCID-30059, Lawrence Livermore Lab., University of California, Livermore, Calif., Mar 1975.
46. R. D. Richtmeyer and K. W. Morton, Difference Methods for Initial Value Problems, New York Interscience Publishers, 1967, Chap. 8.

# DISTRIBUTION LIST

<u>No. of Copies</u>		<u>No. of Copies</u>	
2	Defense Documentation Center ATTN: DDC-TCA Cameron Station (Bldg. 5) Alexandria, VA 22314	1	Commander Harry Diamond Laboratories ATTN: Library 2800 Powder Mill Road Adelphi, MD 20783
1	Office of Naval Research Code 427 Arlington, VA 22217	1	Commander U.S. Army Material Development and Readiness Command ATTN: DRCDE-R 5001 Eisenhower Ave. Alexandria, VA 22333
1	Naval Ship Engineering Ctr. ATTN: Code 6157D Prince Georges Center Hyattsville, MD 20782	2	NASA Scientific & Tech. Info Facility ATTN: Acquisition BR (S-AK/DL) P.O. Box 33 College Park, MD 20740
1	Commander Naval Electronics Lab Ctr. ATTN: Library San Diego, CA 92152	2	Advisory Group on Electron Devices 201 Varick Street, 9th Floor New York, NY 10014
1	Commander US Naval Ordnance Lab ATTN: Technical Library White Oak Silver Springs, MD 20910	1	Director Naval Research Laboratory ATTN: Code 2627 Washington, D.C. 20375
1	Rome Development Center ATTN: Documents Library (TILD) Griffiss AFB, NY 13441	1	USA Security Agency ATTN: IARDA Arlington Hall Station Arlington, VA 22212
1	HQ ESD (DRI) L.G. Hanscom Field Bedford, MA 01731	1	Director Defense Communications Agency Technical Library Center Code 205 Washington, D.C. 20305
1	Deputy for Science & Technology Office, Assist. Sec. Army (R & D) Washington, D.C. 20310	1	Director Naval Research Laboratory ATTN: Mr. Eliot Cohen Code 5211 Washington, D.C. 20375
2	Commander US Army Missile Command Redstone Scientific Info Ctr. ATTN: Chief, Documents Section Redstone Arsenal, AL 35809		

No. of  
Copies

1 Commander  
Harry Diamond Laboratories  
ATTN: Mr. Horst W.A. Gerlach  
2800 Powder Mill Road  
Adelphi, MD 20783

1 GIDEP Engineering & Support  
Dept.  
TE Section  
P.O. Box 398  
Norco, CA 91760

1 Institute of Defense Analysis  
Arlington, VA 22209

1 Mr. Jack Kilby  
5924 Royal Lane  
Suite 150  
Dallas, TX 75230

1 Commander  
Harry Diamond Laboratories  
ATTN: Mr. A.J. Baba  
2800 Powder Mill Road  
Adelphi, MD 20783

1 Naval Research Laboratory  
ATTN: Dr. David F. Barbe  
(Code 5260)  
4555 Overlook Ave., S.W.  
Washington, D.C. 20375

1 Commander  
Naval Electronics Laboratory  
Center  
ATTN: Mr. C.E. Holland Jr.  
271 Catalina Blvd.  
San Diego, CA 92152

1 Air Force Avionics Lab  
ATTN: AFAL/DHE  
(Mr. Stanley E. Wagner)  
Wright-Patterson AFB, OH 45433

1 Commander  
Rome Air Development Center  
ATTN: Mr. Joseph E. Brauer  
(RBRM)  
Griffiss AFB, NY 13441

No. of  
Copies

1 Dr. Gerald B. Herzog  
Solid-State Technology Center  
RCA David Sarnoff Research Center  
Princeton, NJ 08540

1 Mr. Harold D. Toombs  
Texas Instruments, Inc.  
P.O. Box 5474; M/S 72  
Dallas, TX 7522

1 Dr. W. Bandy  
NSA  
Operations Bldg. #3  
S-27 Ft. George Meade  
MD 20755

Commander, ERADCOM

2 ATTN: DRSEL-MS-TI  
1 ATTN: DELET-DT  
1 ATTN: DELET-E  
1 ATTN: DELET-M  
1 ATTN: DELET-P  
1 ATTN: DELET-PL-ST  
1 ATTN: DELET-I  
2 ATTN: DELET-I (CPC File)  
1 ATTN: DELET-IT  
1 ATTN: DELET-IC  
1 ATTN: DELET-ID  
1 ATTN: DELET-IR  
1 ATTN: DELET-IG (R. Sproat)  
27 ATTN: DELET-IS  
1 ATTN: DELET-IJ  
1 ATTN: DELET-DD

Fort Monmouth, NJ 07703